

14 Bull-46-pt-5

Bulletin 46
(Part 5 of 5 Parts)

ADA 033 423

6

THE SHOCK AND VIBRATION BULLETIN

Part 5 •
Dynamic Analysis, Modal Test and Analysis •

1

11

AUG 1976

12 253p.

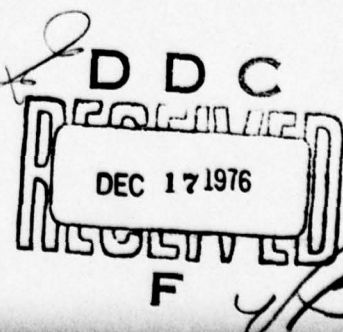
A Publication of
THE SHOCK AND VIBRATION
INFORMATION CENTER
Naval Research Laboratory, Washington, D.C.



Office of
The Director of Defense
Research and Engineering

Approved for public release; distribution unlimited.

Copy available to DDC does not
permit fully legible reproduction



389004

SYMPOSIUM MANAGEMENT

THE SHOCK AND VIBRATION INFORMATION CENTER

Henry C. Pusey, Director
Rudolph H. Volin
J. Gordan Showalter
Barbara Szymanski
Carol Healey

Bulletin Production

Graphic Arts Branch, Technical Information Division,
Naval Research Laboratory

Bulletin 46
(Part 5 of 5 Parts)

THE SHOCK AND VIBRATION BULLETIN

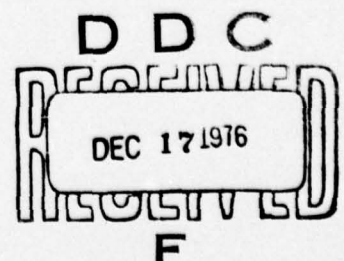
AUGUST 1976

A Publication of
THE SHOCK AND VIBRATION
INFORMATION CENTER
Naval Research Laboratory, Washington, D.C.

The 46th Symposium on Shock and Vibration was held at the Royal Inn at the Wharf, San Diego, California on October 20-23, 1975. The Naval Electronics Laboratory Center and the Naval Undersea Center, San Diego, California were the hosts.

ADDITION for	
NTIS	White Section <input checked="" type="checkbox"/>
DEC	Buff Section <input type="checkbox"/>
UNANNOUNCED	<input type="checkbox"/>
JUSTIFICATION	
BY	
DISTRIBUTION/AVAILABILITY CODES	
Dist.	AVAIL. and/or SPECIAL
A	

Office of
The Director of Defense
Research and Engineering



CONTENTS

PAPERS APPEARING IN PART 5

Dynamic Analysis

<p><i>Partial contents:</i></p> <p>DYNAMIC EARTHQUAKE ANALYSIS OF A BOTTOM SUPPORTED INDUSTRIAL BOILER N. J. Monroe and N. Dasa, The Babcock & Wilcox Company, North Canton, Ohio</p> <p>DYNAMIC RESPONSE OF LAMINATED COMPOSITE SHELLS C. T. Sun, Department of Engineering Science and Mechanics and Engineering Research Institute, Iowa State University, Ames, Iowa</p> <p>SPECTRUM AND RMS LEVELS FOR STRESSES IN CLOSELY SPACED STIFFENED CYLINDRICAL SHELLS, SUBJECTED TO ACOUSTIC EXCITATION G. Maymon, Armament Development Authority, Haifa, Israel</p> <p>ANALYSIS OF SPACE FRAMEWORKS CONTAINING CURVED BEAMS M. A. Cassaro and M. Paz, University of Louisville, Louisville, Kentucky</p> <p>THE VIBRATIONS IN CONSTRUCTION EQUIPMENT P. A. Drakatos, Institute of Technology, University of Patras, Patras, Greece</p> <p>MODEL OF SOIL VIBRATING MACHINE P. A. Drakatos, Institute of Technology, University of Patras, Patras, Greece</p> <p>A GENERAL PURPOSE COMPUTER GRAPHICS DISPLAY SYSTEM FOR FINITE ELEMENT MODES H. N. Christiansen, Brigham Young University, Provo, Utah, University of Utah, Salt Lake City, Utah, B. E. Brown, University of Utah, Salt Lake City, Utah and L. E. McCleary, Naval Undersea Center, San Diego, California</p> <p>VIBRATION CHARACTERISTICS OF 1/8-SCALE DYNAMIC MODELS OF THE SPACE SHUTTLE SOLID ROCKET BOOSTERS S. A. Leadbetter, W. B. Stephens, J. L. Sewall and J. W. Majka, NASA Langley Research Center, Hampton, Virginia and J. R. Barrett, Rockwell International, NASA Langley Research Center, Hampton, Virginia</p> <p>LONGITUDINAL VIBRATION CHARACTERISTICS OF THE SPACE SHUTTLE SOLID ROCKET BOOSTER TEST SEGMENT J. C. Bartlett and D. L. Linton, IBM Federal Systems Division, Huntsville, Alabama</p> <p>MECHANICAL IMPEDANCE TECHNIQUES IN SMALL BOAT DESIGN B. E. Douglas and H. S. Kenchington, David W. Taylor Naval Ship R&D Center, Annapolis Laboratory, Annapolis, Maryland</p> <p>FREQUENCIES AND MODE SHAPES OF GEOMETRICALLY AXISYMMETRIC STRUCTURES: APPLICATION TO A JET ENGINE P. Trompette and M. Lalanne, Institut National des Sciences Appliquées, Villeurbanne, France</p> <p>EIGENSOLUTION SENSITIVITY TO PARAMETRIC MODEL PERTURBATIONS C. W. White and B. D. Maytum, Martin Marietta Corporation, Denver, Colorado</p> <p>MATRIX METHODS FOR THE ANALYSIS OF ELASTICALLY SUPPORTED ISOLATION SYSTEMS G. L. Fox, Barry Division, Barry Wright Corporation, Burbank, California</p> <p>AXISYMMETRIC STRUCTURAL LOADING FOR A TRAVELING OVERPRESSURE PULSE J. J. Farrell, D. J. Ness, and G. M. Teraoka, TRW Defense and Space Systems Group, Redondo Beach, California</p>	<p>1</p> <p>17</p> <p>25</p> <p>37</p> <p>49</p> <p>57</p> <p>61</p> <p>67</p> <p>93</p> <p>107</p> <p>117</p> <p>123</p> <p>135</p> <p>147</p>
---	---

(cont. from p. iii)

Modal Test and Analysis

MODAL LABIA NEW SYSTEM FOR STRUCTURAL DYNAMIC TESTING	153
R. C. Stroud, Lockheed Missiles and Space Company, Sunnyvale, California, S. Smith and G. A. Hamma, Lockheed Missiles and Space Company, Palo Alto, California	
DYNAMIC BEHAVIOR OF COMPLEX STRUCTURES, USING PART EXPERIMENT, PART THEORY	177
J. C. Cromer and M. Lalanne, Institut National des Sciences Appliquees Villeurbanne, France	
THE EXPERIMENTAL DETERMINATION OF VIBRATION PARAMETERS FROM TIME RESPONSES	187
S. R. Ibrahim, NASA Langley Research Center, Hampton, Virginia and E. C. Mikulcik, Department of Mechanical Engineering, The University of Calgary, Calgary, Alberta, Canada	
IDENTIFICATION OF STRUCTURAL MODAL PARAMETERS BY DYNAMIC TESTS AT A SINGLE POINT	197
N. Miramand, J. F. Billaud, F. Leleux, Centre Technique des Industries Mecaniques, SENLIS (FRANCE) and J. P. Kernevez, Universite de Technologie de Compiègne COMPIEGNE (FRANCE)	
EXPERIENCES IN USING MODAL SYNTHESIS WITHIN PROJECT REQUIREMENTS	213
J. A. Garba, B. K. Wada and J. C. Chen, Jet Propulsion Laboratory, Pasadena, California	
VIBRATION ANALYSIS OF THE BSE SPACECRAFT USING MODAL SYNTHESIS AND THE DYNAMIC TRANSFORMATION	231
E. J. Kuhar, General Electric Company, Valley Forge, Pennsylvania	
VIBRATION ANALYSIS OF STRUCTURES USING FIXED-INTERFACE COMPONENT MODES	239
C. Szu, TRW Defense and Space Systems Group, Redondo Beach, California	
AN INTRODUCTION TO THE APPLICATION OF MODAL ANALYSIS SURVEYS IN THE TEST LABORATORY	253
H. Caruso, Westinghouse Electric Corporation, Baltimore, Maryland	

PAPERS APPEARING IN PART 2

KEYNOTE ADDRESS

Rear Admiral Samuel L. Gravely, Jr., Commandant 11th Naval District, San Diego, California

Invited Papers

S AND V IN T AND E

Captain Louis Colbus, USN, Ship Evaluation Division, COMOPTEVFOR, Norfolk, Virginia

REVIEW OF NUCLEAR BLAST AND SHOCK ENVIRONMENT SIMULATION

Dr. Eugene Sevin, Defense Nuclear Agency, Washington, D. C.

METRICATION IN THE NAVY

Mr. John Haas, Chairman, Navy Metrication Group, Naval Ship Engineering
Center, Hyattsville, Maryland

Panel Session

VIBRATION REQUIREMENTS FOR RELIABILITY DEMONSTRATION TESTS

Shock Testing and Analysis

EARTHQUAKE TEST ENVIRONMENT - SIMULATION AND PROCEDURE FOR COMMUNICATIONS
EQUIPMENT

N. J. DeCapua, M. G. Hetman, and S. C. Liu, Bell Telephone Laboratories,
Whippany, New Jersey

AN ALTERNATE APPROACH TO MODAL DAMPING AS APPLIED TO SEISMIC-SENSITIVE EQUIPMENT

L. A. Bergman and A. J. Hannibal, Lord Kinematics, Erie, Pennsylvania

ACTUATOR DEVELOPMENT FOR SYSTEM-LEVEL SHOCK TESTING

G. Richard Burwell, Boeing Aerospace Company, Seattle, Washington

BOUNDED IMPACT A REPEATABLE METHOD FOR PYROTECHNIC SHOCK SIMULATION

R. T. Fandrich, Jr., Harris Electronic Systems Division, Melbourne, Florida

DYNAMIC RESPONSE OF ELECTRICAL CABLES TO SHOCK MOTION

R. W. Doll, TRW Defense and Space Systems Group, Redondo Beach, California

AUTOMATED WHEEL-ON-THE-GROUND DETECTION BY DERAILMENT IMPACT SENSING ANALYSIS AND FULL SCALE TEST RESULTS

W. W. Wassmann and J. H. Armstrong, Naval Surface Weapons Center, White Oak, Silver Spring, Maryland

THE DEVELOPMENT OF A GENERALIZED IMPACT RESPONSE MODEL FOR A BULK CUSHIONING MATERIAL

D. McDaniel, U. S. Army Missile Command, Redstone Arsenal, Alabama and R. M. Wyskida, The University of Alabama in Huntsville, Huntsville, Alabama

BARREL-TAMPED, EXPLOSIVELY PROPELLED PLATES FOR OBLIQUE IMPACT EXPERIMENTS

F. H. Mathews and B. W. Duggin, Sandia Laboratories, Albuquerque, New Mexico

ESTIMATION OF SHIP SHOCK PARAMETERS FOR CONSISTENT DESIGN AND TEST SPECIFICATION

G. C. Hart and T. K. Hasselman, J. H. Wiggins Company, Redondo Beach, California and W. N. Jones, Naval Weapons Center, China Lake, California

PLANE HARMONIC WAVES IN LIQUID OVERLYING A MONOCLINIC, CRYSTALLINE LAYER

S. De, Old Engineering Office, Birbhum, West Bengal (India)

POWER SERIES EXPANSION OF THE DYNAMIC STIFFNESS MATRIX INCLUDING ROTARY INERTIA AND SHEAR DEFORMATION

M. Paz and L. Dung, University of Louisville, Louisville, Kentucky

EFFECT OF PHASE SHIFT ON SHOCK RESPONSE

C. T. Morrow, Vought Corporation Advanced Technology Center, Dallas, Texas

Fluid-Structure Topics

DETERMINATION OF DYNAMIC LOADS FROM MISSILE MODEL WIND TUNNEL DATA

P. G. Bolds and D. K. Barrett, Air Force Flight Dynamics Laboratory, Wright-Patterson AFB, Ohio

FEASIBILITY STUDY OF AN ACOUSTIC ENCLOSURE FOR SHUTTLE PAYLOADS

M. Ferrante and C. V. Stahle, General Electric Space Division, Philadelphia, Pennsylvania and F. J. On, NASA Goddard Space Flight Center, Greenbelt, Maryland

EXPERIMENTAL DETERMINATION OF ROCKET MOTOR STRUCTURAL RESPONSE TO INTERNAL ACOUSTIC EXCITATION

F. R. Jensen and L. R. West, Hercules Incorporated, Bacchus Works, Magna, Utah

VISCOELASTIC DAMPING SYSTEM USE AS A REMEDY FOR POGO EFFECT ON THE DIAMANT SATELLITE LAUNCH VEHICLE

M. Poizat and P. Vialatoux, Societe METRAVIB, Ecully - France and P. Cochery and M. Vedrenne, Centre National D'Etudes Spatiales, Evry - France

VIBRATION AND STABILITY OF FLUID-CONVEYING PIPES

H. Lin and S. Chen, Argonne National Laboratory, Argonne, Illinois

EXPERIMENTAL LIQUID/POSITIVE EXPULSION BLADDER DYNAMICS

M. Wohltmann, Martin Marietta Aerospace, Orlando, Florida

PAPERS APPEARING IN PART 3

Acoustic and Vibration Testing

SIMULATING TACTICAL MISSILE FLIGHT VIBRATION WITH PNEUMATIC VIBRATORS
D. G. VandeGriff, W. D. Ayers and J. G. Maloney, General Dynamics Corporation,
Pomona, California

A THREE DIRECTIONAL VIBRATION SYSTEM
F. M. Edgington, Army Missile Test and Evaluation Directorate, White Sands
Missile Range, New Mexico

DUAL SHAKER VIBRATION FACILITY
C. V. Ryden, Pacific Missile Test Center, Point Mugu, California

ANALYSIS OF FATIGUE UNDER RANDOM VIBRATION
R. G. Lambert, General Electric Company, Utica, New York

RANDOM VIBRATION FATIGUE TESTS OF WELDBONDED AND BONDED JOINTS
F. Sandow, Jr., and O. Mauer, Air Force Flight Dynamics Laboratory,
Wright-Patterson AFB, Ohio

FATIGUE PREDICTION FOR STRUCTURES SUBJECTED TO RANDOM VIBRATION
W. J. Kacena and P. J. Jones, Martin Marietta Corporation, Denver, Colorado

**MEAN LIFE EVALUATION FOR A STOCHASTIC LOADING PROGRAMME WITH A FINITE
NUMBER OF STRAIN LEVELS USING MINER'S RULE**
G. Philippin, T. H. Topper and H. H. E. Leipholz, Department of Civil Engineering,
University of Waterloo, Waterloo, Ontario, Canada

THERMO-ACOUSTIC SIMULATION OF CAPTIVE FLIGHT ENVIRONMENT
W. D. Everett, Pacific Missile Test Center, Point Mugu, California

THE EFFECT OF SIGNAL CLIPPING IN RANDOM VIBRATION TESTING
A. G. Ratz, Vibration Instruments Company, Anaheim, California

Impact and Blast

PREDICTION OF STANDOFF DISTANCES TO PREVENT LOSS OF HEARING FROM MUZZLE BLAST
P. S. Westine and J. C. Hokanson, Southwest Research Institute, San Antonio, Texas

**A STUDY OF THE SPACE SHUTTLE SOLID ROCKET BOOSTER NOZZLE WATER IMPACT
RECOVERY LOADS**
E. A. Rawls, Chrysler Corporation - Space Division, New Orleans, Louisiana and D. A. Kross,
NASA, Marshall Space Flight Center, Alabama

**AN EXPERIMENTAL INVESTIGATION OF THE AXIAL FORCES GENERATED BY THE OBLIQUE
WATER ENTRY OF CONES**
J. L. Baldwin, Naval Surface Weapons Center, White Oak, Silver Spring, Maryland

DELAMINATION STUDIES OF IMPACTED COMPOSITE PLATES
C. A. Ross, University of Florida Graduate Engineering Center, Eglin Air Force Base, Florida and
R. L. Sierakowski, Engineering Sciences Department University of Florida, Gainesville, Florida

**SIMULATION OF X-RAY BLOWOFF IMPULSE LOADING ON A REENTRY VEHICLE AFT END USING
LIGHT-INITIATED HIGH EXPLOSIVE**
R. A. Benham, Sandia Laboratories, Albuquerque, New Mexico

AN ARC SOURCE FOR INITIATING LIGHT-SENSITIVE EXPLOSIVES
P. B. Higgins, Sandia Laboratories, Albuquerque, New Mexico

BLAST PRESSURES INSIDE AND OUTSIDE SUPPRESSIVE STRUCTURES
E. D. Esparza, W. E. Baker and G. A. Oldham, Southwest Research Institute,
San Antonio, Texas

DEVELOPMENT OF STRUCTURES FOR INTENSE GROUND MOTION ENVIRONMENTS
T. O. Hunter and G. W. Barr, Sandia Laboratories, Albuquerque, New Mexico

DESIGN STUDY OF AN EXPERIMENTAL BLAST CHAMBER
W. E. Baker and P. A. Cox, Southwest Research Institute, San Antonio, Texas

FRAGMENT VELOCITIES FROM BURSTING CYLINDRICAL AND SPHERICAL PRESSURE VESSELS

R. L. Bessey and J. J. Kulesz, Southwest Research Institute, San Antonio, Texas

DESIGN OF A BLAST LOAD GENERATOR FOR OVERPRESSURE TESTING

P. Lieberman, J. O'Neill, D. Freeman, and A. Gibbs, TRW Defense and Space Systems Group, Redondo Beach, California

DEVELOPMENT OF A SHRAPNEL CONTAINMENT SYSTEM FOR EXPLOSIVE-TO-ELECTRIC TRANSDUCERS

P. H. Prasthofer, Exxon Production Research Company, Houston, Texas

ANALYSIS OF CONCRETE ARCH MAGAZINE USING FINITE ELEMENT TECHNIQUES

J. M. Ferritto, Civil Engineering Laboratory, Naval Construction Battalion Center, Port Hueneme, California

PAPERS APPEARING IN PART 4

Measurements and Criteria Development

BOUNDARY LAYER FLUCTUATING PRESSURE DATA OBTAINED IN A HIGH BACKGROUND NOISE ENVIRONMENT ON A SMALL SCALE WIND TUNNEL MODEL

G. L. Getline, General Dynamics Convair Division, San Diego, California

DYNAMIC MEASUREMENT OF LOW-FREQUENCY COMPONENTS OF TRACK-INDUCED RAILCAR WHEEL ACCELERATIONS

S. A. Macintyre, C. T. Jones and R. E. Scofield, ENSCO, Inc., Springfield, Virginia

DEVELOPMENT AND APPLICATION OF A MINIATURE RECORDER/ANALYZER FOR MEASUREMENT OF THE TRANSPORTATION ENVIRONMENT

M. A. Venetos, Air Force Packaging Evaluation Agency, Wright-Patterson Air Force Base, Ohio and J. J. Lorusso, Bolt, Beranek and Newman, Inc., Cambridge, Massachusetts

ADVANCES IN SHIPPING DAMAGE PREVENTION

H. Caruso and W. Silver II, Westinghouse Electric Corporation, Baltimore, Maryland

COHERENCE METHODS USED TO DEFINE TRANSMISSION PATHS IN AIRBORNE ANTENNA VIBRATION

J. Pearson and R. E. Thaller, Air Force Flight Dynamics Laboratory, Wright-Patterson Air Force Base, Ohio

DEVELOPMENT OF COMPONENT RANDOM VIBRATION REQUIREMENTS CONSIDERING RESPONSE SPECTRA

C. V. Stahle and H. R. Gongloff, General Electric Company, Space Division, Philadelphia, Pennsylvania and W. B. Keegan, NASA-Goddard Space Flight Center, Greenbelt, Maryland

STATISTICAL DETERMINATION OF RANDOM VIBRATION REQUIREMENTS FOR SUBASSEMBLY TESTS

J. M. Medaglia, General Electric Company-Space Division, Philadelphia, Pennsylvania

DEVELOPMENT OF SHIP SHOCK LOADS TEST FOR THE RGM-84A MISSILE (HARPOON)

T. L. Eby, Pacific Missile Test Center, Point Mugu, California

EVALUATION OF THE HARPOON MISSILE AIRCRAFT LAUNCH EJECTION SHOCK ENVIRONMENT

J. A. Zara and J. L. Gubser, McDonnell Douglas Astronautics Corporation, St. Louis, Missouri, A. G. Piersol, Bolt, Beranek and Newman, Canoga Park, California and W. N. Jones, Naval Weapons Center, China Lake, California

Isolation and Damping

THE MEASUREMENT OF DAMPING AND THE DETECTION OF DAMAGES IN STRUCTURES BY THE RANDOM DECREMENT TECHNIQUE

J. C. S. Yang and D. W. Caldwell, Mechanical Engineering Department, University of Maryland, College Park, Maryland

RESPONSE ANALYSIS OF A SYSTEM WITH DISCRETE DAMPERS

G. K. Hobbs, D. J. Kuyper and J. J. Brooks, Santa Barbara Research
Center, Goleta, California

THE APPLICATION OF ELASTOMERIC LEAD-LAG DAMPERS TO HELICOPTER ROTORS

D. P. McGuire, Lord Kinematics, Erie, Pennsylvania

EVALUATION OF ISOLATION MOUNTS IN REDUCING STRUCTUREBORNE NOISE

T. F. Derby, Barry Division, Barry Wright Corporation,
Watertown, Massachusetts

POLYURETHANE FOAM ISOLATORS FOR SHOCK ISOLATED EQUIPMENT FLOORS

W. C. Gustafson, Boeing Aerospace Company, Seattle, Washington

**COMPONENT TESTING OF LIQUID SHOCK ISOLATORS AND ELASTOMERS IN SUPPORT
OF RECENT SHOCK ISOLATION SYSTEM DESIGNS**

J. P. Ashley, Boeing Aerospace Company, Seattle, Washington

ANALYSIS AND TESTING OF FULL SCALE SHOCK ISOLATED EQUIPMENT FLOORS

W. R. Milne, Boeing Aerospace Company, Seattle, Washington

FOCALIZATION OF SEMI-SYMMETRIC SYSTEMS

A. J. Hannibal, Lord Kinematics, Erie, Pennsylvania

**THE USE OF GENERAL PURPOSE COMPUTER PROGRAMS TO DERIVE EQUATIONS
OF MOTION FOR OPTIMAL ISOLATION STUDIES**

W. D. Pilkey, University of Virginia, Charlottesville, Virginia
Y. H. Chen, RCA/Astro-Electronics Division, Princeton, New Jersey,
and A. J. Kalinowski, Naval Underwater Systems Center,
New London, Connecticut

**PARTICULATE SILICONE RUBBER: AN EFFECTIVE, REMOVABLE ENCAPSULANT FOR
ELECTRONIC PACKAGING**

R. R. Palmisano and D. W. Neily, Harry Diamond Laboratories,
Adelphi, Maryland

DYNAMIC ANALYSIS

DYNAMIC EARTHQUAKE ANALYSIS OF A BOTTOM SUPPORTED INDUSTRIAL BOILER

N.J. Monroe and N. Dasa
The Babcock & Wilcox Company
North Canton, Ohio 44720

In this paper a dynamic earthquake analysis of a large bottom supported boiler is presented. The assumptions and modeling techniques necessary to developing the mathematical model are stated and the dynamic response of the structure and the resultant stresses are tabulated. The results of the dynamic analysis are compared to the results of the static earthquake analysis which is presently required by the various nationally accepted building codes. In addition, results are presented of a dynamic analysis of the same boiler using a more detailed mathematical model. The advantages of both models are discussed and recommendations are made based on a completion of the results presented.

INTRODUCTION

Most building codes require that a structure be designed to resist earthquakes. The method of analysis usually specified is based on static analysis procedures. An equation, which is a function of the total weight of the structure, is used to determine the total horizontal earthquake force to be resisted by the supports of the structure. This force is then divided into increments acting along the height of the structure. The method used in distributing the horizontal force results in having more force near the top of the structure. The structure is then analyzed, treating the earthquake loads as constant static forces and without considering the structure's response to the dynamic nature of this earthquake loading. A static method of earthquake analysis was a good practical method to use prior to the development of the high speed computers and the various sophisticated programs capable of analyzing very large and complex structures. A better analysis and design can result by using a dynamic earthquake input at the base of a structure and then determine the earthquake loads resulting from the actual response of a structure to the dynamic load. Using such a method the load distribution becomes a function of the structures flexibility

and it changes if the flexibility of certain members is revised. This type of approach is more realistic and it identifies more adequately the structure's behavior during an earthquake. In addition, the designer develops more confidence in the adequacy of the structure to resist an earthquake when he observes its response and understands its structural behavior when subjected to a dynamic force.

The boiler studied in this paper is shown in Figure 1. The actual structure of boiler is represented in the computer by a mathematical model. The accuracy of the results will depend on the accuracy of the model. However, in large complex structures it is impossible to model all structural details. When time and economics allow, the designer can develop more confidence in the mathematical model by observing the changes in its response when certain key members are modeled differently. This way, he can determine the sensitivity of certain members and how detailed their modeling has to be. For this reason the mathematical model used in this paper is compared to a similar but a more detailed model. The results of the analysis using two models are tabulated and compared. Recommendations are made as

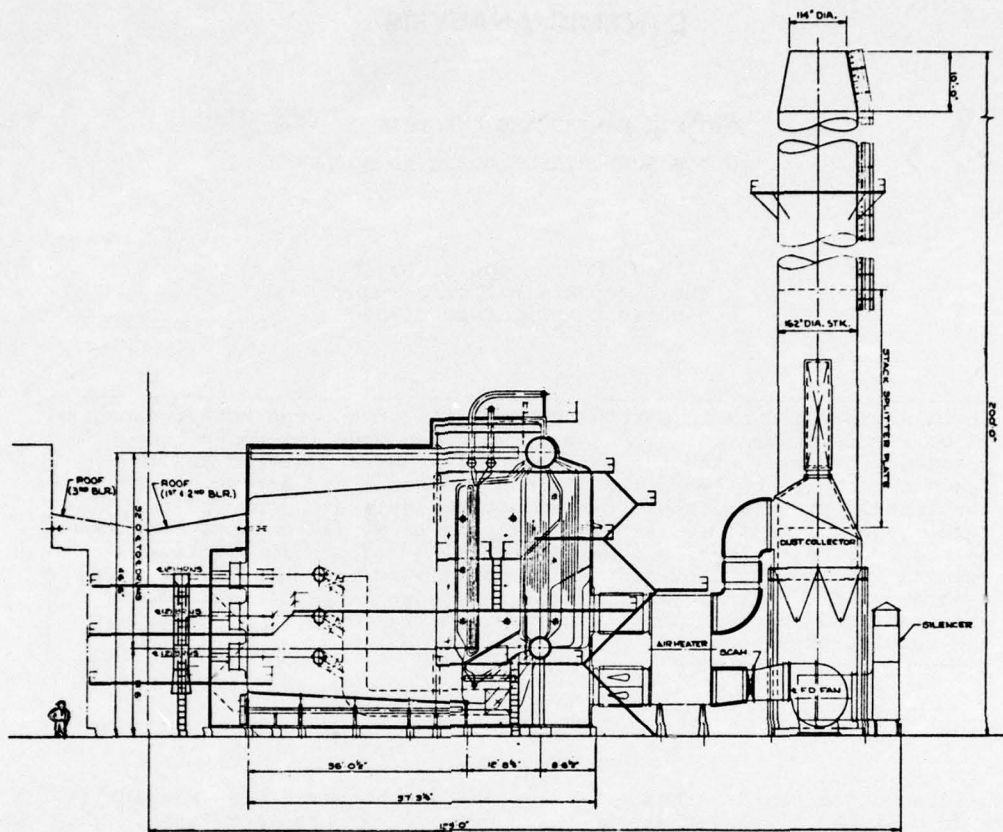


Figure 1 - Typical Arrangement of Boiler and Auxiliary Equipment

to the need for such an effort in designing a structure.

PROCEDURE

In the writer's opinion, the development of the mathematical model is the most important phase to performing a dynamic analysis. Upon the accuracy of the model depend the results of the analysis and how close they represent the actual structure. The computer can do an excellent job in analyzing a model. The designer needs to assure himself that his model truly represents the actual structure. This is easier said than done. Experience coupled with a good understanding of structural dynamics are the best guides.

A boiler is composed of numerous components. It is not possible to include all the components in the mathematical model. In developing the model used in this paper the boiler components were combined and represented as follows:

1. Drums

These are large and thick pressure vessels which are modeled as structural members and are represented by their actual geometric properties.

2. Generating Tubes

There are more than a thousand tubes connecting the upper (steam) drum and the lower (water) drum. Since they are too numerous to individually represent in the model they are combined into equivalent members whose properties represent their total actual flexibility.

3. Superheater Tubes

These tubes, due to their large number, are also represented by equivalent members as is the case with the generating tubes.

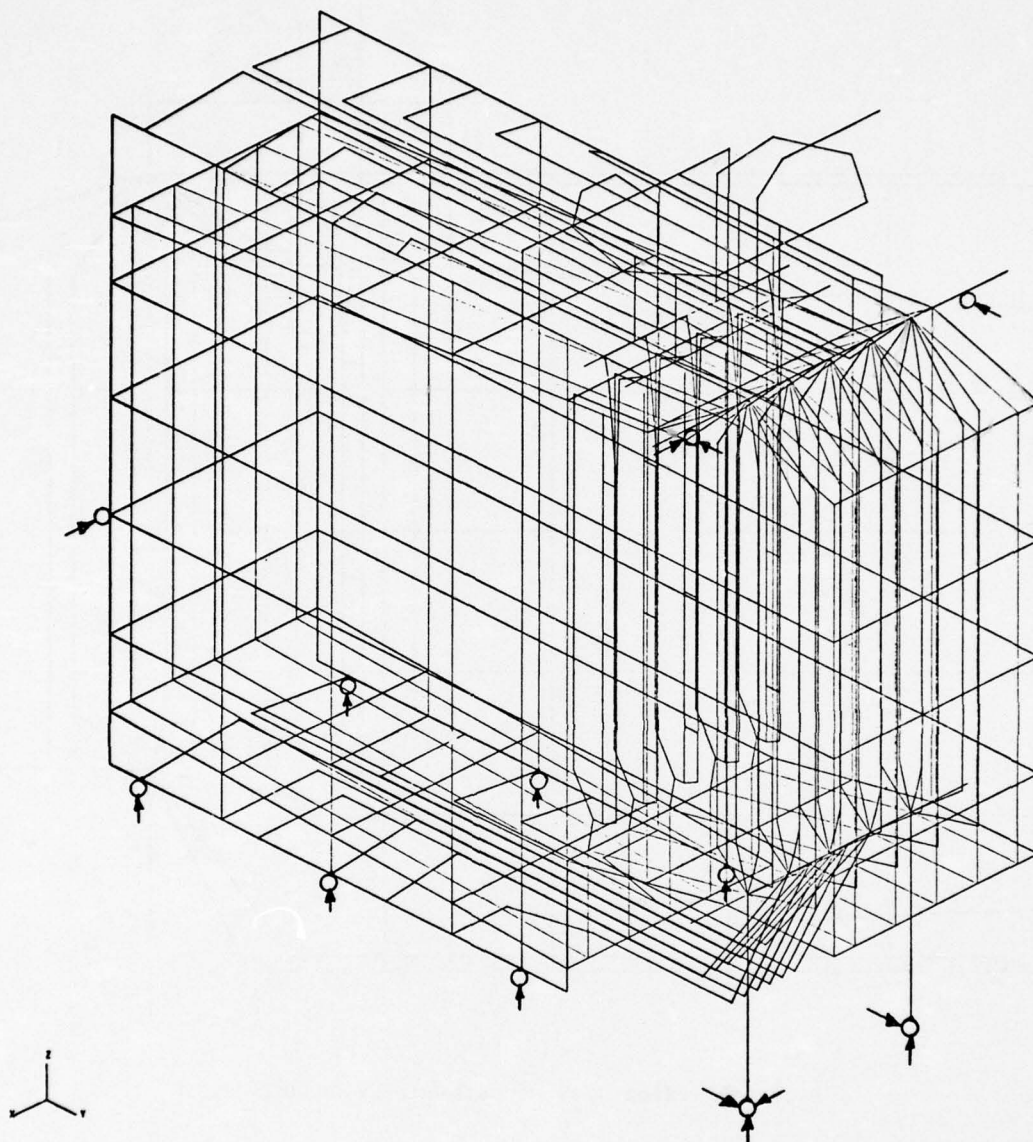


Figure 2 - Mathematical Model of Bottom Supported Boiler 5 Rows of Equivalent Tubes

4. Screen Tubes

These tubes are also modeled using equivalent members.

5. Wall Tubes

These tubes are membraned together. Their properties are best represented modeling them as orthotropic plates.

6. Supports

Careful consideration should be given to modeling the boiler supports to reflect their true behavior during operation. This is necessary since most supports provide resistance in only specific directions while accommodating the thermal expansion of the structure.

7. Pipes and Structural Members

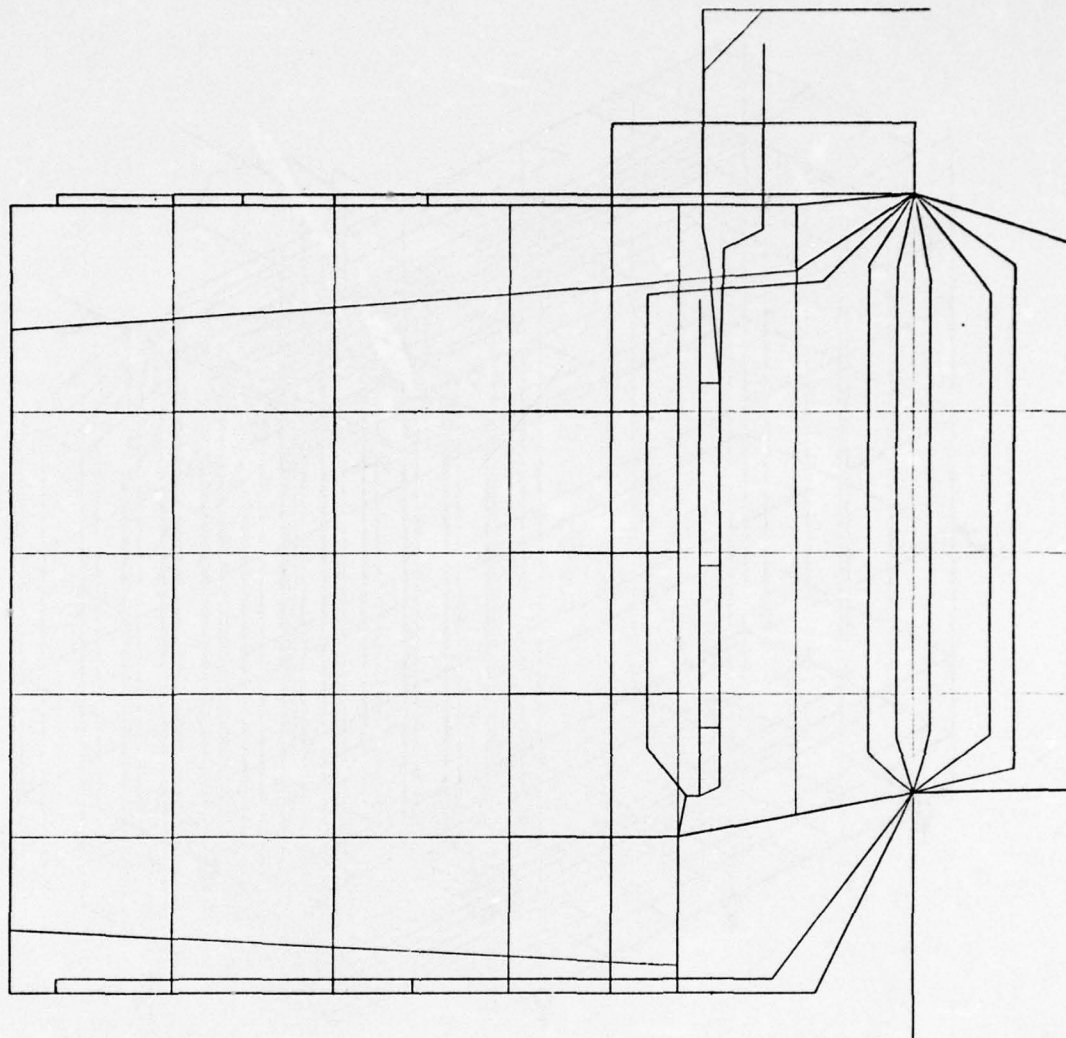


Figure 3 - Side View of Mathematical Model

All these members are modeled using their actual geometry and properties.

Having developed the geometrical configuration and proper ties of all members and establishing their space coordinates, one has fully described the mathematical model to be used in the analysis. The earthquake spectrum required as input is the next step. For the structure analyzed in this paper an input spectrum representing a Zone 2 earthquake with a 2% damping has been used. This response spectrum is typical for a maximum ground motion of 10% of gravity. The

structure is assumed to be supported on bed rock and the soil effects are not considered. The same input has been used in all three directions. The computer program used to analyze the model is titled FESAP. This program is a modified version of the SAP program developed by Dr. E.L. Wilson of the University of California, which has been revised for our Company's own use. The model with five rows has about 700 nodes and 1000 elements. Even though the FESAP program can handle bigger size problems the computer time and resultant expense are the dominant factors in establishing the size of the model. The figures 2 and 3 contain drawings of

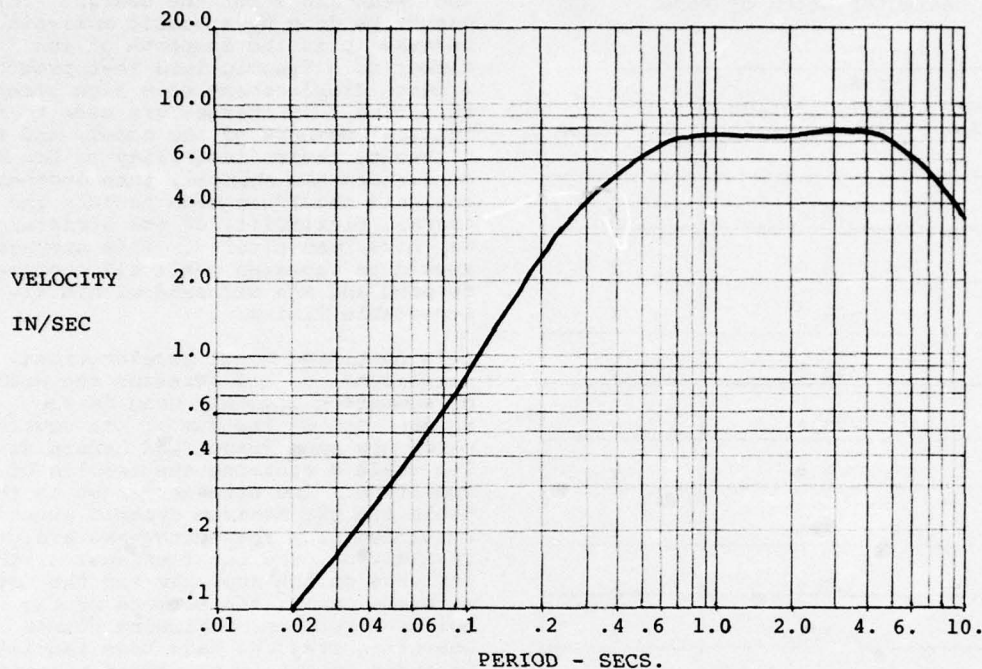


Figure 4 - Earthquake Response Spectrum

mathematical model and figure 4 is a diagram of the earthquake input used in this study.

The work performed may be divided in the following three phases:

1. Dynamic earthquake analysis of a five row of equivalent tube model.

The mathematical model used has lumped the generating, screen and superheater tubes in five rows.

2. Static earthquake analysis of boiler.

The model used is the same as above and a static earthquake input is applied on its members.

3. Dynamic earthquake analysis of a seven row of equivalent tube model.

The mathematical model has been revised to represent the generating screen and superheater tubes by seven rows. The effects of that to the structure's response are reviewed and compared with the original model.

RESULTS

Phase 1

The boiler structure has many components of identical geometry and stiffeners. When analyzed, this results in many closely spaced modal frequencies. As anticipated, the structure's participation in most of these modes is insignificant. Only the dominant modes have large participation factors which results in forces and moments critical to the design of the structure. These are the modes of importance to the designer since they identify the members responding to these modes and the predominant direction of response which is very important in understanding the structure's behavior. Table 1 indicates the predominant frequencies, participation factors and direction of response for the bottom supported boiler being analyzed. The mode shapes corresponding to the three predominant frequencies are indicated on the appendix.

By observing the response of each member and the resulting modal stresses the designer can ascertain what, if any,

TABLE 1

Dynamic Characteristics of Model (5)

Frequency (CPS)	Modal Participation Factor *	Direction
1.6	10.0	X
1.9	5.7	X
2.6	-21.0	X
3.1	-42.8	Y
3.3	-23.4	X
3.7	-8.8	X
4.1	2.6	Y
4.3	-18.9	X
4.8	3.5	Y
5.2	-6.2	Y
5.5	6.2	X
5.6	-8.7	Y
9.9	-6.2	Z
12.5	7.1	Z
13.3	-8.2	X
26.2	-3.0	Z

$$* \text{ M.P.F. }^n = \frac{\sum_1^k M_i \phi_i^n}{\bar{\phi}^{nT} [M] \bar{\phi}^n}$$

Where n = order of mode
 k = number of D.O.F.
 M = generalized mass
 ϕ = mode shape

changes are required to make it earthquake resistant. In other words, he can readily determine which members are the "weak links" of the design. This cannot be done by a static analysis because it is the response of the member to a dynamic load that produces a large displacement or a high stress condition. If changes are made to the critical members of the model, and as a result, their flexibility or boundary conditions are changed, then another analysis should be made because the overall flexibility of the structure may have been altered. This process should be repeated until all components respond and are stressed within the acceptable limits.

In combining modal accelerations, displacements, and stresses the method of summation commonly used is the square root of the sum of the squares which has been identified herein as RSS. The table 2 contains the results of this summation. The stresses shown on this table are the maximum dynamic stresses resulting from the earthquake analysis. In addition, the total effects of the analysis on the supports and the total stresses on all the members of the boiler structure, including normal operating stresses have been tabulated in order to obtain the total stresses of each member. The total stresses obtained using this method are conservative since all maximum stress values are not always at the same location. The results are shown in Table 3 and 4. The allowable stress used is the minimum yield stress for each member. This is an acceptable allowable used in various codes and it appears to be a good practical limitation.

The results of this analysis indicate that this type of boiler can adequately resist an earthquake of a Zone 2 severity. The earthquake spectrum used is one of many established for use in a conventional nuclear installation and in the writer's opinion it is typical for a Zone 2 intensity.

TABLE 2

Results of Dynamic Analysis on Boiler Components
Square Root of the Sum of the Squares - RSS

Component	Acceleration-G			Displacement In. (cm)			Stresses - KSI (MPa)				
	X	Y	Z	X	Y	Z	X Bend	Y Bend	Axial	Max. Princ	Min. Princ
Generating Tubes	2.00	0.89	0.06	2.24 (5.7)	0.70 (1.8)	0.04 (10)	13.7 (94.5)	0.3 (2.1)	0.1 (7)	--	--
Screen Tubes	0.66	0.77	0.14	2.36 (6.0)	0.75 (1.9)	0.82 (2.1)	0.8 (5.5)	16.6 (114.)	0.6 (4.1)	--	--
Roof Tubes	0.09	0.18	0.14	0.84 (2.1)	0.20 (.51)	0.01 (.03)	--	--	--	3.8 (26.2)	0.2 (1.4)
Floor Tubes	0.09	0.20	0.17	0.08 (0.2)	0.20 (.51)	0.20 (.05)	--	--	--	9.3 (64.1)	0.3 (2.1)
Front Wall Tubes	0.01	0.21	0	0.01 (.03)	0.20 (.51)	0	--	--	--	1.1 (7.6)	0.9 (6.2)
Rear Wall Tubes	0.12	0.21	0	0.11 (.28)	0.20 (.51)	0	--	--	--	3.6 (24.8)	0.1 (.7)
Sidewall Tubes	0.37	0.20	0	0.23 (.58)	0.20 (.51)	0	--	--	--	5.2 (35.9)	0.1 (.7)
Superheater Tubes	0.30	0.30	0.30	1.09 (2.8)	0.30 (.67)	0.20 (.05)	7.0 (48.3)	0.4 (2.8)	0.1 (.7)	--	--
Supply Tubes	0.09	0.19	0.14	0.09 (.23)	0.19 (.48)	0.02 (.05)	1.2 (8.3)	0.6 (4.1)	0.1 (.7)	--	--
Riser Tubes	0.10	0.19	0.08	0.07 (.18)	0.20 (.51)	0.01 (.03)	0.6 (4.1)	0.4 (2.8)	0.1 (.7)	--	--
Drum Supports	0.11	0	0	0.10 (.25)	0	0	1.9 (13.1)	4.0 (27.6)	1.0 (6.9)	--	--

Note: Numbers in parenthesis in all tables are in metric units

TABLE 3 Results of Dynamic Analysis on Boiler Supports

Support Points		Accelerations			Displacements In. (cm)			Reactions KIPS (kN)		
		X	Y	X	X	Y	Z	X	Y	Z
Water Drum	Right	0	0	0	0	0	0	22.9 (101.9)	11.0 (48.9)	33.7 (149.9)
	Left	0.11	0	0	0.10 (.25)	0	0	--	6.5 (28.9)	27.3 (121.4)
Steam Drum	Right	0.10	0.19	0	0.10 (.25)	0.20 (.51)	0.002 (.005)	7.3 (32.5)	38.9 (173.0)	--
	Left	0.10	0.19	0	0.10 (.25)	0.20 (.51)	0.002 (.005)	--	38.8 (72.6)	--
Right Side Wall	Rear	0.07	0.20	0	0.06 (.15)	0.20 (.51)	0	--	--	5.3 (23.6)
	Middle	0.06	0.20	0	0.03 (.08)	0.20 (.51)	0	--	--	38.4 (170.8)
	Front	0.04	0.20	0	0.01 (.03)	0.20 (.51)	0	--	--	0.8 (3.6)
Left Side Wall	Rear	0.07	0.20	0	0.06 (.15)	0.20 (.51)	0	--	--	5.3 (23.6)
	Middle	0.08	0.20	0	0.04 (.10)	0.20 (.51)	0	--	--	37.5 (166.8)
	Front	0.05	0.20	0	0.01 (.03)	0.20 (.51)	0	--	--	1.1 (4.8)
Front Wall	Right	0.01	0.20	0	0.01 (.03)	0.20 (.51)	0	15.2 (67.6)	--	--

TABLE 4 Summation of Stresses KSI (MPa)
Design Pressure - 1500 PSI (10.34 MPa)

Component	Pressure (Circ)	Pressure (long)	Earth quake	Dead Load	Total	Allow- able	Material & Temp °F (°C)
Generating Tubes	9.2 (63.4)	4.6 (31.7)	13.7 (94.5)	3.8 (26.2)	22.1 (152.4)	27.7 (191.0)	SA-178C 600 (316)
Screen Tubes	9.2 (63.4)	4.6 (31.7)	16.6 (114.5)	6.3 (43.4)	27.5 (189.6)	27.7 (191.0)	SA-178C 600 (316)
Roof Tubes	10.9 (75.2)	5.5 (37.6)	3.8 (26.2)	1.8 (12.4)	11.1 (76.5)	19.4 (133.8)	SA-178A 600 (316)
Floor Tubes	10.9 (75.2)	5.5 (37.6)	9.3 (64.1)	11.1 (76.5)	25.9 (178.6)	27.7 (191.0)	SA-178C 600 (316)
Front Wall Tubes	10.9 (75.2)	5.5 (37.6)	1.1 (7.6)	3.5 (24.1)	10.1 (69.6)	19.4 (133.8)	SA-178C 600 (316)
Rear Wall Tubes	10.9 (75.2)	5.5 (37.6)	3.6 (24.8)	1.5 (10.3)	10.6 (73.1)	19.4 (133.8)	SA-178A 600 (316)
Sidewall Tubes	10.9 (75.2)	5.5 (37.6)	5.2 (35.8)	7.1 (48.9)	17.8 (122.7)	19.4 (133.8)	SA-178A 600 (316)
Superheater Tubes	8.5 (58.6)	4.3 (29.3)	7.0 (48.3)	7.1 (48.9)	18.4 (126.9)	23.5 (162.0)	SA-210A 900 (482)
Supply Tubes	13.2 (91.0)	6.6 (45.5)	1.3 (9.0)	9.6 (66.2)	17.5 (120.7)	22.4 (154.4)	SA-106A 600 (316)
Riser Tubes	13.2 (91.0)	6.6 (45.5)	0.7 (4.8)	10.3 (71.0)	17.6 (121.3)	22.4 (154.4)	SA-106A 600 (316)
Drum Supports	--	--	4.4 (30.3)	2.3 (15.9)	6.7 (46.2)	32.9 (226.8)	A-36 200 (93)

Phase 2

A static earthquake load of .1g is applied throughout the model in all three directions simultaneously for consistency with the dynamic analysis input. In normal cases the static input will be applied in one direction at a time which will result in considerably lower stresses. The results of the static earthquake analysis have been tabulated and appear on tables 5 and 6. They are compared with the results from the dynamic analysis. One can clearly see that the two types of analysis yield different results. The displacements of the dynamic analysis

are considerably larger than the displacements of the static analysis for the generating and screen tubes. Large differences are also observed in the resultant stresses for several members. In most cases the dynamic analysis yields higher stresses.

TABLE 5 LOADS ON BOILER SUPPORTS - KIPS (kN)

Support Points		Dynamic Analysis			Static Analysis		
		X	Y	Z	X	Y	Z
WATER DRUM	Right	22.9 (101.9)	11.0 (48.9)	33.7 (149.9)	40.6 (180.9)	9.2 (40.9)	26.2 (116.5)
	Left	--	6.5 (29.9)	27.3 (121.4)	--	5.2 (23.1)	22.3 (99.2)
STEAM DRUM	Right	7.3 (32.5)	38.9 (173.0)	--	12.7 (56.5)	35.5 (157.0)	--
	Left	--	38.8 (172.6)	--	--	35.3 (157.0)	--
RIGHT SIDE WALL	Rear	--	--	5.3 (23.6)	--	--	4.6 (20.5)
	Middle	--	--	38.4 (170.8)	--	--	63.7 (293.4)
	Front	--	--	0.8 (3.6)	--	--	0.3 (1.3)
LEFT SIDE WALL	Rear	--	--	5.3 (23.6)	--	--	4.3 (19.1)
	Middle	--	--	37.5 (166.8)	--	--	62.8 (279.3)
	Front	--	--	1.0 (4.9)	--	--	1.1 (4.9)
FRONT WALL	Right	15.2 (67.6)	--	--	25.6 (113.9)	--	--

TABLE 6
COMPARISON OF RESULTS - DYNAMIC AND STATIC ANALYSIS

COMPONENT	DYNAMIC ANALYSIS										STATIC ANALYSIS					
	Displacement In. (cm)			Stresses KSI (MPa)						Displacement In (cm)			Stresses KSI (MPa)			
	X	Y	Z	(X) Bend.	(Y) Bend.	Axial	Max. Princ.	Min. Princ.		X	Y	Z	(X) Bend.	(Y) Bend.	Axial	Max. Princ
Generating Tubes	2.24 (5.7)	.70 (1.8)	.04 (.10)	13.7 (94.5)	0.3 (2.1)	0.1 (.7)	--	--		.33 (.84)	.20 (.51)	.02 (.05)	.87 (6.0)	2.2 (15.2)	0.1 (.7)	--
Screen Tubes	2.36 (6.0)	.75 (1.9)	.08 (.21)	0.8 (5.5)	16.6 (114.)	0.6 (4.1)	--	--		.64 (1.63)	.83 (2.11)	.13 (.33)	2.9 (20.)	12.4 (85.5)	.5 (3.4)	--
Roof Tubes	.08 (.21)	.21 (.51)	.01 (.03)	--	--	--	3.8 (26.2)	0.2 (1.4)		.15 (.38)	.14 (.36)	.008 (.02)	--	--	--	1.5 (10.3)
Floor Tubes	.08 (0.2)	.20 (.51)	.02 (.05)	--	--	--	9.3 (64.1)	0.3 (2.1)		.14 (.36)	.14 (.36)	.025 (.06)	--	--	--	11.7 (80.7)
Front Wall Tubes	.01 (.03)	.20 (.51)	0	--	--	--	1.1 (7.6)	0.9 (6.2)		.008 (.02)	.15 (.38)	0	--	--	--	0.8 (5.5)
Rear Wall Tubes	.11 (.28)	.20 (.51)	0	--	--	--	3.6 (24.8)	0.1 (.7)		.19 (.48)	.15 (.38)	0	--	--	--	2.2 (15.2)
Sidewall Tubes	.23 (.58)	.20 (.51)	0	--	--	--	5.2 (35.9)	0.1 (.7)		.18 (.46)	.14 (.36)	0	--	--	--	2.0 (13.8)
Superheater Tubes	1.09 (2.8)	.30 (.67)	.02 (.05)	7.0 (49.3)	0.4 (2.8)	0.1 (.7)	--	--		.20 (.51)	.32 (.81)	.04 (.10)	9.6 (66.2)	3.9 (26.9)	.5 (3.4)	--
Supply Tubes	.09 (.23)	.19 (.48)	.02 (.05)	1.2 (8.3)	0.6 (4.1)	0.1 (.7)	--	--		.31 (.79)	.17 (.43)	.19 (.48)	1.1 (7.6)	1.2 (8.3)	0.1 (.7)	--
Riser Tubes	.07 (.18)	.20 (.51)	.01 (.03)	0.6 (4.1)	0.4 (2.8)	0.1 (.7)	--	--		.27 (.69)	.14 (.36)	.22 (.56)	1.0 (6.9)	0.9 (6.2)	0.1 (.7)	--

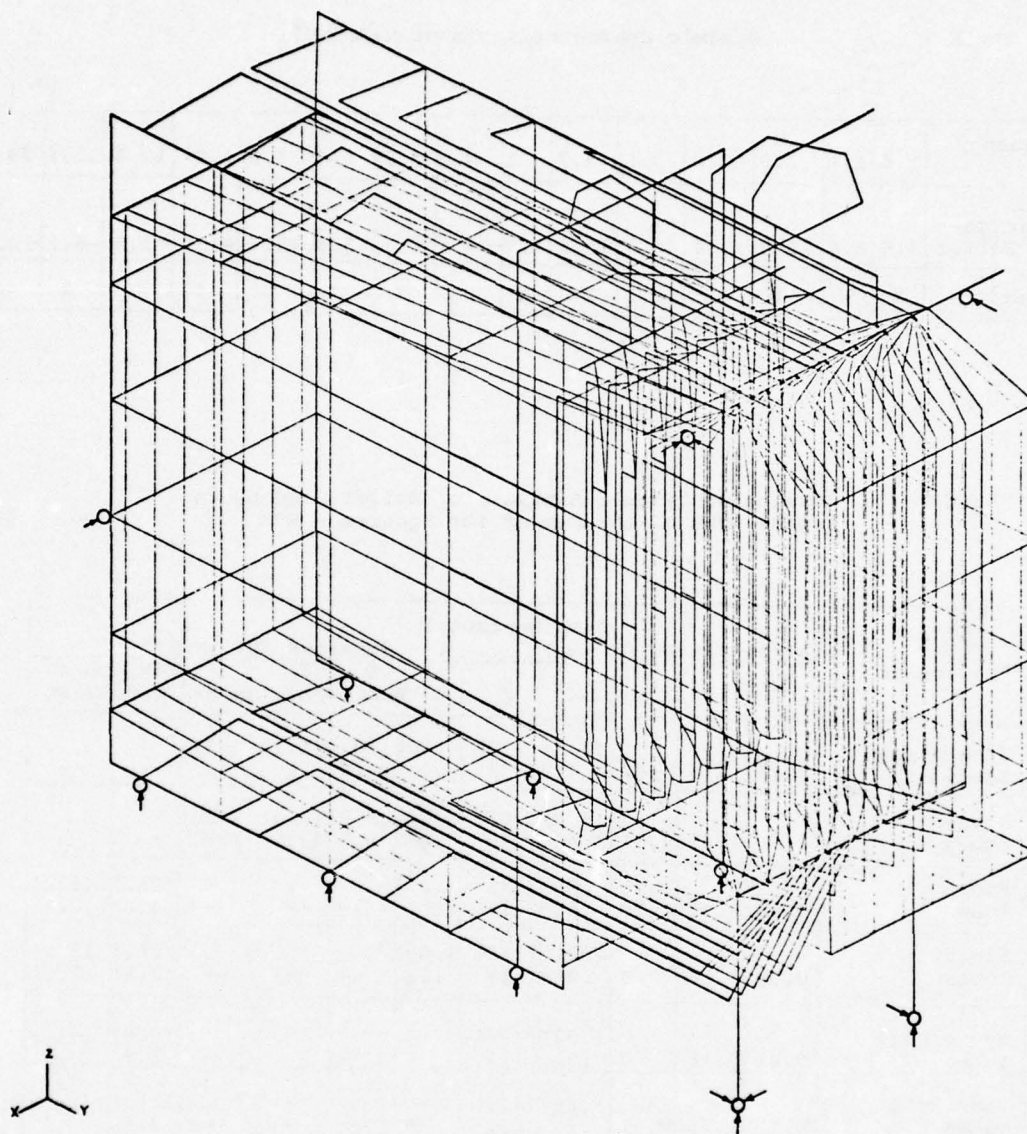


Figure 5 - Mathematical Model of Bottom Supported Boiler
7 Rows of Equivalent Tubes

Phase 3

In order to develop confidence in the modeling techniques used to represent the boiler, the mathematical model was revised by increasing the number of equivalent members representing the boiler tubes. The revised model is shown on figure 5. This model has approximately 200 more joints than the one originally used. The results of a dynamic analysis performed on this

model are tabulated in tables 7, 8 and 9. They are compared to the original model on tables 10 and 11. It can be observed that the two analyses yield very similar results in most areas. However, they differ considerably on the stresses produced on the screen and superheater tubes. These tubes are the most flexible tubes and participate the most at the lower modes. In order to reduce the total stresses on the screen tubes additional internal supports

TABLE 7

Dynamic Characteristics of Model (7)

Frequency CPS	1.6	2.1	2.9	3.3	3.5	3.7	4.1	4.2	5.2	5.5	7.6	9.9	12.4	12.6	29.0
Modal Participa- tion Factor	4.6	8.6	-18.8	26.4	40.3	10.6	4.7	-19.3	-6.8	-5.8	-15.4	6.5	-8.3	-6.1	-10.3
Direction	X	X	X	X	Y	X	Y	X	Y	X	Y	Z	Y	Z	Z

TABLE 8

Results of Dynamic Analysis of Boiler Components
Square Root of the Sum of the Squares - RSS

(7)

Component	Acceleration G			Displacement In (cm)			Stresses KSI (MPa)				
	X	Y	Z	X	Y	Z	X Bend.	Y Bend.	Axial	Max. Princ	Min. Princ
Generating Tubes	2.21	1.46	0.09	(6.1) 2.41	(2.9) 1.14	(.10) .04	(103) 14.9	(1.4) .2	(.7) .1	--	--
Screen Tubes	0.60	1.45	0.35	(6.2) 2.46	(2.8) 1.09	(.24) .09	(9.0) 1.3	(165) 23.9	(20.) 2.8	--	--
Roof Tubes	0.09	0.15	0.19	(.2) .08	(.3) .12	(.03) .01	--	--	--	(21.) 3.0	(6.2) .9
Floor Tubes	0.09	0.16	0	(.2) .08	(.33) .13	(.05) .02	--	--	--	(61.) 9.8	(9.0) 1.3
Front Wall Tubes	0.01	0.16	0	(.03) .01	(.3) .12	0	--	--	--	(9.0) 1.3	(6.2) .9
Rear Wall Tubes	0.12	0.16	0.01	(.28) .11	(.3) .12	0	--	--	--	(18.) 2.6	(.7) .1
Sidewall Tubes	0.40	0.15	0.01	(.61) .24	(.3) .12	0	--	--	--	(31.) 4.5	(.7) .1
Superheater Tubes	0.50	0.87	0.06	(2.6) 1.04	(1.5) .58	(.10) .04	(75.) 10.8	(4.1) .6	(2.8) .4	--	--
Supply Tubes	0.09	0.15	0.17	(.18) .07	(.3) .12	(.03) .01	0.8	(1.4) .2	(.7) 0.1	--	--
Riser Tubes	0.15	0.15	0.10	(.23) .09	(.3) .12	(.05) .02	0.8	(2.8) .4	(.7) 0.1	--	--
Drum Supports	0.1	--	--	(.25) 0.10	0	0	(8.3) 1.2	(27.) 3.9	(1.4) .2	--	--

TABLE 9 Results of Dynamic Analysis on Boiler Supports

Support Points		Accelerations G			Displacements In (cm)			Reactions KIPS (kN)		
		X	Y	Z	X	Y	Z	X	Y	Z
Water Drum	Right	0	0	0	0	0	0	(99.) 22.0	(30.) 6.6	(130) 29.2
	Left	0.11	0	0	(.25) 0.10	0	0	--	(18.) 4.1	(104) 23.3
Steam Drum	Right	0.11	0.15	0.1	(.25) 0.10	(.31) 0.12	(.005) 0.002	(32.) 7.2	(133) 30.0	--
	Left	0.11	0.15	0.1	(.25) 0.10	(.31) 0.12	(.005) 0.002	--	(133) 30.0	--
Right Side Wall	Rear	0.07	0.15	0	(.15) 0.06	(.31) 0.12	0	--	--	(13.) 2.9
	Middle	0.08	0.15	0	(.08) 0.03	(.31) 0.12	0	--	--	(162) 36.5
	Front	0.05	0.15	0	(.03) 0.01	(.31) 0.12	0	--	--	(2.2) 0.5
Left Side Wall	Rear	0.07	0.15	0	(.15) 0.06	(.31) 0.12	0	--	--	(14.) 3.1
	Middle	0.09	0.15	0	(.10) 0.04	(.31) 0.12	0	--	--	(152) 34.2
	Front	0.06	0.15	0	(.03) 0.01	(.31) 0.12	0	--	--	(3.6) 0.8
Front Wall	Right	0.01	0.15	0	(.03) 0.01	(.31) 0.12	0	(72.) 16.1	--	--

Phase 3 Continued.

will be installed tying them to the roof tubes. For the rest of the boiler components, plus the support end reactions, the original results are considered adequate.

COMMENTS & RECOMMENDATIONS

The effect of this type of earthquake input on the boiler structure was relatively moderate. The reason for this is the fact that most of the important components, generating tubes, screen tubes and superheater tubes, are very flexible. This reduces the shock input into the structure during an earthquake. Therefore, even though numerous modes were considered, the resultant total stresses were not very high.

In comparing a static earthquake analysis with a dynamic earthquake analysis the results of the support end reactions vary considerably. The stresses on most boiler components are similar except for the most flexible members for which the dynamic analysis yields much higher stresses. It should be remembered that the static analysis used was more conservative than the one normally specified since the loads were applied in all three directions simultaneously. It is the writer's opinion that a dynamic analysis procedure should be used in designing most structures and especially those of high human occupancy and of critical nature. In a dynamic analysis, by observing mode shapes and modal stresses, the designer has a more realistic picture of the structures behavior during the earthquake. This strengthens his confidence in the structural integrity

TABLE 10

COMPARISON OF RESULTS

COMPONENT	DYNAMIC ANALYSIS - 5 ROW OF TUBES										DYNAMIC ANALYSIS - 7 ROW OF TUBES									
	Displacement In (cm)					Stresses KSI (MPa)					Displacement In (cm)					Stresses KSI (MPa)				
	X	Y	Z	(X) Bend.	(Y) Bend.	Axial	Princ	Princ			X	Y	Z	(X) Bend.	(Y) Bend.	Axial	Max. Princ	Min. Princ		
Generating Tubes	2.24 (5.7)	.70 (1.8)	.04 (.10)	13.7 (94.5)	.3 (2.1)	.10 (.7)	--	--			2.41 (6.1)	1.14 (2.9)	.04 (.10)	14.9 (102.7)	.2 (1.4)	.1 (.7)	--	--		
Screen Tubes	2.36 (6.0)	.75 (1.9)	.08 (.21)	.8 (5.5)	16.6 (114.)	.6 (4.1)	--	--			2.46 (6.2)	1.09 (2.8)	.09 (.24)	1.3 (9.0)	23.9 (164.8)	2.8 (19.8)	--	--		
Roof Tubes	.08 (2.1)	.20 (.51)	.01 (.03)	--	--	--	3.8 (26.2)	.2 (1.4)			.08 (.20)	.12 (.3)	.01 (.03)	--	--	--	3.0 (20.7)	.9 (6.2)		
Floor Tubes	.08 (.2)	.20 (.51)	.02 (.05)	--	--	--	9.3 (64.1)	.3 (2.1)			.08 (.20)	.13 (.33)	.02 (.05)	--	--	--	8.8 (60.7)	1.3 (9.0)		
Front Wall Tubes	.01 (.03)	.20 (.51)	0	--	--	--	1.1 (7.6)	.9 (6.2)			.01 (.03)	.12 (.3)	0	--	--	--	1.3 (9.0)	.9 (6.2)		
Rear Wall Tubes	.11 (.28)	.2 (.51)	0	--	--	--	3.6 (24.8)	.1 (.7)			.11 (.28)	.12 (.3)	0	--	--	--	2.6 (17.9)	.1 (.7)		
Sidewall Tubes	.23 (.58)	.2 (.51)	0	--	--	--	5.2 (35.9)	.1 (.7)			.24 (.61)	.12 (.3)	0	--	--	--	4.5 (31.0)	.1 (.7)		
Superheater Tubes	1.09 (2.8)	.3 (.67)	.02 (.05)	7.0 (48.3)	.4 (2.8)	.1 (.7)	--	--			1.04 (2.6)	.58 (1.47)	.04 (.10)	10.8 (74.5)	.6 (4.1)	.4 (2.8)	--	--		
Supply Tubes	.09 (.23)	.09 (.48)	.02 (.05)	1.2 (8.3)	.6 (4.1)	.1 (.7)	--	--			.07 (.18)	.12 (.30)	.01 (.03)	.8 (5.5)	.2 (1.4)	0.1 (.7)	--	--		
Riser Tubes	.07 (.18)	.20 (.51)	.01 (.03)	.6 (4.1)	.4 (2.8)	.1 (.7)	--	--			.09 (.23)	.12 (.30)	.02 (.05)	.8 (5.5)	.4 (2.8)	0.1 (.7)	--	--		

TABLE 11 LOADS ON BOILER SUPPORTS KIPS (kN)

Support Points		DYNAMIC ANALYSIS Original Model			DYNAMIC ANALYSIS Revised Model		
		X	Y	Z	X	Y	Z
Water Drum	Right	22.9 (101.9)	11.0 (48.9)	33.7 (149.9)	22.2 (98.7)	6.6 (29.4)	29.2 (130.)
	Left	--	6.5 (29.9)	27.3 (121.4)	--	4.1 (18.4)	23.3 (103.6)
Steam Drum	Right	7.3 (32.5)	38.9 (173.6)	--	7.2 (32.0)	30.0 (133.4)	--
	Left	--	38.8 (172.6)	--	--	30.0 (133.4)	--
Right Side Wall	Rear	--	--	5.3 (23.6)	--	--	2.9 (12.9)
	Middle	--	--	38.4 (170.8)	--	--	36.5 (162.4)
	Front	--	--	0.8 (3.6)	--	--	0.5 (2.2)
Left Side Wall	Rear	--	--	5.3 (23.6)	--	--	3.1 (13.8)
	Middle	--	--	37.5 (166.8)	--	--	34.2 (152.1)
	Front	--	--	1.1 (4.9)	--	--	0.8 (3.6)
Front Wall	Right	15.2 (67.6)	--	--	16.1 (71.6)	--	--

of his structure to resist earthquake.

In establishing a mathematical model of a boiler structure numerous assumptions and approximations are required in order to reduce the structure to within practical limitations. The most important task in simplifying or reducing the various components is to first understand their actual behavior and its effect on the total model. This is easy to say and extremely difficult to accomplish. Individual members could be analyzed to determine their natural frequency and compared to the frequencies of the total model. The sensitivity of the model can be checked by modeling important members using more than one modeling technique. This way, it can be determined how sensitive the overall structure is to their modeling. With this type of information available to him, the designer can then finalize the mathematical model and proceed to design the structure.

In testing the modeling techniques used, another mathematical model was developed which yielded higher stresses in two of the most flexible members. These stresses were discovered only because of the additional effort to evaluate and substantiate the adequacy of the original model to represent the boiler structure. Of course, this approach cannot always be followed because of time and economic considerations. However, it should be practiced whenever possible in order to establish the sensitivity of a mathematical model to several of its components and determine the best method of representing them.

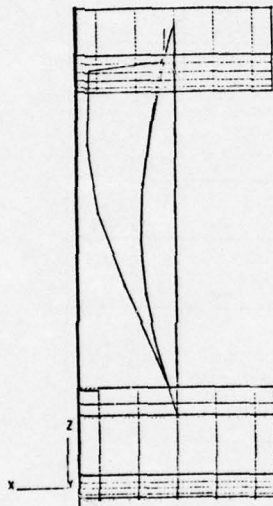
In conclusion, the writer recommends that a dynamic analysis design procedure be developed and incorporated in the present building codes. The procedure will have to be comprehensive in order to safeguard against users' oversimplifying the mathematical model. All users should be required to perform

certain basic steps in modeling to assure them of the adequacy of their model to represent the actual structure. The analysis is an approximation, but with good guidelines and engineering judgement it can be a good approximation. Engineers have the knowledge and facilities available to perform this task. The cost of the analysis will be increased but it is still a very nominal cost when compared to the total cost

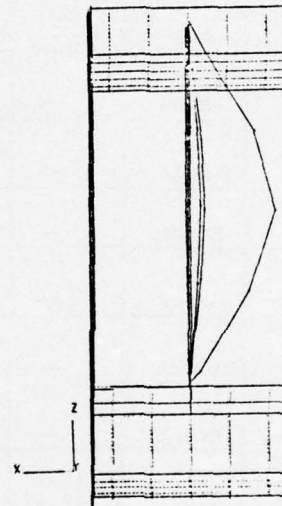
of a structure. Due to the results of a dynamic earthquake analysis, the design of a structure may have to be reinforced or revised which increases its cost. The thing to remember is if a structure affects people every possible precaution should be taken to assure their safety at all costs. As engineers, we are responsible to give our best engineering effort in all of our designs.

APPENDIX

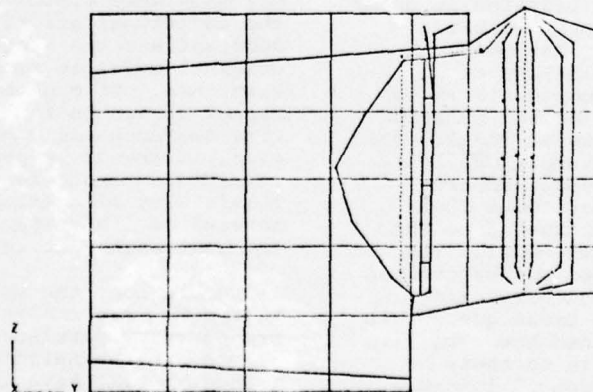
MODE SHAPES



Frequency = 1.6 CPS
Displacement Factor = 263



Frequency = 2.6 CPS
Displacement Factor = 248



Frequency = 3.1 CPS
Displacement Factor = 140

DYNAMIC RESPONSE OF LAMINATED COMPOSITE SHELLS

C. T. Sun

Department of Engineering Science and Mechanics
and Engineering Research Institute
Iowa State University, Ames, Iowa

In this paper the classical method of separation of variables, combined with the Mindlin-Goodman procedure, is employed to analyze the dynamic response of a simply-supported composite shell under a uniform dynamic pressure on the inner surface of the shell. Three cases of dynamic pressures are considered:

1. a rectangular pulse applied for a certain duration
2. a triangular pulse with the same rate of rising and falling
3. a sine pulse applied for a certain duration.

Numerical results for eight-layer graphite-epoxy and glass-epoxy composites with (0/0/45/-45)s stacking sequences are evaluated. Dynamic response characterized in terms of radial displacement w , axial and tangential moment resultants M_x and M_θ , and axial and hoop stresses σ_x and σ_θ are evaluated and compared with the corresponding quantities obtained statically. The ratio of the dynamic response to the corresponding static response (dynamic load factor) is plotted as a function of a geometrical parameter h/R where h is the thickness and R is the radius of the middle surface of the shell. It is observed that the dynamic load factor for w , M_θ and σ_θ decreases as the ratio h/R increases and the dynamic load factor for M_x and σ_x almost remains as a constant value. It is also observed that under the same type of dynamic loading, the dynamic load factor for graphite-epoxy is always higher than the dynamic load factor for glass-epoxy.

INTRODUCTION

Composite materials are in current use in a wide variety of applications. Important examples include composite materials for aircraft structural components, composite ablative materials for ABM and re-entry vehicles, filament-wound solid-propellant motor cases and nozzles, fiber reinforced rotor blades for helicopters, composite turbine blades for jet engines and fiber reinforced gun tubes.

An element common to all of these applications is that the composite materials are subjected to dynamic loads. In particular, most composite materials are brittle, and they are vulnerable to dynamic impact loading in these applications. In order to perform adequate design studies for such usage, methods are needed which will make it possible to determine the response of composite materials to dynamic loads. The solutions to dynamic boundary value problems often are, however, very difficult and

time consuming compared to corresponding static problems. Thus, the establishment of dynamic load factors (DLF), the ratio of dynamic response to static response, which would allow dynamic problems to be analyzed statically, is of considerable importance to materials engineers and structural designers.

In this paper, the classical method of separation of variables is employed to analyze the dynamic response of composite cylindrical shells under time-dependent uniform pressure at the inner surface of the shell. This method was first developed by Mindlin and Goodman [1] to evaluate the dynamic response of beams under time-dependent forces prescribed at the boundary and was subsequently extended to sandwich plates by Yu [2]. C. T. Sun and P. W. Sun [3] applied this method to investigate the dynamic response of laminated composite shells. This paper is a direct extension of the work published in [3]. In order to avoid repetition, the general development of the method of separation of variables

applied to composite cylindrical shells is omitted here but can be found in detail in [3].

GENERAL THEORY

Recently a dynamic theory which includes the effects of transverse shear deformation and rotary inertia was developed for anisotropic laminated shells [3]. By the application of the classical method of separation of variables, combined with the Mindlin-Goodman procedure [1-3] for treating time-dependent boundary conditions and/or dynamics external loadings, a solution for the five displacement variables under axisymmetric dynamic loading is assumed in the form

$$y_i(x, t) = \sum_{n=1}^{\infty} Y_{in}(x) T_n(t) + \sum_{j=1}^{10} g_{ij}(x) f_j(t) \quad (i = 1, 2, 3, 4, 5) \quad (1)$$

where y_i ($i=1, 2, 3, 4, 5$) stands for five displacement variables u^0 , v^0 , w , ψ_x and ψ_θ , respectively. In Eq. (1) $Y_{in}(x)$ represents the n th principal mode of y_i associated with the n th natural frequency ω_n of free vibration; $f_j(t)$ ($j=1, 2, \dots, 10$) represents the applied forcing function at the boundaries and $T_n(t)$ and $g_{ij}(x)$ are unknown functions time t and the axial coordinate x , respectively. Physically, the first term in Eq. (1) represents the solution due to surface tractions under homogeneous boundary conditions while the second term represents the solution generated by the forcing function $f_j(t)$ prescribed at the boundary. The function $g_{ij}(x)$ is determined from the Mindlin-Goodman procedure, and it vanishes identically when all $f_j(t) = 0$ at the boundary [1-3]. It has been shown [3] that for a laminated shell with the same density ρ of each layer, simply supported at both ends $x = 0, L$ under uniform normal pressure $p(x, t) = p_0 F(t)$ at the inner surface, the solution of $T_n(t)$ is given by

$$T_n(t) = \frac{2p_0 L h G_n}{n\pi \omega_n J_{nn}} \int_0^t F(\tau) \sin \omega_n(t - \tau) d\tau \quad (2)$$

where

$$J_{nn} = \frac{G_n^2 \rho h^3}{2\alpha_n} \quad (3)$$

and

$$\alpha_n = \left[1 + \left(\frac{E_n}{G_n} \right)^2 + \left(\frac{F_n}{G_n} \right)^2 + \frac{1}{12} \left(\frac{H_n}{G_n} \right)^2 + \frac{1}{12} \left(\frac{K_n}{G_n} \right)^2 \right]^{-1} \quad (4)$$

In Eqs. (2), (3), and (4) E_n , F_n , G_n , H_n , and K_n represent, respectively, the amplitude of free vibration of the displacement variables u^0 , v^0 , w , ψ_x and ψ_θ , and h represents the thickness of the shell.

The dependence of $F(t)$ on the time t is very complex in general. Three different dynamic loadings will be investigated in this paper.

$$\text{Case 1: } F(t) = 1 \quad 0 \leq t \leq t_1 \\ = 0 \quad t_1 < t \quad (5)$$

Geometrically, $F(t)$ given in Eq. (5) corresponds to a rectangular pulse applied for a duration of t_1 .

$$\text{Case 2: } F(t) = \frac{t}{t_1} \quad 0 \leq t \leq t_1 \\ = \frac{2t_1 - t}{t_1} \quad t_1 \leq t \leq 2t_1 \\ = 0 \quad 2t_1 \leq t \quad (6)$$

Equation (6) represents a triangular pulse with equal time rate of rising and falling.

$$\text{Case 3: } F(t) = \sin \frac{\pi t}{t_1} \quad 0 \leq t \leq t_1 \\ = 0 \quad t_1 \leq t \quad (7)$$

Pulse corresponding to Eq. (7) represents a sine pulse applied for a duration of t_1 .

By adjusting the value of t_1 one can evaluate the maximum dynamic response due to the above-mentioned three pulses.

From Eqs. (5)-(7), (2) and (1) and the shell constitutive relations [3] we obtain the solutions for the radial displacement w and moment results M_x and M_θ in the following non-dimensional form:

$$\bar{w}(x,t) = \sum_{n=1,3,5..}^{\infty} \frac{1}{n^3} \sin \frac{n\pi x}{L} \times \sum_{m=1}^5 \alpha_{nm} \left(\frac{\Omega_{11}}{\Omega_{nm}} \right)^2 \phi_{nm}(\bar{T}) \quad (8)$$

$$\bar{M}_x(x,t) = \sum_{n=1,3,5..}^{\infty} \frac{1}{n} \sin \frac{n\pi x}{L} \sum_{m=1}^5 \left[\frac{E_{nm}}{G_{nm}} + \frac{H_{nm}}{G_{nm}} \left(\frac{R}{h} \right) + \frac{D_{16}}{D_{11}} \frac{K_{nm}}{G_{nm}} \left(\frac{R}{h} \right) + \frac{D_{16}}{D_{11}} \frac{E_{nm}}{G_{nm}} \right] \alpha_{nm} \left(\frac{\Omega_{11}}{\Omega_{nm}} \right)^2 \phi_{nm}(\bar{T}) \quad (9)$$

$$\bar{M}_\theta(x,t) = \sum_{n=1,3,5..}^{\infty} \frac{1}{n^2} \sin \frac{n\pi x}{L} \sum_{m=1}^5 \left[\frac{1}{n} + \frac{\pi D_{12}}{D_{22}} \left(\frac{R}{L} \right) \left(\frac{R}{h} \right) \left(\frac{H_{nm}}{G_{nm}} \right) + \frac{\pi D_{26}}{D_{22}} \left(\frac{R}{L} \right) \left(\frac{R}{h} \right) \times \frac{K_{nm}}{G_{nm}} \right] \alpha_{nm} \left(\frac{\Omega_{11}}{\Omega_{nm}} \right)^2 \phi_{nm}(\bar{T}) \quad (10)$$

where

$$\bar{w} = \left(\frac{\pi \rho h \omega_{11}^2}{4 p_o} \right) w \quad \bar{M}_x = \left(\frac{\rho h R L \omega_{11}^2}{4 p_o D_{11}} \right) M_x$$

$$\bar{M}_\theta = \left(\frac{\pi \rho h R^2 \omega_{11}^2}{4 p_o D_{22}} \right) \bar{M}_\theta \quad \bar{T} = \sqrt{\frac{E_T}{\rho}} \frac{t}{L}$$

$$\Omega_{nm}^2 = \frac{\rho L^2 \omega_{nm}^2}{E_T n^2 \pi^2} \quad (11)$$

In Eq. (1), \bar{T} , Ω_{nm} are non-dimensional time and frequency, respectively, E_T represents the Young's modulus along a direction normal to the fibers, and R is the radius of the middle surface of the shell.

Using the composite material constitutive relations in conjunction with solutions of the displacement variables one obtains the normal stress components σ_x and σ_θ for each layer

$$\bar{\sigma}_x = \sum_{n=1,3,5..}^{\infty} \frac{1}{n^2} \sin \frac{n\pi x}{L} \sum_{m=1}^5 \left[\frac{1}{n} \frac{1}{1 + \frac{z}{R}} - \frac{\pi C_{11}}{C_{12}} \left(\frac{R}{L} \right) \left(\frac{E_{nm}}{G_{nm}} + \frac{z}{h} \frac{H_{nm}}{G_{nm}} \right) - \frac{\pi C_{16}}{C_{12}} \left(\frac{R}{L} \right) \left(\frac{F_{nm}}{G_{nm}} + \frac{1}{1 + \frac{z}{R}} \frac{z}{h} \frac{K_{nm}}{G_{nm}} \right) \right] \alpha_{nm} \left(\frac{\Omega_{11}}{\Omega_{nm}} \right)^2 \phi_{nm}(\bar{T}) \quad (12)$$

$$\bar{\sigma}_\theta = \sum_{n=1,3,5..}^{\infty} \frac{1}{n^2} \sin \frac{n\pi x}{L} \sum_{m=1}^5 \left[\frac{1}{n} \frac{1}{1 + \frac{z}{R}} - \frac{\pi C_{12}}{C_{22}} \left(\frac{R}{L} \right) \left(\frac{E_{nm}}{G_{nm}} + \frac{z}{h} \frac{H_{nm}}{G_{nm}} \right) - \frac{\pi C_{26}}{C_{22}} \left(\frac{R}{L} \right) \times \left(\frac{F_{nm}}{G_{nm}} + \frac{1}{1 + \frac{z}{R}} \frac{z}{h} \frac{K_{nm}}{G_{nm}} \right) \right] \alpha_{nm} \left(\frac{\Omega_{11}}{\Omega_{nm}} \right)^2 \times \phi_{nm}(\bar{T}) \quad (13)$$

where

$$\bar{\sigma}_x = \frac{\pi \rho h R \omega_{11}^2}{4 p_o C_{12}} \sigma_x \quad \bar{\sigma}_\theta = \frac{\pi \rho h R \omega_{11}^2}{4 p_o C_{22}} \sigma_\theta \quad (14)$$

and z represents the thickness coordinate of the shell.

The function $\phi_{nm}(\bar{T})$ in Eqs. (8)-(10), (12) and (13) is given by the following form for different cases.

Case 1: rectangular pulse

$$\phi_{nm}(\bar{T}) = 1 - \cos \Omega_{nm} \lambda_n \bar{T}, \quad 0 \leq \bar{T} \leq \bar{T}_1$$

$$= \cos \Omega_{nm} \lambda_n (\bar{T} - \bar{T}_1) - \cos \Omega_{nm} \lambda_n \bar{T}, \quad \bar{T}_1 \leq \bar{T} \quad (15)$$

Case 2: triangular pulse

$$\phi_{nm}(\bar{T}) = \frac{\bar{T}}{\bar{T}_1} = \frac{\sin \Omega_{nm} \lambda_n \bar{T}}{\Omega_{nm} \lambda_n \bar{T}_1} \quad 0 \leq \bar{T} \leq \bar{T}_1$$

$$\begin{aligned}
&= \frac{\bar{T}}{\bar{T}_1} - \frac{\sin \Omega_{nm} \lambda \bar{T}}{\Omega_{nm} \lambda \bar{T}_1} - \frac{2(\bar{T} - \bar{T}_1)}{\bar{T}_1} \\
&+ \frac{2 \sin \Omega_{nm} \lambda (\bar{T} - \bar{T}_1)}{\Omega_{nm} \lambda \bar{T}_1}, \quad \bar{T} \leq \bar{T} \leq 2\bar{T}_1 \\
&= -\frac{\sin \Omega_{nm} \lambda \bar{T}}{\Omega_{nm} \lambda \bar{T}_1} + \frac{2 \sin \Omega_{nm} \lambda (\bar{T} - \bar{T}_1)}{\Omega_{nm} \lambda \bar{T}_1} \\
&- \frac{\sin \Omega_{nm} \lambda (\bar{T} - 2\bar{T}_1)}{\Omega_{nm} \lambda \bar{T}_1}, \quad 2\bar{T}_1 \leq \bar{T} \quad (16)
\end{aligned}$$

Case 3: sine pulse

$$\begin{aligned}
\phi_{nm}(\bar{T}) &= \frac{\Omega_{nm} \lambda \bar{T}_1}{\pi^2 - (\Omega_{nm} \lambda \bar{T}_1)^2} \left[\pi \sin \Omega_{nm} \lambda \bar{T} \right. \\
&\quad \left. - \Omega_{nm} \lambda \bar{T}_1 \sin \frac{\pi \bar{T}}{\bar{T}_1} \right] \quad 0 \leq \bar{T} \leq \bar{T}_1 \\
&= \frac{\Omega_{nm} \lambda \bar{T}}{\pi^2 - (\Omega_{nm} \lambda \bar{T}_1)^2} \left[\pi \sin \Omega_{nm} \lambda \bar{T} \right. \\
&\quad \left. + \pi \sin \Omega_{nm} \lambda (\bar{T} - \bar{T}_1) \right] \quad \bar{T}_1 \leq \bar{T} \quad (17)
\end{aligned}$$

where

$$\begin{aligned}
\bar{T}_1 &= \sqrt{\frac{E_T}{\rho}} \frac{t_1}{L} \\
\lambda_n &= n\pi h/L
\end{aligned} \quad (18)$$

NUMERICAL RESULTS AND DISCUSSION

Numerical results for maximum deflection w , maximum normal moment resultants M_x and M_θ and maximum normal stresses σ_x and σ_θ are evaluated for eight layer 0/0/45/-45/-45/45/0/0 laminates. The maximum values of the above quantities occur at $x = L/2$ and $\bar{T} = \bar{T}^*$. The evaluation of \bar{T}^* for each case is achieved by plotting w , M_x , etc. as a function of \bar{T} for a given value of \bar{T}_1 . Two different composite materials, graphite-epoxy and glass-epoxy, are used in the numerical examples. For graphite-epoxy each ply has the following unidirectional properties:

$$\begin{aligned}
E_L &= 20 \times 10^6 \text{ psi } (13.788 \times 10^{10} \text{ Pascal}) \\
E_T &= 10^6 \text{ psi } (0.689 \times 10^{10} \text{ Pascal}) \\
\nu_{LT} &= \nu_{TT} = 0.25 \\
G_{LT} &= 0.6 \times 10^6 \text{ psi } (0.414 \times 10^{10} \text{ Pascal}) \\
G_{TT} &= 0.5 \times 10^6 \text{ psi } (0.345 \times 10^{10} \text{ Pascal})
\end{aligned} \quad (19)$$

and for glass epoxy,

$$\begin{aligned}
E_L &= 5.5 \times 10^6 \text{ psi } (3.791 \times 10^{10} \text{ Pascal}) \\
E_T &= 2 \times 10^6 \text{ psi } (1.379 \times 10^{10} \text{ Pascal}) \\
\nu_{LT} &= \nu_{TT} = 0.25 \\
G_{LT} &= 0.8 \times 10^6 \text{ psi } (0.552 \times 10^{10} \text{ Pascal}) \\
G_{TT} &= 0.6 \times 10^6 \text{ psi } (0.414 \times 10^{10} \text{ Pascal})
\end{aligned} \quad (20)$$

where L and T are the directions parallel and normal to the fibers, respectively. We assume that $h/L = 1/200$. It can be observed in Eqs. (19) and (20) that the principal rigidity ratio E_L/E_T for graphite-epoxy is 20 and for glass-epoxy is only 2.75. This implies that graphite-epoxy is a stronger anisotropic material than glass-epoxy. In order to evaluate the dynamic load factor, the static response for both materials is also calculated. The static problem is a laminated composite shell under uniform internal pressure p_0 . The problem is solved by using a similar approach to that used by Whitney and Sun [4].

A detailed examination of the numerical results reveals that the dynamic load factors can be grouped into two categories; one is for w , M_θ and σ_θ and another is for M_x and σ_x . In order not to duplicate the results only the numerical values for w and M_x will be presented.

Figure 1 shows the dynamic load factor for w as a function of h/R under the rectangular pulse. The values of h/R range from 0.02, a thin shell, to 0.1, a relatively thick shell. Since we are using linear elastic theory, the value of h/R must be small. Thus it is not necessary to evaluate the numerical results for w , M_x , etc. corresponding to large values of h/R . In Fig. 1 we observe that for both graphite-epoxy and glass-epoxy the dynamic load factor for w decreases as h/R increases. This implies that a thin composite shell is more liable to dynamic loading than a thick shell. We also observe that the dynamic load factor for w for graphite-epoxy is always higher than the dynamic load factor for glass-epoxy. This is attributed to the fact that graphite-epoxy is a stronger anisotropic material than glass-epoxy. In Figs.

2 and 3 the dynamic load factor for w is plotted as a function of h/R under the sine and triangular pulses respectively. The results are similar to the rectangular pulse; but the dynamic load factors are smaller than the rectangular pulse for both cases.

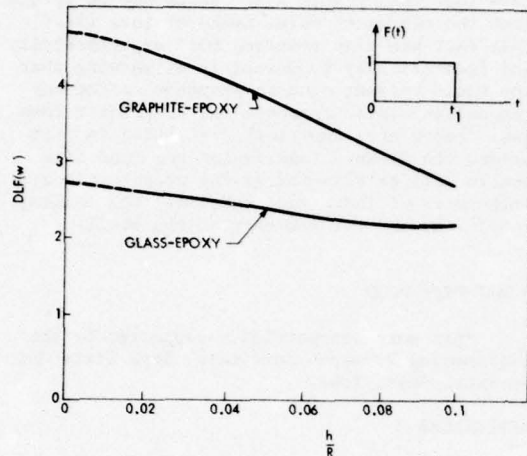


Fig. 1. Dynamic load factor for radial displacement as function of h/R under rectangular pulse.

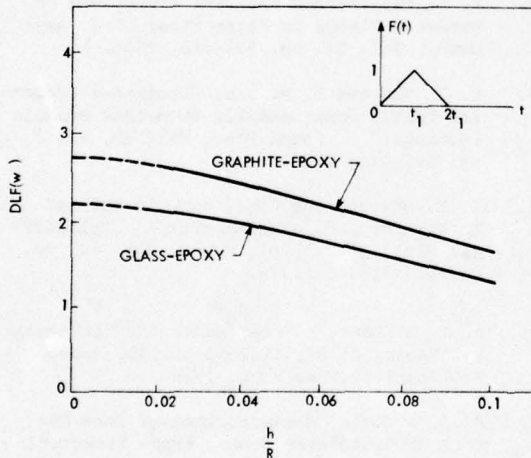


Fig. 2. Dynamic load factor for radial displacement as a function of h/R under triangular pulse.

Figures 4, 5, and 6 show the dynamic load factor for M_x as a function of h/R under the rectangular, sine and triangular pulses respectively. It is observed that the dynamic load factor remains almost unchanged. It decreases slightly as h/R increases. The dynamic load factor for M_x for both materials under the rectangular pulse is surprisingly high. At the present time, it is difficult to offer a physical interpretation.

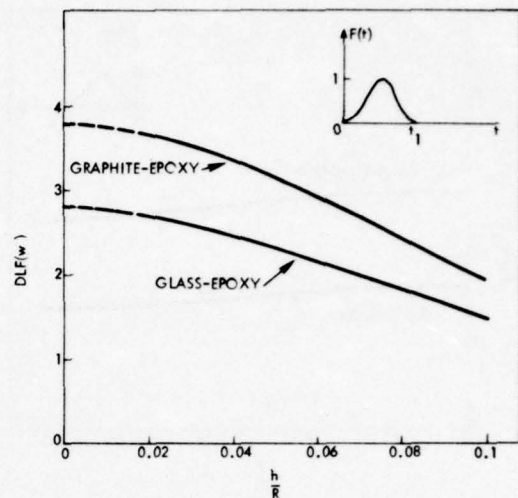


Fig. 3. Dynamic load factor for radial displacement as function of h/R under sine pulse.

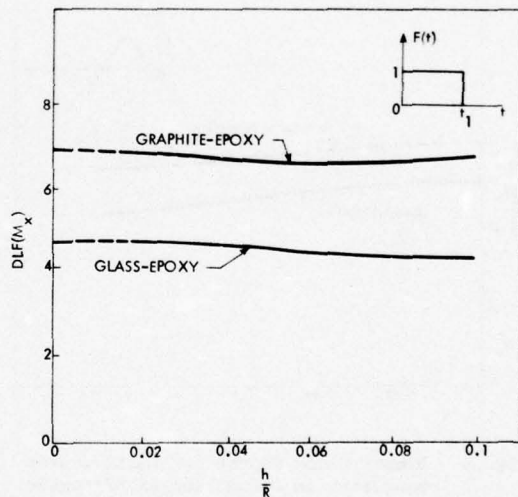


Fig. 4. Dynamic load factor for axial moment resultant as a function of h/R under rectangular pulse.

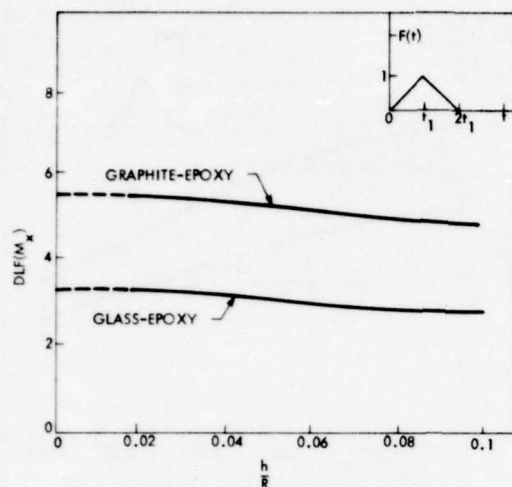


Fig. 5. Dynamic load factor for axial moment resultant as a function of h/R under triangular pulse.

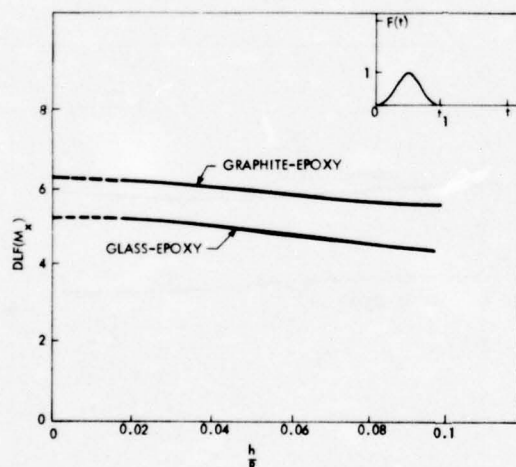


Fig. 6. Dynamic load factor for axial moment resultant as a function of h/R under sine pulse.

CONCLUDING REMARKS

In this paper dynamic load factors for graphite-epoxy and glass-epoxy composite shells under the rectangular, sine and triangular pulses are evaluated. Numerical results indicate that the dynamic load factor may be greater than the classical value found by Love [5]. This fact was also observed both experimentally and theoretically by Suzuki [6-8] showing that the ratio between dynamic response to the corresponding static response may be greater than two. Based upon numerical evaluation in this paper, the dynamic load factor for composite shells will be affected by the unidirectional properties of individual material, the loading conditions and the geometry of the shell.

ACKNOWLEDGEMENT

This work was partially supported by the Engineering Research Institute, Iowa State University, Ames, Iowa.

REFERENCES

1. R. D. Mindlin and L. E. Goodman, "Beam Vibrations with Time-dependent Boundary Conditions," *J. Appl. Mech.*, Vol. 17, pp. 377-380, 1950.
2. Y. Y. Yu, "Forced Flexural Vibrations of Sandwich Plates in Plane Strain," *J. Appl. Mech.*, Vol. 27, pp. 535-540, 1960.
3. C. T. Sun and P. W. Sun, "Laminated Composite Shells Under Axially Symmetric Dynamic Loadings," *J. Sound Vib.*, Vol. 35, No. 3, pp. 395-414, 1974.
4. J. M. Whitney and C. T. Sun, "A Refined Theory for Laminated Anisotropic Cylindrical Shells," *J. Appl. Mech.*, Vol. 41, No. 2, pp. 471-476, 1974.
5. A. E. H. Love, *A Treatise on the Mathematical Theory of Elasticity*, p. 181, Dover Publications, New York, 1926.
6. S. I. Suzuki, "Measured Dynamic Load Factors of Cantilever Beams, Frame Structures and Rings Subjected to Impulsive Loads," *Exp. Mech.*, pp. 76-81, Feb. 1971.
7. S. I. Suzuki, "The Effects of Axial Forces to Dynamic Load Factors of the Beam Subjected to Transverse Impulsive Loads," *J. R. Aeronaut. Soc.*, Vol. 61, pp. 860-864, 1967.
8. S. I. Suzuki, "The Effects of Solid Viscosities to Dynamic Load Factors of the Ring and Hollow Sphere Subjected to Impulsive Loads," *J. R. Aeronaut. Soc.*, Vol. 72, pp. 971-976, 1968.

Discussion

Mr. Baker (Southwest Research Institute):
I noticed that your dynamic load factors are
all well in excess of 2.

Dr. Sun: Most anisotropic materials behave
this way.

Mr. Baker: So this is a function of the
anisotropy?

Dr. Sun: I believe so I have no theoretical
proof.

Mr. Baker: Were your pulse lengths shorter on
the same order of magnitude as the fundamental
period of your shells?

Dr. Sun: We adjusted t_1 , the fundamental
period of the shells, to produce the maximum
response.

SPECTRUM AND RMS LEVELS FOR STRESSES IN CLOSELY SPACED STIFFENED CYLINDRICAL
SHELLS, SUBJECTED TO ACOUSTIC EXCITATION (U)

G. MAYMON

Armament Development Authority
Haifa, Israel

A formulation, by which RMS values of stresses in cylindrical shells with closely spaced stiffeners subjected to acoustic excitation can be obtained, is presented. Donnell type equations are used to analyze the stiffened shells. Effects of eccentricity of stiffeners and the existence of constant axial stress in the structure are included. Analysis of deformation is done by smearing the stiffeners, but stresses are calculated discretely for the stringers, the rings and for the shell. A digital computer program, based on the present formulation was written, and numerous examples for unstiffened shells are presented. As a by product, noise reduction is also obtained.

LIST OF SYMBOLS

- | | |
|--|--|
| <p>a- Acceleration
a- Distance between rings
A_1- Area of stringer
A_2- Area of ring
b- Distance between stringers
c- Speed of sound in acoustic medium
D- Shell rigidity
E- Young's modulus
e_1- Eccentricity of stringer } (positive for
e_2- Eccentricity of ring } inner stiffener)
F- Stress function
f- Frequency
f_R- Ring frequency
f_C- Coincidence frequency
F_x
F_y } Parameters defined in Ch. 2
F -
h- Thickness of shell
\bar{h}- Equivalent thickness
I_{11}- Moment of inertia of stringer
I_{22}- Moment of inertia of ring
I_{t1}- Polar moment of inertia of stringer
I_{t2}- Polar moment of inertia of ring
K_a- Axial wavenumber
K_c- Circumferential wavenumber
$K_{m,n}$- Rigidity of (m,n) mode
K_x- Curvature in x direction
K_y- Curvature in y direction
L- Length of cylinder
m- Number of axial half waves
M- Mass per unit area of the shell
n- Number of circumferential full waves</p> | <p>N- Axial static force (ch. 2.1)
N- Number of modes in a given bandwidth (ch. 2.3)
N_x- Axial membrane force
N_y- Circumferential membrane force
P- Pressure
$q()$- Coefficients defined in ch. 2.3
R- Radius of shell
R_{rad}- Acoustic radiation impedance
R_{mech}- Mechanical impedance
S- Ratio of axial static stress to classical buckling stress
S_{pext}- PSD of pressure excitation
v- Velocity
w- Radial displacement
x- Longitudinal direction
y- Circumferential direction
Z_B- Batdorf parameter = $\sqrt{1-\nu^2} \left(\frac{L}{h} \right) \left(\frac{L}{R} \right)$
Z_{max}- Distance between shell median line to top of stiffener
β- Parameter in ch. 2.1
ϵ_x- Axial strain
ϵ_y- Circumferential strain
$\mu_1 = (1-\nu^2) A_1 / bh$
$\mu_2 = (1-\nu^2) A_2 / ah$
ν- Poisson ratio
ω_0- Center normalized frequency
$\omega_{m,n}$- Angular frequency of mode (m,n)
ρ- Density of acoustic media
ρ_m- Density of shell material
σ- Acoustic efficiency</p> |
|--|--|

G_x - Axial stress in the shell
 G_y - Circumferential stress in the shell
 G_{RR} - Stress in the ring
 G_{xx} - Membrane stresses in the shell
 G_{yy} - Bending stresses in the shell
 G_{cl} - Classical buckling load $= E h / R \sqrt{3(1-\nu^2)}$

$\chi_1 = \mu_1 e_1$
 $\chi_2 = \mu_2 e_2$
 η - Loss factor
 $\eta_{01} = 12(1-\nu^2) [I_{11}/bh^3 + A_1/bh (e_1/h)^2]$
 $\eta_{02} = 12(1-\nu^2) [I_{22}/ah^3 + A_2/ah (e_2/h)^2]$
 $\eta_{t1} = GI_{t1}/bD$
 $\eta_{t2} = GI_{t2}/aD$
 $\delta_1 = 12 \chi_1 / h^2$
 $\delta_2 = 12 \chi_2 / h^2$

1. INTRODUCTION

In the future qualification tests of externally carried stores, an acoustic test of the whole structure will be required. Since the acoustic test of a complete store requires very expensive test facilities, e.g. large acoustic cells with high sound pressure levels and high power requirements, it is worthwhile to be able to assess the necessity of such test with respect to the specific case investigated. One can think of cases in which the calculated factor of safety of acoustical excitation response is so large, that all parties involved can be sure that no experimental or qualification verification is necessary. In addition, the developer wishes to predict, during the preliminary design stages, the effect of the acoustic environment on the structure, so that a change in design can be introduced early enough, if catastrophic results are predicted.

This lead to the conclusion that an analytical tool is required in order to predict two main characteristics of the structure:

- Levels of stresses created by acoustic excitation;
- Noise reduction through the store envelope.

The former will give insight about the possibility of the store to withstand acoustic fatigue. The latter will enable to define realistic acoustic test envelope for internal equipment, in those cases where external noise levels are given.

It seems that theories on cylindrical shells should be attempted first for external stores, before other geometries are undertaken. These theories will be useful tools for the investigation of the effects of main parameters.

A theory for the prediction of stress levels in closely spaced stiffened cylindrical shells is presented in this paper. Donnell type equations for the stiffened shell are given, from which spectrum and rms levels for stresses in the shell and in the stiffeners can be calculated. Effects of eccentricity of stiffeners and the presence of axial static load are included. Numerical examples for the application of the theory are given for several unstiffened shells. Using known theories, noise reduction spectrum is also calculated as by product.

2. BASIC EQUATIONS

2.1 Frequency Equation

The analysis of closely spaced stiffened shell can be approximated by "smearing" the stiffeners while calculating the deflections of the shell, however taking into account the discreteness of the stiffeners while calculating stresses from the deflections.

Two Donnell type equations can be used for the analysis of the smeared shell (1), (2), (3):

Equilibrium equation

$$\begin{aligned}
 D \nabla^4 w + D \{ \eta_{01} w_{,xxxx} + \eta_{02} w_{,yyyy} + (\eta_{t1} + \eta_{t2}) w_{,xxyy} - \\
 - \beta [(1+\mu_2) \delta_1 \chi_2 w_{,xxxx} - 2 \delta_1 \delta_2 \chi_2 w_{,xxyy} + (1+\mu_1) \delta_2 \chi_1 w_{,yyyy}] \} - \\
 - \beta \{ \chi_1 [(1+\mu_2) h F_{,yyxx} - \nu h F_{,xxxx}] + \chi_2 [(1+\mu_1) h F_{,yyxx} - \nu h F_{,yyyy}] \} \\
 - \frac{h F_{,xx}}{R} + N w_{,xx} + \rho h w_{,tt} = 0
 \end{aligned} \quad (2.1)$$

Compatibility equation

$$L_1(F) + L_2(w) = - \frac{w_{,xx}}{R} \quad (2.2)$$

where

$$\begin{aligned}
 L_1(F) &= \frac{\beta(1-\nu^2)}{E} \{ (1+\mu_2)(F)_{,yyyy} + (1+\mu_1)(F)_{,xxxx} + 2 \left[\frac{1+\nu}{\beta(1-\nu^2)} - \nu \right] (F)_{,xxyy} \} \\
 L_2(w) &= \beta \{ -\nu \chi_1 (w)_{,xxxx} - \nu \chi_2 (w)_{,yyyy} + [(1+\mu_2) \chi_1 + (1+\mu_1) \chi_2] (w)_{,xxyy} \} \\
 \beta &= 1 / (1 - \nu^2 + \mu_1 + \mu_2 + \mu_1 \mu_2)
 \end{aligned} \quad (2.2.a)$$

other parameters are defined in the list of symbols.

A Fourier series solution for the deflection and for the stress function can be assumed for simply supported conditions as follows:

$$\begin{aligned}
 w &= \sum_{m=1}^{\infty} \sum_{n=1}^{\infty} w_{m,n} \sin \left(\frac{m\pi x}{L} \right) \cos \left(\frac{n\pi y}{R} - \phi_n \right) \\
 F &= \sum_{m=1}^{\infty} \sum_{n=1}^{\infty} F_{m,n} \sin \left(\frac{m\pi x}{L} \right) \cos \left(\frac{n\pi y}{R} - \phi_n \right)
 \end{aligned} \quad (2.3)$$

Although this is not always the case in reality, it was shown (e.g. (4)) that, due to the response of the shell in high wavenumbers, the effect of boundary conditions can be neglected.

Substituting eq. (2.3) into eq. (2.2), the relationship between $W_{m,n}$ and $F_{m,n}$ is as follows:

$$F_{m,n} = \frac{\frac{Eh}{h\beta R(1-\nu^2)} \left(\frac{m\pi}{L}\right)^4 - \frac{Eh}{1-\nu^2} \left\{ \nu \frac{\chi_1}{h} \left(\frac{m\pi}{L}\right)^4 + \nu \frac{\chi_2}{h} \left(\frac{n}{R}\right)^4 - \right.}{(1+\mu_1) \left(\frac{m\pi}{L}\right)^4 + 2 \left[\frac{1+\nu}{(1-\nu^2)} \beta - \nu \right] \left(\frac{m\pi}{L}\right)^2 \left(\frac{n}{R}\right)^2} - \left. \frac{[(1+\mu_2) \frac{\chi_1}{h} + (1+\mu_1) \frac{\chi_2}{h}] \left(\frac{m\pi}{L}\right)^2 \left(\frac{n}{R}\right)^2}{(1+\mu_2) \left(\frac{n}{R}\right)^4} \right\} W_{m,n} \quad (2.4)$$

and, substituting eq. (2.4) into eq. (2.1) yields the final equations for the free vibration of the stiffened shell:

$$\ddot{W}_{m,n} + K_{m,n} W_{m,n} = 0 \quad (2.5)$$

where

$$K_{m,n} = \frac{\pi^2}{\sqrt{3(1-\nu^2)}} \cdot \frac{h}{R} \cdot \frac{E}{\rho L^2} \cdot Z_{m,n} \quad (2.6)$$

$$Z_{m,n} = \frac{\pi^2}{4\sqrt{3}} \cdot \frac{1}{Z_0} \cdot \frac{h}{R} \left\{ \left[m^2 + \left(\frac{1}{\pi R}\right)^2 n^2 \right]^2 - \eta_{01} m^4 + \eta_{02} \left(\frac{1}{\pi R}\right)^4 n^4 + \right. \\ \left. + (\eta_{11} + \eta_{12}) m^2 \left(\frac{1}{\pi R}\right)^2 n^2 - \beta f_1 \chi_1 (1+\mu_2) m^4 - \beta f_2 \chi_2 (1+\mu_1) \left(\frac{1}{\pi R}\right)^4 n^4 \right. \\ \left. + 2\nu \beta f_1 \chi_1 m^2 \left(\frac{1}{\pi R}\right)^2 n^2 \right\} - S m^2 + \\ + \sqrt{3(1-\nu^2)} \cdot \frac{1}{h} \cdot \frac{1}{\mu_0} \left\{ m^2 + \frac{\pi^2 \beta \sqrt{1-\nu^2}}{Z_0} \frac{\chi_1}{h} \left[\nu m^4 - (1+\mu_2) m^2 \left(\frac{1}{\pi R}\right)^2 n^2 \right] + \right. \\ \left. + \frac{\pi^2 \beta \sqrt{1-\nu^2}}{Z_0} \frac{\chi_2}{h} \left[\nu \left(\frac{1}{\pi R}\right)^4 n^4 - (1+\mu_1) m^2 \left(\frac{1}{\pi R}\right)^2 n^2 \right] \right\}$$

in which

$$\alpha_0 = \frac{1}{1-\nu^2} \left\{ \frac{\chi_1}{h} m^2 \left[\nu m^2 - (1+\mu_2) \left(\frac{1}{\pi R}\right)^2 n^2 \right] + \frac{\chi_2}{h} \left(\frac{1}{\pi R}\right)^2 n^2 \left[\right. \right.$$

$$\left. \left. \nu \left(\frac{1}{\pi R}\right)^2 n^2 - (1+\mu_1) m^2 \right] + \frac{Z_0 m^2}{\pi^2 \beta (1-\nu^2)^{3/2}} \right\}$$

$$\mu_0 = (1+\mu_1) m^4 + 2 \left[\frac{1+\nu}{\beta(1-\nu^2)} - \nu \right] m^2 \left(\frac{1}{\pi R}\right)^2 n^2 + \left(\frac{1}{\pi R}\right)^4 n^4 (1+\mu_2)$$

$K_{m,n}$ is the "rigidity" of the (m,n) mode, which can be negative due to the term $-Sm^2$ and other terms in eq. (2.7.a). It will be positive if $S \leq 0$, which means that no axial compression load is acting on the shell. It should be noted that when analysis of the frequency of compressed shells is done, non linear effects have to be taken into account, thus

eq. (2.6) is not valid for high levels of S . From past investigations (5) and experience, it is believed that values of $S \leq 0.3$ are the upper limit for eq. (2.6) to be valid.

Once $K_{m,n}$ is known in terms of m and n , eq. (2.6) is normalized, and a relationship is established between ν_0 , the nondimensional frequency which is defined by

$$\nu_0 = \frac{f}{f_R} \quad (2.8)$$

and the normalized wavenumbers k_a and k_c , which are defined by

$$k_a = \frac{m\pi \left(\frac{1}{L} \frac{R}{L}\right)^{1/2}}{[12(1-\nu^2)]^{1/4}} \quad (\text{axial wavenumber})$$

and

$$k_c = \frac{n \left(\frac{1}{R}\right)^{1/2}}{[12(1-\nu^2)]^{1/4}} \quad (\text{circumferential wavenumber}) \quad (2.9)$$

The equation for the normalized frequency takes the following form:

$$\nu_0^2 \frac{h}{R} = \left\{ 1 + \eta_{01} - \beta f_1 \chi_1 (1+\mu_2) \right\} k_a^4 + \left\{ 1 + \eta_{02} - \beta f_2 \chi_2 (1+\mu_1) \right\} k_c^4 \\ + \left\{ 2 + \eta_{11} + \eta_{12} + 2\nu \beta \chi_1 \right\} k_a^2 k_c^2 - 2 S \frac{h}{R} k_a^2 + \\ + \left\{ \frac{\sqrt{12}}{1-\nu^2} k_a^2 + 12\nu \beta \frac{\chi_1}{h} k_a^4 - 12(1+\mu_2) \beta \frac{\chi_1}{h} k_a^2 k_c^2 + \frac{\nu \beta}{1-\nu^2} \frac{\chi_2}{h} k_c^4 - \right. \\ \left. - 12(1+\mu_1) \beta \frac{\chi_2}{h} k_a^2 k_c^2 \right\} + \\ + \left\{ \frac{\nu \chi_1}{h} k_a^4 - \frac{\chi_1}{h} (1+\mu_2) k_a^2 k_c^2 + \nu \frac{\chi_2}{h} k_c^4 - \frac{\chi_2}{h} (1+\mu_1) k_a^2 k_c^2 + \frac{k_a^2}{\beta \sqrt{12(1-\nu^2)}} \right\} \\ + \left\{ (1+\mu_1) k_c^4 + 2 \left[\frac{1+\nu}{\beta(1-\nu^2)} - \nu \right] k_a^2 k_c^2 + k_c^4 (1+\mu_2) \right\} \quad (2.10)$$

2.2 Wavenumber Diagram

Wavenumber diagram is plotted by connecting all points having the same value of ν_0 in the k_a - k_c plane. Several interesting parameters are calculated from this diagram.

1. Number of modes within a given bandwidth (as shown in Fig. 1);
2. Total number of modes below a given frequency (e.g. ref. (4) and (6));
3. Modal density function of a given shell (e.g. refs. (4) and (6));
4. Acoustic efficiency of the shell as function of frequency (e.g. ref. (4)).

In order to calculate mean square values of displacements, velocities and accelerations it is sufficient to know the number of modes in a certain bandwidth. However, in order to compute mean square values for stresses, the modes are to be identified, since second derivatives with respect to coordinates appear in the formulation.

For this purpose a program for a digital computer was written as part of the complete solution of the problem. The computation is done by scanning the wavenumber diagram in vertical lines, for any given center frequency and bandwidth.

2.3 Stresses In The Shell And In The Stiffeners

Although the deformation analysis (and thus the frequencies, as well) is carried out using the smeared shell differential equations, the stresses are analysed discretely for the shell and the stiffeners.

Stresses in the deformed shell are obtained from two different sources:

1. Bending stress due to the curvature of the deflected structure;
2. Membrane stresses due to the deformation w .

Generally, one can write:

for the shell

$$\bar{\sigma}_x = \frac{E}{1-\nu^2} \left[(\epsilon_x + \nu \epsilon_y) - Z (\kappa_x + \nu \kappa_y) \right] \quad (2.11)$$

$$\bar{\sigma}_y = \frac{E}{1-\nu^2} \left[(\epsilon_y + \nu \epsilon_x) - Z (\kappa_y + \nu \kappa_x) \right]$$

for a stringer

$$\bar{\sigma}_{xs} = E (\epsilon_x - Z \kappa_x) \quad (2.12)$$

and for a ring

$$\bar{\sigma}_{xr} = E (\epsilon_y - Z \kappa_y) \quad (2.13)$$

The internal forces N_x and N_y will be given by

$$N_x = \int_{-h/2}^{+h/2} \bar{\sigma}_x dz + \frac{1}{b} \int_{A_s} \bar{\sigma}_x dA \quad (2.14)$$

$$N_y = \int_{-h/2}^{+h/2} \bar{\sigma}_y dz + \frac{1}{a} \int_{A_r} \bar{\sigma}_y dA$$

The second term in each of eqs. (2.14) is, in fact the "smearing" of the stiffeners.

In ref. (1), the following expressions were derived for N_x and N_y in eccentrically stiffened cylindrical shell:

$$N_x = \frac{Eh}{1-\nu^2} \left[\epsilon_x (1+\mu_1) + \nu \epsilon_y - \chi_1 \kappa_x \right] \quad (2.15)$$

$$N_y = \frac{Eh}{1-\nu^2} \left[\epsilon_y (1+\mu_2) + \nu \epsilon_x - \chi_2 \kappa_y \right]$$

from eq. (2.11) it can be seen that

$$\int_{-h/2}^{+h/2} \bar{\sigma}_x dz = \frac{Eh}{1-\nu^2} (\epsilon_x + \nu \epsilon_y) \quad (2.16)$$

$$\int_{-h/2}^{+h/2} \bar{\sigma}_y dz = \frac{Eh}{1-\nu^2} (\epsilon_y + \nu \epsilon_x)$$

let

$$\bar{\sigma}_{ox} = \frac{E}{1-\nu^2} (\epsilon_x + \nu \epsilon_y) \quad (2.17)$$

$$\bar{\sigma}_{oy} = \frac{E}{1-\nu^2} (\epsilon_y + \nu \epsilon_x)$$

be the membrane stresses. The second part of eq. (2.11) is due to the contribution of the bending.

As consequence of (2.15), one can write

$$N_x = \bar{\sigma}_{ox} h + \frac{Eh}{1-\nu^2} (\mu_1 \epsilon_x - \chi_1 \kappa_x) \quad (2.18)$$

$$N_y = \bar{\sigma}_{oy} h + \frac{Eh}{1-\nu^2} (\mu_2 \epsilon_y - \chi_2 \kappa_y)$$

thus

$$\bar{\sigma}_{ox} = \frac{N_x}{h} - \frac{E}{1-\nu^2} (\mu_1 \epsilon_x - \chi_1 \kappa_x) \quad (2.19)$$

$$\bar{\sigma}_{oy} = \frac{N_y}{h} - \frac{E}{1-\nu^2} (\mu_2 \epsilon_y - \chi_2 \kappa_y)$$

The stress function which appears in eq. (2.2) is defined by

$$\frac{N_x}{h} = \frac{\partial^2 F}{\partial y^2} \quad (2.20)$$

$$\frac{N_y}{h} = \frac{\partial^2 F}{\partial x^2}$$

and thus eq. (2.19) takes the form

$$\bar{\sigma}_{ox} = \frac{\partial^2 F}{\partial y^2} - \frac{E}{1-\nu^2} (\mu_1 \epsilon_x - \chi_1 \kappa_x) \quad (2.21)$$

$$\bar{\sigma}_{oy} = \frac{\partial^2 F}{\partial x^2} - \frac{E}{1-\nu^2} (\mu_2 \epsilon_y - \chi_2 \kappa_y)$$

From Hook's law

$$\begin{aligned} E \epsilon_x &= \sigma_{ox} - \nu \sigma_{oy} \\ E \epsilon_y &= \sigma_{oy} - \nu \sigma_{ox} \end{aligned} \quad (2.22)$$

thus

$$\begin{aligned} \sigma_{ox} &= \frac{\partial^2 F}{\partial y^2} - \frac{E}{1-\nu^2} \left[\frac{\mu_1}{E} (\sigma_{ox} - \nu \sigma_{oy}) - \chi_1 K_x \right] \\ \sigma_{oy} &= \frac{\partial^2 F}{\partial x^2} - \frac{E}{1-\nu^2} \left[\frac{\mu_2}{E} (\sigma_{oy} - \nu \sigma_{ox}) - \chi_2 K_y \right] \end{aligned} \quad (2.23)$$

Solving eq.(2.23) for σ_{ox} and σ_{oy} using eq.(2.4) and the following notations

$$\begin{aligned} \bar{F} &= \frac{1}{\beta R h} \left(\frac{m\pi}{L} \right)^2 + \nu \frac{\chi_1}{h} \left(\frac{m\pi}{L} \right)^4 - \nu \frac{\chi_2}{h} \left(\frac{n}{R} \right)^4 - \\ &\quad - \left[(1+\mu_1) \frac{\chi_1}{h} + (1+\mu_2) \frac{\chi_2}{h} \right] \left(\frac{m\pi}{L} \right)^2 \left(\frac{n}{R} \right)^2 \end{aligned} \quad (2.24)$$

$$\begin{aligned} F_x &= \frac{1}{\mu_0} \left(\frac{m\pi}{L} \right) \cdot \bar{F} \cdot W_{m,n} \\ F_y &= \frac{1}{\mu_0} \left(\frac{n}{R} \right) \cdot \bar{F} \cdot W_{m,n} \end{aligned} \quad (2.25)$$

one obtains the following solution for the membrane stresses:

$$\begin{aligned} \sigma_{ox} &= -\beta \frac{E h}{1-\nu^2} \left[(1-\nu^2 \mu_1) F_x + (1-\nu^2 \mu_2) \frac{\chi_1}{h} \left(\frac{m\pi}{L} \right)^2 + \nu \mu_1 F_x \right. \\ &\quad \left. + \nu \mu_2 \frac{\chi_2}{h} \left(\frac{n}{R} \right)^2 \right] \end{aligned}$$

$$\begin{aligned} \sigma_{oy} &= -\beta \frac{E h}{1-\nu^2} \left[(1-\nu^2 \mu_1) F_x + (1-\nu^2 \mu_2) \frac{\chi_1}{h} \left(\frac{m\pi}{L} \right)^2 + \nu \mu_1 F_y \right. \\ &\quad \left. + \nu \mu_2 \frac{\chi_2}{h} \left(\frac{n}{L} \right)^2 \right] \end{aligned} \quad (2.26)$$

It should be noted that eq.(2.26) refers only to the contribution of the (m,n) mode to the total membrane stress.

The bending moments are obtained by multiplying eq.(2.11) by Z, and integrating it with respect to the thickness. Using the definitions

$$\begin{aligned} K_x &= -\frac{\partial^2 w}{\partial x^2} \\ K_y &= -\frac{\partial^2 w}{\partial y^2} \end{aligned} \quad (2.27)$$

the well known equations

$$\begin{aligned} \sigma_{bx} &= \frac{E h}{2(1-\nu^2)} \left[\frac{\partial^2 w}{\partial x^2} + \nu \frac{\partial^2 w}{\partial y^2} \right] \\ \sigma_{by} &= \frac{E h}{2(1-\nu^2)} \left[\frac{\partial^2 w}{\partial y^2} + \nu \frac{\partial^2 w}{\partial x^2} \right] \end{aligned} \quad (2.28)$$

are obtained.

Knowing σ_{ox} , σ_{oy} , σ_{bx} and σ_{by} , one can obtain from eqs.(2.12), (2.13) and (2.27)

$$\begin{aligned} \sigma_{xs} &= \sigma_{ox} - \nu \sigma_{oy} - 2 \frac{Z_{max}}{h} (\sigma_{bx} - \nu \sigma_{by}) \\ \sigma_{ys} &= \sigma_{oy} - \nu \sigma_{ox} - 2 \frac{Z_{max}}{h} (\sigma_{by} - \nu \sigma_{bx}) \end{aligned} \quad (2.29)$$

The maximum stress in the shell is obtained by adding the contributions of the membrane and bending stresses. It can be shown that the maximum stress in the shell appears in the opposite side to the stringer.

2.4 Mean Square Of Stresses

It was shown in ref.(7), and presented more clearly in ref. (8) that the mean square velocity of the r^{th} mode due to excitation with fluctuating pressure of spectral density $S_{pext}(\omega_r)$ is given by:

$$\langle v^2 \rangle = \frac{2 \pi^2 C S_{pext}(\omega_r)}{\rho \omega_r^2 \rho_m \bar{h} A} \cdot \frac{R_{rad}(r)}{2 R_{rad}(r) + R_{mech}(r)} \quad (2.30)$$

The acoustic radiation impedance in eq.(2.30) is given by

$$R_{rad}(r) = G(r) \rho C A \quad (2.31)$$

where $G(r)$ is the acoustic efficiency.

The mechanical impedance is given by

$$R_{mech}(r) = \eta_r \rho A h \omega_r \quad (2.32)$$

where η_r is the loss factor ($= 2 \zeta_r$, ζ_r being the damping coefficient).

Analysing a bandwidth $\Delta \omega$ around a center frequency ω_0 , and assuming that each quantity in eq.(2.30) is constant through the bandwidth $\Delta \omega$, the following expression is written for the mean square velocity of that band:

$$\langle v^2 \rangle = \frac{2 \pi^2 C S_{pext}(\omega_0) N}{\rho \omega_0^2 \rho_m \bar{h} A} \cdot \frac{R_{rad}(\omega_0)}{2 R_{rad}(\omega_0) + R_{mech}(\omega_0)} \quad (2.33)$$

where N is the number of modes within the bandwidth

The assumption of constant quantities throughout the band is justified when bandwidth is not too wide. 1/3 octave bandwidth was shown in the past

to yield good results.

As a result of eq.(2.33), the following equations are written for the mean square of accelerations and displacements, respectively:

$$\langle a^2 \rangle = \frac{2 \pi^2 C S_{\text{ext}} N}{\rho \rho_m \bar{h} A} \cdot \frac{R_{\text{rad}}}{2 R_{\text{rad}} + R_{\text{mech}}} \quad (2.34)$$

$$\langle w^2 \rangle = \frac{2 \pi^2 C S_{\text{ext}} N}{\rho \omega_0^4 \rho_m \bar{h} A} \cdot \frac{R_{\text{rad}}}{2 R_{\text{rad}} + R_{\text{mech}}} \quad (2.35)$$

by eqs.(2.26),(2.28),(2.29) and (2.35) the mean square values for the stresses are obtained:

$$\langle G_i^2 \rangle_r = \frac{2 \pi^2 C S_{\text{ext}}(r)}{\rho \omega_r^4 \rho_m \bar{h} A} \cdot \frac{R_{\text{rad}}(r)}{2 R_{\text{rad}}(r) + R_{\text{mech}}(r)} \sum_{i=1}^N q_i^2(m, n) \quad (2.36)$$

In these equations, r represents a given bandwidth with center frequency ω_r . The index i is

- 1 for stresses in \bar{x} direction
- 2 for stresses in y direction
- 3 for stresses in stringers
- 4 for stresses in rings.

The functions q_i are obtained from eqs.(2.26), (2.28) and (2.29) and are listed below:

$$q_x^{(1)} = \frac{BEh}{1-\nu^2} \left[(1-\nu^2+\mu_1)F_x + (1-\nu^2+\mu_1)\frac{\chi_1}{h} \left(\frac{m\pi}{L} \right)^2 + \nu\mu_1 F_x + \nu\mu_1 \frac{\chi_1}{h} \left(\frac{n}{R} \right)^2 \right]$$

$$q_y^{(1)} = -\frac{BEh}{1-\nu^2} \left[(1-\nu^2+\mu_1)F_x + (1-\nu^2+\mu_1)\frac{\chi_1}{h} \left(\frac{m\pi}{L} \right)^2 + \nu\mu_1 F_y + \nu\mu_1 \frac{\chi_1}{h} \left(\frac{m\pi}{L} \right)^2 \right]$$

$$q_x^{(2)} = \frac{Eh}{2(1-\nu^2)} \left[\left(\frac{m\pi}{L} \right)^2 + \nu \left(\frac{n}{R} \right)^2 \right] \quad (2.37)$$

$$q_y^{(2)} = \frac{Eh}{2(1-\nu^2)} \left[\left(\frac{n}{R} \right)^2 + \nu \left(\frac{m\pi}{L} \right)^2 \right]$$

$$q_1 = |q_x^{(1)}| + q_x^{(2)}$$

$$q_2 = |q_y^{(1)}| + q_y^{(2)}$$

$$q_3 = q_x^{(1)} - \nu q_y^{(1)} - 2 \frac{Z_{\text{max}}}{h} (q_x^{(2)} - \nu q_y^{(2)})$$

$$q_4 = q_y^{(1)} - \nu q_x^{(1)} - 2 \frac{Z_{\text{max}}}{h} (q_y^{(2)} - \nu q_x^{(2)}) \quad (2.38)$$

3. NUMERICAL EXAMPLES

3.1 General Data

The theory presented provides means for calculating the response in terms of stresses, while the following data must be given:

1. Geometry of the shell and stiffeners;
2. Material properties (for the shell and for the acoustic medium);
3. Damping coefficient of the structure, as function of the frequency;
4. Acoustic efficiency of the shell, as function of the frequency.

The last parameter is obtained by analysing the wavenumber diagram, as was done in (4) for unstiffened shells. For the numerical examples, the acoustic efficiency curves obtained in (4) were taken into account. In the near future, acoustic efficiency curves for stiffened shell will be available, by extending the computer program to include this calculation too. The damping coefficient γ , which was taken into account is described in Fig. 2. It is a line which lies between recommended values from refs. (9) and (10).

The analysis was done in 1/3 octave bandwidth, with external excitation of 160 DB across the whole spectrum, up to 25000 cps. This excitation is not a real one since it has high sound pressure levels in the high frequency regions. This was done in order to eliminate, in the calculations, the effects of external excitation, focusing the attention on the effects of the shell itself. The 160 DB level refers to 1/3 octave SPL, and one has to correct the input to true pressure levels by taking into account the given bandwidth.

3.2 Shell Data

Eleven unstiffened shells were calculated, in order to examine a wide range of shell geometry parameters. In order to create a common basis for comparison, most of the computed shells has the same ring frequency. The effect of different ring frequencies was examined on three examples.

Table I summarizes several properties of the calculated shells.

TABLE I: SUMMARY OF DATA

Aluminum, $\rho_m = 0.0000286 \frac{\text{kg}}{\text{cm}^3}$ $E = 0.7 \times 10^6 \text{ kg/cm}^2$

example	R Cm	L Cm	h Cm	R/h	L/R	Z_B	f_R Cps	f_C Cps
1	20	40	0.2	100	2	381	3960	5900
2	20	80	0.2	100	4	1526	"	5900
3	20	140	0.2	100	7	4675	"	5900
4	20	40	0.08	250	2	954	"	14750
5	20	80	0.08	250	4	3816	"	14750
5a	30	120	0.12	250	4	3816	2640	9833
5b	10	40	0.04	250	4	3816	7920	29500
6	20	140	0.08	250	7	11687	3960	14750
7	20	40	0.04	500	2	1908	"	29500
8	20	80	0.04	500	4	7632	"	29500
9	20	140	0.04	500	7	23373	"	29500

3.3 Results

The calculation give numerous results in terms of stresses, velocities, accelerations, transmission ratios and noise reduction. The latter was calculated using smoothed results of ref.(9) for absorption coefficients. As representative results, the power spectral density function of stresses in axial and circumferential directions are shown in Figures 3-5. Noise reduction spectrum is shown in Fig.7. The root mean square values of several parameters are tabulated in Figures 3-5, and plotted in Figures 7 and 8. The effect of axial force (tension and compression) was examined on shell No.5, and the results are shown in Fig.9. The influence of S on noise reduction was of no significance, inspite of the qualitative analysis presented in (6). The effect of the change in ring frequency (keeping the nondimensional geometric parameters constant) was also examined on shell no.5. Results are presented in Fig. 10.

3.4 Discussion of Numerical Results

Figures 3-5 show some interesting results on the influence of shell geometry on the PSD of the stresses. In the low frequency regions ($f \ll f_R$) irregularity of results can be seen. This is due to the small number of modes involved in the low frequencies. As frequency increases the PSD of stresses increasingly depends on the value R/h, but independant of the ratio L/R. The PSD levels themselves increase as the ratio R/h increase. It should be noticed that this occurs only for shells with the same ring frequency. For shells of the same nondimensional geometric parameters, but with different dynamic parameters (ring frequency and coincidence frequency) one can see, from Fig. 10, that for larger cylinder lower stresses were obtained, for a given input. This is due to the increased thickness of that shell, regardless of the increased number of modes which participate

in the response motion.

An interesting numerical result can be seen in Fig.7, for the very thin and long shell: There is a decrease in the total rms values of stresses beyond a certain value of L/R. No physical explanation has yet been found to this numerical result, and no effort was made, at this stage, to generalize this phenomena in terms of geometric or dynamic parameters. It is suspected that this happens due to the fact that the very thin shell ($R/h = 500$) is the only one in which the coincidence frequency is higher than the maximum frequency taken into account in the calculation. One has to bear in mind that constant excitation input over such a large frequency range is unreal, and in practical cases there is a significant attenuation in input levels at frequencies higher than few thousands cycles pe second.

4. CONCLUDING REMARKS

The theoretical tool presented enables the structural dynamics engineer to predict the magnitude of the expected levels of stresses in the shell. It can be seen from the numerical examples that for some cases, which are of practical use in aeronautical structures, significant levels are predicted. These levels are to be taken into account in the prediction of acoustic fatigue life of the system. More research efforts are to be invested in order to include, in the numerical tool, the automatic computation of acoustic efficiency, and in order to verify the theoretical analysis by experimental means.

5. REFERENCES

1. Baruch, M., Singer, J., Effect of eccentricity of stiffeners on the general instability of stiffened cylindrical shells under hydrostatic pressure. *J. Mech. Eng. Sci.* 5 23 (1963)
2. Singer, J., Baruch, M., Harari, O., On the instability of eccentrically stiffened cylindrical shells under axial compression. *Int. J. Solids & Struc.* 3 (1967), pp. 445-470.
3. Maymon, G., On the dynamic elastic buckling of stiffened and unstiffened cylindrical shells under axial impact, Technion D.Sc. Thesis, 1974.
4. Szechenyi, E., Modal densities and radiation efficiencies of unstiffened cylinders using statistical methods, *J. of Sound and Vibrations* 19, 1, (1971) pp. 65-81.
5. Rosen, A., Singer, J., Vibration of axially loaded stiffened cylindrical shells, *J. of Sound and Vibration*, 34 3, (1974) pp. 357-378.
6. Maymon, G., Modal densities of stiffened, axially loaded cylindrical shells, *J. of Sound and Vibration*, 42, 4, (1975) pp. 115-127.
7. Smith, P.W. Jr., Response and radiation of structural modes excited by sound, *J. of the Acous. Soc. of America*, 34, 5, 1963, pp. 640-647.
8. Szechenyi, E., Sound transmission through cylinder walls using statistical considerations, *J. of Sound and Vibration* 19, 1, (1971), pp. 83-94.
9. Cummins, R.J., Sound transmission into cylinders, ISVR M.Sc. Thesis, (1970).
10. Fahy, F.J., Statistical energy methods, *The Shock and Vibration Digest*, 6, 7, (1974).

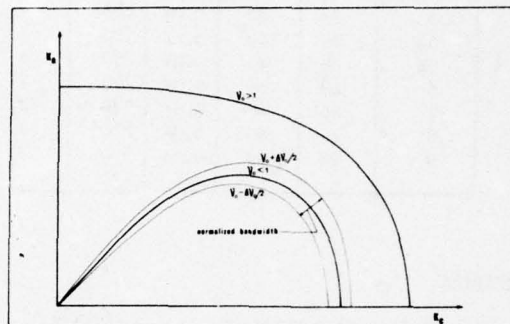


Fig. 1: Wavenumber diagram

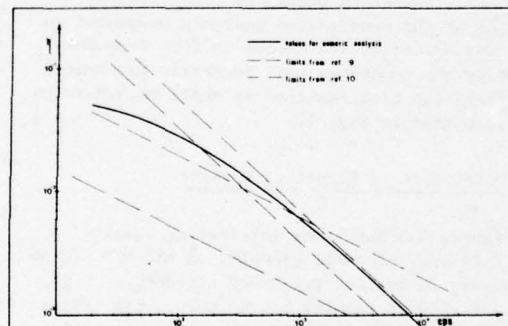


Fig. 2: Loss factor for numerical examples

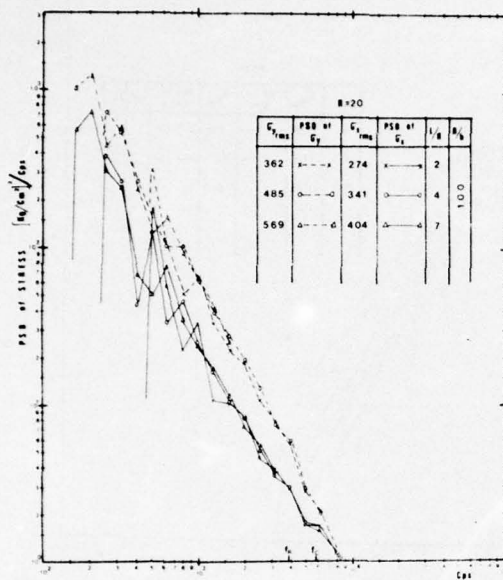


Fig. 3: Effects of L/R on PSD of stresses for shells with $R/h=100$.

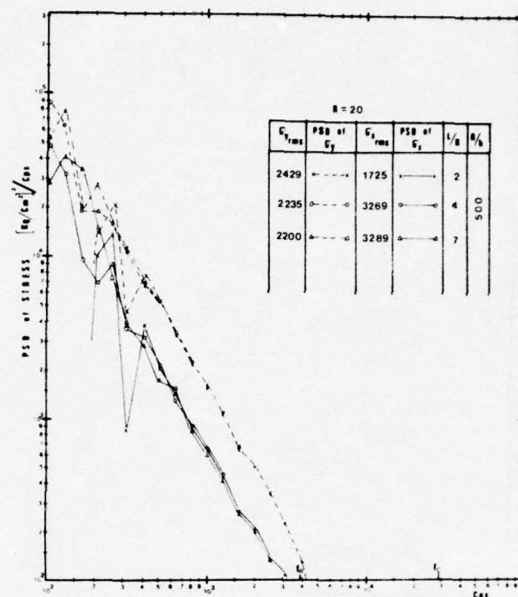


Fig. 5: As fig. 3, for $R/h=500$.

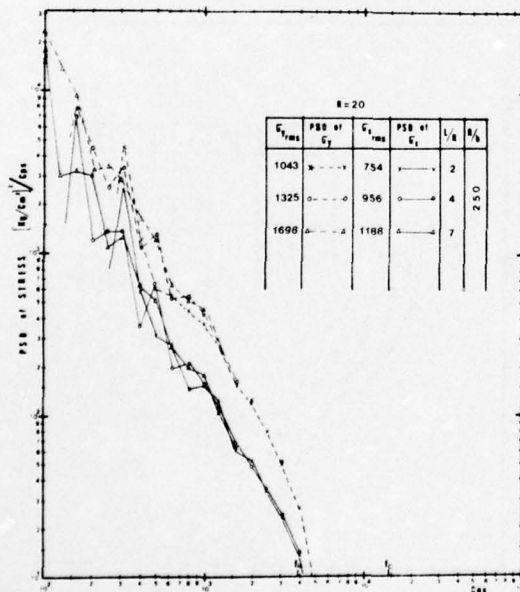


Fig. 4: As fig. 3, for $R/h=250$.

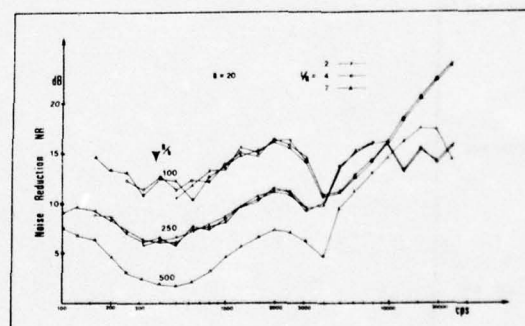


Fig. 6: Noise reduction for several shells

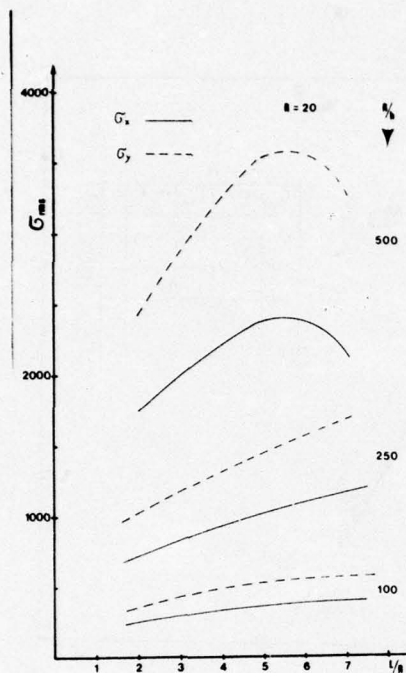


Fig. 7: Rms values for stresses

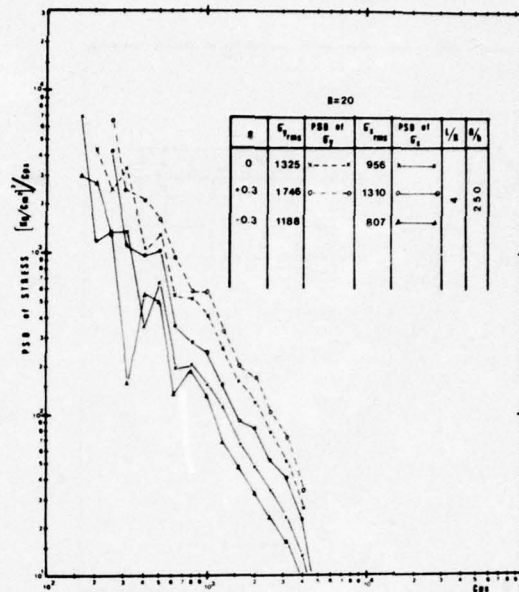


Fig. 9: Effects of axial stress (S) on PSD of stresses

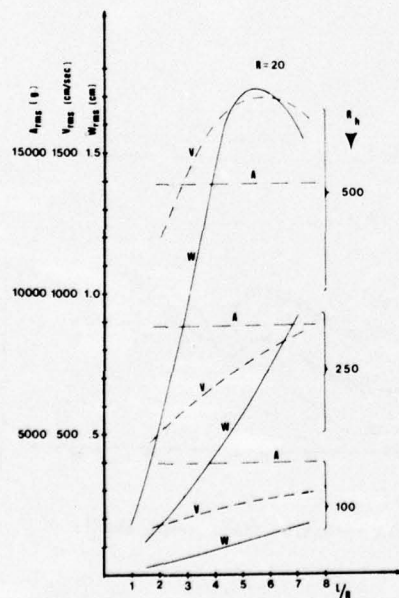


Fig. 8: Rms values for displacements, velocities and accelerations

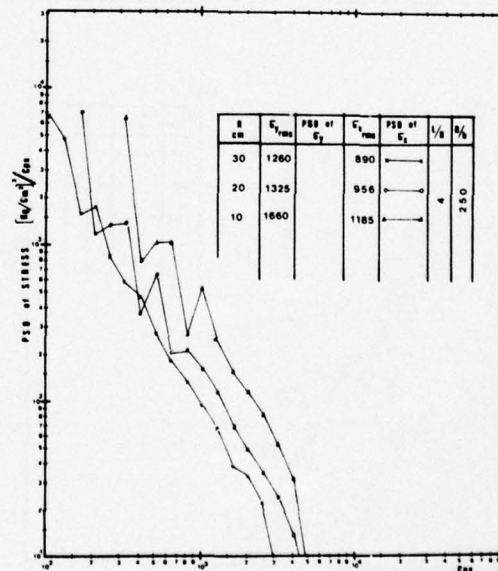


Fig. 10: Effect of radius on PSD of stresses

Discussion

Mr. Henderson (Air Force Materials Lab): I'm left with the impression that your theory is more valid for the higher wave numbers, that is as you increase the number of node lines around the circumference it would be more valid. Do you have any feel for how this effects your assumption of smearing, particularly the stringers, and at what point these two opposing views get to the point that you have to start considering discrete stringers?

Mr. Maymon: There were several works done in the Technion and it was the conclusion that you have to have at least two stiffeners for a wave length in order that you will be able to do the smearing analysis with logical results. So that is one limitation of the analysis. But nevertheless we felt that if you have a closed form solution, and this is a closed form solution in a way, we will be able to see the trends which affect the phenomena and that is why I said that more research needs to be invested in the problem.

ANALYSIS OF SPACE FRAMEWORKS CONTAINING CURVED BEAMS

Michael A. Cassaro and Mario Paz
University of Louisville
Louisville, Kentucky

In the general analysis of structures complications arise in the determination of the internal forces and performance of curved beam elements. These complications result from the difficulty in establishing the elastic and inertial properties for curved beam elements. It is a fact that even a simple loading on a curved beam in space tends in general to produce components of each element of the state vector, including torsion, shear, bending, axial forces, and the associated displacements. In most analyses which idealize the curved beam by projecting it onto the horizontal plane, some force components are eliminated from the analysis, and others are significantly effected. Further idealization of the general curved beam to a straight beam results in gross inaccuracies in many cases.

This paper presents a study of the analysis of curved beams in space by use of the transfer method. The analysis is capable of handling beams having additional distortions such as built-in twist with respect to the longitudinal axis, as well as coordinate transformations producing super-elevation and inclination of the beam axis. Comparisons are made between internal forces produced in straight beams and curved beams to evaluate the effects of beam curvature and the additional distortions of built-in twist, super-elevation and beam inclination.

INTRODUCTION

In the general analysis of structures complications arise in the determination of the internal forces and performance of curved beam elements. These complications result from the difficulty in establishing the elastic and inertial properties for curved beam elements. It is a fact that even a simple loading on a curved beam in space tends in general to produce components of each element of the state vector, including torsion, shear, bending, axial forces, and the associated displacements. In most analyses which idealize the curved beam by projecting it onto the horizontal or vertical planes, some force components are eliminated from the analysis, and others are significantly effected. Further idealization of the general curved beam to a straight beam results in gross inaccuracies in many cases.

This paper presents a study of the analysis of curved beams in space by use of the transfer method. The general transfer matrix is developed in numerical form to include curved beams with horizontal and vertical curvature. The

analysis is capable of handling beams having additional distortions such as built-in twist with respect to the longitudinal axis, as well as coordinate transformations producing super-elevation and inclination of the beam axis. Comparisons are made between internal forces produced in straight beams and curved beams to evaluate the effects of beam curvature and the additional distortions of built-in twist, super-elevation and beam inclination.

As it is well known, the transfer matrix method is most effective for chain type structures in which the structural elements are arranged in sequence with no branches. This limitation of the method may be overcome, and the advantages for analysis of framed structures containing curved beam elements may still be realized by developing the stiffness matrix from the transfer matrix between branch points.

The transfer matrix expresses the state vector (equation (1)) at one section of a beam in terms of the state vector at another section. The state vector at a section in a beam is defined as a column vector the components of

which are the displacements and the corresponding internal forces at the section. Once the transfer matrix is obtained for the general curved beam, it is a routine matter to perform a static or dynamic analysis to determine forces, displacements, natural frequencies, etc.

$$Z_i = \{u \ v \ -w \ \theta_x \ \theta_y \ \theta_z \ M_x \ M_y \ T \ V_x \ -V_y \ N\}_i \quad (1)$$

The sign convention uses the right-hand cartesian coordinate system with the x-axis coinciding with the centroidal axis of the elastic member. Positive displacements coincide with positive directions of the coordinate system, and forces are positive when acting as shown in Figure 1.

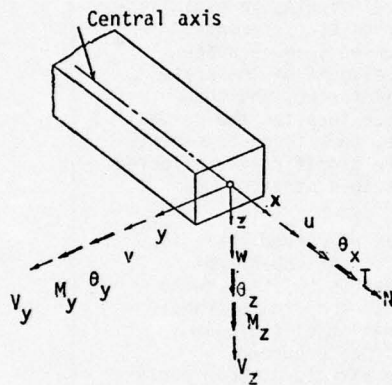


Fig. 1. Beam Coordinate System With Vector Notations.

The Transfer Matrix method of analysis for beam systems is thoroughly described by Pestel and Leckie (1). Therefore, only a brief discussion is presented here to provide sufficient clarity for the use of the method in analysis of space frames.

To illustrate the concept for application of the transfer matrix consider the bending of a simple straight beam element vibrating in the x-z plane. The differential equations defining the flexural behavior are expressed in matrix form by equation (2);

$$\frac{dz}{dx} = Az \quad (2)$$

where z is the state vector and A is a matrix of coefficients in the system of equations. In its complete form equation (2) is,

$$\frac{d}{dx} \begin{bmatrix} -w \\ \theta_y \\ M_y \\ V_z \end{bmatrix} = \begin{bmatrix} 0 & 1 & 0 & 0 \\ 0 & 0 & \frac{1}{EI_y} & 0 \\ 0 & 0 & 0 & 1 \\ \mu\omega^2 & 0 & 0 & 0 \end{bmatrix} \begin{bmatrix} -w \\ \theta_y \\ M_y \\ V_z \end{bmatrix} \quad (3)$$

where: E is the elastic modulus of the beam material,

μ is the mass per unit length,

ω is the vibrating frequency, and

I is the moment of inertia of the cross section.

In the analysis of a general curved beam in space, the entire state vector given by equation (1) is required. The expanded form of equation (2) for the general curved beam contains the matrix of coefficients A , as given by Pestel and Leckie (1), and shown in the Appendix.

THE TRANSFER MATRIX

The solution of equation (2) for a beam segment of length L between end points a and b is,

$$Z_b = e^{AL} Z_a = U_B Z_a \quad (4)$$

In equation (4) the matrix e^{AL} is the beam transfer U_B relating the state vectors at section a and b in the beam. Most direct methods for solution of equation (2) to find the transfer matrix U_B fail when the elements of matrix A are variables of the space coordinates or when it becomes impossible to find the eigenvalues of the matrix A . In that event, for the case of the general curved beam, the transfer matrix can be readily determined by applying the Runge-Kutta method (1). The procedure requires the numerical integration of the function over the range from a to b in the beam as shown in Figure 2.

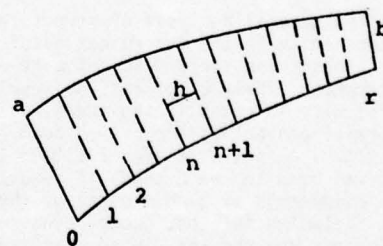


Fig. 2. The Subdivision of the Interval Between Sections a and b .

The interval is subdivided into smaller elements of length h along the central axis of the element. By selecting matrix A to be constant for any sub-element (i.e., from n to $n+1$), equation (4) becomes,

$$Z_{n+1} = \left[I + \frac{Ah}{1!} + \frac{(Ah)^2}{2!} + \frac{(Ah)^3}{3!} + \frac{(Ah)^4}{4!} \right] Z_n \quad (5)$$

The complete transfer from section a to section b in Figure 2 is obtained by successive multiplication of the subelement transfers yielding the beam transfer U_B .

$$Z_b = [U_1 U_2 \dots U_r] Z_a = U_B Z_a \quad (6)$$

FRAME ANALYSIS - DETERMINATION OF MEMBER STIFFNESS MATRIX

Space frames may be analyzed by using the transfer matrix to determine the stiffness matrix for the curved beam members. The construction is performed numerically in the computer. As given by equation (1), the state vector at a section of beam contains displacement and force components. The first six elements in the state vector represent the displacement vector and the second group of six elements represent the force vector. Equation (6) represents a system of twelve equations from which any combination of twelve elements in the state vectors at the ends of a member may be determined as a function of the remaining twelve elements at the ends. The member stiffness matrix is numerically obtained within the computer by successively setting all the elements except one in the displacement vectors in equation (6) equal to zero. The displacement component not set equal to zero is given a value of unity. Equation (7) illustrates the procedure for the condition $\theta_y = 1$ at end b. The force vectors for the beam sections at a and b as computed from equation (7) are the elements in the column of the member stiffness matrix corresponding to the unit displacement assigned.

$$\begin{bmatrix} 0 \\ 0 \\ 0 \\ 0 \\ 1 \\ 0 \\ 0 \\ M_z \\ M_y \\ T \\ V_z \\ -V_y \\ N \end{bmatrix}_b = U_B \begin{bmatrix} 0 \\ 0 \\ 0 \\ 0 \\ 0 \\ 0 \\ 0 \\ M_z \\ M_y \\ T \\ V_z \\ -V_y \\ N \end{bmatrix}_a \quad (7)$$

In like manner, the process is repeated for the remaining eleven displacement components and the entire stiffness matrix may be systematically computed.

Construction of the structure stiffness matrix from the member stiffnesses is accomplished by conventional methods.

DETERMINATION OF EQUIVALENT MEMBER END FORCES

The transfer matrix may be used to compute end equivalent forces in members subjected to applied forces. To illustrate the method, consider a beam element acted upon by a concentrated force as shown in Figure 3. The transfer from points a to d in the beam may simply be accommodated by considering the segment b-c to be a point containing the applied force F. The point transfer matrix is a unit matrix extended to include the point loads in the thirteenth column. The state vector is also extended to include unity in the thirteenth element. A point force may be similarly applied in any of the six coordinates at a beam section by simply including the magnitude of the applied force in the appropriate position (7th to 12th rows) in the thirteenth column of the extended point transfer matrix, U_F . The force transfer, U_F , from b to c is completely described by Pestel and Leckie (1) and for convenience is shown in equation (8).

$$\begin{bmatrix} u \\ v \\ -w \\ \theta_x \\ \theta_y \\ \theta_z \\ M_z \\ M_y \\ T \\ V_z \\ -V_y \\ N \\ 1 \end{bmatrix}_c = \begin{bmatrix} 1 & & & & & & & & & & & 0 \\ & 1 & & & & & & & & & & 0 \\ & & 1 & & \text{zero} & & & & & & & 0 \\ & & & 1 & & & & & & & & 0 \\ & & & & 1 & & & & & & & 0 \\ & & & & & 1 & & & & & & 0 \\ & & & & & & 1 & & & & & 0 \\ & & & & & & & 1 & & & & 0 \\ & & & & & & & & 1 & & & 0 \\ & & & & & & & & & 1 & & -F \\ & & & & & & & & & & 1 & 0 \\ & & & & & & & & & & & 1 & 0 \\ & & & & & & & & & & & & 1 \end{bmatrix} \begin{bmatrix} u \\ v \\ -w \\ \theta_x \\ \theta_y \\ \theta_z \\ M_z \\ M_y \\ T \\ V_z \\ -V_y \\ N \\ 1 \end{bmatrix}_b \quad (8)$$

or

$$Z_c = U_F Z_b \quad (9)$$

The complete transfer for the beam is obtained by successive multiplication of the extended beam and point transfer matrices as prescribed by equation (10).

$$Z_d = U_B^{ab} U_F^{bc} U_B^{cd} Z_a = U Z_a \quad (10)$$

Equivalent end forces are computed from equation (10) by setting the displacement in the vectors Z_a and Z_d equal to zero and solving for the force vectors at the positions a and d.

DETERMINATION OF NATURAL FREQUENCIES

The usual procedure used in a finite element analysis for determination of natural frequencies from the frequency equation (11),

$$(K - \omega^2 M) y = 0 \quad (11)$$

is not convenient when the dynamic matrix is obtained from the transfer matrix by the numerical methods discussed earlier. As seen from equation (5), the transfer matrix for a beam contains components of the natural frequency in every term of the matrix in a polynomial form as given by,

$$U_{ij} = a_{ij} + b_{ij}\lambda + c_{ij}\lambda^2 + d_{ij}\lambda^3 + \dots \quad (12)$$

In equation (12) a_{ij} , b_{ij} , ... represent numerical constants and λ represents the square of the natural frequency, ω^2 .

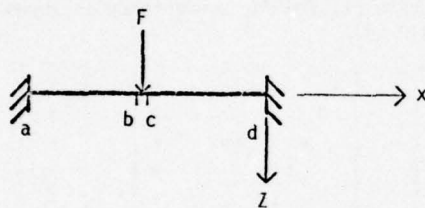


Fig. 3. Loaded Beam

Two methods are available for determination of frequency response of vibrating structures. When the forcing frequency is known, there is not a need to find all the natural frequencies of the framework. It is more convenient to determine whether a natural frequency exists within certain frequency ranges which bound the forcing frequencies. The frequency determinant can be evaluated for values of frequency ω within the selected frequency range in a search procedure as illustrated in Figure 4. A thorough description of this method is provided in Reference 1.

Where the natural frequencies must be found as, for example, in the case of impulsive loadings, the exact dynamic stiffness matrix does not offer a convenient method for solution. It can be shown that the transfer U_{ij} from the Runge-Kutta solution given by equation (5), is the fourth order approximation of the infinite series expansion of the exact transfer given by equation (4). Paz (2) has shown that the elements of the dynamic matrix formed using the finite element method, as given by equation (11), are the second order approximation in a Taylor Series expansion of the corresponding coefficients in the exact dynamic matrix.

It is possible to reduce the elements of the quasi-exact dynamic matrix developed from the transfer matrix to a form similar to the

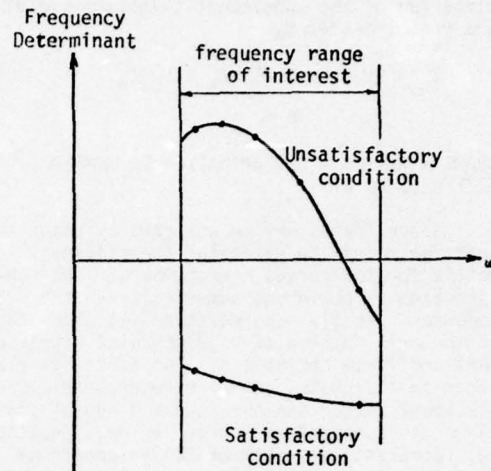


Fig. 4. Plot of Frequency Determinant

dynamic matrix obtained by the finite element method. When all members in the structure, including curved beam members, are expressed in finite element form a typical eigenvalue problem results. The solution for natural frequencies may then be performed by conventional methods of matrix analysis.

To illustrate the reduction of the quasi-exact dynamic matrix to a finite element form consider the member stiffness matrix computed as described from the transfer matrix. Each element of the stiffness matrix expressed as a number, represents the series,

$$\left[K_{ij} - \sum_{n=1}^{\infty} (M_{ij})_n \omega^{2n} \right] = S_{ij} \quad (13)$$

where S_{ij} is the dynamic stiffness element in the i th row, j th column,

K_{ij} and $(M_{ij})_1$ are respectively the stiffness and consistent mass coefficients and $(M_{ij})_n$ ($n=2,3,\dots$) higher order mass coefficients.

It is required to solve for K_{ij} and $(M_{ij})_1$, in each element to reduce the dynamic stiffness matrix to the standard finite element form given by equation (11).

The reduction of equation (13) to the finite element form is accomplished by successive substitution of selected values of frequency (e.g.; $\omega = 0,1,2$) into the coefficient matrix A (see Appendix) when constructing the dynamic stiffness matrix in which the term represented by equation (13) is one of the elements. When ω is set equal to zero in the

construction, the static stiffness coefficients K_{ij} are found directly. By manipulation of the values of S_{ij} computed using the selected values of ω it is possible to extract the value $(M_{ij})_1$, the consistent mass coefficient. The procedure is repeated for each element resulting in a dynamic stiffness matrix in the form given in equation (11) from which the natural frequencies are readily found.

APPLICATION OF THE TRANSFER MATRIX TO ANALYSIS OF FRAMED STRUCTURES

The solution of space frameworks containing curved beams may be obtained using a numerical determination of the curved member dynamic stiffness matrix discussed in the previous sections. It is interesting to examine the influence of beam curvature on the equivalent end forces. Stiffnesses will be similarly affected.

For comparison, the end forces are illustrated as a proportion of the equivalent end force in a straight beam of equal span, subjected to the same loading. Figures 5 to 16 consider the influence of such factors as the ratio of initial radius of curvature to span length (R/L), inclined beam axes (α, β), and twist rate of central axis (σ).

Any type of beam curvature may be analyzed by the method presented; however, for convenience circular curved beams are illustrated. The extent of beam curvature may vary over a wide range. The amount of curvature is usually described by the angle subtended by the radii to the beam ends. For example, a complete 180° curve represents a ratio $R/L = 0.5$, whereas a relatively small curve of 10° corresponds to a ratio $R/L = 5.75$. All members in the analysis are subjected to a concentrated load at midspan.

Figures 5 and 6 illustrate the bending moments about the y-axis of fixed end beams as a ratio of moment in curved beam to corresponding moment in a straight beam with the same span length. The load is applied transverse to the plane of beam curvature. The beam is subjected to various degrees of inclination by rotating about its y-axis (β) placing the beam ends at different elevation, and is also subjected to initial twist of its centroidal axis (σ). The effect of these geometric variations are illustrated in Figure 5 for beams with large degrees of initial curvature and in Figure 6 for beams with small initial curvature.

Figures 7 and 8 show the influence of rotation of the longitudinal axis (α) producing superelevation of the beam. The beam ends are maintained at the same elevation. Figures 9

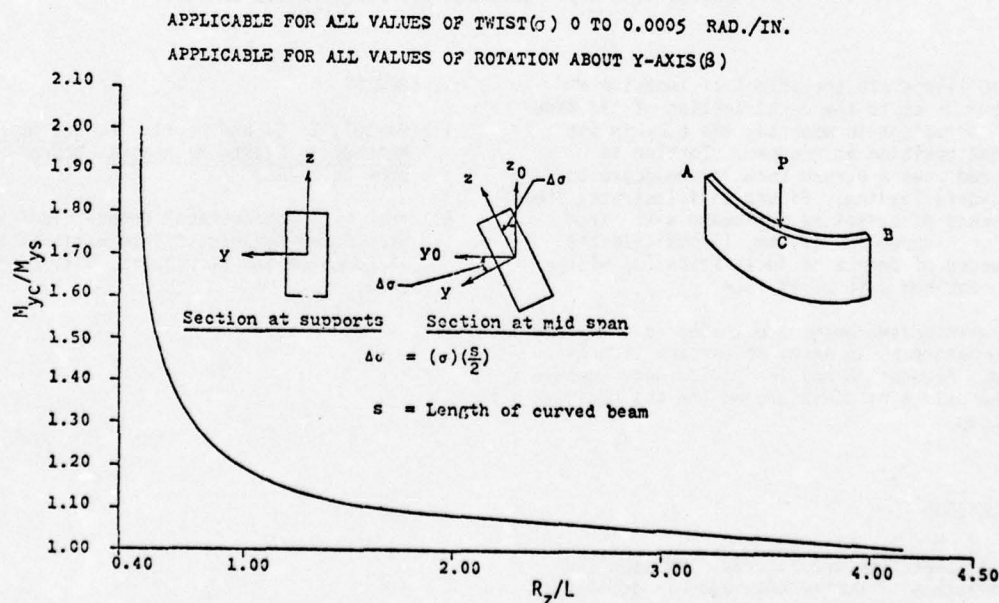


Fig. 5. Support Ratios for Fixed End Beams Transversely Loaded at Midspan for Varying R_z/L

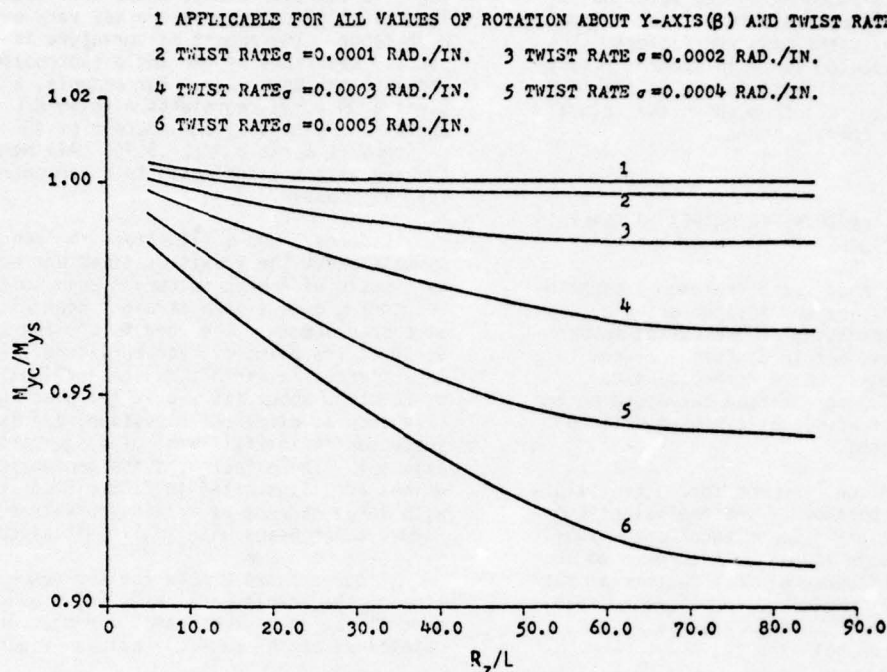


Fig. 6. Support Moment Ratios for Fixed End Beams Transversely Loaded at Midspan Extended for Large Ratios of R_2/L

and 10 illustrate the effect of imposing a uniform twist to the cross section of the same beam sufficient to maintain the beam in its upright position at midspan. Torsion is produced when a curved beam is subjected to transverse loading. Figure 11 illustrates the influence of curvature for beams with large radii. Figures 12, 13, and 14 indicate the influence of degree of inclination (β) of the beam combined with twist rate (σ).

When curved beams are loaded in the plane of curvature as an arch, no torsion is produced. Figures 15 and 16 provide some measure of the effect of curvature on the end moments produced.

CONCLUSIONS

As seen from the figures, the magnitude of influence of curved beam axes is greatest for small ratio of R/L . However, curvature may produce as much as a ten to twenty percent difference over straight beam analysis for a wide range of values of R/L .

REFERENCES

1. Pestel, E. C. and Leckie, F. A., Matrix Methods in Elasto Mechanics, McGraw-Hill Book Co., 1963.
2. Paz, M., "Mathematical Observations in Structural Dynamics," International Journal of Computer and Structures, Vol. 3, March 1973.

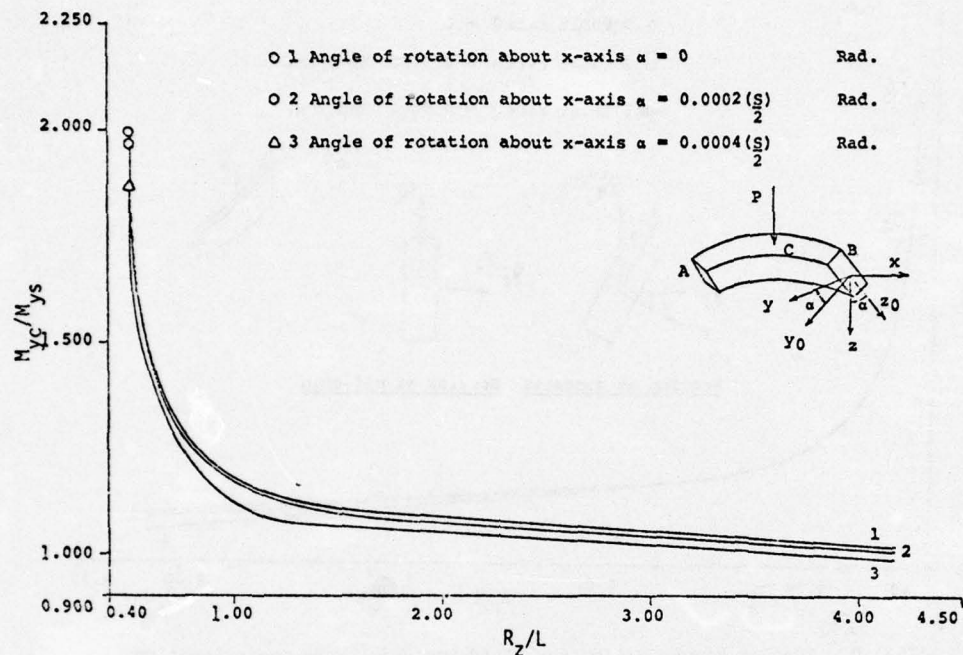


Fig. 7. Support Moment Ratios for Fixed End Beams With Superelevation Transversely Loaded at Midspan

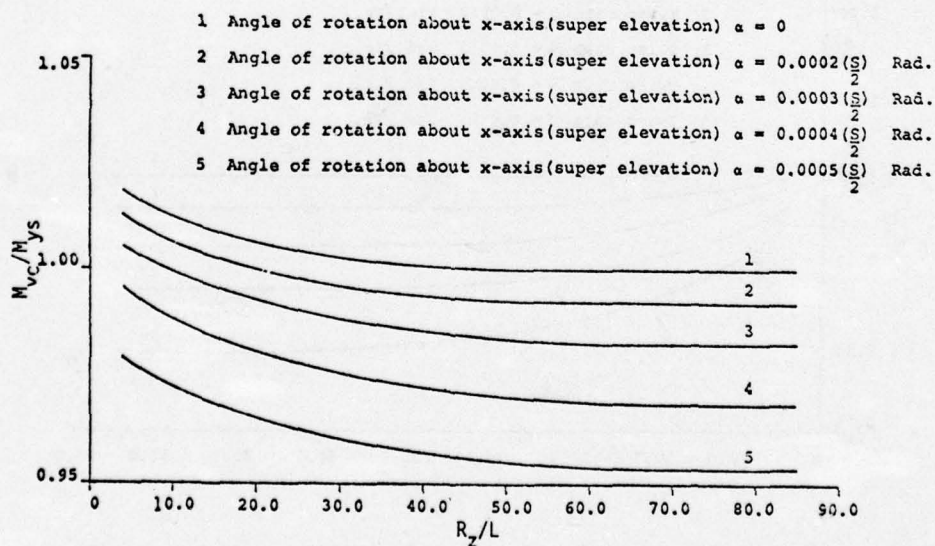


Fig. 8. Support Moment Ratios for Beams Represented in Figure 7 Extended for Large Ratios of R_z/L

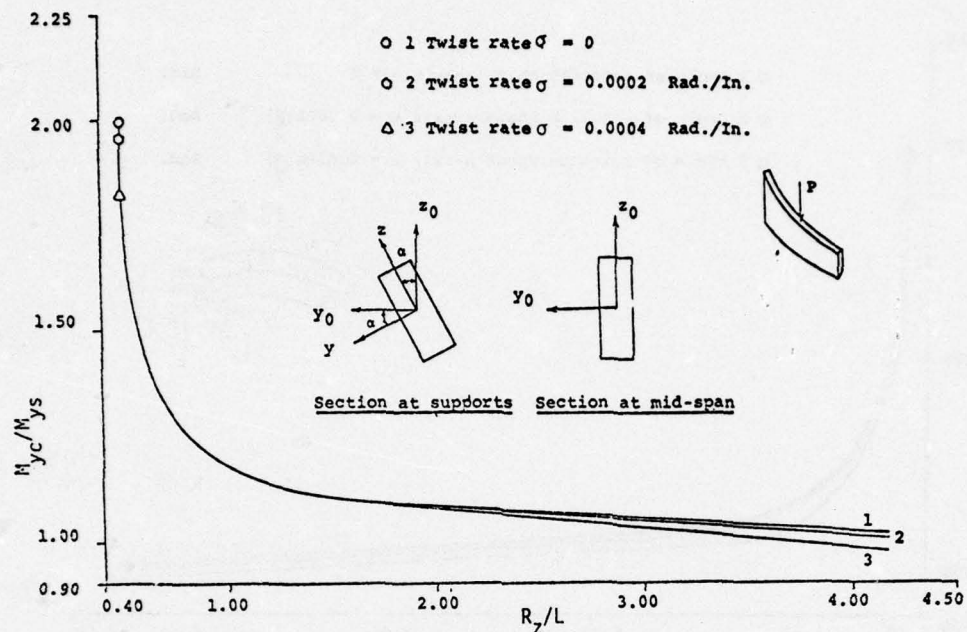


Fig. 9. Support Moment Ratios for Fixed End Beams With Superelevation Compensated by Uniform Twist to Provide Upright Position at Midspan

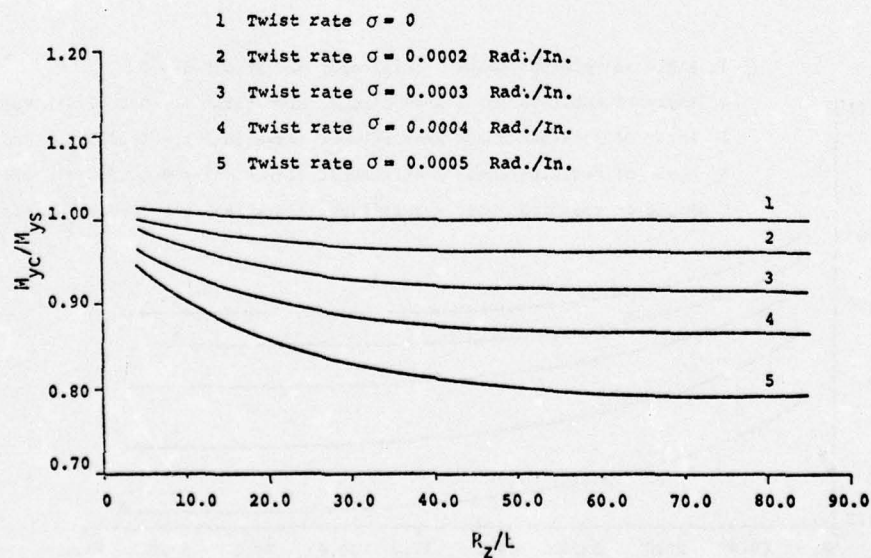


Fig. 10. Support Moment Ratios for Beams Represented in Figure 9 Extended for Large Ratios of R_z/L

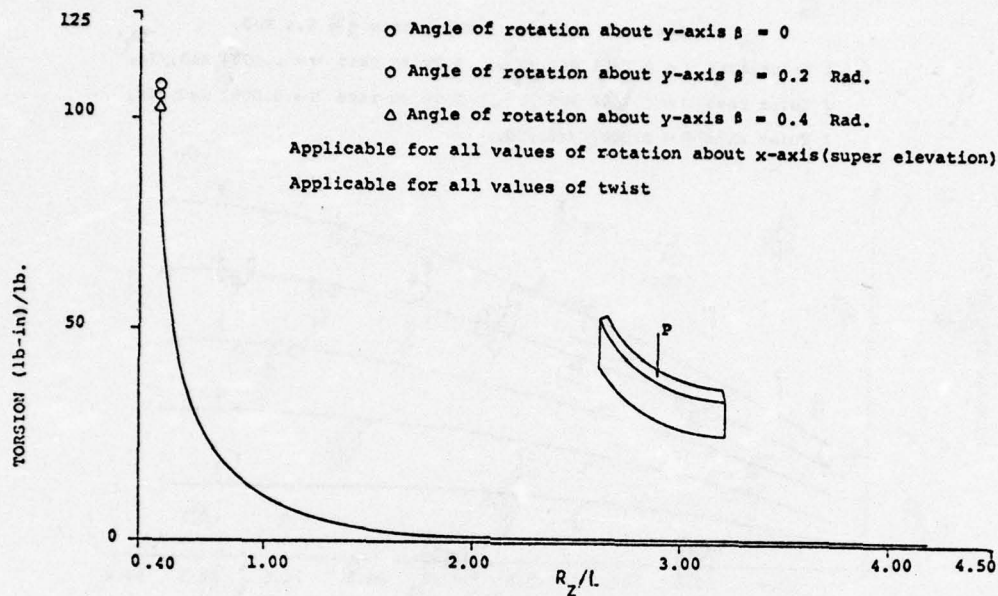


Fig. 11. Support Torsion in Fixed End Beams Transversely Loaded at Midspan for Varying R_z/L

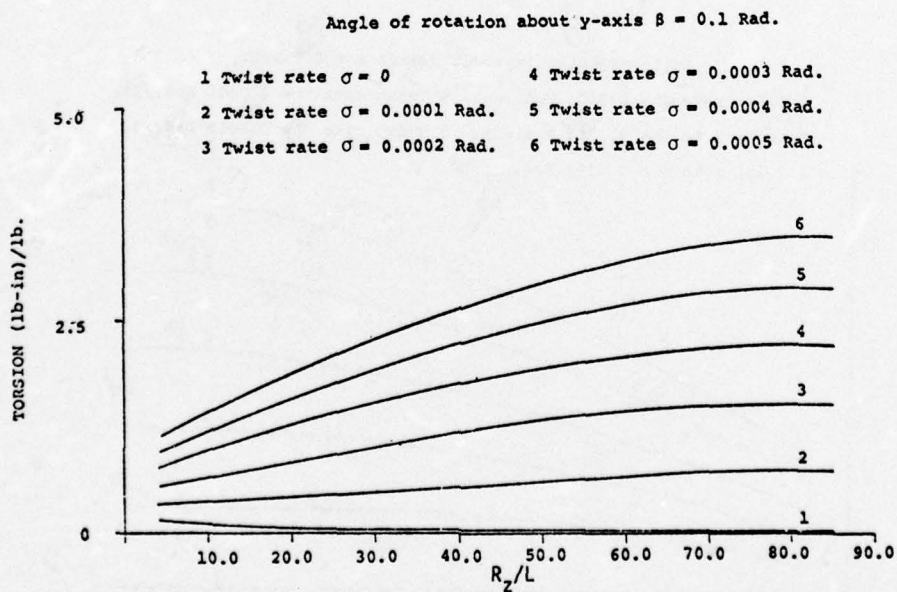


Fig. 12. Support Torsion in Beams Represented in Figure 11 With Rotation About y-Axis Equal to 0.1 Radian

Angle of rotation about y-axis $\beta = 0.4$ Rad.

- 1 Twist rate $\sigma = 0.0001$ Rad./In. 4 Twist rate $\sigma = 0.0004$ Rad./In.
 2 Twist rate $\sigma = 0.0002$ Rad./In. 5 Twist rate $\sigma = 0.0005$ Rad./In.
 3 Twist rate $\sigma = 0.0003$ Rad./In.

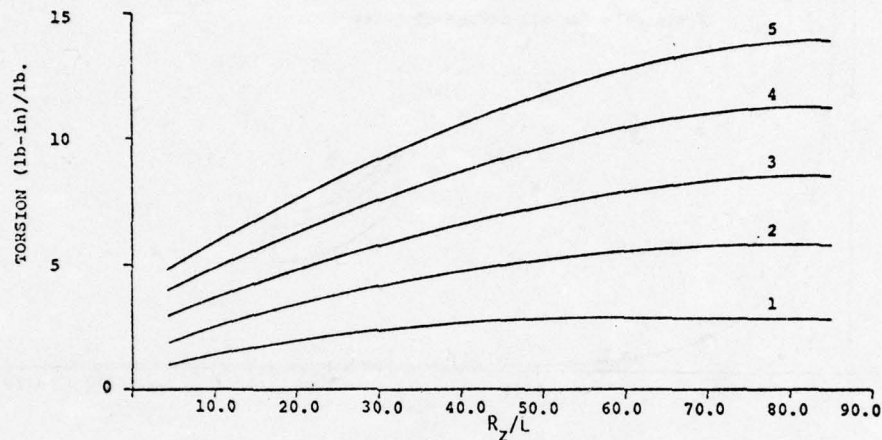


Fig. 13. Support Torsion in Beams Represented in Figure 11
 With Rotation About y-Axis Equal to 0.4 Radian

Angle of rotation about y-axis $\beta = 0.7$ Rad.

- 1 Twist rate $\sigma = 0.0001$ Rad./In. 4 Twist rate $\sigma = 0.0004$ Rad./In.
 2 Twist rate $\sigma = 0.0002$ Rad./In. 5 Twist rate $\sigma = 0.0005$ Rad./In.
 3 Twist rate $\sigma = 0.0003$ Rad./In.

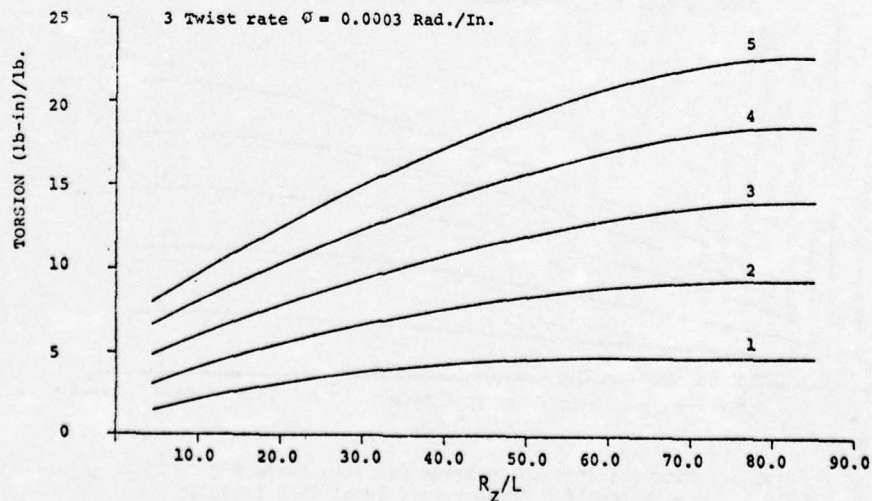


Fig. 14. Support Torsion in Beams Represented in Figure 11
 With Rotation About y-Axis Equal to 0.7 Radian

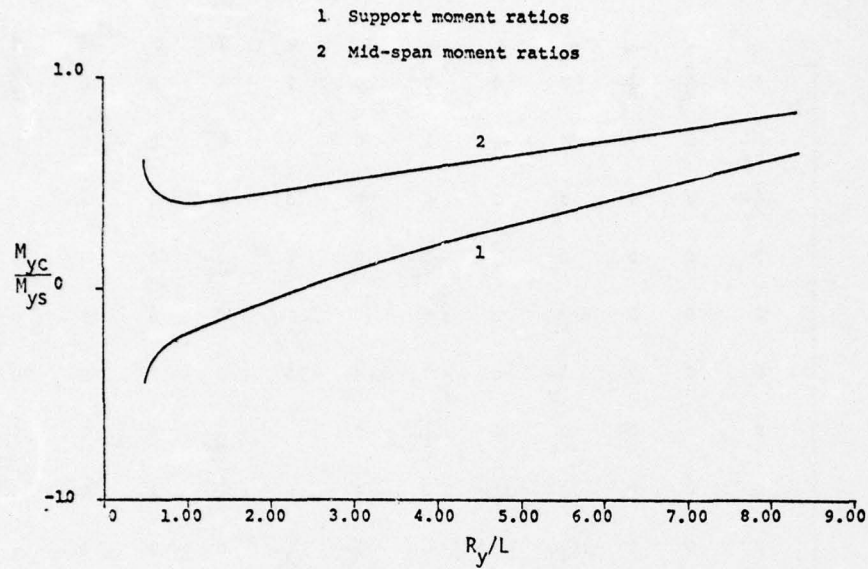


Fig. 15. Moment Ratios in Fixed End Beams Loaded at Midspan as an Arch

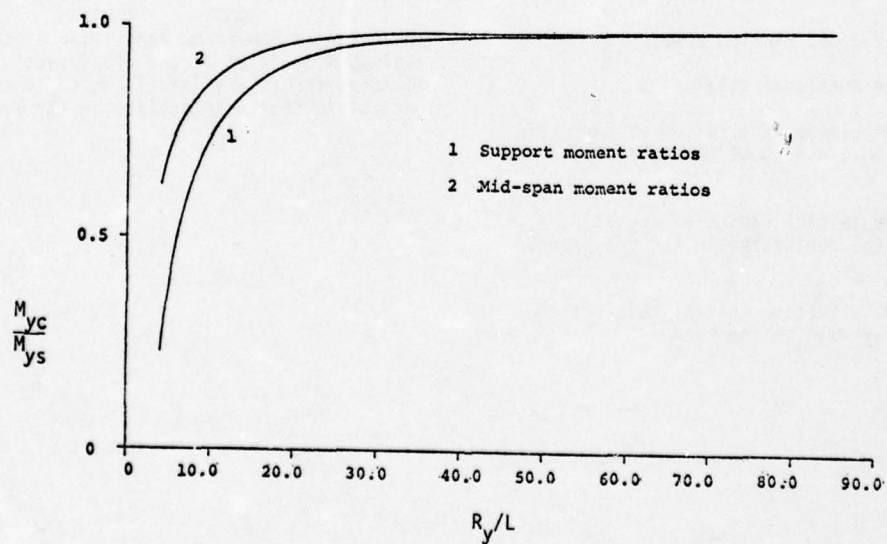


Fig. 16. Moment Ratios in Beams Represented in Figure 15 for Extended Values of R_y/L

APPENDIX: MATRIX A OF COEFFICIENTS OF THE
STATE VECTOR

$$A = \begin{bmatrix} u & v & -w & \theta_x & \theta_y & \theta_z & M_z & M_y & T & V_z & -V_y & N \\ 0 & \frac{1}{R_z} - \frac{1}{R_y} & 0 & 0 & 0 & 0 & 0 & 0 & 0 & 0 & 0 & \frac{1}{EA} \\ -\frac{1}{R_z} & 0 & -\sigma & 0 & 0 & 1 & 0 & 0 & 0 & 0 & 0 & 0 \\ \frac{1}{R_y} & \sigma & 0 & 0 & 1 & 0 & 0 & 0 & 0 & 0 & 0 & 0 \\ 0 & 0 & 0 & 0 & \frac{1}{R_z} & \frac{1}{R_y} & 0 & 0 & \frac{1}{GJ_T} & 0 & 0 & 0 \\ 0 & 0 & 0 & -\frac{1}{R_z} & 0 & \sigma & 0 & \frac{1}{EI_y} & 0 & 0 & 0 & 0 \\ 0 & 0 & 0 & -\frac{1}{R_y} & -\sigma & 0 & \frac{1}{EI_z} & 0 & 0 & 0 & 0 & 0 \\ 0 & 0 & 0 & 0 & 0 & \mu i_z^2 \omega^2 & 0 & -\sigma & -\frac{1}{R_y} & 0 & 1 & 0 \\ 0 & 0 & 0 & 0 & -\mu i_y^2 \omega^2 & 0 & \sigma & 0 & -\frac{1}{R_z} & 1 & 0 & 0 \\ 0 & 0 & 0 & -\mu i_x^2 \omega^2 & 0 & 0 & \frac{1}{R_y} & \frac{1}{R_z} & 0 & 0 & 0 & 0 \\ 0 & 0 & \mu \omega^2 & 0 & 0 & 0 & 0 & 0 & 0 & 0 & \sigma & -\frac{1}{R_y} \\ 0 & \mu \omega^2 & 0 & 0 & 0 & 0 & 0 & 0 & 0 & -\sigma & 0 & \frac{1}{R_z} \\ -\mu \omega^2 & 0 & 0 & 0 & 0 & 0 & 0 & 0 & 0 & \frac{1}{R_y} & -\frac{1}{R_z} & 0 \end{bmatrix}$$

where A is the cross section area,

GJ_T is the torsional stiffness,

i is the radius of gyration of the cross sectional area about the subscripted axis,

R_y is the initial radius of curvature of the beam centerline in the y-z plane, and

σ is the effective initial twist of the central axis of the beam.

Inclusion of the terms containing i, the radius of gyration of the cross sectional areas accounts for rotary inertia which is considered without further complication in the analysis.

THE VIBRATIONS IN CONSTRUCTION EQUIPMENT

Dr. Panagiotis A. Drakatos
Research Scientist
Institute of Technology
University of Patras
Patras, Greece.

In applications, where construction equipment are used, such as vibrating compactors, best soil compaction is achieved by the appropriate combination of the operation frequency and the vibration amplitude of the vibrating roller. In this process the propagation speed of the longitudinal waves created on soil during the operation of compactor is a function of the frequency and vibration amplitude. In the field, the above parameters are measured with great accuracy by means of a Laser device. In practice, the stochastic model for construction equipment - soil system can be determined with a very good approximation if the various soil parameters are taken into consideration in the design of the machines.

INTRODUCTION

This study represents an attempt for creating stochastic models of vibrations by combination of soil and compacting equipment properties. Any material has a basic property which makes it capable of receiving vibrations and further transmitting or damping them.

In some elastic-plastic materials, the longitudinal waves are affected by the properties of the material. Here, an appropriate nonlinear theory is developed to describe the propagated wave [1]. The waves created within their mass, as well as on the surface of the elastic material are of different kinds.

In an isotropically elastic material, when the concentrated elastic stresses reaches a limit, the elastic waves created are further transmitted from the point of their origin to every direction and with a speed which depends on the elastic properties of the material [2].

In the elastic - plastic materials the sto-

chastic variation is intensive. Thus, statistical methods are offered for solving this type of problems [3].

One of these problems is soil vibrations created during its compaction by means of vibrating machinery.

ANALYSIS

During soil compaction by a vibrating machine, the frequency of operation (f), the dynamic load (F) applied by the machine on the soil, and the acceleration of vibration, put particles of soil into a pulsating motion.

Forces of inertia are thus created, which are proportional to the mass of the particles, and which differ from particle to particle. These differences, in turn, result in new forces which act in counteracting with the forces of cohesion [4].

If the cohesion forces prevail, the displacements of the particles are elastic.

Otherwise, the particles are put in an independent random vibrating motion, the cohesion that exist between them is destroyed, and the soil falls into an intermediate condition [5].

The dynamic compaction of soil is achieved [6] when the particles, due to their own weight, tend to occupy the voids of air (pores) that exist between them and to form a more closely cemented material of increased density. Now, let us consider the speed of propagation (v) as a function of the frequency ($\omega=2\pi f$) of the vibrating machine under the so created intensive condition of the soil.

The propagation speed in homogeneous soils increases with the depth and is proportional to the square root of depth [7].

Therefore, the propagation speed does not remain constant during soil compaction because of the reasons mentioned above.

The dynamic load (F) vertically applied to the soil depends on the vibration amplitude (α), operation frequency (f), mass of the vibrating roller (m_w), centrifugal forces of rotating eccentric mass inside the cylinder as well as the constant spring of machine supports (k_m), e.t.c. [6,8,22].

Best soil compaction is achieved by the appropriate combination of the frequency (f) and the vibration amplitude (α) of the vibrating roller as a function of the propagation speed (v) of the longitudinal waves, which are created during the operation of compactor.

Consequently, the change in soil's density (ρ) under the influence of the soil frequency (ω) during the passes (j) of compactor, can be followed by observing the changes in the propagation speed (v) [9]. For this depth of soil layer from the point at which the propagation speed of the wave changes nearly linearly (the curve is of second degree) with the vibration frequency of soil (ω), the soil is compacted [10]. In other words, the air and the water which previously occupied the pores of the soil have been expelled and the soil behaves as a solid at a fixed density [11]. It is thus evident that changes in the propagation speed con-

stitutes an important criterion in characterizing the soil's state of compaction.

EXPERIMENTS

The experiments are carried out in several kinds of soil shown on Table 1. Before subjecting each soil to compaction [12], its various characteristics, such as its optimum moisture (w), maximum unit wet weight ($\gamma = \rho g$), degree of uniformity (U), cohesion (c), angle of friction (ϕ), e.t.c. are determined. The frequencies (f, ω), amplitude (α), propagation speed (v), length (λ) of longitudinal waves and force (F) are measured by means of a Laser device (Fig.1), [13]. The propagation speed is measured between points 3,4 which are mirrors supported on the soil surface. The wave length (λ) is equal to $\lambda = \frac{v}{f}$.

TABLE 1

Data taken of ω, v, λ for $j = 10$ th pass and operation frequency of vibrating roller $f = 47 \text{ sec}^{-1}$, $G = 231,72 \text{ kp/cm}$, $B = 70 \text{ cm}$, $\alpha = 0,45 \text{ cm}$.

Kind of soil	Frequency $\omega(\text{rad/sec}) \times 2\pi$	Propagation speed $v(\text{cm/sec}) \times 10^3$	Wave length $\lambda(\text{cm})$
Sand	42.00	16.50	392.86
	42.65	18.00	422.04
	43.80	20.00	456.62
	45.25	22.20	490.61
	46.05	22.50	488.60
Clay	47.50	23.60	496.84
	42.50	18.00	423.52
	43.60	18.60	426.60
	45.25	21.50	475.14
	46.50	30.70	660.22
Sand+Clay	47.40	36.30	765.82
	47.47	40.75	858.80
	43.65	16.85	386.02
	43.62	24.20	554.80
	44.00	28.75	653.41
	44.96	34.00	757.24
	46.50	40.90	879.60

For various passes (j) of a compactor of which the width is (B), several frequencies (ω) are given from a position 7 (Fig.1) and the amplitude (α), applied specific loading ($G = \frac{E}{B}$) [14] and propagation speed (u) of the wave are measured, as well as the density (ρ) of soil in several depths (z) of which the maximum is 25cm. According to the measurements shown on table 1, the graphs of Fig.2 are drawn. Fig.2 shows changes of speed (u) and length (λ) of longitudinal waves as a function of frequency ($\omega = 2\pi f$) for $J=10$ th and $f=47\text{sec}^{-1}$.

G_{1j}	ω_{1j}	α_{1j}	u_{1j}	γ_{1j}	z_{1j}
G_{2j}	ω_{1j}	α_{1j}	u_{1j}	γ_{1j}	z_{1j}
G_{3j}	ω_{3j}	α_{3j}	u_{3j}	γ_{3j}	z_{3j}
\vdots	\vdots	\vdots	\vdots	\vdots	\vdots
G_{nj}	ω_{nj}	α_{nj}	u_{nj}	γ_{nj}	z_{nj}

It is probable, to measure $z_{1j} = z_{2j} \dots \dots = z_{nj}$ which correspond in same pass of

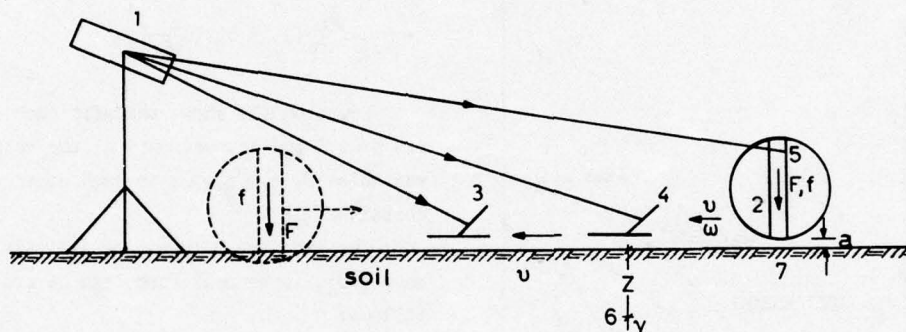


Fig. 1. Diagram showing the experimental procedure

1. Laser device, 2. Vibrating machine, 3,4,5. Mirrors, 6. Mass of soil of density (ρ) in a depth (z), 7. Position of vibrating roller after each pass.

For first pass of compactor $j=1$, the following measurements result by changing of frequency ω from a position (7) of soil (Fig.1).

G_{11}	ω_{11}	α_{11}	u_{11}	γ_{11}	z_{11}
G_{21}	ω_{21}	α_{21}	u_{21}	γ_{21}	z_{21}
G_{31}	ω_{31}	α_{31}	u_{31}	γ_{31}	z_{31}
\vdots	\vdots	\vdots	\vdots	\vdots	\vdots
G_{n1}	ω_{n1}	α_{n1}	u_{n1}	γ_{n1}	z_{n1}

After passes j of compactor results

compactor but the G_{nj} , ω_{nj} , u_{nj} , γ_{nj} will be different.

It

$$\begin{aligned}\omega_{11} &= \omega_{12} = \dots = \omega_{1j} \\ \omega_{21} &= \omega_{22} = \dots = \omega_{2j} \\ \omega_{n1} &= \omega_{n2} = \dots = \omega_{nj}\end{aligned}$$

The G_{nj} , ω_{nj} , u_{nj} , γ_{nj} , z_{nj} will be different, because after each pass the spring constant and damping coefficient of soil are changed [15].

THEORY

The stochastic model for the machine - soil system can be determined by the application of the theorem of Buckingham or Pi terms

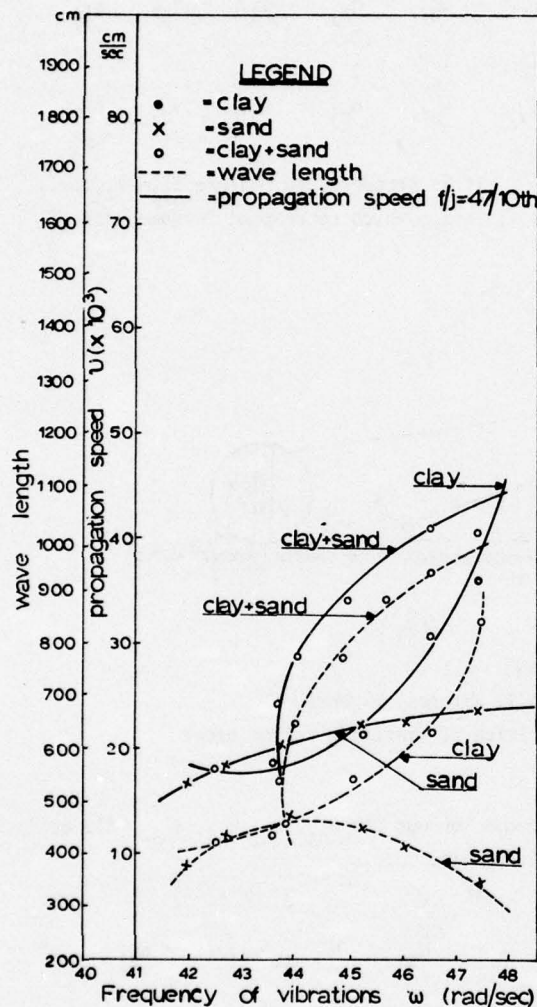


Fig. 2. Graphic representation of a change of the speed of propagation and the wave-length as a function of the frequency of vibration f , corresponding to the maximum achieved density for each type of soil at the corresponding pass $j=10$ and operational frequency $f = 47\text{sec}^{-1}$ of the vibrating machine.

on above data. Thus, using the same procedure the terms of similarity can be defined [16].

The non dimensional terms resulted are several but the most important of them are the following [17].

$$\frac{G}{\gamma z^2}, \frac{v}{\alpha \omega}, j$$

By means of Correlation Analysis and according to the method of Least Square (LSE) [18], it is possible to find the relationship between the above terms of similarity.

In general, this relationship is:

$$\left(\frac{G}{\gamma z^2}\right)_j = b_{0j} + b_{1j} \left(\frac{v}{\alpha \omega}\right)_j + b_{2j} \left(\frac{v}{\alpha \omega}\right)_j^2 + b_{3j} \left(\frac{v}{\alpha \omega}\right)_j^3 + b_{4j} \left(\frac{v}{\alpha \omega}\right)_j^4 \quad (1)$$

Equation (1) shows that for each compactor, its pass j and measurements n , the relation of variables $G, \alpha, \omega, z, \gamma, v$, to each other can be ascertained [19].

The problem, by means of Analysis of Variance [20], in general form, can be stated as follows:

$$\underline{Y} = \underline{X}' \underline{\beta} + e \quad (2)$$

where

$$\underline{Y} = Y_1 \ Y_2 \ \dots \ Y_n$$

$$\underline{\beta} = \beta_1 \ \beta_2 \ \dots \ \beta_p$$

$$\underline{X}' = \begin{matrix} x_{11} & x_{21} & \dots & x_{p1} \\ x_{12} & x_{22} & \dots & x_{p2} \\ \vdots & \vdots & & \vdots \\ x_{1n} & x_{2n} & \dots & x_{pn} \end{matrix}$$

$$e = e_1 \ e_2 \ \dots \ e_n, \ e_1 \dots e_n =$$

= corresponding error during the measurements. These errors are included in the measurements n , and by combination of (1), (2) for j passes, we obtain:

$$\begin{array}{l} X_{11j} = \left(\frac{v_1}{\alpha_1 \omega_1} \right)_j, \dots, X_{41j} = \left(\frac{v_1}{\alpha_1 \omega_1} \right)_j, X_{51j} = 1 \\ \vdots \qquad \qquad \qquad \vdots \qquad \qquad \qquad \vdots \\ X_{1nj} = \left(\frac{v_n}{\alpha_n \omega_n} \right)_j, \dots, X_{4nj} = \left(\frac{v_n}{\alpha_n \omega_n} \right)_j, X_{5nj} = 1 \end{array}$$

$$\begin{aligned} Y_{1j} &= \left(\frac{G_1}{Y_1 Z_1} \right) j \\ &\vdots \\ Y_{nj} &= \left(\frac{G_n}{Y_n Z_n} \right) j \end{aligned}$$

Of course, the assumption is that values distribution of variables Y is normal [21], that is $Y : N(X' \beta, \sigma^2 I)$.

$$(t - \hat{\Psi})' B^{-1} (t - \hat{\Psi}) \leq q s^2 F_{\alpha}, q, n-p \quad (3)$$

Applying the above method for each pass (j) of compactor, it is possible to find the total ellipsoid which is valid for every compactor and soil. The total ellipsoid constitutes the stochastic model with a probability $(1-\alpha)$ in a level of significance α , in a space $q = 4$ and for P degrees of freedom in Snedecor

The author wishes to thank C. Georgopoulos, P. Papadopoulos and J. Cosmopoulos, Patras Univ., for their help during this work.

REFERENCES

- [1] A.G., Hegemeier, " Finite Amplitude Elastic Wave Propagation in Laminated Composites ", Calif. Univ., San Diego, Dept. Appl. Mech. Engr, Rept. No. TR - 14, 1974.
- [2] N.B. Howel, Introduction to Geophysics, p.147, Mc Graw - Hill Book Company, London, 1959.
- [3] S.F.R. Hearmon, An Introduction to Applied Anisotropic Elasticity, P. 68, Oxford Univ. Press, 1961.
- [4] The University of Michigan, Vibration of Soils and Foundation, 1968.
- [5] K.E. Bender, " Optimization of the Random Vibration Characteristics of Vehicle Suspensions ", Ph D dissertation, Mass. Inst. Tech., Cambridge, Mass., 1969.
- [6] N.B. Panagiotopoulos, Construction Equipment, Part II, P. 451, Thessaloniki, 1969.
- [7] L. Bendel, Ingenieurgeologie, Ester Teil, P. 373, Springer Verlag, Wien, 1940.
- [8] P.J. Den Hartog, Mechanical Vibrations, Mc Graw - Hill Publishing Co., New York, N.Y.
- [9] N.R. Arnold, N.G. Bycroft, and B.G. Warburton, " Forced Vibrations of a Body on an Infinite Elastic Solid ", Journal of Applied Mechanics, P.P. 391, 1968.
- [10] D.W. Pilkey, and P.B. Wang, " Limiting Performance Characteristics of Randomly Disturbed Dynamic Systems ", The Shock and Vibration Digest, Vol. 7, No 1, P. 108, 1975.
- [11] A.C. Ross and L.R. Siera Kowski, " Elastic Waves in Fiber - Rein - forced Composites", The Shock and Vibration Digest, Vol. 7, No. 1, P. 96, 1975.
- [12] L.I. Kortchinski, Computation of Building Structures for Vibration Load, Stroyizdat, Moscow.
- [13] P. A. Drakatos, " Soil Compaction Checks by Means of a Laser Device ", IEEE/CLEA, Washington, 1975.
- [14] J. Haener, " Viscoelastic Wave Propagation in Unidirectional Composites ", AFML, 1970.
- [15] A.D. Dimarogonas, Mechanical Vibration P.P. 6-14 Lehigh Univ., 1973.
- [16] D.F. Young, " Similitude of Soil - Machine Systems ", Journal of Terramechanics, New York, Pergamon Press, Vol.3, No2, P.P. 61-69, 1966.
- [17] A. Soltynski, " Physical Similarity and Scale Effects in Soil - Machine Systems", Journal of Terramechanics, New York, Pergamon Press, Vol. 5, No 2, P.33, 1968.
- [18] F. Scheid, Theory and Problems of Numerical Analysis, P. 241, Schaum's Outline Series, Mc Graw - Hill, 1968.
- [19] A.R. Johnson and G.G. Roussas, " Applications of Contiguity to Multiparameter Hypotheses Testing ", Cal. Univ., P. 195, 1970.
- [20] H. Scheffé, The Analysis of Variance, P.29, John Wiley and Sons, Canada, 1959.
- [21] G.G. Roussas, A First Course in Mathematical Statistics, P. 356, Addison - Wesley, 1973.
- [22] P.A. Drakatos., Model of Soil - Vibrating Machine, 46th Symposium of SVIC, Oct.1975.

APPENDIX

The symbols of relationship (3) are:

\vec{t} = vector from a fixed point.

$(\vec{t}-\vec{\Psi})$ = the radius vector of ellipsoid in a space of q dimensions.

$$\vec{\Psi} = \vec{A} \vec{Y}$$

where

$$\vec{A} = \begin{vmatrix} \alpha_{11} & \alpha_{12} & \dots & \alpha_{1n} \\ \vdots & \vdots & & \vdots \\ \alpha_{q1} & \alpha_{q2} & \dots & \alpha_{qn} \end{vmatrix}$$

$$\hat{\underline{\beta}} = \underline{S}^{-1} \underline{X}' \underline{Y} = \begin{pmatrix} \hat{\beta}_1 \\ \vdots \\ \hat{\beta}_p \end{pmatrix} =$$

$$= \begin{pmatrix} \alpha_{11} y_1 + \dots + \alpha_{1n} y_n \\ \vdots \\ \alpha_{p1} y_1 + \dots + \alpha_{pn} y_n \end{pmatrix}$$

$$\underline{S} = \underline{X}' \underline{X}$$

$$\underline{B}^{-1} = \underline{A} \underline{A}' = \text{the volume of ellipsoid}$$

$$q = \text{the dimensions of space}$$

$$S \left(= \frac{J_0}{n-p} \right) = \text{The mean square of error}$$

$$J_0 = (\| \underline{Y} - \underline{X}' \hat{\underline{\beta}} \|)^2 = \text{the error of sum of squares}$$

$$F_{\alpha}; q, n-p = \text{the highest point or level of importance } \alpha \text{ in the distribution of Snedecor } F_{q, n-p}.$$

$$n = \text{the number of measurements}$$

$$\sigma^2 = \text{Variance of distribution}$$

$$\underline{I} = \text{Identity matrix}$$

MODEL OF SOIL - VIBRATING MACHINE

Dr. Panagiotis A. Drakatos
Research Scientist
Institute of Technology
University of Patras
Patras, Greece.

During soil compaction by means of vibrating machinery changes in the density of the soil affect changes in the damping and elastic characteristics of the soil which, in turn, render the calculation of the force F_D applied in the process very difficult. Up to now this force F_D has been estimated experimentally. By means of a Laser device invented by the author and capable of measuring the frequency and the amplitude of the vibrations of the vibrating machine, the force F_D can now be calculated with ease and great precision as the following will demonstrate.

NOTATION

- F_D Dynamic loading applied on the soil
 α Vibration amplitude of the cylinder
 K_m Spring constant of the machine's elastic supports
 C Damping factor of soil
 f Vibration frequency of the motor
 f_r Frequency of the vibrating cylinder's rotating mass
 F Centrifugal force of vibrating cylinder's rotating mass
 W_m The weight of the cylinder
 m_w The mass of the cylinder
 F_m The weight of the motor
 m_o Mass of vibrating cylinder's rotating masses
 G_D The special dynamic loading ($G_D = F_D/B$) of the vibrating machine
 B Cylinder's width

CALCULATION

In order to study the dynamic load F_{Dm} ap-

plied to the soil, the vibrating machine and the soil may be considered as a vibrating system with a mass m_w , a spring constant K and a damping coefficient C . (Fig.1).

The dynamic load F_{Dm} [5] applied to the soil is given then by the relationships (1) and (2).

$$F_{Dm} = \alpha \sqrt{K^2 + (C\omega)^2} \quad (1)$$

where α is the amplitude of vibration [2] given by

$$\alpha = \frac{2m_o r \omega^2}{\sqrt{(K^2 - m_w \omega^2)^2 + (C\omega)^2}} \quad (2)$$

By eliminating C in both (1) and (2), the following relationship results:

$$F_{Dm} = \sqrt{F^2 + \alpha^2 [K^2 + (K - m_w \omega^2)^2]} \quad (3)$$

where $\omega = 2\pi f$

f = The system's vibration frequency

F = The centrifugal force of the rotating masses inside the cylinder, corresponding to the frequency f .

Knowing the centrifugal force F_r of the vibrating machine for a known frequency f_r , the centrifugal force F for a given frequency f is:

$$\frac{F}{F_r} = \frac{2m_o r 4\pi^2 f^2}{2m_o r 4\pi^2 f_r^2}$$

or

$$\frac{F}{F_r} = \frac{f^2}{f_r^2}$$

$$\text{when } F = F_r \frac{f^2}{f_r^2} \quad (4)$$

On the basis of the initial assumption that the soil and the machine constitute a vibrating system [1], the spring constant K of the machine's elastic supports may be taken as K_m and the relationship then becomes:

$$F_{D_m} = \sqrt{F^2 + \alpha^2 [K_m^2 + (K_m - m_w \omega^2)^2]} \quad (5)$$

Equation (5) gives the force F_{D_m} applied to the soil by the vibrating cylinder.

The vibration amplitude α of the cylinder itself may also be taken as the amplitude of the cylinder (Fig.1).

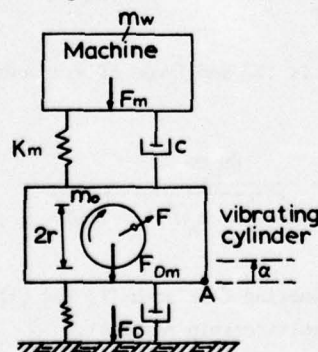


Fig.1. The model for the soil-vibrating machine system used in calculating F_D .

Consequently, and in order to calculate the force F_{D_m} the values of F , α , K , m_w , and ω must be known.

The centrifugal force F is calculated on the basis of the relationship (4), since the values F_r and f_r for the particular machine are known. The amplitude α and the frequency of vibration f are then measured by means of a specially constructed Laser device, constructed by the author [3,4].

Because of the small amplitude α of vibrations and the vibrating cylinder position, it would not be possible to use a common micrometric apparatus. In the experiments a low power, red Laser beam was used. Its high density of energy, creates more sensitive and distinct signs on the oscillograph and so the results are more reliable.

The measurements of amplitude α take place at the point A of Fig. 1. During the vibrations of the cylinder the observer can read displacements of the luminous spot on the oscillograph that is the amplitude α and frequency f .

The frequencies f employed in the experiment and the obtained values of the amplitude α of the vibrations of the three cylinders used, are shown in Table 1.

The spring constant K_m was calculated after the motor of the compactor was removed and the average value of yield of the supports under various weights was measured.

The mass m_w was calculated by the relationship $m_w = W_m/g$ after the weight of the cylinder was taken.

The angular speed ω was calculated from the relationship $\omega = 2\pi f$, where the frequency f was measured.

Table 2 shows the values of K_m , W_m , and m_w thusly obtained.

The total force F_D applied to the soil is calculated by adding the weight of the motor F_m to the force F_{D_m} exerted by the vibrating cylinder:

$$F_D = F_{D_m} + F_m \quad (6)$$

The values (Table 1) for the specific loading G_D were then calculated from the relationships (4), (5), and (6) by computer according to the computational program. (Appendix 1).

TABLE 1.

Frequencies f used, and values of amplitude α obtained in the experiment.

Cylinder: $D = 50$ cm, $b = 70$ cm, $G_0 = 6.79$ kp/cm			
Frequency f (Hz)	42.5	45	47
α (cm)	0.20	0.35	0.45
G_D (kp/cm)	86.73	166.04	231.72
Cylinder: $D = 50$ cm, $b = 75$ cm, $G_0 = 5.4$ kp/cm			
Frequency f (Hz)	42.5	45	47
α (cm)	0.18	0.30	0.38
G_D (kp/cm)	59.46	109.27	150.52
Cylinder: $D = 40$ cm, $b = 65$ cm, $G_0 = 3.78$ kp/cm			
Frequency f (Hz)	42.5	45	47
α (cm)	0.17	0.25	0.32
G_D (kp/cm)	47.7	68.018	94.59

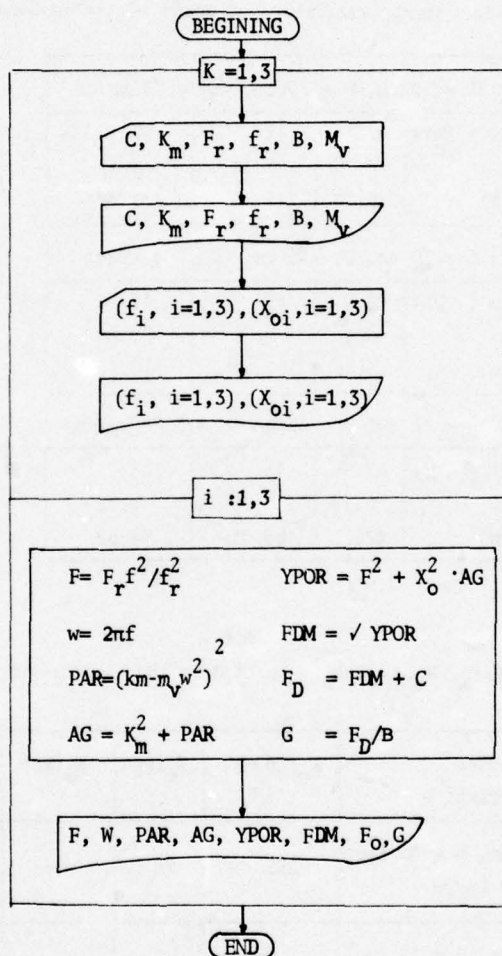
TABLE 2.

Values of K_m , W_m , F_m , m_w obtained in the experiments.

Cylinder Characteristics	K_m (kp/cm)	F_m (kp)	W_m (kp)	m_w (kp/cm ⁻¹ sec ²)
$D = 50$ cm, $b = 70$ cm, $G_0 = 6.79$ kp/cm	255	70	405	0.412
$D = 50$ cm, $b = 75$ cm, $G_0 = 5.4$ kp/cm	600	60	338	0.344
$D = 40$ cm, $b = 65$ cm $G_0 = 3.78$ kp/cm	380	50	217.5	0.222

APPENDIX "1"

FLOW CHART



REFERENCES

- [1]. F. Ames and D. Mumaghan, Theoretical Mechanics and Introduction to Mathematical Physics, p.283, Dover Publications, Inc., New York, 1957.
- [2]. P.J. Den. Hartog, Mechanical vibrations, p.70, Fourth edition, McGraw-Hill Book Company, 1956.
- [3]. P.A. Drakatos, The Interference of Construction Equipment and Laser in the Study of Soil Surface Wave, Technology, Aug., P.P. 2-5, 1975.
- [4]. C.W. Kilmister and J.E. Reeve, Rational Mechanics, p.63, Longmans, 1966.
- [5]. N.B. Panagiotopoulos, Construction equipment, Part II, P. 454, Thessaloniki, 1969.

A GENERAL PURPOSE COMPUTER GRAPHICS DISPLAY SYSTEM
FOR FINITE ELEMENT MODELS

H. N. Christiansen
Brigham Young University/Provo, Utah
University of Utah/Salt Lake City, Utah

B. E. Brown
University of Utah
Salt Lake City, Utah

L. E. McCleary
Naval Undersea Center
San Diego, California

This paper describes a Fortran computer program which generates displays of finite element models* in line drawing and/or continuous tone format. The system reads data generated by other analysis routines, accepts a variety of control commands, and produces line drawings with (or without) hidden line removal and/or black and white or full color continuous tone images with hidden surface removal. The display features are appropriate to both static and dynamic math models and allow output in single frame or smooth animation movie format.

INTRODUCTION

The Fortran computer program described in this paper is called MOVIE-NUC. It is a general purpose routine for the display of three-dimensional mathematical models. The models are defined in terms of mosaics of triangular and quadrilateral panel systems. This definition quite naturally lends the routine to the display of two- and three-dimensional finite element models.

MOVIE-NUC has evolved from MOVIE-UTAH, a code originally written by Christiansen [1] at the University of Utah. The Utah code was used to produce raster-driven displays with the option of hardware or software proces-

sing to solve the hidden surface problem. Both options were based upon Watkin's Algorithm [2], with Gary Watkins designing and building the "Visible Surface Processor" and Michael Archuleta writing the software version (called HIDDEN).

In 1973, Archuleta became an employee of Lawrence Livermore Laboratories (LLL) and converted his routine to their computer system. During this process, the line drawing capability of the program was significantly improved. During the same year, MOVIE-UTAH was implemented at LLL and, after modification to interface it with the new version of HIDDEN and various finite element codes, became known as SAMPP-LLL [3].

*The program is, in fact, applicable to any scene which may be described in terms of triangular and quadrilateral panels. For example, a pre-processor exists, and is available, which will generate a panel system definition of two- and three-dimensional alphanumeric character sets. Examples of the use of this pre-processor are found in this paper.

The present implementation of MOVIE-UTAH uses a modification of the LLL version of HIDDEN and a combination of MOVIE-UTAH and SAMPP-LLL. The installation of the system at the Naval Undersea Center (NUC) has further generalized the system and made it as machine independent as possible. About 96 percent of the coding is written in standard Fortran with the remaining 4 percent being machine dependent Fortran. This total does include HIDDEN but does not include the display interface programs. At NUC, the routines currently produce line drawing plots on a Tektronix 4012 scope or Calcomp plotter, and continuous tone black and white or color images on a Comtal 8300 display. Perspective views are produced with the hidden lines (optional) and surfaces removed. The general purpose digital computer being utilized in both a batch and time-sharing mode is a Univac 1110.

COMMAND STRUCTURE

The features of MOVIE-NUC are discussed in terms of the command structure. The exact inputs required for each command are detailed in the MOVIE-NUC User Manual [4]. A session begins with the user-initiated commands to READ the geometry, displacements and/or special function files. The geometry file consists of the nodal coordinates, an element connectivity array, and a definition of the division of the connectivity array into separate smooth surfaces and/or parts. Special function files are used to read scalar functions such as stress or strain components and temperature. These files may be later used as a basis for "pattern type" displays using color fringes and/or surface warping techniques. The user then RESTores the geometry which initialize the translation and rotation transformations. The content of the scene is controlled by specifying the PARTs to be displayed. The complete model or any subset may be shown.

A command SCOPE is utilized to select the output device. Line drawing plots or continuous tone color images may be selected. If line drawings are selected, the user is asked if hidden line removal calculations is desired. The frustum of vision is partly controlled in SCOPE by the perspective scale factor. The position of the model within the frustum can be controlled by the DISTance command. Clipping is performed for the frustum of vision and for two planes parallel to the X, Y plane. These are known as the near and far Z-clipping planes. Their location along

the Z-axis is specified in DISTance.

If a color picture is to be made, then a diffuse light factor will be requested in SCOPE. This is the amount of ambient light in the picture. The COLOR command must be executed. To assign a part (or the background) a color, the user specifies a combination of green, blue, and red light. The shading method to be used must also be specified for a color picture. The choices are: FLAT, UNIFORM, and SMOOTH. The shade of each element displayed by MOVIE-NUC is proportional to the cosine squared of the angle between the normal to the element and the direction to the observer. This produces a simulation of the light source being at the eye of the observer. FLAT and UNIFORM produce what is known as faceted shading. The discontinuities of the shading function across element boundaries produce the faceted look. To produce a more realistic simulation of a curved surface SMOOTH shading was developed by Gouraud [5] at the University of Utah, and is used by the routine.

The viewing positions of the model are controlled by the ROTate, TRANsLate, and CENTer commands. CENTER has been implemented for the user's convenience. It executes a SUMMary command which prints out the range of the model's three coordinate values and the ranges of the displacements and/or special functions. CENTER then performs a TRANsLate to the center of the model. The DISTance command is executed and all variables are set to default values. At appropriate times, the user may request a VIEW of the scene he has defined.

Frequently, the results of finite element analysis can be effectively displayed by distorting the geometry of the model according to the calculated displacements multiplied by an appropriate SCALE factor. The user may also distort the geometry in accordance with the special scalar function. This is accomplished by specifying scale factors for the WARPing in the model's coordinate directions. This works well for planar areas of the model when the warping is in the direction normal to the plane. Pattern information contained in the displacement and special function files may also be displayed through the use of color FRINGes. This command requires the selection of displacement or special function fringing and the range of values for which color fringes are to be assigned. The definition of the color components for the individual fringes is accomplished in the COLOR command.

The FAST command is an option to help speed up the hidden surface process. It removes all polygons which face away from the observer. EXPLode is the local motion or exploded view option of the code. Here the user specifies translation patterns for each part. This option is useful when displaying a model for those who are unfamiliar with the relationships of the several parts.

MOVie is the command in which the animation is specified. The total number of frames and the vibration cycles per frame for display of harmonic motion are requested. The user then specifies the total animation change for translations and rotations. Motion toward or away (zooming) from the model may also be defined in MOVie.

All four letter commands either result in completion of the request or ask specific questions before returning to a command wait status. An extra carriage return or an unrecognized instruction produces a list of the commands available. The result is a system for which minimum training is required.

DISPLAY EXAMPLES

The first six figures depict the results of a finite element analysis of a low frequency sonar device called a Helmholtz Resonator. The particular model shown has a flared neck, but is

otherwise identical to the straight necked Helmholtz Resonator described in the paper by C. S. Nichols, entitled "Finite Element Analysis of Low Frequency Transducers," which was also presented at the 46th Shock and Vibration Symposium.

Figure 1 is a line drawing which provides a view of the top and side of the resonator. The slight inaccuracy (in the removal of hidden line segments) is a consequence of the calculation process. By increasing the resolution (specified by the user in terms of the number of raster scan lines), this inaccuracy may be reduced at the cost of increased processing time. Figure 2 is the same view as Figure 1 shown as a flat shaded picture. Figure 3 provides a smooth shaded image of the side and bottom of the device. Figure 4 is a cross-sectional view of the fluid medium contained within a hemispherical region surrounding one-half of the device. Notice that the cross section of the device itself is missing. Color fringing has been used to indicate the pressure pattern in the surrounding fluid at a resonant frequency. These color fringes show up as varying intensities of grey when reproduced as black and white pictures. The primary colors (blue, red, and green) appear dark as compared with yellow, for example, which has increased brightness (being full intensity red and green). Figure 5 illustrates the pattern of the motion

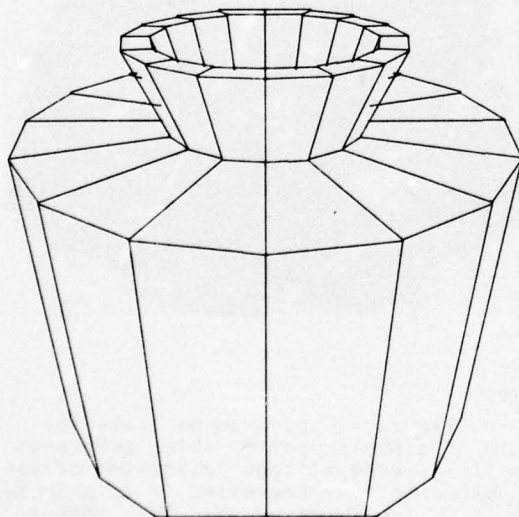


Figure 1

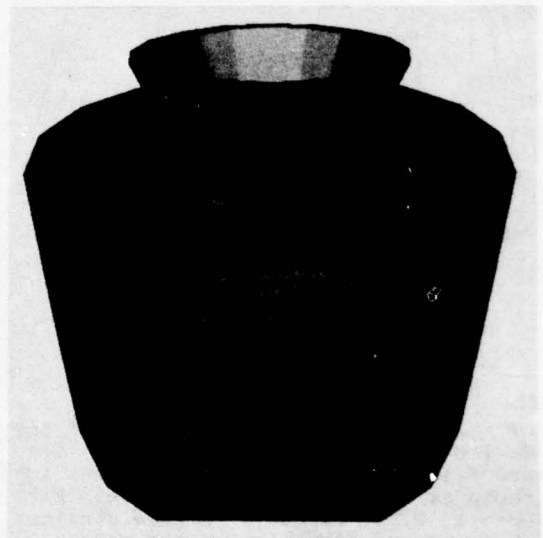




Figure 3

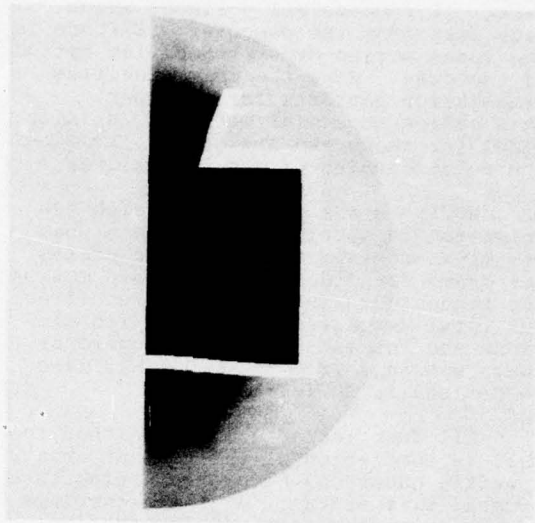


Figure 4

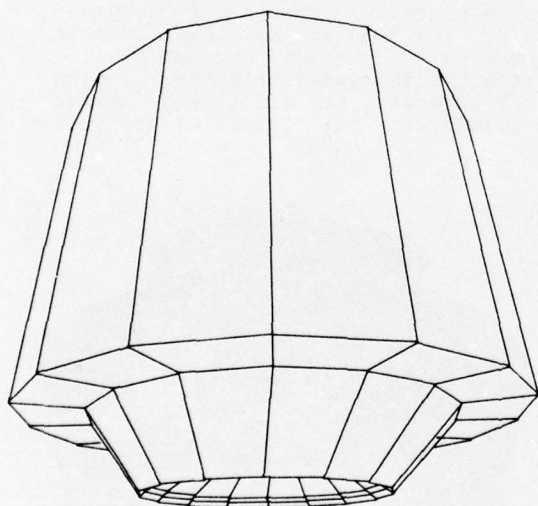


Figure 5

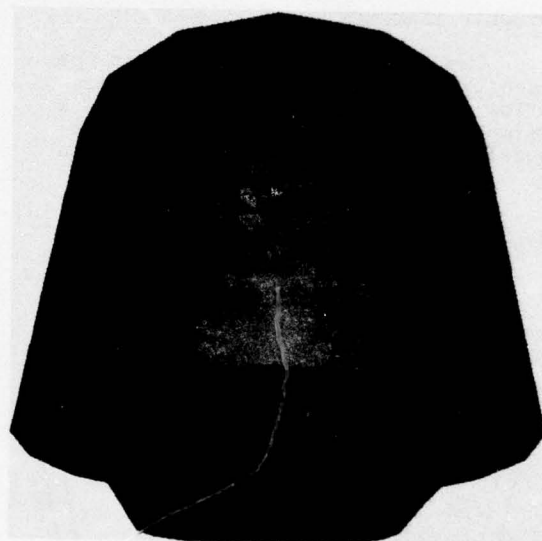


Figure 6

of the hinged disk on the bottom of the device during resonant conditions. Figure 6 is identical to Figure 5, but is shown as a smooth shaded picture. Figures 1, 2, 3, 5, and 6 provide a rather sharp perspective view of the resonator. This was the result of positioning the viewer in close to the model with a wide angle or view.

Figures 7 and 8 demonstrate the use of a pre-processor which generates a finite element type definition of alphanumeric text (referred to in a footnote on the first page). Note that line two is portrayed in terms of three-dimensional characters.

COMPUTER GRAPHICS DISPLAY SYSTEM

Figure 7

COMPUTER GRAPHICS DISPLAY SYSTEM

Figure 8

CONCLUDING COMMENTS

The development of the system has been sponsored by ARPA, ERDA, and the Naval Undersea Center. The documented system, including the pre-processing for title generation, is available upon request to both governmental and private users. Although considerable effort has been made to achieve as much machine independence as possible, some changes will be necessary to drive other display devices.

It is believed that the system provides a versatile display tool for panel systems which can be readily implemented on most display configurations. The NUC version provides low cost line drawings and connection to a relatively low cost continuous tone display terminal.

REFERENCES

1. H. N. Christiansen, "Applications of Continuous Tone Computer-Generated Images in Structural Mechanics" Structural Mechanics Computer Programs--Surveys, Assessments, and Availability, University Press of Virginia, Charlottesville, Virginia, June 1974. pp. 1003-1015.
2. G. S. Watkins, "A Real time Visible Surface Algorithm," Dept. Computer Sci., University of Utah, Salt Lake City, Tech. Rep. UTEC-CSc-70-101, July 1970.
3. B. E. Brown, "Structural Analysis Movie Post-Processor (SAMPP) User Manual," University of California, Lawrence Livermore Laboratory, UCID-30097 Rev. 1 (Oct. 1975), Livermore, California.
4. L. E. McCleary, H. N. Christiansen, and B. E. Brown, "MOVIE-NUC: A Computer Program to Display Two and Three Dimensional Models as Line Drawing or Continuous-Tone Color Images," December 1975, NUC Tech. Pub. 501 (Advance Copy), Available from L. E. McCleary, Code 302, Naval Undersea Center, San Diego, California 92132.
5. H. Gouraud, "Computer Display of Curved Surfaces," Dept. Computer Sci., University of Utah, Salt Lake City, Tech. Rep. UTEC-CSc-71-113, June 1971. Also in IEEE Trans. C-20, June 1971, pp. 623-629.

Discussion

Mr. Chapman (Jet Propulsion Laboratory): I would like to know the size of this program as it is currently available to us and the mode that the programs is obtained in. Is it on magnetic tape or on cards? What type of language is it written in?

Dr. Christiansen: The program is written in Fortran. It is probably about 96 to 97% standard Fortran with a little machine dependent Fortran which needs to be changed for different programs or different machines. The other 4% is in Fortran that the 1108 Computer understands and other machines have comparable subroutines. We need to do some packing and unpacking for economy. The program is relatively small it is about 2500 cards and I think it will be made available on a card basis so it is slightly over one box of cards and that includes all of the hidden surface hidden line capabilities as well as the rest of this. How big in terms of core? Running these kinds of problems requires about 40K. But if you want big models you have to have a lot of core or disc and if you need to go to disc then you need to modify the program somewhat. It expects to have a fairly large host computer available and to be run in either a timesharing or a batch mode interactive basis from Tektronix or cheaper display units. As compared to some of the expensive equipment that you saw in the previous paper, the continuous tone color pictures can be put out on equipment which currently costs about \$60,000 dollars and we hope that the cost will be down to \$30,000 for a complete system within a year.

VIBRATION CHARACTERISTICS OF 1/8-SCALE DYNAMIC MODELS
OF THE SPACE SHUTTLE SOLID ROCKET BOOSTERS

Sumner A. Leadbetter, Wendell B. Stephens,
John L. Sewall, and Joe W. Majka
NASA Langley Research Center
Hampton, Virginia

and

Jack R. Barrett
Rockwell International
NASA Langley Research Center
Hampton, Virginia

Results of vibration tests and analyses of six 1/8-scale models of the space shuttle solid rocket booster tanks are reported. Natural vibration frequencies and mode shapes were obtained for these aluminum shell models having internal solid fuel configurations corresponding to launch, midburn (maximum dynamic pressure), and near end-burn (burn-out) flight conditions. Test results for longitudinal, torsional, bending, and shell vibration frequencies are compared with analytical predictions derived from thin shell models, and finite-element plate and beam models. The lowest analytical, longitudinal, torsional, bending and shell vibration frequencies were within 10% of experimental values. The effects of damping and asymmetric end skirts on natural vibration frequency were also considered. The analytical frequencies of an idealized full-scale space shuttle solid rocket booster structure are computed with and without internal pressure and compared with the 1/8-scale model results.

INTRODUCTION

The structural dynamic characteristics of all launch structures must be predicted and understood during vehicle development and operations. Knowledge of the vibration frequencies, mode shapes, and damping is fundamental to the prevention of aeroelastic and POGO instabilities and for the prediction of dynamic loads. Analytical methods, normally used to determine these structural dynamic properties, must be verified by experiments to insure their adequacy. Test data, needed to evaluate the analytical methods, are most often obtained from ground vibration tests of flight vehicle prototypes and are generally obtained with the expenditure of considerable effort and cost.

Another and sometimes more expedient method of obtaining experimental data for validating analytical approaches is the use of dynamic scale models as described in Refs. [1] and [2]. Specialized vibration models have been used extensively to obtain data on launch vehicles as indicated in Refs. [3] through [7].

The space shuttle vehicle will have more complex structural dynamic characteristics than previous launch vehicles because four separate, large elements are joined asymmetrically at discrete interfaces. This multielement configuration will have a high modal density in the frequency range of expected dynamic loading and the dynamic response will have a high degree of directional coupling. Thus, it is important to develop the analytical methods needed to accurately compute frequencies and mode shapes of the various vehicle elements and subsequently to couple these element dynamic properties to predict the total vehicle response characteristics.

To provide a better assessment of analytical modeling capabilities with which to understand the dynamic behavior of shuttle-like configurations, a 1/8-scale dynamic model of an early shuttle vehicle concept was designed and fabricated for structural dynamics investigations at the NASA Langley Research Center. The 1/8-scale dynamic model details are described in Refs. [8-10].

The complete 1/8-scale shuttle dynamic model is shown in Fig. 1. The assembled model has a simulated lift-off mass of 3975 kg, is 7.43 m long, and consists of four major elements: the orbiter, external tank, and two solid rocket boosters (SRB). Data from vibration studies of the 1/8-scale model orbiter are reported in Refs. [8] and [11].

The purpose of the present paper is to report the results of vibration studies of the 1/8-scale SRB. Vibration tests of six SRB models containing inert solid fuel are reported and compared with results from analyses based on thin shell theory, and finite-element plate and beam theory. Additional model studies showing the effects of propellant damping and the addition of end skirts are discussed. Finally, an analytical comparison of the 1/8-scale model response with that of an idealized full-scale shuttle SRB propellant cylinder with and without internal pressure is presented.

LIST OF SYMBOLS

A	Cross-sectional area
E	Modulus of elasticity
E_p	Modulus of elasticity of the propellant
G	Modulus of rigidity in shear
g	Acceleration due to gravity
k	Shear factor
k_x, k_y, k_z	Linear spring constants along roll, pitch, and yaw axes
I_x, I_y, I_z	Area moments of inertia with respect to roll, pitch, and yaw axes
I_{xx}	Torsional mass moment of inertia
J	Torsional constant
m	Number of circumferential nodal circles along a meridian
n	Number of full circumferential waves
N_x, N_θ	Membrane stress resultants in SRB in the axial and circumferential directions, respectively
p	Internal pressure
r_i	Inner radius of the propellant layer
r_r	Radius of the casing reference surface

t_c	Thickness of the casing
t_p	Thickness of the propellant
$\bar{x}, \bar{y}, \bar{z}$	Cross-section centroid eccentricity along roll, pitch, and yaw axes from point of attachment (or model grid point), respectively
$\beta_x, \beta_y, \beta_z$	Rotational spring constants along roll, pitch, and yaw axes
ρ	Mass density
$\bar{\rho}$	Effective mass density at the casing reference surface
μ	Poisson's ratio
μ_p	Poisson's ratio for the propellant

Abbreviations

FEB	Finite-Element Beam model
FEP	Finite-Element model using plate and/or hexahedral elements
SOR	Shell-of-Revolution model
SRB	Solid Rocket Booster

TEST MODELS AND PROCEDURES

The design and fabrication of the 1/8-scale SRB dynamic models is based on an early vehicle concept [10] and does not include a significant amount of the structural details. In particular, uniform skin thicknesses are used in lieu of stepped thicknesses or ring reinforced skins. Also, aluminum is used in place of steel for the construction of the major components. Each SRB model consists of three separate parts: a forward skirt, a propellant cylinder, and an aft skirt. A photograph of the SRB model is shown in Fig. 2.

The scaling relationships between the models and shuttle prototypes are shown in Table I. These relationships directly follow from a dimensional analysis of the parameters that control the dynamic behavior of the structure, and from the choice of material used in the model. Extrapolating prototype behavior from model test data is accomplished by using these scaling relationships directly. However, full-scale shuttle SRB flight hardware design approved for fabrication is significantly different from the structural concept upon which the 1/8-scale model design is based. For example, the model SRB consists of one continuous cylindrical section, a forward skirt, and an aft skirt, while the flight hardware prototype consists of an aft propellant segment, including engine section, six propellant

sections, a forward skirt, and a nose cone. Also, the 1/8-scale model dimensions are based on an overall length of 45.72 m and a diameter of 3.96 m as compared to the 43.94 m (excluding the engine nozzle) length and 3.70 m diameter called for in the planned flight prototype.

In this study, a comprehensive assessment was made of the propellant cylinder dynamic response. More limited data were gathered on propellant cylinders with end skirts attached.

Model Description

The assembled 1/8-scale model includes a forward end skirt, a propellant cylinder, and an aft end skirt as shown in Fig. 2. The end skirts, the casing of the propellant cylinder, and the attachment end rings are all constructed of aluminum. As indicated in Table I, the model aluminum component thicknesses are three times the nominal smeared thicknesses of the prototype steel components so that stiffnesses and masses can be properly proportioned. The forward skirt is a short cylinder which is 0.495 m in diameter and 0.533 m in length. The basic skin thickness of the forward skirt is 0.102 cm and has local reinforcement in the region of the external tank connection. Details of local reinforcements and attachment frames are given in Ref. [10]. The aft skirt consists of a short cylindrical section and a larger conical section, each with a nominal skin thickness of 0.157 cm. The cylindrical section is attached to the propellant cylinder and is 0.113 m long. The conical section is 0.551 m long and flares to an outer diameter of 0.775 m. Details of local reinforcement and attachment frames are given in Ref. [10].

End rings used for the attachment of the forward and aft skirts to the propellant cylinders are shown in Fig. 2. Fastening of the SRB elements to other 1/8-scale model elements is achieved through the skirt structures.

The propellant cylinder is composed of an outer aluminum casing, an inert interior solid cylindrical propellant layer, and two end frames for attachment to the end skirts. Six 1/8-scale propellant cylinders were fabricated and tested. Two propellant cylinders were used to simulate each of the lift-off, approximate maximum dynamic pressure (midburn), and near end-burn (burnout) flight conditions. The cylinder casings are 0.476 cm thick, 3.73 m long, and have a 0.495 m outer diameter. The length of the simulated propellant layer is 3.69 m which allows for a propellant recess of 2.0 cm from each edge. The length of the propellant cylinder is 3.74 m since each attachment ring extends 0.005 m past the casing edge. The propellant layer thicknesses are 0.173 m, 0.089 m, and 0.198 m for the lift-off, midburn, and burnout flight conditions, respectively. End views of each of the cylinders for the various flight conditions are shown in Fig. 3. The masses of the various SRB components are given in Table II.

The solid propellant is a viscoelastic material whose elastic properties are characterized by dynamic moduli defined as complex quantities that vary with frequency, temperature, and strain level. The simulated propellant used for the 1/8-scale dynamic model was inert UTI-610 manufactured by the UTC Division of United Aircraft Corporation. The simulant consists of essentially the same binder-fuel-curable components as the UTP-3001 propellant used in the Titan launch vehicle. Inert sodium chloride and inert ammonium sulphate were substituted for the ammonium perchlorate in the inert UTI-610.

The particular batch of UTI-610 that was used in the 1/8-scale model yielded samples having a density of 4.407 kg/m³. Estimates of the elastic moduli of propellant were provided by the manufacturer [10] and were based on a low strain level of approximately 10⁻⁶. Measurements of moduli based on moderate-to-high strains of 0.005 to 0.05 using specimens of the same propellant material are reported in Ref. [12]. Both sets of material properties are listed in Table III. The large differences in moduli are consistent with those due to high and low strain observed elsewhere* for propellant materials similar to that used in the 1/8-scale SRB. These large differences suggest that the propellant properties deserve careful attention, particularly with regard to the strain environment. Other factors such as strain rate, frequency, temperature, and aging may also have large effects on the propellant modulus. An in-house series of low-to-moderate strain level tests on a specimen taken from one of the models indicated better agreement with the low moduli values of Ref. [12]. Therefore, the studies presented are based on the low moduli values of Ref. [12] unless otherwise noted.

Suspension System

The tests were conducted to determine the lower natural frequencies and mode shapes of an SRB model in an unrestrained condition. To simulate free-free boundary restraint conditions for the experimental study, the SRB model was supported in a horizontal position as shown in Figs. 2 and 4, and as discussed in Ref. [13]. Steel cables and rope slings were used to support the model and were located near the node lines of the mode being studied. For the tests to determine the first longitudinal and torsional responses, the cables were located near the model midlength and small elastic cables were attached to the skirt attachment rings, as shown on Fig. 4, to statically stabilize the test configuration. The vibration exciters were suspended with separate steel cables, and were

* Unpublished report by Duane Linton and John Bartlett, "Dynamic Characterization of Solid Rockets," IBM Report No. 73W-05271, IBM Federal Systems Division, Electronic Systems Center, Huntsville, Ala., Sept. 1973.

attached to the model as needed to excite the modes of interest. For torsional response two exciters were required as shown in Fig. 4.

Data Acquisition and Reduction

The instrumentation for the SRB vibration studies provided continuous electronic signals that were a measure of the dynamic response of the model to the sinusoidal input force. The data acquisition system provided a means for monitoring exciter inputs and accelerometer and force gage output signals and for performing on-site data analyses. Transducers used during the test program included piezoelectric accelerometers and force gages that were attached to the test article by means of either a mechanical fastener or a movable vacuum mount. The movable accelerometers were used primarily to obtain detailed mode shapes and shell response data. Electromagnetic exciters were used to vibrate the model at discrete frequencies to obtain modal response data.

A schematic layout of the data acquisition system is given in Fig. 5. The accelerometer and force gage output signals were indicated on meters and recorded on an $x_1 - y_1y_2$ recorder in the form of amplitude and phase components referenced to the input force signal. The servo-oscillator indicated in Fig. 5 was used to control the exciter force level. The data were analyzed to obtain the required modal response information by means of either the so-called co-quad method, discussed in Refs. [14] and [15], or the Kennedy-Pancu or phase-plane method discussed in Refs. [16, 17, and 18]. Structural damping was determined from the power-off decrement, the co-incident response, or from the phase-plane diagram.

Typical data for a test article representing the midburn flight condition is shown in Figs. 6 and 7. A single electrodynamic exciter, oriented such that a constant sinusoidal force could be applied in the pitch direction, was located at one end of the cylinder. The output from an accelerometer located at the other end of the cylinder provided the response signal. On Fig. 6 the out-of-phase (quadrature or quad) and in-phase (co-incident or co) components of the output acceleration with respect to the input force are shown for a limited frequency range. As shown in Refs. [14] and [15], the modal amplitude and frequency can be determined from the quadrature peak value while a measure of the damping can be obtained from the co-incident component. On Fig. 7, for the same test data the quadrature component and the frequency is plotted as a function of the co-incident component of the acceleration referred to the force. As shown in Ref. [16], an indication of modal purity, modal amplitude, frequency, and damping can be obtained from these data.

The data on Figs. 6 and 7 exemplify uncoupled (labeled first bending) and coupled (labeled second bending) response conditions of a 1/8-scale SRB model. The first bending mode

occurred at a frequency well separated from other modes while the second bending mode occurred at a frequency near the model first torsion mode and is a shell response. These coupled modes could be adequately separated in the laboratory by the use of appropriate test methods; namely, adjusting the suspension system as well as the location and direction of the vibration exciters.

ANALYTICAL MODELS

Analysis Approach

The 1/8-scale SRB model is complicated by thick shell effects, that is, transverse shear deformation and motion between the aluminum casing and the propellant simulant. In addition, the SRB structure is not symmetrical since end skirts are reinforced for attachment to the rest of the shuttle system. In order to properly account for these effects in the 1/8-scale models and the comparative full-scale SRB configuration analyses were performed with three types of analytical models: a finite-element plate model, a finite-element beam model, and a shell of revolution model. Flat-plate elements were used for the finite-element shell model (FEP) to represent the casing and hexahedral elements were used to represent the thick propellant layer present at midburn and lift-off flight conditions. This model also is capable of accounting for the asymmetries of the end skirts as well as external tank attachment supports. The ability of this model to predict accurately the SRB response is of interest, since this class of models is a candidate for use in full-scale shuttle tankage analysis. Inherent in this dynamic model are many degrees of freedom which can be reduced for computational efficiency by the application of a Guyan reduction technique and by taking advantage of axial planes of symmetry, which exist in the propellant cylinder of the 1/8-scale SRB.

A more computationally efficient finite-element model was used to study the effects of asymmetrically attached end skirts and damping, and the overall agreement with test data for the membrane (longitudinal and torsional) and bending modes. This simpler model uses linear beam elements to represent the casing and propellant and is referred to as the finite-element beam (FEB) model. It is computationally more efficient than the previous model but cannot be used to calculate general shell modes involving distortion of the cylinder cross section.

A shell-of-revolution (SOR) analysis based on thin shell theory was used when analytical data were needed to show shell response trends such as the effect of high internal pressure on shell response at SRB burnout. This method is the most computationally efficient of the three analytical approaches. However, circumferential structural asymmetries, transverse shear deformations, and thick shell effects are either approximated or ignored in this approach.

The finite-element models are based on the displacement formulation of the NASTRAN code [19] and the shell-of-revolution code [20] is based on a numerical integration technique.

Finite-Element Shell Model

In order to simplify FEP model, the forward and aft skirts are not included. Therefore, the length of the cylinder model is that of the casing. The SRB was originally modeled for an earlier NASTRAN vibration study [10], and this model has been modified for use in this study. The relatively coarse grid used in Ref. [10] was satisfactory since only the lower mode responses are of interest and shell responses higher than two circumferential waves ($n = 1$) and three axial half waves ($m = 3$) generally yield frequencies above the range of interest. By use of axial symmetry planes, only a one-quarter (90°) model of the SRB propellant cylinder with proper combinations of symmetric, antisymmetric, and antisymmetric-symmetric boundary conditions along the longitudinal edges is required. This reduces the number of degrees of freedom by a factor of almost 4 and the total run time by a factor of 3. Thus, the basic grid for the FEP analysis is a 3 by 12 rectangular mesh which allows a rectangular element size spanning 30° circumferentially and one-twelfth of the propellant cylinder length axially. The casing is modeled using the NASTRAN isotropic flat-plate element, CQUAD2, and the propellant layer for the midburn and lift-off flight conditions is modeled using the NASTRAN isotropic solid hexahedron element, CHEXAL. The propellant thickness is modeled by two and three equal thickness layers for the midburn and lift-off flight conditions, respectively, using the CHEXAL element. The propellant layer at burnout is thin enough for a single layer of CQUAD2 elements to be used to represent its behavior. The beam element, CBAR, is used to represent the ring frames at the forward and aft edges of the cylinder. The CQUAD2 and CBAR elements both include membrane and bending stiffnesses. The CQUAD2 node motion is described by three displacements and two inplane rotational degrees of freedom. The constant-strain CHEXAL element is described by three displacements at each node. A preliminary study showed that a Guyan reduction equivalent to seven equally spaced longitudinal stations yielded well converged results. The number of degrees of freedom for the lift-off, midburn, and burnout models is 253, 211, and 71, respectively, for symmetry-symmetry axial boundary conditions and slightly higher for the asymmetry-asymmetry and asymmetry-symmetry boundary conditions.

The accuracy of this 90° model with the Guyan reduction is shown in Table IV for the casing without the interior propellant layer for the relevant response modes. The converged solutions were obtained using a shell-of-revolution code. The data show that longitudinal, torsional, and bending behavior is quite accurately predicted for the first several modes of response. The shell response predictions ($n \geq 2$) degenerate rapidly, however, as

the axial mode number increases. The first two frequencies at these circumferential wave numbers are of acceptable accuracy if it is recalled that the propellant is not included and that the stiffer models which have the propellant layer included were found to be more accurate. Comparison at burnout, midburn, and lift-off flight conditions are made in subsequent sections of this report.

The propellant is an incompressible material with a Poisson's ratio that approaches a value of 0.5. This value will cause the stress-strain matrix for the NASTRAN solid element, CHEXAL, to become singular since terms are present which contain the factor $(1 - 2\mu)$ in the denominator. Even with μ_p equal to 0.49, the stresses are overly magnified and the element consequently becomes overly stiff. For the FEP model, therefore, μ_p was taken to be 0.4 to avoid possible numerical instabilities for μ_p near 0.5. The effect of varying μ_p is considered further subsequently.

Finite-Element Beam Model

The finite-element beam model (FEB) was used to investigate the transverse shear and damping effects of the propellant mass as well as the effect of the forward and aft skirts on the frequencies. This FEB model can be used to investigate only the longitudinal, torsional, and bending modes of the SRB test model. The length of the FEB model was that of the propellant cylinder, 3.74 m.

The propellant cylinder was modeled as two six-element beams of equal length. One beam represents the casing and the other beam represents the propellant. Two beam elements of equal length were used to model the forward skirt. These beam elements were offset from the shell neutral surface to account for the asymmetric character of the stiffening in the forward skirt. The aft skirt cylinder is modeled as one beam element and the aft skirt cone is modeled by two equal length elements. The cross-sectional and mass properties are given in Tables V and VI. These tables include data required for modeling the lift-off, midburn, and burnout flight conditions.

The two beams representing the casing and the propellant can either be rigidly connected at common grid points, or by springs to allow relative motion between the two beams. The rigidly attached model results (without end skirts) were verified by excellent agreement with elementary beam theory [21] for longitudinal and torsional frequencies as shown in Table VII. Results by the FEB analysis for the bending response are slightly lower than those based on beam theory because the beam shear effect is accounted for in the element formulation.

The mass distribution matrix was generated in this analysis using the coupled mass matrix formulation described in Ref. [22]. The number

of degrees of freedom retained for this model was 84 without end skirts and 114 with skirts.

Shell-of-Revolution Model

The simplest and most computationally efficient manner of calculating frequencies for this study is to use a one-dimensional shell-of-revolution code. Since the thin shell criterion of the theory is violated in the midburn and lift-off flight condition studies, some caution must be used in interpreting the results for cases in which propellant stiffness contribution exceeds the magnitude for the casing stiffness. For the cases studied, this occurred only for the lift-off shell modes ($n \geq 2$). Also, the total mass of the thick propellant layer must be accounted for by using an effective mass density, $\bar{\rho}$, defined by

$$2\pi \bar{\rho} r_p t_p = \pi \rho \left[\left(r_r - \frac{t_c}{2} \right)^2 - \left(r_r - \frac{t_c}{2} - t_p \right)^2 \right]$$

Here, r_r is the radius to the reference surface located at the casing midsurface, ρ the mass density of the propellant, and t_c and t_p the layer thickness of the casing and propellant, respectively.

More details such as the different lengths of the propellant layer and the casing can be easily and accurately modeled using the shell-of-revolution approach. However, shear deformations and circumferential asymmetries in the shell could not be accounted for using this approach. Therefore the asymmetrically stiffened end skirts are not analyzed using this model. For the SOR model, the casing length is taken to be 3.73 m and extends 2.0 cm past each end of the propellant layer. The end frames are attached 1.27 cm from each edge of the casing. The elastic properties of the discretely modeled end frames are given in Table VIII.

RESULTS AND DISCUSSION

The results are presented as four main topics. First, experimental data for the propellant cylinders are presented. Second, a comparison of these results is made with the various analytical models. Third, the influence of propellant damping, addition of end skirts, and propellant material variations on shell response is presented. Fourth, a brief study of the effect of internal pressure on the 1/8-scale SRB and the full-scale shell dynamic response is presented. Unless otherwise specified, all discussions refer to SRB models without the end skirts, and the moduli of the propellant used are based on the values given in Ref. [12].

Test Results for the SRB 1/8-Scale Model

The frequencies obtained experimentally for the six 1/8-scale propellant cylinders at

the three flight conditions and with free-free boundary conditions are tabulated in Table IX. Two SRB scale models are tested at each flight condition and are identified by numbers 1 through 6. The responses excited are characterized as longitudinal and torsional membrane modes ($n = 0$), bending modes ($n = 1$), and general shell modes ($n \geq 2$) which involve distortion of the cylinder cross section. The n -number identifies the number of full harmonic circumferential waves and the m -number identifies the number of nodal circles occurring along a longitudinal generatrix which is analogous to the number of axial half waves for a freely supported shell. For the free-free cylinders, the rigid body modes in each direction are present but are ignored in the presentation of results. Higher longitudinal modes could not be excited. Modes involving a local motion of the propellant layer were found in the 200-Hz range for the lift-off and midburn flight conditions. Also, there were some shell modes ($n \geq 2$) which could not be identified due to the close coupling of modes and the resulting modal interference. These modes were ignored since their behavior could not be determined over the length of the models. In general, frequencies higher than about 250 Hz were not considered.

Comparison of Test and Analysis

To demonstrate the effect of the propellant modulus on the stiffness of the shell, a longitudinal frequency and a general shell ($n = 2$) frequency at the lift-off flight condition are compared in Fig. 8 with the results of an analysis in which the propellant stiffness contribution is ignored. For the longitudinal response, the membrane stiffness of the propellant is negligible compared to the casing stiffness and very little error is introduced if the propellant modulus is in error. For the shell mode, however, the contribution of the propellant bending stiffness is larger than that of the casing bending stiffness and variations in the modulus of the propellant directly affect the accuracy of the analysis. This effect should be less pronounced as the propellant layer stiffness contribution becomes less than that of the casing, that is, as the burnout condition is approached.

Shell-of-Revolution Results. A comparison of the experimental data with the SOR model analysis is presented first since the 1/8-scale SRB propellant cylinders are rotationally symmetric and since all modes of response can be accounted for by this analytical procedure. The longitudinal mode frequencies for the three flight conditions as a function of axial mode number m are shown in Fig. 9 for both the experimental data and the SOR analysis. The experimental results for these models are denoted by the symbols in the legend and correspond to the average of the frequencies obtained at the various model responses of a particular flight condition. At the midburn and lift-off flight conditions, the analysis overestimates the frequency because transverse

shear effects were neglected. The agreement becomes much better as the propellant mass becomes progressively less, that is, approaches burnout. The error varies from 15% at lift-off to less than 1% at burnout.

The analytical torsion mode frequencies for the three flight conditions along with available experimental data are linear functions of the axial mode number as shown in Fig. 10. Excellent agreement with experimental data is obtained for the burnout flight condition but transverse shear effects cause the analytical prediction to differ as much as 15% at lift-off.

The bending mode ($n = 1$) frequencies are shown in Fig. 11 and again frequencies are essentially linear functions of axial mode number. The agreement between experiment and analysis is quite good in all cases for m equal to 2 and 3 (i.e., first and second bending modes) and for m equal to 4 the agreement is within 10%.

The general shell modes are presented in Figs. 12 to 14 as functions of circumferential wave number for the lift-off, midburn, and burnout flight conditions. The shell-response frequencies ($n \geq 2$) decrease with decreasing mass. This result occurs because the bending stiffness of the propellant is equal to or greater than the bending stiffness of the casing. Thus, the propellant stiffness decreases as the cube of the propellant layer thickness while the mass decreases only as a linear function of the thickness. This is quite the opposite of the situation shown in Figs. 9 to 11 where the membrane stiffness remains nearly constant for all flight conditions because the casing membrane stiffness is much larger than the propellant membrane stiffness. In these cases, the increase in frequency as mass decreases is due to the mass loss.

There are no experimental data for comparison with analysis in Fig. 12 for the shell responses at lift-off, but the trend of the analytical behavior indicates that n equal to 2 is the minimum frequency shell mode. (The n equal to 1 results are bending modes and not shell modes.) The agreement between analysis and experiment is good except for the higher m values in the n equal to 2 and 3 modes of the midburn case (Fig. 13). For these modes, analysis and experiment differ by as much as 33% with analysis underestimating the frequency. This discrepancy for the shell modes ($n \geq 2$) of the midburn flight condition suggests that the error is due to a low estimate of the propellant modulus, since the agreement between analysis and experiment is excellent for the burnout flight condition (Fig. 14) where the propellant stiffness is small compared to the casing stiffness.

A typical set of mode shapes for normal displacements is shown in Fig. 15 for the first six modes at n equal to 2 for the burnout

flight condition. The straight lines indicate the profile of an undeformed SRB meridian, and the mode shape is superimposed on this meridian. The circular symbols on the undeformed meridian denote the attachment ring locations.

First, longitudinal, torsional, bending, and shell modes at n equal to 2 are compared in Fig. 16 for the three flight conditions with the available experimental data. The increase in longitudinal, torsional, and bending frequencies is due primarily to decrease in the mass of the propellant layer. For the shell modes, however, the propellant layer contributes a significant portion of the total bending stiffness at lift-off and the decrease in response frequency is attributed to the decrease in propellant stiffness. Thus at lift-off, the bending mode is the lowest and at burnout the general shell mode is the lowest. Shell modes greater than n equal to 2 do not yield minimum frequencies, as shown previously in Figs. 12 to 14.

Finite-Element Plate Results. A further comparison of experimental and analytical results is shown in Figs. 17 and 18 using the finite-element plate (FEP) model. The analytical results based on the NASTRAN FEP model are presented and compared with both the SOR analysis and the experimental data for various flight conditions. The frequencies for both the bending and shell modes are shown as a function of axial mode number in Figs. 17 and 18. In Fig. 17 the FEP analysis gives excellent agreement with experiment for the three flight conditions. The first two bending frequencies are within 5% of the experimental values. The agreement between the analyses and experiment for the first three axial modes at burnout and midburn in Fig. 18 is no worse than 17%. At lift-off, the agreement between the analyses is particularly good but no experimental data were obtained.

The FEP model yielded modes which could not be defined in terms of n and m numbers in the 200-Hz region of response for the lift-off and midburn flight conditions. These modes involved a local motion of the propellant layer and were high enough not to be of interest in this investigation.

Table X shows that the FEP model accurately predicts the membrane (longitudinal and torsional) and bending ($n = 1$) frequencies in the lower range of axial mode numbers. In general, the FEP models have yielded results for all modes of response and flight conditions that differ from the expected results by as much as 16% but usually differ by only 5%.

Finite-Element Beam Results. Also shown in Table X are the results from the NASTRAN finite-element beam (FEB) analysis along with the previously discussed SOR results. The separate beam elements of the case and propellant may be attached either rigidly or by

springs at common node points. For the results presented in Table X the elements are attached rigidly. The agreement of the FEB model with experiment is generally good, although the analytical longitudinal frequency is 17% in error at lift-off and the error for higher bending frequencies tends to grow. These analytical errors can be corrected by adding spring stiffnesses for all six degrees of freedom. It was hypothesized elsewhere* that the propellant shears with respect to the casing (with the bond line still maintained). This behavior was modeled by the introduction of springs. The stiffnesses of the springs were first estimated by static structural analyses and then adjusted by a simple curve-fitting procedure, based on an acceptable agreement between test and analytical frequencies, to establish an approximate model. Table XI shows the final stiffnesses used in the analytical models for the three flight conditions, and Table XII summarizes the analytical results of the spring-beam-element model. The agreement with experimental data for the beam model with springs is 10% or better. The remaining comparisons in this report for the beam model (FEB) are based on the inclusion of springs.

Additional Model Studies

Damping Results. Theoretical and experimental results for models that consider damping effects in the propellant cylinders are summarized in Tables XIII and XIV. Experimental damping coefficients in Table XIV are highest for the first longitudinal mode (0.17), which helps to explain why this mode was difficult to excite and the higher longitudinal modes could not be found. Damping coefficients in torsion and bending are significantly lower (0.008 to 0.08) and more typical of all-metal structures.

Because the propellant is a viscoelastic material, its elastic moduli are complex quantities representing the inherently combined elastic and material damping properties. Referring to Ref. [12], the dynamic modulus may be defined as

$$E_p = E'_p + i E''_p$$

where the real quantity E'_p is the storage modulus and the imaginary quantity E''_p is the loss modulus. This expression may also be written as

$$E_p = E'_p \left(1 + i \frac{E''_p}{E'_p} \right)$$

where $\frac{E''_p}{E'_p}$ is a loss factor or loss tangent

which can be shown to be equal to the material structural damping coefficient. The shear

moduli and shear damping properties can be described similarly. In the present analytical studies, these effects were simulated in the NASTRAN beam model by including the propellant structural damping coefficient with the storage modulus (E'_p) in the material property input data and then solving for the eigenvalues of the resulting complex frequency equation using NASTRAN's Rigid Format 7. This is essentially the same approach as that used in a NASTRAN SRB model† made up of contiguous ring elements. The frequencies and damping coefficients given in Tables XIII and XIV were obtained for a loss factor of 0.5; the frequencies in Table XIII come from the imaginary parts and the damping coefficients in Table XIV from the real parts of the complex eigenvalues. As shown in Table XIII, the agreement of analysis with experiment is good and the changes from the FEB frequencies given in Table XII are slight for the cases studied. Also, the change in frequency due to the different propellant moduli amounts to no more than a 3% difference for the cases studied. In Table XIV it is shown that the agreement between theory and experiment for damping coefficients is poor for the bending modes but reasonably good for the membrane modes. The analysis predicts the damping trends for both bending and membrane modes. The undamped frequencies for these beam and membrane modes have been shown previously to be only slightly affected by the propellant modulus.

SRB Skirt Results. The FEB model was also used to compare the analytical and experimental frequencies of the SRB with forward and aft skirts attached for the three flight stages. Table XV summarizes the results of this study and shows the agreement for the burnout and midburn frequencies to be within 5% (except for the third bending mode at midburn). Experimental data for the lift-off flight condition model with skirts are not available for comparison. On examining the results, the analysis showed that the torsion mode and second beam bending mode are strongly coupled for the midburn and lift-off flight conditions. A comparison of Tables XII and XV shows that the addition of the skirts lowers the lift-off and midburn frequencies and the burnout membrane frequencies by approximately 10% while burnout bending frequencies may be lowered by as much as 25%.

Elastic Property Variation Results. Two problems related to the modeling of the propellant material have been noted in this report. One problem is related to the wide variation in the elastic modulus which is apparently a function of strain level and frequency. The other problem is related to numerical singularities which occur as a result of using solid finite elements that are based on a displacement formulation to model incompressible materials. The former problem is expected to affect only the shell modes since the total membrane stiffness is derived almost entirely from the casing

* See report referred to in first footnote.

† See report referred to in first footnote.

stiffness. The effect on the shell frequencies of using the higher modulus values of Ref. [10] rather than the lower modulus values of Ref. [12] for the lift-off and burnout flight conditions is shown in Figs. 19(a) and 19(b) where comparisons are made using the SOR models. The curves indicate that the lower modes (i.e., the lower m values) are influenced the most and that frequencies are increased by as much as 125% and 29% for the lift-off and burnout cases, respectively.

The variation in natural frequency response with changes in Poisson's ratio for the FEP analysis is shown in Fig. 20 for the first shell mode at n equal 2 of the lift-off flight condition. The bar graph shows relatively wide variations in frequency for values of Poisson's ratio above about 0.4. The changes due to values higher than 0.4 are suspected to be due to numerical singularities induced in the NASTRAN solid element as Poisson's ratio approaches 0.5. The value of 0.4 for Poisson's ratio was selected in the present report to avoid such numerical instabilities when the CHEXAL solid elements were used in the FEP models.

Comparison With Idealized Full-Scale Behavior

Some appreciation of the differences in the behavior of the scale model and the full-scale model can be determined by studying analytically the behavior of the full-scale model at the burnout flight condition. An SOR analysis is used to obtain the frequencies and mode shapes of an idealized full-scale SRB without skirts or bulkheads. The geometric and material properties used are given in Table XVI. The SRB is composed of six equal-length propellant cylinder segments and a motor case skirt. Each of the propellant cylinders is 4.06 m long. The motor case skirt is composed of four cylindrical segments which are 2.18, 3.04, 3.04, and 0.50 m long, respectively. The 2.18-m segment attaches to the aft propellant cylinder and the 0.50-m segment is the aft component of the motor case skirt. The six propellant cylinders and the four segments of the motor case skirt are all cylinders. Asymmetries in the structure are neglected for the analysis. The 10 cylindrical segments are connected by joint rings with the elastic properties shown in Table XVII. Such a joint ring is also placed at the forward edge of the model. At the aft edge of the motor case, the aft skirt ring (referred to in Table XVII) is used. The two 3.04-m segments of the motor case skirt are each reinforced at one-third points along the meridian with the motor case ring. Finally, the support ring is located on the 2.18-m segment of the motor case skirt at a distance of 0.495 m from the motor case skirt juncture to the aft propellant cylinder. For modeling purposes, this large support ring is divided into two equal parts located 0.343 m and 0.648 m from the propellant cylinder and motor case skirt juncture.

The membrane and beam frequencies are shown in Fig. 21 as a function of longitudinal mode number and the shell mode frequencies are shown in Fig. 22 as a function of circumferential wave number for the burnout flight condition. Also shown in Fig. 21 with dashed lines are frequencies at which the SRB is subjected to a static pressure loading that is present during combustion of the propellant. A simple membrane stress state was assumed that neglects ring loads and rotations and assumes the stress resultants to be given by

$$N_x = \frac{pr_i^2}{2r_r}$$

$$N_\theta = pr_i$$

where r_i is the inner radius of the propellant and r_r is the radius of the casing reference surface. The applied pressure, p , is 4.02 MPa. The responses shown in Fig. 21 are essentially unaffected by the static pressure.

The results in Fig. 21 are similar in character to those in Figs. 9 to 11 except that the free vibration frequencies for first longitudinal and torsional modes are lower by a factor of about 9.5 and the bending mode response is lower by a factor of 11.

Additional results in Fig. 22 show the influence of the large internal pressure expected at burnout on shell frequency for both the 1/8-scale and full-scale models. The ordinate axes in Fig. 22 are at an 8:1 ratio for comparison purposes. The shell frequencies are affected significantly and the static stress state increases the lower axial mode burnout frequencies by at least a factor of 2.5. The free vibration frequencies of the full-scale model show a behavior similar to that of the 1/8-scale model but the frequencies are lower by a factor of about 13. Deviation of the full-scale free vibrations results from the scaled results based on a scale factor of 8 are attributed primarily to differences in the full-scale structural designs. Thus, direct scaling comparisons cannot be made for free vibrations. For frequencies with static pressure added, however, the response ratio closely approximates the 8:1 factor.

Typical mode shapes for the n equal to 2 frequencies are shown in Fig. 23 (at $p = 0$). The straight lines indicate the profile of the undeformed SRB meridian and the mode shape is superimposed on this meridian. The circular symbols on the undeformed meridian denote ring locations.

CONCLUDING REMARKS

Vibration characteristics of six 1/8-scale rocket booster dynamic models have been

determined both experimentally and analytically. Two models were used to represent each of three flight conditions corresponding to lift-off, midburn, and burnout conditions. Frequencies have been determined for these SRB propellant cylinder models with and without end skirts, and damping coefficients have been presented for the propellant cylinder at the lift-off flight condition.

The study showed that the finite-element shell model composed of flat-plate elements could be used to calculate frequency responses to within 3% of experimental data for the lowest membrane and bending modes and within 6% for the lower shell modes. However, discrepancies with experiment as large as 33% were noted for the higher shell modes and were attributed to the relatively coarse grid used in the finite-element analyses. Also, the NASTRAN three-dimensional element used in some of the analyses cannot account for material incompressibility and a value of Poisson's ratio less than measured material values for the propellant was used to avoid singularities in the stiffness matrix. A value of Poisson's ratio equal to 0.4 was found to be sufficient to avoid the stiffness singularity occurring at a value of 0.5. Wide variations in the propellant layer modulus due to frequency and strain level cause difficulty in assessing the accuracy of the various models for thick propellant layers.

A finite-element beam model was used to assess the effects of end skirts and damping. The addition of end skirts does not appreciably affect the correlation of the experimental and analytical results and lowers the frequency of membrane and bending modes by no more than 10%. The effect of damping on analytical frequencies is small, and reasonably accurate damping coefficients for torsional and longitudinal responses were calculated. The high damping present in the first longitudinal response mode accounts for the inability to find the higher longitudinal natural frequencies experimentally.

A shell-of-revolution analysis was effectively used to determine the effects of changes in propellant layer thickness and internal pressure on dynamic response even though the thin shell criterion for this analysis is violated. The shell-of-revolution analysis gave good agreement with all vibration modes in the near burnout propellant condition. For thicker propellant conditions, beam and torsional mode agreement was good, but agreement for the shell modes was only fair at higher frequencies.

Analytical comparisons were made between the behavior of an idealized full-scale shuttle SRB with scale models in the near burnout condition. Results show that full-scale models give similar trends in behavior but results cannot be directly compared to scale models due to significant differences in the full-scale structural designs. The effects of internal pressure on both scaled model and full-scale models is shown to be small or negligible for bending,

longitudinal, and torsion modes. The internal pressure, however, raised the shell frequencies significantly.

The present study was intended to provide early data on vibrations of space shuttle-like solid fuel tanks. Experimental results suggest that in tests of unpressurized tankage, some difficulty may be experienced in separating shell modes from bending modes in near-burnout fuel conditions. Significant damping is likely to be observed only in the longitudinal vibration modes. Analytical results suggest that elementary beam finite-element and plate finite-element models can be used effectively to predict membrane, bending, and lower shell modes. For higher shell modes, more refined finite-element or shell-of-revolution analysis will be required.

REFERENCES

- [1] H. L. Runyan, H. G. Morgan, and J. S. Mixon, "Use of Dynamic Models in Launch Vehicle Development," AGARD Report 479, May 1964.
- [2] P. R. Guyett, "The Use of Flexible Models in Aerospace Engineering," RAE Technical Report 66335, Nov. 1966.
- [3] John S. Mixon, and John J. Catherines, "Comparison of Experimental Vibration Characteristics Obtained From a 1/5-Scale Model and From a Full-Scale Saturn SA-1," NASA TN D-2215, 1964.
- [4] Ivan J. Jaszlics, and George Morosow, "Dynamic Testing of a 20 Percent Scale Model of the Titan III," Proceedings of the AIAA Symposium on Structural Dynamics and Aeroelasticity, pp. 477-485, 1965.
- [5] S. A. Leadbetter, and J. P. Raney, "Analytical and Experimental Studies of the Dynamics of Launch Vehicles," J. Spacecraft and Rockets, Vol. 3, No. 6, June 1966.
- [6] L. D. Pinson, and H. W. Leonard, "Longitudinal Vibration Characteristic of 1/10-Scale Apollo/Saturn V Replica Model," NASA TN D-5159, April 1969.
- [7] Anon., "Advancements in Structural Dynamic Technology Resulting From Saturn Programs," NASA CR-1540, 1969.
- [8] P. W. Mason, H. G. Harris, J. Zalesak, and M. Bernstein, "Analytical and Experimental Investigation of a 1/8-Scale Dynamic Model of the Shuttle Orbiter," May 1974, NASA CR-132488, Vol. I, Summary Report, NASA CR-132489, Vol. II, Technical Report, NASA CR-132490, Vol. IIIA, Supporting Data, NASA CR-132491, Vol. IIIB, Supporting Data.

- [9] M. Bernstein, R. Coppolino, J. Zalesak, and P. W. Mason, "Development of Technology for Fluid-Filled Structure Interaction Modeling of a 1/8-Scale Dynamic Model of the Shuttle External Tank (ET)," Aug. 1974, NASA CR-132549, Vol. I, Technical Report, Vol. II, Supporting Data, Appendices A through C.
- [10] A. Levy, J. Zalesak, M. Bernstein, and P. W. Mason, "Development of Technology for Modeling of a 1/8-Scale Dynamic Model of the Shuttle Solid Rocket Booster (SRB)," NASA CR-132492, July 1974.
- [11] L. D. Pinson, coordinator, "Analytical and Experimental Vibration Studies of a 1/8-Scale Shuttle Orbiter," NASA TN D-7964, 1975.
- [12] William L. Hufferd, "Measured Elastic Properties of Propellant for Solid Rocket Booster of One-Eighth-Scale Dynamic Shuttle Model," NASA CR-144938, 1976.
- [13] Robert W. Herr, "Some Cable Suspension Systems and Their Effects on the Flexural Frequencies of Slender Aerospace Structures," NASA TN D-7693, Sept. 1974.
- [14] Anton C. Keller, "Vector Component Techniques: A Modern Way to Measure Modes," *Sound and Vib.*, Vol. 3, No. 3, pp. 18-26, Mar. 1969.
- [15] Robert A. Salyer, J. Jung, Jr., Ed., Stacy L. Huggins, and Barry L. Stephens, "An Automatic Data System for Vibration Model Tuning and Evaluation," NASA TN D-7945, April 1975.
- [16] James A. Schoenster, "Measured and Calculated Vibration Properties of Ring-Stiffened Honeycomb Cylinders," NASA TN D-6090.
- [17] James A. Schoenster, and Nancy L. Taylor, "A Sinusoidal-Vibration Analysis Program for Experimental Data," NASA TM X-2789, Oct. 1973.
- [18] Lloyd J. Turner, Jr., "An Analytical Investigation of a Vector Technique for Determining Normal Mode Amplitudes From Vibration Data," Master of Science Thesis, Virginia Polytechnic Institute, May 1968.
- [19] Caleb W. McCormick, "The NASTRAN User's Manual (Level 15)," NASA SP-222(01), 1972, Washington, D.C., May 1973.
- [20] Gerald A. Cohen, "User Document for Computer Programs for Ring-Stiffened Shells of Revolution," NASA CR-2086, Mar. 1973.
- [21] J. P. Den Hartog, *Mechanical Vibrations*, 2nd edition, McGraw-Hill Book Company, Inc., New York and London, 1940.
- [22] Richard H. MacNeal, "The NASTRAN Theoretical Manual," NASA SP-221(01), pp. 5.5-4, Washington, D.C., April 1972.

TABLE I. Pertinent Scaling Relations for 1/8-Scale Model of SRB

Physical quantity	Magnitude	
	Propellant	Structure*
Length (overall) and displacement	$8L_m = L_p$	$8L_m = L_p$
Mass density	$\rho_m = \rho_p$	$3\rho_m = \rho_p$
Modulus of elasticity	$E_m = E_p$	$3E_m = E_p$
Area	$8^2 A_m = A_p$	$8^2 A_m = 3A_p$
Area moment of inertia	$8^4 I_m = I_p$	$8^4 I_m = 3I_p$
Volume	$8^3 V_m = V_p$	$8^3 V_m = 3V_p$
Weight	$8^3 \rho_m V_m = \rho_p V_p$	$8^3 \rho_m V_m = \rho_p V_p$
Longitudinal stiffness	$8^2 E_m A_m = E_p A_p$	$8^2 E_m A_m = E_p A_p$
Bending stiffness	$8^4 E_m I_m = E_p I_p$	$8^4 E_m I_m = E_p I_p$
Frequency	$f_m = 8f_p$	$f_m = 8f_p$

* Aluminum used in model to represent steel in the prototype.

Subscripts: p = prototype
m = scaled model

TABLE II. Mass of the Components of the 1/8-Scale SRB Model

Component	Mass, kg
Casing	76.02
Propellant, lift-off	1065.86
Propellant, midburn	698.40
Propellant, burnout	171.00
Forward ring	1.50
Aft ring	1.09
Forward skirt	6.58
Aft skirt	14.86

TABLE III. Material Properties of the 1/8-Scale SRB

Property	Casing	Propellant ^a [10]	Propellant ^a [12]
E, GPa	72,994	172.4	30.0
ρ , kg/m ³	7.164	4.407	4.407
μ	.3	.5	.5

^aProperties selected at a nominal room temperature of 22° C and a frequency range of 100 to 120 Hz.

TABLE IV. Convergence Study for Frequencies of FEP Model 1/8-Scale Aluminum Casing Compared With SOR Analysis (Frequencies in Hz)

Type	Mode		SOR	FEP	% error
	n	m			
1st longitudinal	0	1	661.9	663.7	0.3
2nd longitudinal		2	1312.8	1335.7	1.7
3rd longitudinal		3	1931.9	2008.2	3.9
1st torsional	0	1	410.3	397.5	-3.1
2nd torsional		2	820.7	804.4	-2.0
3rd torsional		3	1231.5	1222.1	-0.8
1st bending	1	2	195.8	206.3	5.4
2nd bending		3	465.8	486.5	4.4
Shell	2	0	58.4	65.2	11.6
		1	87.6	107.4	22.6
		2	126.6	161.3	27.4
	3	3	207.7	266.1	28.1
		0	146.5	157.5	7.5
		1	159.0	189.2	19.0
	4	2	195.3	265.3	35.8
		3	255.0	368.0	44.3
		0	279.3	297.8	6.6
		1	283.6	315.9	11.4
		2	295.5	364.0	23.2
		3	319.7	448.4	71.3

TABLE V. Cross-Sectional Properties for Elements Used in NASTRAN FEB Model of SRB With Skirts Attached

Property	Casing elements	Propellant elements			Forward skirt elements		Aft skirt elements		
		Lift-off	Midburn	Burnout	Inner	Outer	Cylinder	Core inner	Core outer
Area, cm ²	73.39	1523.80	1111.48	272.13	23.68	19.87	24.41	36.01	43.83
I _z , cm ⁴	22,077.	271,162.	229,547.	74,378.	5011.	5003.	7442.	12942.	24563.
I _y , cm ⁴	22,077.	271,162.	229,547.	74,378.	9103	6701.	7442.	16256.	30374.
J, cm ⁴	44,154.	542,308.	459,095.	148,757.	15,026.	11672.	14884.	29207.	54934.
\bar{y} , cm					7.99	4.92			
k	.5	.9	.52	.5	.5	.5	.5	.8	.8

TABLE VI. Discrete Mass and Torsional Mass Moments of Inertia Properties of NASTRAN FEB Model of 1/8-Scale SRB With Skirts Attached

Grid point position	I _{xx} , g · m ²	Mass, kg	I _{xx} , g · m ²		
			Lift-off	Midburn	Burnout
Casing, forward edge	1.244	0.00394			
Casing, aft edge	1.171	.00280			
Casing interior points	1.972				
Propellant, forward edge			7.153	5.791	1.877
Propellant, aft edge			7.153	5.791	1.877
Propellant, interior points			14.920	12.610	4.087
Forward skirt, outer edge	.282	.00399			
Forward skirt, interior point	.206	.00064			
Forward skirt, attachment	.389	.00486			
Aft skirt, attachment	.372	.00726			
Aft skirt, cylinder-cone edge	.681	.00726			
Aft skirt, cone interior point	.811	.00086			
Aft skirt, outer edge	1.364	.00604			

TABLE VII. Comparison of FEB Model Frequencies With Theory
(E_p = 172.4 MPa, μ_p = 0.50). Frequencies in Hz

Type	Mode		Lift-off		Midburn		Burnout	
	n	m	FEB	Ref. [21]	FEB	Ref. [21]	FEB	Ref. [21]
1st longitudinal	0	1	181.4	181.4	215.15	215.47	376.45	379.80
1st torsion	0	1	146.3	148.0	156.15	155.89	238.14	239.0
1st bending	1	2	56.13	59.03	66.26	71.24	117.17	127.17

TABLE VIII. Ring Elastic and Cross-Sectional Properties Used in the SOR Analysis of the 1/8-Scale SRB Model

Property	Forward ring	Aft ring
E, GPa	72.394	72.394
A, cm ²	3.258	2.426
I _x , cm ⁴	1.973	1.428
I _z , cm ⁴	1.819	1.274
I _{xz} , cm ⁴	-.982	.753
GJ, GNm ²	20.06	6.74
\bar{x} , cm	1.024	1.120
\bar{z} , cm	.975	.871

TABLE IX. Experimental Frequencies (Hz) for 1/8-Scale SRB Model Propellant Cylinders With Free-Free Boundary Conditions

Mode description			Burnout		Midburn		Lift-off	
Type	Shape		Model 1	Model 2	Model 3	Model 4	Model 5	Model 6
	n	m						
1st longitudinal	0	1	373.4	369.5	187.5	185.9	149.7	156.6
1st torsional	0	1	237.2	235.5	147.5	145.5	135.3	135.1
1st bending	1	2	112.6	112.2	64.6	64.8	54.1	54.2
2nd bending		3	265.6	263.4	150.2	150.9	126.5	126.6
3rd bending		4		435.3	240.0	241.7	201.8	204.8
Shell	2	1	54.7	52.9				
		2	77.6	75.6	103.0	114.7		
		3	121.7	120.0	131.0			
		4	196.7	195.4				
		5	297.0	290.5	200.0	194.4		
		6				247.5		
	3	5	230.2	227.0				
	4	5	268.0					

TABLE X. Frequencies (Hz) for Three Analyses and Experiment for Membrane and Bending Modes for Three Flight Conditions

Type	Mode		Test	Analysis									
	n	m		FEP	FEB (rigid)	SOR							
			(a) Lift-off										
			Model #5	Model #6									
			1st longitudinal	0				1	149.7	156.6	128.7	177.4	175.3
			1st torsional	0				1	135.3	135.1	131.6	144.8	155.7
			1st bending	1				2	54.1	54.2	56.8	55.3	54.4
2nd bending		3	126.5	126.6	126.1	134.0	130.7						
3rd bending		4	201.8	204.8	177.3	227.9	216.6						
			(b) Midburn										
			Model #3	Model #4									
			1st longitudinal	0				1	187.5	185.9	178.0	211.2	214.2
			1st torsional	0				1	147.5	144.5	145.0	154.2	158.9
			1st bending	1				2	64.6	64.8	69.8	65.3	66.4
2nd bending		3	150.2	150.9	153.9	158.3	157.8						
3rd bending		4	240.0	241.7		268.6	262.3						
			(c) Burnout										
			Model #1	Model #2									
			1st longitudinal	0				1	373.4	369.5	366.9	375.5	369.4
			1st torsional	0				1	237.2	235.5	227.9	237.6	237.5
			1st bending	1				2	112.6	112.2	115.9	116.2	111.8
2nd bending		3	265.6	263.4	272.5	282.0	264.6						

TABLE XI. Spring Stiffnesses at Element Nodes for the NASTRAN FEB Model of the 1/8-Scale SRB Propellant Cylinders

Spring constant	Lift-off	Midburn	Burnout
k_x , GN/m	0.377	0.516	6.031
k_y, k_z , GN/m	.613	.533	.296
β_x , kNm	20.999	27.070	163.097
β_y, β_z , kNm	7.744	26.638	329.696

TABLE XII. Propellant Cylinder Test Comparisons With FEB Models With and Without Springs. (Frequencies in Hz.)

Type	Mode		Test		FEB models	
	n	m			Rigid	With springs
			(a) Lift-off			
			Model #5	Model #6		
			149.7	156.6		
			135.3	135.1		
			54.1	54.2		
1st longitudinal	0	1	149.7	156.6	177.4	143.2
1st torsional	0	1	135.3	135.1	144.8	132.1
1st bending	1	2	54.1	54.2	55.3	54.5
2nd bending		3	126.5	126.6	134.0	121.8
3rd bending		4	201.8	204.8	227.9	183.7
			(b) Midburn			
			Model #3	Model #4		
			187.5	185.9		
			147.5	145.5		
			64.6	64.8		
1st longitudinal	0	1	187.5	185.9	211.2	183.0
1st torsional	0	1	147.5	145.5	154.2	144.5
1st bending	1	2	64.6	64.8	65.3	65.9
2nd bending		3	150.2	150.9	158.3	149.2
3rd bending		4	240.0	241.7	268.6	229.9
			(c) Burnout			
			Model #1	Model #2		
			373.4	369.5		
			237.2	235.5		
			112.6	112.2		
1st longitudinal	0	1	373.4	369.5	375.5	371.8
1st torsional	0	1	237.2	235.5	237.6	235.6
1st bending	1	2	112.6	112.2	116.2	115.0
2nd bending		3	265.6	263.4	282.0	261.5

TABLE XIII. Comparison of Experimental and Analytical Frequencies at Lift-Off of 1/8-Scale SRB Propellant Cylinder With Structural Damping Added

Type	Mode		Experiment		FEB ^a	
	n	m	Model #5	Model #6	Ref. [10] ^a	Ref. [12] ^b
1st longitudinal	0	1	149.7	156.6	152.7	147.4
1st torsional	0	1	135.3	135.1	135.9	134.2
1st bending	1	2	54.1	54.2	55.6	54.7
2nd bending		3	126.5	126.6	127.1	123.8
3rd bending		4	201.8	204.8	197.2	189.3

^aLoss factor = 0.5.

^bSee Table III for propellant material properties.

TABLE XIV. Comparison of Experimental and Analytical Damping Factors at Lift-Off for the 1/8-Scale SRB Propellant Cylinder With Structural Damping Added (Loss Factor = 0.5)

Type	Mode		Experiment		FEB ^a	
	n	m	Model #5	Model #6	Ref. [10] ^b	Ref. [12] ^b
1st longitudinal	0	1	0.174	0.166	0.180	0.160
1st torsional	0	1	.056	.068	.083	.070
1st bending	1	2	.009	.008	.030	.020
2nd bending		3	.027	.026	.090	.080
3rd bending		4	.078	.066	.168	.161

^aLoss factor = 0.5.

^bSee Table III for propellant material properties.

TABLE XV. Comparison of Experimental and Analytical Frequencies of the 1/8-Scale SRB With End Skirts Attached (Frequencies in Hz)

Type	Mode		Experiment	FEB with skirts
	n	m		
1st longitudinal 1st torsional 1st bending 2nd bending 3rd bending	0 0 1 3 4	1 1 2 3 4	(a) Lift-off	142.1 128.2 51.5 115.1 177.7
			Model #5 with skirts	
			143.4	
			129.7	
			50.7	
			117.3	
1st longitudinal 1st torsional 1st bending 2nd bending 3rd bending	0 0 1 3 4	1 1 1 3 4	(b) Midburn	180.2 139.4* 60.7 137.8 214.7
			Model #4 with skirts	

			139.8	
			59.3	
			135.2	
1st longitudinal 1st torsional 1st bending 2nd bending	0 0 2 3	1 1 2 3	(c) Burnout	341.8 212.0* 93.0 210.0

TABLE XVI. Material and Geometric Properties of Full-Scale SRB Without Skirts

Property	Casing	Propellant
E, MPa	199,955.0	30.0
μ	.3	.5
ρ , kg/m ³	20.27	4.407
Length, m	33.16	-----
Radius (outer), m	1.85	1.84
Radius (inner), m	1.84	1.69

TABLE XVII. Ring Properties for Full-Scale SRB Without Skirts

Type	A, cm ²	I_x , cm ⁴	I_z , cm ⁴	I_{xz} , cm ⁴	J, cm ⁴	\bar{x} , cm	\bar{z} , cm
Joint ring	17.48	39.25	161.83	8.16	4.25	-0.165	0.536
Motor case ring	18.00	819.98	34.55	15.61	1.91	10.795	3.800
Aft skirt ring	110.45	14277.56	934.44	-287.32	138.19	9.357	6.764
Support ring, forward	15.73	847.45	72.38	122.33	1.47	13.360	-.874
Support ring, aft	15.73	847.45	72.38	-122.33	1.47	13.360	+.874

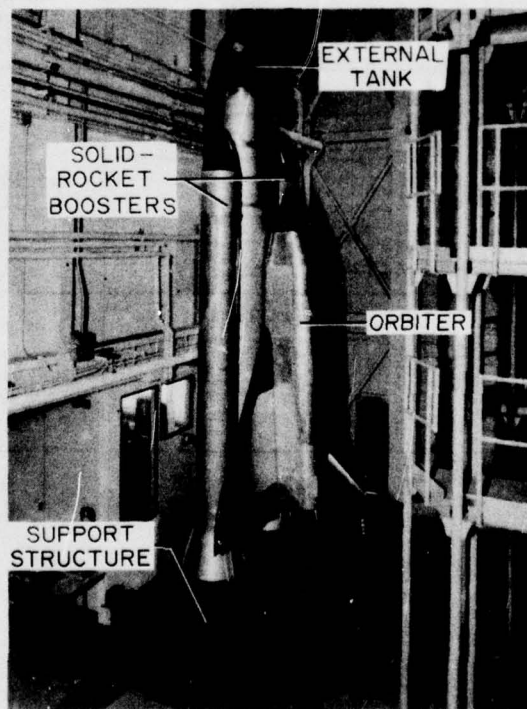


Fig. 1 - Space shuttle 1/8-scale dynamic model

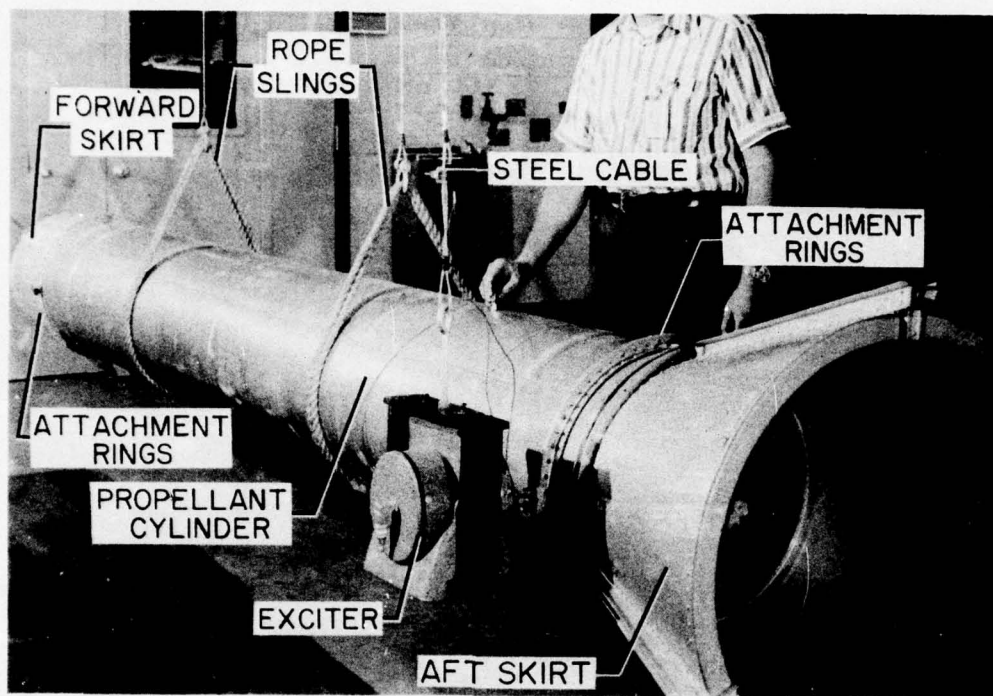


Fig. 2 - Solid rocket booster 1/8-scale dynamic model

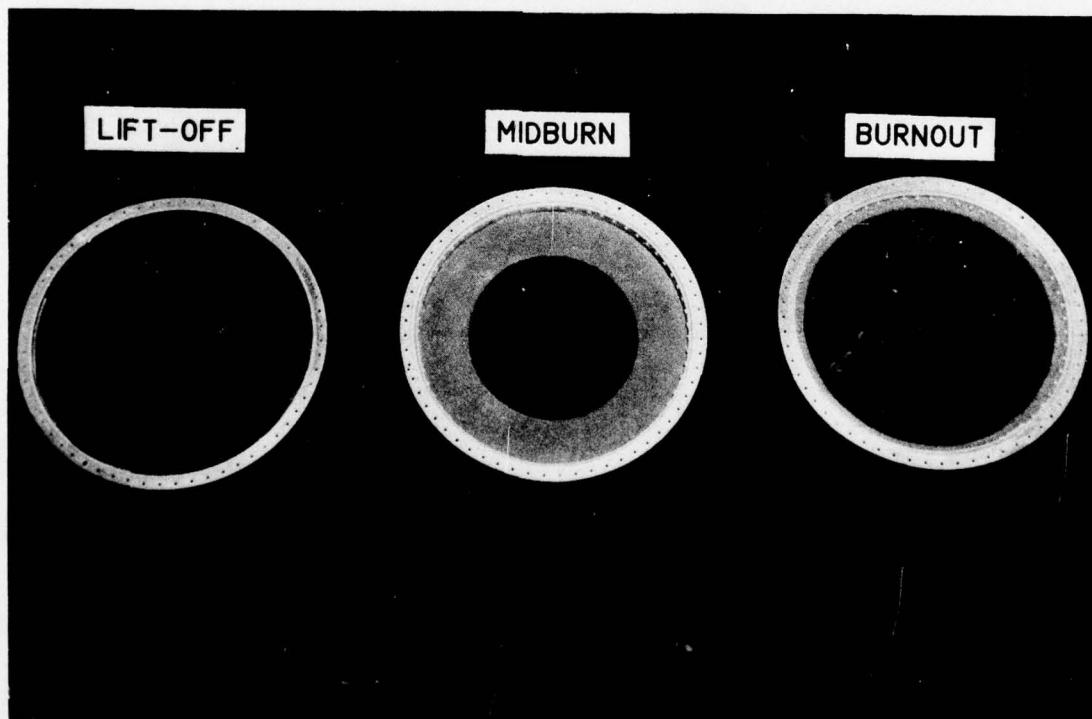


Fig. 3 - The 1/8-scale SRB model propellant cylinders for different flight conditions

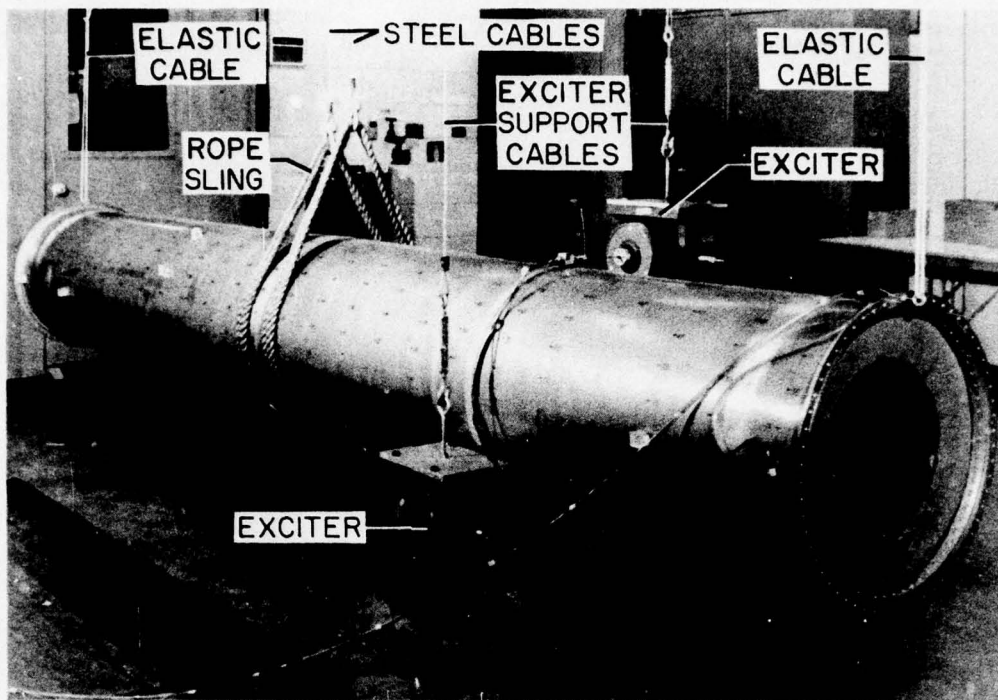


Fig. 4 - The 1/8-scale propellant cylinder at midburn flight condition suspended for testing

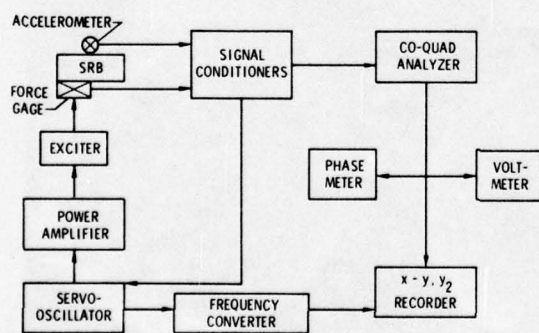


Fig. 5 - Schematic diagram of data acquisition system

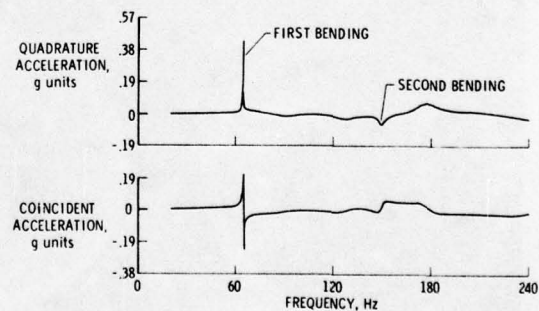


Fig. 6 - Typical SRB model co-quad data with simulated free-free support for the midburn flight condition. The components are referenced to a constant servo-controlled force input of 13 N

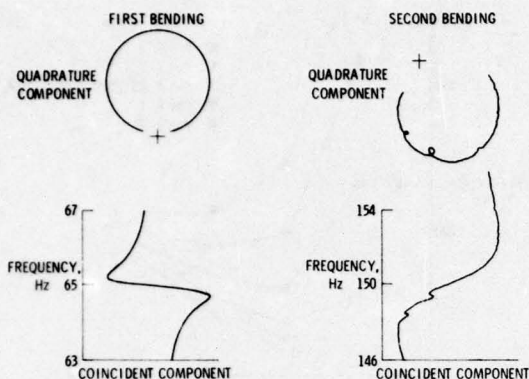


Fig. 7 - Typical SRB model phase-plane (Kennedy-Pancu) data with simulated free-free support for the midburn flight condition. Components are referenced to a constant servo-controlled force input of 13 N

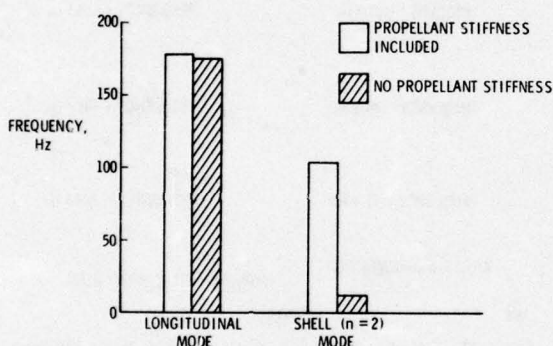


Fig. 8 - Effect of propellant membrane and bending stiffnesses on frequency at lift-off flight condition

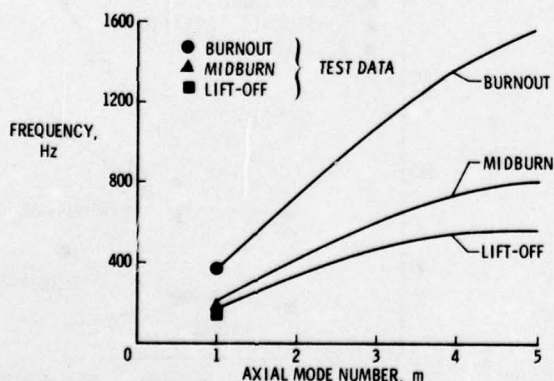


Fig. 9 - Comparison of the experimental free-free longitudinal ($n = 0$) vibration frequencies of the 1/8-scale model propellant cylinders with the shell-of-revolution analysis

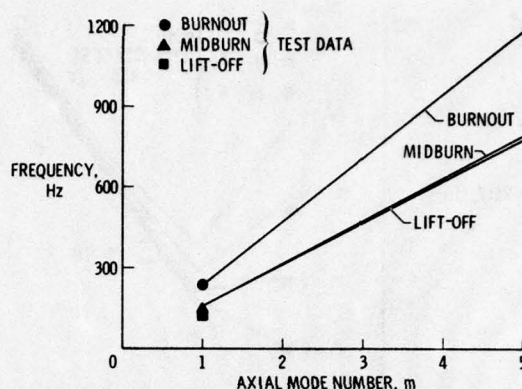


Fig. 10 - Comparison of the experimental free-free torsional ($n = 0$) vibration frequencies of the 1/8-scale model propellant cylinders with the shell-of-revolution analysis

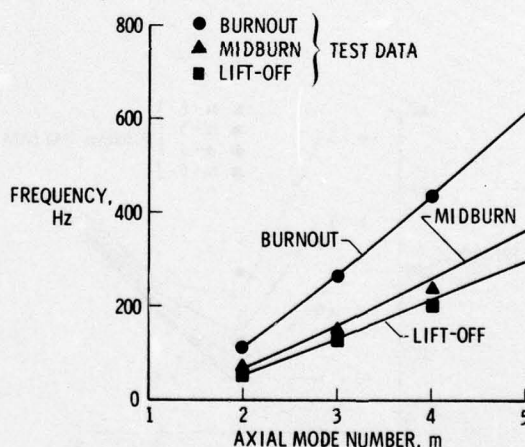


Fig. 11 - Comparison of the experimental free-free bending ($n = 1$) vibration frequencies of the 1/8-scale model propellant cylinder with the shell-of-revolution analysis

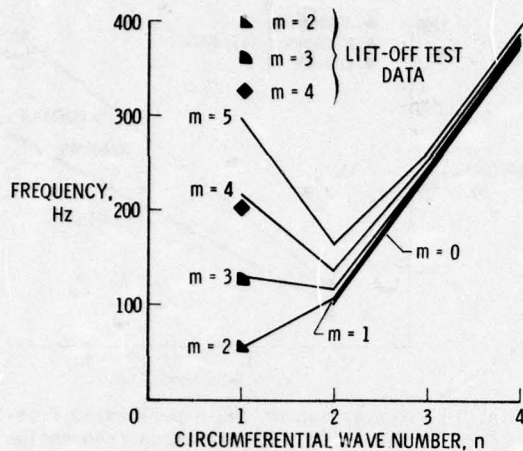


Fig. 12 - Comparison of the experimental free-free shell vibration frequencies at lift-off of the 1/8-scale model propellant cylinder with the shell-of-revolution analysis

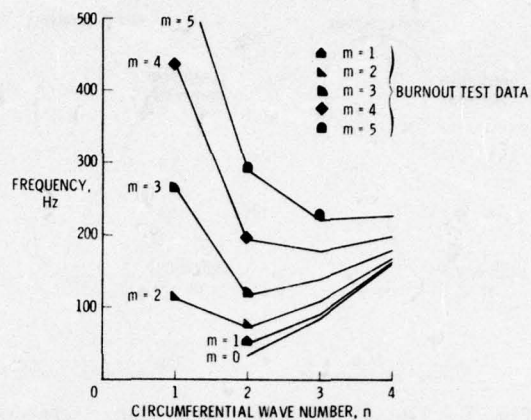


Fig. 14 - Comparison of the experimental free-free shell vibration frequencies at burnout of the 1/8-scale model propellant cylinder with the shell-of-revolution analysis

FREQUENCY = 33.4 Hz

FREQUENCY = 117.1 Hz

FREQUENCY = 49.3 Hz

FREQUENCY = 193.6 Hz

FREQUENCY = 71.9 Hz

FREQUENCY = 289.5 Hz

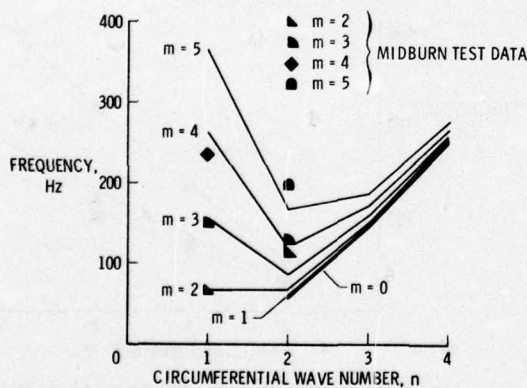


Fig. 13 - Comparison of the experimental free-free shell vibration frequencies at midburn of the 1/8-scale model propellant cylinder with the shell-of-revolution analysis

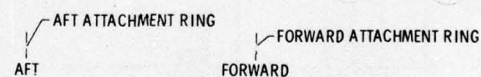


Fig. 15 - Mode shapes and frequencies for normal displacement of the 1/8-scale SRB at burnout along a meridian using SOR analysis with $n = 2$

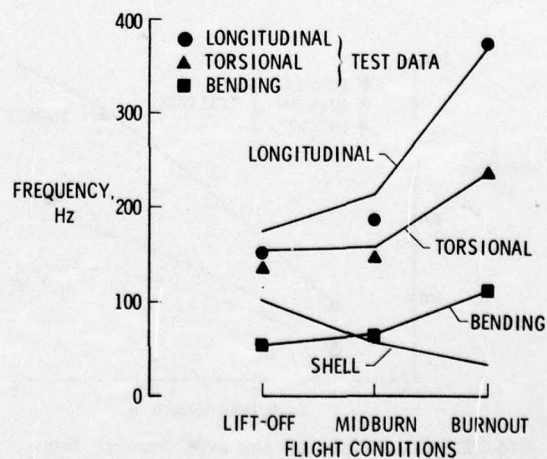


Fig. 16 - First membrane, bending, and shell frequencies for 1/8-scale propellant cylinders at different flight conditions

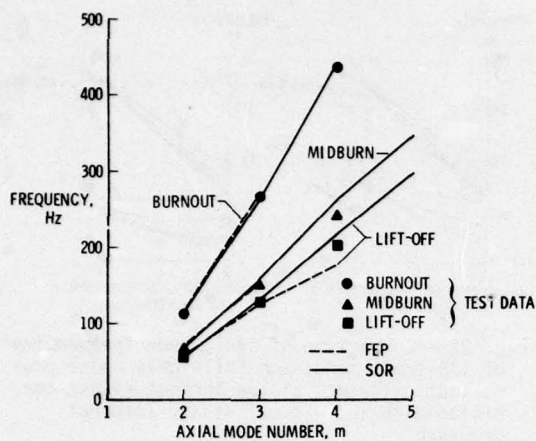


Fig. 17 - Comparison of FEP and SOR model bending ($n = 1$) frequencies with experiment for the 1/8-scale propellant cylinders

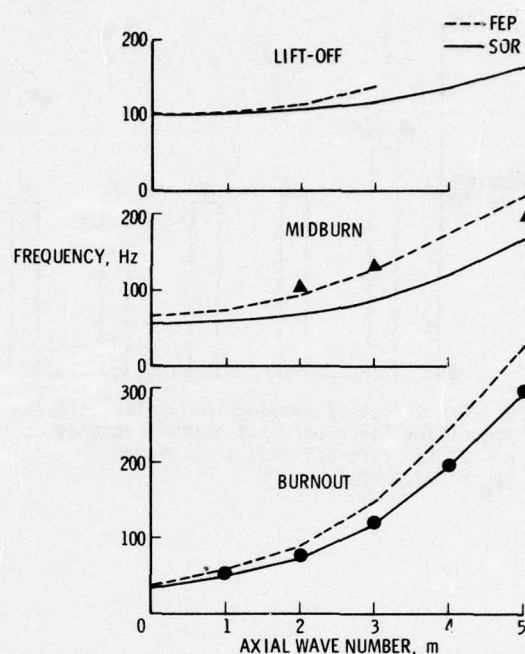


Fig. 18 - Comparison of FEP and SOR models and experimental data for the 1/8-scale SRB propellant cylinders at $n = 2$

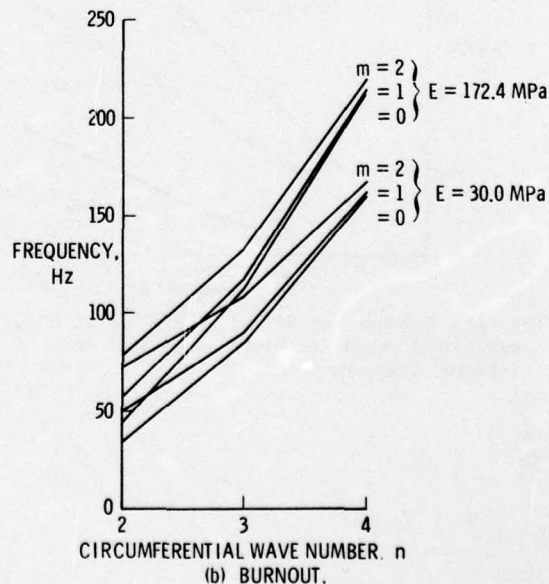
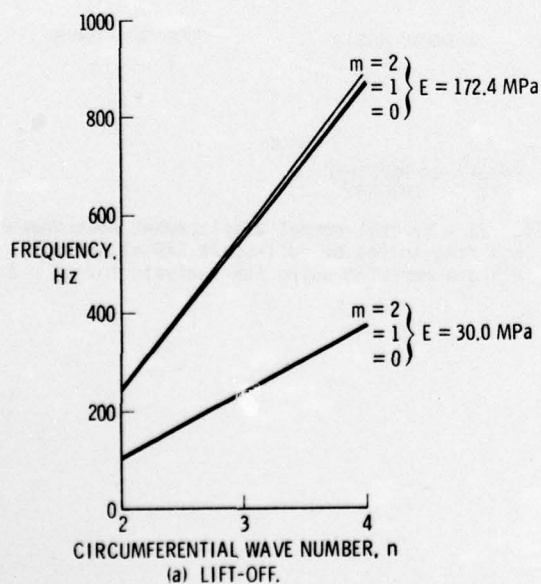


Fig. 19 - Variation of frequency with changes in the elastic modulus of the propellant using the SOR analysis

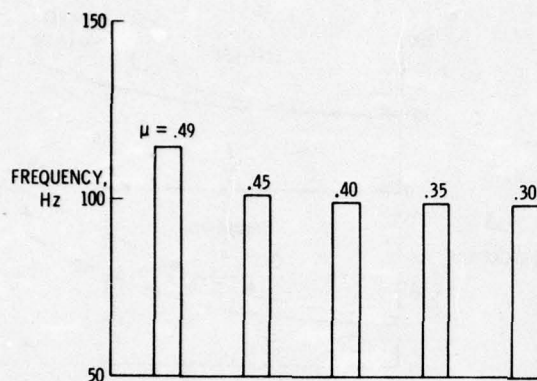


Fig. 20 - Effect of varying Poisson's ratio for propellant layer on first shell frequency at $n = 2$ for lift-off flight condition ($E_p = 172.4$ MPa)

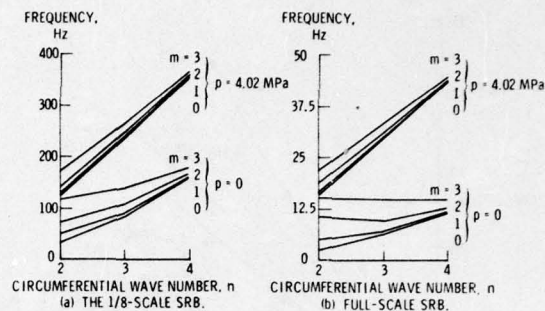


Fig. 22 - Comparison of shell mode frequencies of 1/8-scale model and full-scale model propellant cylinders at the burnout flight condition with and without static internal pressure

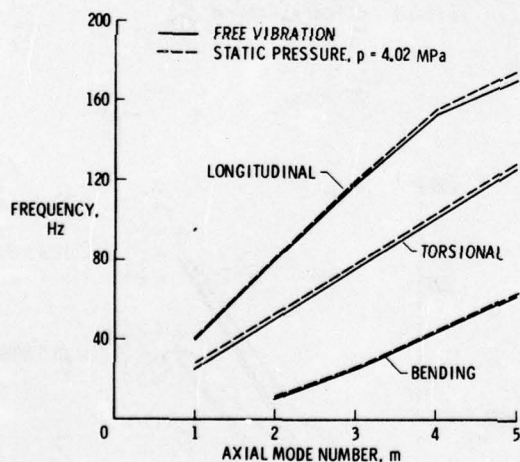


Fig. 21 - Frequencies of full-scale SRB at burnout flight condition with and without an internal pressure

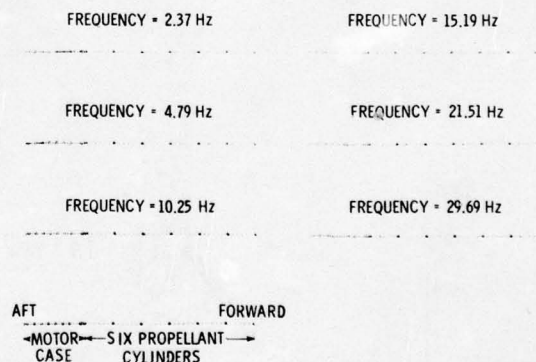


Fig. 23 - Typical normal displacement mode shapes and frequencies of full-scale SRB at burnout along a meridian using SOR analysis for $n = 2$

Discussion

Mr. Snell (McDonnell Douglas Astronautics Co.): Was this model constructed purely for the sake of conducting the vibration tests? If so, was the analysis in which you compared the model which had different types of structural configurations or simplifications, was that comparison made before or after the model was constructed?

Mr. Stephens: Are you talking about the Grumman model, the physical model? It was designed for a ground vibration type test at the Langley Research Center. As in all experimental work some of the analyses were performed prior to the experimentation but most of the agreement comes after the experimentation where you have to go back and correct your model and make the various improvements that are necessary. One of the major improvements we found necessary was that we had originally started off with a propellant modulus which was about 6 times too high; when we got into the lab and found the frequencies that were present, even though these modulus tests were run by sub contractors, we also took a specimen and made our own studies to help us determine what the propellant modulus should be to help us know which way to jump. We may have chosen too conservative or too low a value but we feel that it is a lot closer to the real structure. We also ran into certain modeling problems such as the number of layers to use. We had to run convergence study which we should have done before hand but we didn't do it until after the experiment and we came up with the aspect ratio problem in the mid-burn case.

Mr. Snell: Was the close agreement in the trend lines between the two cases obtained by modification to your analysis?

Mr. Stephens: No, this was all analytical work. That work was performed after we felt that we understood how to model the problem. But I might add that all of these analyses were performed using the Shellof Revolution code which is the simplest modeling technique and that other than changing the modulus there were no further improvements that were needed.

Mr. Snell: Is a report available that describes the method, the fabrication, and the logic behind the construction of the particular model, not only the SRB but also the Orbiter and the External tank?

Mr. Stephens: There is a series of contractor reports from Grumman Aircraft Corporation which we have at the Langley Research Center.

Mr. Lalanne (Institut National des Sciences Appliques): Did you want to know the different generalized parameters and did you get good agreement between the computed and the experimentally determined mode shapes?

Mr. Stephens: We did get good agreement, in most cases the response was fairly classical in the experimental results and it was fairly easy to get the lower mode numbers using either the Shellof Revolution code or the finite element code.

LONGITUDINAL VIBRATION CHARACTERISTICS OF THE SPACE
SHUTTLE SOLID ROCKET BOOSTER TEST SEGMENT*

J. C. Bartlett and D. L. Linton
IBM Federal Systems Division
Huntsville, AL 35805

This paper deals with the axisymmetric longitudinal vibration modes of the Space Shuttle Solid Rocket Booster (SRB) Test Segment. An explanation of the methods used to conduct this dynamic analysis is given and the finite element models used with the NASTRAN Computer Program are defined. A short test segment of the SRB was analyzed with and without a test fixture, to evaluate the longitudinal dynamic characteristics of the test segment and to demonstrate the feasibility of determining these modes by testing with a 100,000 force-pound (444,822 newton) vibration exciter. The results of the SRB test segment analysis show the effects that a test fixture can have on the test results. Also, the vibration modes and the magnitude of the response displacements and strains that can be developed within the propellant, with both constant force and constant acceleration vibration control, are presented.

INTRODUCTION

Several liquid fueled launch vehicles in the space program have encountered low frequency longitudinal vibration anomalies called pogo. Pogo is a stability problem peculiar to liquid propellant vehicles with thin skinned tanks which can be caused by coupling of structural motions and the tank pressure regulation system. Although the Titan IIIC vehicle has both liquid and solid propellant motors, the Space Shuttle will be the first vehicle where the liquid motors burn before the solid propellant is depleted. In the Space Shuttle the liquid and solid propellant motors burn simultaneously and of special interest to the control and stability of the vehicle is the coupling between the pogo vibration mode of the liquid motor and the longitudinal vibration modes of the solid motor.

The primary longitudinal vibration modes of interest of the Space Shuttle Solid Rocket Booster (SRB) involve coupling between the rod modes of the motor case and the thickness shear modes of the solid propellant. The analysis of these coupled vibration modes is more complex than the analysis of other structural modes due to the properties of the propellant. Solid propellant is a highly damped viscoelastic material whose moduli are complex quantities which vary with temperature, pressure, frequency, and strain. The dependence of the moduli on the latter

two quantities results in the stiffness of the propellant being a function of the forcing frequency and the response deflection. Analytical techniques have been developed to analyze the longitudinal vibration characteristics of a solid rocket motor, but before any theory can be accepted it must be compared with test results. Because of the difficulty and cost of a vibration test of the entire SRB, a vibration survey test is planned for a segment of the SRB. This paper presents the analytical techniques that have been developed to analyze the longitudinal vibration characteristics of a solid rocket motor and the analysis of the longitudinal vibration characteristics of the model survey test segment of the SRB.

ANALYTICAL TECHNIQUES

The purpose of this section is to show the methodology needed to dynamically analyze a structure that contains sufficient quantities of solid propellant so that the vibration modes of the structure are dependent on both the mass and stiffness of the propellant. To understand the effects of the solid propellant on such structures the mechanical properties of the propellant must be noted. It was previously shown [1] that solid propellant is a viscoelastic material and the dynamic moduli of such materials are complex

*Work was sponsored by the NASA, Marshall Space Flight Center (MSFC), AL under Contract NAS8-14000.

numbers whose values are dependent on frequency, strain, temperature, and pressure. For the analysis of a solid propellant rocket during flight, the dependence of the moduli on temperature and pressure are easily handled because temperature and pressure are essentially constant.[†] The burning rate of the propellant is greater than the heat flow rate, therefore, the temperature of the propellant is not significantly affected by the combustion process.[‡] Also, the pressure in the combustion chamber during flight does not vary significantly with regards to effects on moduli. However, the dynamic moduli of the propellant change significantly with both frequency and strain. Therefore, the stiffness of the propellant varies with both frequency and amplitude of response. This section will present the techniques needed to analyze structures whose stiffness is a function of frequency and strain.

To adequately analyze a solid propellant structure, three different types of analyses have to be performed. These analyses are real eigenvalue analysis, complex eigenvalue analysis, and frequency response analysis. The purpose of each analysis will be discussed in this section along with methods which can be used to account for the dependence of stiffness on frequency and strain.

Real eigenvalue analysis must be performed in a dynamic analysis of a solid propellant structure for several reasons. Some of these reasons are readily apparent and the others will become apparent later in this section. To aid in understanding the terminology used in real eigenvalue analysis, Appendix A gives the mathematical formulation of real eigenvalue analysis. The purpose of the real eigenvalue analysis is to determine the real eigenvalues and the real eigenvectors of the structure. The square roots of the real eigenvalues are the resonant circular frequencies of the undamped structure. The resonant frequencies of the undamped structure aid in understanding the dynamic characteristics of the structure. The real eigenvalues also aid in determining the search region for the complex eigenvalue analysis if a searching technique is used for eigenvalue extraction. The real eigenvectors give the mode shape of the undamped structure and also aid in understanding the dynamic characteristics of the structure. They are also used in transforming from physical coordinates to principal coordinates so that the structure may be represented as part of a larger structure by a modal formulation.

The purpose of the complex eigenvalue analysis is to determine the damped resonant frequencies and the damping at each frequency of the structure. The damping at each frequency is used to form the damping matrix in principal coordinates for the modal formulation. Since the dynamic shear modulus of solid propellant is a complex number, the stiffness in the complex eigenvalue analysis should be a complex number. Appendix B gives the mathematical formulation of complex eigenvalue analysis using complex stiffness.

The frequency response is required to determine which vibration modes of the structure are excited when the structure is driven at the points and in the frequency range of interest. It is also used to determine the deflections and the shear strain in the propellant for the excited modes. These strain values are used to ensure that the dynamic moduli used in the real eigenvalue analysis and the complex eigenvalue analysis are appropriate. As in the complex eigenvalue analysis, the stiffness in the frequency response should be a complex number. Appendix C gives the mathematical formulation of frequency response analysis using complex stiffness.

The dependence of the propellant stiffness on frequency and strain can be accounted for by writing a computer program where the stiffness can be a function of frequency and strain or by using an existing computer program [2] with an iterative technique. In the iterative method the response frequency of interest and the strain levels at this frequency are first estimated. Using these estimates an initial selection of the dynamic moduli of the propellant is made. A frequency response analysis is then made using an existing computer program where the moduli are independent of frequency and strain. The frequency response is obtained at many frequencies in the frequency range of interest so that the response frequency of interest and the propellant strain at this frequency can be accurately determined. This response frequency could be either a resonant frequency of the structure where the relative displacement is a maximum or another frequency where the absolute displacement is a maximum. These two conditions do not necessarily occur at the same frequency. Using the response frequency and the associated strain from the frequency response, new values for the shear moduli are determined. The values are used in the next frequency response. This procedure is repeated

[†]Preliminary analysis at Thiokol, as reported in the Solid Rocket Booster proposal, has shown that combustion is stable and therefore only slight pressure fluctuations are expected during combustion.

[‡]Propellant authorities have stated that if the heat flow rate were greater than the burning rate, the burning rate would be nonuniform but this is not the case for the propellant.

until the shear moduli are compatible with the response frequency and the shear strain.

It should be noted that the strain in the propellant will vary throughout the propellant from the inside radius to the outside radius. This effect should be incorporated in the model by changing the moduli throughout the propellant.

This section has presented a methodology which was developed to analyze the longitudinal vibration modes of the SRB (or any structure containing large quantities of viscoelastic material and subjected to harmonic excitation). The following section will present an example of this method based on the Space Shuttle Solid Rocket Booster Modal Survey Test Segment. It was not possible to show a complete example of the methodology due to the limitations in the availability of propellant material properties. The propellant data available for the analysis were for one strain value, therefore the example illustrates the dependence of the moduli on frequency but does not illustrate the dependence of the moduli on strain. It has been recommended that the analysis be repeated when adequate data are available.

SRB TEST SEGMENT ANALYSIS

A longitudinal vibration test is planned on a typical factory splice segment of the SRB. One of the purposes of the test is to determine how closely analysis using the methodology presented in the previous section agrees with test results. The primary purpose of the analysis described in this section is to identify the dynamic characteristics of the segment and to show how a test fixture can affect these results. Three basic configurations of the segment were analyzed. Configuration I consisted of the segment and a rigid drive cone. Configuration II consisted of the segment with an aluminum drive cone. Configuration III consisted of the "segment only". In Configuration II, a 45° (0.785 rad) aluminum drive cone, was assumed to couple the segment to a vibration exciter. A 156 in. (3.962m) long segment was selected for analysis because it is one of six similar segments which make up the major portion of the SRB. The math models of the segment and segment with cone are illustrated in Fig. 1 and 2, respectively, and were generated using axisymmetric, finite elements. These elements allow easy modeling of 360° (6.283 rad) structures but limit the eigenvalues to those with axisymmetric mode shapes.

The segment test fixture design was not available when this analysis was undertaken. A simple test fixture design was therefore conceived for analytical purposes. The fixture is a 45° (0.785 rad) conical frustum with a one inch thick aluminum wall. At the driving point end of the frustum, a 6 in. (0.152m) diameter aluminum plate, 2 in. (0.0508m) thick, is

used. A 1 in. (0.0254m) thick flat aluminum plate ring, 4 in. (0.102m) wide, is located at the large end of the frustum and serves to connect the drive cone to the segment shell. The cone weighs approximately 2,500 pounds (1135 Kg). No attempt was made to reduce weight by cutting lightening holes or slots in the fixture.

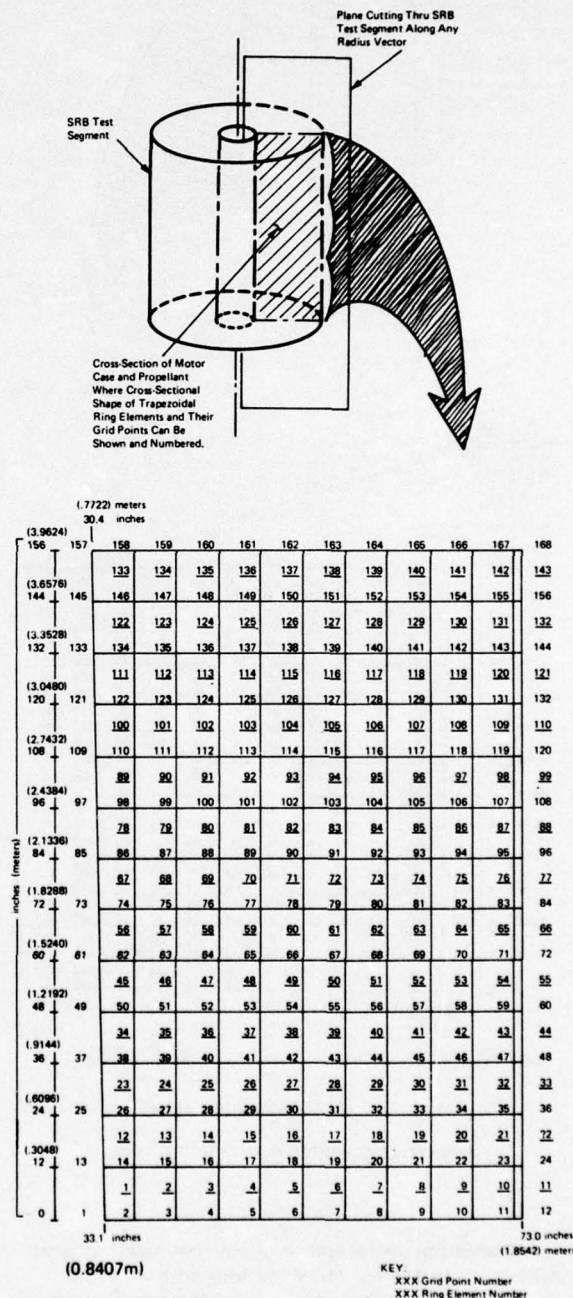


Fig. 1. Solid rocket booster test segment

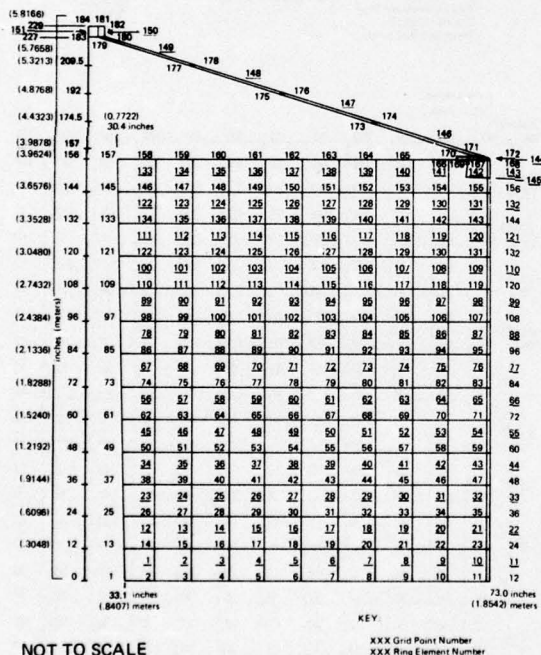
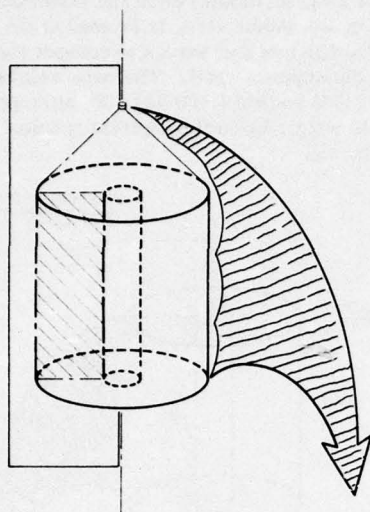


Fig. 2. Model of solid rocket booster test segment with drive cone

Definition of the test segment was obtained from MSFC. It is 156 in. (3.962m) long with a 146 in. (3.708m) outside diameter and weighs approximately 143,000 pounds (64922 Kg). It is typical of the second segment aft of the forward bulkhead of the SRB. The

preignition propellant bore has a uniform taper from a 60.8 in. (1.544m) diameter at one end to a 66.2 in. (1.681m) diameter at the other end. The motor case has a 0.52 in. (0.0132m) uniform thickness of D6AC tool steel. The case design complexity at the splice joints was not considered warranted for modeling in this analysis. Also, no attempt was made to model liner, insulation and flap design.

The test segment was analyzed in each of the three configurations previously described. The segment was divided into 143 axisymmetric elements with 168 grid points and is illustrated in Fig. 1. The drive cone was separated into eight elements with 18 grid points as shown in Fig. 2. Material properties utilized in the model are shown in Table 1. The storage modulus of rigidity, G' , and the loss tangent G''/G' , were selected by estimating the resonant frequency of the first longitudinal mode of vibration of the test segment and using equation $G' = 900 f^{0.145}$ psi ($G' = 6.206 \times 10^6 f^{0.145} \text{ N/m}^2$) [1] and Fig. 3 [3]. The equation relating the storage modulus to frequency is an empirical relationship based on test data furnished by Thiokol. This equation is based on room temperature and atmospheric pressure data due to the lack of test data for other conditions. These values for shear moduli were used throughout the analysis for all modes. Iteration of the analysis to obtain the correct shear moduli for each mode was not considered necessary until such time as more complete shear moduli data becomes available.

Three types of analyses (normal mode, complex eigenvalue, and frequency response) were conducted on each of the three configurations for both the free-free and fixed-free boundary conditions. In the eigenvalue analyses all eigenvalues were determined in the frequency range of 0 to 50 Hertz. The frequency response was determined for harmonic excitation between 10 and 50 Hertz and the segment was restrained on one end of the shell for the fixed-free "segment only" analyses. In the fixed-free cases with drive cone, the model is restrained at the driving point end of the frustum. Reasons for performing the three types of analyses were previously presented and procedures for performing the three analyses are available [2]. Excitation forces for the frequency response models were applied in two different ways. In the first method, a constant level sinusoidal force was applied to the model. A total force of 100,000 pounds (442822 N) was divided equally between the grid points of application as follows:

Model	Grid Points	Description
Segment with Alum Cone	181, 182, 184	Small end of Frustum
Segment with Rigid Cone	181, 182, 184	Small end of Frustum
Segment only	167, 168	End of segment case

TABLE 1
Test Segment Material Properties

AREA	MATERIAL	ρ	μ	E	G'	G''/G'
MOTOR CASE	D6AC STEEL	7.25×10^{-4} (20.07)	0.330	28×10^6 (19.3×10^{10}) (-)	--	0.04
PROPELLANT	PBAN	1.658×10^{-4} (4.59)	0.495	--	1390 (9.584×10^6) (-)	0.246
DRIVE CONE	ALUMINUM	2.59×10^{-4} (7.17)	0.330	10×10^6 (6.89×10^{10})	--	0.04
RIGID DRIVE CONE	--	2.59×10 (7.17)	0.330	10×10^6 (6.89×10^{10})*	--	0.04

UNITS

ρ = mass density lbs. sec²/in⁴ (Kg/m³)
 μ = Poisson's ratio
E = Elastic Modulus lbs./in² (Kg/m³)
G' = Shear Modulus lbs./in² (N/m²)
G''/G' = Loss tangent (N/m²)

NOTES

*Multipoint restraints were used with NASTRAN to make the cone perfectly rigid.

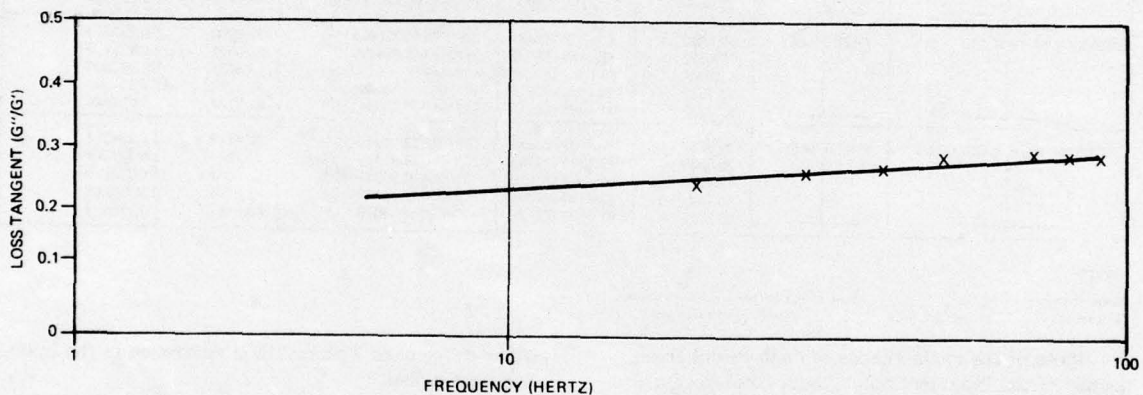



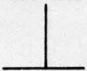
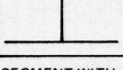
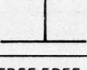
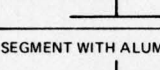
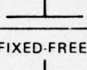
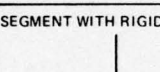
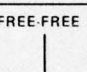

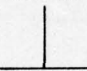
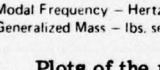
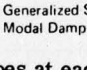
Fig. 3. Loss tangent vs frequency for PBAN propellant obtained from Reference 3

In the second method, a one g peak constant sinusoidal acceleration was specified for a seismic element, i.e., an element with a mass many orders of magnitude higher than the model. For the "segment only" model, element 143 is the seismic mass (Fig. 1). For the models of segment with the aluminum or rigid cones, element 150 is the seismic mass. Initially, frequency response was conducted at only the discrete modal frequencies that were identified in the complex eigenvalue analysis. During the review of this data it was determined that frequency responses at many additional frequencies in the range from 10 to 50 Hertz were required. Additional frequency response analysis was therefore conducted at 0.5 Hz intervals throughout the range of interest.

Modal frequencies obtained from the normal mode analysis and complex eigenvalue analyses for all cases analyzed are tabulated in Table 2 for modes to

50 Hertz. Review of this data shows the first fixed-free coupled motor case and propellant mode of all configurations, except the segment with aluminum drive cone, to be approximately 20 Hertz and the first free-free mode for all configurations to be approximately 30 Hertz. The mode at approximately 14.5 Hertz for the fixed-free segment with aluminum drive cone is the fundamental mode of the drive cone. This condition is undesirable because it causes amplitude and phase changes between the exciter and test specimen. It is suggested that the fundamental frequency of the drive cone be greater than 1.5 to 2 times the highest test frequency. The results of the complex eigenvalue analysis shows that adding the damping properties to the propellant has the effect of increasing the modal frequencies that were determined by Normal Mode Analysis. This increase in frequency is expected when using complex stiffness [1, Sect. 4.3.3].

TABLE 2
Test Segment Modal Analysis Summary

CONFIGURATION	BOUNDARY CONDITION	NORMAL MODE ANALYSIS			COMPLEX EIGENVALUE ANALYSIS	
		MODAL FREQUENCY	GENERALIZED MASS	GENERALIZED STIFFNESS	MODAL FREQUENCY	MODAL DAMPING
SEGMENT ONLY 	FREE-FREE 	30.6931 32.9735 43.0616 46.0999 52.6467	61.0816 (10695) 69.4493 (12160) 58.3782 (10221) 38.4062 (6724) 31.1037 (5446)	2271696 (3.97835x10 ⁸) 2980978 (5.22049x10 ⁸) 4273562 (7.48415 x 10 ⁸) 3222266 (5.64305x10 ⁸) 3403414 (5.96029x10 ⁸)	30.9291 33.2267 43.3940 46.4685 53.0849	0.235867 0.236022 0.236586 0.228052 0.227237
SEGMENT ONLY 	FIXED-FREE 	20.0253 30.8885 42.6807 46.5441 50.5150	119.2288 (20875) 73.1324 (12805) 65.7458 (11511) 42.3809 (7420) 41.7312 (7307)	1887560 (3.30562x10 ⁸) 2754630 (4.82410x10 ⁸) 4728133 (8.28023x10 ⁸) 3624594 (6.34764x10 ⁸) 4203988 (7.36231x10 ⁸)	20.1777 31.1241 43.0099 46.9113 50.9166	0.234391 0.237368 0.237070 0.232069 0.229594
SEGMENT WITH ALUM CONE 	FREE-FREE 	30.8162 32.7461 43.1187 46.3487 52.6895	63.1417 (11055) 74.1514 (12983) 60.7035 (10628) 42.1124 (7373) 30.5901 (5356)	2367191 (4.14559x10 ⁸) 3139040 (5.49730x10 ⁸) 4455575 (7.80291x10 ⁸) 3571446 (6.25456x10 ⁸) 3352651 (5.87139x10 ⁸)	31.0434 32.9903 43.4512 46.7168 53.0964	0.237394 0.237453 0.237361 0.230094 0.227406
SEGMENT WITH ALUM CONE 	FIXED-FREE 	14.4820 30.8592 39.3505 43.4719 46.3802	181.1840 (31723) 72.9314 (12769) 97.9443 (17149) 64.3496 (11267) 41.4920 (7265)	1500157 (2.62718x10 ⁸) 2741852 (4.80172x10 ⁸) 5987414 (10.48557x10 ⁸) 4800905 (8.40767x10 ⁸) 3523610 (6.17078x10 ⁸)	14.5719 31.0953 39.5856 43.7654 46.7472	0.130107 0.236948 0.194405 0.231306 0.230716
SEGMENT WITH RIGID CONE 	FREE-FREE 	30.8686 32.8333 43.2007 46.5523 52.7836	65.6276 (11491) 78.5468 (13752) 64.6882 (11326) 43.3883 (7597) 31.4740 (5511)	2468769 (4.32348x10 ⁸) 3342843 (5.85422x10 ⁸) 4766140 (8.34679x10 ⁸) 3712051 (6.50080x10 ⁸) 3461859 (6.06264x10 ⁸)	31.0850 33.0509 43.4981 46.8277 53.2133	0.237774 0.238262 0.237860 0.231097 0.228198
SEGMENT WITH RIGID CONE 	FIXED-FREE 	20.0231 30.8885 42.6804 46.5441 50.5115	119.2502 (20879) 73.1335 (12805) 65.7502 (11512) 42.3799 (7420) 41.7622 (7312)	1887468 (3.30546x10 ⁸) 2754673 (4.82417x10 ⁸) 4728384 (8.28067x10 ⁸) 3624509 (6.34749x10 ⁸) 4206530 (7.36676x10 ⁸)	20.1777 31.1241 43.0099 46.9114 50.9167	0.234391 0.237368 0.237070 0.232069 0.229594

UNITS

Modal Frequency - Hertz
Generalized Mass - lbs. sec²/in. (Kg)
Generalized Stiffness - lbs/in. (N/m)
Modal Damping - dimensionless

Plots of the mode shapes at each modal frequency of the "segment only", both fixed-free and free-free boundary conditions, are shown in Fig. 4 thru 13. These plots were NASTRAN generated from normal mode analyses and represent a cross-section through the model as shown on a plane formed by the longitudinal and any radial axis through the model. The eigenvectors from the normal mode analysis are normalized to the maximum value. In order to show mode shapes, the displacements are exaggerated by specifying an exaggeration factor for the plot routine. The maximum displacement from each of the particular modes of the normal mode analysis were then set equal to 5 in. (0.127m) and all other normalized displacements are proportional.

General mass, generalized stiffness, modal damping and modal frequencies are tabulated in Table 2. The generalized mass is useful in determining the amount of mass in motion, i.e., the higher the generalized mass the greater amount of mass is in motion. All four parameters are required in coupling a substructure model to a larger structure. For example, these parameters could be used to couple the 156 in. (3.962m) segment (only) to the 45° (0.785 rad) aluminum drive cone or any

other drive cone with no other reference to the initial segment model.

Displacement values used in the analysis were the maximum displacements at the grid points. The frequency response displacement data is given by NASTRAN in phase and amplitude. Unless noted, no attempt was made to compensate for the slight phase differences between adjacent grid points. This could result in slight inaccuracies which could be corrected if greater accuracies are required. Propellant shear strains were determined from the frequency response displacement data. Free-free and fixed-free restraints were analyzed, each with 100,000 pound (442822 N) and 1 g excitation. Shear strains and stresses can normally be obtained directly from NASTRAN; however, because of Level 15.1 NASTRAN limitations, the request for shear stresses and strains was ignored. (The latest released version of NASTRAN determines the strain for the axisymmetric elements). Shear strains were therefore calculated manually from displacement response data as follows:

$$\epsilon = \frac{d_1 - d_2}{L} \times 100$$

where ϵ = average shear strain in percent

d_2 = displacement at grid point 2

d_1 = displacement at grid point 1

L = distance between grid point 1 and 2

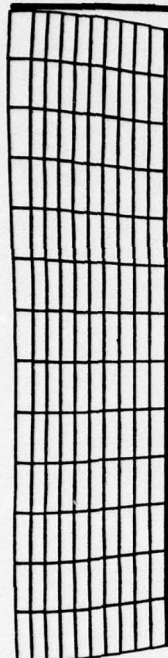


Fig. 4. First mode free-free segment only - 30.69 Hz

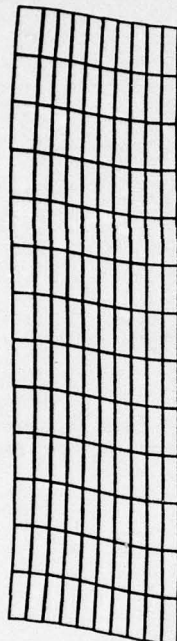


Fig. 5. Second mode free-free segment only - 32.97 Hz

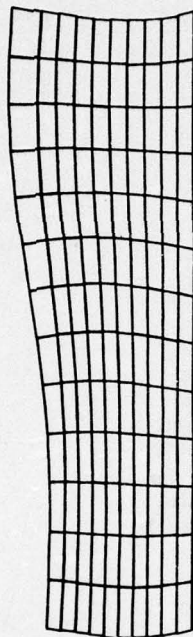


Fig. 6. Third mode free-free segment only - 43.06 Hz

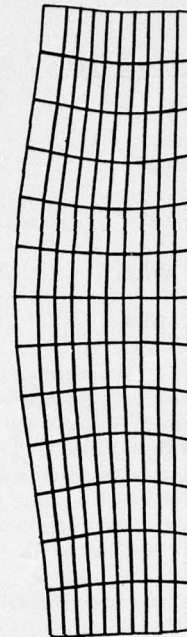


Fig. 7. Fourth mode free-free segment only - 46.10 Hz

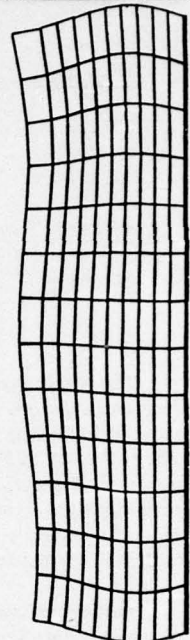


Fig. 8. Fifth mode free-free segment only - 52.65 Hz

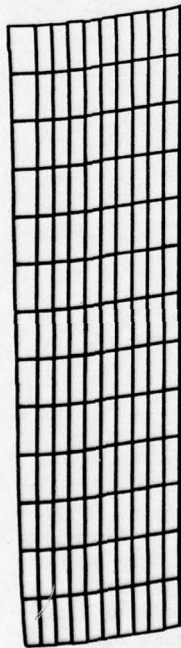


Fig. 9. First mode fixed-free segment only - 20.03 Hz

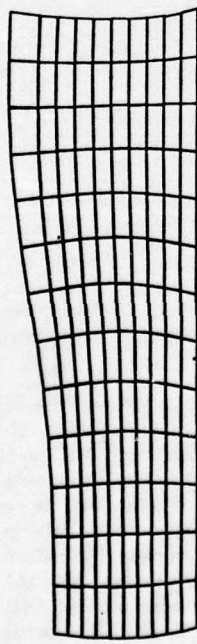


Fig. 10. Second mode fixed-free segment only - 30.89 Hz

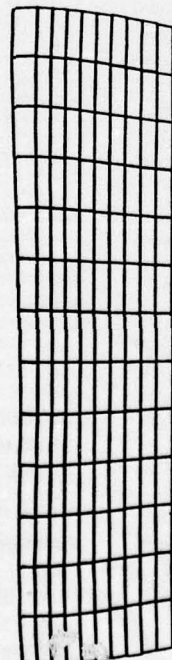


Fig. 11. Third mode fixed-free segment only - 42.68 Hz

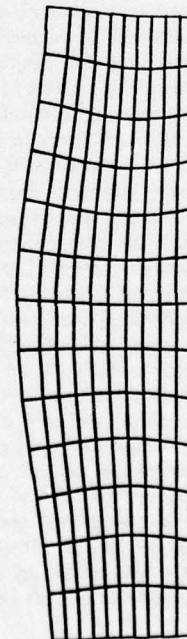


Fig. 12. Fourth mode fixed-free segment only - 46.54 Hz

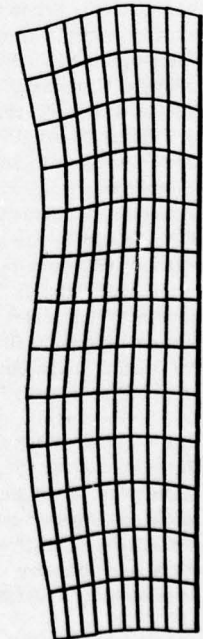


Fig. 13. Fifth mode fixed-free segment only - 50.52 Hz

Shear strains were determined for one end of the propellant. The maximum strains and the location of these strains, for the "segment only" free-free model are tabulated below:

Mode (Hz)	Between Grid Points	Strain
30.929	5 and 6	.29%
33.227	5 and 6	.35%
43.394	3 and 4	.15%
46.468	3 and 4	.15%
53.085	2 and 3	.12%

The shear strains for the aluminum cone free-free second mode configuration were calculated for several layers of propellant throughout the segment. The variation in strain is from 0.000384 to 0.255053 percent. This suggests that variations in shear modulus with strain may be required throughout the model to improve accuracy when propellant sample test data for shear moduli becomes available.

Before reviewing the frequency response displacement data for mode shapes, it was assumed that the model was responding at each discrete frequency in the mode shape identified for that frequency in the normal mode analysis; however, this was not the case. To explain some of the modal variations between the fixed-free and free-free restraint configurations, sufficient frequency responses were obtained so as to determine how the models respond throughout the frequency range of interest. These frequency responses were incremented at 0.5 Hertz intervals from 10 to 35 Hertz in all cases, or to 50 Hertz in some cases. The NASTRAN X-Y Plotter was used to generate data plots from the 0.5 Hertz incremented frequency response analyses. Fig. 14 and 15 are computer generated displacement versus frequency plots for the free-free, 100,000 pound (442822N) excited segment with aluminum drive cone and segment with rigid drive cone respectively. The driving point displacement, grid point 184, and propellant at the bore, grid point 1, displacements are plotted in both figures. Of the five modes identified by the normal mode analysis for each of the three models analyzed, only two modes were excited for each model. These two modes peak at approximately 20 and 54 Hertz and are the first and second thickness shear modes of the propellant respectively. These two modal frequencies agree with the closed-form solutions for infinitely long hollow cylinders developed by Baltrakonsis and Gottenberg [4].

Frequency response analysis with constant force excitation was conducted on the segment with aluminum

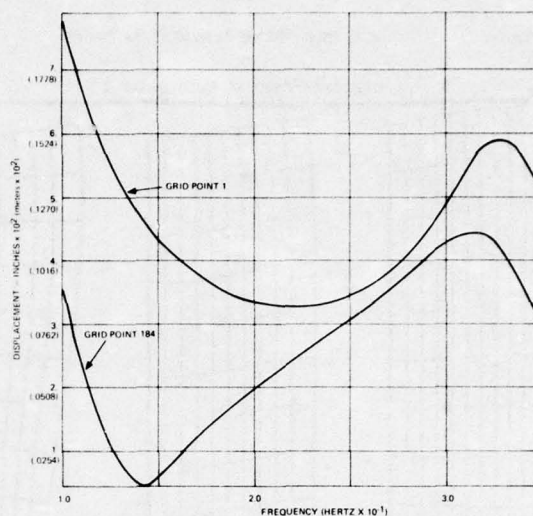


Fig. 14. Test segment with aluminum drive cone frequency response analysis

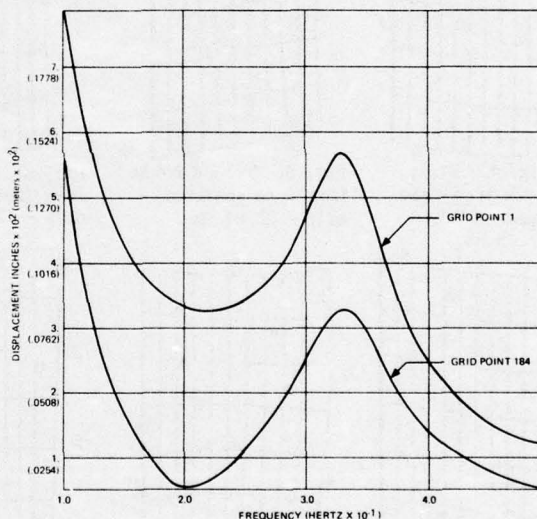


Fig. 15. Test segment with rigid drive cone frequency response analysis

drive cone and on the segment with rigid drive cone at discrete frequencies corresponding to the modes identified in their respective normal mode analyses and also at 0.5 Hertz increments from 10 to 35 Hertz in all cases, or to 50 Hertz in some cases. Response displacement is plotted for the grid points throughout the radius of the propellant at the end of the segment opposite the drive cone, grid points 1 through 11, for the rigid drive cone model. Displacement data was obtained from NASTRAN in terms of maximum amplitude and phase. Displacement data plotted was therefore adjusted so that the displacement at each grid

point would be represented at the same time. Fig. 16a and 16b shows plots of displacement vs frequency from the incremented frequency response run at 20, 32, 40 and 50 Hertz. The mode shapes excited at 20, 32, and 40 Hertz are clearly the first thickness shear mode of the propellant. The mode shape at 50 Hertz shows the presence of the second thickness shear mode. The first thickness shear mode of the propellant is much like the coupled case rod and propellant thickness shear mode identified by normal mode analysis for the free-free rigid drive cone at 32.75 Hertz. The second thickness shear mode of the propellant is much like the coupled case rod and propellant thickness shear mode identified in the free-free rigid drive cone normal mode analysis at 46.6 and 52.8 Hertz, except the longitudinal nodes are not present. It is significant to note that the thickness shear resonance at 20 Hertz which is being excited with constant force control is not the first mode that was identified in the free-free normal mode analysis, but rather the first mode identified in the fixed-free normal mode analysis.

drive cone, grid points 1 through 11. Displacement data from NASTRAN is given for maximum amplitude and phase. Displacement data plotted was therefore adjusted so that the displacements at each grid point would be shown at the same time. Fig. 18 is a plot of displacement vs frequency data from the frequency response with constant acceleration at 31.09, 39.61, 43.77, 46.75 and 53.20 Hertz. ** The mode shapes identified with the frequency response at 31.09, 39.61 and 43.77 Hertz are clearly the first thickness shear mode of the propellant. The mode shapes at 46.75 and 53.2 Hertz show the presence of the second thickness shear mode. The first thickness shear mode is much like the mode identified in the normal mode aluminum drive cone fixed-free analysis at 39.35 Hertz. The second thickness shear mode is somewhat like the mode identified in the normal mode aluminum drive cone fixed-free analysis at 53.2 † † Hertz since there are two nodes along a radius through the propellant grain; however, in the frequency response, there is no reversal of the shape of mode lines from one end to the other of the propellant grain

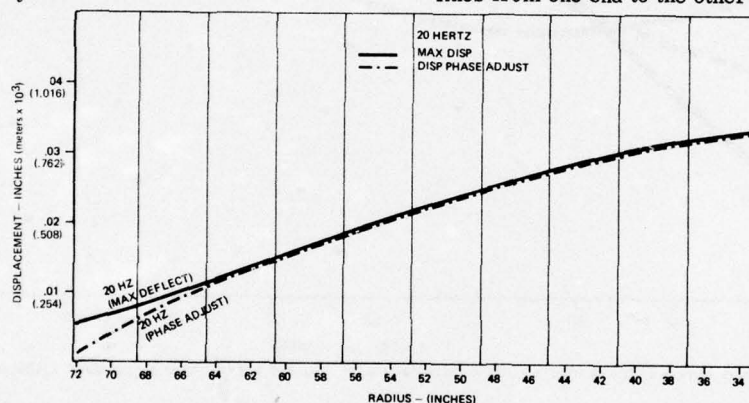


Fig. 16a. SRB test segment rigid drive cone constant force frequency response (100,000 pounds)

Similar results were obtained with the constant force frequency response analyses for the test segment with rigid drive cone and the "segment only" models.

Constant acceleration control for the segment test appears rather unlikely because of the large forces required. Fig. 17 shows the vibratory acceleration obtainable with the 100,000 force pound (442822 N) exciter as obtained from a frequency response of the segment with rigid drive cone. The 100,000 pound (442822 N) excitation force is insufficient to maintain the 1 g acceleration at frequencies up to 26 Hertz. Above 26 Hertz, the driving force must be reduced to maintain the 1 g excitation. Frequency response analysis with 1 g constant acceleration excitation was conducted on the test segment with aluminum drive cone at frequencies corresponding to the modes identified in the normal mode analysis. Response displacement from NASTRAN is plotted for the grid points throughout the radius of the propellant at the end of the segment opposite the

(i.e., longitudinal node near center of grain). The results of the frequency response analysis show how the test segment can be excited with a 100,000 force-pound (442822 N) vibration shaker when driven at one end of the motor case. Vibratory maximum accelerations with a rigid drive cone vary from a low value of 0.06 g at 10 Hertz at the exciter end of the motor case to a high value of 6.3 g at the propellant bore at the end opposite the exciter. These response values indicate that ordinary vibration test methods and instrumentation can be used to evaluate the dynamic characteristics of the motor segment.

This section has presented a summary of the analysis of the SRB Test Segment. These results have been reported as part of a larger task which includes an analysis of the total SRB [5]. This reference contains examples of the NASTRAN inputs and outputs used to generate the results reported in this paper. The reader is referenced to that document if additional information is required.

**These frequencies were chosen from the aluminum drive cone, fixed-free complex eigenvalue analysis.
† † Modal characteristics for this mode are not shown in Table 2.

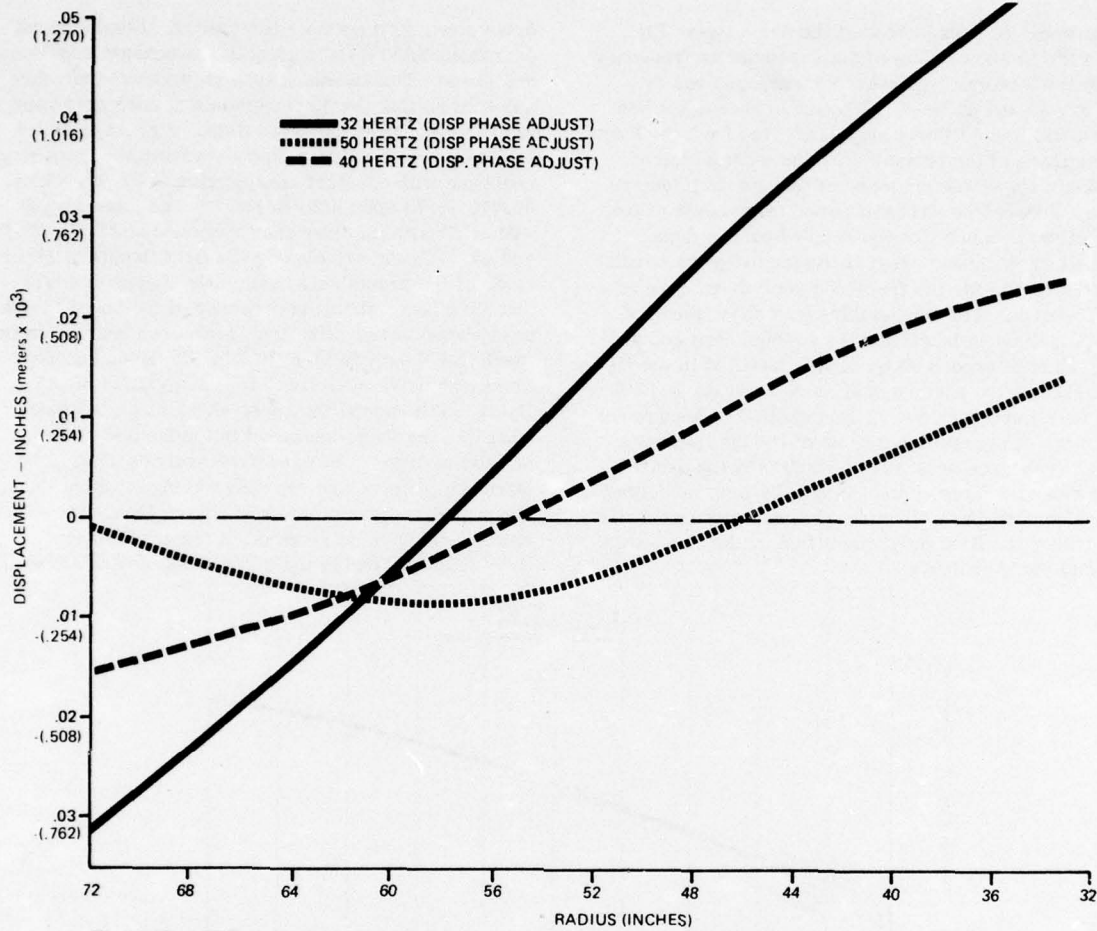


Fig. 16b. SRB test segment rigid drive cone constant force frequency response (100,000 pounds)

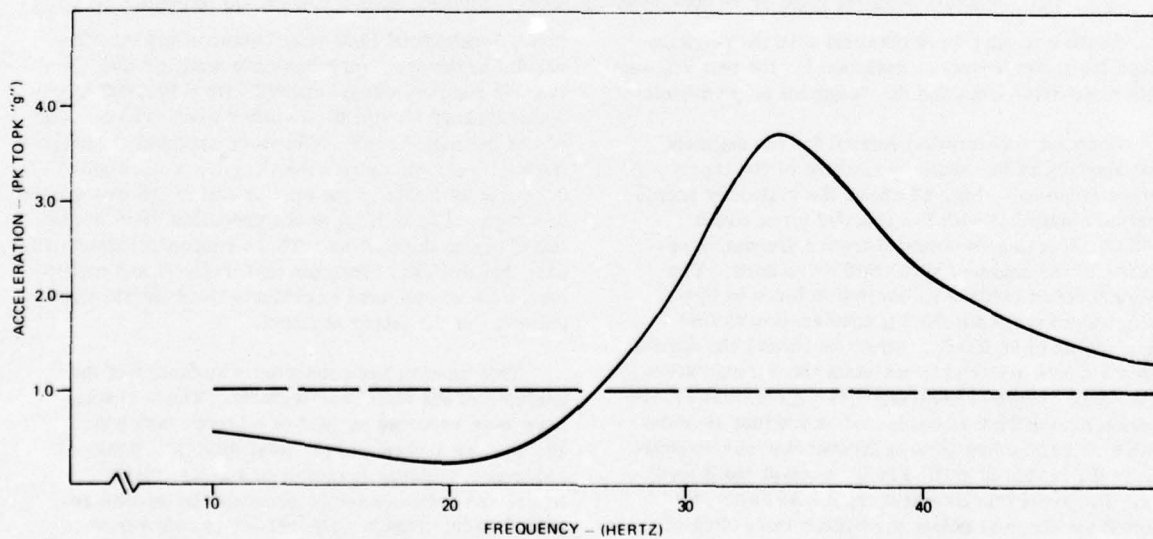


Fig. 17. Driving point acceleration vs frequency with 100,000 pound exciter force

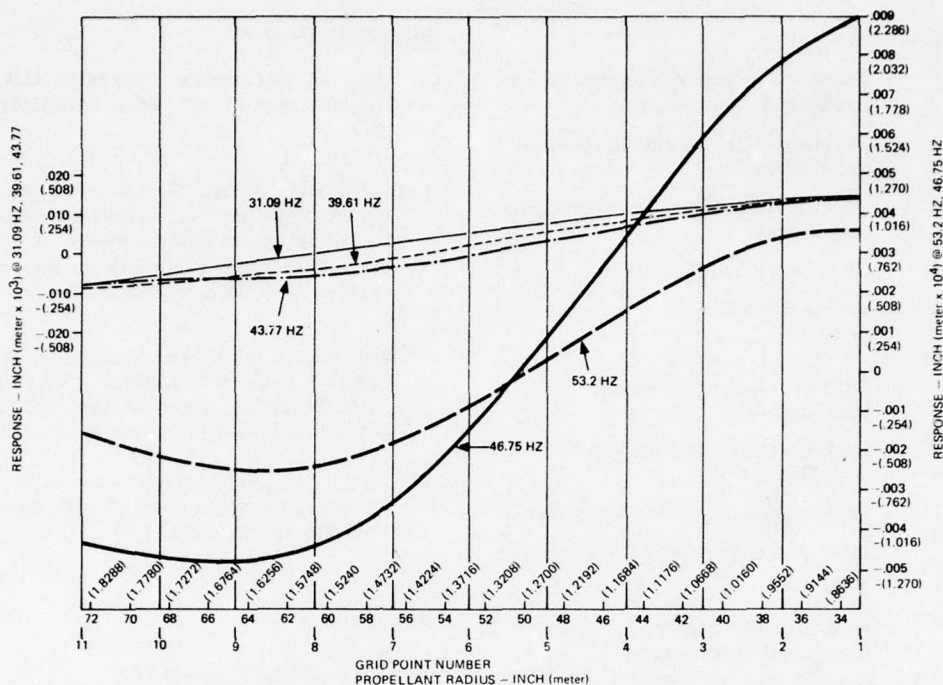


Fig. 18. Aluminum drive cone constant acceleration frequency response (1g excitation)

CONCLUSIONS

Since the results from the segment test will be used to judge the adequacy of analytical techniques, the design of the test fixture should be kept simple so that it can be simply and accurately analyzed. The results of this study show that the vibration test proposed for the SRB test segment will excite only the first and second axisymmetric thickness shear mode. The other coupled motor case rod and propellant thickness shear modes that were identified in the normal mode will not be excited.

The analysis performed was made with the aid of NASTRAN using the axisymmetric ring elements. Antisymmetric modes were therefore not determined. Since the proposed test calls for symmetrical loading, it is unlikely that antisymmetric modes can be excited.

When the aluminum drive cone was found to have a longitudinal resonance at a frequency lower than the first mode of the test specimen, it was expected that the drive cone would act as a vibration isolator and attenuate the vibratory excitation in the frequency range of interest. A comparison of the response data from the aluminum drive cone and rigid drive cone shows however, that the response with the aluminum drive cone was greater throughout the frequency range of the analysis, 10 to 35 Hertz. It is recommended, though, that the drive cone be resonant free in the frequency range from 0 to 100 Hertz.

Since the second axisymmetric thickness shear mode is centered at approximately 54 Hertz which is outside the frequency of interest, only the first axisymmetric thickness shear mode is available for test-analysis evaluation with the proposed segment test. Other modes could possibly be excited by trying other points of excitation. For example, two exciters with one on either end of the motor case driven 180 degrees (3.14 rad) out of phase with each other could be evaluated by analysis to determine if the first coupled free-free mode could be excited. Also, unsymmetrical axial loading to either end or both ends could possibly excite the first antisymmetric thickness shear mode of the propellant.

When the actual test fixture design becomes available for review, an analysis of the fixture-segment should be conducted before going into fabrication. Additionally, when propellant coupon test data becomes available representative shear moduli should be used throughout the model and iteration with strain used to apply correct shear moduli throughout, at each element of propellant, in order to obtain representative model frequencies and responses.

NOMENCLATURE

$\{ A \}$	Magnitude of forcing function vector in physical coordinates
$\{ F \}$	Forcing function vector in physical coordinates
$\{ F_p \}$	Forcing function vector in principal coordinates
g	G''/G' or Gravitational acceleration
i	Frequency number
j	$\sqrt{-1}$
$[K]$	Stiffness matrix in physical coordinates
$[k]$	Stiffness matrix in principal coordinates
$[M]$	Mass matrix in physical coordinates
$[m]$	Mass matrix in principal coordinates
t	Time
$\{ X \}$	Magnitude of displacement vector in physical coordinates
$\{ x \}$	Displacement vector in physical coordinates
$\{ \ddot{x} \}$	Acceleration vector in physical coordinates
$\{ X_{mi} \}$	Displacement amplitude vector in physical coordinates
$[X_n]$	Normalized modal matrix
α	Damping coefficient
$(\alpha + j\omega_d)_i^2$	Complex eigenvalues
ϕ	Phase angle
$\{ \phi_i \}$	Normalized eigenvectors
ω	Circular frequency
ω_d	Damped circular frequency
ω_i^2	Real eigenvalues
ζ	Viscous damping ratio
$[]^T$	Transposed matrix

REFERENCES

1. Anon. "Dynamic Characterization of Solid Rockets", IBM Report No. 73W-00271, September 1973

REFERENCES (cont)

2. Caleb W. McCormick, "The NASTRAN User's Manual (Level 15.0)", NASA SP-222(01), May 1973.
3. Gottenberg, W.G., "Results of Minuteman Engine Associate Contractors Round-Robin Propellant Mechanical Properties Test", Space Technology Laboratories, Inc., Report 6121-7244-KU000, July 26, 1963.
4. Baltrukonis, J.H., and Gottenberg, W.G., "Thickness-Shear Vibrations of Circular Bars", Space Technology Laboratories, Inc., Report No. GM-TR-0165-00518, November 1958.
5. Anon. "Dynamic Analysis of the Solid Rocket Motor for the Space Shuttle", IBM Report No. 75W-00144, July 1975.

APPENDIX A

REAL EIGENVALUE ANALYSIS

The homogeneous differential equation of motion for an undamped multi-degree-of-freedom system using matrix notation is

$$[M] \{ \ddot{x} \} + [K] \{ x \} = 0. \quad (1)$$

Assuming that the motion is harmonic

$$\{ x \}_i = \{ X_{mi} \} e^{j\omega_i t}, \quad (2)$$

equation (1) reduces to

$$[K - \omega_i^2 M] \{ X_{mi} \} = 0. \quad (3)$$

Equation (3) is the general form of the eigenvalue problem for undamped vibration. A trivial solution to equation (3) is $\{ X_{mi} \} = 0$, but this solution is of no consequence. The nontrivial solutions are the values of ω_i^2 that satisfy equation (3). These values of ω_i^2 are the eigenvalues of the system and are the squares of the circular natural frequencies. There exists an eigenvalue for each degree of freedom of the system. Also for each eigenvalue there exists an eigenvector which gives the mode shape of the vibrating system at that frequency. Since at each frequency there are $n + 1$ unknowns (ω_i , $\{ X_{mi} \}$) and only n equations, the eigenvectors are only known as ratios of displacements, not as absolute magnitudes. The eigenvectors $\{ \phi_i \}$, are found by solving equation (3) for each eigenvalue. It is desirable to normalize the eigenvectors with respect to the largest component.

APPENDIX A (cont)

The diagonal terms, m_{ii} and k_{ii} , are the generalized mass and the generalized stiffness of the i th mode. The diagonalized matrices can be used in transforming from physical coordinates to principal coordinates.

APPENDIX B

COMPLEX EIGENVALUE ANALYSIS

The homogeneous differential equation of motion for a multi-degree-of-freedom system with uniform damping represented by complex moduli in matrix notation is

$$[M] \{\ddot{x}\} + (1+jg) [K] \{x\} = 0. \quad (1)$$

Assuming the solution is of the form

$$\{x\}_i = \{X_{mi}\} e^{(\alpha + j\omega_d)_i t} \quad (2)$$

equation (1) reduces to

$$[(\alpha + j\omega_d)_i^2 [M] + (1+jg)[K]] \{X_{mi}\} = 0. \quad (3)$$

Equation (3) is a form of the complex eigenvalue equation. As in real eigenvalue analysis, the trivial solution is of no consequence. The nontrivial solutions are the values of $(\alpha + j\omega_d)_i^2$ that satisfy equation (3) where α is the damping coefficient and ω_d is the damped circular frequency. The significance of the terms may be seen by recalling that the complex eigenvalue for a viscous damped system with less than critical damping is $-\zeta\omega_n + j\sqrt{1-\zeta^2}\omega_n$.

An $n \times n$ matrix, called the normalized modal matrix, can be formed by merging the normalized eigenvectors. The columns of the modal matrix, $[X_n]$, correspond to the n system normalized eigenvectors, therefore

$$[X_n] = \begin{bmatrix} \phi_1 & \phi_2 & \dots & \phi_n \end{bmatrix} \quad (4)$$

The normalized modal matrix is used to uncouple the equations of motion by diagonalizing the mass and stiffness matrix in transforming from physical to principal coordinates. The diagonal principal mass matrix, $[m]$, is given by

APPENDIX B (cont)

$$[m] = [X_n]^T [M] [X_n] \quad (5)$$

and the diagonal principal stiffness matrix, $[k]$, is given by

$$[k] = [X_n]^T [K] [X_n]. \quad (6)$$

APPENDIX C

FREQUENCY RESPONSE

The nonhomogeneous differential equation of motion for a multi-degree-of-freedom system with uniform damping represented by complex moduli in matrix notation is

$$[M] \{\ddot{x}\} + (1+jg)[K] \{x\} = \{F\}. \quad (1)$$

To obtain the frequency response of the system, the forcing function, $\{F\}$, is defined as

$$\{F\} = \{A\} \sin \omega t. \quad (2)$$

The forcing frequencies, ω , and the magnitudes of the forcing function, $\{A\}$, are determined from inputs to the system. The shear strain in the propellant can be found from the frequency response since the shear strain can be determined from the deflections and physical geometry. Equation (2) is solved by assuming that the solution is of the form

$$\{x\} = \{X_i \sin(\omega t - \phi_i)\}. \quad (3)$$

Substituting equation (2) and (3) into (1)

$$-\omega^2 [M] + (1+jg)[K] \{X_i \sin(\omega t - \phi_i)\} = \{A\} \sin \omega t \quad (4)$$

Equation (4) can be solved for the magnitude of the displacements, X_i , and the phase angles, ϕ_i .

MECHANICAL IMPEDANCE TECHNIQUES

IN SMALL BOAT DESIGN*

B. E. Douglas and H. S. Kenchington
David W. Taylor Naval Ship R&D Center
Annapolis Laboratory
Annapolis, Maryland 21402

This paper is concerned with the use of mechanical impedance technology to isolate and diagnose the structural cause of airborne-noise problems on small boats. A normal mode interpretation is given to analog mechanical impedance and structural radiation factor spectra in order to (1) identify hull and decking resonances, (2) examine noise transmission path strengths, and (3) differentiate between radiating structural modes and the normal acoustic modes of the room. These techniques were applied to solve an airborne-noise problem on a 36-foot high performance naval landing craft.

INTRODUCTION

The performance standards set or envisioned for many classes of small boats have placed an increasingly high premium on structural weight. The recent advanced development [1] of the hydrofoil and surface effects ship illustrates the emphasis placed in controlling weight which, in some cases, has forced tradeoffs with vibroacoustic design considerations. This trend is particularly apparent in small boats designed for military applications where structural weight directly affects speed, maneuverability, and payload. As a result, extensive use of lightweight hull and deck plating has been made which has resulted in severe low frequency vibration and airborne-noise problems from resonance amplification and radiation by "high Q" plating modes. When the natural frequencies of these modes coincide with major forcing frequencies of the propulsion unit such as blade rate, piston firing frequency, tooth-contact frequency and their harmonics, the hull and decking can experience significant vibratory displacements which at a minimum cause crew discomfort and fatigue and could ultimately result in structural failure [2].

In addition, the above described resonance conditions can give rise to low frequency airborne-noise problems detrimental to crew health as well as speech intelligibility.

The objective of this paper is to examine the utility of mechanical impedance technology as an aid in diagnosing hull and decking related vibroacoustic problems on small boats. Specifically, this paper is concerned with the application of impedance methods to identify hull and decking resonances and associated damping loss factors, and to examine modal density, vibration transmission path strengths, and acoustic radiation factor spectra of small boat hull and deck structures. Emphasis is placed on structural contributions to airborne noise. (Note: The term mechanical impedance, as used in this paper, refers simply to the ratio of the applied dynamic force to the resultant velocity response (i.e., inverse mobility). For a discussion of impedance and mobility of complex structures, the reader is referred to O'Hara.) [3]

*All opinions or assertions made in this paper are those of the authors and are not to be construed as official or necessarily reflecting the views of the Navy or the naval service at large.

IMPEDANCE TECHNIQUES

Mechanical impedance and mobility techniques have long been recognized as powerful methods for analyzing the vibratory response of complex structures. Considerable attention [2, 4, 5] has been given to developing methods of collecting and interpreting impedance spectra in order to isolate and examine the response of structural elements. These methods have ranged from simple lumped parameter to complex normal mode descriptions. The technique utilized in the analysis presented herein assumes a normal mode interpretation [6] of analog impedance spectra. This approach was chosen due to the predominantly plate-like behavior of small boat hull, decking, and support structures. In addition, such an approach results in a field-oriented evaluation method which can be economically applied to diagnose vibroacoustic problems with the ease of standard structureborne- and airborne-noise surveys.

From normal mode theory, the impedance response on the surface of a viscous-damped structure with a concentrated sinusoidal load applied at x_p, y_p can be written (assuming the damping is small so that there is no appreciable coupling between normal modes):

$$\bar{Z}(x, y) = (i\omega)^{-1} \left[\sum_n \frac{W_n(x_p, y_p) W_n(x, y)}{M_n(\omega_n^2 - \omega^2 - i\eta_n \omega_n \omega)} \right] + i\omega M \quad (1)$$

where: $M_n = \int_0^L \int_0^L W_n^2(x, y) m \, dx \, dy$ = generalized mass of n^{th} mode

M = rigid body mass

ω_n = natural frequency of n^{th} mode

η_n = loss factor of n^{th} mode

ω = excitation frequency

$W_n(x, y)$ = deflection form of n^{th} mode.

The last term of this equation accounts for rigid body motion, and the series terms represent the impedance response of the vibrational modes of the structure.

If the normal modes are well separated in the frequency domain, i.e., $\eta_n < (\omega_{n+1} - \omega_n)/\omega_n$, the response of individual modes can be isolated as distinct minima in an impedance spectrum which are the resonance frequencies of the structure. In this case, the resonance response is predominantly

governed by the response of only one structural mode, and single mode methods can be utilized to determine the modal damping loss factor. One of the oldest and most popular techniques for determining damping directly from impedance spectra is the standard half-power bandwidth method, $\eta_n = (\Delta\omega_{3dB})/\omega_n$, where $\Delta\omega$ is the bandwidth of the structural response 3 dB below the resonance response. However, this method can be subject to considerable magnification of instrument error in lightly damped structures ($\eta_n < 0.01$) as well as large inherent error in highly damped structures due to modal overlap (i.e., coherent modal response). This last consideration is important, since all bandwidth methods are particularly sensitive to the selection of the off-resonance response measurement [7]. That is, bandwidth methods assume that both the resonance response measurement and the off-resonance response measurement are governed by the response of only one structural mode. As a result, the modal density of a structure often influences a bandwidth determination of modal damping to a larger degree than methods which utilize only a resonance response measurement, such as a free decay (reverberation) measurement. However, bandwidth methods can be directly applied to impedance or radiation factor data so that these methods have the advantage of consolidating instrumentation and thus reducing the time required to conduct such evaluations. The measurement range of the half-power bandwidth method can be significantly increased by generalizing the selection of the off-resonance response measurement so that

$$\eta_n = \left\{ \frac{(\omega/\omega_n)^2 + (\omega_n/\omega)^2 - 2}{|Z(\omega)|^2 / |Z(\omega_n)|^2 - 1} \right\}^{1/2} \quad (2)$$

where:

$|Z(\omega_n)|$ = impedance magnitude at resonance

$|Z(\omega)|$ = impedance magnitude at ω (off-resonance).

Besides extending the range and flexibility of the half-power bandwidth method, this expression provides a method for evaluating the damping arising from degenerate modes in which structural irregularities act as perturbations, such as in the case of a periodically stiffened hull.

Upon identifying the structural resonances, the impedance instrumentation

can, also, be directly utilized to obtain mode shape information. By exciting the structure at the resonance frequencies and examining transfer impedance utilizing a mobile accelerometer, the mode shapes can be determined by probing the structure. Nodal lines are indicated by relative maxima in transfer impedance. Impedance phase information (e.g., lissajous figures) can also be utilized as a convenient aid in describing the motion of structures at resonance by determining the areas of the structure which are moving in phase with the drive point.

The application of the impedance techniques mentioned above to small boats is straightforward at low frequencies where low order transverse (plate) modes dominate response, and the damping capacity and modal density of the hull and decking are relatively low so that $\eta_n < (\omega_{n+1} - \omega_n) / (\omega_n)$. In this spectral region, a normal mode interpretation should give an adequate description of the dynamic response of small boat structures. However, at higher frequencies, the modal density and damping capacity of these structures increase so that significant modal overlap occurs, thus making the identification of individual modes very difficult by the methods described above. Fortunately, even in this spectral region

the impedance methods for characterizing vibroacoustic energy transport still yield valuable design information.

Finally, it should be noted that the impedance methods discussed above are deemed best suited to either analog data systems or the new fast Fourier transform instrumentation with frequency translation capability where the structure is excited by random noise. These systems have sufficient frequency resolution to obtain accurate measures of the resonance frequency and resonance impedance magnitude. A block diagram of the instrumentation utilized in the studies presented herein is shown in Figure 1.

RADIATION FACTOR MEASUREMENTS

The radiation factor, i.e., mechano-acoustic transfer function, $S(\omega)$, is a measure of the sound energy radiated by a structure due to a known applied force. It is the ratio of the sound-pressure level in the acoustic medium, usually an enclosed space, to the concentrated sinusoidal force applied either to a structural radiating surface in the medium or to a structure directly coupled to a radiating surface. These measurements are used to examine the radiating efficiency of structural modes

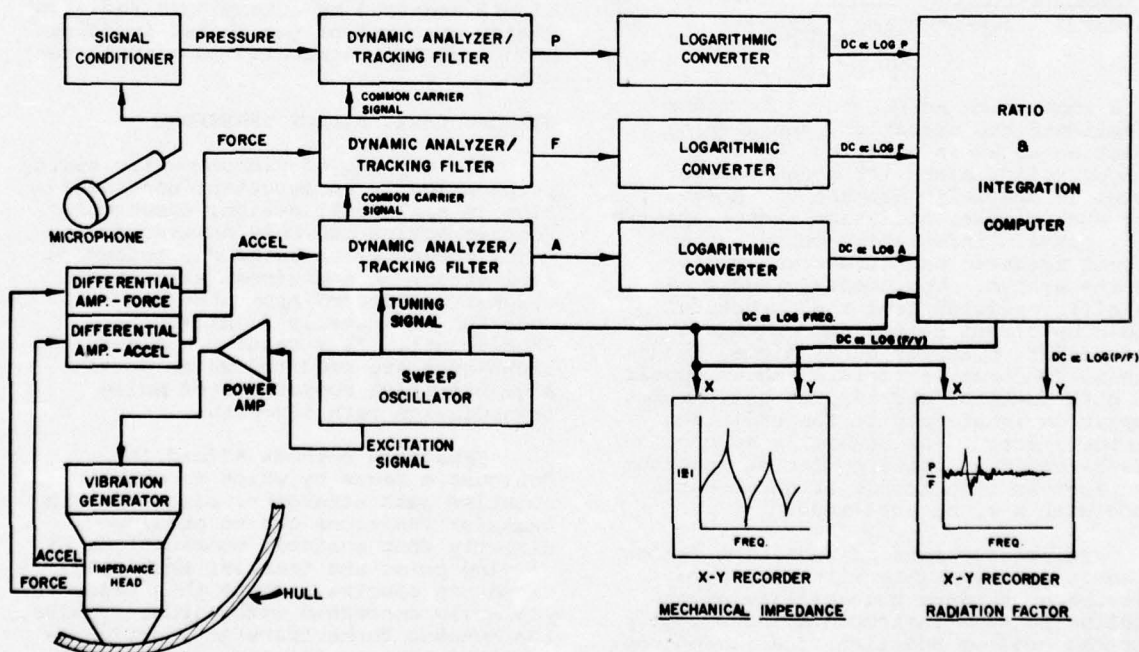


Fig. 1 - Instrumentation block diagram for impedance and radiation factor measurements

and to differentiate between radiating structural modes and normal acoustic modes in the room.

The radiation factor can be shown to be related directly to the ratio of the power radiated in a "live" completely diffuse room to the power imparted to the structure. The mechanical power, W_m , imparted to a structure due to an applied concentrated force, F , can be written [8]

$$W_m = \langle F^2 \rangle R_e \left\{ \frac{1}{Z} \right\}. \quad (3)$$

The sound power radiated by an acoustic source into a "live" diffuse room is simply

$$W_r = \langle p^2 \rangle \frac{a}{4\rho c} \quad (4)$$

where $\langle p^2 \rangle$ is the final steady-state effective acoustic pressure, ρc is the characteristic acoustic impedance, and a is the total absorptive power of the room. Thus, for each case, the ratio of the radiated power to the power imparted to a radiating surface of the room can be shown to be

$$\frac{W_r(\omega)}{W_m(\omega)} = \frac{\langle p^2 \rangle}{\langle F^2 \rangle} \frac{a}{4\rho c R_e \left\{ \frac{1}{Z} \right\}}. \quad (5)$$

In a room where normal acoustic modes complicate the situation, the simple relation shown in equation (5) is no longer valid, since the sound-pressure level is spatially dependent. However, for such a case, radiation factor spectra will contain information on both the normal acoustic and structural modes of the system. The acoustic modes can be differentiated from the structural modes by direct comparison of impedance and radiation factor data, since, assuming no feedback, structural modes appear in both spectra; whereas, acoustic modes appear dominant only in the radiation factor spectra. An unusually strong resonance in a radiation factor spectrum can suggest coincidence of an acoustic mode with a structural mode.

The measurement of radiation factor spectra is compatible with impedance measurements since both utilize essentially the same instrumentation except for the obvious addition of a microphone, see Figure 1. However, several additional considerations as to technique are important in obtaining these measurements. The frequency sweep rate

must allow the energy density in the enclosure to reach steady-state. The differential equation governing the time build-up in energy density, ϵ , in a "live" diffuse room is

$$V \frac{d\epsilon}{dt} + \frac{ac}{4} \epsilon = W \quad (6)$$

where V is the volume of the room, a is the total absorptivity, and W is the rate at which energy is produced. The solution of this equation for a source turned on at $t = 0$ in terms of the mean square acoustic pressure, $\langle p^2 \rangle$, can be shown to be

$$\langle p^2 \rangle = \frac{4W\rho c}{a} \left(1 - e^{-\frac{ac}{4V}t} \right). \quad (7)$$

In addition to sweep rate, direct acoustic radiation from the vibration generator can mask results. At high frequencies, an absorptive shield can be wrapped around the shaker and constrained by a high mass density material, such as lead vinyl, which is mechanically decoupled from the shaker. At low frequencies, direct radiation from the source does not appear to be a major factor in most cases. However, the influence of the direct path can be simply examined by obtaining a radiation factor spectrum of the shaker-impedance head assembly terminated on a small test mass.

VIBROACOUSTIC ENERGY TRANSPORT

The mapping of vibroacoustic energy propagation is an important consideration in small boat design, since corrective action can only be afforded to major transmission paths due to severe limitations on additional structural weight. "Shotgun" approaches to redesign are usually dismissed as inefficient. As a result, analysis techniques are required which provide a quantitative comparison of noise transmission path strengths.

Impedance methods afford the designer a means by which to examine relative path strengths, since dynamic transfer functions can be obtained directly from suitable combinations of driving point and transfer mechanical impedance spectra. Since this paper is primarily concerned with airborne noise, the dynamic force transfer function is utilized because it allows the designer to classify airborne-noise paths by direct comparison with radiation factor spectra. The dynamic force transfer

function can be simply defined as:

$$\left| H_{ab}^f(\omega) \right| = \frac{|F_b|}{|F_a|} = \frac{|Z_{bb}(\omega)|}{|Z_{ab}(\omega)|} \quad (8)$$

If the transmission paths are assumed to be decoupled both acoustically and mechanically, then the transfer function described by equation (8) can be combined with appropriate structural radiation data to investigate individual paths for the airborne noise, that is:

$$|S_{ab}(\omega)| = |H_{ab}^f(\omega)| \cdot |S_p(\omega)| \quad (9)$$

The spectra resulting from the operation described above can then be directly compared to the path from the source to the room, $|S_a(\omega)|$, in order to determine relative path strength.

APPLICATION

The analysis techniques described above were applied to diagnose an airborne-noise problem observed on a 36-foot naval landing craft, the LCP(L).

The LCP(L) is currently used by the Navy as a personnel and patrol boat as well as a guide and control boat in amphibious operations. A plan arrangement of this boat is depicted in Figure 2.

High airborne-noise levels were observed in the forward cabin at cruising speed (2100 rpm) which were deemed detrimental to its performance. Subsequently, an airborne-noise analysis was made to identify the sources of the noise. Figure 3 shows a narrow-band spectral analysis of the airborne noise which reveals that the major sources are discrete lines occurring at 69, 140, and 208 Hz which correspond to the blade rate, a coincidence of the firing frequency and twice blade rate and three times blade rate, respectively.

As a result of this airborne-noise survey, driving point and transfer mechanical impedance and radiation factor spectra were measured at positions deemed critical to the generation and propagation of vibroacoustic energy on this craft. These spectra are presented in figures 4 through 8. As can be seen from the selection of the measurement positions, emphasis was placed on the area immediately adjacent to the

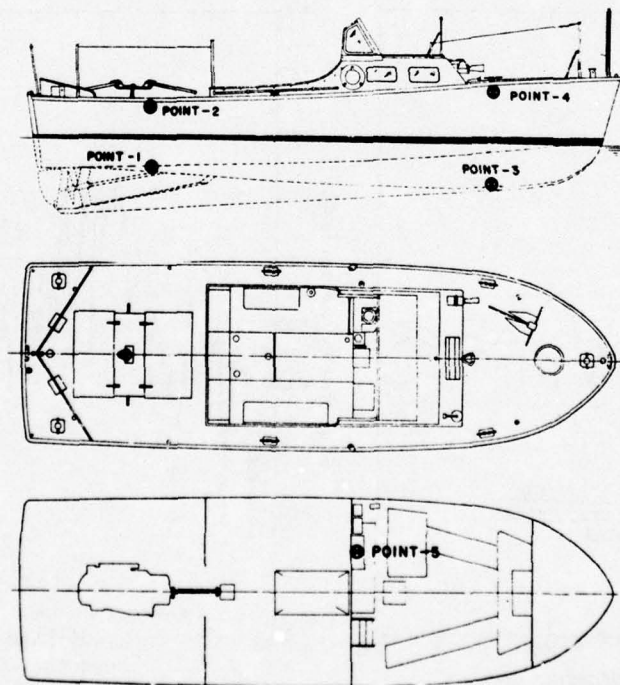


Fig. 2 - Profile and arrangement
36-foot LCP(L) MARK IV

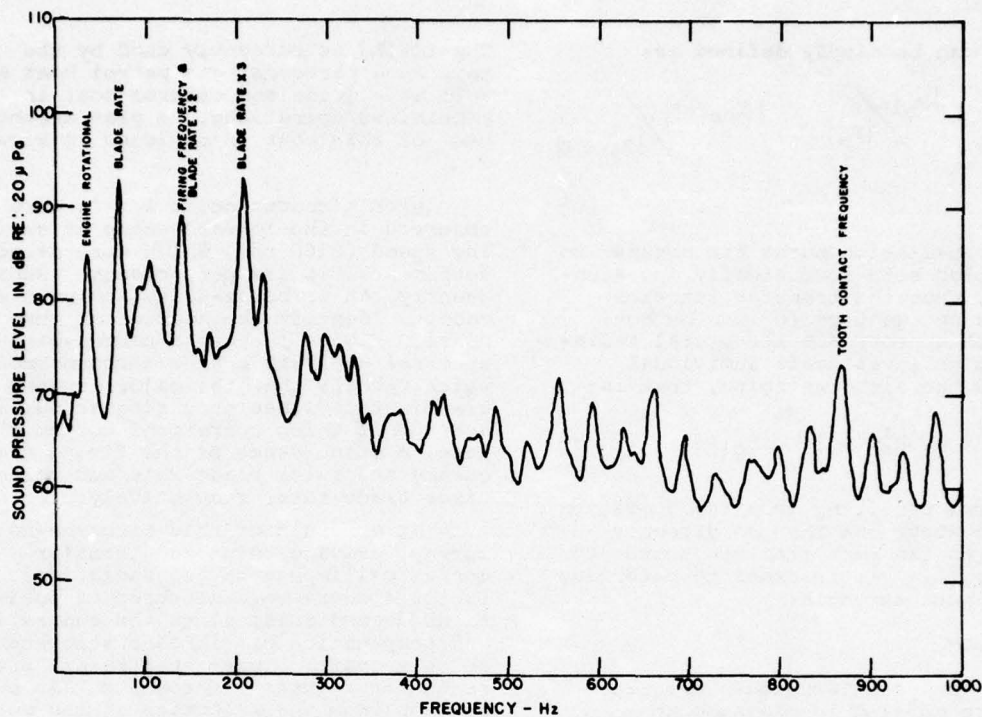


Fig. 3 - Narrow-band analysis of airborne noise in cabin

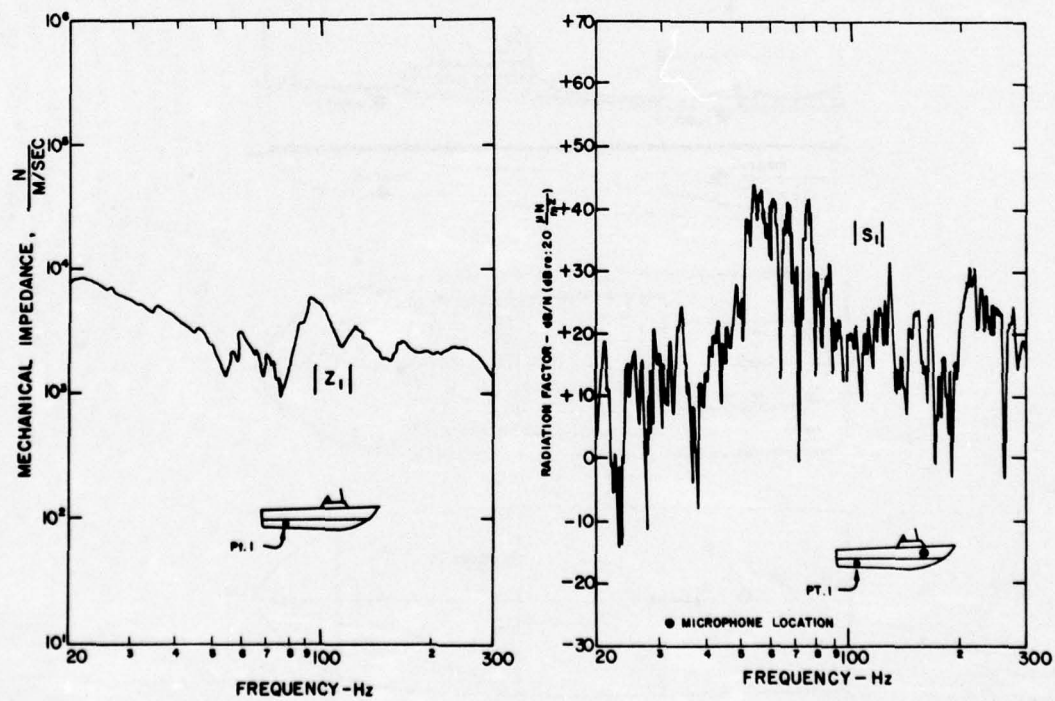


Fig. 4 - Point impedance and radiation factor spectra on the LCP(L) at point 1

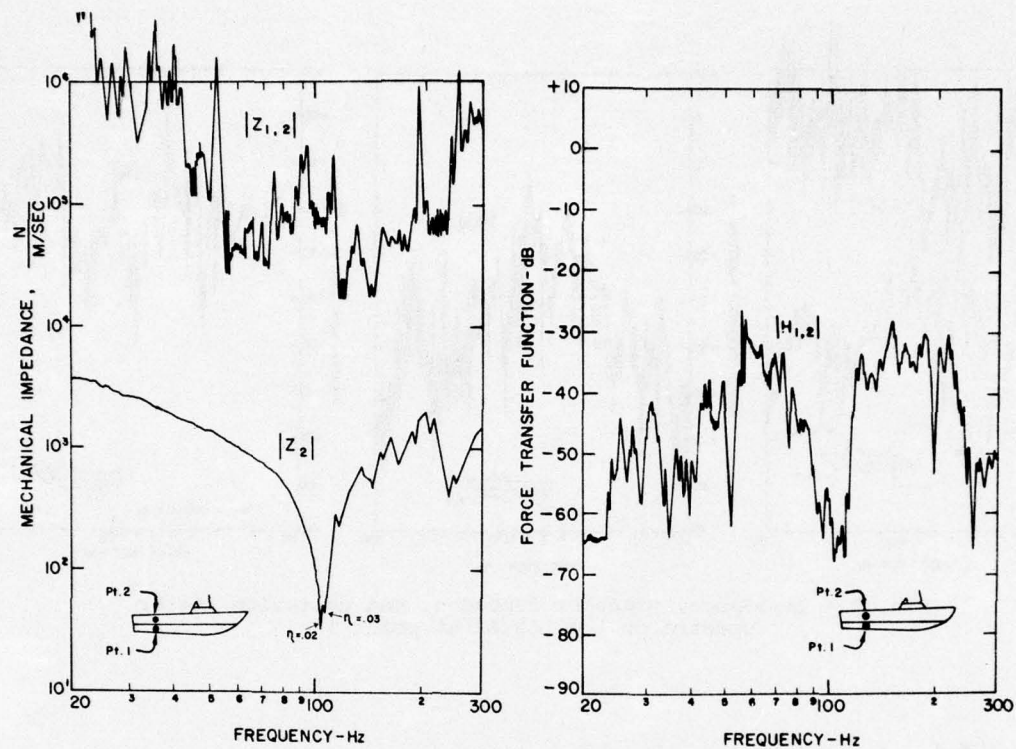


Fig. 5 - Impedance and transfer function spectra on the LCP(L) at point 2

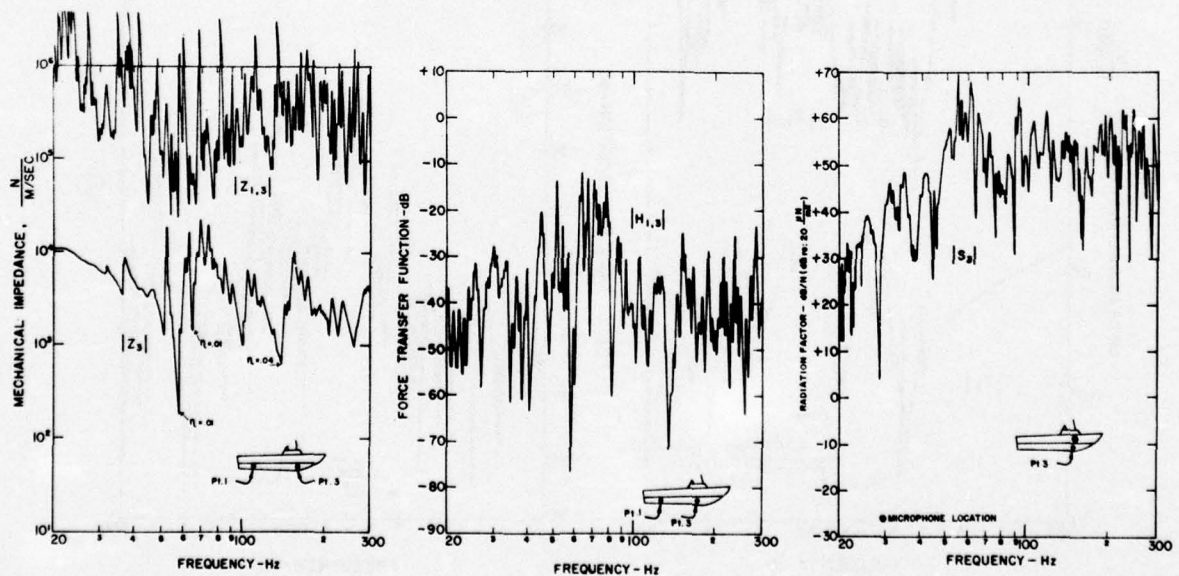


Fig. 6 - Impedance, transfer function, and radiation factor spectra on the LCP(L) at point 3

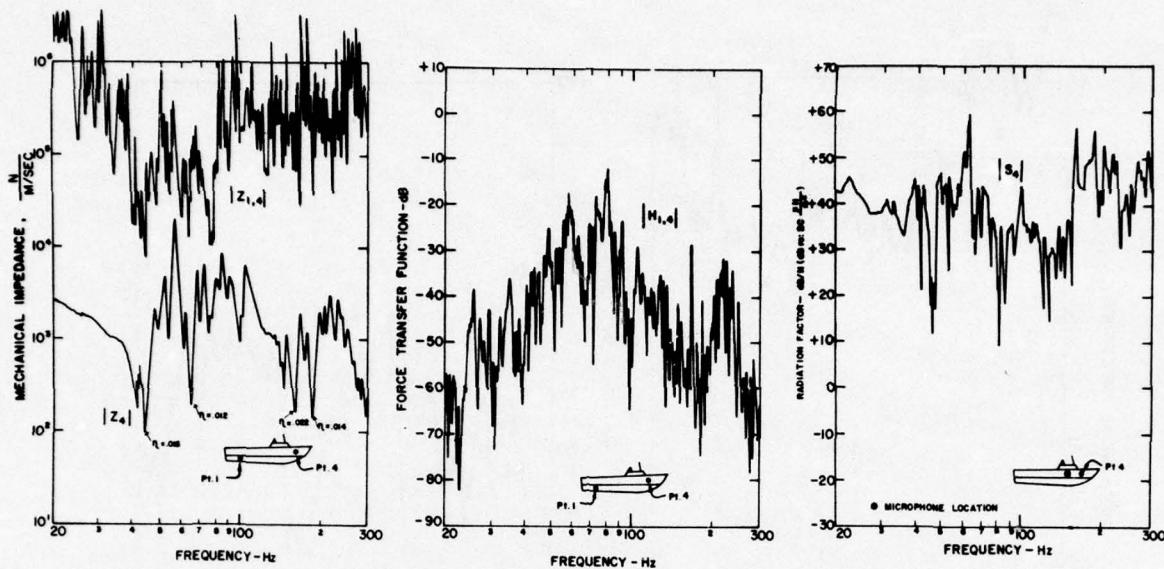


Fig. 7 - Impedance, transfer function, and radiation factor spectra on the LCP(L) at point 4

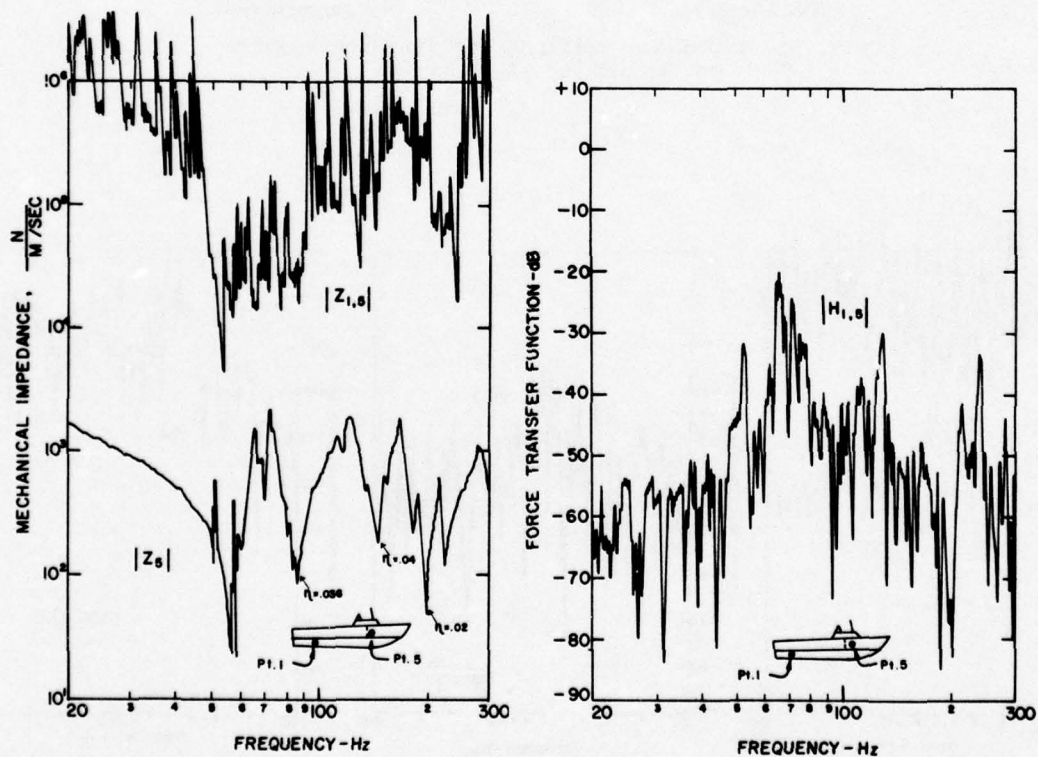


Fig. 8 - Impedance and transfer function spectra on the LCP(L) at point 5

diesel propulsion unit and the propeller shaft on the hull (point 1) since propulsion related sources dominated the airborne noise.

The radiation factor spectrum obtained for the force applied at point 1 and a microphone located in the cabin, figure 4, shows that structural resonances are located at or near all three discrete sources at 69, 140, and 208 Hz. Comparison of the various transfer function spectra with appropriate radiation factor spectra indicate that the blade rate tone at 69 Hz is amplified and radiated by a plating resonance in the overhead decking which is transmitted through a support stanchion located in the cabin. The tone at 140 Hz was found to coincide both with a hull and a decking resonance in the cabin, and the tone at 208 Hz was found to coincide with a plating resonance of decking above the engine compartment.

As a result of this analysis, it was concluded that the selective application of tuned dampers only to the plating identified as resonantly amplifying vibratory energy at 69, 140, and 208 Hz offered the best approach to sufficiently attenuate the airborne noise in the cabin without adding enough weight to jeopardize the performance requirements of this craft. That is, by optimizing the performance of a damping treatment at only one resonance frequency of a plate, a designer need only utilize partial coverage in order to achieve the desired results.

This analysis was also utilized to investigate the potential of other silencing approaches such as localized stiffening or changing the type of propeller so that the blade rate and its harmonics could be shifted out of coincidence with major structural resonances. It was concluded that these alternatives were less desirable due to the relatively high modal density of the hull and deck plating at low frequencies.

DISCUSSION AND SUMMARY

In summary, this paper examined the utility of mechanical impedance technology as a diagnostic design aid for vibroacoustic noise problems on high performance small boats. A normal mode interpretation was given to analog mechanical impedance and radiation factor spectra to characterize the role of hull and decking resonances in amplifying structureborne and airborne noise. Such an interpretation allows the designer to directly determine:

(1) Structural resonance frequencies from relative minima observed in driving point mechanical impedance spectra.

(2) Modal damping loss factors from generalized resonance bandwidth methods applied to driving point mechanical impedance spectra.

(3) Mode shapes from phase information (e.g., lissajous figures) between the applied driving force and a mobile accelerometer.

(4) Relative vibration path strengths from transfer function and radiation factor spectra.

(5) Acoustic radiation characteristics of structural elements from radiation factor spectra.

The above listed information can then be combined with standard structureborne or airborne-noise surveys to identify dynamically deficient structural elements.

The methods described in this paper appear well suited for the low frequency analysis of small boat vibroacoustic problems, where both the modal density and damping are relatively low so that structural modes respond incoherently. At high frequencies, individual resonances are more difficult to identify due to the higher modal densities observed in the light hull and deck plating of these boats. As a result, modal loss factor determinations by the single mode methods described in this paper can be subject to large error.

The critical factors in making impedance measurements on small boats are the selection of measurement positions (which depends, primarily, on source and radiator locations) and the low impedance of hull and decking structures which can limit the frequency range of impedance measuring instrumentation due to transducer mass loading effects and transducer mounting techniques. In addition to measurement technique, it is important to note the effects of random impulse loading due to wave action. Wave slap in rough seas changes the vibratory response of the hull, since the resonance frequencies and resonance response will vary as the radiation impedance of the hull. This consideration should be factored into the assessment of the impedance spectra and favors the use of structural damping in controlling resonance response over reactive methods such as localized

stiffening or mass loading which are used to slightly shift resonances out of coincidence with the major forcing frequencies.

Finally, it is concluded from the application of impedance technology to

diagnose the LCP(L) airborne-noise problem described herein that these techniques offer an economical method for obtaining vibroacoustic design information when used in conjunction with standard airborne- or structureborne-noise surveys.

REFERENCES

- 1 - H. C. Mason, "Small Ships - High Performance," Shock and Vibration Bulletin, Vol. 42, 1972
- 2 - R. B. Tatge, "Failure Detection by Mechanical Impedance Techniques," J. Acoust. Soc. Am., Vol. 41, No. 5, 1967
- 3 - G. J. O'Hara, "Mechanical Impedance and Mobility Concepts," J. Acoust. Soc. Am., Vol. 41, No. 5, 1967
- 4 - N. F. Hunter, and J. V. Otts, "The Measurement of Mechanical Impedance and Its Use in Vibration Testing," Shock and Vibration Bulletin, Vol. 42, 1972
- 5 - R. Plunkett, (ed.), "Mechanical Impedance Methods for Mechanical Vibrations," ASME, 1958
- 6 - J. D. Robson, "An Introduction to Random Vibration," Edinburgh University Press, 1964
- 7 - B. E. Douglas, "Modal Damping from Resonance Spectral Shape Measurements," J. Acoust. Soc. Am., Vol. 58, Suppl. No. 1, 1975
- 8 - I. L. Ver, and C. I. Holmer, "Interaction of Sound Waves with Solid Structures," Chapter 11, Noise and Vibration Control (ed., L. L. Beranek), McGraw-Hill Book Co., 1971

Discussion

Mr. Feldman (NKF Engineering): Your impedance measurements compared your frequency distribution spectrum with the exciting frequencies. How do you separate the airborne noise transmission from the structure borne noise transmission?

Mr. Douglas: The radiation factor spectra will contain information on the normal structural modes as well as any acoustic modes in the enclosures. If you compare that with the impedance spectra one can look for coincidences to determine what are your radiating modes and what is being enhanced by the acoustic modes in the enclosure. Strong comparisons suggest coincidence while weak structural comparisons indicate low radiation efficiency. We identified the structural modes from the impedance spectra, and we could identify the normal modes in the enclosure by overlaying the two. We saw a pretty good spike in the curve where they coincided and this was the technique that we used.

Mr. Feldman: Did you make an attempt to drive airborne noise with speakers?

Mr. Douglas: No, we were doing it totally by structure.

Mr. Lepor (Naval Undersea Center): What do you intend to do on the SES? That is a real serious weight problem and you will have all kinds of problems. How do you intend to apply damping treatments to keep the airborne noise levels down?

Mr. Douglas: We were hoping to get into the problem, we have some people in our lab that are working on the SES who are associated with the Patuxent Lab and this has been another group up to now; we are working on our results from the LCPL and we are giving it to them to see if they have some use for it.

Mr. Lepor: Will you design light-weight highly damped structures?

Mr. Douglas: I would like to have shown you the results of our work on noise control unfortunately the program was cut.

Mr. Lepor: We have been using methods similar to yours also; we talk sound level measurements and we try to relate on a narrow band on a narrow frequency analysis what we measure from a structure and what is in the space itself. Many times you can get something radiating in the hull and it doesn't radiate efficiently into the air and that is where the problem is.

Mr. Douglas: I know the method has been around but we have tried to emphasize in the paper that the modes that are associated with this are usually of a high modal density and that the techniques for extracting information have become a little more sophisticated and we just tried to prove a point.

FREQUENCIES AND MODE SHAPES OF GEOMETRICALLY AXISYMMETRIC STRUCTURES :

APPLICATION TO A JET ENGINE

P. Trompette and M. Lalanne
Institut National des Sciences Appliquées,
Villeurbanne, France

The vibrations of axisymmetric structures are studied using a Fourier series development and the finite element technique. The general differential equation for rotating thin or thick structures is presented. Here the Coriolis effect is neglected and frequencies and mode shapes of the system are obtained using a simultaneous iteration technique. The method is first tested on simple examples and then applied to a part of a jet engine.

INTRODUCTION

In order to predict the dynamical behaviour of systems subjected to external forces it is often necessary to know from calculations and with sufficient accuracy their frequencies and associated mode shapes. Amongst these systems let us mention specifically thin or thick rotating axisymmetric parts of jet engine components. In previous work [1], [2], [3], [4], studies of three dimensional rotating structures have been reported and also many papers for example [5], [6], [7], [8], have already been published concerning the linear or non linear behaviour of axisymmetric structures without rotation. In this paper, the general differential equation of motion of an axisymmetric rotating system is given using a Fourier series development and the finite element method. The Coriolis matrix is neglected in the applications described here. First, the method and the computer program are tested with some known examples. Then, they are applied to the calculation of a jet engine part. The agreement between experimental and calculated frequencies is shown to be satisfactory.

DIFFERENTIAL EQUATIONS OF THE SYSTEM

Kinetic and potential strain energies for the whole structure need to be calculated in order to apply Lagrange's equations [9]. Because of the symmetry of the structure, displacements are developed in terms of a Fourier series. The calculations are performed using the finite element method. The material characteristics, Young's modulus E , Poisson's ratio ν , mass per unit volume ρ , are assumed to be constant. Both thick and thin structures are considered. For the first, the potential strain energy U is obtained as in [8] but large strains have been introduced here (Appendix 1). For the

second, U is obtained as in [6] (Appendix 2). Now the method for determining the kinetic energy T is briefly presented.

Let V be the velocity of $M(r, \theta, z)$ with respect to an absolute fixed coordinate system, expressed by its components in R , the rotating system. M coordinates become $(r + u_r, \theta + u_\theta, z + u_z)$.

$$2T = \int_{\tau} \rho V^t V d\tau \quad (1)$$

with
 τ , volume of the solid
 t , transposition symbol
with,

$$V = \begin{bmatrix} \dot{u}_r \\ \dot{u}_\theta \\ \dot{u}_z \end{bmatrix} + \begin{bmatrix} 0 \\ 0 \\ \Omega \end{bmatrix} \times \begin{bmatrix} r + u_r \\ \theta + u_\theta \\ z + u_z \end{bmatrix} = \begin{bmatrix} \dot{u}_r - \Omega u_\theta \\ \dot{u}_\theta + \Omega(r + u_r) \\ \dot{u}_z \end{bmatrix} \quad (2)$$

and (2) becomes

$$\begin{aligned} 2T = & \int_{\tau} \rho (\dot{u}_r^2 + \dot{u}_z^2 + \dot{u}_\theta^2) d\tau + \Omega^2 \int_{\tau} (u_r^2 + u_\theta^2) d\tau \\ & + 2\Omega \int_{\tau} \rho (u_r \dot{u}_\theta - \dot{u}_r u_\theta) d\tau + 2\Omega^2 \int_{\tau} \rho r u_r d\tau \\ & + 2\Omega \int_{\tau} \rho r \dot{u}_r d\tau + \Omega^2 \int_{\tau} \rho r^2 d\tau \end{aligned} \quad (3)$$

These six integrals may be represented by

I_1, \dots, I_6 respectively, I_5 and I_6 disappear in Lagrange's equations. The displacements are those of Appendix I or II (formula A1 (1), A2 (1)). Due to the orthogonality of the sine and cosine functions on the interval $(0, 2\pi)$ the integrals are only dependent on r and z . The structure is modelled by finite elements whose meridian is,

- for thick elements : a triangle with three degrees of freedom per node.
- for thin elements : a line segment with four degrees of freedom per node.

From Lagrange's equations,

$$I_1 \rightarrow M_n \delta_n^{\circ\circ} (M_n \text{ classical mass matrix}),$$

$$I_2 \rightarrow \Omega^2 M_{gn} \delta_n (\Omega^2 M_{gn} \text{ supplementary stiffness matrix}),$$

$$I_3 \rightarrow C_n \delta_n^{\circ} (C_n \text{ Coriolis matrix}),$$

$$I_4 \rightarrow F(\Omega^2) (\text{centrifugal forces vector}).$$

The potential strain energy U is obtained from

$$2U = \int_{\tau} \sigma^t \epsilon \, d\tau \quad (4)$$

with,

σ , stress vector
 ϵ , strain vector

As the material is supposed to be "hookean" :

$$2U = \int_{\tau} \epsilon^t D \epsilon \, d\tau \quad (5)$$

D , elasticity matrix.

In terms of displacements, the components of ϵ are given in Appendix A1 or A2, (formula A1 (2), A2 (2)). There are non linear terms in the displacement gradients although these are assumed to be infinitesimal.

From Lagrange's equation U gives :

$$[K_{en} + K_{gn}(\sigma_0)] \delta_n \quad (6)$$

with,

K_{en} , classical stiffness matrix
 $K_{gn}(\sigma_0)$, geometric matrix function of initial stresses σ_0 .

The differential matrix equation for the structure is :

$$M_n \delta_n^{\circ\circ} + C_n \delta_n^{\circ} + [K_{en} + K_{gn}(\sigma_0) - \Omega^2 M_{gn}] \delta_n = F(\Omega^2)$$

where,

$$F(\Omega^2) = 0 \quad \text{for } n \neq 0 \quad (7)$$

The Coriolis matrix C_n is now neglected. For the first step, σ_0 is n calculated by solving :

$$[K_{eo} + K_{go}(\sigma_0) - \Omega^2 M_g] \delta_0 = F(\Omega^2) \quad (8)$$

with an iterative Newton-Raphson procedure.

Next, for each n , frequencies and associated modes are obtained from the matrix equation :

$$[\omega^2 M_n] \delta_n = [K_{en} + K_{gn}(\sigma_0) - \Omega^2 M_g] \delta_n \quad (9)$$

by solving the classical eigenvalue problem using a simultaneous iterative technique [10].

APPLICATIONS

The first test of the method is the calculation of stresses in a circular rotating disk of varying profile. The theoretical results are those of C.D. Mote [11]. The angular velocity Ω is 10^3 rd/sec, and the thickness of the disk is given by the formula : $h = e^{\lambda r}$. ($\lambda = 74,8$), (r = radial distance). Results are presented in table 1.

The second test is concerned with the free vibrations of a centrally clamped circular disk spinning with an angular velocity Ω . Results are due to W. Eversman and R.O. Dodson [12]. This disk is modelled in the finite element program by only twelve shell elements. Frequencies are presented in table 2 for the Fourier series order 2.

$r(m)$	σ_{rr} , TH $\times 10^8$ (N/m ²)	σ_{rr} , FE $\times 10^8$ (N/m ²)	$\sigma_{\theta\theta}$, TH $\times 10^8$ (N/m ²)	$\sigma_{\theta\theta}$, FE $\times 10^8$ (N/m ²)
0.0266	0.481	0.485	0.482	0.486
0.0666	0.471	0.477	0.476	0.482
0.106	0.443	0.450	0.462	0.468
0.15	0.361	0.370	0.422	0.432
0.19	0.121	0.136	0.316	0.327

Table : 1

Nodal circles	$\Omega = 0$		$\Omega = 1886$ rd/sec	
	TH	FE	TH	FE
0	63.48	63.64	472.5	470.4
1	426.4	397.8	1128.3	1103.6
2	1095	1058.8	2036.8	1975.3

Table : 2

The third example gives the linear buckling analysis of a thin annular plate - outer edge clamped, inner edge free-under uniform compression. Results are compared with those obtained by S. Majumbar [13]. The computer program calculates the first eigenvalue of the matrix equation

$$|K_{en} + \lambda K_{gn}(\sigma_0)| \delta_n = 0$$

for different values of the circumferential wave number n . Results are given in table 3 :

n	TH	EXP	FE
0	1630	2140	1634
1	2480	2465	2620
2		3186	4060
3		4388	6200

Table : 3

Frequencies and modes shapes of a jet engine component.

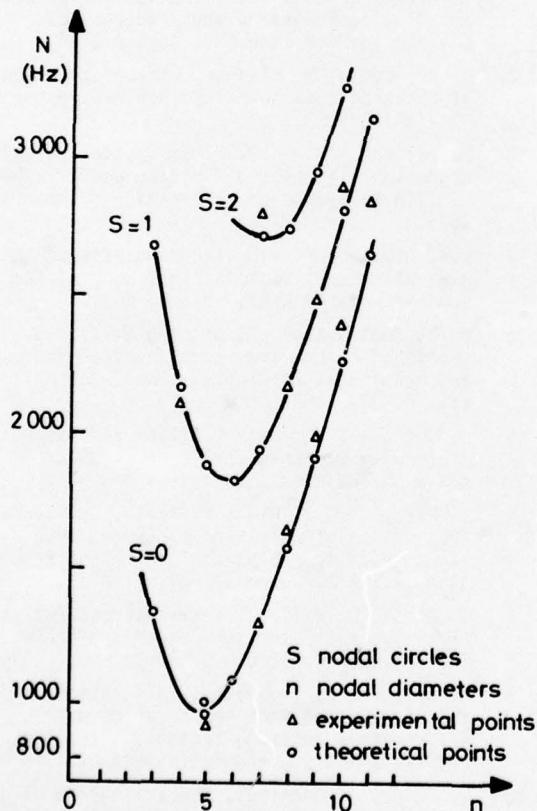


Fig. 1 Frequencies of the cone-cylinder

Roughly, the structure is built up from a cylinder connected to a cone. The thickness of the structure is not constant and so the two kinds of element have been used. One of the boundaries is clamped and the other is modelled by springs and masses. Experimental results have been performed at rest. The results are presented in figs. 1,2,3.

- For a number of circumferential waves $n > 3$ modes shapes are generally predominant either for the cone (fig.1) or for the cylinder (fig. 2). For the lowest frequencies (at an n given) the two parts of the system seem to be uncoupled. Fig.3 shows the mode shapes for $n = 7$.
- For $n = 2$ the two parts are coupled, for $n = 3$ this coupling is slight.
- The agreement between experimental and finite element results is shown to be satisfactory.
- At operating speeds all frequencies are seen to increase. For $n = 7$ the six first frequencies increase respectively by 32 %, 20 %, 15 %, 15 %, 10 %, 9 %.

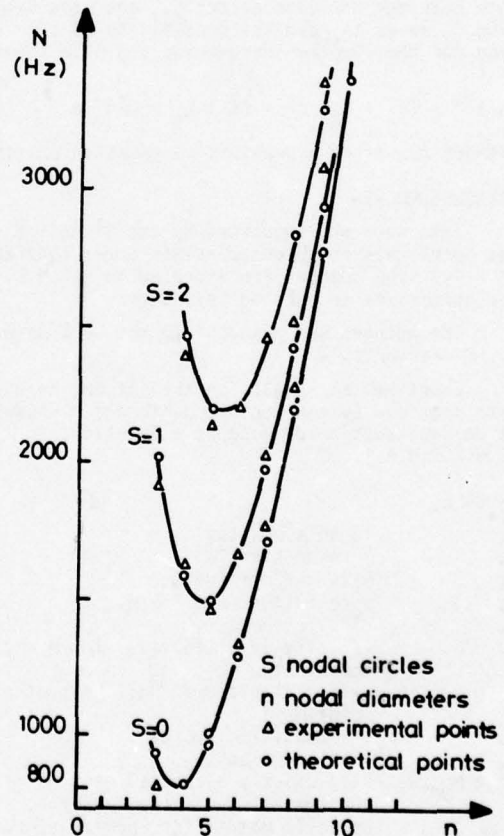


Fig. 2 Frequencies of the cylinder-cone

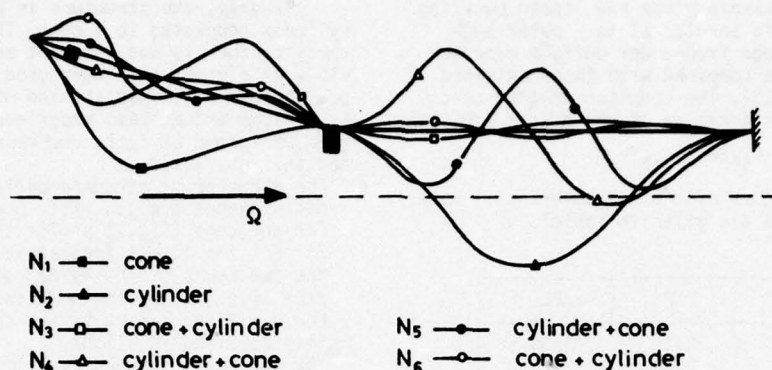


Fig. 3 Cylinder-cone mode shape, $n = 7$

CONCLUSION

Calculations of rotating thin or thick axisymmetric structures have been presented using the finite element technique. It is considered that it would be now very interesting to introduce both the Coriolis effect C_1 , and also damping C_2 so as to have the possibility of solving for the complex frequencies and mode shapes of:

$$M \delta'' + (C_1 + C_2) \delta' + (K + K_g - \Omega^2 M_g) \delta = 0 \quad (10)$$

without requiring a prohibitive computation time.

ACKNOWLEDGMENTS

This work was supported by the Direction des Recherches et Moyens d'Essais under contract 73 - 741. The authors are indebted to D.R.M.E. for permission to publish this paper.

The authors are grateful to the work done by Mr. G. Ferraris.

Experimental results on the jet engine have been provided by the Société Nationale d'Etude et de Construction de Moteurs d'Aviation, (S.N.E.C.M.A.).

SYMBOLS

E ,	Young's modulus
ν ,	Poisson's ratio
ρ ,	mass per unit volume
U ,	potential strain energy
T ,	kinetic energy
V ,	velocity of a typical point M whose coordinates are r, θ, z
u_r, u_θ, u_z ,	vector displacement of the typical point M
t ,	transposition symbol
Ω ,	angular velocity
$M_n, \Omega^2 M_{gn}, C_n$,	respectively classical mass matrix, supplementary stiffness matrix, Coriolis matrix for Fourier's order n
$F(\Omega^2)$,	centrifugal force vector
σ ,	stress vector
ϵ ,	strain vector
D ,	elasticity matrix

$K_{en}, K_{gn}(\sigma_0)$, respectively classical stiffness matrix and geometric matrix for Fourier's order n .

REFERENCES

1. R. Henry, M. Lalanne, Vibration analysis of rotating compressor blades. Journal of Engineering for Industry, august 1974.
2. P. Trompette, M. Lalanne, Vibration analysis of rotating turbine blade. A.S.M.E. paper 74 - WA/DE - 23.
3. M. Lalanne, R. Henry, P. Trompette, Rotating blade analysis by the finite element method. I.U.T.A.M. Symposium on dynamics of rotors, 1974.
4. K.K. Gupta, Free vibration analysis of spinning structural systems. Int. Journal for Num. Methods in Eng., vol. 5, 1973.
5. D. Bushnell, Analysis of ring stiffened shells of revolution under combined thermal and mechanical loading. A.I.A.A. Journal, vol. 9, n°3, 1971.
6. D. Bushnell, Stress, stability and vibration of complex branched shells of revolution. Analysis and user's manual of BOSOR IV.
7. J. Percy, T.H.H. Pian, S. Klein, D. Navaratna. Application of matrix displacement method to linear elastic analysis of shells of revolution. A.I.A.A. Journal, vol. 3, n°11, 1965.
8. S. Ghosh, E. Wilson, Dynamic stress analysis of axisymmetric structure under arbitrary loading. Rapport E.E.N.C. 69-10, sept. 1969.
9. M. Lalanne, P. Trompette, Calculation of frequencies and mode shapes of geometric axisymmetric rotating systems. 45th Shock and Vibration Conferences, Short Discussion.
10. M. Clint, A. Jennings, The evaluation of eigenvalues and eigenvectors of real symmetric matrices by simultaneous iteration. Computer Journal, vol. 13, n°1, 1970.
11. C.D. Mote, Free vibration of initially stressed circular disks. Journal of Eng. for industry, may 1965.

- 12 W. Eversman, R.O. Dodson, Free vibration of a centrally clamped spinning circular disk. A.I.A.A. Journal, vol. 7, n°10, 1969.
- 13 S. Majumbar, Buckling of a thin annular plate under uniform compression. A.I.A.A. Journal, vol. 9, n°9, sept. 1971.
- 14 V.V. Novozhilov, Thin shell theory. Wolters - Noordhoff, 1970.

APPENDIX I

THICK ELEMENT

It is a three nodes element with three degrees of freedom per node, (u_r, u_z, u_θ) . The displacements functions are :

$$\begin{aligned} u_r &= \sum_{n=0}^N u_{rn}(r, z) \cdot \cos n\theta \\ u_z &= \sum_{n=0}^N u_{zn}(r, z) \cdot \cos n\theta \\ u_\theta &= \sum_{n=0}^N u_{\theta n}(r, z) \cdot \sin n\theta \end{aligned} \quad A1(1)$$

n , Fourier's series order.

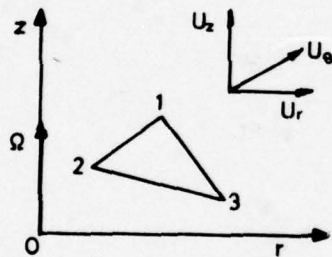


Fig. 4 Thick element

The large strain expressions are :

$$\begin{aligned} \epsilon_{rr} &= \frac{\partial u_r}{\partial r} + \frac{1}{2} \left[\left(\frac{\partial u_r}{\partial r} \right)^2 + \left(\frac{\partial u_z}{\partial r} \right)^2 + \left(\frac{\partial u_\theta}{\partial r} \right)^2 \right] \\ \epsilon_{zz} &= \frac{\partial u_z}{\partial z} + \frac{1}{2} \left[\left(\frac{\partial u_r}{\partial z} \right)^2 + \left(\frac{\partial u_z}{\partial z} \right)^2 + \left(\frac{\partial u_\theta}{\partial z} \right)^2 \right] \\ \epsilon_{\theta\theta} &= \frac{u_r}{r} + \frac{1}{r} \frac{\partial u_\theta}{\partial \theta} + \frac{1}{r^2} \left[\left(\frac{\partial u_r}{\partial \theta} \right)^2 + \left(\frac{\partial u_z}{\partial \theta} \right)^2 + \left(\frac{\partial u_\theta}{\partial \theta} \right)^2 \right] \\ &\quad + \frac{1}{2r^2} (u_r^2 + u_\theta^2) + \frac{1}{r^2} (u_r \frac{\partial u_\theta}{\partial \theta} - u_\theta \frac{\partial u_r}{\partial \theta}) \\ 2\epsilon_{rz} &= \frac{\partial u_r}{\partial z} + \frac{\partial u_z}{\partial r} + \frac{\partial u_r}{\partial r} \frac{\partial u_r}{\partial z} + \frac{\partial u_z}{\partial r} \frac{\partial u_z}{\partial z} + \frac{\partial u_\theta}{\partial r} \frac{\partial u_\theta}{\partial z} \end{aligned}$$

$$\begin{aligned} 2\epsilon_{r\theta} &= \frac{1}{r} \frac{\partial u_r}{\partial \theta} + \frac{\partial u_\theta}{\partial r} - \frac{u_\theta}{r} + \frac{1}{r} \left(\frac{\partial u_r}{\partial r} \frac{\partial u_r}{\partial \theta} + \frac{\partial u_z}{\partial r} \frac{\partial u_z}{\partial \theta} \right. \\ &\quad \left. + \frac{\partial u_\theta}{\partial r} \frac{\partial u_\theta}{\partial \theta} \right) + \frac{1}{r} (u_r \frac{\partial u_\theta}{\partial r} - u_\theta \frac{\partial u_r}{\partial r}) \quad A1(2) \\ 2\epsilon_{z\theta} &= \frac{1}{r} \frac{\partial u_z}{\partial \theta} + \frac{\partial u_\theta}{\partial z} + \frac{1}{r} \left[\frac{\partial u_r}{\partial z} \frac{\partial u_r}{\partial \theta} + \frac{\partial u_z}{\partial z} \frac{\partial u_z}{\partial \theta} + \frac{\partial u_\theta}{\partial z} \frac{\partial u_\theta}{\partial \theta} \right] \\ &\quad + \frac{1}{r} (u_r \frac{\partial u_z}{\partial z} - u_\theta \frac{\partial u_r}{\partial z}) \end{aligned}$$

The relation ship between stresses σ and strains ϵ is :

$$\sigma = D \epsilon$$

with

$$D = \frac{E(1-\nu)}{(1+\nu)(1-2\nu)} \cdot \begin{bmatrix} 1 & \frac{\nu}{1-\nu} & \frac{\nu}{1-\nu} & 0 & 0 & 0 \\ & 1 & \frac{\nu}{1-\nu} & 0 & 0 & 0 \\ & & 1 & 0 & 0 & 0 \\ & & & \frac{1-2\nu}{2(1-\nu)} & 0 & 0 \\ & & & & \frac{1-2\nu}{2(1-\nu)} & 0 \\ & & & & & \frac{1-2\nu}{2(1-\nu)} \end{bmatrix}$$

(A1(3)) Symmetric

APPENDIX II

THIN ELEMENT

It is a straight element with two nodes and four degrees of freedom per node $(u, v, w, \psi = \frac{\partial w}{\partial s})$.

The displacements functions are :

$$\begin{aligned} u &= \sum_{n=0}^N u_n(r, z) \cdot \cos n\theta \\ v &= \sum_{n=0}^N v_n(r, z) \cdot \sin n\theta \\ w &= \sum_{n=0}^N w_n(r, z) \cdot \cos n\theta \end{aligned} \quad A2(1)$$

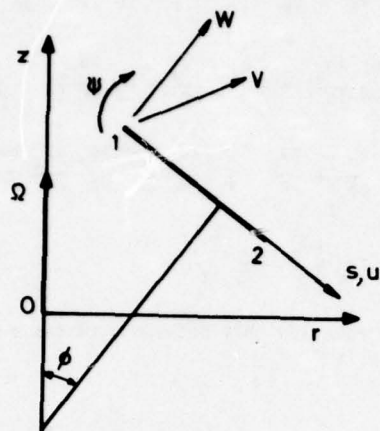


Fig. 5 Thin Element

The large strain expressions are these of Novozhilov's thin shell theory [14].

$$\epsilon_{ss} = \frac{\partial u}{\partial s} + \frac{1}{2} (\chi^2 + \gamma^2) - z \frac{\partial^2 w}{\partial s^2}$$

$$\epsilon_{\theta\theta} = \frac{1}{r} \left(\frac{\partial v}{\partial \theta} + u \cos \phi + w \sin \phi \right) + \frac{1}{2} (\psi^2 + \gamma^2)$$

$$+ z \left[\frac{1}{r^2} \left(\frac{\partial v}{\partial \theta} \sin \phi - \frac{\partial^2 w}{\partial s^2} \right) - \frac{1}{r} \frac{\partial w}{\partial s} \cos \phi \right]$$

$$\gamma_{s\theta} = \frac{\partial v}{\partial s} - \frac{v}{r} \cos \phi + \frac{1}{r} \frac{\partial u}{\partial \theta} + \chi \psi$$

$$+ 2z \left[\frac{1}{r^2} \left(\frac{\partial w}{\partial \theta} \cos \phi - r \frac{\partial^2 w}{\partial s \partial \theta} \right) + \frac{1}{r} \left(\frac{\partial v}{\partial s} - \frac{v}{r} \cos \phi \right) \sin \phi \right] \quad A2(2)$$

with

$$\chi = \frac{\partial w}{\partial s}$$

$$\psi = \frac{1}{r} \frac{\partial w}{\partial \theta} - v \frac{\sin \phi}{r}$$

$$\gamma = \frac{1}{2} \left[\frac{1}{r} \frac{\partial u}{\partial \theta} - \frac{\partial v}{\partial s} - v \frac{\cos \phi}{r} \right]$$

and :

$$D = \frac{E}{1-\nu^2} \begin{vmatrix} 1 & \nu & 0 \\ \nu & 1 & 0 \\ 0 & 0 & \frac{1-\nu}{2} \end{vmatrix} \quad A2(3)$$

EIGENSOLUTION SENSITIVITY TO
PARAMETRIC MODEL PERTURBATIONS

Charles W. White, and Bruce D. Maytum
Martin Marietta Corporation
Denver, Colorado

An anatomical study of the eigenproblem is pursued to find an economical answer to the questions:

- 1) What effect will a specified perturbation of a dynamic model finite element have on analytical mode shapes and frequencies?
- 2) What dynamic model finite element perturbations are required to produce mode shapes and frequencies that satisfy design requirements or that agree with test results?

A three dimensional array of the energy distribution (kinetic and/or potential) among the finite elements and the modal coordinates of the nominal model is identified. It is shown that this array contains the information required to define an eigenproblem size reduction that provides an accurate and economical answer to the first question.

The second question is the inverse of the first. It is shown how the energy array information can be used in an algorithm to solve this second problem. Of particular value is the identification of a method of theoretical/experimental correlation improvement which does not require calculations involving measured mode shapes.

INTRODUCTION

The dynamic model of an aerospace structure is a collection of mathematical simulations of component or subcomponent parts of that structure. The manner in which the structure is so divided is subject to the judgment of the analyst and restricted by computer capability available to him. Further restrictions are imposed by the fact that each piece must be represented as a finite approximation of what, in reality, is a continuous system. Average mechanical properties and assumptions regarding velocity and strain distributions are uncertainties necessarily assigned to a specific representation. All of these factors combine to produce a dynamic model for which the eigensolution is unique.

Thus, if one is faced with the requirement to evaluate tolerance effects or design changes the model must be revised to reflect these changes and the eigensolution must be recalculated. A similar problem for the dynamicist arises when he must define an optimum design

change that will produce a configuration which conforms to some specified frequency or mode shape requirement. The size of present day dynamic models generally makes the costs of an adequate parametric study approach to these problems prohibitive. Therefore, the first purpose of this paper is to present an anatomical study of the eigenproblem that results in an economical and accurate method to identify the sensitivity of mode shapes and frequencies to dynamic model perturbations.

The value of any purely mathematical scheme to evaluate model perturbation is academic until the validity of the nominal model is established. The veracity of the model can be established only by correlation with dynamic test results. Presently, there is no assurance that test results will be sufficient or conclusive, or that modeling errors discovered by test can be corrected. The reason for this situation is that no mathematical procedure now exists by which to associate overall model dynamic behavior with individual model components short of a parametric study of eigensolutions, perturbing

each component in turn. Again, this is a costly process. Therefore, the second purpose of this paper is to apply the knowledge of dynamic model sensitivity to the task or theoretical/experimental correlation improvement.

The procedure used to arrive at the method presented may be summarized as follows.

A brief review of the energy methods by which the eigenproblem is formulated is made to introduce the notion of nominal component kinetic and potential energy contributions in a discrete coordinate system. The component terms are then collected as mass and stiffness matrices used to formulate the nominal eigenproblem. At this point, the significance of component kinetic and potential energy in the modal coordinate system is discussed. Then, it is shown how component perturbations may be made to appear as explicit terms in a perturbed eigenproblem. This step produces a three dimensional array of modal data which defines the distribution of potential and kinetic energy among the model elements in each mode, and identifies the coupling between the nominal model modes produced by each of the model elements. It is shown how the data in this array may be used to obtain an approximate solution to the perturbed eigenproblem, and to define a procedure for theoretical/experimental correlation improvement.

Finally, a quantitative evaluation of the methodology is obtained from an example structure.

ELEMENTS OF A DYNAMIC MODEL

Energy methods by which dynamic models are generated are well known [2]. A broad overview of dynamic modeling techniques is presented here to lay the ground work for later development.

A dynamic model is a collection of mathematical simulations of component or subcomponent parts of the structure being considered. Hereafter, these parts will be referred to as elements. The initial step in the simulation is to define the kinetic and potential energy in each of the elements. The general form of these expressions are,

$$\text{Kinetic Energy, (K.E.)}_j = \frac{1}{2} \int_{r_j} \rho v^2 dV \quad (1)$$

$$\text{Potential Energy, (P.E.)}_j = \frac{1}{2} \int_{r_j} E \epsilon^2 dV \quad (2)$$

where r_j = the volume of j th structural element
 dV = a differential volume
 ρ = mass density of the differential volume

v = the velocity of the differential volume
 ϵ = the strain in the differential volume
 E = Young's modulus of the differential volume

Exact evaluation of these integrals is seldom, if ever, possible. Usually, they are approximated by assuming constant or linearly varying material properties and by assuming velocity and strain distributions throughout the volume, r_j . In order to remain within computer size constraints and budget limitations, these approximations, in many instances, are necessarily gross. Gross approximations may be insufficient for those elements which control the dynamic behavior in the frequency range of interest. For this reason, it is the object of this paper to determine which elements of the model do control the dynamic behavior, so that modeling effort can be concentrated in these areas to improve the representation, and so that specific dynamic tests may be planned to assure sufficient test data is obtained in these areas.

It must be remembered that overly gross assumptions or outright errors can introduce completely erroneous behavior within the frequency range of interest or shift a true dynamic characteristic well outside of that range. One should not expect a perturbation approach such as is being developed here to detect these situations. However, state of the art techniques properly employed, should provide an adequate initial model.

Once the assumptions required to form the energy integrals have been made, Eq. (1) and (2) may be written in matrix form as,

$$(K.E.)_q = \frac{1}{2} [h] [m]_q \{\dot{h}\} \quad (3)$$

where $\{\dot{h}\}$ = the global system absolute discrete velocity

$[m]_q$ = the q th element mass matrix which contains all material and velocity distribution assumptions and any necessary coordinate transformations into the global system

$$(P.E.)_p = \frac{1}{2} [h] [k]_p \{h\} \quad (4)$$

where $\{h\}$ = the global system absolute discrete displacement vector

$[k]_p$ = the p th element stiffness matrix which contains all material and strain distribution assumptions and any necessary coordinate transformation into the global system

Now, the energy expressions for the total structure are obtained by addition of the element

contributions. That is,

$$\begin{aligned} (K.E.)_{\text{total}} &= [\dot{h}] \left(\sum_{q=1}^Q [m]_q \right) \{\dot{h}\} \\ &= [\dot{h}] [M_o] \{\dot{h}\} \end{aligned} \quad (5)$$

$$\begin{aligned} (P.E.)_{\text{total}} &= [h] \left(\sum_{p=1}^P [k]_p \right) \{h\} \\ &= [h] [K_o] \{h\} \end{aligned} \quad (6)$$

where Q = the total number of mass elements

P = the total number of stiffness elements

$[M_o]$ = the initial model mass matrix

$[K_o]$ = the initial model stiffness matrix

Application of Lagrange's equation[2] may now be used to form the homogeneous equations of motion for the structure as,

$$[M_o] \{\ddot{h}\} + [K_o] \{h\} = \{0\} \quad (7)$$

Dynamic analyses can be conducted using the discrete coordinate system, as in Eq. (7). Moreoften, a transformation into the normal mode coordinate system is made to uncouple the equations and, thus, allow a reduction of the number of coordinates used in subsequent analyses. This decoupling of coordinates is essential to the following development. How the decoupling is accomplished is explained briefly in the discussion of the eigenproblem.

PROPERTIES OF THE EIGENSOLUTION

One may define the transformation from discrete to normal mode coordinates as,

$$\{h\} = [\phi_o] \{\xi\} \quad (8)$$

where $\{\xi\}$ is the normal modes coordinate vector and $[\phi_o]$ is obtained as the solution of the eigenproblem [2],

$$[M_o] [\phi_o] [\omega_o^2] = [K_o] [\phi_o] \quad (9)$$

which is derived from the equations of motion given by (7).

All valid solutions of Eq. (9) produce a set of eigenvectors which are orthogonal with respect to both the mass and stiffness matrices of the system [2,3,4,5,6]. That is,

$$[\phi_o]_i [M_o] \{\phi_o\}_j = \begin{cases} \text{Meq}_{oi} & \text{when } i=j \\ 0 & \text{when } i \neq j \end{cases} \quad (10)$$

and

$$[\phi_o]_i [K_o] \{\phi_o\}_j = \begin{cases} \omega_o^2 \text{Meq}_{oi} & \text{when } i=j \\ 0 & \text{when } i \neq j \end{cases} \quad (11)$$

where Meq_{oi} often is called the generalized mass of the i th mode.

An eigenvector defines the shape, or relative motion, that the discrete coordinate system of the model will display when vibrating freely in a normal mode. The absolute values of the individual numbers in the vector are arbitrary, provided the shape is retained. This attribute allows one to normalize any eigenvector such that the generalized mass of that mode has a particular value. In the remaining discussions, all initial, or "nominal", model eigenvectors must be thought of as having been normalized so that all generalized mass values are unity.

ELEMENT ENERGY DISTRIBUTION IN THE MODES

The kinetic and potential energies of the system may be expressed in terms of element data and modal coordinates by substitution of Eq. (8) into Eqs. (5) and (6) to give,

$$\begin{aligned} (K.E.)_{\text{total}} &= \\ [\dot{\xi}] [\phi_o]^T \left(\sum_{q=1}^Q [m]_q \right) [\phi_o] \{\dot{\xi}\} \end{aligned} \quad (12)$$

$$\begin{aligned} (P.E.)_{\text{total}} &= \\ [\xi] [\phi_o]^T \left(\sum_{p=1}^P [k]_p \right) [\phi_o] \{\xi\} \end{aligned} \quad (13)$$

Recalling the orthogonality relationships of Eqs. (10) and (11), the relationships between system and element matrices given by Eqs. (5) and (6), and the normalization to unity generalized mass, one may write

$$[\phi_o]^T \left(\sum_{q=1}^Q [m]_q \right) [\phi_o] = [I] \quad (14)$$

and

$$[\phi_0]^T \left(\sum_{p=1}^P [k]_p \right) [\phi_0] = [\omega_0^2] \quad (15)$$

Although the summed contributions of all mass elements or all stiffness elements result in the respective diagonal modal kinetic energy and modal potential energy matrices, the contribution of any single element is not necessarily a diagonal matrix. However, the individual element energy contributions have a propensity to be less than fully coupled matrices. If one considers that certain modes contain no significant strain among those degrees of freedom by which the p th stiffness element strain energy is defined, or that other modes contain no significant amplitudes among those degrees of freedom by which the q th mass element kinetic energy is defined, the reason for this particular disposition of character becomes obvious. Thus, it is possible to examine the individual element contributions to Eqs. (14) and (15) to determine the extent of modal coupling produced by each. Since the sum of the diagonal term must equal the total modal energy, each element's diagonal contribution defines that element's fractional part of the total energy. (Note that $[\phi]_i [k]_p \{\phi\}_i$ must be divided by ω_{0i}^2 to

obtain a fractional form)

At this point, intuition suggests that if any element contains a large percentage of the total energy in a given mode, variations of that element will have a significant impact on the eigensolution. That is, the energy content of an element in a mode is a dynamic sensitivity indicator. Furthermore, those elements having the same geometry, material, boundary conditions and modeling assumptions may be categorized by type. The total energy percentage in a particular element type (e.g.,

$$100 \times \frac{1}{\omega_{0i}^2} \sum_{p=R}^V [\phi_0]_i [k]_p \{\phi_0\}_i$$

where R through V are like elements) should serve as a dynamic sensitivity indicator, since a change in a single element of that type would result in the same change in the entire population of the type by similarity. If the number of elements in a model is large, that is, if the energy is divided into many parts, this collection of energy by element type may be necessary to arrive at significant numerical values. Therefore, subscripts p and q will refer to groups of like elements in all subsequent equations.

A method of using these indicators in predicting eigensolution changes and to facilitate theoretical/experimental correlation will now be developed.

MODEL PERTURBATIONS

Perturbations may reflect some prescribed structural geometric or material tolerance considerations, or they may represent element adjustments required to produce a model that agrees with test results. In the discussion that follows, these perturbations will be limited to linear variations of the nominal model element definitions. Perturbed system stiffness and mass matrices may, therefore, be defined as

$$[K] = [K_0] + \sum_{p=1}^P \delta_p [k]_p \quad (16)$$

$$\text{and } [M] = [M_0] + \sum_{q=1}^Q \delta_q [m]_q \quad (17)$$

respectively, where δ_p and δ_q denote the linear variations of the affected element stiffness and mass matrices.

Using the notation of Eqs. (16) and (17), the perturbed eigenproblem can be formulated as

$$\begin{aligned} & \left([M_0] + \sum_{q=1}^Q \delta_q [m]_q \right) [\phi_0] [\psi] [\Omega^2] \\ & = \left([K_0] + \sum_{p=1}^P \delta_p [k]_p \right) [\phi_0] [\psi] \end{aligned} \quad (18)$$

The transformation from discrete to normal mode coordinates implied by Eq. (18) is

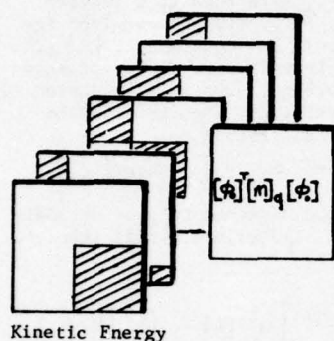
$$\{h\} = [\phi_0] [\psi] \{\gamma\} \quad (19)$$

where $\{\gamma\}$ = the normal modes coordinate vector of the perturbed system

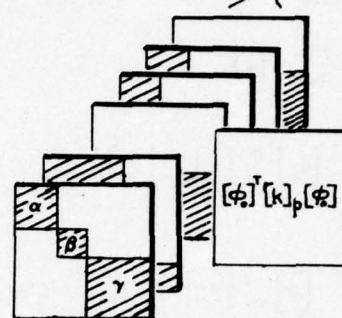
Premultiplication of Eq. (18) by $[\phi_0]^T$, and substitution of the nominal model orthogonality relationships gives Eq.(20) as shown in Figure 1.

In Figure 1, each element contribution matrix is represented as a plane. If the modal vectors are rearranged so that strongly coupled modes are grouped, the kinetic and potential energy distributions can be depicted by Figure 1. The shaded areas represent strong modal coupling, the unshaded areas weak coupling. The cost of an eigensolution to obtain $[\psi]$ and $[\Omega^2]$ for prescribed values of δ_q and δ_p is roughly proportional to the cube of the order of the matrices defined by Eq. (20). Thus,

$$\left([I] + \sum_{q=1}^Q \delta_q [\phi_0]^T [m]_q [\phi_0] \right) [\psi] [\Omega^2] = \left([\omega_0^2] + \sum_{p=1}^P \delta_p [\phi_0]^T [k]_p [\phi_0] \right) [\psi] \quad (20)$$



Kinetic Energy



Potential Energy

Figure 1. Schematic Energy Distribution

any reduction in order will result in significant computer cost savings. The method proposed here to approximate the perturbed modal data is the direct solution of the reduced eigenproblem that results from the limited modal coupling produced by the various model elements. For example, if certain sets of eigenvectors (e.g., $[\phi_0^\alpha], [\phi_0^\beta], \dots, [\phi_0^\gamma]$,

are strongly coupled, but negligible coupling exists between these sets on the p th element (e.g., $[\phi_0^\alpha]^T [k]_p [\phi_0^\beta] \approx 0$), the p th stiffness element contribution to potential energy in the $[\phi_0^\beta]$ mode set (indicated by the shaded β area in Figure 1) is $[\phi_0^\beta]^T [k]_p [\phi_0^\beta]$.

Thus, if one is interested in the effect of only p th element stiffness variations on the modes in a specific frequency range, Eq. (20) reduces to

$$[\psi^\beta] \left[(\Omega^\beta)^2 \right] = \left([\omega_0^\beta]^2 + \delta_p [\phi_0^\beta]^T [k]_p [\phi_0^\beta] \right) [\psi^\beta] \quad (21)$$

where $[\psi^\beta]$ is a square matrix.

Now, the size of the eigenproblem required to evaluate the perturbation is reduced to the number of modes in the coupled set, $[\phi_0^\beta]$. Variations of several mass or stiffness elements can be evaluated simultaneously. How-

ever, the size of the required eigenproblem will increase if different elements couple different mode sets.

When a single mode is uncoupled from all others by the p th stiffness element, and no mass perturbation is considered, a linear hand solution is given by

$$\Omega_i^2 \approx \omega_{0i}^2 + \delta_p [\phi_{0i}]^T [k]_p \{ \phi_{0i} \} \quad (22)$$

Note that Eq. (22) has been divided through by ψ_i indicating that the i th eigenvector is unaffected except for a normalization factor.

Eq. (22) is also the result obtained by the first order Taylor's series expansion of the eigenvalue about its initial value. [1,7] Indeed, all diagonal elements of Eq. (20) are the first order Taylor's series approximation of the eigenvalue perturbations. The advantage of the approach taken here over the Taylor's series expansion is the visibility of the need for higher order terms. That is, if strong coupling exists between modes, it is immediately apparent that a linear (first order) extrapolation is not adequate. Accounting for this coupling is equivalent to including higher order terms in the Taylor's series.

CORRELATION IMPROVEMENT METHODOLOGY

We will now focus our attention on the inverse problem, that of determining what dynamic model finite element perturbation are

required to produce mode shapes and frequencies that satisfy design requirements or that agree with test results. Again, the proposed solution relies upon the limited modal coupling produced by the elements of the nominal model. The perturbed eigenproblem has been given by Eq. (20). The eigenproblem for the i th mode is the i th column of Eq. (20). It may be written in the form,

$$\begin{aligned} & (\Omega_i^2 [I] - [\omega_o^2]) \{\psi\}_i \\ & - \left(-\Omega_i^2 \sum_{q=1}^Q \delta_q [\phi_o]_i^T [m]_q [\phi_o]_i \right. \\ & \left. + \sum_{p=1}^P \delta_p [\phi_o]_i^T [k]_p [\phi_o]_i \right) \{\psi\}_i \end{aligned} \quad (23)$$

If Ω_i^2 and $\{\psi\}_i$ are known (either specified or determined by test) the right hand side of Eq. (23) may be defined as

$$(\Omega_i^2 [I] - [\omega_o^2]) \{\psi\}_i = [E]_i \{\delta\} \quad (24)$$

where the columns of $[E]_i$ are

$$-\Omega_i^2 [\phi_o]_i^T [m]_q [\phi_o]_i \{\psi\};$$

$$\text{or } [\phi_o]_i^T [k]_p [\phi_o]_i \{\psi\}.$$

N equations are defined by (24) and a possible $S = Q + P$ unknown δ 's. (N is the number of modes in the nominal model set, $[\phi_o]$.) If $S > N$, more equations are required for a solution. An additional set of N equations is available from every Ω_i^2 and $\{\psi\}_i$, $i = 1, N$, giving a possible total of N^2 equations. In general, far fewer than N^2 equations will be required for a solution (i.e., $N^2 \gg S$). Therefore, the problem becomes one of selecting the most suitable set of equations that will allow a solution for $\{\delta\}$ by inversion of $[E]$.

The suitable set of equations will depend upon whether the modal data is specified or is determined by test. In either case, a vector $\{\psi\}_i$ must be determined from

$$\{\psi\}_i = [\phi_o]_i^{-1} \{h\}_i \quad (25)$$

If $\{h\}_i$ is a specified vector, the operation indicated by Eq. (25) can be performed directly. The corresponding Ω_i^2 is also specified. The

resulting $\{\psi\}_i$ may indicate that only a limited number of initial modes participate significantly in the linear combination required to form $\{h\}_i$. If so, the determination of certain element scaling factors may not be required when a review of the energy distributions reveals those elements do not carry significant energy in the participating modes indicated by $\{\psi\}_i$. As a result, a reduced set of equations, $\hat{S} < S$, will be required for a solution. If only one mode shape, $\{h\}_i$, is specified, an insufficient number of equations may be generated, even if a reduction to size \hat{S} can be justified. When this is the case, additional constraints

$$(\text{e.g., } \Omega_m^2 = \omega_m^2 \text{ and } \psi_{jm} = \begin{cases} 1 & \text{when } j=m \\ 0 & \text{when } j \neq m \end{cases})$$

where $m \neq i$) can be assigned to provide additional equations. The solution will then take the form

$$\{\delta\} = \begin{bmatrix} [E]_i \\ [E] \end{bmatrix}^{-1} \begin{bmatrix} \Omega_i^2 [I] - [\omega_o^2] \\ [0] \end{bmatrix} \{\psi\} \quad (26)$$

where the assembled $[E]$ matrix is of rank S .

The choice of additional constraints is not completely arbitrary. Care must be taken that $\{\phi_o\}_m$ is not one of the primary participating modes in the linear combination forming $\{h\}_i$ or else the rows of $[E]$ will be linearly dependent and $[E]$ will be singular.

A rigorous application of this approach, when attempting to force an analytical model to agree with test data, is hindered by the inaccuracies and incompleteness of measured mode shapes, $\{h\}_T$. The impact of inaccuracies is easily appreciated by substituting Eq. (25) into (23). One of the resulting products is $[k]_p \{h\}_T$. Thus, we encounter calculations involving small differences of large numbers (measured strains) which can distort the associated energy distributions, and therefore, $[E]$, by a significant amount. The impact of incomplete vectors (i.e., fewer measurements than required to define all analytical model degrees of freedom) is illustrated by Eq. (25). Implementation of this equation requires the introduction of some artificial constraint to reduce the analytical model or to expand the test data to achieve conformity. Therefore, a solution, such as that described below, that does not require calculations involving measured modal amplitudes is desirable. Consider Eq. (23). Dividing all rows by ψ_{ii} is equivalent to normalizing the vector $\{\psi\}_i$ to unity at ψ_{ii} and the i th row of Eq. (23) becomes

$$\begin{aligned} \Omega_i^2 - \omega_o^2 &= \left(-\Omega_i^2 \sum_{q=1}^Q \delta_q \{\phi_o\}_i^T [m]_q [\phi_o]_i \right. \\ & \left. + \sum_{p=1}^P \delta_p \{\phi_o\}_i^T [k]_p [\phi_o]_i \right) \{\psi\}_i (1/\psi_{ii}) \end{aligned} \quad (27)$$

If the measured vector $\{h\}_T$ has the essential character of $\{\phi_o\}_i$, a good approximation to Eq. (27), by virtue of Eq. (25), is given by

$$\begin{aligned} \Omega_T^2 - \omega_{o_i}^2 &\approx -\Omega_T^2 \sum_{q=1}^Q \delta_q \{\phi_o\}_i^T [m]_q \{\phi_o\}_i \\ &+ \sum_{p=1}^P \delta_p \{\phi_o\}_i^T [k]_p \{\phi_o\}_i \\ &= [E_o]_i \{\delta\} \end{aligned} \quad (28)$$

where $[E_o]_i$ defines the energy distribution in the i th mode of the nominal model among the finite elements. The approximation is tantamount to constraining the analytical model to have an i th eigenvalue equal to the test value, Ω_T^2 , and an eigenvector unchanged from the nominal vector, $\{\phi_o\}_i$.

A review of the energy distributions will identify at least one mode for each element in which that element contains significant energy. Thus, a strongly diagonal $[E_o]$ matrix can be assembled to assure a valid inversion. Therefore, if a test is conducted to obtain the eigenvalues Ω_T^2 that clearly represent the modes of the corresponding rows of $[E_o]$, a solution for the required model correction factors can be obtained from

$$\{\delta\} = [E_o]^{-1} \{\Omega_T^2 - \omega_o^2\} \quad (29)$$

Note that the calculations involve only eigenvalues which can be measured accurately.

The correction values, $\{\delta\}$, obtained from Eq. (29) can be used to calculate the revised model mode shapes and frequencies by the reduced eigenproblem method defined earlier. If the results are not satisfactory, the energy distributions in the revised model may be calculated and the procedure repeated until acceptable theoretical/experimental correlation is achieved.

In the event that a best-pairing of modes and elements is not obvious, more than one mode per element can be selected. This will result in more equations than unknowns. The solution may then be obtained from a least-squares fit as determined by

$$\{\delta\} = ([E_o]^T [E_o])^{-1} [E_o]^T \{\Omega^2 - \omega_o^2\} \quad (30)$$

This least-squares fit was used in the application of the correlation improvement methodology to the example problem.

EXAMPLE PROBLEM

The structural model for the example problem is illustrated by Figure 2. It con-

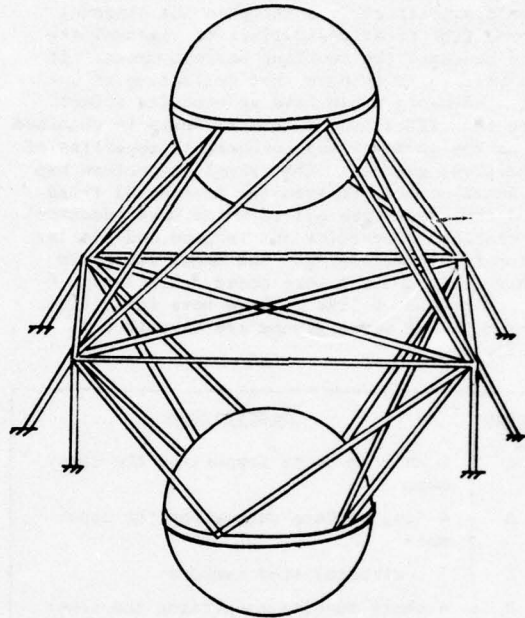


Figure 2. Example Problem Structure

sists of two rigid concentrated masses supported by a pinned-end truss comprised of 30 axial members. The geometry and member sizing were specifically chosen to produce coupling between all degrees of freedom, to produce multiple roots, and to result in a large frequency separation between the first six low frequency suspension modes (considered grounded members in Figure 2 as test suspension hardware) and the higher frequency truss modes. This selection was made to demonstrate the applicability of the method to structure whose complexity is typical of that encountered in the Aerospace industry.

The potential and kinetic energy of the truss members and rigid masses in their respective local coordinate systems were transformed into a global rectangular coordinate system of 24 retained degrees of freedom (DOF); 6 DOF at the center of gravity of each rigid mass and 3 DOF at each of the four corner joints. 24 modes of the nominal model were calculated using an existing computerized eigenproblem routine. Then the transformation from local to modal coordinates was formed and

the potential energy distribution among the modal coordinates and each of the thirty members was calculated as described by Eq. (20) and Figure 1 (only stiffness perturbations will be presented). From a review of this 30 element distribution it was obvious that a collection of like elements, as discussed in the text would significantly strengthen the diagonal terms (the first derivatives of eigenvalues) and decrease the coupling between modes. It is worthwhile to note that collecting of unlike elements would have an opposite effect. The identification of like elements is obtained from the geometry and mechanical properties of the truss members. The example structure has 4 short members between the horizontal truss and the upper mass all of which have identical mechanical properties and lengths and similar geometric positioning. The modal energy in these like numbers were added. Similarly, 6 other groups of like members were identified. The total of seven groups are described in Table 1.

Group	Description
A	4 short members supporting the upper mass
B	4 long members supporting the upper mass
C	4 horizontal side members
D	4 short members supporting the lower mass
E	4 long members supporting the lower mass
F	2 horizontal cross members
G	8 "suspension" system members
	30 total number of stiffness elements

Table 1. Element Grouping Identification

The lower truss member lengths and geometry are different than those in the upper truss. Thus, the total description of the potential energy array consists of seven 24x24 matrices. This data is too voluminous to present here. However, the character of this array may be described as follows:

SUSPENSION MEMBERS PERTURBATIONS

The potential energy in the first six low frequency (.28 Hz to 1.5 Hz) suspension modes is contained almost entirely in the suspension system, Group G, members. That is, the diagonals of $[\phi_0]^T [k]_G [\phi_0]$ contain over 98% of the energy in the first six modes. No significant coupling is produced between any of the nominal model modes by the suspension member group. Therefore, a hand solution using Eq. (22) can be used to determine the

frequency change of the first six modes due to suspension member perturbations. The lack of coupling between the first six modes indicates that their mode shapes will not be changed by Group G perturbations. Insignificant energy (<1%) is contained in these members in the higher frequency (>8.3 Hz) truss modes. Thus, no changes to any, except the first six, mode shapes or frequencies will be produced by Group G perturbations.

These results were expected. The example was configured to have these characteristics so that the methodology could be checked against known results.

MAIN TRUSS MEMBERS PERTURBATIONS

Insignificant potential energy in the first six suspension modes is contained in any of the Groups A through F. Also, no significant coupling between these low frequency (<1.5 Hz) modes and the high frequency (>8.3 Hz) modes is produced by the A through F group members. Therefore, no changes in suspension mode shapes or frequencies will result from Groups A through F perturbations. The potential energy distribution among these members in modes numbers 7 through 24 can be summarized by the diagonals of $[\phi_0]^T [k]_p [\phi_0]$ where $p = A, F$. Table 2 presents this data in percentage form. (i.e., $100 \times ([\phi_0]_i [k]_p \{\phi\}_i) / \omega_{0i}^2$)

The first column of Table 2 indicates the coupling between modes by the A through F element groups. Each element group produced the same coupling of three sets of modes. The number following the / indicates the coupled mode set. (e.g., 16/3, 20/3 and 21/3 indicates that modes 16, 20 and 21 are coupled and this set of three modes is designated as the 3rd set.)

"Significant" coupling of modes was easily identifiable since the off diagonal terms of $[\phi_0]^T [k]_p [\phi_0]$, $p = A, F$ are either the order of magnitude of the diagonals or at least two orders of magnitude less. Thus, three reduced eigenproblems for each of Groups A through F stiffness element perturbation evaluation were identified. The stiffness of a single group was doubled (e.g., $\delta_A = 1.0$) and the reduced eigenproblem mode shapes and frequencies were calculated. These results were compared with a 24 mode solution and frequencies agreed within four significant figures. Mode shapes were compared by a cross orthogonality check, $[\phi_{24}]^T [M_0] [\phi_N]$, where $[\phi_{24}]$ are the 24 mode solution and $[\phi_N]$ are the $N = 10, 5$ or 3 mode solution of a reduced eigenproblem. The results were strongly diagonal matrices.

Note that coupled mode set 1, in Table 2, contains all double root modes. 10 of the 24 modes are contained in this set. The appendix proposes a method for obtaining further reduction of eigenproblem size. This method is a

Mode No. Set	Freq. Hz.	Energy in Group ~ %					
		A	B	C	D	E	F
7/1	8.303	20.8	36.0	5.71	12.2	24.8	0
8/1	8.303	20.8	36.0	5.71	12.2	24.8	0
9/2	9.135	30.6	34.6	19.4	30.2	2.51	13.7
10/1	9.816	19.0	13.0	12.1	30.4	25.5	0
11/1	9.816	19.0	13.0	12.1	30.4	25.5	0
12/2	12.78	7.46	32.4	3.56	13.0	41.1	2.52
13/2	106.8	21.2	36.0	0	15.7	25.7	0
14/1	194.6	15.9	18.3	34.6	14.6	16.3	0
15/1	194.6	15.9	18.3	34.6	14.6	16.3	0
16/3	317.8	9.92	.438	78.7	10.6	0	0
17/1	347.9	24.0	12.2	1.63	36.7	24.6	0
18/1	347.9	24.0	12.2	1.63	36.7	24.6	0
19/2	348.9	27.3	15.1	.209	33.9	22.3	0
20/3	351.2	15.4	13.3	10.3	30.3	28.5	1.33
21/3	410.7	23.5	22.7	0	6.98	8.95	37.7
22/1	411.2	19.9	17.8	45.7	5.96	8.50	0
23/1	411.2	19.9	19.8	45.7	5.96	8.50	0
24/2	510.2	12.7	12.6	35.4	6.50	7.81	25.1

Table 2. Diagonals of Potential Energy Distribution (Nominal Model)

recent development which has not, as yet, been exercised by an example problem.

CORRELATION IMPROVEMENT RESULTS

Two models are required to demonstrate the theoretical/experimental correlation improvement methodology. One, whose modal characteristics were assumed to represent test results, is identical to that defined for the reduced eigenproblem example. The other, which represents the nominal model (the analysts' original representation) was established by applying arbitrary stiffness scaling factors to the seven groups of test model truss members. The scaling is defined in Table 3.

Type	Description	Stiffness Scaling
A	Upper truss short members	+ .60
B	Upper truss long members	- .30
C	Middle frame side members	- .20
D	Lower truss short members	- .40
E	Lower truss long members	+ .60
F	Middle frame cross members	- .30
G	Support members	+ .10

Table 3. Scaling to Generate Analysts' Model

No mass scaling was considered. The strain energy distributions in the nominal (scaled) model were calculated and reviewed. A set of ten modes were selected to obtain a solution for the seven element scaling factors which would force ten analytical model frequencies to agree with the corresponding ten test

model frequencies. Correspondence was determined from cross-orthogonality products between the two models on the mass matrix. Table 4 shows the diagonal of the potential energy distribution in the scaled model in those modes selected to obtain a first iteration least square fit solution as defined by Eq. (30). The columns of $[E]$ in Eq. (30) correspond to columns headed A through G in Table 4. Note the difference in energy distribution and frequencies between the nominal model in Table 2 and the scaled model in Table 4. Four iterations were required to arrive at an "acceptable" improved model. Table 5 presents the frequency comparisons of the nominal model, the test model, and the fourth iteration improved model produced by the correlation improvement method. Only data from those modes indicated by * were used in the calculations. Note that the agreement of the improved model frequencies with those of the test model improved in all modes. (In practice, this complete comparison could not be made since all test mode frequencies probably would not be known.) Cross-orthogonality checks showed comparable improvement in mode shapes with the exception of the double root pairs of modes. Even then, linear dependency was indicated only between the respective pairs.

APPENDIX

The perturbed eigenproblem is defined by Eq. (20) which can be rearranged, as

Mode No.	Freq. Hz.	Energy in Group ~ %						
		A	B	C	D	E	F	G
1	.29	0	0	0	0	0	0	99.5
7	7.949	13.6	44.4	8.24	19.6	11.8	1.54	0
8	8.001	12.6	47.8	6.32	18.5	14.0	0	0
9	8.398	15.1	6.53	20.1	41.9	3.97	11.9	0
10	9.274	10.1	15.8	13.9	45.3	14.9	0	0
11	9.288	10.5	16.2	14.0	44.6	14.3	0	0
12	12.41	3.90	44.4	5.46	18.1	24.7	3.38	0
16	286.0	3.14	4.91	81.8	7.43	0	2.47	0
19	363.5	11.4	3.41	4.69	21.8	53.2	4.82	0
21	414.8	53.5	17.5	0	0	5.89	21.7	0

Table 4. Diagonals of Potential Energy Distribution (Scaled Model)

Mode Number	Nominal Model Freq. (Hz)	Test Model Freq.	Improved Model Freq.
1*	.2901	.2767	.2767
2	.2901	.2767	.2767
3	1.126	1.076	1.076
4	1.126	1.076	1.076
5	1.247	1.190	1.191
6	1.584	1.511	1.512
7*	7.949	8.303	8.287
8*	8.001	8.303	8.314
9*	8.398	9.135	9.131
10*	9.274	9.816	9.803
11*	9.288	9.816	9.828
12*	12.41	12.78	12.78
13	107.7	106.8	106.9
14	188.2	194.6	194.7
15	188.2	194.6	194.7
16*	286.0	317.8	317.8
17	362.3	347.9	347.5
18	362.3	347.9	347.5
19*	363.5	348.9	348.8
20	367.1	351.2	350.6
21*	414.8	410.7	410.8
22	417.0	411.2	412.5
23	417.0	411.2	412.5
24	489.9	510.2	509.8

Table 5. Correlation Improvement, Frequency Comparisons

$$\begin{aligned}
 & [\psi] [\Omega^2] - [\omega_o^2] [\psi] = \\
 & - \sum_{q=1}^Q \delta_q [\phi_o] T [m]_q [\phi_o] [\psi] [\Omega^2] \\
 & + \sum_{p=1}^P \delta_p [\phi_o] T [k]_p [\phi_o] [\psi] \quad (31)
 \end{aligned}$$

The first derivative of the eigenvalues with respect to the scaling factors [7] are the diagonal terms that remain after making the approximations that $[\psi] \approx [I]$ on both sides of Eq. (31) and $[\Omega^2] \approx [\omega_o^2]$ on the right hand side (RHS) only.

Similarly, the first derivatives of the eigenvectors with respect to the scaling factors [7] can be obtained by making the approximations that $[\psi] \approx [I]$ only on the RHS of Eq. (31) and $[\Omega^2] \approx [\omega_o^2]$ on both sides. The equations that remain are,

$$\begin{aligned}
 & [\hat{\psi}] [\omega_o^2] - [\omega_o^2] [\hat{\psi}] \approx \\
 & - \sum_{q=1}^Q \delta_q [\phi_o] T [m]_q [\phi_o] [\omega_o^2] \\
 & + \sum_{p=1}^P \delta_p [\phi_o] T [k]_p [\phi_o] \quad (32)
 \end{aligned}$$

where $[\hat{\psi}]$ denotes the approximate solution. Note that the diagonal terms on the left hand side (LHS) of Eq. (32) are zero. Thus, the usual solution found in the literature [7] can be obtained by deleting the diagonal terms and solving for the j th vector $\{\psi\}_j$ alone from

$$\begin{aligned}
 & \{\psi\}_j = \left([\omega_o^2] [I] - [\omega_o^2] \right)^{-1} \\
 & \left(- \sum_{q=1}^Q \delta_q [\phi_o] T [m]_q \{\phi_o\}_j \omega_o^2 \right. \\
 & \left. + \sum_{p=1}^P \delta_p [\phi_o] T [k]_p \{\phi_o\}_j \right) \quad (33)
 \end{aligned}$$

where the notation $[-]$ indicates that nominal model j th mode data has been deleted. An alternate approach to the solution for $[\hat{\psi}]$ is replace $[\hat{\omega}^2]$ in Eq. (31) by $[\hat{\omega}^2]$, where $[\hat{\omega}^2]$ are the approximate eigenvalues obtained from a first order approximation solution. With this approximation the alternative to Eq. (32) becomes

$$\begin{aligned} & [\hat{\psi}] [\hat{\omega}^2] - [\omega_o^2] [\hat{\psi}] \approx \\ & - \sum_{q=1}^Q \delta_q [\phi_o]^T [m]_q [\phi_o] [\hat{\omega}^2] \\ & + \sum_{p=1}^P \delta_p [\phi_o]^T [k]_p [\phi_o] \end{aligned} \quad (34)$$

The general term, A_{ij} , of the LHS matrix of Eq. (34) is

$$A_{ij} = \psi_{ij} (\hat{\omega}_j^2 - \omega_{oi}^2) \quad (35)$$

where i and j refer to the i th nominal mode and the j th perturbed mode respectively. Thus, $[\hat{\psi}]$ can be defined by dividing the corresponding terms of both sides of Eqs. (34) by $(\hat{\omega}_j^2 - \omega_{oi}^2)$

Consider, for simplicity, the case where $\delta_q = 0$ for all q and $\delta_p = 0$ for all p except one (e.g., $p = A$). Let $\delta_A = 1.0$. Allowing the notation that an asterisk indicates this term by term operation on a matrix, the solution can be written as

$$[\hat{\psi}]_A = (\hat{\omega}_j^2 - \omega_{oi}^2)^{-1} * [\phi_o]^T [k]_A [\phi_o] \quad (36)$$

The j th approximate eigenvalue is

$$\hat{\omega}_j^2 = \omega_{oj}^2 + \{\phi_o\}^T [k]_A \{\phi_o\}_j \quad (37)$$

Then

$$\begin{aligned} & \hat{\omega}_j^2 - \omega_{oi}^2 = \omega_{oj}^2 - \omega_{oi}^2 \\ & + \{\phi_o\}_j^T [k]_A \{\phi_o\}_j \end{aligned} \quad (38)$$

Therefore, the diagonal results from Eq. (36) are unity. The participation of the i th nominal mode in the j th perturbed vector, ψ_{ij} , will diminish as the difference, $\omega_{oj}^2 - \omega_{oi}^2$

increases in absolute value. This dramatically reduces the apparent coupling between modes with appreciable frequency separation. Thus, the use of the LHS of Eq. (36) to select the modes required for a valid reduced eigenproblem provides the potential for even greater reduction than that indicated by the coupling in $[\phi_o]^T [k]_p [\phi_o]$. This is consistent with the results obtained in the example problem, where coupled mode set 1 included 10 modes but $[\hat{\psi}]$ obtained from the eigenproblem showed at most 4 close frequency nominal modes participating in any significant coupling.

REFERENCES

1. C. W. White: "Dynamic Test Reflected Structural Model Methodology Report". Contract NAS8-24000, Skylab Program Payload Integration Technical Report, ED-2002-1577, Martin Marietta Corporation, Denver, Colorado, December 1972.
2. R. L. Bisplinghoff, H. Ashley and R. L. Halfman: "Aeroelasticity". Addison-Wesley Publishing Company, Inc., November 1957, pp. 114-124.
3. W. T. Thomson: "Vibration Theory and Application". Prentice-Hall, Inc., 1965.
4. M. F. Rubinstein: "Matrix Computer Analysis of Structures". Prentice-Hall, Inc., 1966.
5. R. Wohlen, W. Benfield and R. Philippus: "Evaluation of Modal Analysis Techniques". Contract NAS8-26750, MCR-73-310, Martin Marietta Corporation, Denver, Colorado, December 1973.
6. J. R. Admire: "Modal Analysis of Structures by an Iterative Rayleigh-Ritz Technique". NASA TMX-64528, Marshall Space Flight Center, 1970.
7. R. L. Fox and M. P. Kapoor: "Rates of Change of Eigenvalues and Eigenvectors", AIAA Journal, Vol. 6, No. 12, December 1968, pp. 2426-2429.

MATRIX METHODS FOR THE ANALYSIS OF ELASTICALLY
SUPPORTED ISOLATION SYSTEMS

Gary L. Fox
BARRY DIVISION
Barry Wright Corporation
Burbank, California

This paper presents a new method for calculating stiffness, damping and inertia matrices for lumped parameter linear systems. After a discussion of the solution to the equations for a six degree of freedom rigid body, the analysis is extended to a two-mass, twelve degree of freedom system. In the limiting case that the second mass inertia matrix can be ignored, some especially simple relationships are obtained.

NOMENCLATURE

$[\quad]$	6 x 6 matrix
	6 x 1 (1 x 6) column (row) vector
$[\quad]^T$	Transpose of matrix
$[\quad]^{-1}$	Inverse of matrix
$\begin{bmatrix} - & - & - \\ - & - & - \\ - & - & - \end{bmatrix}$	Matrix partitioned into 3 x 3 submatrices
$\{a'\}, \{a''\}$	Quantity referenced to a local coordinate system
$\{a\}, \{a''\}$	Quantity referenced to a local coordinate system colinear to the global
$\{A\}, \{A''\}$	Quantity referenced to the global coordinate system
$\{\ddot{A}\}, \{\dot{A}\}$	Acceleration and velocity of A
P_1, P_2, P_3	Location of an element (mass, spring or damper), or vector (force or displacement)
θ, ψ, ϕ	Euler angles defining the angular orientation of an element or vector
$\{\}^*$	The adjoint of $\{\}$

INTRODUCTION

It has been shown [1,2,3] that when a rigid body is supported by a

number of linear springs and dampers, the resulting six coupled, linear, second order differential equations can be written in matrix notation. With the availability of matrix routines in digital computer libraries, this has become a popular representation.

To be presented is a scheme whereby the matrices of coefficients in the equations are developed using six-rank square matrices. The advantage of this technique is that instead of computing four or five three-rank sub-matrices which must be placed in the proper locations of the six-rank matrix, the six-rank matrix is computed directly. This is accomplished by allowing the translational and rotational coordinates to appear on an equal footing. Because torques or rotations do not have to be "added in", but appear automatically in the equations, a greater unity and simplicity is achieved and the meanings of the terms become more transparent.

The basic problem is to transform known vectors and matrices from a point and orientation in space, the local coordinate system, to a common, global, coordinate system in which the differential equations will be solved. This is accomplished by applying a rotation transformation and then a position transformation. The transformations are performed, as usual, by matrix multiplication, except that in the scheme presented the vectors have six components, three translational and three rotational, and the matrices are all square and of six rank.

A rotational transformation employing Euler angles is developed in detail. Rotations about all three axes are included for generality. The displacement transformation is derived; the inverse is shown to transform vectors in the reverse direction. For completeness, the final matrices are written out in detail. The solution of the differential equations is discussed for certain cases. Free vibration results in an eigenvalue equation. It is shown that the eigenvalues and eigenvectors are complex if the damping is not zero. This gives rise to phase differences and exponential decays of the modes.

The method is then generalized to multi-mass systems. If the isolators themselves are mounted on a resilient support of negligible inertia and described by its own stiffness and damping matrices, a second set of six coupled differential equations must be solved simultaneously with the first set.

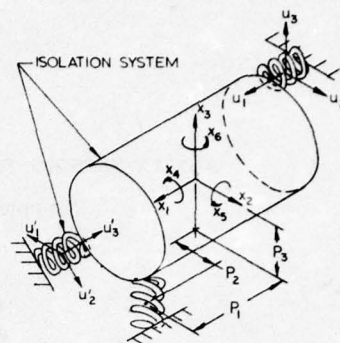
For steady-state sinusoidal foundation excitation or free vibration the equations of motion are shown to reduce to a form that is identical to that of a rigid support, but with an equivalent stiffness-damping matrix which has elements that are complex numbers.

MATRIX FORM OF THE EQUATIONS

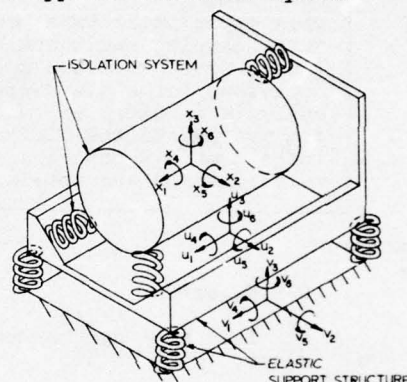
The differential equations of motion for a rigid body supported by linear springs and viscous dampers can be written in matrix form [2] as

$$[H]\{\ddot{X}\} + [C]\{\dot{X}\} + [K]\{X\} = [C]\{\dot{U}\} + [K]\{U\} + \{F\} \quad (1)$$

Where $[H]$, $[C]$ and $[K]$ are 6×6 symmetric matrices of coefficients for the inertia, damping and stiffness terms respectively, and $\{X\}$ and $\{U\}$ are 6×1 displacement vectors of the mass and foundation respectively. The dot denotes a derivative with respect to time. $\{F\}$ is a 6×1 force vector applied to the body at the origin of which the prior terms were defined. Capital letters will be used to denote quantities referred to this "global" coordinate system as shown in Figure 1. Lower case letters will be reserved to denote those quantities in a "local" reference system. The local system quantities will be primed if the axes are not parallel to the global axes.



(a)
A Typical Isolation System



(b)
An Elastically Supported Isolation System
FIGURE 1

Equation (1) is valid only when all the quantities are evaluated in a common reference system. In most practical problems, however, the matrices $[H]$, $[C]$ and $[K]$ are known in the local coordinate system, and the force and displacements, $\{f\}$ and $\{u\}$ are known at the point of application.

TRANSFORMATION OF $\{f\}$ AND $\{u\}$

Since the only matrix that transforms a 6×1 matrix into a 6×1 matrix is a 6×6 matrix, a transformation of the type

$$\{F\} = [Q]\{f'\} \quad (2)$$

is assumed. It is well known [2,4] that a rotation may be effected by matrix operations so one may assume that $[Q]$ can be written as a product of two 6×6 matrices

$$[Q] = [T][R] \quad (3)$$

where $[R]$ is a rotation operator and $[T]$ is a translation operator. Let $\{f'\}$ be written as

$$\{f'\} = \begin{Bmatrix} f'_t \\ f'_r \end{Bmatrix} \quad (4)$$

where $\{f'_t\}$ represents the three translational forces and $\{f'_r\}$ represents the three rotational forces (torques). It is clear that if $[R]$ is written as

$$[R] = \begin{bmatrix} r & 0 \\ 0 & r \end{bmatrix} \quad (5)$$

then $[r]$ is the familiar 3×3 rotation matrix. This matrix is often written with direction cosines as the elements. The author feels that the following development, using a set of Euler angles (θ, ψ, ϕ) has certain advantages, especially if an element possesses axial symmetry.

The development can be considered in three steps since $[r]$ is a product of three Euler rotation matrix operators. Each operator rotates the local coordinate system about one of its own axes, three rotations being necessary in general to bring a local coordinate system parallel to the global system. In order to determine θ, ψ, ϕ and the elements of $[r]$, define a right handed coordinate system u_1, u_2, u_3 as shown in Figure 2. The components of the force lie along the u_1, u_2, u_3 axes. (When transforming the matrices $[h]$, $[d]$ and $[k]$, the local reference axes are u_1, u_2, u_3).

STEP 1. Rotate the u_1, u_2, u_3 system about the u_3 axis θ degrees until the u_1' axis lies in the u_1-u_2 plane (Fig. 2a). The sign of θ is determined by the right hand rule. Curl the fingers of the right hand in the direction of the rotation; if the thumb points along the $+u_3$ axis then the rotation is positive, $+\theta$; if it points along the $-u_3$ axis then the rotation is negative, $-\theta$. The rotation shown is positive. The Euler matrix for this rotation is

$$[r_{u_1}(\theta)] = \begin{bmatrix} \cos \theta & 0 & -\sin \theta \\ 0 & 1 & 0 \\ \sin \theta & 0 & \cos \theta \end{bmatrix} \quad (6a)$$

STEP 2. Next, rotate the u_1', u_2', u_3' system about the u_1' axis ψ degrees until the u_2'' axis lies in the $u_1'-u_3'$ plane (Fig. 2b). The u_3'' axis will then line up with the u_3 axis. The sign of ψ is also

determined by the right hand rule. The rotation shown is negative. The Euler matrix is

$$[r_{u_2'}(\psi)] = \begin{bmatrix} 1 & 0 & 0 \\ 0 & \cos \psi & \sin \psi \\ 0 & -\sin \psi & \cos \psi \end{bmatrix} \quad (6b)$$

STEP 3. Finally, rotate the u_1'', u_2'', u_3'' system about the u_3'' axis ϕ degrees until u_1''' axis lies along the u_1 -axis and the u_2''' -axis lies along the u_2 -axis. The sign of ϕ is again determined by the right hand rule. The rotation shown in Figure 2c is negative. This Euler matrix is

$$[r_{u_3''}(\phi)] = \begin{bmatrix} \cos \phi & \sin \phi & 0 \\ -\sin \phi & \cos \phi & 0 \\ 0 & 0 & 1 \end{bmatrix} \quad (6c)$$

The total rotation matrix, $[r]$, is simply a matrix product of the three matrices in the proper order.

$$[r(\theta, \psi, \phi)] = [r_{u_3''}] [r_{u_2'}] [r_{u_1}] \quad (7)$$

Written out in detail

$$[r] = \begin{bmatrix} \cos \theta \cos \phi & \cos \theta \sin \phi & \cos \theta \sin \psi \sin \phi \\ +\sin \theta \sin \phi & -\cos \theta \sin \phi & -\cos \theta \cos \phi \\ \cos \phi \sin \theta & \cos \phi \cos \theta & \cos \phi \sin \psi \sin \theta \\ -\cos \phi \sin \theta & -\cos \phi \cos \theta & -\cos \phi \sin \psi \sin \theta \\ \sin \phi \sin \theta & -\sin \phi \cos \theta & \sin \phi \sin \psi \sin \theta \\ -\sin \phi \sin \theta & \sin \phi \cos \theta & -\sin \phi \sin \psi \sin \theta \end{bmatrix}$$

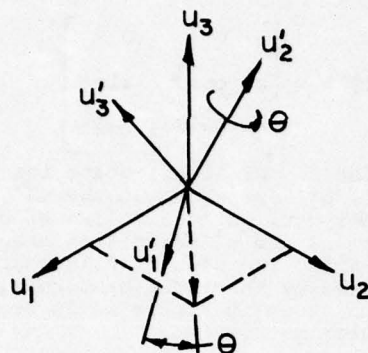
To derive $[T]$, the matrix to transform a force in one reference system to another, in the equation $\{F\} = [T]\{f\}$, let

$$[T] = \begin{bmatrix} A & B \\ D & E \end{bmatrix} \quad (8)$$

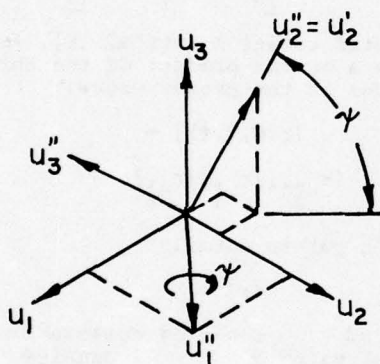
where $[A]$, $[B]$, $[D]$ and $[E]$ are 3×3 submatrices, and $\{f_t\}$ and $\{f_r\}$ are the 3×1 translational and rotational force vectors. With these definitions the transformed force vector is

$$F = \begin{Bmatrix} [A]\{f_t\} + [B]\{f_r\} \\ [D]\{f_t\} + [E]\{f_r\} \end{Bmatrix} \quad (9)$$

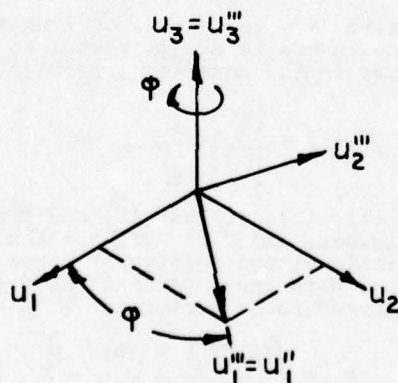
From the laws of mechanics it is clear that $[A]=[E]=1$ and that $[B]=[0]$ and that $[D]\{f_t\} = \{p\} \times \{f_t\}$; forces transform into



(a)
Rotation about u_2' axis



(b)
Rotation about u_1'' axis



(c)
Rotation about u_3''' axis

FIGURE 2

forces and torques, but torques transform as torques. Writing the cross product in tensor notation

$$(p \times f_t)_k = p_i f_j e_{ijk} \quad (10)$$

where e_{ijk} is the Levi-Cevita tensor density which has the following values

$$e_{ijk} = \begin{cases} 0 & \text{if any index is repeated} \\ +1 & \text{if } ijk \text{ is an even permutation of } 123 \\ -1 & \text{if } ijk \text{ is an odd permutation of } 123 \end{cases}$$

The repeated indices in (10) indicate a sum on that index. To write (10) as a matrix product note that

$$\begin{aligned} (p \times f_t)_k &= -p_i e_{ijk} f_k \\ &\equiv D_{jk} f_k \end{aligned} \quad (11)$$

The matrix $[D]$ is given by

$$D_{jk} = -p_i e_{ijk} \quad (12)$$

where the sum over i is indicated.

Since the matrix is antisymmetric only the diagonal and upper half of $[D]$ need be calculated. The diagonal elements are zero since $l = m$ results in a repeated index. The three independent elements are

$$l = 1, m = 2$$

$$\begin{aligned} D_{12} &= -[p_1 e_{112} + p_2 e_{212} + p_3 e_{312}] \\ &= -p_3 \end{aligned}$$

$$l = 1, m = 3$$

$$\begin{aligned} D_{13} &= -[p_1 e_{113} + p_2 e_{213} + p_3 e_{313}] \\ &= +p_2 \end{aligned}$$

$$l = 2, m = 3$$

$$\begin{aligned} D_{23} &= -[p_1 e_{123} + p_2 e_{223} + p_3 e_{323}] \\ &= -p_1 \end{aligned}$$

$$D_{21} = -D_{12}; \quad D_{31} = -D_{13}; \quad D_{32} = -D_{23}$$

Equation (11) can now be written in matrix form (note that $\{p\} \times \{f\}$ is actually a second rank antisymmetric tensor, usually referred to as a pseudovector).

$$[\{p\} \times \{f\}] = \begin{bmatrix} 0 & -p_3 & p_2 \\ p_3 & 0 & -p_1 \\ -p_2 & p_1 & 0 \end{bmatrix} \begin{Bmatrix} f_1 \\ f_2 \\ f_3 \end{Bmatrix} \quad (13)$$

The transformation matrix is seen to be

$$[T] = \begin{bmatrix} 1 & 0 & 0 & | & 0 & 0 & 0 \\ 0 & 1 & 0 & | & 0 & 0 & 0 \\ 0 & 0 & 1 & | & 0 & 0 & 0 \\ \hline 0 & -p_3 & p_2 & | & 1 & 0 & 0 \\ p_3 & 0 & -p_1 & | & 0 & 1 & 0 \\ -p_2 & p_1 & 0 & | & 0 & 0 & 1 \end{bmatrix} \quad (14)$$

Therefore

$$\{F\} = [T][R]\{f'\} \quad (15)$$

Note that since $[T][R] \neq [R][T]$, the order of application of the transformations is important. This is true because $[T]$ was derived assuming a colinear coordinate system.

Since $\{f\} = [R]\{f'\}$ is usually known, then written in detail (15) is

$$\{F\} = [T]\{f\} = \begin{Bmatrix} f_1 \\ f_2 \\ f_3 \\ f_4 + p_2 f_3 - p_3 f_2 \\ f_5 + p_3 f_1 - p_1 f_3 \\ f_6 + p_1 f_2 - p_2 f_1 \end{Bmatrix} \quad (15a)$$

The derivation of the matrix to transform displacements follows similar reasoning. Let

$$\{x\} = [T']\{X\} = \begin{Bmatrix} [A']\{X_T\} + [B']\{X_R\} \\ [D']\{X_t\} + [E']\{X_j\} \end{Bmatrix} \quad (16)$$

Again, $[A'] = [E'] = [I]$, but $[D'] = [0]$ and $[B']\{X_R\} = -[\{p\} \times \{X_R\}]$ for $\sin X_R \approx X_R$. Since $[t(p_i)] = -[t(p_i)]^T$ implies $[B'] = [T]^T$ so that Equation (16) is finally

$$\{x\} = [T]^T\{X\}. \quad (17)$$

Since $\{x\} = [R]\{x'\}$ and $[R]^{-1} = [R]^T$, Equation (17) can be written

$$\{x'\} = [R]^T[T]^T\{X\} \quad (17a)$$

Similarly, the foundation motion $\{u\}$ must also be transformed to the global system. Inverting Equation (17),

$$\{U\} = [T(p_i)]^T\{u\} \quad (18)$$

To find the inverse of $[T]$ note that the form of $[T]$ in general is the result of a vector cross product. Consequently one would expect that

$$[T(p)] [T(-p)] = [I] \quad (19)$$

This is indeed the case. Similarly,

$$[T(p_i)]^T [T(-p_i)]^T = [I] \quad (20)$$

Using these results, Equation (18) becomes

$$\{U\} = [T(-p_i)]^T\{u\} \quad (21)$$

Written out in detail, this is

$$\{U\} = \begin{Bmatrix} u_1 + p_2 u_6 - p_3 u_5 \\ u_2 + p_3 u_1 - p_1 u_6 \\ u_3 + p_1 u_5 - p_2 u_4 \\ u_4 \\ u_5 \\ u_6 \end{Bmatrix} \quad (21a)$$

Equations (19) and (20) can also be used to invert Equations (15) and (17).

TRANSFORMATION OF $[K]$ AND $[C]$

It is assumed that the stiffness (or damping) matrix is known in a local coordinate system, i.e.

$$\{f'\} = -[k']\{x'\} \quad (22)$$

In lumped parameter models such as the one that we are discussing the values for $[k']$ or $[c']$ are assumed to be known along the principal axes of the isolator [6]. In that case the matrices would be diagonal. The following derivation assumes that $[k']$ and $[c']$ are diagonal. Operating on the right of (22) with $[T][R]$ and employing Equation (15)

$$\{F\} = -[T][R][k']\{x'\} \quad (23)$$

Substitution of Equation (17a) results in

$$\{F\} = -[T][R][k'] [R]^T [T]^T \{X\} \quad (24)$$

Comparison of (24) with (22) shows the desired relationship

$$[K]_i = [T]_i [R]_i [k']_i [R]_i^T [T]_i^T \quad (25)$$

Equation (25) gives the stiffness matrix evaluated in the global coordinate system for a single, i^{th} , spring. The stiffness matrix appearing in Equation (1) is the sum of all the n individual stiffness matrices.

$$[K] = \sum_{i=1}^n [K]_i \quad (26)$$

The stiffness matrix for a single spring located at $\begin{Bmatrix} p_1 \\ p_2 \\ p_3 \end{Bmatrix}$ with a stiffness matrix referenced to the local system

$$[k] = [R] [k'] [R]^T$$

$$= \begin{bmatrix} k_{11} & k_{12} & k_{13} & 0 & 0 & 0 \\ k_{21} & k_{22} & k_{23} & 0 & 0 & 0 \\ k_{31} & k_{32} & k_{33} & 0 & 0 & 0 \\ 0 & 0 & 0 & k_{44} & k_{45} & k_{46} \\ 0 & 0 & 0 & k_{54} & k_{55} & k_{56} \\ 0 & 0 & 0 & k_{64} & k_{65} & k_{66} \end{bmatrix} \quad (27)$$

is written out in detail on the following page. In the case of viscous damping the damping force transforms like the spring force [2,5]. In this case the transformation of $[c']$ is analogous to Equation (25). Equation (25) is called a congruent transformation.

TRANSFORMATION OF $[H]$

Let the mass matrix be known in a local coordinate system. From Newton's law

$$\{f'\} = [h'] \{\ddot{x}'\} \quad (28)$$

If the local coordinate system is located at the Center of Gravity with the axes along the principle axes of the Body

$$[h'] = \begin{bmatrix} m & 0 & 0 \\ 0 & m & 0 \\ 0 & 0 & m \end{bmatrix} \begin{bmatrix} i'_{11} & 0 & 0 \\ 0 & i'_{22} & 0 \\ 0 & 0 & i'_{33} \end{bmatrix}$$

where m is the mass of the body and i'_{11} , i'_{22} and i'_{33} are the mass moments of inertia about the 1, 2, 3 axes. Since $[H]$ is constant Equation (28) can be written as

$$\{f'\} = \frac{d^2}{dt^2} [h'] \{x'\} \quad (29)$$

Comparison of Equation (29) with Equation (22) yields the immediate result

$$[H] = [T] [R] [h'] [R]^T [T]^T \quad (30)$$

Therefore, the inertia matrix transforms exactly like the stiffness and damping matrices. The inertia matrix, $[H]$, with the Center of Gravity located at $\begin{Bmatrix} p_1 \\ p_2 \\ p_3 \end{Bmatrix}$ and

a local inertia matrix defined by

$$[h] = [R] [h'] [R]$$

$$= \begin{bmatrix} m & 0 & 0 & 0 & 0 & 0 \\ 0 & m & 0 & 0 & 0 & 0 \\ 0 & 0 & m & 0 & 0 & 0 \\ 0 & 0 & 0 & i_{11} & i_{12} & i_{13} \\ 0 & 0 & 0 & i_{21} & i_{22} & i_{23} \\ 0 & 0 & 0 & i_{31} & i_{32} & i_{33} \end{bmatrix}$$

is written out on the following page.

GENERALIZATION OF $[T]$ AND $[R]$

The above derivation employed the diagonal matrices $[k']$ and $[h']$. It is reasonable to ask if the more general forms $[K]$ and $[H]$ can be treated in the same manner. This question is the same as asking if the matrix $[K_2]$ in Figure 3, which, calculated directly by Equation (26),

$$[K_2] = \sum_i [T_i] [R_i] [k_i'] [R_i]^T [T_i]^T \quad (31)$$

is the same as the matrix transformed from the X_1 system to the X_2 system,

$$[K_2] = [T] [R] [K_1] [R]^T [T]^T \quad (32)$$

where

$$[K_1] = \sum_i [T_i] [R_i] [k_i'] [R_i]^T [T_i]^T \quad (33)$$

The coordinate systems X_1 and X_2 are colinear and related by $[T]$; X_1 and X_2 are also colinear and related by $[T]$; both X_1 , X_1 and X_2 , X_2 are

$$\begin{bmatrix}
 k_{11} & k_{12} & k_{13} & -k_{12}p_3 + k_{13}p_2 & +k_{11}p_3 - k_{13}p_1 & -k_{11}p_2 + k_{12}p_1 \\
 k_{21} & k_{22} & k_{23} & -k_{22}p_3 + k_{23}p_2 & +k_{21}p_3 - k_{23}p_1 & -k_{21}p_2 + k_{22}p_1 \\
 k_{31} & k_{32} & k_{33} & -k_{32}p_3 + k_{33}p_2 & +k_{31}p_3 - k_{33}p_1 & -k_{31}p_2 + k_{32}p_1 \\
 -k_{21}p_3 + k_{31}p_2 & -k_{22}p_3 + k_{32}p_2 & -k_{23}p_3 + k_{33}p_2 & k_{44} + k_{22}p_3^2 + k_{33}p_2^2 & k_{45} - k_{21}p_3^2 - k_{33}p_1p_2 & k_{46} - k_{31}p_2^2 - k_{22}p_1p_3 \\
 & & & -k_{23}p_2p_3 - k_{32}p_3p_2 & +k_{23}p_1p_3 + k_{31}p_3p_2 & +k_{21}p_2p_3 + k_{32}p_1p_2 \\
 k_{11}p_3 - k_{31}p_1 & +k_{12}p_3 - k_{32}p_1 & k_{13}p_3 - k_{33}p_1 & k_{54} - k_{12}p_3^2 - k_{33}p_2p_1 & k_{55} + k_{11}p_3^2 + k_{33}p_1^2 & k_{56} - k_{32}p_1^2 - k_{11}p_2p_3 \\
 & & & +k_{32}p_3p_1 + k_{13}p_2p_3 & -k_{31}p_3p_1 - k_{13}p_1p_3 & +k_{31}p_2p_1 + k_{12}p_1p_3 \\
 -k_{11}p_2 + k_{21}p_1 & -k_{12}p_2 + k_{22}p_1 & -k_{13}p_2 + k_{23}p_1 & k_{64} - k_{13}p_2^2 - k_{22}p_1p_3 & k_{65} - k_{23}p_1^2 - k_{11}p_2p_3 & k_{66} + k_{11}p_2^2 + k_{22}p_1^2 \\
 & & & +k_{12}p_2p_3 + k_{23}p_1p_2 & +k_{13}p_2p_1 + k_{21}p_1p_3 & -k_{12}p_1p_2 - k_{21}p_2p_1
 \end{bmatrix}$$

THE STIFFNESS MATRIX [K] FOR AN ISOLATOR LOCATED AT (p_1, p_2, p_3)

$$\begin{bmatrix}
 m & 0 & 0 & 0 & mp_3 & -mp_2 \\
 0 & m & 0 & -mp_3 & 0 & mp_1 \\
 0 & 0 & m & mp_2 & -mp_1 & 0 \\
 0 & -mp_3 & mp_2 & i_{11} + m(p_2^2 + p_3^2) & i_{12} - mp_1p_2 & i_{13} - mp_1p_3 \\
 mp_3 & 0 & -mp_1 & i_{21} - mp_2p_1 & i_{22} + m(p_1^2 + p_3^2) & i_{23} - mp_2p_3 \\
 -mp_2 & mp_1 & 0 & i_{31} - mp_3p_1 & i_{32} - mp_3p_2 & i_{33} + m(p_1^2 + p_2^2)
 \end{bmatrix}$$

THE INERTIA MATRIX [H] FOR A MASS LOCATED AT (p_1, p_2, p_3)

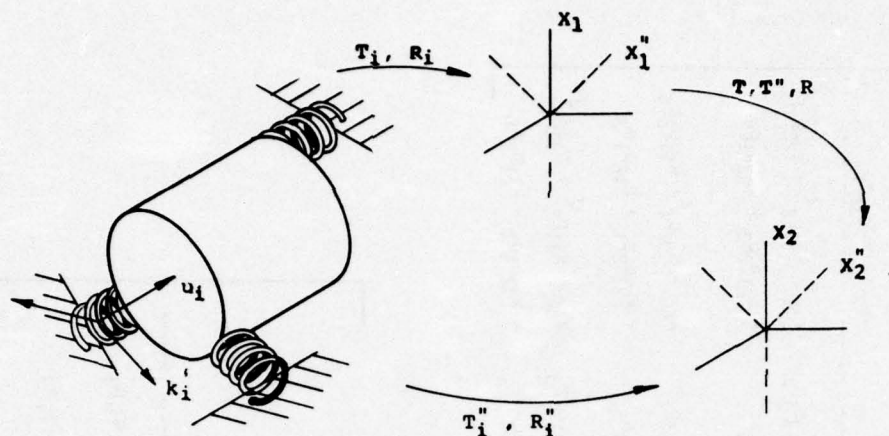


FIGURE 3
Calculation of the Matrices in Two Coordinate Systems

related by $[R]$.

The relationship between $[T]$ and $[T'']$ is found from Equations (15) and (2). Let $[R]\{F_1\} = \{F_1''\}$ and $R\{F_2\} = \{F_2''\}$. Since $\{F_2\} = [T]\{F_1\}$ then

$$\{F_2''\} = [R][T][R]^T\{F_1''\}$$

which implies

$$[T''] = [R][T][R]^T \quad (34)$$

The individual isolator rotation transformation derives in a similar manner. Now $[R_1]\{f_1'\} = \{f_1\}$ and $[R]\{f_1\} = \{f_1''\}$ so that

$$[R][R_1]\{f_1'\} = \{f_1''\}$$

which implies

$$[R_1''] = [R][R_1] \quad (35)$$

It is clear from Equation (34) and the form of $[T]$ that

$$[T_1''] = [R][T][T_1][R]^T \quad (36)$$

Substituting Equation (35) and Equation (36) into Equation (31)

$$\sum_k [R][T][T_1][R_1][k_1'] [R_1]^T [T_1]^T [T]^T [R]^T [K_2''] = 0 \quad (37)$$

Since $[R]$ and $[T]$ do not depend on i , and using Equation (33)

$$[K_2''] = [R][T][K_1][T]^T [R]^T \quad (38)$$

Substitution of Equation (34) into Equation (32) yields the same result. The important idea here is that the $[T]$ transformation can only be used on colinear coordinate systems. The transformation Equation (34) results in the same matrix that would be formed if the coordinates were measured in the X_2 system, transformed to the X_2'' , and then substituted into Equation (14).

FORMS OF SOLUTION OF THE EQUATIONS

Before analyzing an elastically supported system it is useful to consider the solution to Equation (1) for various conditions. In the absence of forces or support motions, $\{F\} = \{U\} = 0$, the solution $\{X\} = \{E\}e^{i\omega t}$ is assumed. Writing a complex matrix $[S(\omega)] = [K] + i\omega[C]$, Equation (1) becomes a complex Eigenvalue equation:

$$([S(\omega)] - \omega^2[M])\{E\}e^{i\omega t} = 0 \quad (39)$$

The determinant set equal to zero

$$|[S(\omega)] - \omega^2[H]| = 0$$

determines the six roots, ω_i^2 , which are in general complex numbers.

The Eigenvectors, $\{E_i\}e^{i\omega t}$, are then the solution to Equation (39) for each ω_i^2 and will in general also be complex. Since $[S]$ is a function of ω , the excitation frequency, the orthogonality of the Eigenvectors do not have the same form as in the real case. To show this

assume that there exist two different Eigenvalues w_r and w_s with the resulting Eigenvectors X_r and X_s . They therefore satisfy Equation (39)

$$[K + iw_r c]\{x_r\} = w_r^2 [H]\{x_r\} \quad (40a)$$

$$[K + iw_s c]\{x_s\} = w_s^2 [H]\{x_s\} \quad (40b)$$

Pre-multiply Equation (40b) by $\{x_r\}^T$ and post-multiply the transpose of Equation (40a) by $\{x_s\}$

$$\{x_r\}^T [K + iw_r c]\{x_s\} = w_r^2 \{x_r\}^T [H]\{x_s\} \quad (41a)$$

$$\{x_r\}^T [K + iw_s c]\{x_s\} = w_s^2 \{x_r\}^T [H]\{x_s\} \quad (41b)$$

Since $[K]$, $[C]$ and $[H]$ are symmetric these equations result in two orthogonality conditions. Subtraction of Equation (41b) from Equation (41a) yields

$$(w_r + w_s) \{x_r\}^T [H]\{x_s\} - i \{x_r\}^T [C]\{x_s\} = 0 \quad (42)$$

Multiplication of Equation (41a) by w_s and multiplication of Equation (41b) by w_r and subtracting yields

$$w_r w_s \{x_r\}^T [H]\{x_s\} + \{x_r\}^T [K]\{x_s\} = 0 \quad (43)$$

The Eigenvectors are a product of a 6×1 column vector with complex elements, a decaying exponential, and a sinusoid with a frequency equal to the damped frequency. Since the elements of the column vector are complex the phase relations are not just $\pm 1 = e^{i(\pi/2 \pm \pi/2)}$ as in the undamped case, but can take on intermediate values.

Let the adjoint (transpose, complex conjugate) be represented by $(*)$. Pre-multiply Eq. (39a) by $\{X_r\}^*$ and post-multiply the adjoint of Eq. (39b) by $\{X_r\}$.

$$\begin{aligned} \{X_r\}^* [K]\{X_r\} + iw_r \{X_r\}^* [C]\{X_r\} \\ = w_r^2 \{X_r\}^* [H]\{X_r\} \end{aligned} \quad (44)$$

$$\begin{aligned} \{X_r\}^* [K]\{X_r\} - iw_r \{X_r\}^* [C]\{X_r\} \\ = w_r^2 \{X_r\}^* [H]\{X_r\} \end{aligned} \quad (45)$$

Subtracting Equation (45) from Equation (44) yields

$$\begin{aligned} i \{X_r\}^* [C]\{X_r\} \\ = (w_r - w_r^*) \{X_r\}^* [H]\{X_r\} \end{aligned} \quad (46)$$

Multiplying Equation (44) by w_r^* and adding the product of Equation (45) and w_r results in

$$\begin{aligned} \{X_r\}^* [K]\{X_r\} \\ = w_r w_r^* \{X_r\}^* [H]\{X_r\} \end{aligned} \quad (47)$$

If w_r is assumed to have the form

$$w_r = \bar{w}_r (\sqrt{1 - \xi^2} + i\xi) \quad (48)$$

then Equation (46) and Equation (47) show

$$2\bar{w}_r \xi = \frac{\{X_r\}^* [C]\{X_r\}}{\{X_r\}^* [H]\{X_r\}} \quad (49)$$

$$\bar{w}_r^2 = \frac{\{X_r\}^* [K]\{X_r\}}{\{X_r\}^* [H]\{X_r\}} \quad (50)$$

Equation (49) shows ξ as the damping ratio and Equation (50) shows \bar{w}_r as the undamped natural frequency analogous to the single degree of freedom case. The Eigenvector in Equation (39) is written

$$\begin{aligned} \{X_r\} = \\ \{E_r\} e^{i\bar{w}_r (-\xi_r + i\sqrt{1 - \xi_r^2}) t} \end{aligned} \quad (51)$$

If the foundation undergoes a sinusoidal motion, $\{U\}e^{i\omega t}$, and assuming a steady state solution, Equation (1) becomes

$$([S(\omega)] - \omega^2 [H]) \{X\} = [S(\omega)] \{U\} \quad (52)$$

The solution vector $\{X\}$ is found by inverting the complex matrix $[S] - \omega^2 [H]$ for a given frequency, ω , and excitation vector $\{U\}$.

$$\{X\} = ([S(\omega)] - \omega^2 [H])^{-1} [S(\omega)] \{U\} \quad (53)$$

If instead of motion excitation the mass is acted on by a force, $\{F\}$, Equation (1) becomes

$$([S(\omega)] - \omega^2 [H]) \{X\} = \{F\} \quad (54)$$

the solution to which becomes

$$\{X\} = ([S] - \omega^2 [H])^{-1} \{F\} \quad (55)$$

If both sides of Equation (55) are multiplied by $[S]$ then the force on the body, $\{F_B\}$, due to the springs and dampers is

$$\{F_B\} = [S]([S] - \omega^2 [H])^{-1} \{F\} \quad (56)$$

Comparison of Equation (56) with Eq. (53) shows the difference between the displacement and force "transmissibility" matrices. If $[S]$ and $[H]$ are diagonal, then $[S]$ will commute with $([S] - w^2[H])^{-1}$ indicating that only when the modes are not coupled the force transmissibility is equal to motion transmissibility.

ELASTICALLY SUPPORTED SYSTEM

If the isolation system is mounted on an elastic structure, schematically shown in Figure 1b, the equations of motion become

$$[H_1]\{\ddot{X}\} = [C_1](\dot{U} - \dot{X}) + [K_1](U - X) \quad (57a)$$

$$[H_2]\{\ddot{U}\} = [C_1](\dot{X} - \dot{U}) + [K_1](X - U) + [C_2](\dot{V} - \dot{U}) + [K_2](V - U) \quad (57b)$$

In these equations, $[C_1]$, $[K_1]$ and $[C_2]$, $[K_2]$ represent the stiffness and damping matrices for relative motion of $\{X\}$, $\{U\}$ and $\{U\}$, $\{V\}$ respectively. Equations (57) are 12 coupled differential equations where all the matrix coefficients are evaluated with respect to the global coordinate system. Many physical conditions arise with $[H_2]$ much less than $[H_1]$ such that the sum of the forces on $[H_2]$ can be considered equal to zero. Examples of this are engine mounting systems where the airplane wing mass is small compared to that of the engine, for pneumatic isolation systems where the sprung damper is an approximation to the pneumatic system response, or a combined Maxwell-Voigt model of an elastomer spring. For free vibration or sinusoidal excitation the solution of $\{E\}e^{i\omega t}$ where $\{E\}$ is complex can again be assumed. Equations (57) become

$$[S_1]\{X\} - w^2[H_1]\{X\} = [S_1]\{U\} \quad (58a)$$

and

$$([S_1] + [S_2])\{U\} = [S_1]\{X\} + [S_2]\{V\} \quad (58b)$$

where

$$[S_1(w)] = [K_1] + i\omega[C_1]$$

$$[S_2(w)] = [K_2] + i\omega[C_2]$$

Now $\{U\}$ can be eliminated from Equations (58) to give one set of six equations.

$$([S_1] - [S_1]([S_1] + [S_2])^{-1}[S_1] - w^2[H_1])\{X\} = ([S_1]([S_1] + [S_2])^{-1}[S_2])\{V\} \quad (59)$$

Let an equivalent matrix $[S_e]$ be defined as

$$[S_e] = [S_1] - [S_1]([S_1] + [S_2])^{-1}[S_1] \quad (60a)$$

and noting the identity

$$[S_e] = [S_1]([S_1] + [S_2])^{-1}[S_2] \quad (60b)$$

Equation (59) reduces to (53), a system of six coupled differential equations with an equivalent matrix, $[S_e]$.

$$\{X\} = ([S_e] - w^2[H_1])^{-1}[S_e]\{V\} \quad (61)$$

From Equations (60a) or (60b) the identity can be obtained

$$[S_e]^{-1} = [S_1]^{-1} + [S_2]^{-1} \quad (62)$$

which shows that the total "dynamic" influence coefficients, $[S_e]^{-1}$, are the sum of the individual coefficients. Equation (62) can be used if two isolators are in series at a certain point by inverting Equation (25), using Equations (19) and (20).

$$[K]_i^{-1} = [T(-p)]_i^T [R]_i^T [k']_i^{-1} [R]_i^T [T(-p)] \quad (63)$$

If the linear dimensions of the isolator approach those of the mass, then the evaluation of $[k']$ in Equation (22) is not obvious. A detailed treatment for this case is given in reference [7]. Application of Equation (25), on the resultant stiffness matrix, $[K]$, will allow the analysis to proceed.

ACKNOWLEDGEMENTS

The author is indebted to Dr. David Gregorich of California State University at Los Angeles for many stimulating conversations on this subject, to Don Bailey and Terrence Dowell for their comments, and to his wife, Marianne, for patiently typing the manuscript.

REFERENCES

- [1] Crandall, Stephen H., and Robert B. McCalley, Jr., "Numerical Methods of Analysis", in Shock and Vibration Handbook, C. Crede and

- C. Harris, Eds. (McGraw-Hill Book Co., Inc., New York, 1961) Vol. 2, Chapter 28.
- [2] Smollen, Leonard E., "Generalized Matrix Method for the Design and Analysis of Vibration-Isolation Systems", The Journal of the Acoustical Society of America, Vol. 40, No. 1, 195-204 (July 1966)
 - [3] Derby, Thomas F., "Decoupling the Three Translational Modes from the Three Rotational Modes of a Rigid Body Supported by Four Corner-located Isolators", The Shock and Vibration Bulletin, Bulletin 43, Part 4, 91-108 (June 1973)
 - [4] Gouldstein, Herbert, Classical Mechanics, (Addison-Wesley Publishing Co., Inc., Massachusetts, 1950). Chapters 4 and 5
 - [5] Himmelblau, Harry Jr. and Sheldon Rubin, "Vibration of a Resiliently Supported Body", The Shock and Vibration Handbook, C. Crede and C. Harris, Eds. (McGraw-Hill Book Co., Inc., New York, 1961). Vol. 1, Chapter 3
 - [6] Doll, Robert W., "Modal Decoupling of Multi-Degree of Freedom Systems Using the Tensor Properties of the Stiffness Matrix". Qualifying Examination Report, University of California, Berkeley. Professor G.W. Brown, Chairman. 1973
 - [7] Brock, J.F., "A Matrix Method for the Flexibility Analysis of Piping Systems", Trans. ASME., J. Appl. Mech., Vol. 74, 501-516, 1952

AXISYMMETRIC STRUCTURAL LOADING
FOR A TRAVELING OVERPRESSURE PULSE

J. J. Farrell, D. J. Ness, G. M. Teraoka
TRW Defense and Space Systems Group
Redondo Beach, California 90278

Survivability evaluation of protective structures under nuclear attack environments is often aided by finite element analyses. Such analyses have considered two-dimensional axisymmetric models. This paper examines several implications of using a zeroth order Fourier expansion of the nuclear loading on an axisymmetric finite element structural model. Sample problem results are presented and discussed. General considerations of this locally axisymmetric representation of the nuclear blast loading are also discussed.

INTRODUCTION

Survivability evaluation of protective structures under nuclear attack environments is often aided by finite element analyses. Such analyses have considered two-dimensional axisymmetric models. This paper examines several implications of using a zeroth order Fourier expansion of a traveling nuclear airblast loading for calculation of the response of a surface-flush axisymmetric structure.

Various calculational schemes have been used to approximate a nuclear traveling pressure loading in an axisymmetric structural-media interaction (SMI) calculation. The simplest approximation can be made when the airblast is very superseismic with respect to the ground media. In such a case, a uniform (or pancake) load applied simultaneously to all surface nodes would be a reasonable approximation. The time history of this uniform load is usually taken to be the pressure pulse at the structure centerline (axis of symmetry) modified by addition of a rise time sized to minimize spurious oscillations within the grid. A more complex approach has considered computing the average force acting on the structure plan area at any instant of time and then dividing this by the plan area to obtain an "Impulse Averaging Load" exhibiting a more realistic rise time and smoothed peak based on the structure transit time; this average loading function is then applied simultaneously to all surface nodes. Although adequate for superseismic airblast loading conditions, it is obvious that such simultaneous loading procedures cannot introduce the effects of uprange loads propagating through the earth media; loads which are extremely important when the airblast is subseismic

or when "outrunning" of the ground shock waves occurs.

Another approximation which has been used is the so called "converging shock" load. In this scheme, the centerline time history pulse is swept across the grid at the proper shock front velocity, thus axisymmetrically modeling a blast load converging on the structure from all sides. This technique does introduce the effects of uprange loads but results in too severe a loading condition.

Fundamentally, an axisymmetric model for a structure-media interaction calculation assumes that the loading and subsequent response is identical for all points lying on a circular ring of radius r centered upon the symmetry axis of the structure. The method presented in this paper is based on applying, to a given loaded surface node at a radius r in the 2-dimensional axisymmetric grid, the zeroth order coefficient $P_0(r, t)$ of a Fourier expansion of the traveling nuclear overpressure pulse acting upon the entire circular ring of radius r .

Quantitatively, the derived pressure time history $P_0(0, t)$ applied to the surface node on the symmetry axis is identical to the nuclear pressure pulse at that location since this unique node corresponds to a degenerate ring of radius $r = 0$ for which the average pressure is equal to the pressure at that discrete point. For surface nodes off the symmetry axis at a radius r , a rise time plus a lowering of the initial shock peak is introduced, both effects increasing monotonically with r . The arrival

time of the applied load pulse at a given node is a monotonically decreasing function of r , indicating a traveling load traversing the grid toward the structure centerline. Thus, the present method yields a converging type loading which approximates the asymmetry in the actual 3-dimensional nuclear loading.

THEORETICAL DEVELOPMENT

Figure 1 depicts schematically the general nature of a nuclear height-of-burst airblast loading on a surface-flush structure. Below an altitude of 30 kilometers, approximately 50% of the energy yield from a typical nuclear detonation is in blast and shock effects. The tremendous pressures produced by the expanding hot gases generate a blast wave which propagates radially outward at a very high, but ever decreasing, velocity. As the blast wave arrives at a given point, the overpressure rises very rapidly (essentially instantaneously) from ambient to its peak value and then decreases much more slowly. As shown, the peak overpressure value also decreases with radial distance from ground zero (the detonation point).

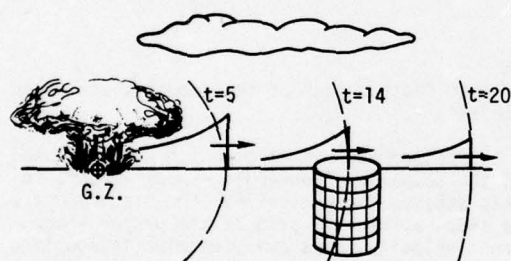


Fig. 1 - Airblast loading on a surface flush structure

For the case of an axisymmetric structure subjected to such an overpressure loading, there are two symmetry axes as shown in Figure 2.

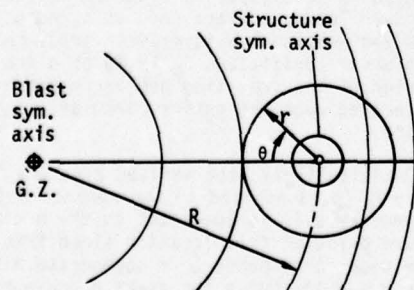


Fig. 2 - Axes of symmetry for airblast and structure

The loading function is symmetric about a vertical line through ground zero while the structure exhibits its own symmetry axis which, for all further developments in this paper, is taken to lie parallel to the air blast symmetry axis and separated from it at a range R .

In an axisymmetric structure, all points located a radial distance r and a vertical distance z (from some reference origin) are identical. Thus, all points on the surface rings A and B of the cylindrical structure shown in Figure 3 are mapped into the two nodal points a and b respectively. The nature of the airblast loading on a typical ring (B) is shown as $P(r, \theta, t)$ in Figure 3. It is obvious that this loading is not symmetric relative to the symmetry axis of the structure. One method of handling such an asymmetric loading in an axisymmetric calculation is to expand the loading function in a Fourier series on the circumference of each circular node.

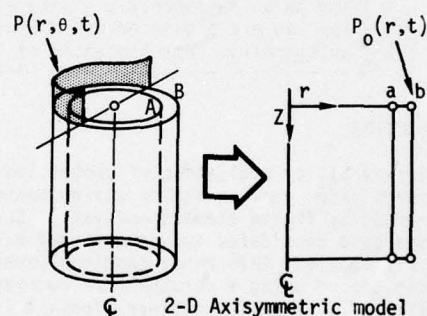


Fig. 3 - Asymmetric loading on the symmetric structure

During the nineteen-sixties, a number of computer codes were developed which could model static and dynamic effects of Fourier expansions of non-axisymmetric loads on elastic finite element structures. The theoretical development for the zeroth order term of the Fourier expansion is not novel. However, the outrunning nature of ground shock problems is unusual and the forms of the zeroth order load time histories are not at all intuitively obvious.

Measuring θ from the uprange radial as shown in Figure 2, the loading function $P(r, \theta, t)$ is seen to be an even function of θ and thus can be expanded in a Fourier cosine series as follows:

$$P(r, \theta, t) = \sum_{n=0}^{\infty} a_n(r, t) \cos n \theta \quad (1)$$

$$a_n(r, t) = \frac{1}{\pi} \int_0^{\pi} P(r, \theta, t) \cos n \theta \, d\theta$$

Due to the shock discontinuity, the above Fourier expansion for a given circular node would have to retain many terms if the shape of the pressure distribution were to be represented accurately. However, the higher-order terms of the expansion excite only the higher-frequency modes of vibration of the finite element structural model, modes which are normally represented poorly and are also highly damped in typical finite element analyses. Often, there is insufficient reason to retain the higher-order terms and, in this present limiting case, only the zeroth order term will be considered.

Thus, to a first (or zeroth) order approximation, the traveling overpressure load on a given loaded surface node at a radius r in the axisymmetric finite element grid is given by

$$P_0(r,t) = \frac{1}{\pi} \int_0^\pi P(r,\theta,t) d\theta \quad (2)$$

For the height of burst case under consideration, no analytical expression exists for evaluating the overpressure function $P(r,\theta,t)$; thus, it must be evaluated numerically. A typical SMI grid will contain approximately 50 loaded surface nodes. If $P(r,\theta,t)$ were numerically calculated for a sufficient number of θ values to accurately integrate Equation (2), an inordinate amount of core storage and computer time would be required. Thus, the following approximation to $P(r,\theta,t)$ is used in the present analysis:

$$P(r,\theta,t) \approx P(r,0,t) + \Delta P [1 - \cos \theta]/2 \quad (3)$$

$$\Delta P(r,t) = P(r,\pi,t) - P(r,0,t)$$

In performing the integration indicated by Equation (2), three distinct cases are possible as shown in Figure 4:

- 1) $P(r,0,t) = P(r,\pi,t) = 0$
- 2) $P(r,0,t) > 0$; $P(r,\pi,t) = 0$
- 3) $P(r,0,t) > 0$ and $P(r,\pi,t) > 0$

The first case (Figure 4(a)) implies that the overpressure pulse has not yet reached the circular node and obviously $P_0(r,t) = 0$ for this case.

The third case (Figure 4(c)) implies that the overpressure pulse has completely engulfed the circular node and it is readily verified that here $P_0(r,t)$ is given by

$$P_0(r,t) = [P(r,0,t) + P(r,\pi,t)]/2 \quad (4)$$

which represents the average of the uprange (minimum) and downrange (maximum) overpressure values acting on the circular node.

The second case (Figure 4(b)) represents the situation in which the overpressure shock front is traversing the circular node and the entire ring is not yet totally engulfed. In this case,

$$P_0(r,t) = \frac{1}{\pi} \int_0^{\theta^*} P(r,\theta,t) d\theta \quad (5)$$

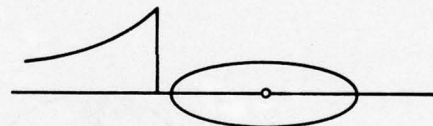
where θ^* denotes the instantaneous shock front location on the ring of radius r . For this case, ΔP can be approximated by the linear extrapolation

$$\Delta P = \left[\frac{P(r,\theta^*,t) - P(r,0,t)}{r(1 - \cos \theta^*)} \right] 2r \quad (6)$$

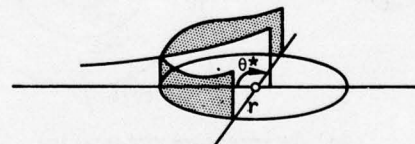
so that the required relation for P_0 becomes

$$P_0(r,t) = \left\{ P(r,0,t) \theta^* + \Delta P [\theta^* - \sin \theta^*]/2 \right\} / \pi \quad (7)$$

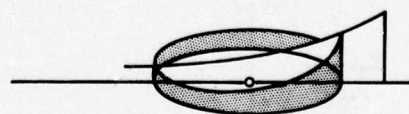
with ΔP given by Equation (6) above. Thus, P_0 can be calculated for all three cases shown in Figure 4.



(a) Before overpressure arrival



(b) Partial engulfment



(c) Total engulfment

Fig. 4 - Generation of zeroth order approximation

NUMERICAL EXAMPLE

The equations for $P_0(r,t)$ have been numerically implemented into a FORTRAN subroutine using the Brode Simple Fit expressions for a nuclear height-of-burst overpressure pulse [1]. This forcing-function subroutine was then incorporated into the SAMSON finite element code [2] in order to assess its capability to approximate a 3-dimensional traveling pulse on a 2-dimensional axisymmetric grid.

Figure 5 presents an example of the forcing function $P_0(r,t)$ produced for a typical air-blast loading on representative axisymmetric circular nodes. As depicted in Figure 5(a), the nuclear burst is taken to have a yield of 4×10^6 kilograms (kg) at a height-of-burst of 21 meters above ground level. The symmetry axis of the structure is chosen to lie at a range of 74 meters. Circular nodes are exhibited at radial distances of 1, 4, 8 and 16 meters.

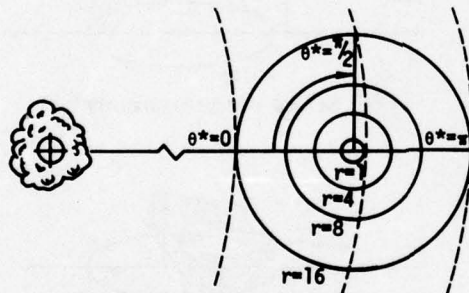
Figure 5(b) presents the spatial distribution of the overpressure pulse on the $r = 16$ meters ring for three values of θ^* : $\theta^* = 0$, $\theta^* = \pi/2$ and $\theta^* = \pi$. For $\theta^* = 0$, the shock front has just reached the uprange edge of the ring; thus, the spatial distribution of the pressure pulse is a singular spike at $\theta = 0$

having a magnitude equal to the peak overpressure value at the appropriate range of 58 meters from ground zero. The time associated with this condition is indicated by t_0 on Figure 5(c) and it is to be noted that $P_0(16,t) = 0$ for all t less than t_0 since this represents Case 1 described in the previous section.

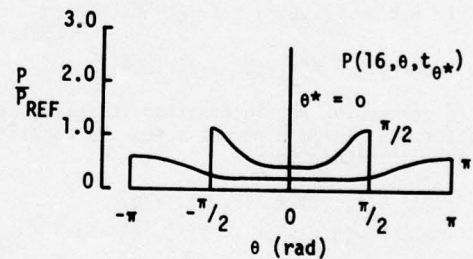
For $\theta^* = \pi/2$, the spatial distribution is again shown in Figure 5(b) and the time history of $P_0(16,t)$ during this phase of the loading is as shown in Figure 5(c) for $t_0 \leq t \leq t_1$ (note: $t = t_1$ at $\theta^* = \pi/2$). This represents Case 2 with the circular ring one-half engulfed by the overpressure pulse at $t = t_1$.

At $\theta^* = \pi$, the overpressure loading has totally engulfed the ring yielding Case 3 of the preceeding section. The appropriate spatial distribution $P(16,\theta,t_2)$ is shown in Figure 5(b) and the time history of $P_0(16,t)$ for this phase of the loading is shown in Figure 5(c) for $t_1 \leq t \leq t_2$ (note: $t = t_2$ at $\theta^* = \pi$). Beyond $t = t_2$, the entire ring is loaded (Case 3) and the appropriate time history for $P_0(16,t)$ is shown in Figure 5(c) for time out to 25 msec.

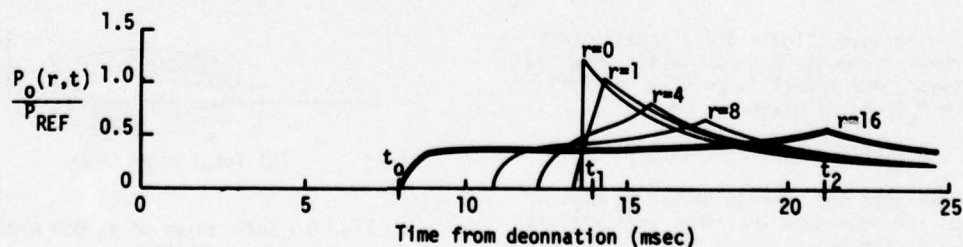
Time histories of $P_0(r,t)$ for nodes at radii of 8, 4, 1 and 0 meters are also shown in Figure 5(c). Several qualitative statements



(a) Overpressure propagation



(b) Spatial distribution of overpressure



(c) Overpressure time histories

Fig. 5 - Example of zeroth order approximation

are obvious from the time histories presented:

1. The arrival time of $P_0(r,t)$ is an ever decreasing function of r ; i.e., loading initiates first on the outermost circular node and progresses inward toward the axis of symmetry. Thus, the zeroth order approximation yields a converging type of loading.
2. The rise time (time interval between initiation and peak value of loading) is an ever increasing function of r . Thus, the zeroth order approximation introduces a rise time proportional to the radial distance to a given node.
3. The double curvature rise time is due to the rapid increase in circumferential distance as the wavefront angle θ^* is near 0° and 180° . This accounts for the sharp rise initially and again the sharp rise immediately before the peak.
4. The peak loading value of $P_0(r,t)$ is an ever decreasing function of r ; i.e., the zeroth order approximation tends to lower the peak pressure applied to the circular nodes as one moves radially outward from the symmetry axis.
5. For each circular node, the peak applied pressure occurs at the time of total engulfment of the node by the wavefront. This is due to the rapid increase of circumferential distance near the $\theta^* = 180^\circ$ point.
6. The derived pressure time history $P_0(o,t)$ applied to the surface node on the symmetry axis is identical to the nuclear pressure pulse at that range since this unique node corresponds to a degenerate ring of radius $r = 0$ for which the average pressure is equal to the instantaneous pressure at that discrete point.

GENERAL CONSIDERATIONS

As mentioned above, the zeroth order forcing function has a time history which becomes increasingly different from the three dimensional forcing function as distance from the centerline of an axisymmetric structure is increased. Nevertheless, if all materials in the structural model are linear the solution for this forcing function is the zeroth order term of the Fourier expanded response. The zeroth order term is the term which governs crushing in the hoop mode and the hoop mode is a relatively accurate predictor of survivability for an important class of buried axisymmetric structures.

For nonlinear material models, Fourier expansions of the loads and the resulting responses are not strictly applicable. However, since this loading function provides the first order traveling air blast loading effects in addition to preserving the exact force history on the structure it is considered the most appropriate of the presently available forcing functions for use in linear or nonlinear axisymmetric response analysis.

Important considerations for the application of this technique include appropriately sizing the finite element grid to the duration of the peak loading on the structure in an outrunning geology, and appropriately inputting the boundary and initial conditions to be compatible with the accuracy of the engineering solution which is to be sought.

REFERENCES

1. "Height of Burst Effects at High Overpressures", RM-6301-DASA, H. L. Brode, July 1970.
2. "A Computer Code for Dynamic Stress Analysis of Media - Structure Problems with Non-Linearities" (SAMSON), AFWL-TR-72-104, Vol. I, Theoretical Manual, T. Belytschko, IIT Research Institute, February 1973.

MODAL TEST AND ANALYSIS

MODALAB

A NEW SYSTEM FOR STRUCTURAL DYNAMIC TESTING

Richard C. Stroud
Space Systems Division
Lockheed Missiles & Space Company
Sunnyvale, California

and

Strether Smith and George A. Hamma
Palo Alto Research Laboratory
Lockheed Missiles & Space Company
Palo Alto, California

The subject of this paper is the MODALAB (MOBILE Dynamic Analysis LABoratory). Objectives of the MODALAB development are discussed. The theoretical concepts supporting the current MODALAB modal-test procedures are outlined along with alternate testing theories. The MODALAB hardware and software systems are described. There is a delineation of the current modal-test procedure. Results of an early application are presented.

INTRODUCTION

A modal test is the experimental determination of some of the modal characteristics (i.e., natural frequencies, modal-damping behavior, and mode shapes) of a structural system.

Modal testing is an essential phase in the development of an aerospace vehicle or any sophisticated structure that may be subjected to dynamic excitation. In fact, there is a strong argument for performing modal surveys on complicated structures that should experience only static loads.

Experimentally determined modal parameters are frequently used directly as analytical parameters in the theoretical prediction of control-system behavior. Modal-test results are used in flutter studies, to determine design loads, and to help predict functional behavior of complex structural systems. Modal tests have a growing role as a qualification test, particularly for substructures whose design is influenced by the frequency characteristics of their host vehicle.

The most common use for modal-test results is the verification of analytical models. A structure's design is frequently dictated by exposure to static and/or dynamic excitations that are impossible or impractical to simulate under laboratory conditions. In such instances, it is necessary to theoretically predict the system's response to these "design" environments. The analyst can have great confidence in his predictions if his analytical idealization of the structure possesses theoretical modal characteristics that are similar to measured modal properties of the actual structure. When experimental modal data are available, the mathematical

model can be refined to exhibit nearly the same modal behavior as the test article. A structure is often subject to geometry variations (e.g., variable-sweep wings, directional antennae) and/or mass variations (e.g., consumption of propellants, different payloads). If the credibility of an analytic model has been established for one configuration, the analyst may have confidence in the results given by reasonable modifications of that model to reflect mass and/or geometry changes. Experimentally verified models can be similarly altered to assess the consequences of proposed design perturbations.

Determination of modal characteristics by ground vibration testing has been practiced in the Aerospace Community for about 40 years. Excitation, instrumentation, and analysis hardware have been continually refined during this period. These improvements have, however, been outpaced by more complex test articles and more ambitious test requirements. As a result, modal tests have frequently fallen short of their objectives. Cost- and schedule-conscious managers have come to look on ground vibration testing as an expensive gamble. While realizing the real need for this test data, technical risk may seem more acceptable than entering into a test program that could extend schedules, overrun budgets, and yield less than the desired data.

Researchers have recognized this dilemma and have sought alternate techniques for vibration testing. Several important suggestions have appeared in the literature, but, with few exceptions, these proposals have, for practical reasons, been ignored in the testing of large structures. Application of these more sophisticated techniques typically requires rapid acquisition of large volumes of data

and extensive manipulation of this information. Recent advances in small computers and data-acquisition equipment have made practical the application of these techniques to testing of large aerospace structures. MODALAB (MOBILE Dynamic Analysis LABORatory) is an automated test system designed to use the newly developed data-acquisition/processing hardware and to apply existing but unused theoretical procedures.

A popular approach to modal testing has been simultaneous excitation by several coherently phased shakers (Reference 1). Certain factors have precluded a satisfactory, systematic procedure for multipoint-excitation modal testing.

Two significant problems have been: 1) lack of a reliable procedure for establishing the appropriate distribution of shaker forces for pure excitation of a mode and, 2) an effective criterion for identifying modal purity. Theoretical data-processing techniques capable of overcoming these problems have existed but gone unused because of stringent data-acquisition/processing requirements. The development of MODALAB permits practical application of many of these techniques. Two of these are of particular importance to successful multishaker testing. They are:

- 1) A method first proposed by Asher (Reference 2), but not previously used in a practical application, is used to identify resonances in high modal-density situations and to determine the appropriate force distributions to tune the associated modes. This technique uses the data acquired during a series of wideband, single-shaker sinusoidal sweeps. These data are assembled into a coincident-response matrix, the determinant of which is examined as a function of frequency. Those frequencies for which this determinant vanishes are resonant frequencies and the solution of the corresponding set of homogeneous equations yields the force distributions required to tune the respective modes. Modal tuning by this method is an objective procedure.
- 2) The energy-admittance method of Smith and Woods (Reference 3) provides a single, concise measure of modal response for an entire structure. The total-energy admittance is defined as the complex ratio of kinetic energy of the entire structure to the power input by shakers. This quantity is analogous to the complex displacement/force admittance first discussed by Kennedy and Pancu (Reference 4). Consequently, if the real and imaginary components of the total-energy admittance are plotted against each other, the locus of data points will, for a well-tuned mode, form a circle which is centered on the imaginary axis and tangent to the real axis. Deviations from this pattern indicate a lack of modal purity. The total-energy admittance is used to determine the modal frequency and damping based on overall structural behavior. Local-energy admittances provide the basis for accurate determination of the mode shape.

These methods have been programmed and are a part of MODALAB's modal-test procedure. The steps in the modal survey conducted with MODALAB are:

- 1) A series of wideband, single-shaker, sinusoidal sweeps.
- 2) Resonance determination and force-distribution analysis.
- 3) Interactive refinement of modal tuning.
- 4) Decay test.
- 5) A narrowband, multiple-shaker sinusoidal sweep.
- 6) Immediate postprocessing to determine modal properties and to critique results.
- 7) Momentum/orthogonality check.

This procedure is unique for modal testing in that it is almost entirely objective. It has been used on several practical applications. The results of one such use will be subsequently presented.

It is the objective of this paper to define the objectives of MODALAB's software, outline experimental and analytical procedures followed in performing a modal test with MODALAB, and present results from such a test.

DISCUSSION

MODALAB Development Objectives

In preparation for a large-scale modal test, the state of structural dynamic testing was reviewed. An industry-wide view of the state of modal testing indicated a situation wherein continually improving test capabilities were falling behind the demands of more and more ambitious test requirements. A review of testing literature revealed a number of sophisticated theoretical procedures that had not been fully exercised in practical test operations. In most instances, this lack of application was because the newer methods required the acquisition and processing of an impractically large volume of data. Recent advances in small computers and digital data-acquisition hardware suggested the assembly of a system that was capable of applying these unused, or incompletely used, theoretical procedures. Thus, the fundamental objective of the MODALAB development was to exploit recent advances in data-acquisition and -processing hardware to assemble an automated structural dynamic test system capable of adapting theoretical techniques to practical operating procedures.

Because MODALAB was being developed to apply unproven methods, it was decided to assemble a system that was not committed to any particular procedure. This decision led to procurement of the most powerful miniprocessor available at that time (see section on MODALAB Hardware), and a policy of emphasizing software rather than hardware.

This software-oriented philosophy produced a versatile and flexible test system. Although MODALAB was developed to be a specialized modal-test system, its rapid data-acquisition system and powerful data-processing system can, with appropriate software modifications, be adapted to a large array of experimental and/or analytical tasks.

To further accentuate this versatility, it was an objective to generate system software in FORTRAN language, thus permitting engineers to revise programs for new applications without becoming involved in assembly-language programming. With the exception of a few seldom-changed routines for controlling peripheral equipment, all MODALAB software is coded in FORTRAN language.

The availability of a powerful data processor at the test site provided a new dimension to modal testing in that test data could be evaluated as it was acquired. The traditional modal test involves the acquisition of great quantities of force and acceleration data. Analysts then take this data and, in a matter of days or weeks or even months, produce the sought-after modal characteristics. If the analysts conclude their data are inadequate, too often the test setup has been dismantled and the specimen is unavailable for further testing. With a system like MODALAB, the Test Director can, in a matter of minutes, assess the acceptability of data and, if it is found unsatisfactory, he has the option to reacquire the faulty data.

In summary, it was the objective of the MODALAB development to exploit recent developments in data-acquisition and -processing hardware to assemble a system for structural dynamic testing that had the following unique features:

- 1) capability to apply previously unused theoretical procedures,
- 2) capability to substantially reduce the time required to perform a large-scale modal test,
- 3) mobility,
- 4) immediate data-evaluation capability, and
- 5) versatility afforded by the minimum hardware, maximum FORTRAN-software approach.

Theoretical Considerations

The theoretical basis for the MODALAB modal-test procedure is the complex energy-admittance method described in Reference 3. This technique was developed to take advantage of the best features of two popular approaches to modal testing. To put this method in perspective, a review of the classical modal-test theory follows.

Classical Modal-Test Theory - The fundamental approach to modal testing is to sinusoidally excite the test article at a single point, vary the frequency of excitation, observe response of the test specimen, and deduce modal characteristics. In the basic approach, resonant frequencies are identified as those at which the structure responds most

dramatically and "mode shapes" are defined by measuring a series of discrete (in-space) responses. These measurements may be accomplished by dwelling at the resonance or, if adequate test equipment is available, sinusoidal sweeps may be performed. Determination of damping behavior in the fundamental method is ordinarily accomplished by driving the test article at a resonance, quickly stopping the excitation and observing the rate at which motion decreases at one or more locations. Analytical procedures exist for deducing damping properties from response versus frequency plots.

Figure 1 shows the classical plot of response amplitude (per unit excitation force) and response phase (relative to the excitation). This response can be described analytically as

$$\frac{X}{F} = \frac{1}{\omega_n^2 \gamma \sqrt{(1-\beta^2)^2 + g^2}} \quad (1a)$$

$$\phi = \tan^{-1} \frac{-g}{1-\beta^2} \quad (1b)$$

where X is the amplitude of displacement response,

F is the amplitude of force excitation,

ω_n is the natural frequency of the system,

γ is the generalized mass of the system,

β is the ratio of exciting and natural frequencies ($\beta = \omega/\omega_n$),

g is the structural (hysteretic) damping coefficient, and

ϕ is the phase of displacement response relative to the excitation.

The fundamental approach is adequate for those systems which behave as a single degree-of-freedom system or those whose resonances are widely separated in the frequency domain (see Figure 1). As modal density increases (i.e., as the frequency difference between consecutive resonances diminishes), response behavior becomes more complex (see Figure 2) and more sophisticated procedures are required to extract modal properties. Two basic approaches to the problem of modal separation have evolved. One has been the development of analytical techniques which interpret data obtained from the simultaneous response of two or more modes to identify the characteristics of each mode. The other approach has been to simplify the measurement of modal parameters by inducing the structure to vibrate in only one mode at a time. The single-mode response is accomplished by simultaneous excitation with several shakers.

Analytic Mode-Separation Methods - As previously mentioned, one approach to measuring

properties of modes with similar frequencies is to analytically process data that exhibit response of two or more modes. This approach can be generally described as "fitting" theoretically derived analytic response descriptions to measurements of response produced by single-point excitation. The more fundamental of these techniques involves selection of analytic quantities such that the theoretical and experimental results agree at each resonance. More ambitious procedures call for curvefitting of continuous analytic expressions to response versus frequency information.

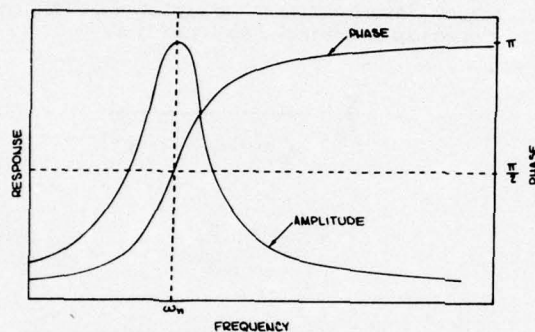


Figure 1. Single-Mode Response

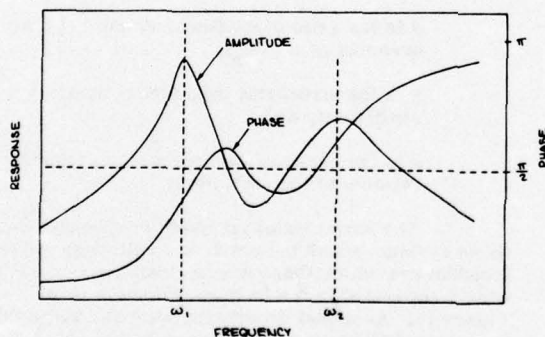


Figure 2. Multiple-Mode Response

Among the methods that fall in the analytic-separation category is the co-quad theory proposed by Kennedy and Pancu (Reference 4). A description of their method is pertinent to this discussion as the basics of their approach are extended and applied in MODALAB's software. Kennedy and Pancu suggested that instead of examining absolute response and its phase behavior, data analysts should consider components of response which are in phase with the excitation and that trail the excitation by 90 degrees. These are referred to as the coincident (or co) and quadrature (or quad) response, respectively. If the complex ratio of displacement response to force

excitation is considered, the real component corresponds to the coincident response whereas the negative imaginary component represents the quadrature response. Kennedy and Pancu's displacement/force admittance relation is

$$\frac{x}{f} = \frac{1}{\omega_n^2 \gamma_n} \frac{1 - \beta_n^2 - i g_n}{(1 - \beta_n^2)^2 + g_n^2} \quad (2)$$

where x is the complex-displacement response

$$(x = X e^{i\omega t + \phi}),$$

f is the complex force ($f = F e^{i\omega t}$), and

i is the imaginary unit ($i = \sqrt{-1}$).

Kennedy and Pancu demonstrated that, for a single degree-of-freedom system or for a mode whose resonance is well-removed from adjacent natural frequencies, the coincident response rapidly passes through zero at resonance and the quadrature response is sharply peaked at resonance. Figure 3a is the single-mode response of Figure 1 displayed in the co and quad versus frequency format. If these co and quad responses are plotted against each other, a circle centered on the quadrature axis and tangent to the coincident axis results (see Figure 3b). The diameter of the circle is the amplitude of modal response. An important feature of such a plot is that the resonant frequency corresponds to the point on the co-quad plot at which the path length derivative with respect to frequency is a maximum. The distance between points on the co-quad plot of Figure 3b represents equal frequency increments. It is apparent that the maximum path-length derivative, $\partial s / \partial \beta$, occurs where the co-quad plot crosses the quadrature axis; i.e., at resonance. Subsequent authors have also derived an expression for structural damping in terms of this maximum path-length derivative and the radius of curvature of the plot at the corresponding point, i.e.,

$$g = \left. \frac{4\rho}{\partial s / \partial \beta} \right|_{\beta=1} = 1 \quad (3)$$

where ρ is the radius of curvature of the co-quad plot, and

s is the path-length.

Multiple-mode response is expressed as a sum of quantities like Equation 2; i.e.,

$$\frac{x}{f} = \sum_{n=1}^N \frac{D_n}{\omega_n^2 \gamma_n} \frac{1 - \beta_n^2 - i g_n}{(1 - \beta_n^2)^2 + g_n^2} \quad (4)$$

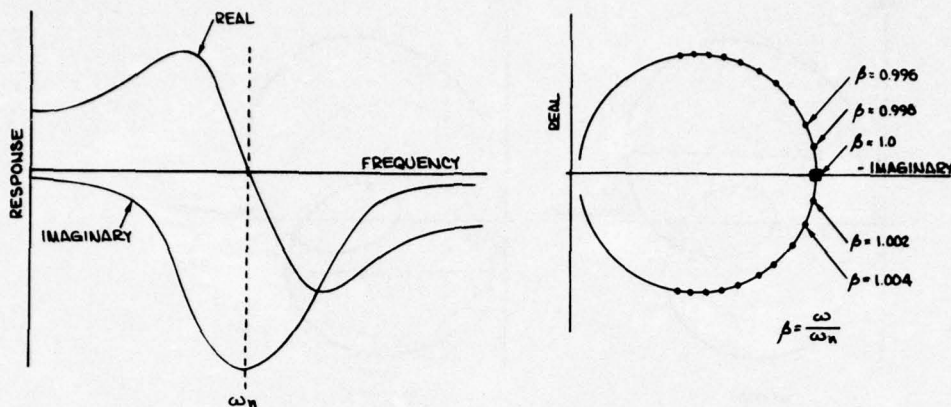


Figure 3. Single-Mode Complex Admittance

where the subscript "n" signifies the nth mode; i.e.,

D_n is the nth modal-displacement amplitude factor,

ω_n is the nth natural frequency,

γ_n is the generalized mass of the nth mode,

β_n is the ratio of the exciting frequency to the nth natural frequency, and

g_n is the structural damping in the nth mode.

Figure 4 is the co-quad presentation of the dual-mode response depicted in Figure 2. Co and quad versus frequency plots no longer explicitly define the resonant frequencies and modal responses. However, the co versus quad plot exhibits a distinct loop for each mode and two maximums of path-length derivative are apparent.

Figure 5 demonstrates that the total response is a complex vector sum composed of

contributions from each mode. The modal response vectors each sweep out a circle by rotation in the co-quad plane. Each vector rotates at a different rate, most rapidly in the vicinity of its resonance as shown in Figure 5. This demonstration can be expanded to include any number of modes. The resulting plots would contain one path-length derivative maximum for each mode present.

The procedure recommended by Kennedy and Pancu to identify modal properties in a mixed-mode response is to first establish a co-quad plot from experimental data. Then identify resonant frequencies by finding (and measuring) the maximums of the frequency derivative of path length. Once resonances are established, modal responses are determined by best-fitting circles to the co-quad plot in the vicinity of each resonance, the diameters of the circles being a measure of each mode's contribution to the total response (see Figure 5). Damping properties for each mode can be obtained by evaluation of Equation 3 using the appropriate diameters and path-length derivatives.

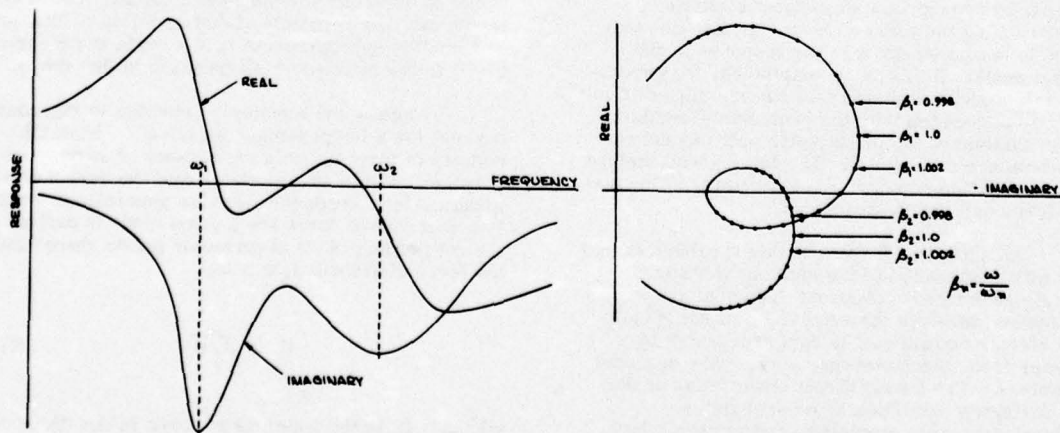


Figure 4. Multiple-Mode Complex Admittance

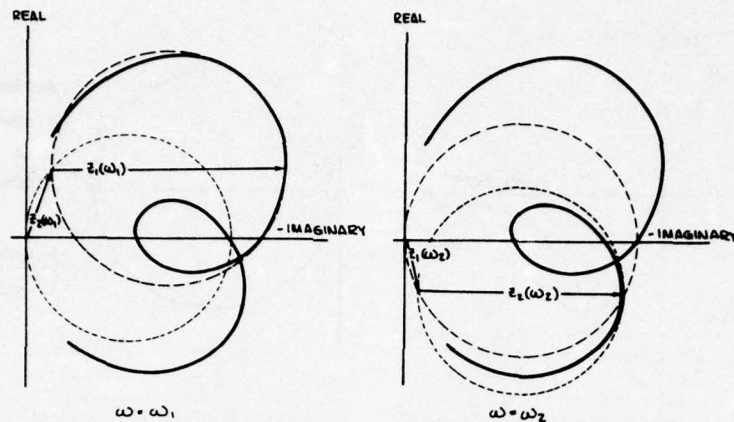


Figure 5. Content of Multiple-Mode Co-Quad Plot

The validity of Kennedy and Pancu's method depends on the assumption that in the vicinity of any resonance the change of total response (amplitude and phase) with respect to frequency is dominated by the mode nearest resonance. In other words, the frequency derivative of response in adjacent modes must be negligible when compared with similar quantities for the resonant mode. It is clear that as resonant frequencies become more nearly equal, the validity of this assumption diminishes. It is also apparent, however, that reduced damping permits this procedure to accommodate greater modal density.

It is noted that earlier test systems have been developed to exploit the methods of Kennedy and Pancu; however, they have not lent themselves to systematic data processing or the efficient acquisition of as many channels of data as is required to perform a large-scale modal test.

Multiple-Shaker Methods - The notion of simplifying the measurement of modal characteristics by excitation with several shakers was first proposed by Lewis and Wrisley (Reference 1). Their objective was to treat two or more modes with similar natural frequencies by successively dwelling at each resonance and, by appropriate adjustment of shaker forces, causing the test article to vibrate such that its motion is almost entirely the response of the resonant mode. If this is accomplished, the experimentalists's measurement tasks are no more difficult than those associated with the fundamental method wherein systems with, effectively, only one degree-of-freedom are considered. The tuned-dwell method has enjoyed broad popularity, particularly in the testing of large aerospace structures.

An appealing feature of this approach is that it permits observation of the mode by measurement of nearly pure modal response. The analytic separation method involves the acquisition of complicated data which are committed to data processing by a computer from which emerges a summary of modal parameters. The nearly direct observation of the mode during its excitation is reassuring to structural-dynamics specialists and is particularly reassuring to those who have a less complete

understanding of modal testing and the theoretical basis of analytic separation.

The appropriate ratios of shaker forces required to produce single-mode responses are seldom apparent and, as a result, obtaining modal purity is not always a simple procedure. Lewis and Wrisley proposed a tuning criterion wherein the appropriate ratios of shaker forces were the same as the ratios of modal response at the corresponding points of force application multiplied by the mass associated with that location. That is,

$$\vec{F} = b [\mathbf{m}_j] \vec{\Phi} \quad (5)$$

where \vec{F} is the force vector,

b is an arbitrary constant,

$[\mathbf{m}_j]$ is a diagonal mass matrix, and

$\vec{\Phi}$ is the modal-displacement vector.

Since the modal-velocity vector is proportional to the modal-displacement vector, this criterion can be alternately stated as follows: the force distribution appropriate to tune a mode is proportional to the momentum distribution in that mode.

Lewis and Wrisley's criterion is rigorously correct for a lumped-mass idealization when the number of forces equals the number of degrees-of-freedom. Modal theory states that the response of a given mode is proportional to its generalized force. The generalized force for a given mode is defined as the dot product of its eigenvector (mode shape) and the force distribution; that is,

$$G_j = \vec{\phi}_j^T \vec{F} \quad (6)$$

where G_j is the generalized force in the j th mode,

$\bar{\phi}_j^T$ is the transpose of the j th eigenvector, and,

\bar{u} is the force distribution vector.

Consider a force distribution based on Lewis and Wrisley's procedure applied to the k th mode, that is,

$$G_j = b \bar{\phi}_j^T [m_k] \phi_k \quad (7)$$

From the classical orthogonality condition, it is clear that the generalized force and modal response will be zero for all except the k th mode. Although Lewis and Wrisley spoke in terms of a lumped-mass idealization, it is apparent from Equation 7 that their criterion could use a consistent mass formulation or full mass matrix which includes mass coupling effects between degrees-of-freedom.

Practical application of Lewis and Wrisley's technique is difficult. First, most contemporary test articles cannot be adequately idealized by a lumped-parameter simulation with a number of degrees-of-freedom equal to or less than the number of shakers available. As a result, computation of the mass matrix required to compute the force vector is often a rather subjective matter. In addition, determination of the force distribution requires *a priori* knowledge of the sought-after mode shape. This information is not, in general, available. As a result, application of Lewis and Wrisley's method ordinarily requires an empirical iteration procedure. Such a process has no assurance of convergence and, in fact, for a high modal-density situation it seems unlikely that iteration would successively converge to all the modes present. In spite of these drawbacks, most contemporary multiple-shaker tests use some variation of the Lewis and Wrisley approach with the iteration or trial-and-error process being performed by skilled experimentalists aided by elaborate test equipment designed for that purpose.

Researchers have recognized the need for an objective process for selecting the correct force distributions and have responded with theoretical proposals. Their efforts will be the subject of a subsequent discussion.

Energy/Power Admittance - Kennedy and Pancu's co-quad theory is incompatible with multiple-shaker techniques because the former method is based on single-point excitation. To exploit the best features of both approaches, Smith and Woods proposed the complex energy-admittance method (Reference 3). A brief discussion of an improved version of this technique follows:

The conventional definition of the kinetic energy associated with the motion of a point mass is

$$T = \frac{m}{2} [\text{Re}(\dot{x})]^2 \quad (8)$$

where m is the mass and $\text{Re}(x)$ is the real part of $\dot{x} = i\omega X e^{i(\omega t + \phi)}$. For this discussion, however, define the kinetic energy as the complex quantity.

$$\begin{aligned} T &= \frac{m}{2} \dot{x}^2 \\ &= \frac{m}{2} (i\omega)^2 X^2 e^{i(2\omega t + 2\phi)} \end{aligned} \quad (9)$$

Consider a structural system whose overall motion can be adequately described by the motion of J discrete displacements (or degrees-of-freedom), X_j . The kinetic energy associated with the motion of the j th degree-of-freedom is

$$T_j = \frac{m_j}{2} \dot{x}_j^2 \quad (10)$$

where m_j is the mass associated with the j th degree-of-freedom.

(Note: This definition implies a structural idealization with mass lumped at the degree-of-freedom locations which, in turn, implies the lack of inertial coupling between degrees-of-freedom. The implications of such an assumption are extensive in the analytic treatment of dynamic response; however, it will be subsequently shown to be of little consequence in this experimental application.)

The quantity, T_j , in Equation 10 is called the local kinetic energy. The total kinetic energy of the entire structure is given by

$$T = \frac{1}{2} \sum_{j=1}^J m_j \dot{x}_j^2 \quad (11)$$

If the system is responding in a single mode, the displacement vector x can be written

$$\bar{x} = \bar{X} e^{i(\omega t + \phi)} \quad (12)$$

or

$$\bar{x} = X_k \bar{\phi} e^{i(\omega t + \phi)} \quad (13)$$

where $\bar{\phi}$ is the eigenvector (mode shape) and X_k is the amplitude of the component to which the eigenvector is normalized (hereinafter referred to as the "key response"), i.e.,

$$X_j = \bar{\phi}_j X_k \quad (14)$$

and φ is the phase difference between excitation and response. Under this circumstance, the kinetic energy can be written

$$T = \frac{(i\omega)^2}{2} X_k^2 \sum_{j=1}^J m_j \phi_j^2 e^{i(2\omega t + 2\varphi)} \quad (15)$$

Now consider the power applied to the test article by a single force. This quantity is ordinarily defined as

$$P = \text{Re}(f) \text{Re}(\dot{x}) \quad (16)$$

where $\text{Re}(f)$ is the real part of the complex force $f = Fe^{i\omega t}$.

Instead, define the power input at the n th degree-of-freedom as the complex product

$$P_n = f_n \dot{x}_n \quad (17)$$

If force is applied at N locations, the total power is given by

$$P = \sum_{n=1}^N f_n \dot{x}_n \quad (18)$$

or for a single-mode response

$$P = \dot{x}_k \sum_{n=1}^N \phi_n f_n \quad (19)$$

If the applied forces are coherently phased and the ratio of their amplitudes are constant, the force vector f can be written

$$\vec{f} = F_m \vec{\psi} \quad (20)$$

where ψ is the normalized force vector and F_m is the normalizing force (hereinafter referred to as the "master force"), i.e.,

$$F_n = \psi_n F_m \quad (21)$$

For this circumstance, the power can be written

$$P = x_k f_m \sum_{n=1}^N \phi_n \psi_n \quad (22)$$

Now consider the complex ratio of the kinetic energy and power, i.e.,

$$\begin{aligned} \frac{T}{P} &= \frac{\frac{(i\omega)^2}{2} X_k^2 \sum_{j=1}^J m_j \phi_j^2 e^{i(2\omega t + 2\varphi)}}{i\omega X_k F_m \sum_{n=1}^N \phi_n \psi_n e^{i(2\omega t + \varphi)}} \\ &= \frac{\sum_{j=1}^J m_j \phi_j^2 X_k}{2 \sum_{n=1}^N \phi_n \psi_n F_m} e^{i\varphi} \end{aligned} \quad (23)$$

Define the complex energy/power admittance as

$$\begin{aligned} A &= \frac{2}{i\omega} \frac{T}{P} \\ &= \frac{\sum_{j=1}^J m_j \phi_j^2 X_k}{\sum_{n=1}^N \phi_n \psi_n F_m} e^{i\varphi} \end{aligned} \quad (24)$$

Examination of this expression reveals that it is the Kennedy and Pancu displacement/force admittance expression (for the key response to the master force) multiplied by a real constant. It is apparent that this complex quantity will exhibit, for a total structural-system response, all the properties exploited so successfully by Kennedy and Pancu in studying individual responses.

The quantity in Equation 24 is defined as the total-energy admittance. Also define the local-energy admittance as

$$\begin{aligned} A_j &= \frac{2}{i\omega} \frac{T_j}{P} \\ &= \frac{m_j \phi_j^2 X_k}{\sum_{n=1}^N \phi_n \psi_n F_m} e^{i\varphi} \end{aligned} \quad (25)$$

This quantity is a similarly analogous expression, in this instance expressing the response of a single degree of freedom to a multiple-force excitation. So, the energy/power admittance principle can be stated: if a structural system is excited by a series of coherently phased shakers with constant force ratios in such a manner that the system response consists of the activity of a single mode,

the complex ratios of the system's total kinetic-energy or local kinetic energies to the applied power is analogous to the complex displacement/force admittance.

The preceding derivation is more general than that presented in Reference 3. Smith and Woods showed the energy admittance to be analogous to the complex ratio of displacement to force where mean values of kinetic energy and power were used; i. e.,

$$T = \sum_{j=1}^J \frac{m_j}{2} \dot{x}_j \dot{x}_j^* \quad (26)$$

and

$$P = \sum_{n=1}^N f_n \dot{x}_n^* \quad (27)$$

where \dot{x}_j^* is the complex conjugate of \dot{x}_j .

This form tacitly assumes that all responses are coherently phased, which is unrealistically restrictive. From Equation 26, it is seen that the mean kinetic energies are always real quantities. Each admittance is computed by multiplying these real values by the complex inverse of the total power. Thus the ratio of real and imaginary components is the same for all the admittances, total and locals. Although such phase coherence is an objective of modal tuning, it can be expected that, even for well-tuned modes, isolated measurements will exhibit substantial phase variations.

The development herein shows that the aforementioned analogy holds for instantaneous complex values of kinetic energy and power. Equations 10 and 11 are, in general, distinct complex quantities and using them to compute admittances accommodates phase variations between individual response measurements.

To apply this technique in a modal survey, acceleration and force measurements are acquired and resolved into components that are in-phase and 90 degrees out-of-phase with some reference sinusoidal signal; i. e.,

$$r = \text{Re } e^{i\omega t}. \quad (28)$$

Then the accelerations and forces can be written

$$\ddot{x}_j = \bar{X}_j e^{i\omega t} \quad (29)$$

and

$$f_n = \bar{F}_n e^{i\omega t} \quad (30)$$

respectively, where \bar{X} and \bar{F} are complex quantities, i. e., their real components in-phase with the reference signal and their imaginary component leading it by a 90 degree phase.

The j th local kinetic energy can be written

$$\begin{aligned} T_j &= \frac{m_j}{2} \dot{x}_j^2 \\ &= -\frac{e^{i2\omega t}}{2\omega^2} m_j (\ddot{x}_{Rj}^2 - \ddot{x}_{Ij}^2 + i2\ddot{x}_{Rj} \ddot{x}_{Ij}) \end{aligned} \quad (31)$$

where \ddot{x}_{Rj} and \ddot{x}_{Ij} are the real and imaginary components, respectively, of \ddot{x}_j . The total kinetic energy is

$$\begin{aligned} T &= \sum_{j=1}^J T_j \\ &= -\frac{e^{i2\omega t}}{2\omega^2} \sum_{j=1}^J m_j (\ddot{x}_{Rj}^2 - \ddot{x}_{Ij}^2 + i2\ddot{x}_{Rj} \ddot{x}_{Ij}) \end{aligned} \quad (32)$$

Power input by the n th force is

$$\begin{aligned} P_n &= f_n \dot{x}_n \\ &= \frac{e^{i2\omega t}}{i\omega} \left[F_{Rn} \ddot{x}_{Rn} - F_{In} \ddot{x}_{In} + i(F_{Rn} \ddot{x}_{In} + F_{In} \ddot{x}_{Rn}) \right] \end{aligned} \quad (33)$$

and the total power is

$$\begin{aligned} P &= \sum_{n=1}^N P_n \\ &= \frac{e^{i2\omega t}}{i\omega} \sum_{n=1}^N \left[F_{Rn} \ddot{x}_{Rn} - F_{In} \ddot{x}_{In} + i(F_{Rn} \ddot{x}_{In} + F_{In} \ddot{x}_{Rn}) \right] \end{aligned} \quad (34)$$

Finally, the local-energy admittance is

$$A_j = \frac{2}{i\omega} \frac{T_j}{P}$$

$$= -\frac{1}{\omega^2} \frac{m_j (\ddot{x}_{R_j}^2 - \ddot{x}_{I_j}^2 + i 2 \ddot{x}_{R_j} \ddot{x}_{I_j})}{\left[\sum_{n=1}^N F_{R_n} \ddot{x}_{R_n} - F_{I_n} \ddot{x}_{I_n} + i (F_{R_n} \ddot{x}_{I_n} + F_{I_n} \ddot{x}_{R_n}) \right]} \quad (35)$$

Similarly, the total-energy admittance is

$$A = \frac{2}{i\omega} \frac{T}{P}$$

$$= -\frac{1}{\omega^2} \frac{\sum_{j=1}^J m_j (\ddot{x}_{R_j}^2 - \ddot{x}_{I_j}^2 + i 2 \ddot{x}_{R_j} \ddot{x}_{I_j})}{\left[\sum_{n=1}^N F_{R_n} \ddot{x}_{R_n} - F_{I_n} \ddot{x}_{I_n} + i (F_{R_n} \ddot{x}_{I_n} + F_{I_n} \ddot{x}_{R_n}) \right]} \quad (36)$$

An important advantage to the energy-admittance method is that it provides a single, concise measure of modal response for an entire structure and thereby presents the opportunity to determine modal parameters on the basis of overall structural response rather than from a series of isolated measurements. If the total-energy admittance is empirically determined, the natural frequency and damping behavior of the subject mode can be determined from the total-energy co-quad plot by application of the techniques described in the discussion of Kennedy and Pancu's co-quad theory; that is, find the resonance frequency from the maximum path-length derivative and determine the damping from Equation 3.

A more reliable means of measuring overall system damping can be obtained by interpretation of Equation 1b. This expression may be rearranged as

$$g = -(1-\beta^2) \tan \varphi \quad (37)$$

Use of this expression permits a computation of damping for each data (frequency) point; that is, measure φ in the co-quad plane for each value of β and compute a corresponding value of g . The resulting sequence of damping values can be treated statistically to attain the appropriate overall damping property.

Another important feature of the energy-admittance method is that it provides an indication of modal purity. Since the complex energy/power admittance is analogous to the classical complex displacement/force admittance, the total-energy co-quad plot for a well-tuned mode will form a circle which is centered on the imaginary axis and is tangent to the real axis. Significant deviations from this pattern indicate a lack of modal purity.

Eigenvector components are determined from local-energy-admittance co-quad plots. The diameter of a circle fit to a local-energy co-quad plot is a measure of the kinetic energy associated with that particular degree-of-freedom. If the diameter of the circle in the j th local co-quad plot is d_j , then the j th eigenvector component is

$$\phi_j = h \sqrt{\frac{d_j}{m_j}} \quad (38)$$

where ϕ_j is the j th component of the mode shape, h is a normalizing constant, d_j is the diameter of the circle in the j th local co-quad plot, and m_j is the mass associated with the j th degree of freedom.

Inspection of Equation 35 shows that d_j is directly proportional to m_j and, therefore (from Equation 38), the value of m_j has no effect on the eigenvector values. Inspection of Equation 36 shows that m_j can be thought of as a "weighting factor" for the kinetic-energy contribution of the j th degree-of-freedom. Theoretically, a well-tuned mode will have all responses in phase and the values of the various m_j 's are inconsequential to the results; that is, the measured natural frequency and damping coefficient. In practice, phase response varies slightly from one accelerometer to another due to experimental error, interference from other modes and nonproportional damping (that is, energy-dissipation distribution that is not proportional to the mass and/or stiffness distribution). So, in practical applications, while the lumped-mass values do have an effect on results, they are, effectively, subjective weighting factors and, therefore, their precise computation is desirable but not mandatory. Refinement of the mass (or weighting) matrix may moderately influence the estimates of natural frequency and modal damping but will not affect the eigenvector measurements.

Analytic-Tuning Method - The preceding discussion of the energy-admittance method described the requirement of reasonably well-tuned modes. This requirement in turn dictates the availability of an objective process for determining force distributions appropriate for pure excitation of selected modes. Such a procedure has been proposed by Asher (Reference 2). It is noted that Trial-Nash (Reference 5) suggested the same procedure,

but Asher extended the method to determine resonant frequencies in the presence of high modal density.

A generally accepted criterion for resonance of a purely excited mode is that all response be in quadrature with the excitation or, conversely, the absence of coincident response. The object of tuning, therefore, should be to select a combination of forces that produces a response devoid of a coincident component.

Consider the expression

$$\vec{x}(\omega) = [a(\omega)] \vec{F} \quad (39)$$

where $\vec{x}(\omega)$ is the complex-displacement vector,

$[a(\omega)]$ is the complex-displacement/force admittance matrix, and

\vec{F} is the excitation-force vector.

The columns of the admittance matrix are the displacement-response vectors for a unit excitation by a single shaker. This matrix can be constructed experimentally by means of a series of wideband, single-shaker, sinusoidal sweeps or by means of Fourier transform techniques applied to response data from impulse, random or rapid sinusoidal-sweep excitation.

The real and imaginary parts of the complex admittance $[a(\omega)]$ are the coincident-admittance matrix $[c(\omega)]$ and the quadrature-admittance matrix $[q(\omega)]$, respectively.

It was stated earlier that the objective of tuning was to achieve a condition of null coincident response; i.e.,

$$[c(\omega)] \vec{F} = 0 \quad (40)$$

If a solution for Equation 40 exists, the columns of $[c(\omega)]$ must be linearly-dependent and the determinant of $[c(\omega)]$ will vanish.

$$\text{Therefore, } |c(\omega_n)| = 0 \quad (41)$$

implies that ω_n is a resonant frequency and solution of the corresponding set of homogeneous equations

$$|c(\omega_n)| \vec{F}_n = 0 \quad (42)$$

yields the force distribution required to purely excite the n th mode.

Thus, Asher's analytic-tuning procedure is:

- 1) establish the coincident-admittance matrix $[c(\omega)]$ by experimental means,

- 2) identify resonant frequencies by finding the zeros of $|c(\omega)|$, and
- 3) find the combination of forces needed to excite that mode by solution of Equation 42.

In order to deal with determinants, it is necessary that the coincident-admittance matrix be square; thus, the number of measured responses must equal the number of forces to be applied. The locations at which these responses are measured are, within practical limitations, arbitrary. A likely choice would be the points of force application. This would satisfy the requirement of an equal number of responses and forces. Effectively positioned shakers would be located at points that participate heavily and diversely in the modes being excited.

It is implicitly assumed in this technique that if responses at selected locations are all in quadrature with the excitation, then the entire structure is in pure quadrature response. This is generally a reasonably safe assumption; however, pathological exceptions can be imagined. The probability of this circumstance occurring might be diminished by replacing the individual responses in the coincident-admittance matrix with linear combinations of coincident responses; that is,

$$[C(\omega)] = [B] [c(\omega)] \quad (43)$$

where $[B]$ is a matrix of real constants.

A likely choice for the elements of $[B]$ would be parameters describing kinematic behavior; e.g., translation or rotation of key specimen components. This process partially relieves the constraint that the number of responses considered equal the number of forces applied. The number of responses entering into the tuning calculations can, with this scheme, exceed the number of excitation points.

Additional generality would be added to the technique if more forces could be applied than responses measured. Trial-Nash recommended the columns of the admittance matrix be the responses to sets of fixed, linearly independent force distributions. In that approach, the solution of Equation 42 yields the combination of force distributions needed. Linear independence of the force distributions requires that the number of forces applied be equal to or greater than the number of distributions considered. Thus, this technique permits more applied forces than measured responses. The necessity of a square admittance matrix requires that the number of force distributions considered equal the number of responses (or combined responses) considered.

The alternatives of the two preceding paragraphs can be combined to make the analytic tuning more versatile.

Although the Asher tuning method was selected as an objective procedure for modal tuning, it is not entirely objective. The selection of locations for response measurements to fill the

admittance matrix is arbitrary and requires judgment on the part of the experimenter. This choice must, if only slightly, affect results. More importantly, if inappropriate excitation points are selected, no amount of data processing can predict the correct force distributions. Even if good excitation and response locations are chosen, different modes require different points for most effective application of forces. Researchers have addressed the problem of how many shakers are required to separate a collection of modes, but little has been written regarding how to select the best places to drive the specimen and where to measure its response.

Hardware Description

MODALAB has been designed to be a flexible, software-oriented system. To provide this, a powerful hardware system is required. This section describes the hardware components that comprise the MODALAB. The system block diagram is shown in Figure 6. For purposes of discussion it may be broken into nine basic subsystems.

- 1) The Computer/Data-Storage System includes the following devices:
 - a) Central Processor: Digital Equipment Corporation PDP-11/45 with the following important features:
 - i) 56K 16-bit words of core memory (960 nsec)
 - ii) 8K words of MOS memory (450 nsec)
 - 2) The Analog-Data System is made up of two Datel 256 multiplexer/analog-to-digital converter units of 128 differential-input channels each. The analog-to-digital converters have 12-bit (1 part in 4096) resolution and a range of $\pm 10.0V$. The units are sampled alternately to provide a maximum system sampling speed of 200,000 channels per second. The analog system also includes 16 digital-to-analog converters used for computer control of the Shaker Control System.
 - 3) The Interface System is a special-purpose device that provides, in addition to conventional
- iii) Hardware floating-point processor

iii) Hardware floating-point processor

(This fast and powerful processor system is essential to the realtime digital-filtering tasks, the FFT processors, and to other heavily used arithmetic routines.)

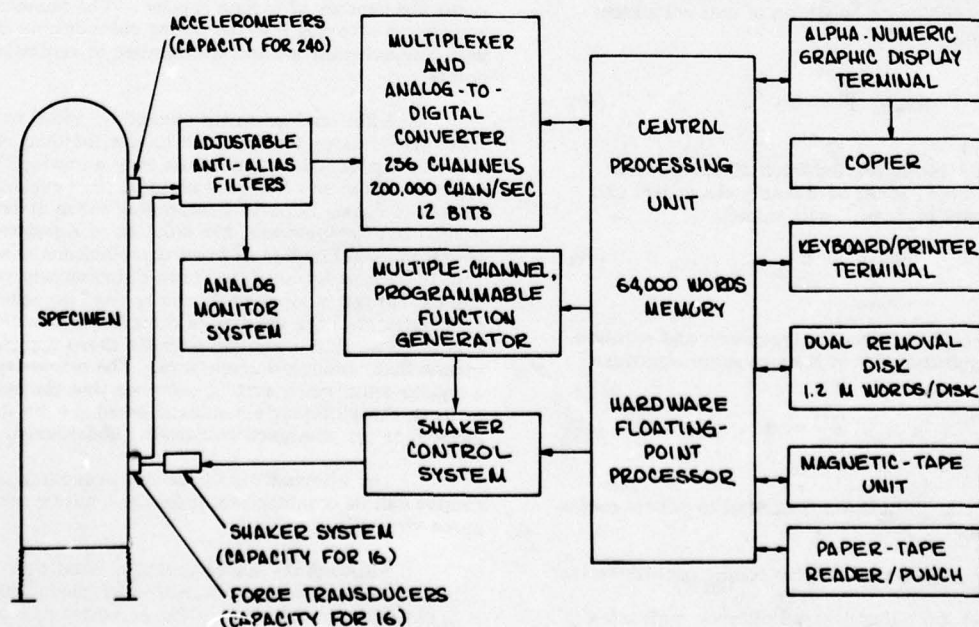


Figure 6. Block Diagram of MODALAB

data-acquisition system control, the following functions for sine-wave testing:

- a) multiple-channel, programmable function generator for experiment control,
 - b) Analog-Data System control, and
 - c) the hardware phase of the realtime digital-filtering algorithm.
- 4) The Shaker-Control System provides amplitude-, phase- and frequency-controlled stimuli to the power amplifiers for multiple-shaker sine-wave testing. These variables may be manually or computer controlled. In addition, an analog-servo system is used to control the excitation level.
 - 5) The Analog-Monitor System includes the following:
 - a) a 32-channel multiplexer/signal-conditioning system to construct a 16 Lissajous-pattern display on the monitor oscilloscope,
 - b) frequency display with .001 Hz resolution, and
 - c) patch panel allowing monitoring access to any system channel by manual patching.
 - 6) The Signal-Conditioning System provides transducer power, amplification, ac coupling, and adjustable low-pass filtering.
 - 7) The Operator-Interaction System includes a conventional keyboard terminal and an alphanumeric/graphics terminal with copier. The keyboard terminal is used for program entry and editing, and the alphanumeric/graphics system is used for high-speed data output and for graphical presentation of results.

The items described above are shown in Figure 7.

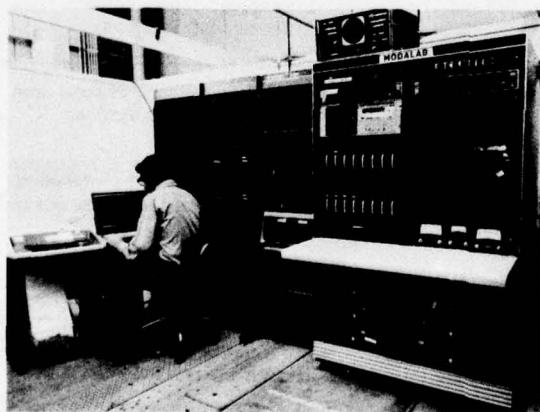


Figure 7. Photo of MODALAB

MODALAB includes instrumentation and excitation systems but the previously described hardware (subsystems 1 through 7) can be used in conjunction with virtually any set of shakers and accelerometers. The units included in the system are described below.

8) The Instrumentation System consists of:

- a) Accelerometers: 250 Unholtz-Dickie 1000-PA devices. These are amplifier-followed piezoelectric instruments whose significant characteristics are:

Sensitivity - 1 v/g

Frequency Response - $\pm 5\%$ from .1 Hz to 2 kHz

Effective self-induced noise less than 10 μ g rms.

- b) Load cells: Strain-gage units with internal amplification having a sensitivity of 2.24 v/Newton (.1 v/lb). The frequency response matches the nominal accelerometer characteristic.

- 9) The Excitation System consists of Acoustic Power Systems Model 113 shakers and Model 114 power amplifiers. They provide up to 1.56 Newtons (35 force-lb) with a stroke of 16 cm (6.25 in.). The amplifiers are dc coupled and have the choice of voltage or current feedback control. They normally operate with current feedback.

A typical shaker/load cell/accelerometer installation is shown in Figure 8.

Modal-Test Software Description

This section discusses the approach taken in MODALAB software development and describes

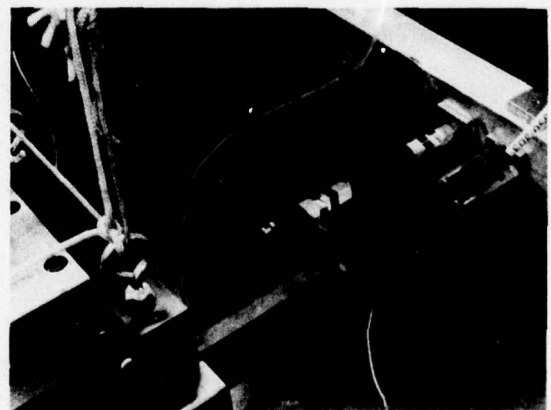


Figure 8. Photo of Shaker/Load Cell/Accelerometer Installation

programs prepared for performance of sinusoidal-excitation modal tests.

One of the objectives of MODALAB's development was to emphasize software rather than hardware in order to provide system versatility. In accordance with this objective, emphasis has been placed on FORTRAN rather than assembly-language programming, thereby enabling engineers to adapt the system to diverse uses without becoming involved in machine-language procedures.

MODALAB's software can be divided into two categories: 1) a generalized software package (that is, FORTRAN-language programs) and 2) a specific software/hardware interface. The latter category is composed of a group of assembly-language subroutines which can be called in FORTRAN routines in the same manner as FORTRAN functions.

The modal-test FORTRAN-language software package can be divided into four categories: 1) input/output routines used to communicate information to the MODALAB and to transmit test/analysis results to other processors, 2) programs to automatically check-out the data-acquisition system, 3) data-acquisition programs, and 4) data-processing programs. The bulk of modal-test software is in categories 3 and 4; that is, data acquisition and processing. The major programs that make up the data-acquisition and data-processing software packages are tabulated below with a brief description of their function.

Procedures

MODALAB's modal-test procedure is a systematic application of the previously discussed method of force-distribution selection and the complex energy-admittance method. The discussion of procedures will be in three parts: 1) pretest procedure, 2) data-acquisition procedure, and 3) data-processing procedure. It will be seen that data processing is an integral part of the data acquisition sequence.

Pretest Procedure - In addition to the preparation ordinarily needed for a modal test, use of MODALAB requires some unique preparation.

The selection of shaker and accelerometer locations is a prerequisite for any vibration test but that selection is, as discussed in the preceding section, particularly important for application of the analytic-tuning procedure. A thorough pretest analysis is helpful in making these selections.

Since most of the data processing is done in realtime or shortly after data acquisition, most of the analytic preparation should be done before the test. Application of the energy-admittance method requires realtime calculation of kinetic energy. Computation-time considerations dictate a diagonal mass matrix for realtime calculations; however, accuracy considerations require a full mass matrix for orthogonality/momentum checks on analytical and experimental modes. These mass matrices and the

DATA-ACQUISITION SOFTWARE		DATA-PROCESSING SOFTWARE	
Wideband Sweep	- Single-shaker, logarithmic, sinusoidal sweep	Wideband-Sweep Processor	- Displays complex admittance and/or co-quad plots
	- Simultaneous acquisition and digital filtering of 1 force and 240 channels of acceleration		- Displays linear combinations of admittance data
	- Realtime display of complex transfer function for selected channel		- Computes and displays complex transmissibility
Narrowband Sweep	- Multiple-shaker, linear, sinusoidal sweep	Modal-Tuning Package	- Processes wideband-sweep data to determine: 1) resonant frequencies 2) force distributions
	- Simultaneous, acquisition, digital filtering and processing of 16 forces and 240 acceleration measurements		
Transient Response	- Realtime display of total energy-admittance plot	Narrowband-Sweep Processor	- Interactive editing of total-and local-energy admittances
	- Computer-controlled sinusoidal decay		- Tabulates resonant frequency, structural damping, and normalized eigenvector
Bulk-Data Acquisition	- Simultaneous acquisition of multiple-channel response transients	Transient-Response Processor	- Momentum/orthogonality check
	- Multiple-channel storage of unfiltered data in memory, on magnetic disk, or on magnetic tape		- Plots decay of individual acceleration measurements
		Fast Fourier Processor	- Plots kinetic-energy decay
			- Generates and plots complex Fourier transforms and power spectral densities for digital histories

analytic mode shapes must be computed and stored before the test begins. Formulation of the mass matrices usually requires reduction from a detailed, discretized mathematical model of the test article to an idealization that has degrees-of-freedom that correspond one-for-one with accelerometer locations.

Finally, programs are mobilized on a large-scale scientific computing system to process data generated by MODALAB. These programs generate tabular and graphic summaries of test results in a more elaborate format than possible with MODALAB's output devices. These programs also include dynamic response programs to quickly determine the effects of new-found modal information on critical responses of the test article.

Data-Acquisition Procedure - After analytic preparation is complete and the excitation and instrumentation devices have been installed and checked out, data acquisition may begin. A flow diagram of this procedure appears in Figure 9. The initial step is a series of logarithmic, single-shaker, wideband, sinusoidal sweeps through the frequency range of interest. These sweeps are not continuous. Excitation dwells at one frequency while the output of each accelerometer is measured, digitized, processed and stored on magnetic disk in the form of a digital, complex measurement of acceleration. Then the frequency is incremented slightly and the process repeated. During the actual data acquisition, the complex transfer function for a selected accelerometer is displayed, in realtime, on the graphic terminal (see Figure 10). Superimposed on this display is a plot of the force history. It is customary to servo control force on the basis of a constant response from a selected transducer. This procedure minimizes the effects of nonlinear behavior. As a result the force diminishes when passing through a resonance. This plot is useful in monitoring the progress of the sweep and quality of the data being acquired. After a sweep is completed, the single-shaker sweep postprocessor converts the digital acceleration data to a digital, complex transfer function for each accelerometer and stores those quantities on another disk file. These data are available on a near-instant basis in the form of an admittance plot on the display terminal. Figure 11 is the typical complex transfer-function plot.

When satisfactory single-shaker sweep data have been acquired, the analytic-tuning analysis is undertaken. The procedure is to assemble selected coincident responses in a sequence of coincident-admittance matrices, one for each frequency. Determinants of these matrices are computed and plotted versus frequency. Figure 12 is typical of such a plot. Zeros of this plot indicate resonant frequencies. The operator may select one of these zeros for examination by placing the graphic-terminal's cursor in the vicinity of the crossing. MODALAB automatically determines the resonant frequency and computes the force distribution needed to tune that particular mode. This procedure is repeated for each zero and the results recorded.

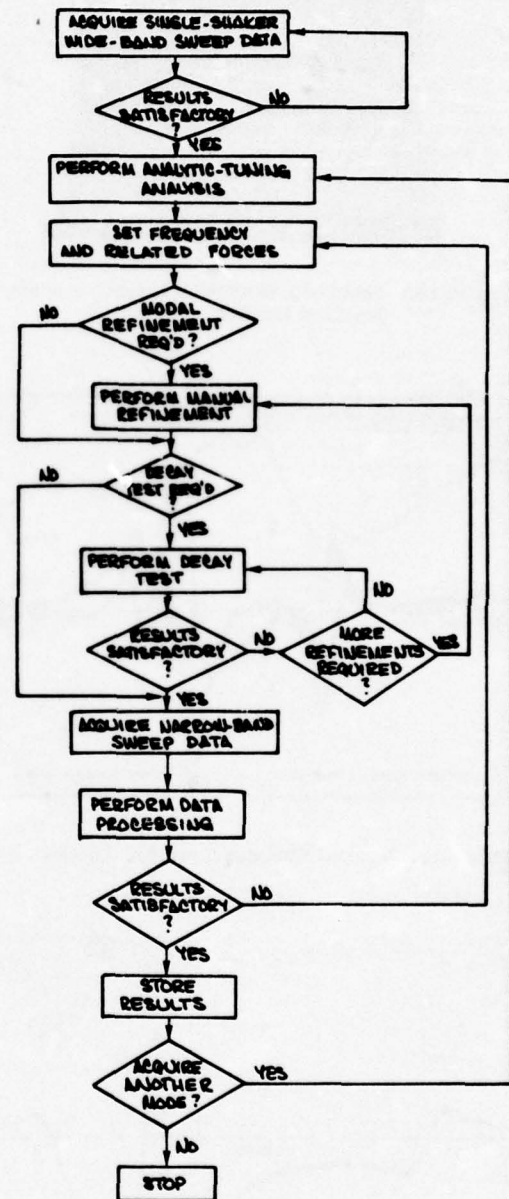


Figure 9. Data-Acquisition Procedure



Figure 10. Photo of a Realtime Complex Transfer-Function Display

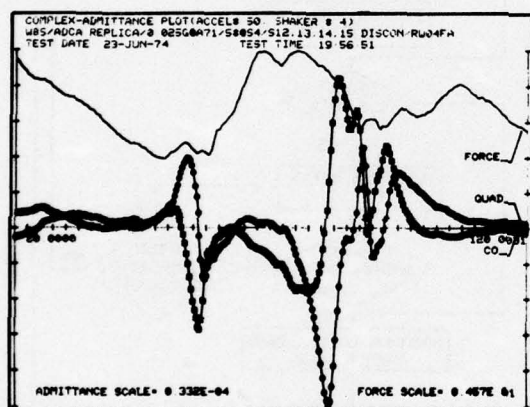


Figure 11. Typical Complex Transfer-Function Plot

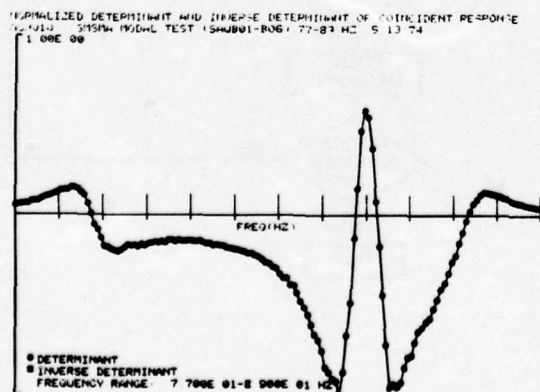


Figure 12. Typical Coincident-Admittance Determinant Plot

The multiple-shaker phase of the test begins by selection of a mode for examination. The choice is based on review of single-shaker sweep data, results of the analytic-tuning analyses, and pretest predictions. The approximate resonant frequency and corresponding forces, as determined by Asher analysis, are set in the frequency generator and the shaker-control system, respectively. If necessary, the excitation parameters can be varied to refine the modal tuning. Effects of these adjustments are observed on the analog monitor which simultaneously displays up to 16 Lissajous figures for selected pairs of force and acceleration responses. Figure 13 is a photo of this display. Refinements are also aided by rapid data processing. A criterion for modal tuning is that the total-energy admittance be a pure quadrature quantity. During the refinement process, data from all accelerometers may be acquired, and a complex value of total-energy admittance computed and plotted in the co-quad plane on the graphic terminal. This plot traces progress towards pure quadrature response as successive sets of excitation parameters are analyzed.



Figure 13. Photo of Multiple-Lissajous Display

When the modal tuning has been adequately refined, the operator has the option to perform a series of decay tests. These decays serve to further verify the purity of modal tuning as a smooth decay demonstrates the absence of participation by neighboring modes. As currently configured, MODALAB accommodates acquisition of decay data from up to sixteen channels. The Decay Postprocessor displays individual decays or combinations of the measured decays including decay of kinetic energy. Figure 14 is a plot of a sum of decaying kinetic energies. The amplitude is plotted on a logarithmic scale which produces a "straight-line" decay. Decay combinations provide a good representation of the test specimen's overall damping behavior.

Multiple-shaker data are acquired in narrowband sweeps. The sweep bandwidth is generally about one or two percent of the resonant frequency for a modal damping on the order of one percent of critical. The multiple-shaker sweeps are

linear; that is, a constant frequency increment is used. When the operator is satisfied with the tuning near resonance, control is passed to the computer which resets the frequency to the low end of the sweep band. Force and acceleration data are acquired, local and total admittances are computed and stored on a magnetic disk. During the multiple-shaker sweep, a realtime display of the total-energy admittance appears on the graphics terminal in either co and quad versus frequency or co versus quad format, at the operator's option. This display, like the transfer-function plot generated during the single-shaker sweep, is useful for monitoring progress and quality of the test.

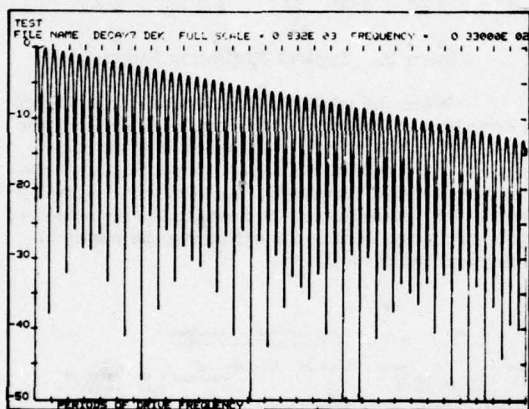


Figure 14. Typical Decay Plot

When the sweep is completed, the acquired data are stored on a disk file along with historical information which includes time and date of data acquisition, excitation and digital-filtering parameters, instrument calibrations and locations, etc.

Data-Processing Procedure - Figure 9 shows that processing of data is an integral part of the data-acquisition procedure. A flow diagram for the postprocessing is shown in Figure 15.

The initial step is interactive editing of the total-energy admittance. The initial display (see Figure 16) is a plot of co, quad and path-length derivative versus frequency. This display presents three criteria for selection of the resonant frequency; i.e., maximum path-length derivative, maximum quadrature response, and zero coincident response. The operator selects the resonance with the vertical cursor. The option to change this selection exists throughout editing of the total-energy admittance.

The next step is to display the total-energy admittance in a co versus quad format (see Figure 17). A circle is fitted to the data points by a least-squares technique. The fit of this circle and its location in the co-quad plane permits the operator to make a subjective assessment of the data. The operator, through use of the cursors, has the option to: 1) select a different resonant frequency, 2) reduce the sweep bandwidth, and 3) eliminate individual data points.

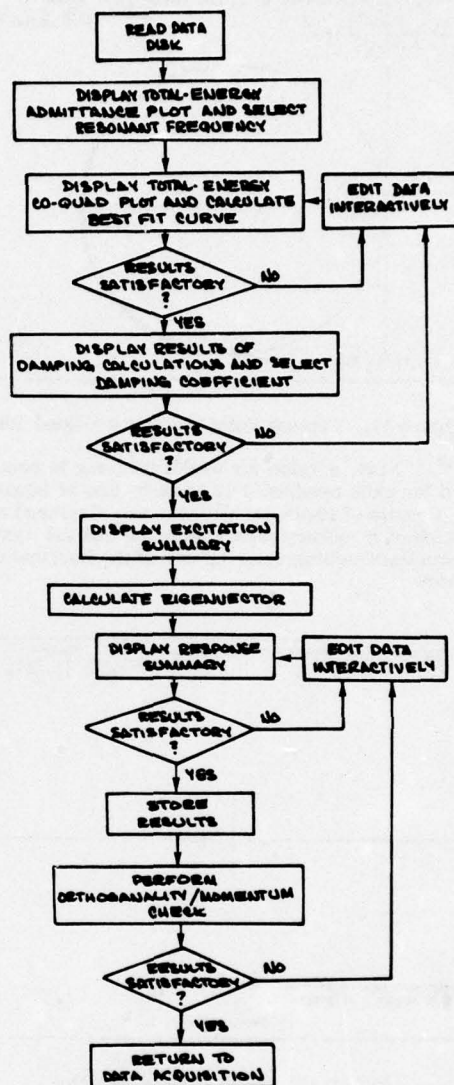


Figure 15. Data-Processing Procedure

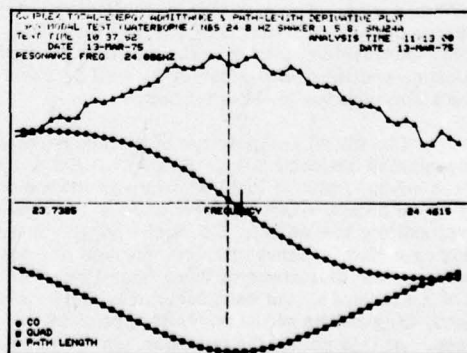


Figure 16. Typical Total-Energy Admittance Plot

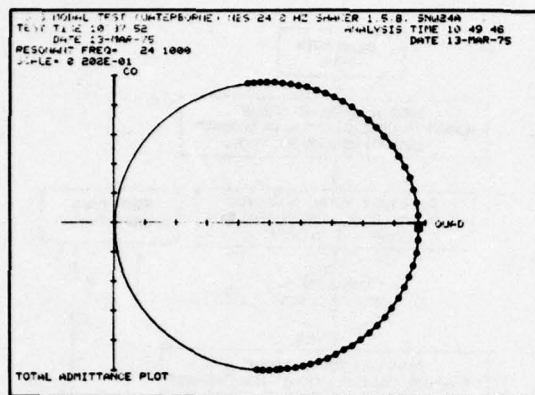


Figure 17. Typical Total-Energy Co-Quad Plot

Next, a value for modal damping is computed for each retained data point by use of Equation 37. Results of these calculations are displayed as a function of frequency (see Figure 18) and the operator selects the damping value by use of the horizontal cursor.

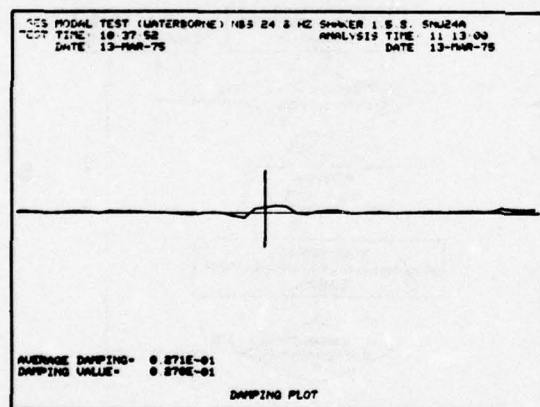


Figure 18. Typical Damping Plot

This completes editing of the total-energy admittance data. The next step is to display a description of the excitation (see Figure 19). This display summarizes the force distribution exerted at resonance and its phase behavior as well as each force's contribution to the total power.

The initial computation of the eigenvector is accomplished automatically. MODALAB fits a circle to each co-quad plot of local-energy admittance data. Only those points which were retained in the total-energy editing are used in the local-energy curve-fitting exercise. Eigenvector components are computed from the diameters of these best-fit circles by use of Equation 38. As each local admittance is processed, diagnostics of the curvefit appear on the screen. At this point, the operator has the option to display any of the local-admittance plots and further

edit them by: 1) reducing the sweep bandwidth, 2) deleting individual data points, 3) substituting new initial values for the curvefit iteration process, or 4) establishing the curvefit subjectively.

EXCITATION SUMMARY

SANB06 SHSMA WITH 100. 87 3516 HZ. CORRECT ASHER TUNING
TEST TIME 16 02 08 ANALYSIS TIME 16 13 53
DATE 13-MAY-74 DATE 13-MAY-74

MEASURED RESONANT FREQUENCY= 87 4231

SHAKER	FORCE			POWER		
	FORCE	NORMALIZED	PHASE	POWER	PUR-TOT	PHASE
1	0.037	1.000	0.0	0.101E-01	0.777	0.0
2	0.018	0.476	-7.3	0.627E-03	0.048	0.0
3	0.019	0.507	-6.2	0.170E-02	0.136	0.0
4	-0.024	-0.647	-8.1	0.410E-03	0.031	0.0
5	0.003	0.001	-18.4	0.103E-03	0.008	106.7
6	0.014	0.376	-8.1	0.220E-03	0.018	0.0

Figure 19. Typical Excitation Summary

When the editing of local-energy admittance is complete, a Response Summary is presented (see Figure 20). This display includes a description of the test, time and data of data acquisition and analysis, the resonant frequency, the structural-damping coefficient, tabulation of the normalized eigenvector, and a tabulation of data for critiquing the purity of tuning and the curvefit.

RESPONSE SUMMARY - FINAL

SANB13 SHSMA WITH 58 UT 82 1427 HZ SANB1
TEST TIME 13 32 39 ANALYSIS TIME 13 35 15
DATE 14-MAY-74 DATE 14-MAY-74

MEASURED RESONANT FREQUENCY= 82 0779
MEASURED STRUCTURAL DAMPING COEFFICIENT, G= 0.0116

ACCEL	EIGENVECTOR		TOTAL RESPONSE		CRITIQUE	
	NORM	GMC	ENERGY ADMIT	ENERGY ADMIT	PHASE	% OF AVE ITER ERROR
1	0.113	0.009	0.200E-04	0.200E-04	-6.6	3.1 7.9 5
2	-0.088	0.001	0.128E-06	0.429E-06	99.7	13.0 0.36 3
3	-0.129	0.018	0.267E-04	0.274E-04	178.8	3.2 5.1 4
4	0.944	0.155	0.360E-03	0.360E-03	-1.1	2.0 7.2 4
5	0.986	0.170	0.393E-03	0.386E-03	-1.1	2.0 8.3 1
6	1.000	0.174	0.404E-03	0.399E-03	-1.2	2.0 7.8 3
7	0.014	0.000	0.600E-06	0.379E-06	-34.9	15.0 5.1 13.0
8	-0.076	0.009	0.205E-04	0.163E-04	-163.2	4.3 8.1 8.0
9	-0.034	0.008	0.390E-06	0.177E-06	112.8	5.0 8.9 131.1
10	-0.038	0.001	0.381E-05	0.280E-05	-178.5	5.0 1.0 30.1
11	0.036	0.001	0.250E-05	0.249E-05	-8.9	4.1 4.8 82.4
12	0.038	0.001	0.310E-05	0.301E-05	22.9	5.0 10.5 30.8
13	0.054	0.001	0.260E-05	0.188E-05	36.0	5.0 1.0 88.9
14	0.471	0.007	0.200E-03	0.200E-03	-3.8	8.1 0.4 4.8
15	0.569	0.127	0.294E-03	0.288E-03	-0.6	2.0 0.0 3.0
16	-0.480	0.241	0.500E-03	0.490E-03	0.0	3.0 0.0 3.0
17	0.008	0.010	0.234E-04	0.231E-04	87.6	4.0 6.8 34.3
18	-0.048	0.002	0.561E-06	0.240E-06	-121.3	13.0 0.0 17.0
TOT		1.004	0.230E-02	0.220E-02		

Figure 20. Typical Response Summary

The first column is the eigenvector normalized to a maximum component equal to unity. The second column is the generalized-mass contribution. This quantity is described in detail in Reference 6. Briefly, the GMC is the fraction of the total kinetic energy associated with the motion of a single accelerometer. The diameter of the circle fit to the total-energy admittance data is equivalent to the total kinetic energy, and diameters of circles fit to local data represent the kinetic energy associated with their respective transducers. Thus each GMC is equal to the diameter of the respective local co-quad plot divided by the diameter of the total-energy data. The sum of GMC's should equal unity. Deviations from this result indicate questionable data or poor phase coherence. The third column is the modal kinetic energy (that is, the diameter of the local co-quad

plot) and the fourth column is the overall kinetic energy (that is, the distance from the origin to the resonance point in the local co-quad plot). The latter quantity includes residual effects of adjacent modes. It is noted that the overall energy is the quantity that would be obtained by the dwell technique. For a well-tuned mode these two quantities should be in reasonable agreement. The fifth column tabulates the phase of each accelerometer's response. For a well-tuned mode these values should be near zero or ± 180 deg. The last three columns constitute a critique of the curvefit. The first of these lists the number of iterations required to attain a satisfactory fit. The error is listed in percent and is equal to the distance from the data point to the best-fit circle divided by the radius of that circle.

When the operator is satisfied with his results, they are stored in the disk file associated with the particular mode.

The final step in the data processing is to perform a momentum/orthogonality check of the just-determined eigenvector with analytically predicted modes and previously measured experimental modes. A mass matrix and theoretical mode shapes are stored on a magnetic disk for this purpose. Orthogonality with respect to a rigid-body mode is a measure of the corresponding residual momentum in the test specimen. For a simulated free suspension, this quantity should be near zero. Figure 21 is a typical summary of an orthogonality/momentum check.

ORTHOGONALITY OF TEST MODES 13 28 02 09-AUG-70

ROW/COLUMN NUMBER IS TEST MODE MASS MATRIX IS RFULL3

TEST MODE ID	RNC01K01	FREQUENCY	11 595 HZ
1	RNC01K01	11 595 HZ	
2	RNC02C01	12 311 HZ	
3	RNC03I01	12 515 HZ	
4	RNC04D01	12 896 HZ	
5	RNC05I01	16 393 HZ	
6	RNC06A01	19 400 HZ	

	1	2	3	4	5	6
1	1.000	0.038	-0.322	-0.020	0.237	0.068
2	0.038	1.000	0.466	0.398	0.667	-0.100
3	-0.322	0.466	1.000	0.076	0.130	-0.014
4	-0.020	0.398	0.076	1.000	0.132	-0.060
5	0.237	0.667	0.130	0.132	1.000	-0.032
6	0.068	-0.100	-0.014	-0.060	-0.032	1.000

Figure 21. Typical Momentum/Orthogonality Check

At this point, the operator has the option to copy the results of postprocessing, on either magnetic or paper tape for transmission to another computer and further processing. If another mode is to be obtained, the preceding procedure is repeated beginning with selection of the excitation parameters from results of the analytic-tuning analysis.

Test Results

One of MODALAB's early applications was a modal survey of a structural simulation of the Large Space Telescope. Figure 22 is a photo of the LST Simulator. This specimen is 9.1 m (30 ft) long and weighs 6,000 kg (13,000 lb).

One of the main concerns in developing the LST is the effect of low-level dynamic excitation on the behavior of the optical system. Figure 23 shows some of the components of the LST system. The control-moment gyros are potential sources of

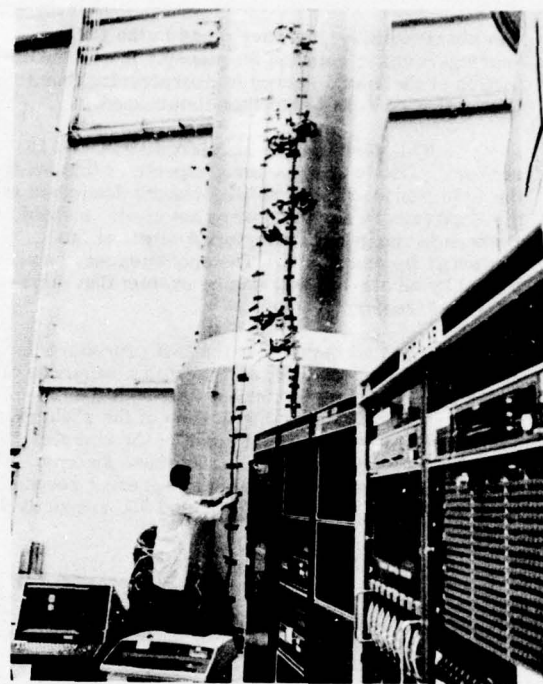


Figure 22. Photo of the Large Space Telescope Simulator

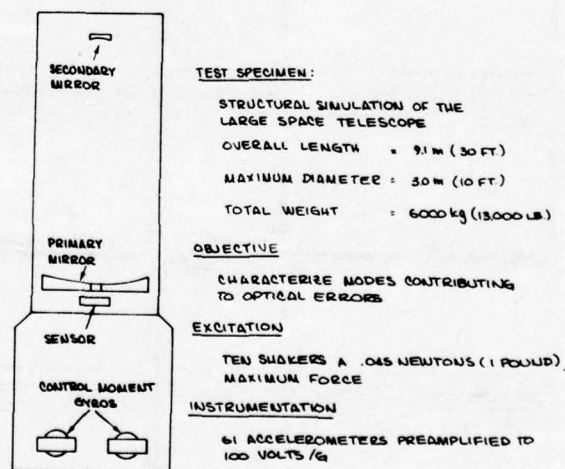


Figure 23. Large Space Telescope Simulator Modal Test

disturbance. Their imbalance may produce enough dynamic activity to create relative motion between key optical components and, thereby, degrade the image quality. Prior to the modal test, a series of transfer-function tests were performed in which low-level forces were applied to the CMG simulator and optical-component motions were measured in order to compute image distortion. A significant disturbance

was observed at a frequency close to the CMG bearing-retainer rotation frequency. It was the objective of the modal survey to characterize those modes that contributed to this disturbance.

This test used 61 accelerometers and 10 shakers. Due to the low-level aspects of this study, the 1.56 Newton (35-lb) output shakers described in the Hardware Description were not used. Instead, shakers having a maximum force output of .045 Newton (1 lb) were used. The specimen was supported by an air-bag suspension system that simulated a "free-free" condition.

The test began (per the test procedure described in the preceding section) with a sequence of wideband, single-shaker sweeps through the frequency ranges of interest with each of the shakers. Figure 24 is a composite of some of the complex transfer functions obtained during these sweeps. The first, second, and third columns represent responses to excitation by shakers #7, #8, and #9, respectively.

The first, second, and third rows represent response at the attachment locations of shakers #7, #8, and #9, respectively. The frequency range of these plots is from 27 to 38 Hz. What appears to be classical single-mode response behavior can be observed in each plot between 34 and 35 Hz. This corresponds to the disturbance measured during the optical-system transfer-function tests.

With regard to the low-level aspects of this test, it is noted that the largest force applied to this 6,000-kg (13,000-lb) specimen was .022 Newton (1/2 lb) and the largest response shown in Figure 24 is less than 1 micron (40 microinches). One plot has a maximum response of .25 microns (10 microinches).

It is also noted that symmetry of the transfer-function array is a demonstration of the dynamic version of Maxwell's Reciprocity Theorem; i.e., the response at point "a" due to excitation at point "b" is identical to the response at point "b" due to a like excitation at point "a".

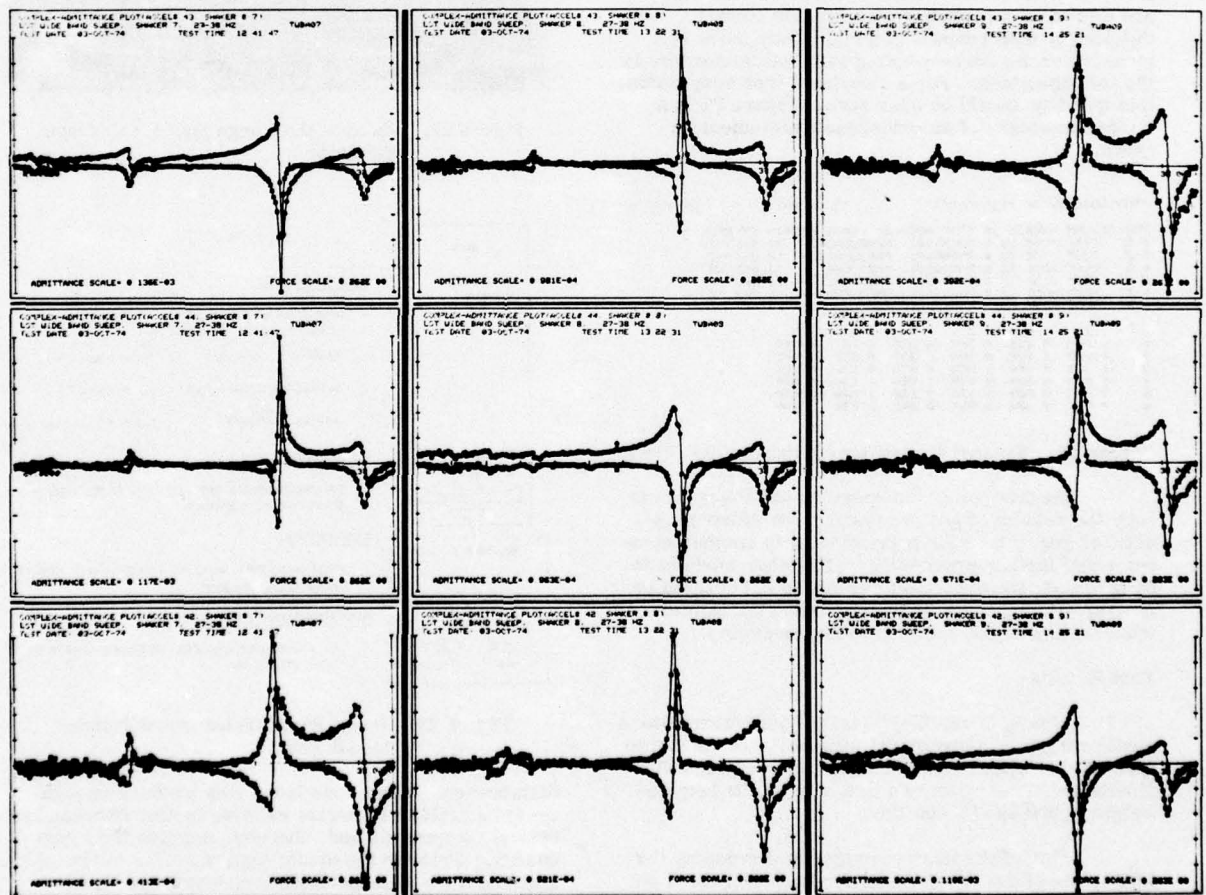


Figure 24. LST Simulator Modal Test - Array of Complex Transfer Functions

The real parts of the admittances shown in Figure 24 were used to identify the resonant frequencies and their associated force distributions using the Asher technique. Figure 25 is a plot of the coincident-admittance determinant as a function of frequency. The two zeros between 34 and 35 Hz indicate the presence of not one, but two modes in that frequency interval. The presence of these dual modes is not readily discernable by inspection of Figure 24.

It is likely that a multiple-shaker test conducted by the traditional iterative-tuning procedure to characterize these modes would have ended in frustration without *a priori* knowledge of the presence of two closely spaced modes. It is also questionable whether analytic mode-separation methods applied to the transfer functions of Figure 24 would have identified two distinct modes between 34 and 35 Hz.

The force distributions determined by the Asher analysis were successively set in the force control system and, without additional tuning, narrow-band multiple-shaker sweeps were performed for each mode. The resulting total-energy admittances

are shown in Figure 26. It is apparent that nearly perfect tuning was achieved for each mode. There is no evidence of modal mixing in either set of plots.

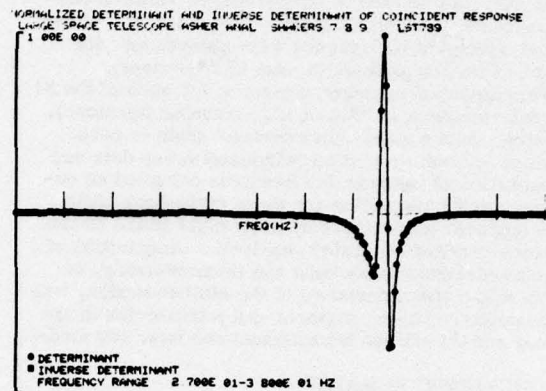


Figure 25. LST Simulator Modal Test - Coincident-Admittance Determinant vs Frequency

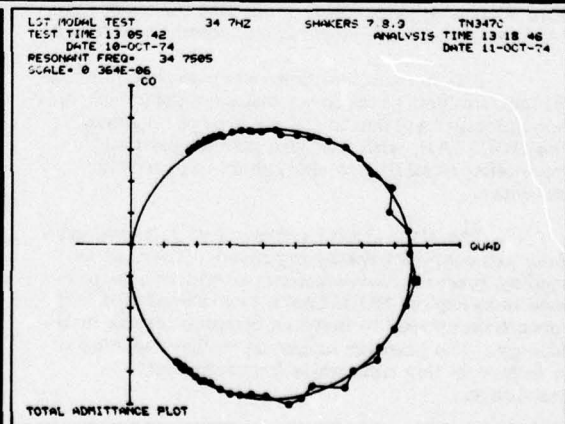
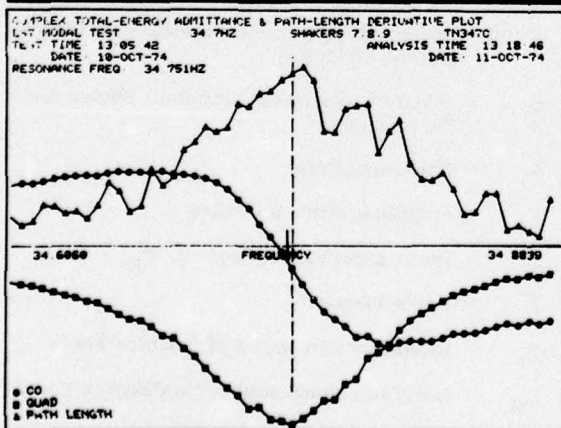
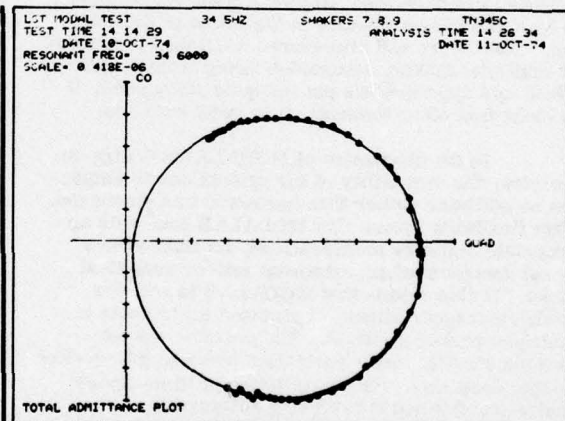
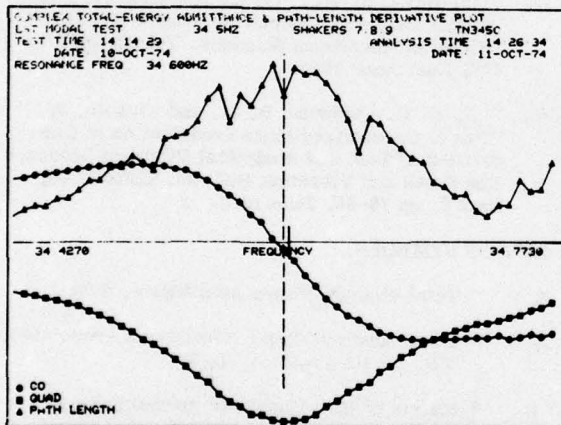


Figure 26. LST Simulator Modal Test - Total-Energy Admittance Plots

Time and manpower requirements are important characteristics of any test technique. The test described above investigated two frequency ranges; 27 Hz to 38 Hz and 50 Hz to 65 Hz. These ranges contained the bearing-retainer rotation frequency and its first harmonic, respectively. Wideband sweeps of both ranges were performed with each of the ten shakers (a total of 20 sweeps). Transfer functions were measured for each of the 61 accelerometers (a total of 1220 transfer functions). Sixteen modes were characterized; eight in each range. Acquisition of the wideband-sweep data and generation of the transfer functions occupied an engineer and a technician for three eight-hour shifts. An engineer spent approximately eight hours on the force-distribution (Asher) analysis. Acquisition of the narrowband-sweep data and its processing, to determine characteristics of the sixteen modes, was accomplished by an engineer and a technician in approximately sixteen hours (about one hour per mode).

CONCLUDING REMARKS

This report has described MODALAB's hardware system, some of its software, and the current procedure for modal testing with MODALAB. Results presented show MODALAB and its methods to be a significant advance in the art of modal testing. The theory and procedures described are based on multiple-shaker, sinusoidal-sweep techniques. While this approach has proved quite successful, it is clear that other methods show great promise.

In the discussion of MODALAB's design objectives, the versatility of the system due to emphasis on software rather than hardware was discussed. This flexibility means that MODALAB can, with appropriate software modifications, be adapted to a broad spectrum of experimental and/or analytical tasks. It also means that MODALAB is not, for modal-test applications, committed exclusively to multiple-shaker methods. The controversy concerning analytic mode separation and multiple-shaker testing continues. The installation of time-series analysis codes and curvefitting software in MODALAB would make it not only the most powerful multi shaker system existing but also the most powerful analytical mode-separation system in existence.

It is certain that there are existing theoretical test/analysis procedures that have gone unused or incompletely used due to the absence of a system, like MODALAB, with adequate data acquisition/processing capability to apply them to practical problems.

The MODALAB hardware and software systems are constantly being improved. There is an ongoing research/development program whose purpose is to exploit MODALAB's data-acquisition and -processing power to improve dynamic testing methodology. The primary emphasis in these studies is to reduce testing time while improving data reliability.

REFERENCES

- (1) Lewis, R. C. and Wrisley, D. L., "A System for the Excitation of Pure Natural Modes of Complex Structures," *Journal of Aerospace Sciences*, Vol 17, No. 11, pp 705-722, November 1950.
- (2) Asher, G. W., "A Method of Normal Mode Excitation Utilizing Admittance Measurements," *Proceedings of the National Specialists Meeting on Dynamics and Aeroelasticity*, Institute of Aerospace Sciences, Fort Worth, Texas, pp 79-76, November 1958.
- (3) Smith, S., and Woods, A. A., Jr., "A Multiple-Driver Admittance Technique for Vibration Testing of Complex Structures," *The Shock and Vibration Bulletin*, Bulletin 42, Part 3, pp 15-23, January 1972.
- (4) Kennedy, C. C. and Pancu, C. D. P., "Use of Vectors in Vibration Measurement and Analysis," *Journal of Aerospace Sciences*, Vol 14, No. 11, pp 603-625, November 1947.
- (5) Trial-Nash, R. W., "On the Excitation of Pure Natural Modes in Aircraft Resonance Testing," *Journal of Aerospace Sciences*, Vol 25, pp 775-778, December 1958.
- (6) Hull, R. E., Bejmuk, B. I., and Nichols, J., "Use of Generalized Mass Contribution in Correlation of Test and Analytical Vibration Modes," *The Shock and Vibration Bulletin*, Bulletin 43, Part 3, pp 79-86, June 1973.

LIST OF SYMBOLS

- A = Total-Energy/Power Admittance, T/P
- A_j = Local-Energy/Power Admittance Associated With the jth Location, T_j/P
- B = Matrix of Real Constants (probably kinematic parameters)
- $[C(\omega)]$ = Combined-Response Coincident-Admittance Matrix, $[B][c(\omega)]$
- D_j = Modal-Displacement Amplitude Factor for the jth Mode
- F = Force Amplitude
- F_j = Amplitude of the jth Force
- \bar{F} = Force Amplitude (Complex), $F_R + iF_I$
- \vec{F} = Force Vector
- F_I = Imaginary Component of Complex Force
- F_{Ij} = Imaginary Component of jth Complex Force
- F_R = Real Component of Complex Force
- F_{Rj} = Real Component of jth Complex Force

G_j	= Generalized Force in the jth Mode	$[q(\omega)]$	= Quadrature Displacement/Force Admittance Matrix
P	= Total Complex Power	r	= Reference Sine Wave, $Re^{i\omega t}$
P_j	= Local Complex Power Associated With the jth Force	s	= Path-Length in Co-Quad Plane
R	= Amplitude of Reference Sine Wave	t	= Time
T	= Total Complex Kinetic Energy	x	= Complex Displacement, $X e^{i\omega t}$
T_j	= Local Complex Kinetic Energy Associated With the jth Location	x_j	= Complex Displacement at the jth Location
X	= Displacement Amplitude	\dot{x}^*	= Complex Conjugate of \dot{x}
X_j	= Displacement Amplitude at the jth Location	$\bar{\Phi}$	= Displacement Eigenvector (Mode Shape)
\bar{X}	= Displacement Vector	Φ_j	= jth Component of the Displacement Eigenvector
\bar{X}	= Displacement Amplitude (Complex), $X_R + iX_I$	$\bar{\Phi}_j$	= Displacement Eigenvector for the jth Mode
X_I	= Imaginary Component of Complex Displacement	Φ_{jk}	= jth Component of the kth Displacement Eigenvector
X_{Ij}	= Imaginary Component of the Complex Displacement at the jth Location	$\bar{\Psi}$	= Force-Distribution Vector
X_R	= Real Component of Complex Displacement	Ψ_j	= jth Component of the Force-Distribution Vector
X_{Rj}	= Real Component of the Complex Displacement at the jth Location	β	= Frequency Ratio, ω/ω_n
$[a(\omega)]$	= Complex Displacement/Force Admittance Matrix	β_j	= Frequency Ratio for the jth Mode, ω/ω_j
b	= Arbitrary Constant	γ	= Generalized Mass
$[c(\omega)]$	= Coincident Displacement/Force Admittance Matrix	γ_j	= Generalized Mass Associated With the jth Mode
$ c(\omega) $	= Coincident Displacement/Force Admittance Determinant	π	= 3.14159 (approx)
d_j	= Diameter of the Circle Fitted to the Local-Energy/Power Admittance Co-Quad Plot Associated With the jth Location	ρ	= Radius of Curvature
e	= 2.71828 (approx)	φ	= Phase Angle
f	= Complex Force, $F e^{i\omega t}$	ω	= Excitation Frequency
f_j	= Complex Force at the jth Location	ω_n	= Natural Frequency
g	= Structural Damping Coefficient	ω_j	= Natural Frequency of the jth Mode
g_j	= Structural Damping Coefficient for the jth Mode		
h	= Normalizing Constant		
i	= Imaginary Unit, $\sqrt{-1}$		
m	= Mass		
m_j	= Mass Associated With the jth Location		
$[m]$	= Diagonal Mass Matrix		

DYNAMIC BEHAVIOUR OF COMPLEX STRUCTURES,
USING PART EXPERIMENT, PART THEORY

J.C. Cromer, M. Lalanne
Institut National des Sciences Appliquées
Villeurbanne, France

The dynamic behaviour of a complex system is obtained using a substructure technique. In order to reduce the large number of degrees of freedom of practical structures, the normal modes of some substructures are used as generalized coordinate. Substructures whose properties are determined by experiments are connected to those modeled by finite element techniques. Tests are conducted on simple beams in bending in order to determine the influence of the number of modes and of the experimental data.

The method is then applied to a complex practical structure and agreement between experimental and theoretical results is shown to be good.

INTRODUCTION

It is often necessary to obtain a mathematical model for the dynamic behaviour of complex structures in order to predict frequencies, mode shapes and the response to external exciting forces. However, dynamic modeling can be practically impossible for some actual cases using only an analytical approach. The basic approach used here is to divide the structure into interconnected components. Each of these can be analysed using a separate analytical model, or an experimental test procedure. To predict the total system behaviour, components are then combined by appropriately coupling their dynamic characteristics. In order to reduce the total number of degrees of freedom of the system, a technique using modal coordinates is applied.

Experimentally determined constrained component modes are used according to a general method developed by Klosterman [1]. In this paper, the basic analysis is presented in terms of kinetic and potential energies. The method is first tested on simple beams in bending, thus the influence of the number of modes and of the required experimental data is analysed.

The method is then applied to a practical example consisting of three components. The first substructure is modeled by a classical finite element technique, the second one by impedance tests and the third by Klosterman's constrained modal method [2].

STRUCTURE ANALYSIS

The method will be illustrated for zero damping but may easily be extended to damped systems. Kinetic and potential energies of the whole structure are obtained by summing the corresponding expressions for each component. Consider a complex structure divided into two substructures SS1 and SS2. The object of this analysis is to predict the characteristics of the complete assembly formed by the two components in Figure 1.

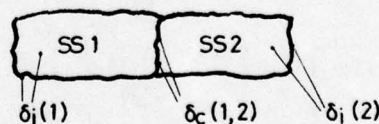


Fig. 1 : General structure

Let the degrees of freedom at the points of connection of the components be designated by the vector $[\delta_c(1,2)]$, while vectors $[\delta_i(1)]$ and $[\delta_i(2)]$ are the remaining degrees of freedom of SS1 and SS2 respectively.

Suppose that for SS1, a finite element analysis is used. Let T_1 be the kinetic energy and U_1 the potential energy of this substructure.

$$2T_1 = \begin{bmatrix} \dot{\delta}_{c(1,2)} \\ \dot{\delta}_{i(1)} \end{bmatrix}^t \cdot \begin{bmatrix} m_{cc(1)} & m_{ci(1)} \\ m_{ic(1)} & m_{ii(1)} \end{bmatrix} \cdot \begin{bmatrix} \dot{\delta}_{c(1,2)} \\ \dot{\delta}_{i(1)} \end{bmatrix} \quad (1)$$

$$2U_1 = \begin{bmatrix} \delta_{c(1,2)} \\ \delta_{i(1)} \end{bmatrix}^t \cdot \begin{bmatrix} k_{cc(1)} & k_{ci(1)} \\ k_{ic(1)} & k_{ii(1)} \end{bmatrix} \cdot \begin{bmatrix} \delta_{c(1,2)} \\ \delta_{i(1)} \end{bmatrix}$$

The constrained modal method is used for the dynamic representation of SS2. The substructure SS2 is tested, clamped at the connection nodes. This demands that the masses at the connection nodes be not significant in the modeling of SS2. The dynamic behaviour can be evaluated using a modal base represented by a well chosen set of eigenvectors [5].

If $\psi_j(2)$ is the j th eigenvector of the component $\delta_{i(2)}$ (abbreviated to include, only the coordinates $\delta_{c(1,2)} = 0$), the motion of the points $\delta_{i(2)}$ is related to the modal coordinates $\gamma_j(2)$ of SS2 by the equation:

$$\delta_{i(2)} = \psi(2) \cdot \gamma(2) = \sum_{j=1}^s \psi_j(2) \cdot \gamma_j(2) \quad (2)$$

s = sum of all modes considered.

Thus with respect to:

$$2T_2 = \begin{bmatrix} \dot{\delta}_{c(1,2)} \\ \dot{\delta}_{i(2)} \end{bmatrix}^t \cdot \begin{bmatrix} 0 & 0 \\ 0 & m_{ii(2)} \end{bmatrix} \cdot \begin{bmatrix} \dot{\delta}_{c(1,2)} \\ \dot{\delta}_{i(2)} \end{bmatrix} \quad (3)$$

and

$$\begin{bmatrix} \delta_{c(1,2)} \\ \delta_{i,2} \end{bmatrix} = \begin{bmatrix} 1 & 0 \\ 0 & \psi(2) \end{bmatrix} \cdot \begin{bmatrix} \delta_{c(1,2)} \\ \gamma(2) \end{bmatrix} \quad (4)$$

we obtain expressions for the kinetic and potential energies of SS2.

$$2T(2) = \begin{bmatrix} \dot{\delta}_{c(1,2)} \\ \dot{\gamma}(2) \end{bmatrix}^t \cdot \begin{bmatrix} 0 & 0 \\ 0 & M(2) \end{bmatrix} \cdot \begin{bmatrix} \dot{\delta}_{c(1,2)} \\ \dot{\gamma}(2) \end{bmatrix} \quad (5)$$

$$2U(2) = \begin{bmatrix} \delta_{c(1,2)} \\ \gamma(2) \end{bmatrix}^t \cdot \begin{bmatrix} k_{cc(2)} & k_{ci(2)} \cdot \psi(2) \\ \psi^t(2) \cdot k_{ic(2)} & k_{ii(2)} \end{bmatrix} \cdot \begin{bmatrix} \delta_{c(1,2)} \\ \gamma(2) \end{bmatrix}$$

Using this modal representation, with constrained modes, the well chosen (experimentally determined) dynamic characteristics are obtained from Klosterman's method [1].

CONSTRAINED MODAL METHOD

Application of Lagrange's equations to $2T(2)$ and $2U(2)$ gives the equations of motion of SS2:

$$\begin{bmatrix} M(2) & 0 \\ 0 & 0 \end{bmatrix} \cdot \begin{bmatrix} \ddot{\gamma}(2) \\ \ddot{\delta}_{c(1,2)} \end{bmatrix} + \begin{bmatrix} K(2) & \psi^t(2) \cdot k_{ic(2)} \\ k_{ci(2)} \cdot \psi(2) & k_{cc(2)} \end{bmatrix} \cdot \begin{bmatrix} \gamma(2) \\ \delta_{c(1,2)} \end{bmatrix} = \begin{bmatrix} \psi^t(2) \cdot F_i(2) \\ F_c(1,2) \end{bmatrix} \quad (6)$$

$F_i(2)$ are the external forces applied on the inner nodes, $F_c(1,2)$ are the external forces applied on the connection nodes. Then:

$$\begin{bmatrix} K(2) & \psi^t(2) \cdot k_{ic(2)} \\ k_{ci(2)} \cdot \psi(2) & k_{cc(2)} \end{bmatrix} \cdot \begin{bmatrix} \gamma(2) \\ \delta_{c(1,2)} \end{bmatrix} = \begin{bmatrix} \psi^t(2) \cdot F_i(2) - M(2) \cdot \ddot{\gamma}(2) \\ F_c(1,2) \end{bmatrix} \quad (7)$$

and from equation (7), with $\delta_{c(1,2)} = 0$ (constrained modal method),

$$[k_{ci(2)} \cdot \psi(2)] \cdot [\gamma(2)] = [F_c(2)] = [R(2)] \cdot [\gamma(2)] \quad (8)$$

where $R(2)$ represents a set of modal forces which must be applied at the connection nodes to restrain the normal modes $\psi(2)$.

$$[k_{ci(2)} \cdot \psi(2)] = [R(2)]$$

and

$$\begin{bmatrix} \psi(2) \\ \vdots \end{bmatrix} \cdot k_{ic}(2) = \begin{bmatrix} R(2) \\ \vdots \end{bmatrix}$$

An experimental dynamic test of SS2, with the connection nodes $\delta_{c(1,2)}$ restrained, gives :

ω^2 natural frequencies

$M(2)$ modal masses

$K(2)$ modal stiffnesses

$\psi(2)$ natural modes of vibration

$R(2)$ modal forces at connection nodes.

$k_{cc}(2)$ (Equation 6) is to be obtained : consider a dead static test (where $\dot{\gamma}(2) = 0$ and $F_i(2) = 0$ in equation 7) :

$$\begin{bmatrix} K(2) \\ \vdots \end{bmatrix} \cdot \begin{bmatrix} \gamma(2) \\ \vdots \end{bmatrix} + \begin{bmatrix} R(2) \\ \vdots \end{bmatrix} \cdot \begin{bmatrix} \delta_{c(1,2)} \\ \vdots \end{bmatrix} = 0 \quad (9)$$

$$\begin{bmatrix} R(2) \\ \vdots \end{bmatrix} \cdot \begin{bmatrix} \gamma(2) \\ \vdots \end{bmatrix} + \begin{bmatrix} k_{cc}(2) \\ \vdots \end{bmatrix} \cdot \begin{bmatrix} \delta_{c(1,2)} \\ \vdots \end{bmatrix} = \begin{bmatrix} F_c(2) \\ \vdots \end{bmatrix}$$

Then, a relation between $F_c(2)$ and $\delta_{c(1,2)}$ may be obtained by eliminating $\gamma(2)$, thus :

$$\begin{bmatrix} \gamma(2) \\ \vdots \end{bmatrix} = - \begin{bmatrix} K(2) \\ \vdots \end{bmatrix}^{-1} \cdot \begin{bmatrix} R(2) \\ \vdots \end{bmatrix} \cdot \begin{bmatrix} \delta_{c(1,2)} \\ \vdots \end{bmatrix}$$

$$\left\{ - \begin{bmatrix} R(2) \\ \vdots \end{bmatrix} \cdot \begin{bmatrix} K(2) \\ \vdots \end{bmatrix}^{-1} \cdot \begin{bmatrix} R(2) \\ \vdots \end{bmatrix} + \begin{bmatrix} k_{cc}(2) \\ \vdots \end{bmatrix} \right\} \cdot \begin{bmatrix} \delta_{c(1,2)} \\ \vdots \end{bmatrix} = \begin{bmatrix} F_c(2) \\ \vdots \end{bmatrix}$$

$$\begin{bmatrix} K^* \\ \vdots \end{bmatrix} \cdot \begin{bmatrix} \delta_{c(1,2)} \\ \vdots \end{bmatrix} = \begin{bmatrix} F_c(2) \\ \vdots \end{bmatrix}$$

$k_{cc}(2)$ can be expressed in the following manner :

$$\begin{bmatrix} k_{cc}(2) \\ \vdots \end{bmatrix} = \begin{bmatrix} K^* \\ \vdots \end{bmatrix} + \begin{bmatrix} R(2) \\ \vdots \end{bmatrix} \cdot \begin{bmatrix} K(2) \\ \vdots \end{bmatrix}^{-1} \cdot \begin{bmatrix} R(2) \\ \vdots \end{bmatrix} \quad (10)$$

This last term combines static and dynamic results. If the set of coordinates $\delta_{c(1,2)}$ is non redundant, $K^* = 0$ and

$k_{cc}(2) = R(2) \cdot \begin{bmatrix} K(2) \\ \vdots \end{bmatrix}^{-1} \cdot R(2)$. If the set is redundant, K^* must be determined by a separate experimental static test [2].

A complete experimentally determined modal representation of SS2 is thus obtained. Upon connecting the two components, the equations of motion become :

$$\begin{bmatrix} M(2) \\ \vdots \end{bmatrix} \cdot \begin{bmatrix} \ddot{\gamma}(2) \\ \ddot{\delta}_{c(1,2)} \\ \ddot{\delta}_i(1) \end{bmatrix} +$$

$$\begin{bmatrix} K(2) \\ \vdots \end{bmatrix} \cdot \begin{bmatrix} \gamma(2) \\ \delta_{c(1,2)} \\ \delta_i(1) \end{bmatrix} = \begin{bmatrix} R(2) \\ \vdots \end{bmatrix}$$

$$\cdot \begin{bmatrix} \gamma(2) \\ \delta_{c(1,2)} \\ \delta_i(1) \end{bmatrix} = 0 \quad (11)$$

The mass and stiffness matrices are thus expressed in a standard format used by most finite element computer programs, and the natural frequencies and mode shapes of the complete structure may be readily computed.

NUMERICAL CONSIDERATIONS

Stiffness and mass matrices of the substructure, represented by finite elements, have been set up from a general finite element program : SAP IV [9].

A computer program has been developed to evaluate the global mass and stiffness matrices presented in equation (11). The lowest natural frequencies and corresponding modes of the whole structure were obtained by the method of simultaneous iterations [8].

Written in FORTRAN IV, the program tested by several known examples, is adapted to CDC computers. The greatest part of the computation time is spent in calculating the frequencies and mode shapes. The total computation time for this example, on CDC 7600, is about 130 sec.

EXPERIMENTAL APPROACH

Measurement technique and experiments have been developed by METRAVIB*. The experimental approach is based upon the concept of a single-shaker impedance technique. Transfer functions are obtained by a digital transfer function-

*Société METRAVIB

Société pour la mesure et le traitement des vibrations et du bruit.
24bis, chemin des Mouilles 69130 Ecully FRANCE

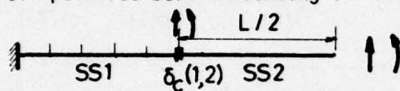
analyser and an identification technique leads to the required modal parameters. Experimental tests have been performed using a new Solartron analyser system.

This work has been described in [3], and will be published later.

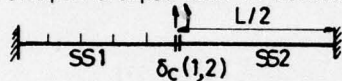
APPLICATIONS : BEAM EXAMPLES

The constrained modal method has been tested on simple examples consisting of beams in bending. Two types of and conditions are considered :

1° - Clamped-free beam in bending :



2° - Clamped-clamped beam in bending :



$$\begin{aligned} L &= 1 \text{ m} & E &= 2.10^{11} \text{ N/m}^2 \\ h &= 1 \text{ cm} & \rho &= 7.8 \cdot 10^3 \text{ Kg/m}^3 \end{aligned}$$

Fig. 2 : Beams in bending

In both cases, SS1 is modeled by five bending-beam elements and SS2 by its five first constrained mode shapes. This study has been performed in order to evaluate the influence of the number of modes of SS2 in the whole structure behaviour, and also to estimate the relation between the quality of the results and the required modal data.

In the first case, the modal characteristics of SS2 are those of a clamped-free beam, while in the second case, data relative to a clamped-clamped beam are necessary ($\delta_{c(1,2)} = 0$).

The modal data used for SS2 are analytical results, in order to test the method and not the effect of experimental data accuracy. The results of the constrained mode program (CMP) are compared with theoretical results (TH) and finite element results (FE) obtained with ten bending-beam elements.

First case : clamped-free beam.

Table 1 : Natural frequencies of the whole structure SS1 + SS2

N_{Hz}	N_1	N_2	N_3	N_4	N_5	N_6	N_7	N_8	N_9
T.H.	8.17	51.26	143.4	281.2	469.8	694.5	970.7	1291.	1658.
F.E.	8.17	51.26	143.5	281.5	466.1	698.3	979.7	1312.	1697
C.M.P.	8.26	53.50	143.6	294.6	466.9	732.4	983.1	1382.	1698.

Second case : Clamped-clamped beam

The results are very similar to the preceding example and do not need to be shown entirely ; for example table 4 shows the natural frequencies of the whole structure (SS1) + (SS2).

Table 4 : Natural frequencies of the whole structure SS1 + SS2

N_{Hz}	N_1	N_2	N_3	N_4	N_5
T.H.	52.04	143.4	279.1	465.2	693.2
F.E.	52.05	143.5	281.5	466.2	698.5
C.M.P.	54.33	143.5	291.7	466.2	724.1

Table 2 : Influence of the number of constrained modes of SS2

N_{Hz}	T.H.	6 modes	5 modes	4 modes	3 modes	2 modes	1 mode
N_1	8.17	8.24	8.25	8.28	8.33	8.42	8.71
N_2	51.26	53.02	53.50	54.10	55.15	57.39	66.40
N_3	143.4	143.5	143.6	143.7	144.0	145.3	263.8
N_4	281.2	291.6	294.6	298.6	306.0	326.4	690.2
N_5	469.8	466.2	466.9	468.4	473.1	701.8	1207.5
N_6	694.5	723.5	732.4	744.8	775.5	1273.4	1957.6
N_7	970.7	977.8	981.3	989.4	1339.6	2025.0	3217.7
N_8	1291.	1359.8	1382.1	1427.8	2096.2	3287.1	4698.1
N_9	1658.	1690.2	1698.6	2172.1	3350.4	4796.8	6792.6

Table 3 : Influence of the required data on the natural frequencies of the whole structure

N_{Hz}	T.H.	A	B	C	D	E
N_1	8.17	8.26	14.14	7.53	7.58	8.96
N_2	51.26	53.50	49.77	52.89	53.26	53.74
N_3	143.4	143.6	156.3	143.6	143.9	143.6
N_4	281.2	294.6	278.8	294.2	297.1	293.2
N_5	469.8	466.9	493.2	467.1	466.8	467.5
N_6	694.5	732.4	711.0	731.0	739.1	729.1
N_7	970.7	981.3	1020.	983.	980.9	982.
N_8	1291.	1382.	1358.	1379.	1396.	1375.
N_9	1658.	1698.	1749.	1700.	1698.	1700.

A : Exact analytical data are taken for SS2.

B : Only displacement is taken in the required mode shapes, rotation is neglected.

C : Displacement and rotation are introduced, but with arbitrary 20 % error on rotation data.

D : Displacement and rotation are introduced, but with arbitrary 20 % error on displacement data.

E : Modal masses are analytically determined with arbitrary 20 % error.

FIRST CASE : CLAMPED-FREE BEAM

Satisfactory results can be observed if the constrained component modes are similar to those of the entire assembly. In fact, this can be observed in tables 1 and 4 for even and uneven modes. The best results are obtained for uneven mode shapes ; at these frequencies, the global mode shapes at connection nodes approach the constrained configuration of SS2.

It can also be seen that all experimental data required are important : displacement and rotation.

As to the number of modes, in this case, every mode shape has to be taken in the frequency range of interest. If one of the constrained modes of SS2 has been neglected, several modes will be missing in global response. Nevertheless the constrained modal method seems suitable for application to experimentally determined substructures and has indeed been applied to an actual example.

ACTUAL EXAMPLE

To evaluate the possible use of this approach for industrial examples, the foundation plate column system shown on Figure 3, was analysed. It consisted of a horizontal plate, supported at four points, on which a vertical cylinder was fixed. The three basic components, foundation, plate and column, are shown in Figure 4.

Each basic component is analysed separately. The dynamic representation for the plate was obtained from finite element analysis while the analytical representation for both the foundation and the cylinder were obtained from experiments.

Component 1 : The foundation. As the frequencies and mode shapes of the plate are significantly influenced by the foundation (up to twice the value of the frequencies of the plate without foundation), it was important to study the dynamic behaviour of the foundation. These data were calculated and determined experimentally : the stiffness characteristics in one translational direction were measured at the four connection nodes, and average values were determined in the frequency range of interest ($k_z \approx 7,4 \cdot 10^7$ N/m) and rotational stiffnesses in two directions were calculated, namely $k_{\theta x} \approx k_{\theta y} \approx 0,4 \cdot 10^5$ N/m.

The dynamic stiffnesses of the foundation were used in the plate finite element calculation as boundary conditions.

Component 2 : The plate. Dynamic characteristics of the plate were determined by a finite element technique : [9]. The agreement between finite element and experimental results were carefully checked in order to ensure a good analytical representation of this component : see Figure 5.

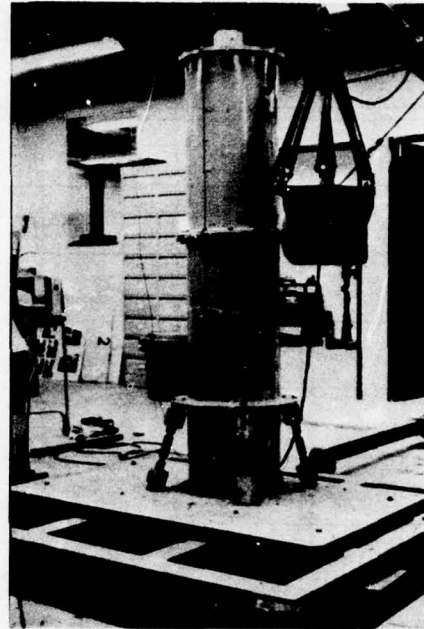


Figure 3 : Foundation-plate-column test system

Component 3 : The column, which was the "complex structure", was not analytically modelled and all its dynamic characteristics were obtained from dynamic test data. $k_{cc}(2)$ could be evaluated by combining experimental data $K(2)$ and $R(2)$. No static test was needed because of a non-redundant set of connection nodes (ball and socket joints).

The modal characteristics of the first six-constrained modes were measured : two rotation modes, two translation modes and two vertical modes. Torsion modes had no influence on the plate and were not taken into account. The experimental data required for this component are given on table 5.

Table 5 : Experimental data required for the column.

Natural frequency N_{Hz}		Modal forces (N/m) at connection nodes				Modal masses	
		1	2	3	4		
N_1	28.4	$-5.5 \cdot 10^6$	$-5.7 \cdot 10^5$	$+5.7 \cdot 10^5$	$+5.5 \cdot 10^6$	M_1	116 Kg
N_2	31.6	$+4.5 \cdot 10^5$	$-6.7 \cdot 10^6$	$+6.7 \cdot 10^6$	$-4.5 \cdot 10^5$	M_2	
N_3	40.9	$+1.7 \cdot 10^6$	$-7.5 \cdot 10^6$	$+7.5 \cdot 10^6$	$-1.7 \cdot 10^6$	M_3	
N_4	45.8	$-1.3 \cdot 10^7$	$-2.0 \cdot 10^6$	$+2.0 \cdot 10^6$	$+1.7 \cdot 10^7$	M_4	
N_5	159.4	$-2.0 \cdot 10^7$	$-2.5 \cdot 10^7$	$-2.5 \cdot 10^7$	$-2.0 \cdot 10^7$	M_5	
N_6	223.0	$-1.3 \cdot 10^7$	$-1.0 \cdot 10^7$	$-1.0 \cdot 10^7$	$-1.3 \cdot 10^7$	M_6	

The modal forces are computed with respect to the modal masses, which are taken arbitrarily as the effective mass of the cylinder.

As to the orthogonality test for the first six frequencies the diagonal terms are :

N_1	N_2	N_3	N_4	N_5	N_6
1.09	1.05	0.84	0.89	1.09	1.1

and the off-diagonal terms are all less than 0.05.

The complete system-simulation results are shown in figure 6. The first eight natural frequencies and mode shapes of the whole structure have been computed and compared with experimental results. Only the second mode of the plate, in the complete system, failed to show up in the experiments.

The seventh mode shape was difficult to observe because of the particular interference of the foundation properties near this frequency (even on the plate experimental test, this can be observed in figure 5). These results appear to be very satisfactory.

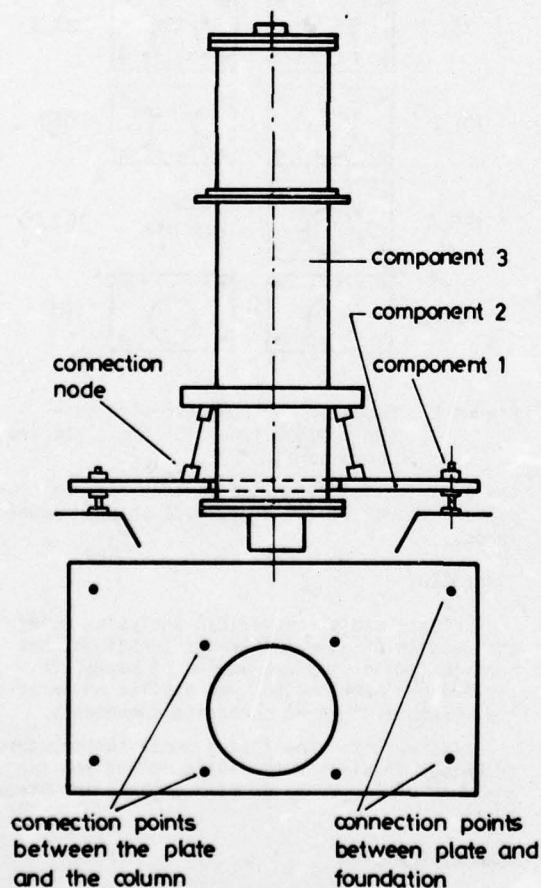


Figure 4 : Schematic design of the structure

Computed results

Experimental results

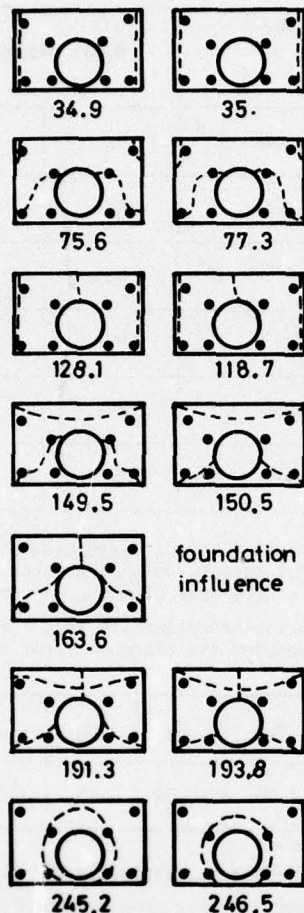


Figure 5 : Modes of the plate with foundation.
(Test of the F.E. representation).

DISCUSSION

The experiments were performed with due regard to analytical restraints. However only the constrained modal method has been tested here. It also seems interesting to study other techniques where modal data are to be determined from free-free excitation tests. Free-free zero frequency modes must then be considered.

Several types of connections between the plate and the cylinder need to be investigated. In fact, in the present case, only forces at the connection points have been measured. We shall, in the near future, consider connection pads or more complex systems where moments are to be determined. Another advantage of the method consists in a simulation technique : any changes in the various components can be readily evaluated with this mathematical model. However, this approach is only practicable when

Computed results

F.E. for the plate and experimental data for the column.

Experimental results

for the whole system (plate + column).

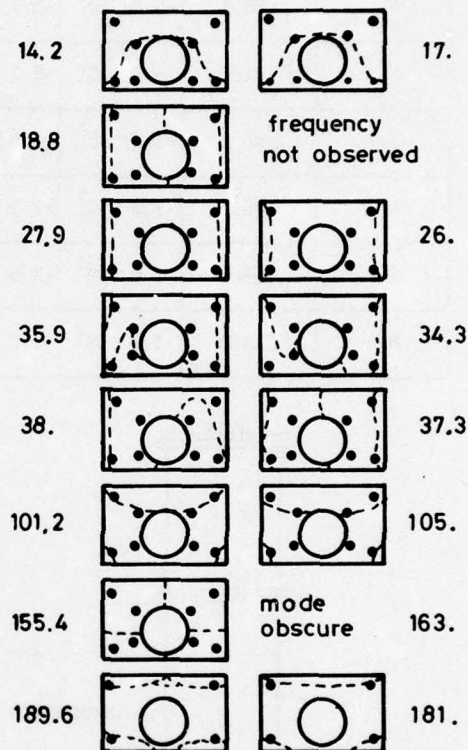


Figure 6 : Modes of the complete structure
(Only nodal lines for the plate are shown here).

the experimental technique is accurate and complete (natural frequencies, mode shapes, modal forces, ...).

CONCLUSION

Klosterman's theoretical analysis, using the results of an experimental technique, has been tested on simple examples of beams. The constrained modal method was applied on an actual example of three connected components.

The results show that a modal substructure technique provides a realistic method for the analysis of large and complex engineering structures.

ACKNOWLEDGEMENTS

This work [3] was supported by the Délégation Générale à la Recherche Scientifique et

Technique, under contract 73-7-1786. The authors are indebted to D.G.R.S.T. for permission to publish this paper. The authors are also indebted to Metravib Cie for experimental data.

REFERENCES

- [1] A.L. Klosterman and J.R. Lemon
Dynamic design analysis via Building block approach. The Shock and Vibration bulletin n°42, Part 1, 1972.
- [2] A.L. Klosterman
On the experimental determination and use of modal representation of dynamics characteristics. Ph. D. Thesis, 1971, University of Cincinnati.
- [3] J.C. Cromer, M. Lalanne, L. Gaudriot
Comportement dynamique des structures complexes. Rapport final, avril 1975. Contrat D.G.R.S.T. n°737.1786.
- [4] J.C. Cromer, M. Lalanne
Comportement dynamique des structures complexes. Rapport intermédiaire, juin 1974, Contrat D.G.R.S.T. n° 737.1786.
- [5] R.R. Craig, M.C.C. Bampton
Coupling of substructures for dynamic analysis. A.I.A.A. Journal, vol.6, n°7, juin 1968.
- [6] W. Hurty
Dynamic analysis of structural systems using component modes. A.I.A.A. Journal, vol.3, n°4, april 1965.
- [7] C.C. Kennedy, C.D.P. Pancu
Use of vectors in vibration measurement and analysis. Journal of Aeronautical Sciences, vol.14, n°11, novembre 1947.
- [8] A. Jennings, D.L.R. Orr
Application of the simultaneous iteration method to undamped vibration problems. Int. J. for Numerical methods in engineering, vol.3, 1971.
- [9] K.J. Bathe, E.L. Wilson, F.E. Peterson
SAP IV, Berkeley, June 1973.

SYMBOLS

SS_k , substructure k ,
 U, T , potential and kinetic energy of the complete structure,
 U_k, T_k , potential and kinetic energy of substructure k ,
 $\delta_{c(k,l)}$, connection degrees of freedom of the two components k and l ,
 $\delta_{i(k)}$, inner degrees of freedom of component k ,
 $m_{(l)}^{k(l)}$, finite element mass and stiffness matrix of component l with respect to connection nodes and inner nodes,

$$[m_{(l)}] = \begin{bmatrix} m_{cc(l)} & m_{ci(l)} \\ m_{ic(l)} & m_{ii(l)} \end{bmatrix}; [k_{(l)}] = \begin{bmatrix} k_{cc(l)} & k_{ci(l)} \\ k_{ic(l)} & k_{ii(l)} \end{bmatrix}$$

$\psi_{j(k)}$, j th eigenvector of component k when restrained at connection nodes ($\delta_{c(k,l)} = 0$),

$\Psi(k)$, set of constrained eigenvectors of component k ,

$\gamma_{j(k)}$, modal coordinate of component k , associated with the j th eigenvector,

$\Upsilon(k)$, set of modal coordinates of component k ,

$$\delta_{i(k)} = \Psi(k) \cdot \Upsilon(k) = \sum_{m=1}^s \psi_{m(k)} \cdot \gamma_{m(k)}$$

s , sum of all modes considered,

$M_{j(k)}$, modal mass of component k , associated with the j th eigenvector,

$$M_{j(k)} = [\psi_{j(k)}]^t \cdot [m_{(k)}] \cdot [\psi_{j(k)}]$$

$$[M_{(k)}] = [\Psi(k)]^t \cdot [m_{(k)}] \cdot [\Psi(k)]$$

$$\left. \begin{matrix} K_{j(k)} \\ [K_{(k)}] \end{matrix} \right\} \text{ idem for the modal stiffness,}$$

$R_{(k)}$, set of modal external forces acting at the connection degrees of freedom, to restrain the considered modes of component k ,

\cdot , derivative with respect to time,

t , matrix transposition symbol.

THE EXPERIMENTAL DETERMINATION OF VIBRATION PARAMETERS FROM TIME RESPONSES

S. R. Ibrahim
NRC Research Associate
NASA Langley Research Center
Hampton, Virginia, U.S.A.

and

E. C. Mikulcik
Associate Professor
Department of Mechanical Engineering
The University of Calgary
Calgary, Alberta, Canada

This paper describes theoretical aspects and experimental verification of the application of a time domain modal vibration test technique. The theory of the technique is based on a reformulation of the ordinary differential equations of motion of a multidegree of freedom system with viscous damping. These equations, in state variable form, comprise the mathematical model that is used for identifying a system's vibration parameters. The theory is applicable to both lumped and distributed parameter systems.

Special attention is directed to applying this technique in practice. Several application problems such as exciting the structure, minimization of measurement data, determination of the order of the mathematical model, minimization of the amount of instrumentation required and averaging of results are examined, and solutions are presented.

The applicability of the technique is verified by two experiments using a cantilever beam and a rectangular plate. The case of the plate involves two very close natural frequencies which could not be identified using a frequency sweep test (peak amplitude) because of interference between modes.

NOMENCLATURE

\underline{M} = mass matrix
 \underline{C} = damping matrix
 \underline{K} = stiffness matrix
 \underline{y} = displacement vector
 \underline{I} = identity matrix
 \underline{x} = state vector
 λ_i = the i -th eigenvalue (characteristic root)
 $\underline{\psi}_i$ = the i -th modal vector

R_i = constants depending on initial conditions
 t = time
 f = frequency (Hz)
 f_d = damped natural frequency
 f_n = undamped natural frequency
 η = damping factor
 $i = \sqrt{-1}$
 \wedge = the symbol on a variable denotes the deviation of that variable from some initial condition.

INTRODUCTION

Experimentally determined natural frequencies, damping, and modal information about a dynamical system are usually obtained through the use of techniques which are based on the frequency response of the system. In the various methods used, the system may be forced using sinusoidal, random, step or other forms of excitation, and either the forced or free response may be utilized. The analysis of the test data, and therefore the determination of vibrational characteristics, is based on frequency domain analysis of the test data. Simple systems or structures can usually be dealt with satisfactorily using simple resonance testing techniques; complex systems (i.e. those containing closely spaced natural frequencies and, perhaps, heavy damping), demand that more complex test procedures be used [1, 2, 3, 4]*. Analyses of frequency domain methods [5, 6] show, however, that there are theoretical limitations on the closeness of natural frequency spacing and heavy damping, beyond which frequency response methods cannot yield accurate vibration information about the system. These limitations are present, basically, because it is assumed that when a system, however complex, is excited at or near a resonant frequency, it behaves as though it has only a single degree of freedom.

The theory of a time-domain based method is presented in [7]. This method circumvents the above described limitations of frequency response methods because there are no approximations involved in determining the vibrational characteristics of a system from the time domain method. The soundness of the theory of the technique was demonstrated through simulated experiments in which the vibrational characteristics of systems having closely spaced natural frequencies and heavy damping were accurately identified.

This paper describes a subsequent theoretical evaluation of several aspects of the practical application of the time domain method, followed by its application in the experimental study of a cantilever beam and a plate.

THE THEORY OF THE TIME DOMAIN METHOD

The time domain method [7] is based on reformulation of the ordinary differential equations of motion for the free response of a multi-degree of freedom linear system with damping, i.e.,

$$\underline{M} \ddot{\underline{y}} + \underline{C} \dot{\underline{y}} + \underline{K} \underline{y} = \underline{0} \quad (1)$$

*Numbers in brackets designate references at end of paper.

into state variable form,

$$\begin{bmatrix} \dot{\underline{y}} \\ \underline{y} \end{bmatrix} = \begin{bmatrix} \underline{0} & \underline{I} \\ -\underline{M}^{-1}\underline{K} & -\underline{M}^{-1}\underline{C} \end{bmatrix} \begin{bmatrix} \underline{y} \\ \dot{\underline{y}} \end{bmatrix} \quad (2)$$

or

$$\dot{\underline{x}} = \underline{A} \underline{x} \quad (3)$$

This first order matrix differential equation is referred to herein as the time domain model of the system. If the A-matrix is known, then the vibration parameters of the system are completely described. The eigenvalues provide knowledge of the natural frequencies and damping, and the eigenvectors give the mode shapes. If the displacement, velocity and acceleration responses at all locations (coordinates) of the system are measured, then the A-matrix can be determined by writing, for \underline{A} of dimension $2n \times 2n$,

$$\begin{bmatrix} \dot{\underline{x}}(t_1) & \dot{\underline{x}}(t_2) & \dots & \dot{\underline{x}}(t_{2n}) \end{bmatrix} = \underline{A} \begin{bmatrix} \underline{x}(t_1) & \underline{x}(t_2) & \dots & \underline{x}(t_{2n}) \end{bmatrix} \quad (4)$$

or

$$\dot{\underline{X}} = \underline{A} \underline{X}, \quad (5)$$

whence

$$\underline{A} = \dot{\underline{X}} \underline{X}^{-1} \quad (6)$$

where

$$\underline{X} = \begin{bmatrix} \underline{x}(t_1) & \underline{x}(t_2) & \dots & \underline{x}(t_{2n}) \end{bmatrix}$$

where $\underline{x}(t_i)$ and $\dot{\underline{x}}(t_i)$ ($i = 1, \dots, 2n$) are vectors whose elements are made up of response measurements at $2n$ different instants of time. Although formulated on the basis of lumped parameter systems, the method is applicable to distributed parameter, or continuous systems.

Direct application of the theory is possible in principle, but several practical problems arise. These problems are discussed below, together with their solutions, approached in such a manner that a step-by-step test procedure utilizing a minimal amount of instrumentation is developed.

APPLICATION PROBLEMS AND THEIR SOLUTIONS

Excitation of the System

In order that the free response contains all the information required, the excitation preceding the free response must excite all the modes that have natural frequencies in the frequency range of interest. Three methods of excitation that could be used are examined here.

An impulse has a uniform spectral density over the entire frequency range making it, theoretically, an ideal method to excite all the

modes of a system. However, a true impulse is unattainable in practice, and the approximations which are possible can transmit only relatively small amounts of energy to the system under test. Thus such excitation should be useful for small lightly damped systems but of little use for large structures.

A rapidly swept sinewave, over a frequency range f_1 to f_2 , could provide good control over the range of natural frequencies which are to be studied in a particular test [8], and could transfer significantly more energy to the system than could an impulse. The time required for the introduction of the test signal should be kept small to avoid the possibility of highly damped modes dying out before the free response is recorded.

Random signals have continuous power spectral density functions, and would therefore be useful in excitation. A narrow band random signal having a power spectral density function of suitable range can be used to excite a system in the frequency range of interest.

Measurement of the Response

Direct application of the theory requires complete knowledge of the acceleration, velocity and displacement responses at the measurement stations. If accelerometers are used in measuring the response, the absolute values of the velocity and displacement are not usually obtainable because their initial values are not accounted for in the integration of the acceleration response.

The dynamic characteristics of a structure and, hence, the A-matrix are, however, not dependent upon the initial conditions of excitation, so it can be concluded that the theory can be modified to eliminate the requirement for knowledge of initial velocity and displacement information. This modification is based upon assuming that the acceleration response measured at n stations on a structure is made up of two components:

$$\ddot{\underline{y}}(t) = \ddot{\underline{y}}(0) + \hat{\ddot{\underline{y}}}(t) \quad (7)$$

where $\ddot{\underline{y}}(0)$ is the acceleration response at some time which is arbitrary (designated as $t = 0$ and $\hat{\ddot{\underline{y}}}(t)$ is the change in acceleration response from time $t = 0$ to t .

Integration of the acceleration response gives the velocity,

$$\dot{\underline{y}}(t) = \int_0^t \ddot{\underline{y}} dt + \dot{\underline{y}}(0) \quad (8)$$

or

$$\underline{\dot{y}}(t) = \hat{\underline{\dot{y}}}(t) + \underline{\dot{y}}(0) \quad (9)$$

where $\underline{\dot{y}}(0)$ is the velocity response vector at time $t = 0$.

Integration of the velocity, equation (8), results in the displacement response,

$$\underline{y}(t) = \int_0^t \int_0^\epsilon \ddot{\underline{y}}(t) dt d\epsilon + t \dot{\underline{y}}(0) + \underline{y}(0) \quad (10)$$

or

$$\underline{y}(t) = \hat{\underline{y}}(t) + \underline{y}(0) \quad (11)$$

where

$$\hat{\underline{y}}(t) = \int_0^t \int_0^\epsilon \ddot{\underline{y}}(t) dt d\epsilon + t \dot{\underline{y}}(0) \quad (12)$$

The state equation must be satisfied for all values of t , including $t = 0$; hence substitution of equations (7), (9), (11) into the state equation for $t = t_1$ results in:

$$\begin{bmatrix} \dot{\underline{y}} t_1 \\ \underline{y} t_1 \end{bmatrix} = \underline{A} \begin{bmatrix} \hat{\underline{y}} t_1 \\ \underline{y} t_1 \end{bmatrix}, \quad (13)$$

and for $t = t_2 = \alpha t_1$

$$\begin{bmatrix} \hat{\underline{y}} \alpha t_1 \\ \underline{y} \alpha t_1 \end{bmatrix} = \underline{A} \begin{bmatrix} \hat{\underline{y}} \alpha t_1 \\ \underline{y} \alpha t_1 \end{bmatrix} \quad (14)$$

Multiplying equation (13) by α and subtracting equation (14) from it gives:

$$\begin{bmatrix} \dot{\underline{y}} \\ \underline{y} \end{bmatrix} = \underline{A} \begin{bmatrix} \underline{\dot{y}} \\ \underline{y} \end{bmatrix} \quad (15)$$

In equation (15) \underline{y} , $\dot{\underline{y}}$ and $\underline{\dot{y}}$ take the following new definitions:

$$\underline{y} = \alpha \int_0^{t_1} \int_0^\epsilon \ddot{\underline{y}}(t) dt d\epsilon - \int_0^{\alpha t_1} \int_0^\epsilon \ddot{\underline{y}}(t) dt d\epsilon, \quad (16)$$

$$\dot{\underline{y}} = \alpha \int_0^{t_1} \ddot{\underline{y}}(t) dt - \int_0^{\alpha t_1} \ddot{\underline{y}}(t) dt, \quad (17)$$

and

$$\underline{\dot{y}} = \alpha \underline{\dot{y}}(t_1) - \underline{\dot{y}}(\alpha t_1) - (\alpha - 1) \underline{\dot{y}}(0) \quad (18)$$

whence \underline{y} , $\dot{\underline{y}}$ and hence the A-matrix, can be obtained from the experimental acceleration records by integration without requiring the knowledge of $\dot{\underline{y}}(0)$ or $\underline{y}(0)$. This procedure reduces the amount of instrumentation required because no on-line integrators are necessary.

Sometimes it may be difficult to measure the acceleration response, as in the case of extremely light structures, or because of space restrictions that do not permit the mounting of accelerometers. If acceleration responses are not available, then either the displacement or the velocity response can be used in the same manner as the acceleration response for the purpose of identifying the A-matrix of a system. This can be shown by examining the displacement response of an n-degree of freedom linear system, expressed as:

$$\underline{y}(t) = \sum_{i=1}^{2n} R_i \underline{\psi}_i e^{\lambda_i t} \quad (19)$$

Differentiation of equation (19) twice gives the velocity and acceleration responses as:

$$\dot{\underline{y}}(t) = \sum_{i=1}^{2n} \bar{R}_i \underline{\psi}_i e^{\lambda_i t}, \quad (20)$$

and

$$\ddot{\underline{y}}(t) = \sum_{i=1}^{2n} \bar{\bar{R}}_i \underline{\psi}_i e^{\lambda_i t}, \quad (21)$$

where R_i is a constant,

$$\bar{R}_i = \lambda_i R_i,$$

and

$$\bar{\bar{R}}_i = \lambda_i^2 R_i$$

Equations (19), (20) and (21) are the same except for the constants R_i , \bar{R}_i and $\bar{\bar{R}}_i$. All three equations are linear combinations of the same set of modes. The set of constants, R_i ($i = 1, 2 \dots 2n$), is dependent only on the initial conditions of excitation and, hence, for the same structure, the response can take as many forms as the possible sets of different initial conditions. Thus, the displacement or velocity responses can be considered to be equivalent to an acceleration response for a set of initial conditions different from those which actually existed.

Determination of the Order of the Model

The development of the method is based on a lumped parameter approximation of the system, in which the number of lumps at which the response is measured equals the number of modes which contribute to the response. The characteristic equation of an n-degree of freedom system is of 2nth order, hence there are 2n characteristic roots and 2n modal vectors. If the modes are underdamped, the characteristic roots and modal vectors occur in complex conjugate pairs, and each pair combines to produce a real mode shape. Henceforth in this paper, the word "mode" implies a real mode shape which is the result of combining a pair of complex conjugate modal vectors. Application to distributed parameter systems requires that the number of stations at which measurements are taken equals the number of modes excited. In each case, the number of degrees of freedom of the model assumed to describe the system must be equal to the number of measurement stations, and also to the number of modes in order that the system parameters can be determined.

In practice, there is not usually control over, or knowledge of, the number of modes excited, and even if there were, it would not always be possible or desirable to employ the same number of measurement stations as there are modes. Thus, three relationships between the number of modes and stations may arise as categorized below:

(i) The number of stations equals the number of modes (referred to herein as an "exactly-specified" system).

(ii) The number of stations is greater than the number of modes (referred to as an "over-specified" system).

(iii) The number of stations is less than the number of modes (referred to as an "under-specified" system).

A procedure is described below, through which the number of modes present in the filtered response can be determined, after which an adjustment can be made to the basic technique to enable system parameter identification to proceed. It is assumed that there are p measurement stations and m modes are excited in the response (hence there are 2m modal vectors). The number of modes is determined on the basis of the determinant of the X-matrix of equation (5). Each column of \underline{X} consists of 2p elements which are the responses recorded at some instant of time, t_j , and can be written as

$$\underline{x}(t_j) = \sum_{i=1}^{2m} R_i \underline{\psi}_i e^{\lambda_i t_j} \quad (22)$$

Each column of X is a linear combination of the $2m$ independent modal vectors ψ_i , hence X is of rank $2m$, and its determinant vanishes if the system is over-specified but not if the system is exactly or under-specified.

The first step of the procedure to determine m is to successively calculate the determinant of X formed by assuming k degrees of freedom, where k takes on values from unity up to a value at which the determinant becomes zero. This value of k equals $2m+1$, whence the responses of only m stations are then used to identify the system.

If the determinant does not become zero during the above procedure, then the system is either exactly or under-specified, i.e. $p < m$. This situation can be dealt with through the addition of more measurement stations, after which the determinant check for an over-specified system can be applied. It is not necessary to physically add measurement equipment and repeat the experiment; it is possible to use "assumed stations" for which the responses are generated using the response of the original, or real, stations. Indeed, if $y(t)$ is the response of the p real stations on a structure, the response at p assumed stations can take the form of $y(t + \Delta t)$. This can be shown by writing the response at time t_j as

$$y(t_j) = \sum_{i=1}^{2m} R_i \psi_i e^{\lambda_i t_j} \quad (23)$$

and at time $t_j + \Delta t$

$$y(t_j + \Delta t) = \bar{y}(t_j) = \sum_{i=1}^{2m} R_i e^{\lambda_i \Delta t} \psi_i e^{\lambda_i t_j} \quad (24)$$

The two responses of equations (23) and (24) can be written as

$$\begin{bmatrix} y(t_j) \\ \bar{y}(t_j) \end{bmatrix} = \sum_{i=1}^{2m} R_i \begin{bmatrix} \psi_i \\ \bar{\psi}_i \end{bmatrix} e^{\lambda_i t_j} \quad (25)$$

where

$$\bar{\psi}_i = e^{\lambda_i \Delta t} \psi_i$$

Equation (25) may be considered to be the response vector for a system with $2p$ stations and m modes. This procedure can be repeated to increase the apparent number of stations to $3p$, $4p$, ... etc. using the determinant check after each increase to see if the number of modes in the response can be determined.

The identification of an under-specified system using the above procedure enables tests to be carried out with a minimum amount of instrumentation. Any structure, however complex, can be identified in stages using two measuring stations at a time with one station in the second and all succeeding tests as a reference. Whatever the number of modes excited in the response of any two points, sufficient transformed stations can be added to make it identifiable.

In practice, because of measurement noise, error and computer round-off, the results of computation to determine the determinant of X for an over-specified system will be small, but not zero. Hence, instead of using the value of the determinant itself, the ratio of two successively calculated determinants [9] should be used. If $|X|_k/|X|_{k+1}$ is very large compared to the values of $|X|_{k-1}/|X|_k$, ..., $|X|_1/|X|_2$, then the number of modes contributing to the response is k .

An over-specified system, $p > m$, may be dealt with by dividing it into a number of exactly-specified subsystems. However, a more efficient method, analogous to the introduction of assumed stations discussed above, is to add a number of assumed modes to the system's response to make the total number of modes equal to the number of stations. The actual displacement response vector y containing m modes at p stations of a structure can be expressed as:

$$y = \sum_{i=1}^{2m} R_i \psi_i e^{\lambda_i t} \quad (26)$$

Let y_a be a hypothetical response of dimension p , being a combination of $(p-m)$ assumed modes as follows:

$$y_a = \sum_{j=1}^{2(p-m)} R_j q_j e^{i\omega_j t}, \quad (27)$$

where q_j is an assumed modal vector and ω_j is an assumed natural frequency.

Adding the hypothetical response y_a to the actual response y results in

$$\bar{y} = \sum_{i=1}^{2m} R_i \psi_i e^{\lambda_i t} + \sum_{j=1}^{2(p-m)} R_j q_j e^{i\omega_j t} \quad (28)$$

which is the response to be used in identification. It represents the response of an exactly specified system since it consists of measurements at p stations and contains p modes.

Averaging of Results

Errors in the identified A-matrix arise due to measurements and recording noise, and in the numerical integration of the measured response. Considering these errors as random, their effects can be reduced by averaging. Either \bar{X} and \bar{X} matrices corresponding to several sets of data (from a single record) can be averaged and then used to calculate a single A-matrix, or equation (6) can be applied to each set of data to produce a set of A-matrices from which the average can be computed. A disadvantage of the first method is that the elements of \bar{X} and \bar{X} are time dependent variables with zero average, so averaging could possibly cause the signal to noise ratio to decrease. The second method is recommended, and was used in the experimental work reported here.

EXPERIMENTAL RESULTS

Experimental employing the methods outlined in the preceding sections were carried out on a cantilever beam and a rectangular plate rigidly clamped along its long edges. Both structures were made of steel. Their dimensions are shown in Figure 1.

Each structure was excited by a narrow band random signal, and the ensuing free responses were recorded using accelerometers at two stations on each structure, located as shown in Figure 1. The frequency range of the filtered responses for the beam was 0-500 Hz and for the plate 50-90 Hz.

The beam's response was digitized at a rate of 7500 samples per second and the free response was recorded for 1/3 of a second (2500 samples for each channel). The determinant check involving \bar{X} required that responses corresponding to "assumed stations" be generated in order that the number of modes excited could be determined. Three such responses were generated using values of Δt , time of delay between original and the artificially generated stations, corresponding to 50 and 100 samples for station 1 and 50 samples for station 2. The results of the determinant check, shown in Table I, then showed that three modes were excited. The ensuing identification calculations of the A matrix were performed using the responses from stations 1 and 2 and the generated response obtained from station 1 delayed by Δt corresponding to 50 samples. The effect of measurements noise and error were reduced by averaging 30 sets (the number 30 was arbitrarily chosen) of A matrix calculations using a total record length corresponding to 1000 samples or 0.133 second.

The plate's response was digitized at 5000 samples per second. Again the determinant check required that responses corresponding to assumed stations be generated. Four such responses were generated using values of

corresponding to 20 and 50 samples for each station with the determinant check, summarized in Table II, then showing that four modes were excited. The calculations were then performed using generated responses with Δt corresponding to 50 samples for both stations. The results presented here were obtained by averaging forty A-matrices obtained from a record length of about 0.3 seconds, corresponding to fifteen hundred samples.

The vibration parameters thus determined are listed in Tables III and IV. Also listed are results obtained from a frequency sweep test employing the peak amplitude method, and theoretical parameters obtained using the Bernoulli Equation for the beam and the procedure described by Claassen and Thorne [10] for the plate. An absolute comparison of the results is not meaningful because the theoretical cases only approximate the actual in respects such as boundary conditions and geometrical dimensions. However, it is of interest to note that the results using three methods compare favourably for the beam, where the natural frequencies are well spaced, but this is not the case for the plate. In this experiment, even though frequency spacing does not appear to be extremely close, the peak amplitude method failed to locate the four resonances of the plate. Interference between modes allowed only three resonances to be observed, with considerable differences between the observed frequencies and those determined by the time domain method as well as those calculated. The agreement between the results of the time domain method and the theoretical calculations is relatively good. It is of interest to note that the time domain technique gives complex modal information, indicating the phase relationship between the test stations.

CONCLUSIONS

It is shown that there exists a choice of fundamental methods, i.e. either frequency domain or time domain based, in the experimental determination of vibration parameters of mechanical systems. The results presented are not intended to illustrate the overall superiority of one method over the other, since either one may have special advantages in certain applications as determined by the type and degree of complexity of the system under test and by the type and accuracy of the information sought. The time domain method described herein might appear somewhat more complex to apply than the simplest frequency response methods, but it is less laborious than some other frequency domain techniques such as in the case of using multiple shaker methods or in construction of Kennedy and Pancu plots. The technique described can be mechanized into a simple measurement and computation procedure which can then be used on both simple and complex systems without the necessity for special adaption for special complexities, and without the requirement for prior

knowledge about the system being tested. The principal advantage in using a time domain model is that no special assumptions were made either in the derivation of the theory of the technique or in obtaining vibration parameters from the identified mathematical model itself.

ACKNOWLEDGEMENT

The work described in this paper was supported by the National Research Council of Canada, Grant No. A-7094 and was completed by Dr. Ibrahim while holding a Resident Research Associateship of the National Research Council of the United States.

REFERENCES

1. Charles C. Kennedy and C.S. Pancu, "Use of Vectors in Vibration Measurement and Analysis," *Journal of Aeronautical Sciences*, Vol. 14, No. 11, pp. 603, 1947.
2. R.C. Lewis and O.L. Wrisley, "A System for the Excitation of Pure Natural Modes of Complex Structures," *Journal of Aerospace Sciences*, Vol. 17, No. 11, November 1950.
3. J.P. Raney, "Identification of Complex Structures Using Near Resonance Testing," *The Shock and Vibration Bulletin*, Bulletin 38, Part 2, August 1968.
4. A.A. Woods, Jr., "A Multiple Driver Admittance Technique for Vibration Testing of Complex Structures," *Shock and Vibration Bulletin*, Bulletin 42, Part 3, January 1972.
5. R.E.D. Bishop, and G.M.L. Gladwell, "An Investigation into the Theory of Resonance Testing," *Phil. Trans. A* 1963, 255 (No. 1055), pp. 241.
6. J.W. Pendered, "Theoretical Investigation into the Effect of Close Natural Frequencies in Resonance Testing," *Journal of Mechanical Engineering Science*, Vol. 7, No. 4, pp. 372, 1965.
7. S.R. Ibrahim and E.C. Mikulcik, "A Time Domain Modal Vibration Test Technique," *Shock and Vibration Bulletin*, Bulletin 43, Part 4, 1973.
8. R.G. White, "Evaluation of Dynamic Characteristics of Structures by Transient Testing," *Symposium on Structural Dynamics*, University of Technology, Loughborough, England, March 1970.
9. C.M. Woodside, "Estimation of the Order of Linear Systems," *IFAC Symposium on Identification in Automatic Control Systems*, Prague, 1970.
10. Ralf W. Claassen and Charles J. Thorne, "Transverse Vibrations of Thin Rectangular Isotropic Plates," NAVWEPS Report 7016, U.S.A. Naval Ordnance Test Station, China Lake, California, August 1960.

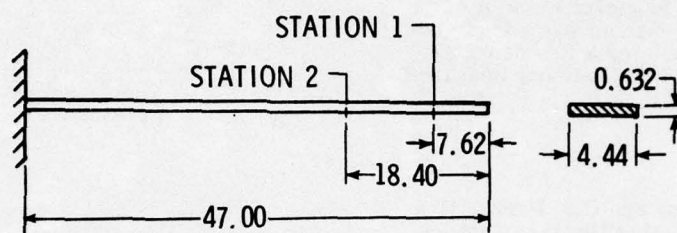


FIG. 1a. GEOMETRY OF THE CANTILEVER BEAM
(DIMENSIONS IN CENTIMETERS)

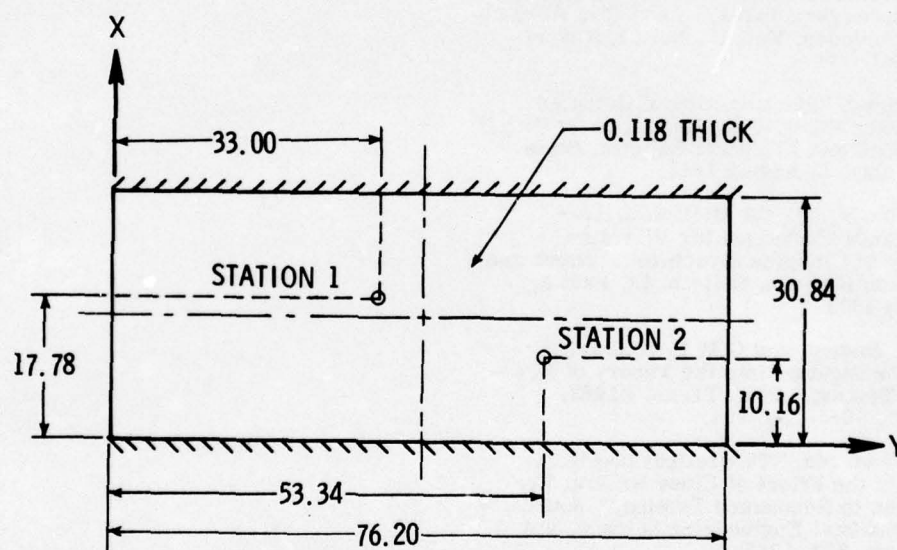


FIG. 1b. GEOMETRY OF THE PLATE
(DIMENSIONS IN CENTIMETERS)

TABLE I
Determinant Check for the Cantilever Beam

Number of Stations	$ X _N$	$ X _N/ X _{N+1}$
1	0.8439×10^{-4}	0.4166×10^5
2	0.2026×10^{-8}	0.4483×10^4
3	0.4518×10^{-12}	0.2754×10^{10}
4	0.1640×10^{-21}	0.1602×10^{10}
5	0.1024×10^{-30}	

TABLE II
Determinant Check for the Plate

Number of Stations	$ X _N$	$ X _N/ X _{N+1}$
1	0.3377×10^{-2}	0.8303×10^3
2	0.4067×10^{-5}	0.1771×10^4
3	0.2296×10^{-8}	0.7204×10^2
4	0.3188×10^{-10}	0.8597×10^6
5	0.3708×10^{-16}	0.3289×10^7
6	0.1127×10^{-22}	

TABLE III
Theoretical and Identified Vibration Parameters of the Cantilever Beam

Mode No.	Theoretical Undamped		Identified (Time Domain)			Identified (Peak Amplitude)	
	f_n (Hz)	Principal Mode*	f_d (Hz)	η	Principal Mode	f_d (Hz)	Principal Mode
1	23.83	100.00 60.66	22.87	0.000615	100.00 58.73-i0.81	22.20	100.00 51.80
2	149.07	100.00 -243.63	145.58	0.000545	100.00 -213.64+i18.53	143.20	100.00 -217.00
3	417.62	100.00 260.64	404.41	0.00129	100.00 237.11+i9.20	401.40	100.00 286.00

TABLE IV
Theoretical and Identified Vibration Parameters of the Plate

Mode No.	Theoretical Undamped		Identified (Time Domain)			Identified (Peak Amplitude)	
	f_n (Hz)	Principal Mode*	f_d (Hz)	η	Principal Mode	f_d (Hz)	Principal Mode
1	69.93	100.00 85.23	64.53	0.031	100.00 63.39-i10.97	69.20	100.00 59.7
2	72.19	100.00 -72.06	69.96	0.021	100.00 -65.83+i13.68	-	-
3	80.24	100.00 33.29	76.73	0.029	100.00 30.18-i3.68	82.20	100.00 40.02
4	96.04	100.00 -148.91	96.51	0.029	100.00 -156.11+i17.07	102.00	100.00 134.00

*mode shapes are listed relative to 100 units for station 1.

Discussion

Voice: You said that there were only three modes in a cantilever beam. My experience is that those beams typically have many modes.

Mr. Ibrahim: No, I felt that was the response in a certain frequency range, I think from 0 to 500 Hz, and there were only 3 modes in this filter response.

Voice: Your data are limited to a model that has a certain number of modes in it. How did you determine how many modes are in a model? Did you look at the frequency domain?

Mr. Ibrahim: We form matrices of increasing order, two by two, three by three, four by four etc. using the response that was measured in the lab and the response that we created from the measured response, which I called transformed stations, until we find a matrix of a certain order that becomes singular. We find the number of modes started, or the number of stations started, that are greater than the number of modes and then we would know how many modes are in this measured response.

Voice: You said something about the modal peaks that were too close in frequency and you couldn't resolve the two modes, that sounds like frequency domain information to me. Did the matrix inversion process give you any better information about how many modes were present?

Mr. Ibrahim: No, that was a comparison. We compared the results to the theoretical results for a plate and to some results that we obtained from a simple frequency sweep, getting the peaks on the oscilloscope to see when the response peaked and we called that resonance. In the frequency range where we were working we were only able to find three peaks using our method. We were also able to find four modes, and the theoretical results indicated that there were four modes; so we tried several times to locate the four modes using the peak amplitude method but we couldn't.

Mr. Klosterman (Structural Dynamics Research Corporation): I have tried this technique and one of the problems I have found is that you have to use anti aliasing filters if you are going to digitize your data. If you use anti aliasing filters then you no longer have a damped sinusoidal response. As soon as you pass a damped sinusoid through a filter it is no longer a damped sinusoid. However you are trying to fit a damped sinusoid to that data that you passed through the anti aliasing filter, so that is one problem that you get into with an approach like this.

Mr. Ibrahim: I didn't meet any constraints on the sampling frequency except as I mentioned the problem of numerically integrating the acceleration. To be successful in the numerical integration the sampling rate should be at least 5, 6, or 7 times the highest frequency, the more the better. I would like to mention here that I didn't like the idea of integrating very much so we will publish another paper where we only use one measured response and we don't integrate it; but I can't see any other constraints on the sampling frequency.

Mr. Klosterman: The problem is that you are putting an anti aliasing filter in front of the data coming in and you have changed the character of that data. It is no longer a damped sinusoid; however your equations and motion are still trying to fit a damped sinusoid to that data.

Mr. Ibrahim: What do I have after passing through the filter?

Mr. Klosterman: You now have a function in the frequency domain that is truncated at the high frequency and it does not fall off on a mass line; that is one problem that you get into with a time domain approach that is not present in a frequency domain approach.

Mr. Ibrahim: I think you are still thinking frequency domain while you are talking about the time domain technique. Are the equations that I have presented applicable at any time?

Mr. Klosterman: They are not. If you have a single-degree-of-freedom system that is supposed to decay in a single damped sinusoid and if you pass that through a filter it will no longer be a single damped sinusoid. It will now have a frequency domain characteristic that is truncated, a single damped sinusoid would go on out to infinite frequency. If you do a Fourier transform on a single damped sinusoid what does it look like? It is a function that continues on out to infinite frequency. But you have truncated the data; you have thrown away a lot of that data in the high frequency range and yet you are fitting an analytical model to it that is not really appropriate. There are some problems that you get into because of that and I have had to devise other techniques to handle those kinds of problems.

Mr. Ibrahim: We obtained damping factors in the three experiments that were carried out that were very reasonable compared to the theoretical ones and I didn't meet the problem that you are talking about. I am not thinking in the frequency domain. I have certain mathematical models and I am getting enough equations to solve for some unknowns in the system. I agree that filters might change the response a little but this wouldn't create a problem for me.

IDENTIFICATION OF STRUCTURAL MODAL PARAMETERS BY DYNAMIC TESTS AT A SINGLE POINT

N. MIRAMAND, J.F. BILLAUD, F. LELEUX
Centre Technique des Industries Mécaniques SENLIS (FRANCE)
and J.P. KERNEVEZ
Université de Technologie de Compiègne COMPIEGNE (FRANCE)

The present work deals with identification, after dynamic excitation tests at a single point, of modal parameters of a structure with arbitrary viscous damping, and possibly with practically coincident frequencies of vibration. Damping values are not necessarily low and the restrictive condition that it be possible to diagonalise the damping matrix on the base of natural modes of the conservative structure is not imposed.

The coefficients of the mobility-displacement functions given by the mathematical model of the structure are calculated by a least squares fit of theoretical values to the experimental results. A variational formulation of the error is established; this leads to the assessment of unknown coefficients by minimising a quadratic functional of the form : $J(Z) = \frac{1}{2} (AZ, Z) - (b, Z)$

where A and b respectively are a nonnegative definite matrix and a vector function of experimental data; Z represents the vector of coefficients to be identified. The modal coefficients are then obtained by decomposition of the so identified mobility-displacement functions into rational fractions. Several examples of the identification from simulated experimental results are presented to illustrate the performance of this method in assessing accurate values for modal characteristics of structures in difficult cases.

The vibratory behaviour of a linear mechanical structure can be determined by knowing its modal parameters and the forces exerted on the structure. The modal representation has a definite advantage because the structure, for a given excitation frequency, can be characterized by the only vibration modes nearly coincident with this frequency.

Modal characteristics can be determined experimentally :

- either by simultaneous excitations at several points of the structure at the resonant frequency of the vibration mode considered
- or by excitation at a single point of the structure using a frequency sweeping.

The first method consists in isolating each vibration mode by so regulating the excitation frequency and the distribution of the exciting forces that the velocity of the different points of the structure is in phase or in opposition of phase with the exciting forces. However, it is

not always possible to make a mode isolated, especially when the damping matrix cannot be diagonalised on the base of the natural modes of the associated conservative structure. On the other hand, the method by excitation at a single point is much easier to be implemented. A single exciter is adequate, the response being measured at several points. The transfer of the structure is shown by the displacement-mobility (or velocity) which is the ratio of the displacement (or velocity) at the point of measurement to the exciting force.

For an excitation frequency nearly coincident with the resonant frequency of an isolated mode of vibration, the structure behaviour is practically similar to that of a system with a unique degree of freedom. The characteristics of this mode then can be easily determined : natural frequency, generalized damping and mass, dynamic shape. On the other hand, when two or more resonant frequencies are nearly coincident, it is not so easy to determine the characteristics of

the corresponding modes of vibration. The problem which is then raised is to find out a method of dynamic identification of the structure, which is generally good, and which is especially applicable to the case of two or more modes being strongly coupled by excitation.

The identification methods can be basically divided into two groups: on the one hand, the iterative methods which proceed from initial estimations (mainly damping and resonant frequencies); on the other hand, the direct methods, with no initial estimations.

Among the numerous published works dealing with the problems of dynamic identification of structures, the following researches representing the various approaches generally used can be mentioned. RANEY [1] * separately identifies each mode from measurements of the response corresponding to frequencies nearly coincident with resonance. It is therefore necessary that the vibration modes be of sufficiently distinct resonant frequencies. FLANELLY [2] determines the dominant mode of vibration using the power method. If two modes are nearly coincident, the convergence is then very slow, and the approximation of the dominant mode might be inadequate to obtain a suitable estimation of the following modes. KLOSTERMAN-LEMON [3] determines the apparent parameters from a limited number of experimental measurements of the transfer functions, using an iterative method of least squares. The values of the resonant frequencies are estimated initially and are no longer revised afterwards.

Moreover, an estimation of the damping is necessary. KLOSTERMAN [4] also envisages the case of modes coupled by damping and considers various damping types. IBANEZ [5] develops a method based on an estimation of the whole modal characteristics. The restrictive hypothesis of diagonal mass matrix is used. Moreover, a specific type of non linear structure is envisaged. The method used by VAN LOON [6] also requires initial estimations. It yields excellent results in the determination of modal characteristics even when resonant frequencies are very near.

The method developed by DAT and MEURZEC [7][8][9] enters into the category of direct methods that do not require a previous estimation of the modal parameters (the number of modes is only to be known). To identify the coefficients of rational fractions which give the mobility-displacement functions, they use a formulation leading to solve an eigenvalue problem. It is very difficult to find an accurate solution to this problem. It is particularly the case when identifying the vibration modes of very near resonant frequencies and/or relatively important damping values. To avoid those difficulties the hereafter proposed method uses a different formulation that leads to the minimisation of a quadratic functional.

* Numbers in brackets designate references at end of paper.

The resolution of the corresponding linear system is then more effective in accurately evaluating modal parameters in the above-mentioned difficult identification cases. Before examining the principle of the latter method, the fundamentals relating to the displacement-mobility functions are first recalled.

I. MODAL PARAMETERS AND TRANSFER FUNCTIONS

The identification methods envisaged relate to linear mechanical systems, that is to say the motion of which is described by a system of linear differential equations with constant coefficients. The damping of the system is considered viscous. The general equation of motion for such systems subjected to external exciting forces, is of the form:

$$[M] \ddot{X} + [C] \dot{X} + [K] X = F \quad (1.1)$$

The motion being defined by n independent variables, the system possesses n degrees of freedom. Each degree of freedom is defined by the displacements x_k of a point i . Matrices $[M]$, $[C]$, $[K]$ are the symmetrical matrices of mass, damping and stiffness. X is the column vector of the x_i displacements for each degree of freedom. If the structure considered is not subjected to any external force, the equation of motion is then:

$$[M] \ddot{X} + [C] \dot{X} + [K] X = 0 \quad (1.2)$$

I.1) Conservative system

When there is no damping, the system is called conservative: In order to determine the general solutions of the matricial equation of the free motion of the structure:

$$[M] \ddot{X} + [K] X = 0 \quad (1.3)$$

Particular solutions are to be found in the form:

$$x_k = x_{0k} \exp(pt) \quad p \text{ complex}$$

$$k = 1, \dots, n$$

Substituting this value for X in (1.3), it follows that:

$$(p^2 [M] + [K]) X_0 = 0 \quad (1.4)$$

or else

* Notations \dot{X} and \ddot{X} indicate the first and second derivatives of X in relation to time.

$$|M|^{-1} |K| X_0 = -p^2 X_0 \quad (1.5)$$

Equation (1.5) leads to a problem of eigenvalues and eigenvectors. There exist n positive eigenvalues $\lambda_j = \omega_j^2$ and n eigenvectors ϕ_j solutions of (1.5); $f_j = \frac{\omega_j}{2\pi}$ is a natural frequency, ϕ_j the corresponding natural form (or natural mode). If the natural frequencies are all distinct, then the particular solutions $X_j = \phi_j \exp(p_j t)$ are linearly independent, and the real general solution of (1.3) is then :

$$\begin{aligned} x_k &= \sum_{j=1}^n \phi_j^k (A_j \cos \omega_j t + B_j \sin \omega_j t) \\ k &= 1, \dots, n \end{aligned} \quad (1.6)$$

where ϕ_j^k indicates the k th component of vector ϕ_j . A_j and B_j are determined by initial conditions. It should be noted that, eigenvectors ϕ_j being real, in each mode, all the points vibrate in phase or in opposition of phase. Moreover, it is known that the modes corresponding to 2 different natural frequencies are orthogonal, that is to say they verify the relations : (*)

$$\begin{aligned} \phi_i^t |M| \phi_j &= 0 & \text{if } \omega_i \neq \omega_j \\ \phi_i^t |K| \phi_j &= 0 \end{aligned} \quad (1.7)$$

Let $|\phi|$ be the matrix of modes, that is to say the matrix the column vectors of which are eigenvectors ϕ_i . The natural frequencies being supposed distinct, the eigenvectors are linearly independent; matrix $|\phi|$ is regular. Let then the vector Y defined by the transformation $X = |\phi| Y$. Coordinates Y_i are termed generalized coordinates. Equation (1.3) is then expressed by :

$$|M| |\phi| \ddot{Y} + |K| |\phi| Y = 0 \quad (1.8)$$

or else

$$|\phi|^t |M| |\phi| \ddot{Y} + |\phi|^t |K| |\phi| Y = 0 \quad (1.9)$$

Now matrices $|\phi|^t |M| |\phi|$ and $|\phi|^t |K| |\phi|$ are diagonal from (1.7). Let m_j and k_j be the dia-

gonal elements of these matrices; parameters m_j are the generalized stiffnesss which verify :

$$k_j = \omega_j^2 m_j \quad (1.10)$$

Equation (1.8) is then equivalent to the system of differential equations :

$$\begin{aligned} m_j \ddot{y}_j + k_j y_j &= 0 \\ j &= 1, \dots, n \end{aligned} \quad (1.11)$$

1.2) Dissipative system

For the models of mechanical structure with damping, particular solutions are to be found in the form :

$$X = \phi \exp(pt); p \text{ complex} \quad (1.12)$$

From (1.2), it follows that :

$$(p^2 |M| + p |C| + |K|) \phi = 0 \quad (1.13)$$

There exist n values $P_j = -\lambda_j + i\Omega_j$ and n complex vectors ϕ_j solutions of (1.13); the ϕ_j complex vectors are the natural forms of the dissipative system. It is to be noted that, in each mode, the points do not vibrate in phase any more. This general case will be further detailed in paragraph I. 4. b. However, there is a particular important case where matrix C can be diagonalised on the base of the natural modes of the conservative structure. CAUGHEY [10] has shown that a necessary and sufficient condition for being so was that the following relation be verified

$$|C| |M|^{-1} |K| = |K| |M|^{-1} |C| \quad (1.14)$$

The natural modes of the dissipative system are then the same as those of the associated conservative system. Let C_i be the diagonal terms of matrix $|\phi|^t |C| |\phi|$, equation (1.13) is then expressed by :

$$\begin{aligned} p^2 m_j + p c_j + k_j &= 0 \\ j &= 1, \dots, N \end{aligned} \quad (1.15)$$

In the case of the modal damping C_j being smaller than the critical damping $c_j < 2\sqrt{k_j m_j}$ equation (15) has 2 complex conjugate roots :

$$\begin{aligned} p_j &= -\lambda_j + i\Omega_j \\ \bar{p}_j &= -\lambda_j - i\Omega_j \end{aligned}$$

where

$$\lambda_j = \frac{c_j}{2 m_j} ; \Omega_j = \frac{\sqrt{4 k_j m_j - c_j^2}}{2 m_j}$$

(*) Symbol t indicates a matrix transposition.

Then a particular solution of (1.2) is :

$$x_j = \phi_j e^{-\lambda_j t} e^{i\Omega_j t} \quad (1.16)$$

The quantity

$$\beta_j = \frac{c_j}{2m_j \omega_j} - \text{ratio of the}$$

generalized damping c_j to the critical damping

$2\sqrt{k_j m_j} = 2\omega_j m_j$ - indicates the reduced damping of the j th mode.

1.3) Complex matrices of impedance and mobility

If a system with n degrees of freedom is subjected to a combination of sinusoidal forces of the same pulsation ω and for a degree of freedom X_r of phase ϕ_r , say in complex notation

$$F = \{F_r(t)\} = \{f_r e^{i\phi_r} e^{i\omega t}\}$$

The response at constant load is harmonic and of the same pulsation :

$$X = \{X_r(t)\} = \{x_r e^{i\theta_r} e^{i\omega t}\}$$

It is a solution of (1.1), say

$$[-\omega^2 |M| + i\omega |C| + |K|] X = F \quad (1.18)$$

The complex matrix of mechanical impedance is by definition :

$$|Z| = -\omega^2 |M| + i\omega |C| + |K| \quad (1.19)$$

It is such as :

$$|Z| X = F$$

The displacement-mobility matrix $|A|$ such as $X = |A| F$ is defined by $|A| = |Z|^{-1}$. Each element a_{ij} of A is given by

$$a_{ij} = (-1)^{i+j} \frac{\text{Cof}(Z_{ij})}{\text{Det}(|Z|)}$$

It is a rational fraction in ω , the numerator and the denominator being polynomials of degrees $2n-2$ and $2n$ respectively.

1.4) Modal mobility

Two cases are to be distinguished according to whether or not the damping matrix C can be diagonalised on the base of the natural modes of the conservative structure.

a) Matrix $|C|$ can be diagonalised

Equation (1.1) is then equivalent to the system of equations :

$$\begin{cases} (-\omega^2 m_j + i\omega c_j + k_j) y_j = \phi_j^L F_L \\ j = 1, \dots, n \end{cases} \quad (1.20)$$

Where F_L corresponds to the nodal excitation at point L . The response at point K is then:

$$x_k = \sum_{j=1}^n \phi_j^k y_j \quad (1.21)$$

From (1.20) it follows that :

$$x_k = \sum_{j=1}^n \frac{\phi_j^k \phi_j^L F_L}{-\omega^2 m_j + i\omega c_j + k_j} \quad k = 1, \dots, n \quad (1.22)$$

The displacement-mobility between the point of excitation L and the point of measurement k is the ratio of x_k to F_L ; it is therefore the function :

$$A_{kL}(i\omega) = \sum_{j=1}^n \frac{\phi_j^k \phi_j^L}{-\omega^2 m_j + i\omega c_j + k_j} \quad (1.23)$$

Relation (1.23) can also be expressed in the form :

$$A_{kL}(i\omega) = \sum_{j=1}^n \frac{\phi_j^k \phi_j^L}{m_j(-\omega^2 + 2i\beta_j \omega_j \omega + \omega_j^2)} \quad (1.24)$$

b) Matrix C cannot be diagonalised

Equations are no longer uncoupled using the base of the natural modes of the conservative system. By means of the DUNCAN method it is possible to calculate the modes of the dissipative system as follows :

equation (1.1) is equivalent to the system :

$$\begin{bmatrix} |C| & |M| \\ |M| & 0 \end{bmatrix} \begin{bmatrix} \dot{X} \\ \ddot{X} \end{bmatrix} + \begin{bmatrix} |K| & 0 \\ 0 & -|M| \end{bmatrix} \begin{bmatrix} X \\ \dot{X} \end{bmatrix} = \begin{bmatrix} F \\ 0 \end{bmatrix} \quad (1.25)$$

$$\text{or } |A| \dot{Y} + |B| Y = P \quad (1.26)$$

$$\text{where } Y = \begin{bmatrix} X \\ \dot{X} \end{bmatrix} \quad \text{and} \quad P = \begin{bmatrix} F \\ 0 \end{bmatrix}$$

The solutions of equations (1.26) with no right-hand side, of the form $Y = Y_0 e^{\lambda t}$, are solutions of

$$\lambda |A| Y = -|B| Y \quad (1.27)$$

$|M|$ being invertible and also $|K|$, when there are no rigid body modes, $|B|$ is then invertible λ and Y are then solutions of the eigenvalue problem:

$$|E| Y = \frac{1}{\lambda} Y \quad (1.28)$$

where $|E| = -|B|^{-1}|A|$

There exist n pairs of conjugate eigenvalues:

$$\lambda_j = u_j + i v_j, \quad \bar{\lambda}_j = u_j - i v_j$$

v_j is termed damped natural frequency, u_j is the damping coefficient.

Moreover, eigenvector ϕ_j are orthogonal in relation to matrices A and B provided that eigenvalues λ_j are distinct. In fact, from (1.27)

$$\begin{aligned} \lambda_j |A| \phi_j &= -|B| \phi_j \\ \lambda_i |A| \phi_i &= -|B| \phi_i \end{aligned}$$

Since A and B are symmetrical, then:

$$(\lambda_j - \lambda_i) \phi_j^t |A| \phi_i = 0 \quad (1.30)$$

Hence if $\lambda_j \neq \lambda_i$, $\phi_j^t |A| \phi_i = 0$

As is the case before, the problem of the response to a sinusoidal excitation is first solved on the base of the natural modes, then by a change of variables, on the geometrical base.

$$\text{Let } P = P_0 e^{i\omega t} \quad (1.31)$$

From (1.26), it follows that:

$$(i\omega |A| + |B|) Y = P \quad (1.32)$$

Let $Y = |\phi| Z$; then equation (1.32) is expressed:

$$\begin{vmatrix} i\omega a_i + b_i \end{vmatrix} Z = |\phi|^t P \quad (1.33)$$

a_i and b_i are the diagonal terms of matrices $\phi^t |A| \phi$ and $\phi^t |B| \phi$. Then Y is defined by:

$$Y = \phi |i\omega a_i + b_i|^{-1} |\phi|^t P \quad (1.34)$$

In the case where E has complex eigenvalues only, matrix $|\phi|$ is of the form:

$$\phi = \begin{vmatrix} |\psi| & |\psi| \\ |\psi| |A| & |\psi| |A| \end{vmatrix} \quad \text{Symbol } ^- \text{ indicates a conjugate matrix}$$

Where $|A|$ is the diagonal matrix which contains only the eigenvalues with positive imaginary part and $|\psi|$ the matrix of complex eigenvectors corresponding to the eigenvalues appearing in $|A|$. Response X is then given by:

$$X = \sum_{j=1}^n \frac{\psi_j \psi_j^t F^{\ell}}{b_j} + \frac{\bar{\psi}_j \bar{\psi}_j^t f^{\ell}}{a_j} \quad (1.35)$$

As $\lambda_j = -\frac{b_j}{a_j}$, the displacement-mobility

corresponding to an excitation at ℓ and to the response at k , is:

$$A_{k\ell}(i\omega) = \sum_{j=1}^n \frac{\psi_j^{\ell} \psi_j^k}{a_j(i\omega - \lambda_j)} + \frac{\bar{\psi}_j^{\ell} \bar{\psi}_j^k}{\bar{a}_j(i\omega - \bar{\lambda}_j)} \quad (1.36)$$

The mobility function between points k and ℓ is the function $A_{k\ell}(p)$, i. e.:

$$A_{k\ell}(p) = \sum_{j=1}^n \frac{\phi_j^{\ell} \phi_j^k}{m_j(p^2 + 2\beta_j \omega_j p + \omega_j^2)} \quad (1.37)$$

if matrix $|C|$ can be diagonalised.

$$A_{k\ell}(p) = \sum_{j=1}^n \frac{\psi_j^k \psi_j^{\ell}}{a_j(p - \lambda_j)} + \frac{\bar{\psi}_j^k \bar{\psi}_j^{\ell}}{\bar{a}_j(p - \bar{\lambda}_j)} \quad (1.38)$$

if matrix $|C|$ cannot be diagonalised.

In both cases, the resolution into simple components is of the form:

$$A_{k\ell}(p) = \sum_{j=1}^n \frac{A_i^{k\ell}}{p - p_j} + \frac{\bar{A}_i^{k\ell}}{p - \bar{p}_j} \quad (1.39)$$

II. IDENTIFICATION OF MODAL PARAMETERS

The identification method proposed for the modal parameters uses the resolution of the mobility functions into simple components and does not require any preliminary estimation of the results to be identified. This method mainly comprises three stages

a. identification of the mobility functions required for the representation of the system,

b. determination of the poles of the rational fractions,

c. Resolution into simple components.

The principal step of this method consists in identifying the mobility function coefficients, the other steps concerning usual operations in linear system modal analyses. DAT and MEURZEC [7, 8, 9] have used such a method and arrived at an eigenvalue problem for determining mobility function coefficients. In order to avoid this eigenvalue problem which may be very difficult to be solved in certain cases, a new formulation of the problem of identification of the modal parameters is put forward. The problem is then reduced to the minimisation of a quadratic functional.

II. 1) Formulation of the problem

Let $A_{uv}^*(i\omega_k)$, $k = 1, \dots, l$ be a sample of the experimental values of the mobility function between points u and v . The problem is to calculate coefficients X^r and Y^r by a least squares fit of the experimental results to the theoretical values given by :

$$A_{uv}(i\omega) = \frac{\sum_{r=1}^m (i\omega)^{r-1} X^r}{\sum_{r=1}^n (i\omega)^{r-1} Y^r} = \frac{P(i\omega)}{Q(i\omega)}$$

$$\text{Where } \begin{cases} m = 2N - 1 \\ n = 2N + 1 \\ N = \text{Number of degrees of freedom} \end{cases}$$

These coefficients are defined to a multiplicative constant. Then the numerator coefficient of the highest degree can be standardised at the value 1.

Let :

$$\begin{aligned} \epsilon(i\omega_k) &= \sum_{r=1}^m (i\omega_k)^{r-1} X^r \\ &- \sum_{r=1}^{n-1} A_{uv}^*(i\omega_k) (i\omega_k)^{r-1} Y^r \\ &- A_{uv}^*(i\omega_k) (i\omega_k)^{n-1} \end{aligned} \quad (2.1)$$

$\epsilon(i\omega_k)$ characterizes the difference between the theoretical values and the experimental results.

Notation :

ϵ Column vector of the $\epsilon(i\omega_k)$

X Column vector of the X^r

Y Column vector of the Y^r

W Column vector of the $A_{uv}^*(i\omega_k)(i\omega_k)^{n-1}$

$|P|$ rectangular matrix defined by

$$p_{kr} = (i\omega_k)^{r-1} \quad \begin{matrix} r = 1 \dots m \\ k = 1 \dots l \end{matrix}$$

$|T|$ rectangular matrix defined by

$$t_{kr} = A_{uv}^*(i\omega_k)(i\omega_k)^{r-1} \quad \begin{matrix} r = 1, \dots, n-1 \\ k = 1, \dots, l \end{matrix}$$

With this notation, (2.1) is expressed as follows :

$$\epsilon = |P| X - |T| Y - W \quad (2.2)$$

Hence

$$\begin{aligned} e = \epsilon^t \epsilon &= \left| |P| X - |T| Y - W \right|^2 \\ &- 2 \operatorname{Re} (|P| X - |T| Y, W) + |W|^2 \end{aligned} \quad (2.3)$$

The expression $\left| |P| X - |T| Y \right|^2$ is also expressed in the form :

$$\begin{vmatrix} X^t Y^t & |P| & |T| \\ |P|^t & |P| & |T| \\ |T|^t & |T| & |T| \end{vmatrix} \begin{vmatrix} X \\ Y \end{vmatrix} = \begin{vmatrix} X^t Y^t & |A| \\ |A|^t & |A| \end{vmatrix} \begin{vmatrix} X \\ Y \end{vmatrix}$$

where $|P|^t$ and $|T|^t$ are the conjugate and transposed matrices of $|P|$ and $|T|$.

II. 2) Identification of coefficients X^r and Y^r

Variational formulation of the error

First, the above - defined matrix $|A|$ is hermitian and nonnegative definite. If Z indicates the column vector X , the error e is expressed in the form of a functional

$$J(Z) = (|A| Z, Z) - 2(b, Z) + |W|^2$$

Since

$$\begin{aligned} (|P| X - |T| Y, W) &= (W_R^t - i W_I^t) \\ ((|P|_R + i |P|_I) X - (|T|_R + i |T|_I) Y) & \end{aligned} \quad (2.4)$$

Hence

$$\begin{aligned} R_e (|P| X - |T| Y, W) &= (|P|_R X - |T|_R Y, W_R) \\ &+ (|P|_I X - |T|_I Y, W_I) \end{aligned} \quad (2.5)$$

If $|O|$ is a real matrix such as a $|M| |O|$ or $|O| |M|$ type matrix obtained by joining $|M|$ and $|O|$ in line that gives a matrix with definite dimensions: $1, n+m-1$; one obtains:

$$R_e(|P|X - |T|Y, W) = ((|P_R||O| - |O||T_R|)Z, W_R) + ((|P_I||O| - |O||T_I|)Z, W_I)$$

considering that:

$$B_R = |P_R||O| - |O||T_R|$$

$$B_I = |P_I||O| - |O||T_I|$$

expression (2.3) is then expressed as follows:

$$e = (|A|Z, Z) - 2(|B_R|^t W_R + |B_I|^t W_I, Z) + |W|^2$$

Matrix $|A|$ is complex, however the real part only is to be considered since $|A| = |A_R| + i|A_I|$ where $|A_R|$ is real and symmetrical, $|A_I|$ real and skew symetric.

$$\text{Now } (|A_I|Z, Z) = Z^t |A_I| Z = Z^t |A_I|^t Z$$

Thus $(|A|Z, Z) = (|A_R|Z, Z)$ and A_R is then a nonnegative definite matrix. The search for coefficients X^r and Y^r is then reduced to minimizing a functional $J(Z)$ of the form:

$$j(Z) = \frac{1}{2} (|A_R|Z, Z) - (b, Z) \quad (2.8)$$

Minimizing J

Matrix $|A|$ is a priori simply nonnegative definite. However, in practice, and provided that the sampling of function $A^*(i\omega)$ is properly chosen, $|A_R|$ will be positive definite. Then J has a unique minimum for u characterized by $j'(u) = 0$, i.e. $|A_R|u = b$. Two methods of solution can be used: 1) the conjugate gradient method, 2) Cholesky's method. It is better to use the latter. In fact, the performance of the gradient method depends, to a great extent, on the initial estimation of the coefficients to be identified. Now, it is practically impossible to have an approximation of these coefficients. On the other hand, Cholesky's method enables direct calculation. Moreover, this method is more suitable than the gradient method to the type of matrices encountered (often ill conditioned).

II. 3) Calculation of modal parameters

The search for the poles of the rational frac-

tion has been carried out by the well-known BAIRSTOW'S method. The principle is to determine the divisors of the polynomial $Q(X)$ of the form $x^2 - sx + p$. This method therefore has the advantage of supplying two conjugate roots for each iteration. Then the rational fraction has been resolved to simple components as follows:

$$A_{uv}(P) = \frac{\sum_{i=1}^m x^i p^{i-1}}{\sum_{i=1}^m y^i p^{i-1}} = \frac{\sum_{i=1}^m x^i p^{i-1}}{\prod_{i=1}^N (p - p_i)(p - \bar{p}_i)} \quad (2.9)$$

the p_i 's are the poles with positive imaginary part. Now, $A(p)$ is expressed, from (1.39)

$$A_{uv}(P) = \sum_{i=1}^N \left[\frac{A_i^{uv}}{p - p_i} + \frac{\bar{A}_i^{uv}}{p - \bar{p}_i} \right]$$

Hence

$$A_{uv}(P)(p - p_i) = A_i^{uv} + \frac{\bar{A}_i^{uv}(p - p_i)}{p - \bar{p}_i} + \sum_{\substack{j=1 \\ j \neq i}}^N \left[\frac{A_j^{uv}}{p - p_j} + \frac{\bar{A}_j^{uv}}{p - \bar{p}_j} \right] (p - p_i) \quad (2.10)$$

and

$$A_{uv}(p)(p - p_i) = \frac{\sum_{j=1}^m x^j p^{j-1}}{(p - \bar{p}_i) \prod_{\substack{j=1 \\ j \neq i}}^N (p - p_j)(p - \bar{p}_j)} \quad (2.11)$$

by identifying (2.10) and (2.11) for $p = p_i$ it follows that:

$$A_i^{uv} = \frac{\sum_{j=1}^m x^j p_i^{j-1}}{(p_i - \bar{p}_i) \prod_{\substack{j=1 \\ j \neq i}}^N (p_i - p_j)(p_i - \bar{p}_j)} \quad (2.12)$$

Explicit formulation of parameters

1) Case of a diagonal generalized damping

Let v be the excitation point, the modes are standardized in relation to component k_0 :

$$\phi_i k_0 = 1 \quad \text{for every } i$$

By identifying expressions (1.37) and (1.39) it follows that :

$$\frac{\phi_i^u \phi_i^v}{m_i(p-p_i)(p-\bar{p}_i)} = \frac{A_i^{uv}}{p-p_i} + \frac{\bar{A}_i^{uv}}{p-\bar{p}_i} \quad (2.13)$$

Hence :

$$\frac{\phi_i^u \phi_i^v}{m_i} = -A_i^{uv} \bar{p}_i - \bar{A}_i^{uv} p_i \quad (2.14)$$

In particular :

$$\frac{\phi_i^v}{m_i} = -A_i^{kv} \bar{p}_i - \bar{A}_i^{kv} p_i \quad (2.15)$$

From (2.14), it follows that :

$$\phi_i^k = \frac{R_e(A_i^{kv} \bar{p}_i)}{R_e(A_i^{ko} \bar{p}_i)} \quad (2.16)$$

The generalized mass is obtained from expressions (2.14), (2.16).

2) Case of a non-diagonal generalized damping

Calculation of modes ψ_j and coefficients a_j

By identifying (1.38) and (1.39), it follows that :

$$\frac{\psi_j^u \psi_j^v}{a_j(p-p_j)} = \frac{A_j^{uv}}{p-p_j}$$

The simplest condition of standardization of the ψ_j 's is : $\psi_j^v = a_j$ $j = 1, \dots, n$

Hence

$$\psi_j^u = A_j^{uv} \quad \text{and} \quad A_j^{vv} = a_j$$

III. RESULTS

In order to verify the accuracy of this new method of identification of structural modal parameters, tests have been carried out on such systems similar to the one represented in figure 1.

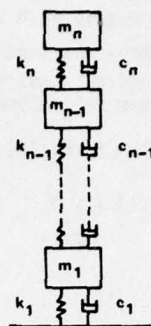


FIG 1.

According to the values of damping coefficients C_i , the damping matrix can be diagonalised or not on the base of the natural modes of the associated conservative system. The displacement-mobility functions which are calculated on these models provide the "experimental values" from which the algorithm of identification establishes the modal characteristics : resonant frequency, generalized damping and mass, modal shape. The experimental values so generated have been willingly disturbed in certain examples in order to simulate the measurement errors unavoidable in practice.

Several numerical examples have been envisaged to illustrate the accuracy obtained in determining the modal characteristics in difficult cases where the resonant frequencies of the vibration modes are very near and where the values of modal damping are not necessarily low. The cases of low damping values (less than 4%) have been especially distinguished from those cases of high damping values (10% approximately). It will also be seen that, when the natural frequencies of two vibration modes are near enough, the ratio of the reduced damping values in each of both modes has an effect on the accuracy (which however remains excellent) of the modal characteristics obtained. This leads to distinguish the cases where the ratio in question is close to unity from the cases where it is sharply different from unity.

For each example, tables show the exact values of the calculated values of the modal characteristics for each pair of modes (excitation - response) which may be envisaged on the structure (*). However, according to MAXWELL-BETTI'S reciprocal theorem, it is not necessary to take into account displacement-mobility functions such as X_j^i

(point j displacement for a point i excitation) if, besides, the mobility function $\frac{X_i}{F_j}$ has already been considered.

The percentages of error relating to each identified value are given. It should be noted that, in the examples given, whatever the pair of points

(*) In the cases where the damping matrix cannot be diagonalised on the base of the natural modes of the associated conservative system, tables show coefficient a_j instead of generalized masses)

considered on the mechanical systems, the modal values identified are in all cases extremely accurate, although the vibration modes are usually strongly coupled by excitation. The displacement mobility functions X_i/F_j (module and phase), obtained from the modal characteristics identified, are shown in continuous lines on the graphs which illustrate each example. The same functions relating to each vibration mode identified are shown in dashed lines. The "experimental points" from which the identification has been carried out are also given.

Finally, for each example, the convergence test used in BAIRSTOW's method is indicated. In the search for the pair of values (s, p) such that the polynomial $x^2 - sx + p$ divides the denominator of the mobility function, the algorithm is discontinued when :

$$\frac{|s^{n+1} - s^n|}{|s^n|} + \frac{|p^{n+1} - p^n|}{|p^n|} < \epsilon$$

with s^n and p^n values of s and p at the nth iteration.

A) Examples with diagonal generalized damping matrix

A.1. System with 2 degrees of freedom

A.1.1. Damping different in each of the 2 modes (fig 2 and 3 ; table 1)

Number of experimental points used : 60

Convergence test for the pole calculation :

$$\epsilon = 10^{-6}$$

The natural frequencies of the two vibration modes are practically coincident

$$\frac{f_2 - f_1}{f_1} = 10^{-6}$$

The accuracy obtained on modal characteristics is however better than 2.10^{-4}

A.1.2. Reduced damping practically identical in both modes (fig 4; table 2)

Number of experimental points : 100

Convergence test for the pole calculation :

$$\epsilon = 10^{-3}$$

Comparative frequency difference $\frac{f_2 - f_1}{f_1} = 10^{-2}$

The accuracy obtained on modal characteristics, while remaining excellent, is not however so good as in the cases where the damping values in each mode are not identical.

A.1.3 High damped values (fig 5)

Number of experimental points : 60

Convergence test for the pole calculation :

$$\epsilon = 10^{-5}$$

Comparative frequency difference $\frac{f_2 - f_1}{f_1} = 10^{-5}$

The accuracy obtained on modal characteristics is better than 5.10^{-5} .

A.2. System with 4 degrees of freedom (fig 6, tables 3a and 3b)

Number of experimental points (in the 9 - 29 Hz frequency band) : 200

Convergence test for the pole calculation :

$$\epsilon = 10^{-3}$$

Two among of the four vibration modes of this system show a comparative frequency difference $\frac{f_2 - f_1}{f_1}$ equal to 2.4×10^{-2} .

f1

A.3 System with 8 degrees of freedom (fig 7)

Number of experimental points : 100

The accuracy obtained on modal characteristics is better than 3.10^{-4} .

B) Examples with non-diagonal generalized damping matrix

System with 4 degrees of freedom (fig 8; table 4)

Number of experimental points : 200

Convergence test for the pole calculation :

$$\epsilon = 10^{-5}$$

C) Effect of truncation of the natural mode base

In order to implement the identification method put forward, it is necessary from the outset to know the number of vibrations modes (number of poles) searched for in the frequency band examined. This number is to be estimated from the number of resonance peaks which are observed on the displacement-mobility functions plotted experimentally. But this does not mean that the number of vibration modes to be searched for should be strictly equal to the number of apparent resonance values. As a matter of fact, the examples above have shown well enough that, for modes of vibrations of very near resonant frequencies, it is not possible to distinguish each constituent mode by simply observing the mobility curves. It is therefore advisable to search initially for more poles to be identified than the simply observed experimental curves show. In addition the frequency band experimental ana-

lysed is necessarily finite, and the value of the natural frequency of a vibration mode may be very little higher than the latest frequency observed. The effect of this vibration mode upon the values of the mobility functions, in the frequency band analysed, is then noticeable. Rather large errors can therefore be made on the identification of the characteristics of the vibration modes the natural frequency of which is within the frequency band analysed. In order to avoid this truncation of the modal base, a greater number of poles should be searched for.

This point is illustrated by the example concerning the system with 4 degrees of freedom and diagonal generalized damping A.2 (tables 3a and 3b). If the experimental points chosen are within the 9-26 Hz frequency band, the last natural frequency (26.36 Hz) of the system is no longer within the frequencies analysed. If the identification of the modal parameters of the system is carried out by searching for 3 poles, the results obtained show rather large errors: up to 58 % for the 3rd mode damping. The errors recorded for generalized masses and modal shapes are still larger. Moreover the results obtained are different according to the pair of points considered. Figure 9 shows an example of the mobility function obtained, in dashed lines, as compared with the mobility function (continuous lines) resulting from an identification carried out from 4 poles within the 9-29 Hz band. The experimental points used are 170 in number and they are identical with the first 170 points considered in the example corresponding to 3a and 3b. The convergence tests in the search for poles are identical in both cases. On the other hand, if four poles are searched for within the 9-26 Hz limited frequency band, the accuracy of the results obtained, especially those relating to the fourth mode, is found to be comparable in accuracy with the results obtained in the table 3a and 3b. It is therefore possible to identify a mode outside the frequency band analysed and especially to improve greatly the accuracy of the modal characteristics the natural frequency of which is within the frequency band analysed.

D) Example with measurement errors

In order to test the identification method with regard to displacement-mobility measurement data containing errors, several examples have been dealt with in which the displacement-mobility values were willingly disturbed. No undue sensitivity of the method to measurement errors has been noticed. The identification of the modal characteristics of four vibration modes carried out from a set of 200 "experimental" points with approximately 5 % of errors and randomly distributed is shown on figure 10. In consideration of the measurement errors, the accuracy obtained on modal characteristics by means of this identification method is therefore good.

4. CONCLUSION

In conclusion, the identification method proposed for structures with arbitrary viscous damping (whether the generalized damping is diagonal or not) yields very accurate results even in difficult cases where the vibration modes are very strongly coupled by excitation because of the vicinity of their natural frequencies. In addition, it is possible to eliminate the effect of truncation of the modal base which affects the accuracy of modal characteristics, by searching for more vibration modes than the observed frequency band actually has. The problem of the identification of the structural modal parameters by a test single point therefore concerns the accuracy only of the measurements carried out since the identification method proposed, even in very difficult cases which may occur in practice, leads to negligible errors as compared with the errors due to experimentation.

REFERENCES

1. RANEY J.P. HOWLETT JT
Identification of Dynamic Systems by Use of Near-Resonance Testing. NASA TN D-5069 February 1969.
2. FLANELLY W.G. BERMAN A. & BARNBY R.M.
Theory of Structural Dynamic Testing Using Impedance Techniques. USAAVLABS Technical Report 70-64 June 1970
3. KLOSTERMAN A.L. 1 LEMON J.R.
Building Block Approach to Structural Dynamics ASME Publication 1969 - Vibr - 30
4. KLOSTERMAN A.L.
On the Experimental Determination and Use of Modal Representations of Dynamic characteristics. University of Cincinnati Ph. D 1971
5. IBANEZ P.
Identification of Dynamic Structural Models from Experimental Data. University of California, Los Angeles Ph. D 1972
6. VAN LOON P.
Modal parameters of mechanical structures. Katholieke Universiteit te Leuven Septembre 1974
7. DAT R. 1 MEURZEC J.L.
Exploitation, par lissage mathématique, des mesures d'admittance d'un système linéaire. Recherche Aérospatiale 1972 n° 4 (July-August) pp 209-215
8. DAT R.
Détermination des modes propres d'une structure par essai de vibration avec excitation non appropriée. Recherche Aérospatiale 1973 n°2 (March-April) pp99-118
9. DAT R.
Détermination des caractéristiques dynamiques d'une structure à partir d'un essai de vibration avec excitation ponctuelle. Recherche Aérospatiale 1973 n° 5 (septembre-octobre) - pp 301-306
10. CAUGHEY TK. O'KELLY M. E. J.
Classical normal modes in damped linear dynamic systems. Journal of Applied Mechanics Vol 32 (1965) pp 583-588

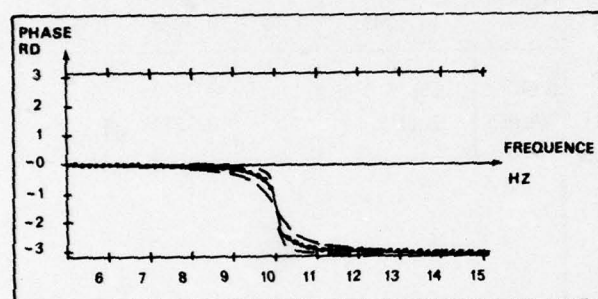
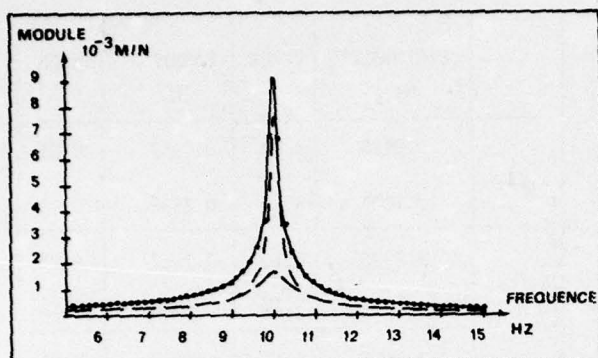


FIG 2 : EXAMPLE A.1.1 (see table 1)

	EIGENVALUES Hz	ERROR %	DAMPING %	ERROR
Exact Values	10 10.00001		0.7959 3.9789	
X_1/F_1	9.99999	1.10^{-4}	0.7957	1.10^{-2}
	9.99999	2.10^{-4}	3.9791	5.10^{-3}
X_1/F_2	9.99999	1.10^{-4}	0.7957	1.10^{-2}
	9.99999	2.10^{-4}	3.9791	5.10^{-3}
X_2/F_2	9.99999	1.10^{-4}	0.7957	1.10^{-2}
	9.99999	2.10^{-4}	3.9791	5.10^{-3}

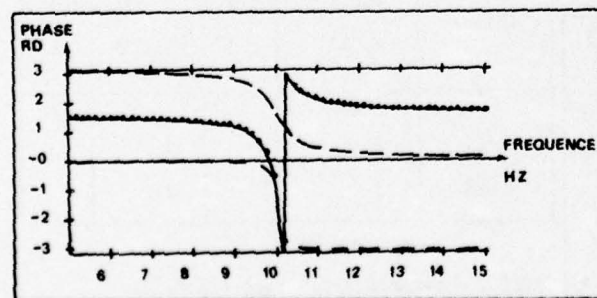
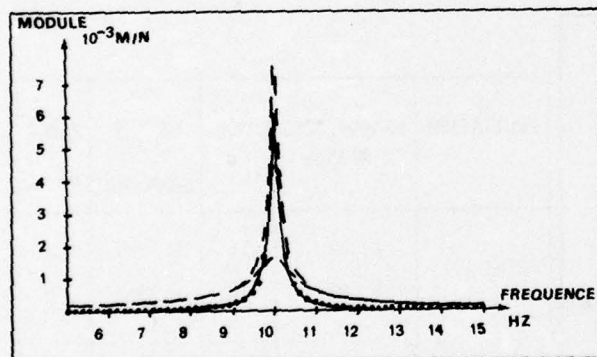


FIG 3 : EXAMPLE A.1.1 (see table 1)

EXCITATION	GENERALIZED MASSES	ERROR	SHAPES 2 nd COMPONENT	ERROR
POINT 1	2.0001	5.10^{-3}	1.0000	$<5.10^{-3}$
	1.9998	1.10^{-2}	-0.9998	2.10^{-2}
POINT 2	2.0001	5.10^{-3}	1.0000	$<5.10^{-3}$
	2.0004	2.10^{-2}	-0.9998	2.10^{-2}
EXACT VALUES	2		1	
	2		-1	

TABLE 1- EXAMPLE A.1.1 (see figures 2 and 3)

$$(f_2 - f_1) / f_1 = 10^{-6}$$

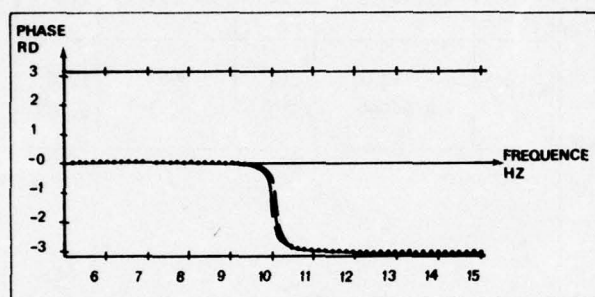
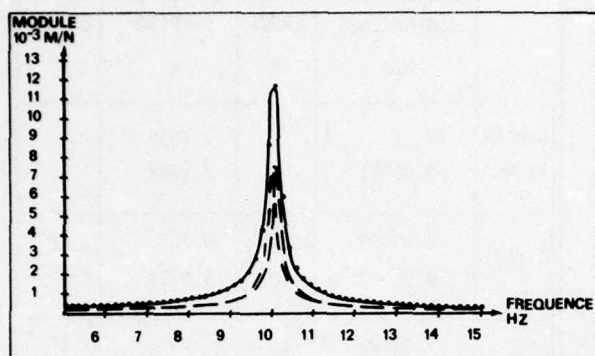


FIG 4 : EXAMPLE A.1.2 (see table 2)

	EIGENVALUES Hz	ERROR %	DAMPING %	ERROR %
X_1/F_1	9.9996	$4 \cdot 10^{-3}$	0.7957	0.01
	10.1003	$3 \cdot 10^{-3}$	0.7888	0.12
X_1/F_2	9.9996	$4 \cdot 10^{-3}$	0.7957	0.01
	10.1003	$3 \cdot 10^{-3}$	0.7888	0.12
X_2/F_2	9.9996	$4 \cdot 10^{-3}$	0.7957	0.01
	10.1003	$3 \cdot 10^{-3}$	0.7888	0.12
EXACT VALUES	10		0.7958	
	10.1		0.7879	

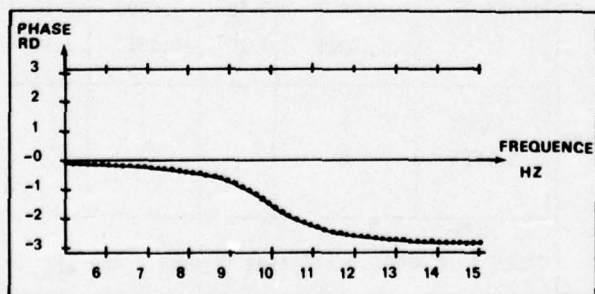
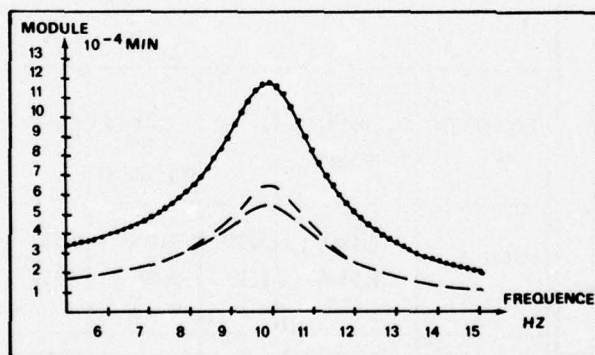


FIG : 5 EXAMPLE A.1.3 $(f_2 - f_1)/f_1 = 10^{-5}$

EXCITATION	GENERALIZED MASSES	ERROR	SHAPES 2 nd COMPONENT	ERROR
POINT 1	2.012	0.6	0.9999	0.01
	1.987	0.6	-0.9877	1.25
POINT 2	2.012	0.6	1.000	<0.05
	2.037	1.8	-1.012	1.2
EXACT VALUES	2		1	
	2		-1	

TABLE 2 - EXAMPLE A.1.2 (see figure 4)
 $(f_2 - f_1)/f_1 = 10^{-2}$

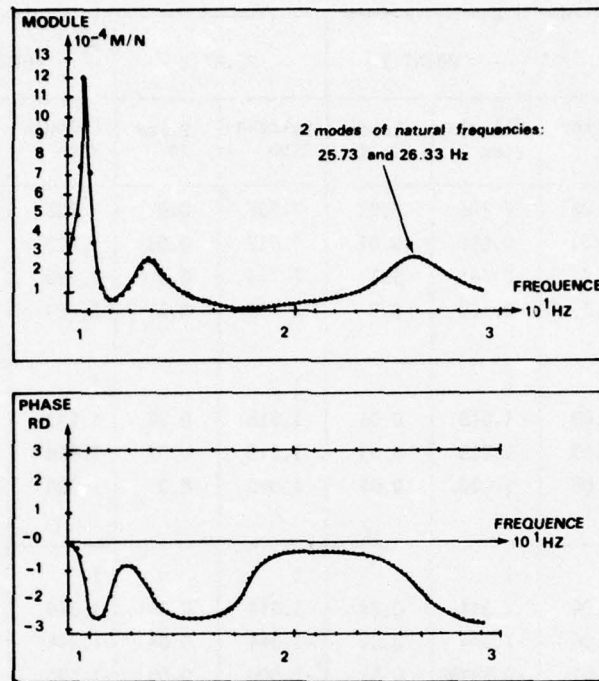


FIG 6 : EXAMPLE A.2 (see tables 3a , 3b)

	X_1/F_1	X_2/F_1	X_3/F_1	X_4/F_1	X_2/F_2	X_3/F_2	X_4/F_2	X_3/F_3	X_4/F_3	X_4/F_3		
											EXACT VALUES	ERROR
EIGENVALUES Hz	9.834	9.834	9.834	9.834	9.834	9.834	9.834	9.834	9.834	9.834	9.836	0.02
	12.87	12.87	12.87	12.87	12.87	12.87	12.87	12.87	12.87	12.87	12.89	0.2
	25.73	25.73	25.73	25.73	25.73	25.73	25.73	25.73	25.73	25.73	25.75	0.03
	26.33	26.33	26.33	26.33	26.33	26.33	26.33	26.33	26.33	26.33	26.35	0.12
REDUCED DAMPING IN %	1.540	1.540	1.540	1.540	1.540	1.540	1.540	1.540	1.540	1.540	1.540	<0.03
	5.207	5.207	5.207	5.207	5.207	5.207	5.207	5.207	5.207	5.207	5.200	0.14
	4.044	4.044	4.044	4.044	4.044	4.044	4.044	4.044	4.044	4.044	4.040	0.1
	4.999	4.999	4.999	4.999	4.999	4.999	4.999	4.999	4.999	4.999	5.000	0.02

TABLE 3 a : EXAMPLE A. 2

EXCITATION	POINT 1		POINT 2		POINT 3		POINT 4		Exact Values
	Calculation	Error in %	Calculation	Error in %	Calculation	Error in %	Calculation	Error in %	
GENERALIZED MASSES	7.235	0.02	7.235	0.02	7.235	0.02	7.235	0.02	7.236
	5.612	0.01	5.612	0.01	5.612	0.01	5.612	0.01	5.612
	2.760	0.2	2.761	0.1	2.754	0.4	2.755	0.4	2.764
	3.110	0.1	3.109	0.1	3.089	0.5	3.085	0.6	3.106
MODE SHAPES 1st mode	1		1		1		1		1
	1.618	0.03	1.618	0.03	1.618	0.03	1.618	0.03	1.618
	1.618	0.03	1.618	0.03	1.618	0.03	1.618	0.03	1.618
	1.000	0.05	1.000	0.05	1.000	0.05	1.000	0.05	1
2nd mode	1.		1		1		1		1
	1.344	0.04	1.344	0.04	1.344	0.04	1.344	0.04	1.344
	1.344	0.04	-1.344	0.04	-1.344	0.04	-1.344	0.04	-1.344
	0.9999	0.01	-0.9999	0.01	-1.000	0.05	-1.000	0.05	1
3d mode	1		1		1		1		1
	-0.6178	0.03	-0.6180	0.01	-0.6180	0.01	-0.6180	0.01	-0.618
	-0.6178	0.03	-0.6188	0.1	-0.6172	0.1	-0.6172	0.1	-0.618
	1.001	0.1	1.001	0.1	0.9987	0.13	0.9990	0.1	1
4th mode	1		1		1		1		1
	-0.7443	0.05	-0.7440	0.01	-0.7438	0.1	-0.7438	0.1	-0.744
	0.7467	0.4	0.7461	0.3	0.7416	0.4	7.414	0.4	-0.744
	1.004	0.4	-1.003	0.3	-0.9968	0.3	-0.9960	0.4	-1

TABLE 3b : EXAMPLE A.2 (see figure 6)

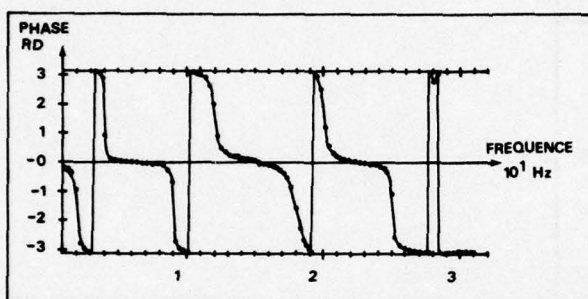
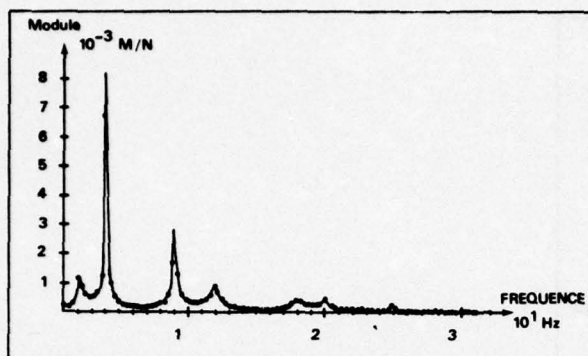


FIG 7 : EXAMPLE A.3

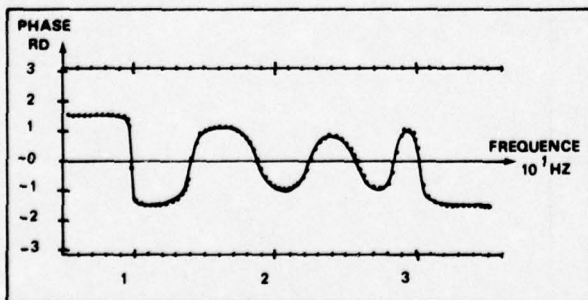
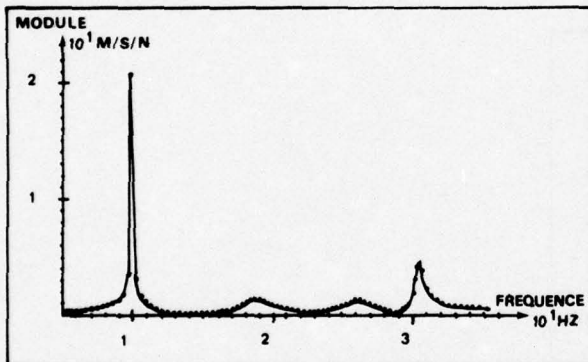


FIG 8 : EXAMPLE B (see table 4)

	DAMPED NATURAL FREQUENCIES Hz	ERROR %	DAMPING COEFFICIENT	ERROR %
X_1 / F_1	9.83	0.05	-0.0463	1.9
	18.72	0.05	-0.806	1.7
	25.77	0.08	-0.806	1.7
	30.26	0.03	-0.215	0.2
X_2 / F_1	9.83	0.05	-0.0468	0.85
	18.72	0.05	-0.806	1.7
	25.76	0.04	-0.829	1.1
	30.25	0.02	-0.214	0.5
X_3 / F_1	9.83	0.05	-0.0477	1.1
	18.72	0.05	-0.8	2.4
	25.77	0.08	-0.8	2.4
	30.25	0.02	-0.214	0.5
X_4 / F_1	9.83	0.05	-0.0476	0.85
	18.72	0.05	-0.813	0.85
	25.76	0.04	-0.823	0.4
	30.25	0.02	-0.215	0.2
EXACT VALUES	9.83		-0.0472	
	18.71		-0.82	
	25.75		-0.82	
	30.25		-0.215	

TABLE 4- EXAMPLE B (see figure 8)
Non diagonal generalized damping

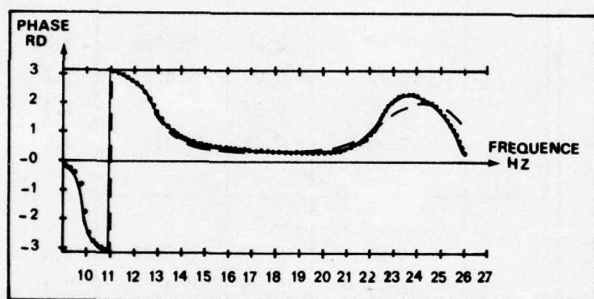
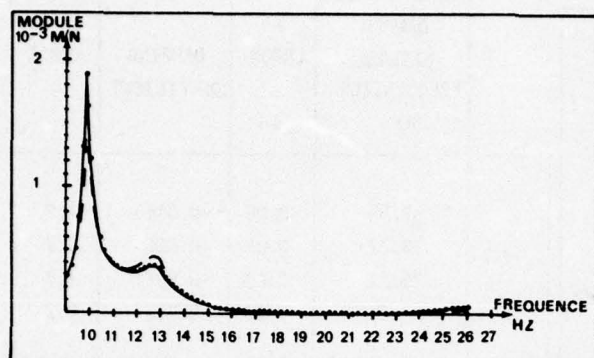


FIG 9 - TRUNCATION OF THE MODAL BASE

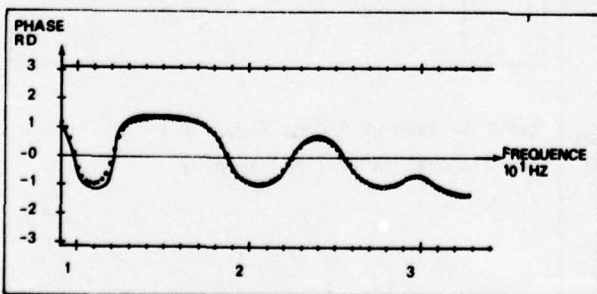
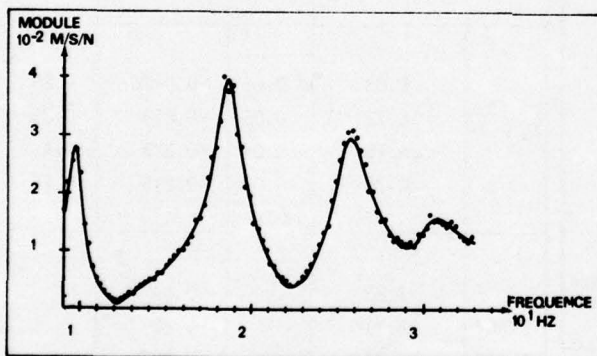


FIG 10 -EXAMPLE WITH MEASUREMENT ERRORS

EXPERIENCES IN USING MODAL SYNTHESIS*
WITHIN PROJECT REQUIREMENTS

J.A. Garba[†]
Member of Technical Staff

B.K. Wada[†]
Group Supervisor

J.C. Chen[†]
Senior Engineer

Modal synthesis methods have been developed for use by engineers for cost-effective solutions of large structural dynamics problems. Different methods have been proposed by various investigators based upon comparative solutions of relatively simple structures using different forms of displacement functions. The paper describes the experiences in the application of modal synthesis methods to a large complex structure in a project environment. The considerations include analysis, hardware interfaces, organizational interfaces, schedules, tests, resources, and other project requirements. Good technical results were obtained through the use of an integrated analysis/test modal synthesis on both substructures and systems. These experiences should be beneficial for engineers contemplating the use of modal synthesis concepts for future projects.

INTRODUCTION

Modal synthesis concepts have been attractive to many engineers involved with the solution of eigenvalues and eigenvectors for large, complex dynamic problems. It is a method that retains the few significant independent coordinates of the various substructures which are combined into the system dynamic equations.

The reduced independent coordinates are selected to provide accuracy in the lower eigenvalues which are of significance to the structural dynamicists. The initial developments were motivated by a requirement for lower eigenvalues of large structures for reasonable computer costs.

The first publication popularizing modal synthesis was a report by W. Hurty [1].[‡] Since then, several other documents on its different aspects, such as optimum selection of displacement functions, have been published [2, 3, 4, 5, and 6]. Other studies [7 and 8] have been made on Shuttle type structures to establish the "best" displacement functions that converge to the correct solution with the least number of independent coordinates. A current research program at Langley Research Center includes a task on a 1/8-scale Shuttle model to verify modal synthesis concepts as applied to the Shuttle.

Although versatile computer codes have been available for eigenvalue solutions of a

*This paper presents the results of one phase of research carried out at the Jet Propulsion Laboratory, California Institute of Technology, under Contract No. NAS 7-100, sponsored by the National Aeronautics and Space Administration.

[†]Structures and Dynamics Section, Jet Propulsion Laboratory, 4800 Oak Grove Drive, Pasadena, California 91103.

[‡]Numbers in brackets designate references at end of paper.

structure, and a few modal synthesis computer programs [9] have been developed, very few projects have successfully implemented a complete modal synthesis substructure and system analysis and test program.

This paper presents the experience at the Jet Propulsion Laboratory (JPL) in a complete modal synthesis analysis and test program. The "best" method for the project was not determined by analytical studies [2 and 3] but by project requirements. The results of the effort are based upon its application to six space projects [10 and 11] at JPL, including the most recent one, Viking*. The Viking results will be used to illustrate the salient points because it incorporated all of the experiences at JPL. The information should be of interest for engineers contemplating the use of modal synthesis concepts for future projects.

The proper use of modal synthesis will result in an efficient and cost-effective support to many projects.

PROJECT REQUIREMENTS

The "best" modal synthesis method and/or a modal synthesis computer program cannot be specified because of their dependence on the particular structure and the project requirements. The Project requirements for Viking [12] should be similar to those for future projects.

Since labor is often the largest cost element, most projects minimize the time for the design, fabrication, and test phases, as shown in Fig. 1. For a series of projects with modifications to the basic structure, higher confidence in the design and minimization of the test program can be achieved by initially developing a good mathematical structures and dynamics model that is verified by a test program. The analysis based on the initially developed mathematical model can be used in subsequent projects for reliable data and elimination of tests.

Schedule - Observations

The Viking Orbiter (VO) schedule pertinent to this discussion is shown in Fig. 2.

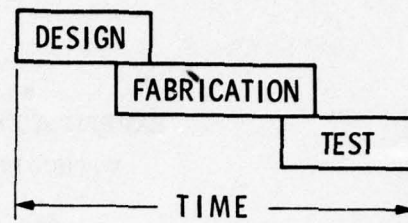


Fig. 1 - Typical project

The current trend is to establish initial design loads using load analysis which are transient analyses based on spacecraft and launch vehicle mathematical models and launch vehicle engine forcing functions. The final model, verified by a system modal test, is used in a load analysis to establish the final flight loads. The results are used to establish the adequacy of the structure and/or the ultimate static qualification test loads. Emphasis is placed on the calculation of spacecraft member dynamic loads rather than accelerations.

The time available between the system modal test and the test-correlated mathematical model is usually a minimum. Thus, if the test and analysis do not correlate, modification of the large system mathematical model to match the test results is an almost insurmountable task. Criteria for the correlation of analysis and test [13] are lacking, and a proven algorithm to automatically modify the mathematical model to match the test data is not available. Consequently, the results from the system modal test are often not used effectively.

The effective use of resources is made possible by

1. Verifying the mathematical models of the substructures with substructure tests. (The term substructure is deliberately used instead of subsystem.)
2. Increasing the probability of a good system test by recognition of potential problems that may be caused by selected substructures. The potential problems include nonlinearities, instrumentation requirements, mass matrix

*JPL is responsible for the Viking Orbiter System, which is part of the overall Viking Project Managed by the Viking Project Office at Langley Research Center (LRC) for NASA.

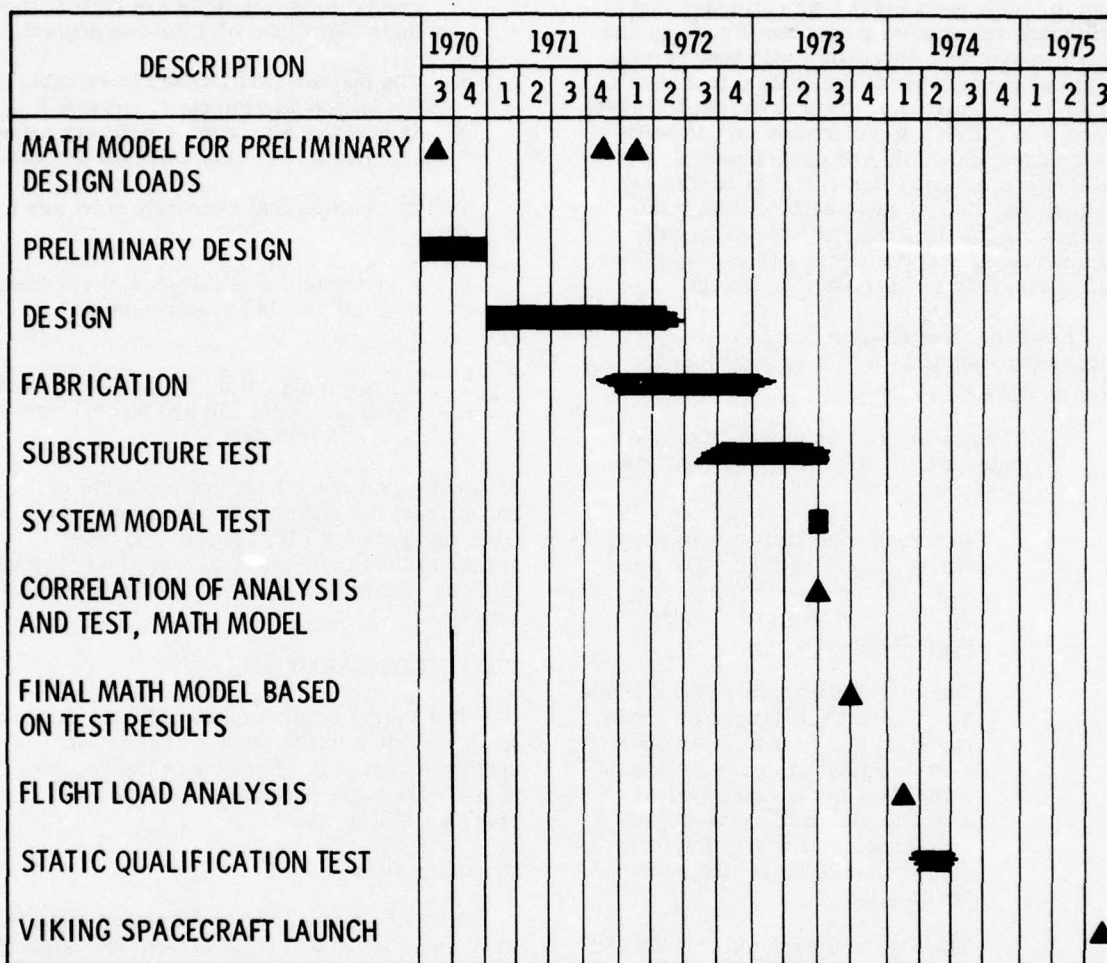


Fig. 2 - Viking Orbiter structures and dynamics overall schedule

- estimations, and identification of significant dynamic characteristics.
3. Distributing the instrumentation and engineering workload over a longer time period.
 4. Performing a good substructure analysis and test program to eliminate the requirements for system tests.

Dynamic Model Requirements

The dynamic model requirements for different projects will vary along with the appropriate modal synthesis approach. The different project uses for a dynamic model are to evaluate the

1. Attitude control interaction
2. Spacecraft/launch vehicle interface loads on accelerations
3. Spacecraft accelerations
4. Spacecraft member forces

Another consideration is whether the significant dynamic forcing function is superimposed with a quasi-static acceleration.

System Modal Test

The need for an accurate analytical model prior to and after a system modal test is dependent on the project requirements. Other

than to obtain good early load estimates and to help guide the system modal test itself, an analytical model that correlates with test results would be superfluous if the system test results could be used directly. This is rarely the case, since it is difficult to determine force coefficients experimentally and experimentally determined models often result in numerical difficulties. For attitude control interaction studies, or for the evaluation of spacecraft/launch vehicle interface loads or accelerations, modal test data are probably sufficient.

However, frequently a modal-test-correlated analytical model is desirable for the following reasons:

1. The modal test configuration may not duplicate the final flight configuration because
 - a. Referee propellants are used for safety considerations. The density of the referee propellants differs from that of the flight propellants.
 - b. The test configuration may exclude a few select substructures. Substructures (e.g., nonlinear ones) may be excluded to assure a good modal test to provide physical space to attach the shakers, or to minimize the number of system eigenvalues to those that require verification.
 - c. The test configuration is modified to allow a meaningful modal test. For instance, discrete dampers may be inactivated or sliding joints may be prevented from sliding.
 - d. Design changes have been made since the fabrication of the hardware for the test.
2. More detailed information is available from the mathematical model than from the test measurements. For instance, detailed modal force distribution can be obtained from the mathematical model, whereas its measurement during the test is impractical.
3. A variety of configurations must be evaluated for its dynamic characteristics. For instance, attitude control studies with various positions of appendages, launch analyses, and

ground condition tests are typical configurations required for one project.

4. The mathematical model is valuable for follow-on projects to provide fundamental information which may allow elimination of some analyses and tests.

Two difficulties that currently exist are a lack of

1. A criterion for the degree of correlation [13 and 14] required by an engineer.
2. A proven algorithm to upgrade a mathematical model [15 and 16] to correlate with test data.

Although several methods are available to reconstruct the stiffness and mass matrix from the test data [17, 18, and 19], they appear to lose their physical significance; thus, their use for analyzing other configurations is limited.

VIKING REQUIREMENTS

The Viking requirements [12] are described to provide a background for the modal synthesis approach. In general, the requirements were more extensive than those of previous JPL projects.

Dynamics Data

Since the design and qualification test loads were established by load analysis, the detailed loads in the various structural members resulting from combined quasi-static and staging transients were required. Load analysis consists of developing a complex finite element model (approximately 32,000 degrees-of-freedom) of the VO (Figs. 3 and 4), which is reduced to about 250 dynamic degrees-of-freedom by modal synthesis. The model is coupled by modal synthesis methods to the Viking Lander capsule and the Titan III/Centaur D-IT launch vehicle (Fig. 5) and excited by the forcing functions shown in Fig. 6. Loads resulting from eigenvalues less than 40 Hz were of interest. (The first Viking spacecraft eigenvalue is 4.42 Hz and the 40th eigenvalue is 43.53 Hz.)

Schedule

As shown in Fig. 1, the modal-test-correlated mathematical model was required within a few weeks after the completion of the VO modal test [20]. The model was required

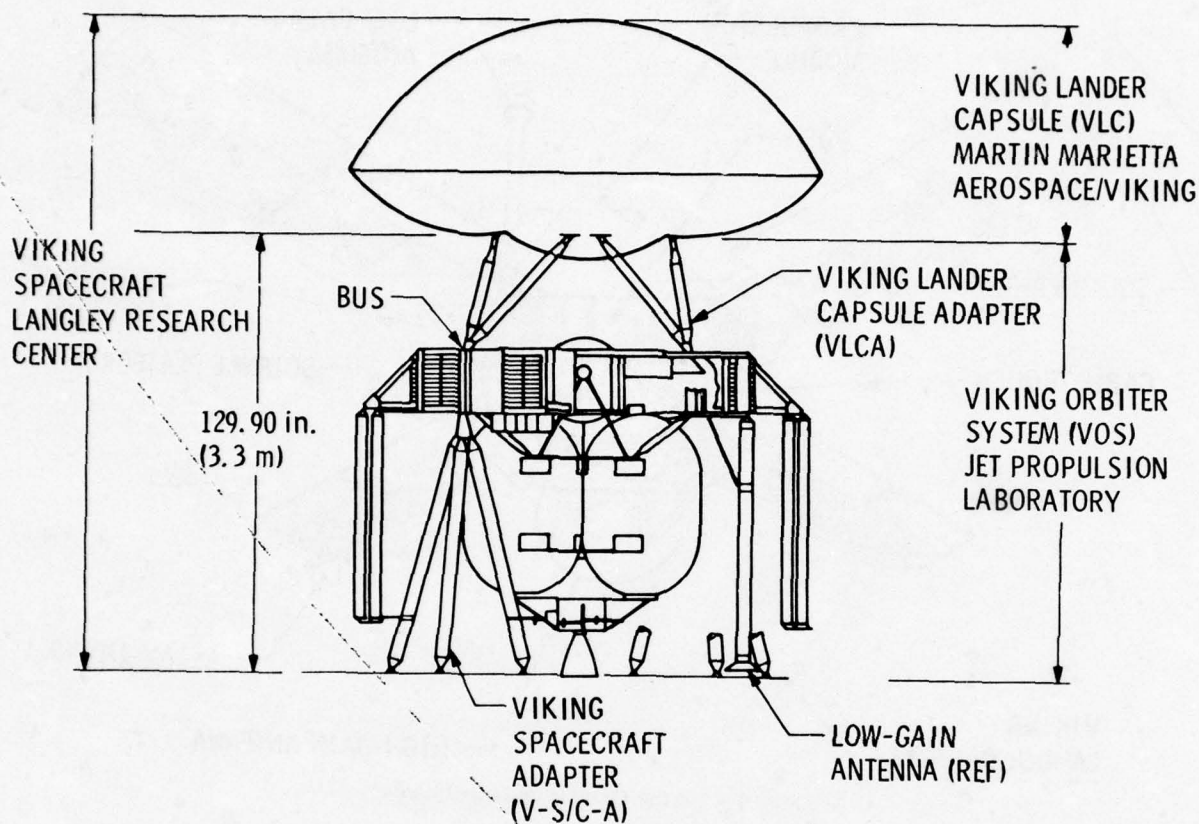


Fig. 3 - Viking spacecraft configuration

for load analysis to establish the ultimate qualification static test loads prior to the scheduled test date. Fortunately, good sub-structure modal tests and the analyses program directly contributed to a successful system test and correlation of the analytical model. The schedule would not have permitted an update of the mathematical model.

A high probability for a good mathematical model, modal test, correlation, and successful ultimate static test was required because a redesign and requalification of the structure prior to launch in the third quarter of 1975 would have been costly.

Dynamic Model Requirements

A mathematical model of the VO was required. The modal-test-verified mathematical model was used to establish ten different models representing a variety of test and flight conditions and approximately six models for attitude control studies in the VO cruise

configuration (Fig. 4). All VO models were generated using the JPL Structural Analysis and Matrix Interpretive System (SAMIS) computer program. The computer used was the Univac 1108.

MODAL SYNTHESIS

Definition of Problem

The major step required to obtain a solution to the system equations of motion

$$[M]\{\ddot{U}\} + [C]\{\dot{U}\} + [K]\{U\} = \{F(t)\} \quad (1)$$

$$\{f\} = [S]\{U\}$$

where

$[M]$ = mass matrix of the system

$\{U\}$ = independent coordinates of the system

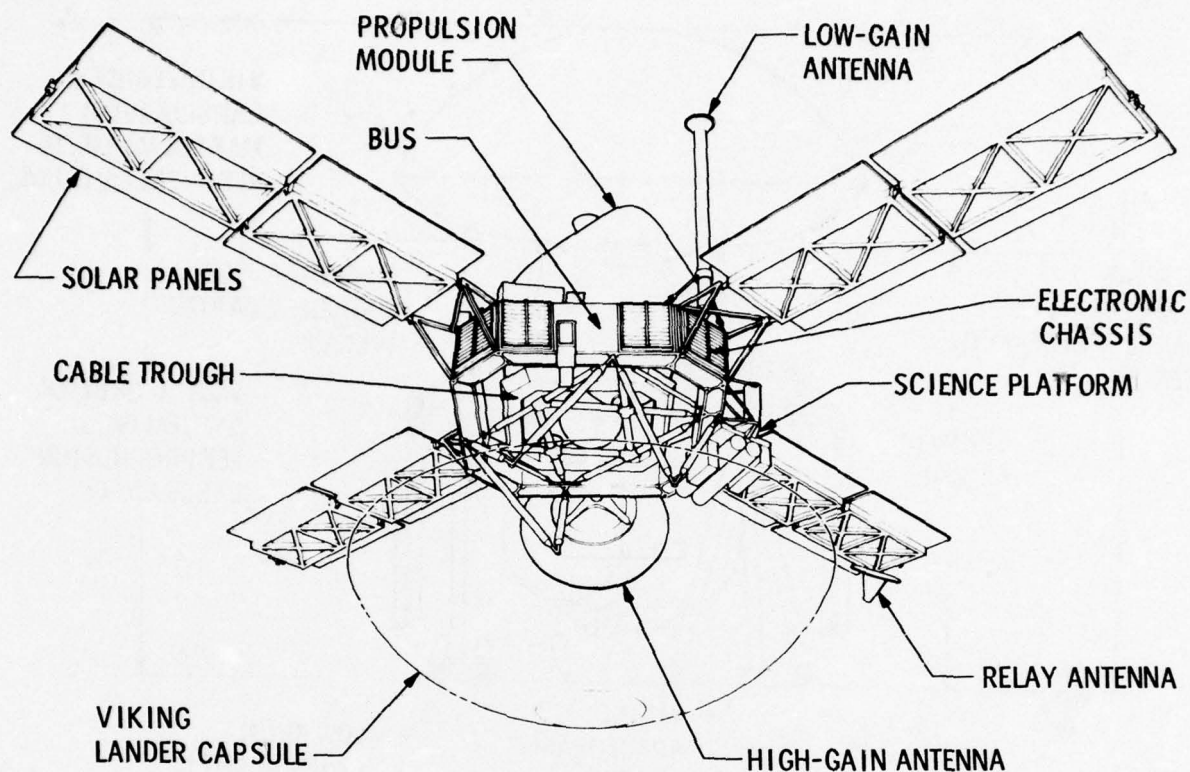


Fig. 4 - Viking Orbiter substructures

$[C]$ = damping matrix of the system

$[K]$ = stiffness matrix of the system

$\{F(t)\}$ = forcing function

$\{f\}$ = member forces

$[S]$ = force transformation

is to reduce the degrees-of-freedom of Eq. (1) by representing $\{U\}$ in terms of various displacement functions. The relationship is

$$\{U\} = [\phi]\{Q\} \quad (2)$$

where

$[\phi]$ = displacement function matrix

$\{Q\}$ = independent generalized coordinates of the system

Substitution of Eq. (2) into (1) and pre-multiplication by $[\phi]^T$ results in

$$\begin{aligned} & [\phi]^T [M] [\phi] \{\ddot{Q}\} \\ & + [\phi]^T [C] [\phi] \{\dot{Q}\} \\ & + [\phi]^T [K] [\phi] \{Q\} = [\phi]^T \{F(t)\} \end{aligned} \quad (3)$$

or

$$[\bar{M}]\{\ddot{Q}\} + [\bar{C}]\{\dot{Q}\} + [\bar{K}]\{Q\} = \{\bar{F}(t)\} \quad (4)$$

The eigenvalue solution of (4) for $[\bar{C}] = 0$ and $\{\bar{F}(t)\} = 0$ results in the system eigenvalues and eigenvectors that are verified by the system modal test.

The main advantage of modal synthesis or the proper establishment of relationship (2) is that the order of the equations of motion is reduced from 32,000 for (1) to 250 for (3), with little loss in accuracy of the desired information.

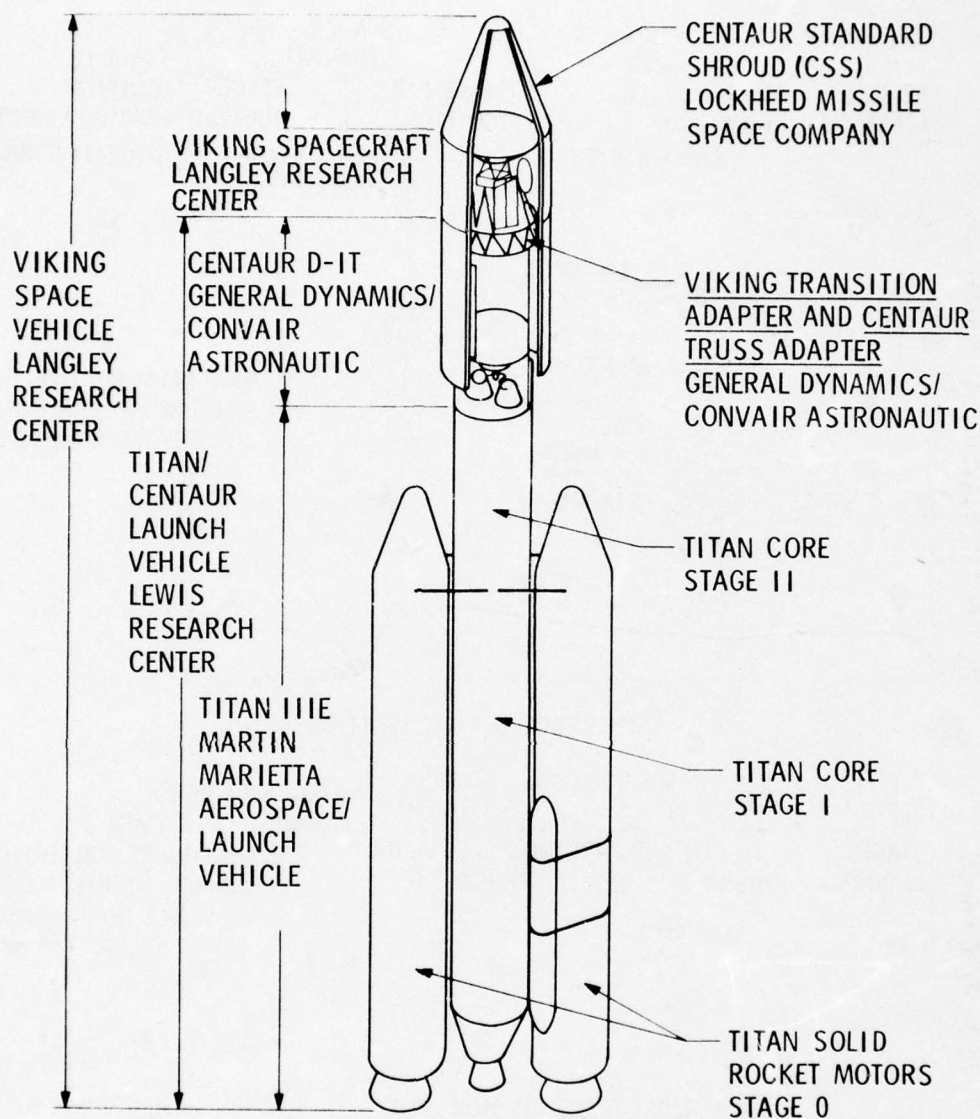


Fig. 5 - Viking space vehicle configuration

Displacement Functions

or

The various displacement functions for a substructure can be obtained from the following two equations for any substructure:

$$[u_0] = [k_{00}]^{-1} ([f_0] - [k_{01}][u_1]) \quad (6)$$

and

$$\begin{bmatrix} k_{11} & k_{10} \\ k_{01} & k_{00} \end{bmatrix} \begin{bmatrix} u_1 \\ u_0 \end{bmatrix} = \begin{bmatrix} f_1 \\ f_0 \end{bmatrix} \quad (5)$$

$$[m]\{\ddot{u}\} + [k]\{u\} = \{0\} \quad (7)$$

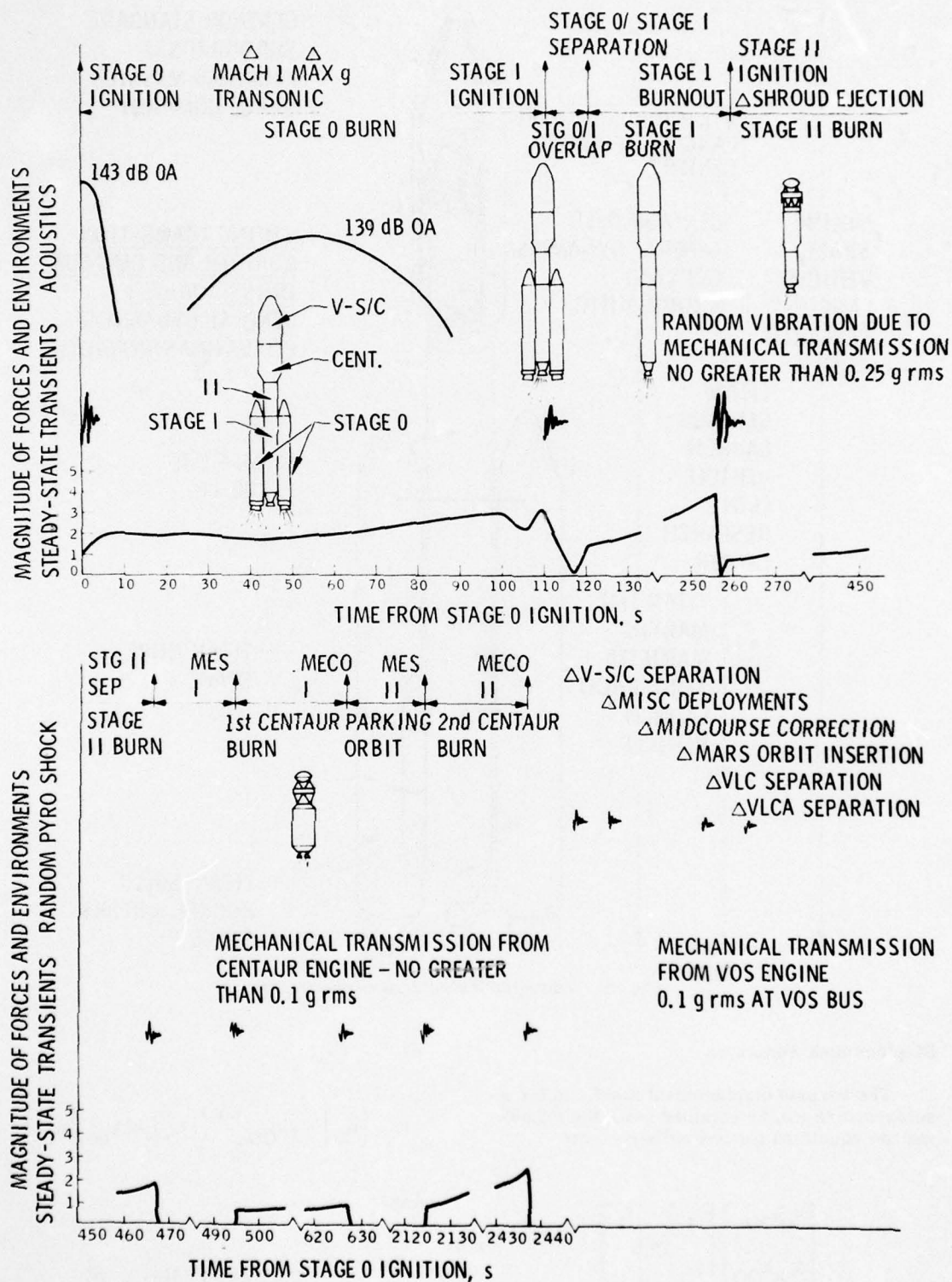


Fig. 6 - Flight loads and environments

where

$\{u\}$ = substructure displacements

$[k]$ = substructure stiffness matrix

$[f]$ = forces on the substructure

$[m]$ = substructure mass

I = subscript to denote interface degrees-of-freedom

O = subscript to denote degrees-of-freedom other than the interface.

The various displacement functions are discussed below.

1. Rigid Body Displacement Function [9]. Rigid body functions represent the motion $[\phi_R]$ when a degree-of-freedom $[u_I]$ is displaced by an arbitrary value without force. The $[\phi_R]$ is a solution to Eq. (6), where $[f_O] = 0$ and $[u_I]$ is a unit matrix (or linear combination of unit matrices) in the degrees-of-freedom associated with the rigid body displacements.

$$\{u_R\} = [\phi_R]\{q_R\} \quad (8)$$

The number of rigid body motions may range from 1 to ∞ . Rigid body motions in excess of 6 are related to linkages within the substructure.

2. Constraint Displacement Functions [1]. Constraint functions represent displacements $[\phi_C]$ of the substructure when a unit displacement of an interface degree-of-freedom requires force as the other interface degrees-of-freedom are restrained. If the interface degrees-of-freedom are statically determinate, the constraint functions are equal to the rigid body functions. The constraint functions are solutions to Eq. (6), where $[f_O] = 0$ and $[u_I]$ is a matrix of displacement vectors with unity associated with the degrees-of-freedom defining a constraint mode. (Other terms of the vector are zero.)

$$\{u_C\} = [\phi_C]\{q_C\} \quad (9)$$

3. Attachment Displacement Functions [9, 5, and 6]. Attachment functions are displacements $[\phi_A]$ of the substructure resulting from concentrated loads $[f_A]$ on the substructure. Displacements $[\phi_A]$ result from the solution to (6), where $[f_O] = [f_A]$ and $[u_I] = 0$.

$$\{u_A\} = [\phi_A]\{q_A\} \quad (10)$$

The $[f_A]$ can be quasi-static inertia loading of the substructure or various combinations of concentrated loads.

4. Imposed Displacement Functions. Imposed functions represent motions $[\phi_{IM}]$ that engineers consider relevant to describe a structural deformation. The displacements are not necessarily a result of any realistic external loads, but are usually directly related to such loads.

$$\{u_{IM}\} = [\phi_{IM}]\{q_{IM}\} \quad (11)$$

5. Eigenvector Displacement Functions. The eigenvector functions are the eigenvector solution of Eq. (7).

$$\{u_E\} = [\phi_E]\{q_E\} \quad (12)$$

Total Displacement Function

The displacements of any substructure are represented by any combination of the displacement functions

$$\{u\} = \begin{bmatrix} [\phi_R] & [\phi_C] & [\phi_A] & [\phi_{IM}] & [\phi_E] \end{bmatrix} \begin{Bmatrix} q_R \\ q_C \\ q_A \\ q_{IM} \\ q_E \end{Bmatrix} \quad (13)$$

or

$$\{u\}_i = [\phi_i]\{q_i\} \quad (14)$$

for the i^{th} substructure.

Equation of Motion of Total System

The independent generalized coordinates of the system are selected by the engineer, who combines the generalized coordinates of the substructures through compatibility relations representing the interconnections. Figure 7 shows that the substructures are attached to the bus for Viking. The selected displacement functions of the substructures (Eq. 13) are combined to obtain the system equations (4).

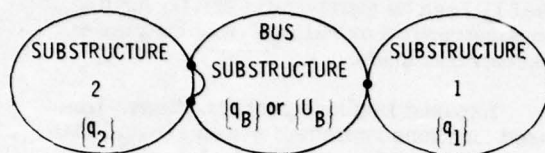


Fig. 7 - Interconnections of substructure

MODAL SYNTHESIS - VO PROJECT REQUIREMENTS

Project Requirements

The experience gained with the modal synthesis process for VO should be applicable to most projects. At the initiation of the Viking Project, the modal synthesis plan was closely integrated with other Project constraints and requirements that included

1. Organizational interfaces external to JPL (Figs. 3 and 5)
2. Organizational interfaces internal to JPL
3. Substructure design, fabrication, and delivery schedules
4. System-related hardware and test program
5. Load analysis definition and requirements

A modal synthesis plan based solely upon the "best" technical approach could not be practically implemented and would not have been acceptable. Two decisions, partially involving analysis and test considerations, were:

1. The responsibility for the Viking Lander capsule adapter (Fig. 3) was assigned to JPL. JPL was cognizant of the hardware which was important in the modal synthesis and the system test plans.
2. The Viking transition adapter (VTA) and Centaur truss adapter (CTA) that interconnect the Viking Orbiter System and Centaur were included in the JPL VO mathematical model, modal, and static qualification test program. The VTA and CTA were designed and fabricated by General Dynamics/Convair Astronautic (GD/CA).

A goal was to minimize the analysis, design, and test interfaces between organizations and people to decrease the coordination effort. Modal synthesis methods minimized interactions and provided a means to effectively obtain good technical results. The complexities associated with the inclusion of the VTA/CTA into the VO effort for technical considerations clearly demonstrated the advantages of minimizing the interfaces whenever possible.

A more detailed schedule is presented in Fig. 8, and the interfaces of the substructures and system are shown in Fig. 9.

All the structural development and structural qualification testing was performed by the JPL Structures and Dynamics Section.

Selection of Substructures

The substructures were defined by the interfaces shown in Fig. 9 rather than an analytical consideration. As noted in the schedule (Fig. 8) and the interfaces (Fig. 9), the substructures were under the cognizance of different engineers and organizations. They were delivered and tested at different times. To provide effective support, analysis, design, and test efforts were performed for each substructure with a minimum of interaction. This naturally resulted in the substructure/modal synthesis approach.

Advantages of Substructure Approach

The goal was to effectively support the VO and develop a mathematical model that would be verified by the system modal and static tests. The plan was to develop the system mathematical model (used for both static and dynamic models) by testing the substructures at the earliest possible time and incorporating the results into the system model.

The advantages of modal synthesis to VO were:

1. A structures engineer provided static and dynamic analysis and test support to his assigned substructure with a minimum of interaction with other substructures.
2. Each engineer and/or organization developed the mathematical model independently of the others. The number of degrees-of-freedom,

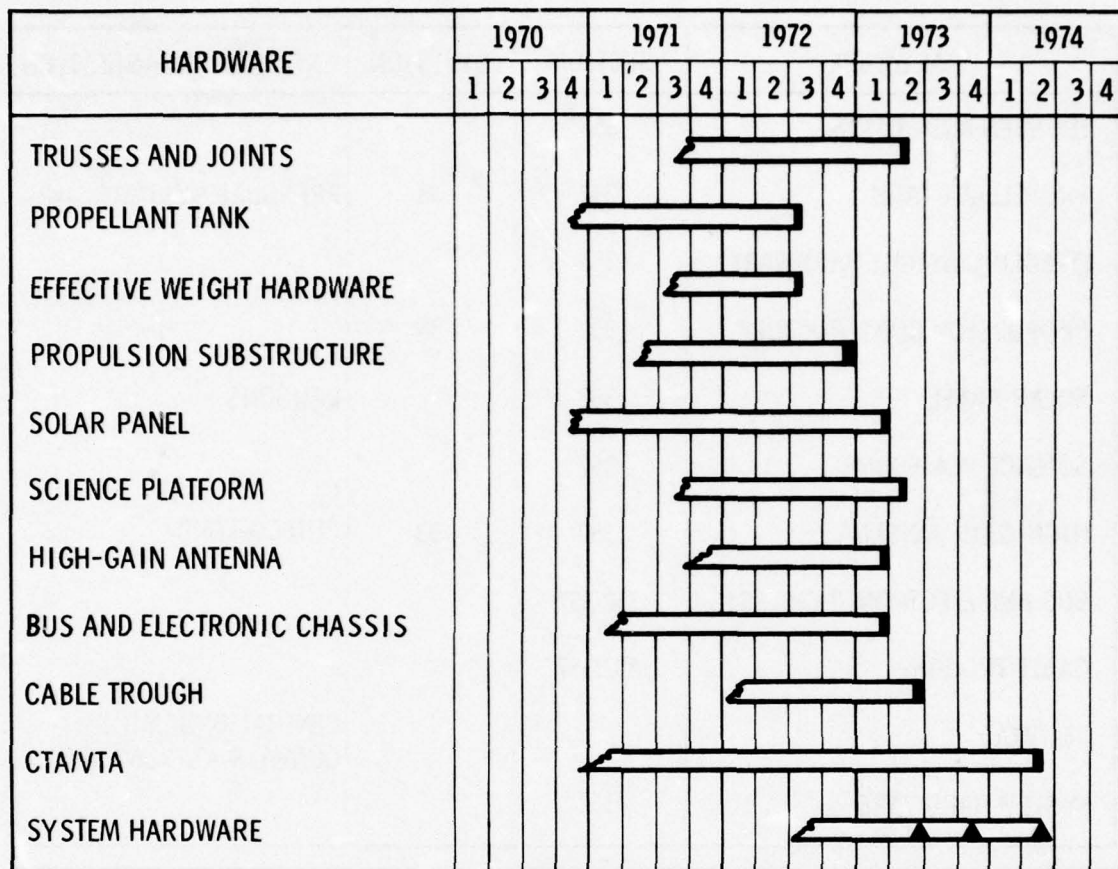


Fig. 8 - Substructure and system schedule

numbering of nodes, and computer program were selected by each engineer. Thus, a special dynamic model with "reduced" degrees-of-freedom was not required. The model was used to evaluate substructure responses, interface distortion, and other parameters.

3. A better engineering estimate of substructures prior to the test was possible when experience on similar hardware was available. Estimates of damping on substructures made of honeycomb or composites are typical examples.
4. An engineer developed a substructure mathematical model, which was correlated and corrected to match the test data. Corrections were made to relatively small mathematical models

prior to their incorporation into the system model.

5. Ninety percent of the strain gages required for the system model and static tests were installed for the substructure tests. This distributed the instrumentation workload and simplified the work by allowing hardware to be instrumented in the instrumentation laboratory. Additionally, the instruments and their calibration were validated during the substructure tests.
6. The substructure tests revealed design deficiencies early in the VO schedule.
7. The potential problems caused by the various substructures during the system modal tests were recognized. For instance, structural nonlinearity

HARDWARE	SECTION	DIVISION	EXTERNAL ORGANIZATION
TRUSSES AND JOINTS	352 ^a		
PROPELLANT TANK	352	38	PRESSURE SYSTEMS, INC.
EFFECTIVE WEIGHT HARDWARE	354		
PROPULSION SUBSTRUCTURE	352	38	
SOLAR PANEL	352		PARSONS
SCIENCE PLATFORM	352		
HIGH-GAIN ANTENNA	352	33	PHILCO-FORD
BUS AND ELECTRONIC CHASSIS	352/357		
CABLE TROUGH	352/357		
CTA/VTA			GENERAL DYNAMICS/ CONVAIR ASTRONAUTIC
SYSTEM HARDWARE	352		

^aTHE NUMBERS DENOTE AN ORGANIZATION WITHIN JPL. WITHIN EACH SECTION, A COGNIZANT ENGINEER WAS ASSIGNED TO EACH OF THE HARDWARE ITEMS.

Fig. 9 - Substructure and system hardware interface

would invalidate the system modal test based upon linear theory. The troublesome substructures were modified or eliminated from the system test.

8. The system modal [20], vibration [21 and 22], and qualification static [23] test results were excellent. Good test results were due to instrumentation and mathematical model verification during the substructure tests.
9. System parameters, such as the pressure in the propellant tank, were established based upon the influence of the pressures on the tank stress and structural nonlinearity.

10. A variety of different system configurations were effectively analyzed by changing only the affected substructures. The configurations analyzed included:

- a. Two different launch configurations with different propellant loadings.
- b. Different launch configurations to establish the maximum or minimum propellant loading which would affect the structural design.
- c. Modal test configuration without selected substructures and

referee propellants in the propellant tanks.

- d. Forced vibration test configurations.
- e. Attitude control cruise configurations.

Description of VO Substructures and Their Displacement Functions

General. All the dynamic and static tests to be described were performed at different magnitudes of loading to establish the nonlinearities and high-level damping trends. Since loads were required when members were subjected to combined quasi-static and dynamic loading, modal acceleration methods (rather than modal displacement) were used. In addition, the selected displacement functions should result in a small residual mass [24] across an interface for which quasi-static loads were important. (This can be achieved by selection of quasi-static attachment functions.) Strain gage readings were measured during the substructure tests to partially verify the eigenvalue force coefficients.

Individual Members and Joints. Whenever feasible, individual truss type members, and occasionally the joints with their instrumentation, were tested in a uniaxial testing machine. The primary objective was to detect a poor design or deficient hardware early in the Project schedule. Additionally, the stiffness of the substructure was verified and the instrumentation was calibrated. A test of the Viking spacecraft adapter truss/fitting revealed a joint that "gapped" when a tension load was applied.

Solar Panels. Eigenvector and constraint functions were used for the solar panel. The solar panel with the relay antenna was verified with a modal and static test in the launch configuration, and a modal test in the cruise or extended configuration. After correlating the mathematical model with the test results, the antenna was removed from the mathematical model to obtain the solar panel model without the relay antenna.

In addition to the solar panel tests, dynamic and static tests were performed on the aluminum honeycomb substrate to verify its structural integrity and the structural properties for the mathematical model.

The analysis indicated more eigenvalues in the frequency range of interest than the test results. Only the analytical eigenvalues corresponding to test eigenvalues were retained, and the eigenvalues were modified to match the test results. The analytical eigenvectors were retained.

The solar panels are connected to the Viking spacecraft adapter with "viscous dampers" that critically damp the panel lowest normal mode. Since the system eigenvalues were limited to real eigenvalues, the dampers were not included. The influence of damping from the viscous dampers was treated as solar panel eigenvalue damping.

Effective Mass Determination of the Propellant. A forced vibration test was performed on a single propellant tank with the propellant management device to measure the effective mass of the propellant in the lateral, longitudinal, and pitch directions for various ullages. The data were used for both the modal test and analysis.

Propellant Tank Tab. The reduced stiffness matrices of the propellant tabs as attached to the members supporting the tanks were calculated and verified by applying static loads similar to attachment functions to confirm the mathematical model to verify the reduced stiffness matrices.

Propulsion Substructure. Eigenvalue and constraint functions were used to describe the motion of the propulsion substructure. Modal and static tests were performed to verify the functions. Tests were made at various internal pressure levels and ullages to establish the threshold of nonlinearity caused by propellants and structural nonlinearities. Zero ullage tests were run in the event that ullages resulted in nonlinearities which would compromise the system modal test. Although a zero ullage condition test was included in the system modal test plan, it was canceled because the ullage conditions did not introduce significant nonlinearities.

Components mounted on isolation pads to the propulsion substructure resulted in local eigenvectors that did not affect the overall significant eigenvectors.

High-Gain Antenna. Eigenvalue and constraint functions were used to describe the motion of the high-gain antenna. Modal and

force vibration sine tests were performed to verify the analytical model. The design, including "snubbers," resulted in a nonlinear (frequency vs force) structure.

Additional modal tests were run for the antenna deployed positions.

Science Platform. Eigenvalue and constraint functions were used to describe the platform motion. Modal tests in the stowed and deployed conditions were performed to verify the model. The design included serrated joints to allow slippage at high loads. However, since the magnitude of the forces in the modal test did not allow slippage, the modal analyses excluded joint slippage, but the model for load analyses did include joint slippage.

During the test, the fixture was not sufficiently rigid, and it rotated. Because of schedule and cost considerations, the test was not repeated. The influence of base rotation could not be eliminated from the test results; thus no experimental results were available for correlation with analyses. An uncorrelated analytical model was used for the system modal test. The science-platform-related eigenvalues and eigenvectors revealed the worst correlation in the system modal test. This deficiency was, however, understood and allowances were made in the loads calculation to cover these uncertainties.

Cable Trough. Prior to the buildup of the structure for the system modal test, a quick modal test of the cable trough was performed to identify the eigenvectors and establish the adequacy of the experimental mass distribution.

Electronic Chassis. Imposed functions were selected for the electronic chassis to establish its generalized stiffness and mass matrix based upon its distortion when it was integrated with the bus. Tests were not run because of the difficulty in imposing the boundary conditions.

Bus. The bus structure included the rigid mass stimulation of the Viking Lander capsule (VLC), Viking Lander capsule adapter (VLCA), Viking spacecraft adapter (V-S/C-A), and the VTA/CTA. The rigid mass of the VLC was included to allow the substructure function to be more representative of its motion in the system response in order to simplify and minimize the selection of bus functions. The inclusion of the rigid mass is identical to mass loading the interface [2]. As mentioned before, the GD/CA hardware referred to as the VTA/CTA between the Centaur and Viking spacecraft,

was included for analysis purposes. The VTA/CTA at the Viking interface was a flexible structure, whereas at the Centaur interface it was considered a rigid plane. The attachment or constraint functions to attach the Viking to the Centaur were eliminated by the inclusion of the CTA/VTA in the bus model.

Three types of functions as independent coordinates were tried for the bus:

1. Attachment functions related to the forces from the substructures.
2. Eigenvector functions with the interfaces to the substructures mass loaded and stiffness loaded (if statically indeterminate). They were linearly combined to obtain super-elements [11] compatible with the substructure degrees-of-freedom.
3. Degrees-of-freedom associated with the bus mass points.

The bus functions were verified by a static test. The static displacements and internal member forces were used to verify the mathematical model.

System Model

The effort to generate a mathematical system model using attachment and eigenvector functions resulted in failure. The resulting mass matrix of Eq. (1) could not be decomposed for the eigenvalue solution. This may be attributed to single-precision arithmetic. It is a limitation of SAMIS using the Univac 1108 computer.

The use of the bus's original degrees-of-freedom and the substructure functions (mixed coordinate system [14]) was successful. The model was verified by a system modal test and a system static test. Eigenvalues, eigenvectors, static displacements, and eigenvalue force coefficients were verified. The system test did not include all the substructures but only those necessary to verify the model and structure.

The eigenvalue damping was estimated by calculating the kinetic energy participation of various substructures in each eigenvalue and proportioning the substructure damping in relation to their contributions.

CONCLUSION

Modal synthesis concepts are valuable in the solution of large dynamic problems as well as effective in the support of a project. However the approach or selection of the methodology must not be based solely on "theory" but must be closely integrated with the overall project plan. Fortunately, the project objectives and modal synthesis desires are often similar (e.g., simplify interfaces). The selected methodology should also consider the ability to verify the mathematical model by an experimental program. A difficulty in modal synthesis is that the dynamicist must have a good understanding of structural dynamics to combine the substructures; automated computer programs to select the "best" methods are not available and may not be feasible for a general type of structure.

The use of modal synthesis resulted in an excellent mathematical model and meaningful test results, as well as a good correlation of analysis and test, for the VO. Its advantages for multiple mission projects are even greater because of the potential savings by elimination of analysis and tests. Using the verified mathematical model, only those substructures to be changed for a mission will require analysis for incorporation into the system model. Modal synthesis provides a means by which past experiences of a project can be fully utilized.

REFERENCES

1. Hurty, W.C., Dynamic Analyses of Structural Systems by Component Mode Synthesis, Technical Report 32-530, Jet Propulsion Laboratory, Pasadena, California, January 1964.
2. Benfield, W.A., and Hruda, R.F., "Vibration Analyses of Structures by Component Mode Substitution," presented at AIAA/ASME 11th Structures, Structural Dynamics, and Materials Conference, Denver, Colorado, April 22-24, 1970.
3. Hou, S.N., "Review of Modal Synthesis Techniques and a New Approach," The Shock and Vibration Bulletin, Bulletin 40, Part 4, pp. 25-30, December 1969.
4. J.H. Wiggins Company, Review and Development of Modal Synthesis Techniques, Technical Report No. 1073-1, NASA Contract NAS8-26192, May 1972.
5. Rubin, S., "An Improved Component-Mode Representation," AIAA paper 74-386, presented at the AIAA/ASME/SAE 15th Structures, Structural Dynamics, and Materials Conference, Las Vegas, Nevada, April 17-19, 1973.
6. Hintz, R.M., Analytical Methods in Structural Mechanics, GD/CA Memo No. SD-73-122, August 16, 1973.
7. Benfield, W.A., Bodley, C.S., and Moranson, G., "Modal Synthesis Methods," Space Shuttle Dynamics and Aeroelasticity Work Group Symposium on Substructuring, Marshall Space Flight Center, Huntsville, Alabama, August 30-31, 1972.
8. Goldenberg, S., and Shapiro, M., A Study of Modal Coupling Procedures for the Space Shuttle, NASA CR-12252, 1972, pp. 14-22.
9. Bamford, R.M., A Modal Combination Program for Dynamic Analyses of Structures, Technical Memorandum 33-290, Jet Propulsion Laboratory, Pasadena, California, August 1966.
10. Holbeck, H.J., Arthurs, T.D., and Gaugh, W.J., "Structural Dynamic Analyses of the Mariner Mars 1969 Spacecraft," The Shock and Vibration Bulletin, Bulletin 38, Part 2, August 1968, pp. 139-155.
11. Bamford, R., et al., "Dynamic Analyses of Large Structural Systems," Synthesis of Vibrating Systems, The American Society of Mechanical Engineers, New York, N.Y., November 1971.
12. Wada, B., "Viking Orbiter-Dynamics Overview," The Shock and Vibration Bulletin, Bulletin 44, Part 2, August 1974, pp. 25-39.
13. Chen J., and Wada, B., "Criteria for Analysis-Test Correlation of Structural Dynamic Systems," Journal of Applied Mechanics, The American Society of Mechanical Engineers (to be published).
14. Wada, B.K., Garba, J.A., and Chen, J.C., "Development and Correlation: Viking Orbiter Analytical Dynamic Model with Modal Test," The Shock and Vibration Bulletin, Bulletin 44, Part 2, August 1974, pp. 125-164.

15. Hall, B.M., Calken, E.D., Sholar, M.S., "Linear Estimation of Structural Parameters from Dynamic Test Data," AIAA/ASME 11th Structures, Structural Dynamics, and Materials Conference, Denver, Colorado, April 1970.
16. White, C.W., Dynamic Test Reflected Structural Model Methodology Report, Martin Marietta Corporation Report No. ED-2202-1577, December 1972.
17. Berman, A., and Flannelly, W.G., "Theory of Incomplete Models of Dynamic Structures," AIAA Journal, Vol. 9, August 1971, pp. 1481-1487.
18. Ross, R.G., "Synthesis of Stiffness and Mass Matrices from Experimental Vibration Modes," SAE Paper 710787, SAE National Aeronautic and Space Engineering and Manufacturing Meeting, Los Angeles, California, September 1971.
19. Pilkey, W.D., and Cohen, R., eds, System Identification of Vibrating Structures, Mathematical Models from Test Data, ASME, New York, 1972.
20. Leppert, E.L., Wada, B.K., and Miyakawa, R., Modal Test of the Viking Orbiter, Technical Memorandum 33-688, Jet Propulsion Laboratory, Pasadena, California, July 15, 1974.
21. Brownlee, G.R., Day, F.D., and Garba, J.A., "Analytical Prediction and Correlation for the Orbiter During the Viking Spacecraft Sinusoidal Vibration Test," presented at the 45th Shock and Vibration Symposium, Dayton, Ohio, October 1974.
22. Fortenberry, J.W., and Rader, W.P., "Fail Safe Vibration Testing of the Viking 1975 Developmental Spacecraft," presented at the 45th Shock and Vibration Symposium, Dayton, Ohio, October 1974.
23. Ugale, M., Volkert, K., and Fortenberry, J., Viking Orbiter 75 Test Report, Static Ultimate Type Approval Test, PD 611-117, Jet Propulsion Laboratory, October 11, 1974 (JPL Internal Document).
24. Bamford, R.M., Wada, B.K., and Gayman, W.H., Equivalent Spring-Mass System for Normal Modes, Technical Memorandum 33-380, Jet Propulsion Laboratory, Pasadena, California, February 1971.

Discussion

Mr. Schendel (Rockwell Space): Did you use any factor at all when you proof loaded it to account for possible errors in the dynamic loads that you determined by your analysis and test?

Mr. Wada: During the ultimate static tests we had an automatic requirement to load it up to the limit loads that we anticipated, meaning a three sigma type load; but we also had a margin of 1.25 on the ultimate test. As it turned out in this whole process when we gave the stress engineers a certain load to design the structure, in their conservatism, they added factors of their own. Consequently right at the end there is a lot more fudge in it you know when the truth really came out. Our project office also wanted to load it, at least to the anticipated flight load, but load it as high as possible before breaking the structure to give them an additional confidence level. So I would say that there are some structural elements that went right up to the anticipated loads but many of them were a factor of 50% above what we had anticipated; on top of that we had a 1.25 factor for the sort of ultimate loading condition.

Mr. Knauer (Hughes Aircraft Co.): It sounds as if the ground vibration survey data were used to check the math model which you then sent to the analysis contractors and they in turn gave you the results out of their force time history studies. Why didn't you use the ground vibration survey data directly?

Mr. Wada: We could not use the ground vibration data directly. I didn't mention this but in our total system model we did not include the total system it was too complex. We looked at what really had to be checked. We had many appendages and solar panels that we felt could be individually attached with a high reliability from a modal combination point of view. They were uncoupled and we checked these individually. Also we had viscous dampers that were highly damped, and we could not account for the highly damped systems in the way we ran our modal test; they have to be lightly damped. Many of the substructures which were sort of irrelevant were left off and we checked those overall motions on a total system that we felt were relevant and then we mathematically added the various subsystems. Another factor is that during these tests we have live fuel which they do not allow us to fly; we have to use referee dummy fluids and these fluids have different masses which change the dynamic characteristics. We have had two launches and we did not know exactly what fuel level they were going to fly; since the configuration of the test article and the flight article are different we have to have a mathematical model that we can adjust to the flight configuration. The other problem is that we needed loads in the individual members to check our stress and we

did not have enough strain gages to get a total; a modal transformation from modal testing, we just had a few points to check to make sure that a modal transformation analysis was correct. We needed 1000 different loads and we could not get that directly from test.

Mr. Knauer: How did you determine the loads in the structures? With the math model that you sent them with the mass and stiffness matrix? Did you send them the loads transformation?

Mr. Wada: Yes, we sent them both a static load and also a dynamic load using mode acceleration methods.

Mr. Stahle (General Electric Co.): At the beginning you mentioned about a dozen different mode synthesis techniques. Which one of those were actually used and by whom?

Mr. Wada: You mean at JPL?

Mr. Stahle: At JPL or in the assembly of the complete system. I guess the 250 degree of freedom eigenvalue solution was for the final system.

Mr. Wada: Yes, I think we used every modal synthesis technique that I mentioned.

Mr. Ferrante (General Electric Co.): Were the loads that you received back from the Martin Company elemental loads?

Mr. Wada: Yes.

Mr. Ferrante: Were they calculated statistically? Did you get three sigma loads?

Mr. Wada: No, they are deterministic. The statistic is on the input forcing function. They came up with an input forcing function sometimes statistically and at other times by applying a certain factor to the input forcing function, but the output is a deterministic result of the statistical input.

Mr. Ferrante: What did you do if there were many events?

Mr. Wada: For example on stage shutdown they have a past history of maybe sixty different motor burning shut down events. They pick what they call a group of 27 and in this case they run 27 different forcing functions. They get the loads in each member 27 different times then they run statistics on that load. There are other flight events which they cover by one deterministic event times the factor.

Mr. Ferrante: You take those loads which you receive and do a stress analysis. How do you account for phase?

Mr. Wada: We did not account for phase. We picked the maximum load due to any one event

regardless of time and we run statistics on
the maximums regardless of time of occurrence.

VIBRATION ANALYSIS OF THE BSE SPACECRAFT USING MODAL SYNTHESIS AND THE DYNAMIC TRANSFORMATION

E. J. Kuhar, Jr.
General Electric Company
Valley Forge, Pennsylvania

This paper presents a unique approach taken for the vibration analysis of the Japanese Broadcast Satellite Experiment (BSE). The total spacecraft structure was defined from substructure analyses using a stiffness coupling modal synthesis approach. A dynamic transformation was used to reduce the size of the eigenvalue problem for accurate coupled modes and frequencies. The analytical approach, the finite element substructures, and the method of solution are described in this paper demonstrating how large, complex structures can be treated conveniently and efficiently with great savings in computer costs.

NOMENCLATURE

$[m]$	=	Mass matrix for substructure in $\{x\}$ physical coordinates
$[k]$	=	Stiffness matrix for substructure in $\{x\}$ physical coordinates
$[\phi]$	=	Matrix of substructure eigenvectors in $\{x\}$ coordinates
$[M]$	=	Mass matrix for total structure in $\{x\}$ physical coordinates
$[K]$	=	Stiffness matrix for total structure in $\{x\}$ physical coordinates
$[\hat{z}]$	=	Matrix of eigenvectors for total structure in $\{x\}$ physical coordinates
$[\bar{K}]$	=	Generalized stiffness matrix for total structure in $\{q\}$ modal coordinates
$[\gamma]$	=	Matrix of eigenvectors for total structure in $\{q\}$ modal coordinates
$\{x\}$	=	Physical coordinates
$\{q\}$	=	Generalized modal coordinates
$\{\omega\}$	=	Substructure circular frequency
$\{\Lambda\}$	=	Eigenvalue

Subscripts

i	=	Refers to the i^{th} subset, term, or substructure
Δ	=	Incremental mass or stiffness from coupling spring
s	=	System Solution

Superscripts

A	=	Attachment coordinates
I	=	Interior coordinates not attached to any other substructure
$-$	=	Revised value
$\ddot{}$	=	Second time derivative
ij	=	Particular submatrix partition

INTRODUCTION

The Japanese Broadcast Satellite Experiment (BSE) is a space satellite (Figure 1) being developed at the General Electric Space Division for Toshiba, Japan. This three-axis-controlled spacecraft is being designed for a stationary equatorial orbit for television rebroadcast after launch on a Thor Delta booster. The basic structural components of the satellite include a fold-up solar array assembly, an antenna dish and feed, a secondary propulsion system, a launch vehicle/spacecraft adapter, and a center body which contains all of the communications and house-keeping electronics.

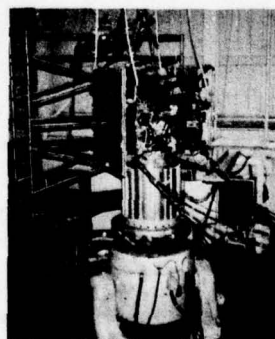


Fig. 1. BSE Z-Axis Test Setup

The optimum design of a new space satellite, such as BSE, requires a complex analytical model in order to accurately evaluate the effects of the satellite's dynamic environment during flight. Current finite-element techniques allow such complex models to be readily developed. However, the resulting analytical model usually consists of several thousand degrees of freedom (DOF). Even though computer programs have been specifically created for analyzing large structural problems, eigenvalue extraction and loads analyses for the total system can result in excessively high computer costs and run times.

Modal synthesis offers one approach for reducing computer costs by partitioning the total system into a set of substructures. Each substructure is analyzed separately, and the system eigenvalue solution is obtained from some combination of truncated substructure modes and frequencies. In addition to reducing computer and analysis costs, some other advantages to a modal synthesis approach include experimental verification at the substructure level, readily identifiable system behavior from substructure results, design changes easily implemented for individual substructures, and accurate results for complex models.

The modal synthesis method that was selected for the vibration analysis of the BSE spacecraft is a stiffness coupling technique which has been used extensively at the General Electric Space Division. The method uses free-free substructure vibration modes and frequencies in determining the coupled system modes of the entire spacecraft. Substructures, as defined by the stiffness coupling method, have no common degrees of freedom and are coupled together by a stiffness matrix relating the substructures' free attachment coordinates. The assembly of the total structure parallels that of the displacement method of the structural analysis.

As in all other methods of modal synthesis, the stiffness coupling method provides an approximate coupled solution in that the effects of the truncated high frequency modes are not included in the solution. Instead of truncating, or omitting the high frequency modes, a Dynamic Transformation [1, 2] is used to include those modes in the solution. The transformation relates the unused (truncated) modes to the retained modes at a selected system frequency. This transformation is then used to reduce the generalized mass and stiffness matrices which describe the dynamic behavior of the coupled system.

A unique computer program called SCAMP (Stiffness Coupling Approach Modal-Synthesis Program) is used to obtain the coupled BSE spacecraft's natural modes and frequencies. The use of SCAMP results in an analytical model accurately representing the dynamic characteristics of the BSE spacecraft even in the higher modes. Design changes

have been handled conveniently and efficiently with great savings in computer costs during the preliminary design phases of the BSE satellite. Accurate solutions have been obtained from small eigenvalue problem solutions due to the unique accuracy of the Dynamic Transformation included in the program.

STIFFNESS COUPLING METHOD

The stiffness coupling method of modal synthesis assembles the complete structure in the same manner as the displacement method for structural analysis. The total structure is represented by a number of substructures connected by flexible links (stiffness matrices). Each substructure is analyzed without the flexible links to determine the component vibration modes with free attachment coordinates. The component modes and frequencies are then used with the flexible links to derive a coupled system of equations describing the total structure.

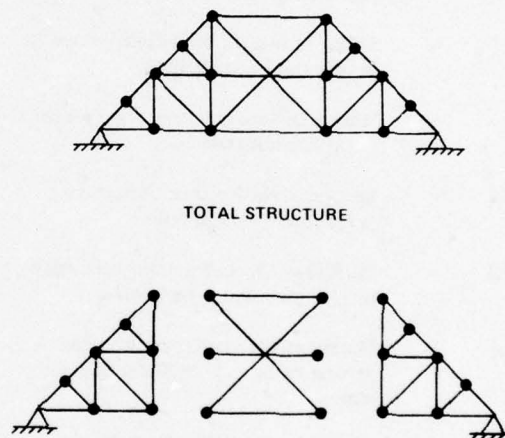


Fig. 2 Stiffness Coupling

The method of substructuring the stiffness coupling may be best illustrated by considering a total structure consisting of only two substructures. As an example, Figure 2 shows a 42 DOF planar truss model partitioned into two stiffness coupled substructures. The flexible link which connects the substructures' free attachment coordinates is modeled from the actual structure connecting them. The general undamped equation of motion for the i th substructure in terms of its mass matrix, $\{m_i\}$, and stiffness matrix, $\{k_i\}$, can be written as

$$\begin{bmatrix} m_i^{AA} & m_i^{AI} \\ m_i^{IA} & m_i^{II} \end{bmatrix} \begin{Bmatrix} \ddot{X}_i^A \\ \ddot{X}_i^I \end{Bmatrix} + \begin{bmatrix} k_i^{AA} & k_i^{AI} \\ k_i^{IA} & k_i^{II} \end{bmatrix} \begin{Bmatrix} X_i^A \\ X_i^I \end{Bmatrix} = \{0\} \quad (1)$$

where the "A" superscript refers to the attachment coordinates (DOF) connected by the link. The "I"

superscript refers to those internal coordinates belonging to the substructure but not connected by a link to another substructure.

Since the attachment degrees of freedom of each substructure are identical to those described by the coupling link, a second equation of motion can be written in terms of the attachment coordinates as

$$\begin{bmatrix} m_{\Delta}^{11} & m_{\Delta}^{12} \\ m_{\Delta}^{21} & m_{\Delta}^{22} \end{bmatrix} \begin{Bmatrix} \ddot{X}_1^A \\ \ddot{X}_2^A \end{Bmatrix} + \begin{bmatrix} k_{\Delta}^{11} & k_{\Delta}^{12} \\ k_{\Delta}^{21} & k_{\Delta}^{22} \end{bmatrix} \begin{Bmatrix} X_1^A \\ X_2^A \end{Bmatrix} = \{0\} \quad (2)$$

where the mass matrix, $[m_{\Delta}]$, and the stiffness matrix, $[k_{\Delta}]$, are obtained from the properties of the link.

By adding Equations (1) and (2) together, the equation of motion for the total coupled system in physical coordinates becomes

$$[M + M_{\Delta}] \{\ddot{X}\} + [K + K_{\Delta}] \{X\} = \{0\} \quad (3)$$

where

$$\{X\} = \begin{Bmatrix} X_1 \\ X_2 \end{Bmatrix}; \quad \{X_i\} = \begin{Bmatrix} X_i^A \\ X_i^I \end{Bmatrix} \quad (4)$$

From the substructure order defined by Equation (4), we have

$$[M] = \begin{bmatrix} m_1 & 0 \\ 0 & m_2 \end{bmatrix} \begin{Bmatrix} X_1 \\ X_2 \end{Bmatrix}; \quad [K] = \begin{bmatrix} k_1 & 0 \\ 0 & k_2 \end{bmatrix} \begin{Bmatrix} X_1 \\ X_2 \end{Bmatrix} \quad (5)$$

where the m_i , k_i , submatrices refer to the total substructure mass and stiffness matrices defined by Equation (1). Similarly, we have

$$[M_{\Delta}] = \begin{bmatrix} m_{\Delta}^{11} & 0 & m_{\Delta}^{12} & 0 \\ 0 & 0 & 0 & 0 \\ m_{\Delta}^{21} & 0 & m_{\Delta}^{22} & 0 \\ 0 & 0 & 0 & 0 \end{bmatrix} \begin{Bmatrix} X_1^A \\ X_1^I \\ X_2^A \\ X_2^I \end{Bmatrix} \quad (6a)$$

$$[K_{\Delta}] = \begin{bmatrix} k_{\Delta}^{11} & 0 & k_{\Delta}^{12} & 0 \\ 0 & 0 & 0 & 0 \\ k_{\Delta}^{21} & 0 & k_{\Delta}^{22} & 0 \\ 0 & 0 & 0 & 0 \end{bmatrix} \begin{Bmatrix} X_1^A \\ X_1^I \\ X_2^A \\ X_2^I \end{Bmatrix} \quad (6b)$$

where the m_{Δ}^{ii} , k_{Δ}^{ii} partitions are defined by Equation (2) for the coupling link. Up to this point, Equation

(3) represents "exactly" the equation of motion that would have been obtained by considering the entire structure.

For each substructure "i" described by $[m_i]$, $[k_i]$ in Equation (1), a set of eigenvalues, $[\omega_i^2]$, and eigenvectors, $[\phi_i]$, can be obtained such that

$$[\phi_i]^T [m_i] [\phi_i] = [I] \quad (7a)$$

$$[\phi_i]^T [k_i] [\phi_i] = [\omega_i^2] \quad (7b)$$

$$[\phi_i] = \begin{bmatrix} A \\ \phi_i^I \\ I \\ \phi_i^I \end{bmatrix} \quad (7c)$$

Defining the coordinate transformation

$$\{x\} = [\phi] \{q\} \quad (8)$$

where

$$[\phi] = \begin{bmatrix} \phi_i & 0 \\ 0 & \phi_2 \end{bmatrix} \quad (9)$$

and

$$\{q\} = \begin{Bmatrix} q_1 \\ q_2 \end{Bmatrix}, \quad (10)$$

Equation (3) can be transformed to a generalized set of coupled modal coordinates, $\{q\}$. Substituting the expression for $\{x\}$ from Equation (8) and pre-multiplying by $[\phi]^T$ yields

$$\begin{aligned} & \{[I] + [\phi^A]^T [m_{\Delta}] [\phi^A]\} \{\ddot{q}\} + \{[\phi^A]^T [k_{\Delta}] [\phi^A]\} \{q\} = \{0\} \\ & \text{where} \end{aligned} \quad (11)$$

$$[\phi^A] = \begin{bmatrix} A & 0 \\ \phi_i^I & A \\ 0 & \phi_2^I \end{bmatrix}; \quad [\Lambda] = \begin{bmatrix} \omega_1^2 & 0 \\ 0 & \omega_2^2 \end{bmatrix} \quad (11a)$$

Solution of Equation (11) will result in a set of coupled systems eigenvalues, $[\Lambda_s]$, and the corresponding eigenvectors, $[\gamma]$. Because of the similarity transformation used to obtain Equation (11) from Equation (3), the eigenvalues of Equation (11) will be equal to those of Equation (3), and the corresponding eigenvectors will be given by

$$[\xi_s] = [\phi] [\gamma] \quad (12)$$

As in other modal synthesis methods, the cost effectiveness in solving for coupled modes and frequencies is obtained by deleting the high frequency substructure modes. The equation is generally solved by partitioning the $\{q\}$ modal coordinates into two groups, kept and truncated. The truncated coordinates correspond to the high frequency substructure modes and are completely omitted from the equation of motion. The partitioned set of kept modal coordinates determine the final "reduced" size of the eigenvalue problem to be solved. To increase the accuracy of the higher modes, a larger number of modal coordinates must be kept. This results in larger eigenvalue solutions and increased cost. The dynamic transformation, however, includes those modes normally truncated without increasing the size of the eigenvalue problem. The accuracy of the method is shown in References 1 and 2.

A reasonable assumption for simplifying even more the calculations necessary to obtain the generalized mass matrix in Equation (11) is to assure that there is no inertial coupling between substructures; i. e., $m_{\Delta}^{12} = m_{\Delta}^{21} = 0$ in Equation (2). Then, by adding the proper m_{Δ}^{ii} terms in Equation (2) to the m_1^{AA} terms in Equation (1), the final form of the coupled equations of motion will be given as

$$[I] \ddot{q} + [\bar{K}] q = \{0\} \quad (13)$$

where

$$[\bar{K}] = [\Lambda] + [K_{\Delta}] \quad (14)$$

and

$$[\bar{k}_{\Delta}] = \begin{bmatrix} \phi_1^A T & k_{\Delta}^{11} & \phi_1^A & \phi_1^A T & k_{\Delta}^{12} & \phi_2^A \\ \phi_2^A T & k_{\Delta}^{21} & \phi_2^A & \phi_2^A T & k_{\Delta}^{22} & \phi_2^A \end{bmatrix} \quad (15)$$

Equation (13) is the equation of motion used to assemble the total structure by SCAMP. Note that for only two substructures, the matrix triple product for \bar{K}_{Δ} is the only calculation required to generate the coupled system dynamic matrix. This calculation is relatively simple since it only involves the attachment DOF's and the number of modes kept from each substructure.

For large systems comprised of several substructures, the \bar{K}_{Δ} calculation becomes cumbersome if formulated with all the substructures at one time. SCAMP simplifies this calculation by extending the two-substructure coupling concept. Stiffness links in SCAMP are defined only between two substructures. The total system $[\bar{K}]$ is then assembled by connecting the common substructure contributions in the same manner stiffness elements are overlaid to connect physical degrees of freedom.

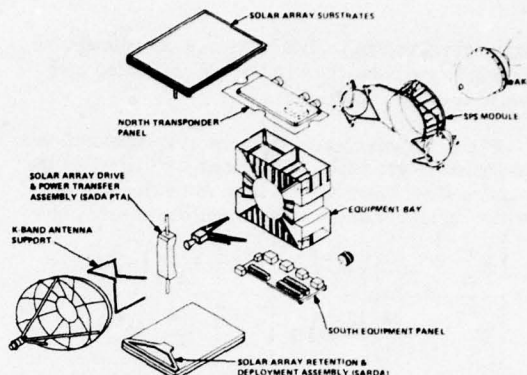


Fig. 3. BSE Structural Subsystem

ANALYTICAL SUBSTRUCTURE DESCRIPTIONS

The analytical model of the BSE spacecraft was developed by considering the major spacecraft segments separately. The structural segments are identified in Figure 3. Mass and stiffness matrices were developed for the fold-up solar array assembly, the antenna disk and feed assembly, the launch vehicle spacecraft adapter, and the center body. The secondary propulsion system tanks were considered as rigid lumped masses attached to the BSE spacecraft by support truss tubes.

1. **Centerbody.** A finite element model of the centerbody was obtained from the General Electric finite element program MASS [3]. Over 400 joints (2400 DOF) connected by beam and panel elements were used to represent the structure. Before reducing the centerbody model to 141 dynamic degrees of freedom (mass points), the 160 joint launch vehicle spacecraft adapter model was used as a grounding spring to cantilever the centerbody at eight attachment points. Fixed-free modes and frequencies were then calculated, analyzed for substructure behavior, and saved for input into SCAMP.
2. **Solar Array.** A stowed configuration of one solar array was modeled with more than 150 joints (900 DOF). The model included two deployable panels and a yoke. A solar array drive shaft connected to the yoke provided the main connection to the centerbody. In order to reduce the dynamic loads in the solar arrays during the initial flight stages, vibration isolators were used at four locations between the centerbody and the stowed solar array assembly. The stiffness links used to couple the solar array assemblies included both the shaft stiffness and the four isolator joints. This particular configuration for the stiffness link permitted several parametric studies of different isolator com-

binations to be easily investigated. Included in the 99 DOF eigenvalue solutions for the solar array were seven rigid body modes, six for the structure and one rotational yoke mode due to the shaft/centerbody connection. Although two solar arrays are used in the system assembly, only one set of modes and frequencies were used in SCAMP. The other solar array model was obtained in SCAMP via a coordinate transformation option.

3. **Antenna.** The 190 joint (1140 DOF) antenna assembly consisted of an antenna dish with a feed/support structure. The substructure assembly has six rigid body modes included in the 78 free-free modes and frequencies used to describe the antenna. The tube support truss between the antenna dish and centerbody was used for generating the stiffness link to couple the substructures together.
4. **SPS Tanks.** The secondary propulsion system tanks were not modeled but considered as rigid lumps. Six degrees of freedom were allowed for each tank mass point. The coupling spring was derived from the truss support structure by assuming a rigid plane where the truss tubes connected to the tanks.

COUPLED SPACECRAFT MODEL

The BSE spacecraft was assembled using the stiffness coupling method in SCAMP by considering stiffness links between two substructures at a time.

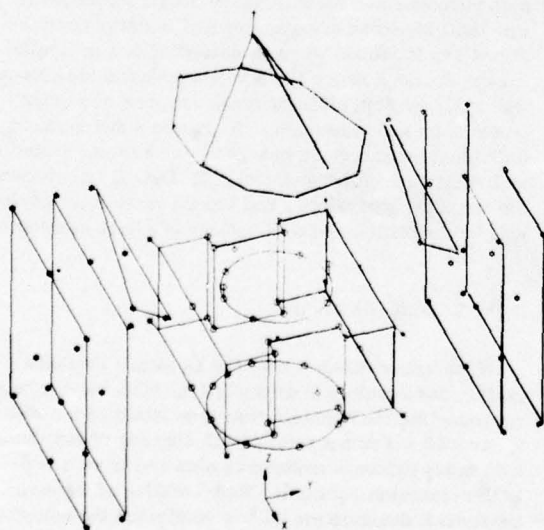


Fig. 4. BSE Analytical Model

From the four previously defined analytical models, five substructure interfaces were defined:

1. Center Body (C/B) to Antenna
2. C/B to South Solar Array
3. C/B to North Solar Array
4. C/B to East SPS Tank
5. C/B to West SPS Tank

Figure 4 shows the complete BSE analytical model. For clarity, the support truss members for the antenna dish, solar arrays, and SPS tanks were deleted. In addition, the stowed solar arrays have been separated and displaced from their correct positions.

TABLE 1.
Substructure DOF Table

SUBSTRUCTURE	JOINTS	DOF	EIGENVALUE SIZE	MODES KEPT	MODES REDUCED	TOTAL MODES USED
1. CENTER BODY	400	2400	141	30	60	90
2. ANTENNA	190	1140	78	18	30	48
3. SOUTH SOLAR ARRAY	150	900	99	20	30	50
4. NORTH SOLAR ARRAY	150	900	99	20	30	50
5. EAST SPS TANK	1	6	6	6	0	6
6. WEST SPS TANK	1	6	6	6	0	6
TOTALS	692	5382	429	100	150	250

The coupled BSE model consists of 429 dynamic degrees of freedom. A tabulation of the dynamic degrees of freedom for each substructure are shown in Table 1 under the column labeled Eigenvalue Size. The DOF column of the table shows the initial size of each substructure before static reduction. Of the 429 available modes, a total of 250 modes were used to synthesize the coupled model. The final size of the eigenvalue problem (100 DOF) was determined from the total number of "modes kept." The distribution of modes "kept" and modes "reduced" for each substructure are also included in Table 1. All modes not kept or reduced were omitted from the coupled solution.

A frequency criterion was used in selecting the modes to be kept and reduced based upon a final frequency requirement for the BSE spacecraft. In order to evaluate various flight load conditions, the final dynamic model was to be used as a substructure for determining a coupled spacecraft/launch vehicle model. This analysis required calculating all of the BSE spacecraft's modes and frequencies up to 100 Hz.

Using the 100 Hz criterion for a final solution, a sufficient number of substructure modes were selected to guarantee the calculation of all system modes under 100 Hz. A total of 90 modes (see Table 1) were used for the centerbody which had 14 flexible modes under 100 Hz. Of the 48 modes used from the antenna, only four had modal frequencies under 100 Hz. These were identified as two dish modes and two antenna/feed support truss modes. For each solar array, 50 modes were used in the assembly. There

were 19 modal frequencies under 100 Hz for the solar array models. The final solution of the 100 DOF eigenvalue problem resulted in 60 spacecraft modes and frequencies satisfying the 100 Hz requirements.

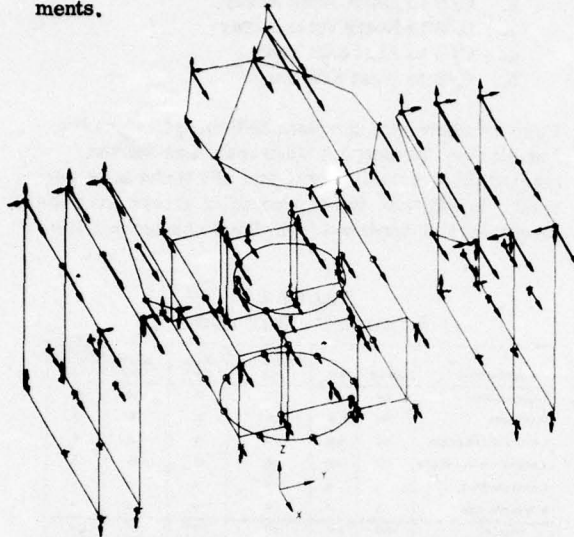


Fig. 5. BSE Spacecraft Bending Mode

Modal plots, such as the spacecraft X-bending mode shown in Figure 5, were used to identify the spacecraft modes. Vector triads located at the undeformed grid points are used to denote the deformed shape in each of the major axis directions. Additional insight to the dynamic behavior of the coupled modes was obtained from examining the participation factors from SCAMP. The participation factors indicated which of the 250 substructure modes were predominant contributors to the coupled modes. Knowing the substructure modes and participation factors simplified the identification and classification of several complex system modes.

The total assembly and eigensolution was solved in less than 15 minutes on a Honeywell 6000 Computer. SCAMP requires only 48K (decimal) core and uses a Jacobi threshold eigenvalue solver subroutine. Although limited to treating a total of 300 modes and 20 substructures at any one time, there is no limit to the number of physical degrees of freedom a substructure can have. The results from one solution in SCAMP can be used to represent one substructure for further coupling by the program.

A modal survey test of a BSE structural dynamic model (SDM) was conducted in order to determine the validity of the analytical model and of the predicted flight loads. Major spacecraft modes were initially identified from resonant responses measured during low-level sine sweeps. Measured test mode

shapes were then obtained, plotted, and compared to the predicted analytical modes. Table 2 contains the analysis/test frequency comparisons for some of the correlated modes. Since the SDM was only excited in the spacecraft X, Y, and Z directions, not all of the spacecraft modes were excited. A total of 19 test modes were correlated with the analytical predictions.

TABLE 2.
Analysis/Test Frequency Comparisons

ANALYTICAL MODE NO.	DESCRIPTION	MODAL AXES	FREQUENCY (Hz)	
			ANALYSIS	TEST
1*	1ST S/A ISOLATOR (ANTI-SYM)	Y	9.10	10.07
3	1ST S/C LATERAL BENDING	X	13.514	12.58
4	1ST S/C LATERAL BENDING	Y	15.82	15.53
9*	2ND S/A ISOLATOR (ANTI-SYM)	Y	22.02	24.27
10	ANTENNA FEED TRUSS BENDING	X	23.74	24.69
15	2ND S/C LATERAL BENDING	X	27.60	25.38
17*	S/A ISOLATOR	Z	30.26	28.98
18	2ND S/C LATERAL BENDING	Y	34.46	30.58
19	S/A MODE	Z	35.99	34.96
20	3RD S/A ISOLATOR	Y	37.02	36.23
28	S/C LONGITUDINAL	Z	48.53	45.24
35	ANTENNA DISH BENDING/S-BAND	Y	55.861	54.05
36	ANTENNA DISH BENDING	Y	56.75	56.82
38	ANTENNA DISH	Z	60.18	54.90

*NON-LINEAR

PROJECT CONSIDERATIONS

In addition to reducing computer costs for complex model solutions, a modal synthesis approach offers several cost effective alternatives for project considerations. 1) Experimental verification of the analytical modeling at the substructure level minimizes or eliminates the need for an extensive integrated test program. 2) Parametric studies for design purposes can be done at the substructure level. For the BSE solar arrays, several isolator combinations and locations were investigated before finalizing the design. Also, the antenna dish and feed model was analyzed for different configurations of support truss tubes and materials. 3) Due to substructuring, individual substructure changes can be incorporated with minimum effort and cost. 4) Data flow between the spacecraft developer and launch vehicle integrator will be simplified and duplications of effort eliminated.

CONCLUDING REMARKS

The use of SCAMP with the Dynamic Transformation has resulted in an analytical model accurately representing the dynamic characteristics of the BSE spacecraft. From a total of 429 degrees of freedom, a 60 mode dynamic model was obtained from a 100-DOF eigenvalue solution. Modal testing of the BSE spacecraft dynamic model has confirmed the analytical model computations.

This analysis has demonstrated how a large complex structure such as the BSE can be handled conveniently and efficiently with great savings in computer costs without modal truncation. Accurate solutions can be obtained for complex systems from small eigenvalue problem solutions due to the unique accuracy of the Dynamic Transformation.

REFERENCES

1. Kuhar, E.J., "Selected System Modes Using the Dynamic Transformation With Modal Synthesis," The Shock and Vibration Bulletin, No. 44, Part 2, pp. 91-102, August 1974
2. Kuhar, E.J. and Stahle, C.V., "A Dynamic Transformation Method for Modal Synthesis," AIAA Journal, Vol. 12, No. 5, pp. 672-678, May 1974
3. Beitch, L., "MASS System-The Computer Program for General Redundant Structures With Vibratory and General Static Loading," General Electric Company, TIS R66 FPG172, September 13, 1966

Discussion

Mr. Chapman (Jet Propulsion Laboratory): I noticed in your summary table of modes in analysis and test that you had two modes in the neighborhood of 24 Hz that were .42 Hz apart. How do you know this? What is your confidence in this?

Mr. Kuhar: Of the modes?

Mr. Chapman: Yes.

Mr. Kuhar: We are currently using a Jacobi threshold method which produces multiple roots and multiple eivenvectors for the solution. We have looked at tje problem in separate pieces such as stripping off the solar arrays, and trying to look at the individual modes of a basic center body spacecraft which were readily identified. When we put the pieces together the modes started coupling and we got pairs of modes for the solar arrays themselves double frequencies up the line, and looking at the individual substructures the modes didn't change that much; if you had an idea what modes were before they coupled and where you were, the frequencies fell right in line with the small shift that they had and I have no doubt that these were valid frequencies.

VIBRATION ANALYSIS OF STRUCTURES USING FIXED-INTERFACE COMPONENT MODES

Charles Szu
TRW Defense and Space Systems Group
Redondo Beach, California

This paper describes a modal coupling program (COUPL) which computes vibration modes of a structural system by using fixed-interface component modes. It contains a complete derivation of equations which lead to efficient algorithms. A sample problem to illustrate the accuracy of the formulations is also included.

The method implemented by COUPL can solve problems where the interfaces are either statically determinate or redundant. It is not necessary to identify statically determinate and redundant interface coordinates. The structural system may have any type of boundary conditions including the free-free type. There is no need to select any specific component as the main one since all components, large or small, are treated alike. There is no constraint on the interconnecting topology of the system of components. Individual components can be modified without affecting the modes of adjacent components, so long as the interface relationships are not changed.

1. INTRODUCTION

Analyses of a complex structure as a whole may require computer facilities of greater capability than may be available. With a modal coupling program, the computer capacity problem is reduced since, in general, only the lower frequency modes of each component are needed. Each component may be modeled in great detail without compromising accuracy. Another advantage is that one component may be changed without remodeling the others. This is particularly useful when components are designed and analyzed by different organizations.

This paper presents in detail an alternate approach to the method developed by Hurty Reference [1] and extended by Craig and Bampton Reference [2] to perform modal coupling analysis. This approach utilizes a procedure to facilitate computer implementation and to achieve computation efficiency.

The method of solution is presented in Section 2. It requires fixed-interface vibration modes as well as constraint modes for each component. However, constraint modes are computed directly from the stiffness matrix of the component. Lagrange equations are used to generate the equations of motion which are expressed in matrix form.

The major features of this approach are described in three appendices. The constraint mode and its corresponding stiffness matrix are contained in Appendix A. Appendix B presents

the dynamic matrix formation. The decomposition of the mass matrix by partitioning is included in Appendix C. A special feature of this approach is the utilization of the mass matrix with a unit submatrix.

Practical application of the method has been demonstrated by implementation of the computer code COUPL*. To illustrate the accuracy of the formulation, a sample problem together with an error study is included in Section 3.

2. METHOD OF SOLUTION

A component is considered to be composed of interface and non-interface degrees of freedom. Interface degrees of freedom are those which are common to two or more components. The total motion of a component can be expressed as a linear combination of its motion relative to a fixed interface and its motion due to its interface motion as

$$\{x\} = \{\bar{x}\} + \{\hat{x}\} \quad (1)$$

*The computer program is divided into one main overlay and four primary overlays. It consists of 43 subroutines having the capability to adjust and determine their field lengths during execution. There is no limitation on the number of components; however, the total number of system modes is limited to approximately 420 (Control Data Cyber 70 Model 74-18, or CDC 6500 computers).

where $\{\bar{x}\}$ is a set of displacements relative to its fixed interface, and $\{\bar{x}\}$ is a set of displacements produced by motion of the interface degrees of freedom.

The displacement relative to the fixed interface can be defined in terms of the component's normal mode shapes as

$$\{\bar{x}\} = [\phi_n] \{p_n\} \quad (2)$$

where $[\phi_n]$ is the normal mode matrix of the component with all interface degrees of freedom fixed in addition to the normal boundary constraints, and $\{p_n\}$ is a vector of generalized displacements.

The displacements caused by interface motion can be obtained from the force-displacement equations for the component. The stiffness matrix of the component can be partitioned as

$$\begin{Bmatrix} F_N \\ F_I \end{Bmatrix} = \begin{bmatrix} K_{NN} & K_{NI} \\ K_{IN} & K_{II} \end{bmatrix} \begin{Bmatrix} x_N \\ x_I \end{Bmatrix} \quad (3)$$

where subscripts N and I refer to non-interface and interface, respectively.

Constraint modes are defined as the deflected shapes of the non-interface degrees of freedom due to successive unit displacement of an interface degree of freedom, all other interface degrees of freedom being totally constrained. To determine constraint modes, the forces at all non-interface degrees of freedom are set equal to zero. Eq. (3) gives

$$\{0\} = [K_{NN}] \{x_N\} + [K_{NI}] \{x_I\}$$

or,

$$\{x_N\} = -[K_{NN}]^{-1} [K_{NI}] \{x_I\} \equiv [\psi_c] \{x_I\} \quad (4)$$

where $[\psi_c]$ defines the non-interface motion in terms of interface motion.

Let $[I]$ denote a unit matrix. The component motion due to its interface motion becomes

$$\{\hat{x}\} = \begin{bmatrix} \psi_c \\ I \end{bmatrix} \{x_I\}$$

or,

$$\{\hat{x}\} = [\phi_c] \{p_c\} \quad (5)$$

where $[\phi_c]$ represents the constraint modes and $\{p_c\}$ replaces $\{x_I\}$.

Using Eqs. (2) and (5), Eq. (1) takes the form

$$\{x\} = [\phi_n] \{p_n\} + [\phi_c] \{p_c\}$$

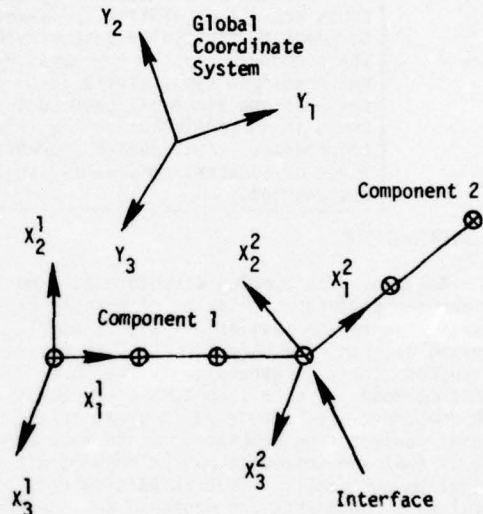
or,

$$\{x\} = [\phi_n | \phi_c] \begin{Bmatrix} p_n \\ p_c \end{Bmatrix} \quad (6)$$

The number of component normal modes may be truncated to reduce the number of generalized displacements. In general, only the lower frequency modes of each component are needed.

As mentioned earlier, the method presented is applicable to n-component systems. To simplify the presentation, two 3-dimensional beams, as shown schematically in Figure 1, are used to illustrate the technique. For convenience, superscript 1 refers to component 1 and superscript 2 refers to component 2.

Figure 1
COORDINATE SYSTEM



x_1^1 : axis 1 of Component 1

x_2^1 : axis 2 of Component 1

x_3^1 : axis 3 of Component 1

x_1^2 : axis 1 of Component 2

x_2^2 : axis 2 of Component 2

x_3^2 : axis 3 of Component 2

Y_1 : axis 1 of the global coordinate system

Y_2 : axis 2 of the global coordinate system

Y_3 : axis 3 of the global coordinate system

$\{x^1\}$: Component 1 displacements in terms of the coordinate system (x_1^1, x_2^1, x_3^1)

$\{x^2\}$: Component 2 displacements in terms of the coordinate system (x_1^2, x_2^2, x_3^2)

$\{y^1\}$: Component 1 displacements in terms of the global coordinate system

$\{y^2\}$: Component 2 displacements in terms of the global coordinate system

For the two-component problem, Eq. (6) takes the form

$$\begin{Bmatrix} x^1 \\ x^2 \end{Bmatrix} = \begin{bmatrix} \phi_n^1 & \phi_c^1 & 0 & 0 \\ 0 & 0 & \phi_n^2 & \phi_c^2 \end{bmatrix} \begin{Bmatrix} p_n^1 \\ p_c^1 \\ p_n^2 \\ p_c^2 \end{Bmatrix} \quad (7)$$

where $\{x^1\}$ and $\{x^2\}$ are the displacement vectors for components 1 and 2 respectively.

Compatibility conditions are needed to insure that the displacements on the interface of component 1 match those of its adjoining components. Since each component has its own discrete coordinate system, a global coordinate system will be used to describe the compatibility conditions. The relationship between the $\{x^1\}$ and $\{y^1\}$ is given by

$$\{x^1\} = \begin{bmatrix} [\lambda^1] & \\ & [\lambda^1] \end{bmatrix} \{y^1\} \quad (8)$$

where $[\lambda^1]$ is the rotation matrix of order 3 by 3.

Eq. (8) may be written in compact form as

$$\{x^1\} = [R^1] \{y^1\} \quad (9)$$

For those interface degrees of freedom, a similar expression is

$$\{p_c^1\} = [R_c^1] \{q_c^1\} \quad (10)$$

where $[R_c^1]$ is a submatrix of $[R^1]$ and $\{q_c^1\}$ is a column of generalized displacements in the global coordinate system.

From Eq. (10), it follows

$$\{p_c^2\} = [R_c^2] \{q_c^2\} \quad (11)$$

Now that $\{q_c^1\}$ and $\{q_c^2\}$ are in terms of the common global coordinate system, it is easy to enforce the compatibility conditions as follows

$$\begin{Bmatrix} q_c^1 \\ q_c^2 \end{Bmatrix} = \begin{bmatrix} \beta^1 \\ \beta^2 \end{bmatrix} \{q\} \quad (12)$$

where $[\beta^1]$ is the displacement compatibility matrix for component 1, $[\beta^2]$ is the displacement compatibility matrix for component 2, and $\{q\}$ is a vector containing the independent interface degrees of freedom for the total structure. It is worthwhile to emphasize that only interface degrees of freedom are transformed into the global coordinate system. The compatibility relationship defined in Eq. (12) is applicable to a system with any number of components.

With Eqs. (10), (11) and (12), it follows

$$\begin{Bmatrix} p_n^1 \\ p_c^1 \\ p_n^2 \\ p_c^2 \end{Bmatrix} = \begin{bmatrix} I & 0 & 0 & 0 \\ 0 & 0 & R_c^1 & 0 \\ 0 & I & 0 & 0 \\ 0 & 0 & 0 & R_c^2 \end{bmatrix} \begin{Bmatrix} p_n^1 \\ p_n^2 \\ q_c^1 \\ q_c^2 \end{Bmatrix} = \begin{bmatrix} I & 0 & 0 & 0 \\ 0 & 0 & R_c^1 & 0 \\ 0 & I & 0 & 0 \\ 0 & 0 & 0 & R_c^2 \end{bmatrix} \begin{bmatrix} I & 0 & 0 \\ 0 & I & 0 \\ 0 & 0 & \beta^1 \\ 0 & 0 & \beta^2 \end{bmatrix} \begin{Bmatrix} p_n^1 \\ p_n^2 \\ q_c^1 \\ q_c^2 \end{Bmatrix} \quad (13)$$

Substitution of Eq. (13) into Eq. (7) yields

$$\begin{Bmatrix} x^1 \\ x^2 \end{Bmatrix} = [MCT] \begin{Bmatrix} p_n^1 \\ p_n^2 \\ q_c^1 \\ q_c^2 \end{Bmatrix} \quad (14)$$

in which

$$[MCT] = \begin{bmatrix} \phi_n^1 & 0 & \phi_c^1 R_c^1 \beta^1 \\ 0 & \phi_n^2 & \phi_c^2 R_c^2 \beta^2 \end{bmatrix}$$

where MCT denotes the modal coupling transformation matrix.

The kinetic energy for the two uncoupled components 1 and 2 may be written in matrix form as

$$KE = \frac{1}{2} \begin{bmatrix} \dot{x}^1 & \dot{x}^2 \end{bmatrix} \begin{bmatrix} m^1 & 0 \\ 0 & m^2 \end{bmatrix} \begin{Bmatrix} \dot{x}^1 \\ \dot{x}^2 \end{Bmatrix} \quad (15)$$

where m^1 and m^2 are the mass matrices for the two components.

Differentiating Eq. (14)

$$\begin{Bmatrix} \dot{x}^1 \\ \dot{x}^2 \end{Bmatrix} = [MCT] \begin{Bmatrix} \dot{p}_n^1 \\ \dot{p}_n^2 \\ \dot{q} \end{Bmatrix} \quad (16)$$

Substituting Eq. (16) into Eq. (15) results in a kinetic energy expression for the coupled system in terms of modal coordinates

$$KE = \frac{1}{2} [\dot{p}_n^1 \mid \dot{p}_n^2 \mid \dot{q}] [CM] \begin{Bmatrix} \dot{p}_n^1 \\ \dot{p}_n^2 \\ \dot{q} \end{Bmatrix} \quad (17)$$

where the coupled modal mass matrix is

$$[CM] = \begin{bmatrix} \phi_n^{1T} m^1 \phi_n^1 & 0 & \phi_n^{1T} m^1 \phi_c^1 R_c^1 \beta^1 \\ \text{SYMMETRIC} & \phi_n^{2T} m^2 \phi_n^2 & \phi_n^{2T} m^2 \phi_c^2 R_c^2 \beta^2 \\ m_{\beta\beta} & & \end{bmatrix}$$

$$= \begin{bmatrix} m_{nn}^1 & 0 & m_{nc}^1 R_c^1 \beta^1 \\ \text{SYMMETRIC} & m_{nn}^2 & m_{nc}^2 R_c^2 \beta^2 \\ m_{\beta\beta} & & \end{bmatrix} \quad (18)$$

Let barred matrices below represent rotated quantities. The above equation reduces to

$$[CM] = \begin{bmatrix} \bar{m}_{nn}^1 & 0 & \bar{m}_{nc}^1 \beta^1 \\ 0 & \bar{m}_{nn}^2 & \bar{m}_{nc}^2 \beta^2 \\ \beta^{1T} \bar{m}_{cn}^1 & \beta^{2T} \bar{m}_{cn}^2 & m_{\beta\beta} \end{bmatrix} \quad (19)$$

where

$$m_{\beta\beta} = \beta^{1T} \bar{m}_{cc}^1 \beta^1 + \beta^{2T} \bar{m}_{cc}^2 \beta^2$$

$$\bar{m}_{cc}^1 = R_c^{1T} m_{cc}^1 R_c^1$$

$$\bar{m}_{cc}^2 = R_c^{2T} m_{cc}^2 R_c^2$$

$$\bar{m}_{cc}^1 = \phi_c^{1T} m^1 \phi_c^1$$

$$\bar{m}_{cc}^2 = \phi_c^{2T} m^2 \phi_c^2$$

Note that each element of $[m_{nn}^1]$ represents an uncoupled generalized mass of component 1. In general, it can be made into a unit matrix by normalizing the component modes.

The potential energy for the two uncoupled components 1 and 2 is

$$PE = \frac{1}{2} [x^1 \mid x^2] \begin{bmatrix} K^1 & 0 \\ 0 & K^2 \end{bmatrix} \begin{Bmatrix} x^1 \\ x^2 \end{Bmatrix} \quad (20)$$

where K^1 and K^2 are the stiffness matrices for the two components.

Substituting Eq. (14) into Eq. (20) results in a potential energy expression for the coupled system in terms of modal coordinates

$$PE = \frac{1}{2} [p_n^1 \mid p_n^2 \mid q] [CK] \begin{Bmatrix} p_n^1 \\ p_n^2 \\ q \end{Bmatrix} \quad (21)$$

where $[CK]$ is the coupled modal stiffness matrix.

It can be shown easily that

$$[CK] = \begin{bmatrix} k_{nn}^1 & 0 & 0^+ \\ 0 & k_{nn}^2 & 0^+ \\ 0^+ & 0^+ & \beta^{1T} \bar{K}_{cc}^1 \beta^1 + \beta^{2T} \bar{K}_{cc}^2 \beta^2 \end{bmatrix} \quad (22)$$

From the orthogonality properties of the component normal modes, it can be proved that each element of $[K_{nn}^1]$ represents a product of the circular frequency squared and the corresponding uncoupled generalized mass of component 1. The matrix $[K_{cc}^1]$ is discussed in Appendix A.

The coupled modal mass Eq. (19) and stiffness matrices Eq. (22) are partitioned such that efficient computational algorithms can be easily developed. The algorithm development includes a dynamic matrix formation in Appendix B and a special decomposition technique in Appendix C.

Using Eqs. (17) and (21), Lagrange's Equations can be used to derive the equations of motion.

*Superscript T denotes the transpose of a matrix.

†Based upon the definition of normal and constraint modes, these submatrices can be proved to be zero (Reference [1]).

$$[CM] \begin{Bmatrix} \ddot{p}_n^1 \\ \ddot{p}_n^2 \\ \ddot{q} \end{Bmatrix} + [CK] \begin{Bmatrix} p_n^1 \\ p_n^2 \\ q \end{Bmatrix} = \{0\} \quad (23)$$

[CM] from Eq. (19), and [CK] from Eq. (22) are manipulated to form a symmetric dynamic matrix and are input to an eigenvalue routine based on Householder's method which results in a set of "modal modes" so that an expression may be written

$$\begin{Bmatrix} p_n^1 \\ p_n^2 \\ q \end{Bmatrix} = \begin{Bmatrix} \theta_n^1 \\ \theta_n^2 \\ \theta_q \end{Bmatrix} \{\xi\}$$

or

$$\{p\} = [\theta] \{\xi\} \quad (24)$$

where $[\theta]$ = coupled modal modes (eigenvectors of Eq. (23))

$\{\xi\}$ = coupled modal displacements

The final coupled modes, in terms of the original discrete coordinates $\{x^1\}$ and $\{x^2\}$, may now be calculated by substituting Eq. (24) into Eq. (14), resulting in

$$\begin{aligned} \begin{Bmatrix} x^1 \\ x^2 \end{Bmatrix} &= \begin{bmatrix} \phi_n^1 & 0 & \phi_c^1 R_c^1 \beta^1 \\ 0 & \phi_n^2 & \phi_c^2 R_c^2 \beta^2 \end{bmatrix} \begin{Bmatrix} \theta_n^1 \\ \theta_n^2 \\ \theta_q \end{Bmatrix} \{\xi\} \\ &= \begin{bmatrix} \phi_n^1 \theta_n^1 + \phi_c^1 R_c^1 \beta^1 \theta_q \\ \phi_n^2 \theta_n^2 + \phi_c^2 R_c^2 \beta^2 \theta_q \end{bmatrix} \{\xi\} \\ &= \begin{bmatrix} \text{MODE}^1 \\ \text{MODE}^2 \end{bmatrix} \{\xi\} \end{aligned} \quad (25)$$

where $[\text{MODE}^1]$ denotes the coupled modes of component 1. Each column of $[\text{MODE}^1]$ represents a final coupled mode.

Note that $[\text{MODE}^1]$ is in terms of component 1's discrete coordinate system, and $[\text{MODE}^2]$ is in terms of component 2's. They may be transformed into the global coordinate system defined in Figure 1,

$$\begin{Bmatrix} y^1 \\ y^2 \end{Bmatrix} = \begin{bmatrix} R^{1T} & 0 \\ 0 & R^{2T} \end{bmatrix} \begin{Bmatrix} x^1 \\ x^2 \end{Bmatrix} \quad (26)$$

or,

$$\begin{Bmatrix} y^1 \\ y^2 \end{Bmatrix} = \begin{bmatrix} R^{1T} (\text{MODE}^1) \\ R^{2T} (\text{MODE}^2) \end{bmatrix} \{\xi\} \quad (27)$$

For a n -component problem, the following expression can be written,

$$\begin{Bmatrix} y^1 \\ y^2 \\ \vdots \\ y^n \end{Bmatrix} = \begin{bmatrix} R^{1T} (\text{MODE}^1) \\ R^{2T} (\text{MODE}^2) \\ \vdots \\ R^{nT} (\text{MODE}^n) \end{bmatrix} \{\xi\} \quad (28)$$

The final item to address is the formation of the generalized force vector for the coupled system. Rewrite Eq. (14)

$$\begin{Bmatrix} x^1 \\ x^2 \end{Bmatrix} = \begin{bmatrix} \phi_n^1 & 0 & \phi_c^1 R_c^1 \beta^1 \\ 0 & \phi_n^2 & \phi_c^2 R_c^2 \beta^2 \end{bmatrix} \begin{Bmatrix} p_n^1 \\ p_n^2 \\ q \end{Bmatrix} \quad (14)$$

The generalized force vector is therefore

$$\begin{Bmatrix} p_n^1 \\ p_n^2 \\ q \end{Bmatrix} = \begin{bmatrix} \phi_n^{1T} & 0 \\ 0 & \phi_n^{2T} \\ \beta^{1T} R_c^{1T} \phi_c^{1T} & \beta^{2T} R_c^{2T} \phi_c^{2T} \end{bmatrix} \begin{Bmatrix} F_x^1 \\ F_x^2 \\ F_x \end{Bmatrix} \quad (29)$$

where $\{F_x^1\}$ is the set of forces applied at component 1's degrees of freedom in terms of the discrete coordinate system of component 1.

Using Eqs. (14) and (26), the generalized force vector can also be expressed in terms of the global coordinate system as

$$\begin{Bmatrix} p_n^1 \\ p_n^2 \\ q \end{Bmatrix} = \begin{bmatrix} \phi_n^{1T} R^{1T} & 0 \\ 0 & \phi_n^{2T} R^{2T} \\ \beta^{1T} R_c^{1T} \phi_c^{1T} R^{1T} & \beta^{2T} R_c^{2T} \phi_c^{2T} R^{2T} \end{bmatrix} \begin{Bmatrix} F_y^1 \\ F_y^2 \\ F_y \end{Bmatrix} \quad (30)$$

where $\{F_y^1\}$ is the set of forces applied at component 1's degrees of freedom in terms of the global coordinate system.

3. SAMPLE PROBLEM

A sample problem is included to illustrate the accuracy* of the formulation which is implemented into the computer code COUPL.

*As discussed in Reference [3], the methods that use fixed-interface component modes tend to produce more accurate results than those that use free-free component modes. Moreover, Ref. [3] notes that methods that use component mass and stiffness matrices tend to be more accurate than those that do not.

As shown schematically in Figure 2, component 1 is connected to component 2 at two interface locations. The global coordinate system (X, Y, Z) is defined to coincide with component 1's coordinate system (x, y, z). Component 2's coordinate system (x, y, z) is defined relative to the global coordinate system (X, Y, Z) by a 45 degree rotation about its y-axis.

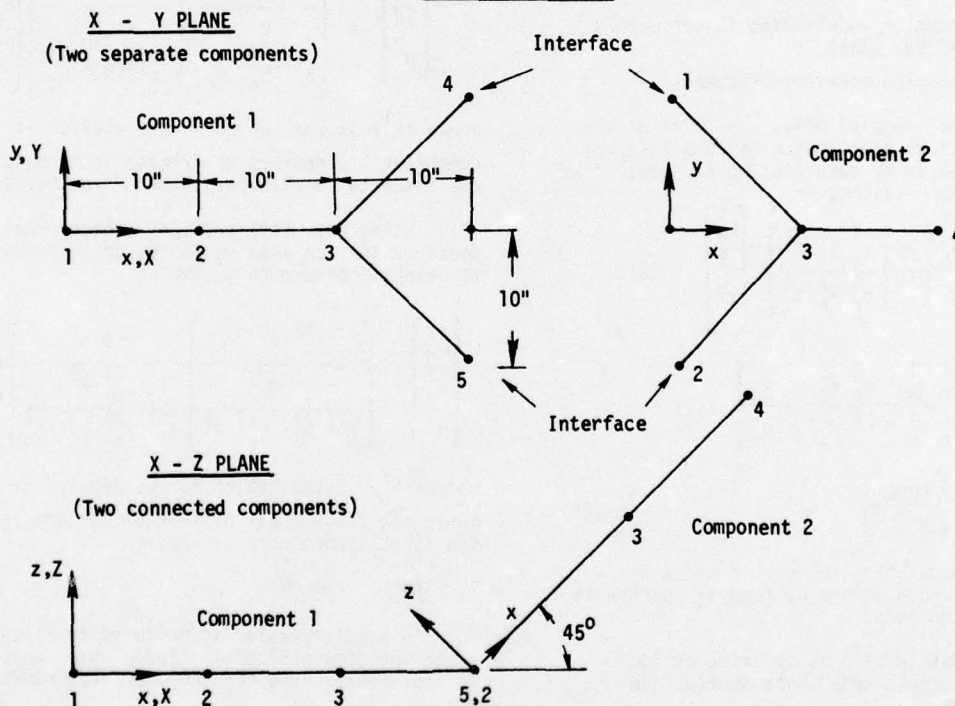
Table 1 depicts the percent frequency errors. The errors are determined by comparing the results obtained using COUPL with those obtained for the complete structure wherein both components are considered to be a single entity. It should be noted that the generalized coordinates used for the eigenvalue solution must contain all 12 interface constraint modes. The maximum per cent frequency error is 0.65 when 10 component normal modes are used (6 from component 1 and 4 from component 2). The

frequencies of the fixed-interface component modes are tabulated in Table 1. It is worth while to mention that the coupled frequency of the 16th mode (the 10th elastic mode) is 409.66 Hz even though the highest frequency of the fixed-interface component mode is 293.148 Hz.

Table 2 identifies the major uncoupled mode contributor to each mode of the coupled structure. It should be noted that uncoupled modes include 10 fixed-interface component modes and 12 interface constraint modes.

Table 3 shows the modal displacements of the first elastic mode (7th coupled mode) together with those obtained for the complete structure with both components considered as a single entity. The excellent agreement of the modes verifies the accuracy of program COUPL.

Figure 2
TWO COUPLED FORKS



Component 1: Left Fork

Joint	x	y	z	Weight	Inertia
1	0.0	0.0	0.0	5	0
2	10.0	0.0	0.0	5	0
3	20.0	0.0	0.0	5	0
4	30.0	10.0	0.0	5	0.1
5	30.0	-10.0	0.0	5	0.1

Component 2: Right Fork

Joint	x	y	z	Weight	Inertia
1	0.0	10.0	0.0	5	0.1
2	0.0	-10.0	0.0	5	0.1
3	10.0	0.0	0.0	5	0
4	20.0	0.0	0.0	5	0

TABLE 1
PERCENT FREQUENCY ERRORS

Mode No.	Frequency (Hz)		Percent Frequency Error
	Complete Structure	Modal Coupling	
7*	9.825714	9.8257155	--
8	15.429395	15.430617	--
9	27.45257	27.452635	--
10	31.843971	31.844421	--
11	33.62594	33.638927	-0.038
12	53.333442	53.333698	--
13	68.034806	68.076275	-0.061
14	79.645058	79.645146	--
15	325.41683	327.53208	-0.65 [†]
16	408.47714	409.66194	-0.29

Fixed-Interface Component Modes

Component 1: Left Fork

5.721 (Hz)
9.301
33.798
62.997
87.526
217.302
458.318
637.776
959.690

} These 3 modes
are truncated.

Component 2: Right Fork

11.476 (Hz)
25.317
64.053
293.148
456.814
839.897

} These 2 modes
are truncated.

* The first six rigid body frequencies are not presented in this table.

[†] The maximum percent frequency error is -0.65 when 10 fixed-interface component modes are used (6 from component 1 and 4 from component 2).

Table 2

IDENTIFICATION OF THE COUPLED MODES

MODE	NCOL	GM CONTRI.	COUPLED FREQ (HZ)	UNCOUPLED* FREQ (HZ)
1	19	.5167	.000	0.000
2	13	.9561	.000	0.000
3	19	.3366	.000	0.000
4	21	.4317	.000	0.000
5	17	.5216	.000	0.000
6	11	1.1429	.000	0.000
7	1	.5884	9.826	5.721
8	2	.9473	15.431	9.301
9	3	.3855	27.453	33.798
10	12 [†]	.3554	31.844	0.000
11	8	.9226	33.639	25.317
12	9	.6167	53.334	64.053
13	4	.9668	68.076	62.997
14	5	.8004	79.645	87.526
15	6	.9661	327.532	217.302
16	10	.9668	409.662	293.148

RIGID BODY
MODES

* This column denotes the modal frequency of the fixed-interface component mode that is the major contributor to the mode of the coupled structure. If this value is zero, the major contributor is one of the constraint modes.

† When two uncoupled modes contribute equally to form the coupled mode, the computer chooses one of them arbitrarily. For example, due to the symmetry of the coupled structure shown in Figure 2, the 12th uncoupled mode (2nd constraint mode) and the 18th uncoupled mode (8th constraint mode) are both major contributors to the 10th coupled mode. They contribute the same amount, 0.3554, to form the 10th mode of the coupled structure.

TABLE 3
MODAL DISPLACEMENT COMPARISON

A. COUPL Output

MODE 7
FREQUENCY (HZ) = 9.8257
GENERALIZED MASS = 1.00000

COMPONENT 1 (GLOBAL COORDINATE SYSTEM)

GLOBAL COMP JOINT	D-X	D-Y	D-Z	R-X	R-Y	R-Z
1	.7618720	0.0000000	4.3397540	0.0000000	.3831651	0.000000000
2	.7615716	0.0000000	.7196382	0.0000000	.3197045	0.000000000
3	.7610193	0.0000000	-1.5961890	0.0000000	.1187996	0.000000000
4	.8928349	-.1323739	-1.9129860	-.0753453	-.1546586	-.033086110
5	.8928349	.1323739	-1.9129860	.0753453	-.1546586	.033086110

COMPONENT 2 (GLOBAL COORDINATE SYSTEM)

GLOBAL COMP JOINT	D-X	D-Y	D-Z	R-X	R-Y	R-Z
6	-1.367051	0.0000000	.5336770	0.0000000	-.3853145	0.000000000
7	-4.488752	0.0000000	3.6550640	0.0000000	-.4695222	0.000000000

B. COMPLETE STRUCTURE AS A SINGLE ENTITY

MODE 7
FREQUENCY (CPS) = 9.8257
GENERALIZED MASS = 1.00000

MODAL JOINT DISPLACEMENTS

JOINT	D-X	D-Y	D-Z	R-X	R-Y	R-Z
1	.7618302	0.0000000	4.3397540	0.0000000	.3831650	0.000000000
2	.7615782	0.0000000	.7196388	0.0000000	.3197045	0.000000000
3	.7610742	0.0000000	-1.5961880	0.0000000	.1187996	0.000000000
4	.8928317	-.1323735	-1.9129850	-.0753453	-.1546585	-.033086080
5	.8928317	.1323735	-1.9129850	.0753453	-.1546585	.033086080
6	-1.3670640	0.0000000	.5336654	0.0000000	-.3853144	0.000000000
7	-4.4887450	0.0000000	3.6550700	0.0000000	-.4695220	0.000000000

Appendix A

Constraint Mode and its Stiffness Matrix

The stiffness matrix of the component can be partitioned as

$$\begin{Bmatrix} F_N \\ F_I \end{Bmatrix} = \begin{bmatrix} K_{NN} & K_{NI} \\ K_{IN} & K_{II} \end{bmatrix} \begin{Bmatrix} x_N \\ x_I \end{Bmatrix} \quad (A-1)$$

where subscripts N and I refer to non-interface and interface, respectively.

To determine constraint modes, the forces at all non-interface degrees of freedom are set equal to zero, i.e.

$$\{0\} = [K_{NN}] \{x_N\} + [K_{NI}] \{x_I\}$$

or,

$$\{x_N\} = -[K_{NN}]^{-1} [K_{NI}] \{x_I\} \equiv [\psi_C] \{x_I\} \quad (A-2)$$

where $[\psi_C]$ is the desired matrix of constraint modes. Eq. (A-1) also gives

$$\{F_I\} = [K_{IN}] \{x_N\} + [K_{II}] \{x_I\}$$

Upon substituting $\{x_N\}$ from Eq. (A-2), the above equation becomes

$$\{F_I\} = ([K_{II}] - [K_{IN}] [K_{NN}]^{-1} [K_{NI}]) \{x_I\} \quad (A-3)$$

Let

$$[K_{CC}] = [K_{II}] - [K_{IN}] [K_{NN}]^{-1} [K_{NI}] \quad (A-4)$$

where $[K_{CC}]$ is the constraint mode stiffness matrix.

A typical element of $[K_{CC}]$, say the i -th row and the j -th column, is equal to the work done by a set of forces associated with the i -th constraint mode acting through displacements associated with the j -th constraint mode.

An alternate method to evaluate $[K_{CC}]$ is to form the triple matrix product,

$$\begin{aligned} [K_{CC}] &= [\psi_C]^T [I] \begin{bmatrix} K_{NN} & K_{NI} \\ K_{IN} & K_{II} \end{bmatrix} \begin{Bmatrix} \psi_C \\ I \end{Bmatrix} \\ &= [\psi_C]^T [K_{NN}] [\psi_C] + [K_{IN}] [\psi_C] \\ &\quad + [\psi_C]^T [K_{NI}] + [K_{II}] \end{aligned}$$

where $[I]$ denotes a unit matrix.

Upon substituting $[\psi_C]$ from Eq. (A-2), the above equation becomes

$$[K_{CC}] = [K_{II}] - [K_{IN}] [K_{NN}]^{-1} [K_{NI}]$$

which is the same as Eq. (A-4).

Thus, Eq. (A-2) is used to evaluate constraint modes, and Eq. (A-4) to evaluate its stiffness matrix $[K_{CC}]$.

Appendix B

Dynamic Matrix Formation

The standard modal analysis technique is repeated for completeness. The derivation deviates from the standard approach in that a special property of the coupled modal mass matrix is utilized to minimize the processing time in inversion and decomposition.

The frequencies and mode shapes of a conservative (undamped) and homogeneous (unforced) system can be determined by

$$[M] \{\ddot{h}(t)\} + [K] \{h(t)\} = \{0\} \quad (B-1)$$

where $[M]$ is the coupled modal mass matrix

$[K]$ is the coupled modal stiffness matrix

$\{h(t)\}$ is the coupled modal coordinate vector.

The time dependence in Eq. (B-1) can be removed by the transformation

$\{h(t)\} = \{p\} e^{i\omega t}$ because its solutions are harmonic in time. For a non-trivial solution, Eq. (B-1) becomes

$$\omega^2 [M] \{p\} = [K] \{p\} \quad (B-2)$$

or,

$$\omega^2 \{p\} = [M]^{-1} [K] \{p\} \quad (B-2a)$$

where $\{p\}$ is a coupled modal mode and ω^2 is a coupled frequency.

The Householder routine cannot be used directly on Eq. (B-2a) because $[M]^{-1} [K]$ is not symmetric in general.

The first operation is to decompose $[M]^*$ into a triple matrix product,

$$[M] = [U]^T [C] [U] \quad (B-3)$$

* The coupled modal mass matrix should be real, symmetric, and positive definite. The coupled modal stiffness matrix should be real and symmetric. Appendix C presents the decomposition of $[M]$ by the partitioning method.

where $[U]$ is an upper triangular matrix with unit values on the diagonal and $[C]$ is a diagonal matrix.

$$\text{Let } [C] = [G] [G] \quad (B-4)$$

It should be noted that each element g_{ii} in $[G]$ is equal to the square root of the corresponding element c_{ii} in $[C]$.

Using Eqs. (B-3) and (B-4), Eq. (B-2) takes the form

$$\omega^2 [U]^T [G] [G] [U] \{p\} = [K] \{p\} \quad (B-5)$$

Let

$$\left. \begin{aligned} [GU]^T &= [U]^T [G] \\ &\quad \text{(a lower triangular matrix)} \\ [GU] &= [G] [U] \\ &\quad \text{(an upper triangular matrix)} \end{aligned} \right\} \quad (B-6)$$

With Eq. (B-6), Eq. (B-5) can be simplified to

$$\omega^2 [GU]^T [GU] \{p\} = [K] \{p\} \quad (B-7)$$

$$\text{Let } \{p\} = [GU]^{-1} \{\psi\} \quad (B-8)$$

In view of the above equation, Eq. (B-7) becomes

$$\omega^2 \{\psi\} = [D] \{\psi\} \quad (B-9)$$

$$\begin{aligned} \text{where } [D] &= ([GU]^T)^{-1} [K] [GU]^{-1} \\ &= ([U]^T [G] [G] [U])^{-1} [K] [U]^{-1} [G]^{-1} \\ &= [G]^{-1} ([U]^{-1})^T [K] [U]^{-1} [G]^{-1} \end{aligned}$$

(B-9a)

$[D]$ is referred to as the dynamic matrix. Because $[K]$ is symmetric, $[D]$ is symmetric.

The coupled frequency ω^2 and the vector $\{\psi\}$ can now be calculated by Householder's method.

It should be emphasized that all relevant matrices and vectors are in partitioned forms. The coupled modal mass matrix can be partitioned as

$$[M] = \begin{bmatrix} I & M_{12} \\ M_{12}^T & M_{22} \end{bmatrix} \quad (B-10)$$

After decomposition, it becomes

$$[M] = [U]^T [G] [G] [U] \quad (B-11)$$

where

$$[U] = \begin{bmatrix} I & M_{12} \\ 0 & U_{22}^* \end{bmatrix}$$

and

$$[G] = \begin{bmatrix} I & 0 \\ 0 & G_{22} \end{bmatrix}$$

The coupled modal mode $\{p\}$ can be evaluated with Eq. (B-8),

$$\begin{aligned} \{p\} &= [GU]^{-1} \{\psi\} \\ &= [U]^{-1} [G]^{-1} \{\psi\} \\ &= \begin{bmatrix} I & -M_{12} U_{22}^{-1} \\ 0 & U_{22}^{-1} \end{bmatrix} \begin{bmatrix} I & 0 \\ 0 & G_{22}^{-1} \end{bmatrix} \{\psi\} \\ &= \begin{bmatrix} I & -M_{12} U_{22}^{-1} G_{22}^{-1} \\ 0 & U_{22}^{-1} G_{22}^{-1} \end{bmatrix} \{\psi\} \\ &= \begin{bmatrix} I & \beta \\ 0 & \alpha \end{bmatrix} \{\psi\} \end{aligned} \quad (B-12)$$

$$\text{where } \alpha = U_{22}^{-1} G_{22}^{-1}$$

$$\beta = -M_{12} U_{22}^{-1} G_{22}^{-1}$$

The coupled modal stiffness matrix can likewise be partitioned in accordance with Eq. (B-10),

$$[K] = \begin{bmatrix} K_{11} & 0 \\ 0 & K_{22} \end{bmatrix} \quad (B-13)$$

Using $[GU]^{-1}$ as defined in Eq. (B-12), the dynamic matrix becomes

$$\begin{aligned} [D] &= ([GU]^T)^{-1} [K] [GU]^{-1} \\ &= \begin{bmatrix} I & 0 \\ \beta^T & \alpha^T \end{bmatrix} \begin{bmatrix} K_{11} & 0 \\ 0 & K_{22} \end{bmatrix} \begin{bmatrix} I & \beta \\ 0 & \alpha \end{bmatrix} \\ &= \begin{bmatrix} K_{11} & K_{11} \beta \\ \beta^T K_{11} & \beta^T K_{11} \beta + \alpha^T K_{22} \alpha \end{bmatrix} \end{aligned} \quad (B-14)$$

The above equation is used to construct the dynamic matrix.

* U_{22} is the only partition that must be inverted. An inversion subroutine designed specifically for an upper triangular matrix is used to compute U_{22}^{-1} .

Appendix C

Decomposition by Partitioning

This appendix presents a method to decompose a matrix with a unit submatrix.

The coupled modal mass matrix [M] can be decomposed into an upper triangular matrix with ones on the diagonal [U] and a diagonal matrix [C] such that,

$$[M] = [U]^T [C] [U] \quad (C-1)$$

The matrix [M] must be real, symmetric, and positive definite. It can be partitioned as,

$$[M] = \begin{bmatrix} I & A \\ A^T & B \end{bmatrix} \quad (C-2)$$

where

$$[A]_{m \times n} = \begin{bmatrix} a_{11} & a_{12} & \dots & a_{1n} \\ a_{21} & a_{22} & \dots & a_{2n} \\ \vdots & \vdots & \ddots & \vdots \\ a_{m1} & a_{m2} & \dots & a_{mn} \end{bmatrix}$$

and

$$[B]_{n \times n} = \begin{bmatrix} b_{11} & b_{12} & \dots & b_{1n} \\ b_{21} & b_{22} & \dots & b_{2n} \\ \vdots & \vdots & \ddots & \vdots \\ b_{n1} & b_{n2} & \dots & b_{nn} \end{bmatrix}$$

The upper triangular matrix [U] can likewise be partitioned in accordance with Eq. (C-2),

$$[U] = \begin{bmatrix} I & A \\ 0 & V \end{bmatrix} \quad (C-3)$$

where

$$[V]_{n \times n} = \begin{bmatrix} 1 & v_{12} & v_{13} & \dots & v_{1n} \\ 0 & 1 & v_{23} & \dots & v_{2n} \\ 0 & 0 & 1 & \dots & v_{3n} \\ \vdots & \vdots & \vdots & \ddots & \vdots \\ 0 & 0 & 0 & \dots & 1 \end{bmatrix}$$

Similarly, the partitioned diagonal matrix becomes,

$$[C] = \begin{bmatrix} I & 0 \\ 0 & D \end{bmatrix} \quad (C-4)$$

where

$$[D]_{n \times n} = \begin{bmatrix} d_1 & & & & \\ & d_2 & & & \\ & & d_3 & & \\ & & & \ddots & \\ & & & & d_n \end{bmatrix}$$

By performing the matrix products indicated by Eq. (C-1), the following algorithms can be derived:

$$d_1 = \frac{b_{11} - \sum_{k=1}^m a_{k1}^2}{v_{1j} = \left(b_{1j} - \sum_{k=1}^m a_{k1} a_{kj} \right) / d_1} \quad (j=2, n)$$

$$d_i = \frac{b_{ii} - \sum_{k=1}^m a_{ki}^2 - \sum_{k=1}^{i-1} v_{ki}^2 d_k}{(i=2, n)}$$

$$v_{ij} = \left(b_{ij} - \sum_{k=1}^m a_{ki} a_{kj} - \sum_{k=1}^{i-1} v_{ki} v_{kj} d_k \right) / d_i \quad (j>i)$$

The above four algorithms are used in the coding of the decomposition subroutine. It is worth mentioning that all underlined terms can be coded by one Fortran statement.

REFERENCES

1. Walter C. Hurty, "Dynamic Analysis of Structural Systems by Component Mode Synthesis", JPL Tech Rpt 32-530, January 15, 1964.
2. Roy R. Craig and Mervyn C. C. Bampton, "Coupling of Substructures for Dynamic Analyses", AIAA Journal, Vol. 6, No. 7, July 1968, pgs. 1313-1319.
3. W. A. Benfield, C. S. Bodley, and G. Morosow, "Modal Synthesis Methods", Presented at the Space Shuttle Dynamics and Aeroelasticity Working Group Symposium on Substructuring, Marshall Space Flight Center, Alabama, August, 1972.

Discussion

Mr. Bejmuk (Rockwell Space Division): Were you surprised that the accuracy in the high frequency range for the coupled mode was so good? Didn't you expect to have difficulty in the frequency when you looked at the coupled modes which were beyond the frequency of truncation of the component modes?

Mr. Szu: I was not surprised, because as you recall the fundamental theory means that the motion of any point inside a structure is superposition; one is the motion with respect to the interface, another is the motion due to the interface. The motion with respect to the interface is already properly defined by the truncated normal modes and the motion due to the interface is taken care of by the computer itself therefore it is not magic. Good guy in good guy out so that is why if I input 10 good modes I would expect 10 good modes to come out. If I don't come out that way I would really be disappointed.

Mr. Bejmuk: The thing that I find surprising is that the modal information that you have truncated out of the components, by truncating the modes, didn't affect the final results. Since you lose some of the modal properties at the higher frequencies for the components I would expect that to be reflected in the higher frequency for coupled modes.

Mr. Szu: It could be above 600 or 800 Hz. I agree with you, but not in this domain, you don't see that yet. Up to a certain higher level truncation definitely brings damage. You know the best method of modal coupling, use all of the modes, if the results show any digit to be wrong then that method is junk. So without truncation we get a perfect answer and with truncation if somebody told me he got a perfect answer I wouldn't believe it. Truncation brings some errors.

AN INTRODUCTION TO THE APPLICATION OF MODAL ANALYSIS SURVEYS IN THE TEST LABORATORY

Henry Caruso
Westinghouse Electric Corporation
Product Qualification Laboratory
Baltimore, Maryland

This paper provides basic guidelines for performing effective modal analyses in the test laboratory. Considerations for appropriate accelerometer placement and significant recording equipment characteristics are detailed. The unique flexibility of modal analysis test fixturing is discussed along with specific test practices that should be employed to ensure the acquisition of uncontaminated modal information. Finally, the use of animated displays to interpret modal data is presented with special attention given to display utility and limitations.

INTRODUCTION

Until recently, detailed modal analyses of complex structures required sophisticated mathematical skills and extensive processing time on limited-access computers. But now, with the widespread introduction of commercially-affordable, high-speed digital equipment, test engineers and technicians with minimal background in mathematics can perform modal surveys of a complexity unattainable a few years ago. However, great care must be taken to ensure that the data used is of high quality and that subsequent analyses do not misrepresent this data. This paper, therefore, provides the basic guidelines for performing effective modal analyses in the test laboratory.

AREAS OF CONCERN

Anyone intending to perform a modal analysis must first be thoroughly familiar with the anatomy of the hardware under consideration and the way in which it is mounted to or restrained by other hardware. A knowledge of the modes and locations of driving inputs will also be of value.

The most common areas of concern for modal surveys include:

- Primary structural elements
- Interfaces between structural or component elements
- Components critical to performance
- Isolated structures

- Structures and components where relative motion (or its lack) is important

ACCELEROMETER LOCATIONS

The selection of accelerometer locations is critical to the validity of the data obtained for analysis. The following criteria should be used:

- Use a sufficient number of locations to adequately define the test item structure and surfaces of interest.
- Establish accelerometer spacings that will allow higher order modes to be identified.
- Instrument both sides of critical structural and component interfaces.
- Be sure that all accelerometers are mounted to surfaces that are representative of the structures under consideration. (As an extreme example, the center of a non-loadbearing skin panel would not yield representative information about the modal behavior of the primary structure to which the skin was attached.)
- Instrumentation of each location must be oriented to identify behavior in the axes of interest. Generally, triaxial accelerometer installations are desirable.

- The mass loading effect of the accelerometers on the structures under study must be considered. Mass loading effects can cause significant frequency shifts in the observed resonance of low mass or high compliance components.

RECORDING EQUIPMENT

The manner in which the accelerometer output signals are recorded can influence the validity of subsequent analyses. Therefore, if magnetic tape is being used as the recording medium, it is important to know if the time displacement error between the recording heads could contaminate phase information.

The extent of phase distortion can be examined by recording a test signal simultaneously on both heads and then determining the time displacement error of the recorded signals with respect to one another. If corrective adjustment is impractical, a decision will have to be made as to whether the equipment on hand will provide sufficiently low phase distortion over a wide enough bandwidth to be of use in a given application.

As a general rule, record both input (reference) and response signals on the same tape head if modal analyses are to consider structural behavior at high frequencies (i. e., greater than 500 Hz). If a large number of accelerometer signals are involved, record the input signal simultaneously on each head.

INPUT/CONTROL ACCELEROMETERS

In the following discussion, the input accelerometer is that accelerometer against whose signal all of the response signals will be compared.

- The input and vibration control accelerometers need not be one and the same nor do they have to be at the same location.
- Mount the input accelerometer on the structure that supplies the forcing function to the structure under consideration (i. e., exciter head input to fixture, fixture input to test items, structure input to component, etc.).
- When the control signal is based upon the averaged signal of several accelerometer responses, it may be desirable to use a separate input

accelerometer, and not one of the control accelerometers, to supply the input signal.

- A signal that is the average of signals from more than one accelerometer CANNOT be used as the input since the phase information will have been distorted by the averaging process.

TEST SETUP

- Mount the structure under consideration by means of its normal mounting provisions. Any other significant restraint or damping that would normally be in effect should also be provided. Examples of these additional boundary conditions are: large diameter hydraulic lines attached to the free end of a cantilevered structure or the coupling to another unit or structure not under analysis.
- It is usually best to excite a structure in a manner similar to that in which it would be driven in service. If this is not practical, the input vibration may be administered at any REPRESENTATIVE point on the primary structure and still yield a valid analysis.
- Since vibration levels for modal analysis can be lower than full test levels, the fixture used to transmit energy from the exciter to the structure can be relatively light and unsophisticated. The presence of off-axis vibration is generally not detrimental and can be of benefit in exciting off-axis modes with the same test setup.

Because input levels may be reduced, it is also practical to use exciters with lower force-pound ratings than those required for testing at full levels. In many instances, this reduction can be quite significant and will allow the use of small, lightweight thrusters.

- Attachment of the driving structure to the test structure can be made in several ways. Among these are bolts or screws, dental cement, contact adhesive, and metal bands. The frequency bandwidth of the analysis and the nature of the mounting surfaces will influence the choice of attachment method.

- All hardware should be appropriately torqued and there must be no loose parts that could rattle against the structure and add noise to the response signals.

TEST DESCRIPTION

Whether the accelerometer signals are recorded on magnetic tape or input directly onto a computer disc, it is imperative to keep accurate records of what data is recorded where. Mislabelled data will result in incorrect analyses and erroneous conclusions. When in doubt, take the data again!

- Vibration time duration is generally at the discretion of the test engineer and may be selected to expedite subsequent data analysis. However, in some instances the sensitivity of the hardware under test may determine the upper limit for vibration time.
- In most instances, a flat random vibration input will be satisfactory. However, any desired input spectrum can be used.
- Before recording any data for analysis, vibrate the structure and listen for noises that could be caused by loose parts or hardware. Correct these conditions to the extent practical to keep accelerometer signal-to-noise ratios high.
- Do not record modal analysis data while other significant noise sources are present (such as other vibration tests, construction noise, etc.). Structural or acoustic coupling with such extraneous sources will result in contaminated modal data. Coherence checks can be used to verify the quality of the data taken.
- Be sure that no one touches the structure to "see what the vibration feels like" while data is being recorded. Such external damping, even though seemingly insignificant, can drastically alter the mode shapes from their true nature and lead to erroneous conclusions.

MODAL DISPLAYS

Animated modal displays are valuable analysis tools, but must be carefully thought out and constructed. A poorly constructed display will be confusing at best. Furthermore, it can lead to totally inaccurate conclusions, for

while many persons are confused by numbers, everyone becomes an expert when presented with a picture. Therefore, when taken out of context, a modal visualization can be extremely misleading. The most important step in the display operation is the reduction of a real, often complex, physical structure into a simple, readily understood outline drawing. Considerations for performing this visualization are presented below.

- Only instrumented structural elements can be represented in an animated display. Therefore, think ahead to the final display when determining accelerometer locations for a modal survey.
- Since straight-line segments are used to connect display points, space accelerometers closely enough to detail a structure's behavior. Do not try to interpolate responses between display points.
- Simplify structural characterizations as much as possible for ease of interpretation. This can often be accomplished by not depicting a structure's thickness.
- It is not necessary to maintain the same proportions between display points as those found between elements of the actual structure. Size and spatial relationships should remain recognizable, but many times exaggerating the proportions of the display outline can make the display easier to interpret.

DISPLAY UTILITY

The value of a particular display will depend on the reason for which the modal survey is run. The most frequently encountered situations are outlined below.

HARDWARE DESIGN ANALYSIS AND FIXTURE SURVEYS. Basic structural behavior or multiple-structure interactions can be analyzed. Modal displays supplemented by numerical data can provide a useful approximation and understanding of behavior that can be expected under subsequent field or test conditions. Design assumptions can be verified and potentially detrimental behavior can be identified and treated.

FAILURE ANALYSIS. Mode shape displays can provide valuable clues to the nature of abnormal or unexpected behavior. (In this respect, phase relationships between structural

elements can be particularly helpful in identifying failure mechanisms.) Conclusions can then be verified by analysis, redesign or modification, and retest.

TEST SETUP ANALYSIS. Vibration test fixture modal behavior can be analyzed to determine the proper placement of control accelerometers and averaging requirements. The display can also indicate loose mounting hardware or isolation pads and misaligned horizontal slip tables.

ANALYSIS OF FIELD DATA. Measurements can be made of structural behavior under field service conditions to verify design predictions, investigate performance hypotheses, or develop test and design criteria. However, due to instrumentation limitations, the data obtained from field measurements may not be of the same high quality as that normally generated under laboratory conditions. Therefore, the display must be viewed with the data acquisition limitations in mind.

DISPLAY LIMITATIONS

There is information that an animated display will not provide and conclusions that the display alone will not support. These limitations must be recognized before the meaning of any display can be completely assessed. It is especially important to explain these limitations to those unfamiliar with modal analysis but who nevertheless will be responsible for making decisions based on the analysis results.

- Accurate numerical values for modal properties cannot be determined from the display. The display depicts the relative magnitudes of acceleration at display points. Even though a rough visual approximation can be made of response acceleration related to input acceleration, numerical data will be required for detailed analysis.
- Animated displays reflect the skill and judgement of the test engineer. Significant modes may be inadvertently deleted from the mode list or structural behavior altered by incorrect measurement techniques. Therefore, test methods and measurements should be carefully double-checked when an animated display yields unexpected significant new information.

- The animated display does not depict a complete and continuing time history of events. Instead, an artificial periodicity of motion is imposed for ease of visualization. In other words, the display will be a repetition of the same "instantaneous" time period.
- The spatial relationships between structural elements may be exaggerated for visualization purposes and therefore may present a potentially misleading picture of actual conditions. For example, if two displayed structures intersect or touch each other, it does not necessarily mean that there is physical contact between the actual test structures. As mentioned above, actual displacements, and therefore potentially damaging situations, can only be verified with accurate numerical data.